



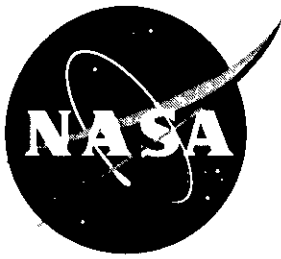
Aluminum-Lithium Alloys for Aerospace Applications Workshop

Edited by
B.N. Bhat, T.T. Bales, and E.J. Vesely, Jr.

NOTICE LIMITED DISTRIBUTION

Because of its significant technological potential, this information, which has been developed under a U.S. Government program, is being given a limited distribution whereby advance access is provided for use by domestic interests. This legend shall be marked on any reproduction of this information in whole or in part. Date for general release December 1996.

Proceedings of a workshop held at
NASA George C. Marshall Space Flight Center
Marshall Space Flight Center, Alabama
May 17-19, 1994



Aluminum-Lithium Alloys for Aerospace Applications Workshop

Edited by
B.N. Bhat
Marshall Space Flight Center • MSFC, Alabama

T.T. Bales
Langley Research Center • Hampton, Virginia

E.J. Vesely, Jr.
IIT Research Institute • Huntsville, Alabama

Proceedings of a workshop held at
NASA George C. Marshall Space Flight Center
Marshall Space Flight Center, Alabama
May 17-19, 1994

National Aeronautics and Space Administration
Marshall Space Flight Center • MSFC, Alabama 35812

December 1994

PREFACE

B.N. Bhat

NASA - George C. Marshall Space Flight Center

Aluminum-Lithium (Al-Li) alloys are the new generation of lightweight, high modulus alloys some of which also have high strength and high fracture toughness. These alloys offer high strength-to-weight ratios which makes them attractive for aerospace applications that require high strength but lightweight materials. For example, in the Space Shuttle External Tank, which is currently made from 2219 (Al-Cu) alloy, it is proposed to use 2195 (Al-Li-Cu) alloy that is 5% lighter and 30% to 40% stronger than 2219. This substitution is expected to result in a weight reduction of nearly 8000 lbs. (3600 kg) and will help to increase the Shuttle payload by nearly as much. Similar applications are being studied in other areas such as Single Stage to Orbit vehicle which also depends for its success on the use of lightweight, high strength materials.

The Workshop on Al-Li Alloys for Aerospace Applications was held as a part of the sixth biennial conference on Advanced Earth-to-Orbit (ETO) Propulsion Technology. The purpose of the workshop was to disseminate to the propulsion community results emerging from government laboratories, industry and universities actively engaged in research, development and testing of Al-Li alloys. The workshop was particularly timely in light of the fact it was being organized at the time when Martin Marietta Manned Space Systems got the go ahead to develop the Al-Li Super Lightweight External Tank for the Space Shuttle.

The Al-Li workshop was sponsored by the office of Advanced Concepts and Technology at NASA Headquarters. A steering committee consisting of members from the government, industry and universities was formed to organize the workshop. In addition, a number of people have contributed to the successful organization of this workshop. These include organizers of the ETO Conference who made the arrangements - R. Richmond and F. Porter of MSFC, and S. Wu and P. Corder of University of Alabama in Huntsville. I would like to thank R.J. Schwinghamer for the opening remarks, and the authors, the presenters, and the participants for making the workshop a success. I would also like to acknowledge the help of NASA-MSFC Technical Publications Department in publishing the workshop proceedings.

TABLE OF CONTENTS

Opening Remarks, R. J. Schwinghammer, NASA/MSFC.....	1
Technical Summary, E. A. Starke, Jr., University of Virginia and B. N. Bhat, NASA/MSFC.....	3
Aluminum-Lithium Alloys, E. A. Starke, Jr., University of Virginia, and C. P. Blankenship, Jr., General Electric Corporate Research and Development.....	6
Al-Li Alloy Development at Reynolds Metals Company for Aerospace Applications, A. Cho, R. E. Greene, M. H. Skillingberg and P. S. Fielding, Reynolds Metal Co.	17
On The Yield Stress Anisotropy of Al-Li Alloys, A. K. Vasudevan, Office of Naval Research, M. A. Przystupa, University of California, Los Angeles	26
Air Force Program for Developing Isotropic Wrought Al-Li Alloys, J. T. Morgan, K. V. Jata, Air Force Wright Laboratory, V. K. Jain, and A. K. Hopkins, University of Dayton.....	43
High Strength Al-Cu-Li Alloys for Launch Systems, J. R. Pickens, Martin Marietta Laboratories, W. T. Tack, Ashurst Corp., F. W. Gayle, National Institute for Standards and Technology, and J. Maisano, Martin Marietta Laboratories.....	57
Ultra-Low Density, High Stiffness Al-Li-X Alloy for Aerospace Structural Applications, D. L. Yaney, Lockheed Missiles & Space Company, Inc.	73
High Fracture Toughness in Al-Li Alloys - The Result of Vacuum Refining to Effect Alkali Metal Impurity Removal, J. L. Mihelich, Commonwealth Aluminum Technologies, C. G. Bennett, Comalco Aluminum Limited, E. D. Sweet and I. Musulin, Comalco Research Centre.....	84
Characterization of Lithium Distribution in Aluminum-Lithium Materials, K. K. Soni, University of Chicago, D. B. Williams, Lehigh University, J. M. Chabala, R. Levi- Setti, University of Chicago, and D. E. Newbury, National Institute of Standards and Technology	95
Stress-Assisted δ' Precipitation on Dislocations in an Al-Li Alloy, Z. M. Wang, and G. J. Shiflet, University of Virginia	105
Aluminum-Lithium Alloy 2195 Reversion Aging Study, I. K. Hall and D. B. Sisk, Martin Marietta Astronautics	114

Critical Electrochemical Potentials Relating to the Rapid Environmentally Assisted Cracking of Advanced Aluminum Alloys, F. D. Wall and G. E. Stoner, University of Virginia.....	122
Environmentally Assisted Cracking and Localized Corrosion Susceptibility of Aluminum Alloys 2195 and 2219, T. J. Langan, P. E. McCubbin, and J. R. Pickens, Martin Marietta Laboratories	133
Stress Corrosion Cracking and Microstructural Evaluations of Aluminum Lithium Alloy 2195-RT 70 Variable Polarity Plasma ARC (VPPA) Weldments, R. M. Diwan, Southern University of Baton Rouge, P. D. Torres, and T. Malone, NASA/MSFC	144
Determining the Crippling Strength of Aluminum Lithium Skin/Stringer Structures, R. Di Tolla, General Dynamics	156
Testing of Aluminum Lithium (AL-Li) Alloy 2095-T8, H. Taketani, McDonnell Douglas Aerospace	167
Microstructure-Cryogenic Fracture Correlations in Weldalite™ Weldments, R. Crooks, Naval Post Graduate School, J. S. Sedlak, U.S. Coast Guard, A. Szabo, Martin Marietta Manned Space Systems and M. R. Mitchell, Rockwell International Science Center	174
Mechanical Testing of 0.5-Inch Welded Aluminum-Lithium Alloy, R. Bond, IIT Research Institute, T. W. Malone, NASA/MSFC	183
Fracture Properties of 0.5-Inch Welded Aluminum-Lithium Alloy, P. McGill, NASA/MSFC, M. Watwood, and B. Malone, IIT Research Institute	194
Analysis of the 2195 Aluminum-Lithium Alloy Weld Microstructure and Fracture Behavior, P. C. Bastias, M. Diehm, G. T. Hahn, K.-Y. Kim, M. Kral, S. R. Shah, and J. E. Wittig, Vanderbilt University	205
Optimization of the VPPA Welding Process for 2195 Aluminum-Lithium Alloy Using Response Surface Techniques, M. O. Roberts, E. F. Scholz, L. W. Locchel, Martin Marietta Astronautics and K. Lawless, NASA/MSFC	216
Backside Shielding Device for Aluminum Lithium VPPA Welding, G. Bjorkman, Martin Marietta Astronautics	229
Laser Beam Welding of Aluminum-Lithium Structures, R. P. Martukanitz, K. G. Lysher, and P. R. Howell, The Pennsylvania State University	237
Analysis of Weld Hot Cracks in Al-Li Alloy 2195, R. G. Thompson, University of Alabama in Birmingham	246

Weld Cracking Susceptibility of Aluminum-Lithium Alloys, J. C. Lippold, W. Lin, Edison Welding Institute, W. A. Baeslack, III and D. Xia, The Ohio State University and A. Szabo, Martin Marietta Manned Space Systems	264
Microstructural Characterization of 0.5-Inch Welded Aluminum-Lithium Alloy, J. H. Sanders and B. Panda, IIT Research Institute	277
Microstructure Evolution in the Heat-Affected Zone of a Gas Tungsten-Arc Welded Al-2195, K. H. Hou, W. A. Baeslack, III, The Ohio State University, J. C. Lippold, Edison Welding Institute, and A. Szabo, Martin Marietta Manned Space Systems	288
Cracking during Welding of 2195 Aluminum-Lithium Alloy: Experimental Approaches towards Mechanism, J. E. Talia, Wichita State University, and A. C. Nunes, Jr., NASA/MSFC	300
Near Net Forging of Aluminum-Lithium Alloy 2195, J. E. Dyer, D. B. Sisk, and I. K. Hall, Martin Marietta Space Systems.....	309
X2096 Aluminum-Lithium Rolled Ring Forging Development, J. E. Dyer, I. K. Hall, Martin Marietta Astronautics Space Systems, A. Cho, Reynolds Metals Company, A. D. Dehbozorgi, Shultz Steel Company	322
Forming of Aluminum-Lithium & High Aspect Ratio Orthogrid Panels, B. F. Graham, NASA/MSFC.....	334
Net Shape Spinformed Aluminum-Lithium Bulkheads for Cryogenic Launch Vehicle Propellant Tanks, D. B. Sisk, Martin Marietta Astronautics and E. Sperlich, Zeppelin Technologie	341

ALUMINUM-LITHIUM WORKSHOP

(Week of May 16, 1994)

STEERING COMMITTEE

Biliyar N. Bhat (Co-chairman)
NASA-MSFC
EH23
Marshall Space Flight Center, AL 35812
(205) 544-2596 FAX: (205) 544-5877

Edward J. Vesely (Vice-chairman)
IIT Research Institute
Building 4618
Marshall Space Flight Center, AL 35812
(205) 544-8055 FAX: (205) 544-7473

Edgar A. Starke, Jr.
Dean, School of Engineering and Applied Science
University of Virginia
Charlottesville, VA 22907-3038
(804) 924-3593 FAX: (804) 924-3555

Alex Cho
Reynolds Metals Company
4th and Canal Street
Richmond, VA 23219
(804) 788-7474 FAX: (804) 788-7416

Carolyn K. Russell
NASA-MSFC
EH 25
Marshall Space Flight Center, AL 35812
(205) 544-4808 FAX: (205) 544-0212

Jeffrey H. Sanders
IIT Research Institute
Building 4618
Marshall Space Flight Center, AL 35812
(205) 544-8685 FAX: (205) 544-6625

Thomas T. Bales (Co-chairman)
NASA/LARC
MS1880A
Hampton, VA 23681-0001
(804) 864-3125 FAX: (804) 864-7893

Don A. Bolstad
Martin Marietta Manned Space Systems
P. O. Box 29304
New Orleans, LA 70189
(504) 257-4651 FAX: (504) 257-4430

Dave B. Sisk
General Dynamics - Space Systems Division
620 Discovery Drive, Suite 200
Huntsville, AL 35806
(205) 922-3347 FAX: (205) 922-3366

Jogender Singh
ARL, Penn State University
P. O. Box 30
State College, PA 16804
(814) 863-9898 FAX: (814) 863-1183

Tina W. Malone
NASA-MSFC
EH 24
Marshall Space Flight Center, AL 35812
(205) 544-2593 FAX: (205) 544-5877

OPENING REMARKS

R.J. Schwinghammer
Deputy Director for Space Transportation Systems,
NASA - George C. Marshall Space Flight Center

Good morning ladies and gentlemen. I wonder if you know how fortunate you are? You may not think you are fortunate but you really are. You're in the process here of creating something in the state of the art and rolling back the frontier, especially in the area of structures and aluminum metallurgy. How many times in one's career do you get to do that? Think back in your own careers, you older folks and you younger ones, how many times do you get to put something into the literature, to make this contribution, that will be a part of you somewhere in this 40 or 50 years hence; And so, in essence, you are establishing data for future generations' use as well as solving an immediate problem. So I think that sometimes we forget that we are making that kind of a contribution. That is very important. Much of what you do here today is probably going to go down in the annals of structures and metallurgy. You can look at it that way. I don't think that's an exaggeration to say that. And I think your work, if you think about it, even has the essence of global competitiveness in it. It is pretty important. If this really works its going to alter how we design aircraft and it certainly is going to influence how we design spacecraft and launch vehicles, so that gets you easily into the sphere of global competitiveness. And I just think it must be gratifying to participate in one of the most outstanding accomplishments in the aluminum industry in the last 30 years or so; its really a stride forward. I can remember 30 years ago when we were excited about 2219. We were going to put that in the Saturn 5 and also in the first stage of the S1C. And I guess you already know how NASA is depending on you. Did you know NASA is depending on you, did you realize that? We depend on you. Because if we are going to have a space station at all and in order to cooperate with the Russians we have to launch in a 51.6 degree inclined orbit. And to do that cuts very heavily into the payload on the Space Shuttle. It cuts so heavily into the payload that we can't get enough payload to fly the modules and so we need aluminum-lithium (Al-Li). We hope to gain in the vicinity of 8000 pounds by using both liquid oxygen and liquid hydrogen tanks made from Al-Li 2195. So you see what you are doing here has international implications. It's not an exaggeration to say that without the successful Al-Li program, we

are not going to have a space station. Of course, we may get preempted by some bad news from Congress and we hope that doesn't happen. We do need that Al-Li to have a space station, so those two things are in tandem and dependent on one another. I'd like to leave another thought with you to encourage you to persevere. I have always admired old T.R. (Teddy Roosevelt) and he gave a Harvard speech that I think captured it very nicely when he said, "Far better it is to dare mighty things to win glorious triumphs, even though checkered with failure than to take rank with those poor spirits, who neither enjoy much nor suffer much because they live in the great twilight that knows neither victory nor defeat". Keep that in mind. You have a chance for victory here. Well, you know you have a very impressive agenda to say the least, I looked through it and it is certainly a very impressive agenda. So I propose to get out of the way so you can get down to business. But I do want to thank you all for coming, and to thank you especially for your strong technical contributions to this activity. Good luck.

TECHNICAL SUMMARY

E.A. Starke, Jr.
University of Virginia, Charlottesville, VA

B.N. Bhat
NASA George C. Marshall Space Flight Center

The Al-Li workshop covered different aspects of Al-Li alloys, viz., physical and process metallurgy, mechanical and corrosion properties, welding and joining, and forming. The first session covered physical metallurgy, characterization, and new refining methods for Al-Li alloys. Starke presented an overview of the relationships between composition, grain and precipitate structure and mechanical properties of these promising materials. There are three generations of Al-Li alloys: 1) Those produced in the 50's and 60's, (e.g., 2020 and 1420) that had either ductility and fracture toughness problems (2020) or were of relatively low strength (e.g., 1420); 2) those produced in the 80's, (e.g., 2090 and 8090) that had attractive high modulus and low density but anisotropic mechanical properties; and 3) the more recent high-strength Weldalite-type alloys, e.g., 2195. Al-Li alloys as a group have attractive fatigue properties, are amenable to superplastic forming, display moderate to good weldability, and can be chemically milled, bonded, anodized, alclad and painted. On the debit side, they often display considerable anisotropy, especially in the short transverse direction. They are more susceptible to surface oxidation and are prone to warping during quenching. Commercial applications of Al-Li alloys have been slow in part because of high cost and processing difficulties.

A presentation by Mihelich and coworkers described vacuum refining of Al-Li alloys developed to achieve low alkali metal impurities (AMI's), i.e., < 1 ppm each of Na, K, Cs, and Rb. The object is to prevent the formation of alkali-rich grain boundary phases that can be liquid at room temperature. Besides the removal of AMI's, vacuum refining removes hydrogen from the melt allowing for residual hydrogen contents of < 0.2 ppm in the wrought products.

Their results showed that low AMI alloys had significant improvements in S-L fracture toughness when compared with those with AMI contents of 5 to 10 ppm that is obtained commercially by conventional melting and casting techniques. The most significant improvement was shown for the lowest strength alloy studied, i.e. 440 MPa (62 ksi). The improvement for the alloy aged to 492 MPa (71 ksi) ultimate tensile strength was very small and possibly within the scatter band for their fracture toughness tests. Although, this refining practice shows some potential, more work needs to be done, especially for the higher strength alloys, e.g., 2195, to determine if the improvement warrants the extra expense associated with the process.

Fundamental papers were presented by Yaney, Soni and coworkers on ultra low density alloys containing high percentages of Li. Yaney reported on successful rapid solidification (spray casting) of Al-5Li-0.2Zr alloy. Wang and Shiflet discussed stress-assisted precipitation of the delta prime (δ'), Al_3Li , phase in a binary Al-2.27Li alloy. Commercial Al-Li alloys exhibit strong yield strength anisotropy when compared to conventional 7XXX and 2XXX aerospace alloys and Vasudevan reviewed the current state of understanding of this behavior. He noted that the observed anisotropic behavior is only due in part to the crystallographic texture developed during processing. Anisotropy may also be associated with the platelet precipitates formed during aging. In addition, grain shape, aspect ratio, and the number of active slip systems can play a role in the anisotropy.

Morgan and coworkers described an Air Force sponsored R&D program that is directed towards correcting the anisotropic behavior of wrought Al-Li alloys containing greater than 2 wt. % Li, (i.e., low density alloys,) e.g., 2090 and 8090. Their research is focused on the development of processing procedures that control the crystallographic texture, grain structure (i.e., degree of recrystallization, grain size and shape), precipitate structure and deformation behavior. The development of processing maps and process modeling is an integral part of this program. If successful, it will make a major impact on the future use of the low density Al-Li alloys since their anisotropic behavior is a major roadblock to their use in advanced aerospace systems. Vasudevan is of the opinion that while this effort is certainly worth pursuing, different design approaches that take advantage of anisotropy, such as the ones used for anisotropic composite materials, should also be examined.

Most of the Workshop focused on the latest generation of Al-Li alloys, i.e., the high strength, Weldalite family of alloys, e.g., 2195 that has been selected for fabricating the super lightweight external tank of the Space Shuttle. This alloy offers a 30%-40% increase in strength, a 5% increase in elastic modulus and a 5% reduction in density compared with the conventional 2219 alloy that it will replace. Pickens, one of the original developers of this alloy system, gave an overview of the relationships among composition, microstructure, and properties. A number of researchers have shown that the Weldalite-type alloys have superior fatigue resistance when compared with conventional 2XXX and 7XXX alloys. Environmentally assisted cracking and localized corrosion of 2195 was described by Wall and Stoner and by Langan and coworkers. The results of their studies suggest that replacing 2219 with 2195 will not result in an increase in susceptibility to corrosion or SCC. Similar results were reported by Diwan and coworkers for variable polarity plasma arc (VPPA) welds of 2195 welded with 2319 filler wire.

A reversion aging study of 2195 was described by Hall and Sisk. Reversion aging is of interest to the aerospace industry for improving producibility and reducing cost for Al-Li structural components. Natural aging occurs at ambient temperature after solution heat treatment and quenching of most age hardenable aluminum alloys, including 2195. The associated strength increase has a detrimental effect on formability. Currently, when the alloys are solution heat treated and quenched (SHT&Q) at one site and shipped to another for forming operations, etc., they must be stored in dry ice to prevent natural aging and to ensure good formability. Hall illustrated that strength and ductility in the reverted conditions are not influenced by the time delay between SHT&Q and the reversion aging treatment. Furthermore, after forming or cold working, the reverted temper material responded normally to artificial aging, achieving T8 properties comparable to non-reversion aged material. Although this study is very promising, the authors pointed out that future work should investigate the effect of reversion on fracture properties and the effect of various reversion temperatures and times. Since the reversion aging treatments of their current study were conducted at relatively high temperatures (up to 390°F), precipitation of equilibrium phases at grain boundaries may occur resulting in an adverse effect on ductility and fracture properties.

Twelve papers were presented on various aspects of welding 2195, an enabling technology for the super lightweight tank. An alloy is considered to have good weldability if it can be joined by conventional welding processes with a minimum of defects such as hot cracks, porosity, lack of fusion, and softening in the heat affected zone (HAZ). Although welding of aluminum-lithium alloys presents technological challenges that exceed those of welding 2219, lower-lithium containing Weldalite alloys are reported to have good weldability without hot cracking. Most authors agreed that when the welds of Al-Cu-Li alloys are fractured the fracture path is intergranular and associated with continuous grain boundary phases. Crooks and coauthors illustrated that ductility increased with leaner alloys in the order 2094 to 2095 to 2195. This corresponds to a shift in the failure location from equiaxed zone (EZ) to HAZ to fusion zone (FZ). The amount of second phases appears much greater at EZ grain boundaries in 2094 than in 2195. It was suggested that the EZ be renamed as unmixed zone in light of the fact that it consists largely of remelted parent metal with very little mixing with the weld pool.

The alloy 2195 exhibits better cryogenic ductility and significantly greater strength than the conventional cryogenic tank alloy 2219. It also exhibits positive fracture toughness ratio (FTR) when going from room temperature to cryogenic temperatures. This is an important consideration in cryotank applications. The higher strength coupled with higher modulus and lower density can lead to significant weight savings. Presentations at the workshop illustrated that the alloy also has good corrosion resistance, excellent fatigue properties, can be near-net-shape formed and, with proper precautions, can be adequately welded. However, further research needs to be conducted to identify optimum processing conditions that will ensure that the required combination of strength and fracture properties is obtained in the final product.

Several papers were presented on the forming of Al-Li alloys. The forming processes included ring rolling, near net forging, spin forming and bump, roll and age forming of orthogrid panels. All the work to date indicates that Al-Li alloys can be successfully formed by these conventional means. The paper by DiTolla covered the crippling strength of 2090; it appears adequate for fabricating riveted structures. More development work is required, however, to perfect these processes. Researchers do not see any major problems in these areas.

It was pointed out that applications of Al-Li alloys have been slow considering the fact that they have been around for some time. One reason appears to be the fact that we still do not understand the Al-Li alloys very well. Al-Li alloys are complex quaternary or even higher order systems, e.g., Al-Cu-Li-Mg-Ag. They produce complex microstructures which

consist of a number of equilibrium and non-equilibrium phases. The kinetics of phase transformation is not well understood. Optical microscopy is not adequate to identify the phases; transmission electron microscopy and secondary ion mass spectrometry (SIMS) are required. Auger spectroscopic analysis may also be required to examine segregation at the grain boundaries. It is also important to understand how the various prior processing steps affect the microstructure and texture, and hence, the mechanical properties of the Al-Li alloys. Further research is required in the above areas to advance the state-of-the-art in Al-Li alloys.

Another important area of research is welding and joining. There is a consensus that Al-Li alloys are weldable, however, the weldability is not as good as that of 2219. They crack more readily than 2219 during weld repairs. It is not clear why these alloys are difficult to weld. The formation of equiaxed unmixed zone with continuous secondary phase at the grain boundary, appears to be unique to Al-Li alloys and explains part of the problem. Another contributing factor may be contamination of the weld metal by shielding gases, such as nitrogen, as suggested by Talia and Nunes. The use of improved backside shielding such as suggested by Bjorkman might help to minimize contamination. Control of weld parameters including weld wire chemistry might hold the key to improving weldability. Alternate welding techniques such as laser welding has been explored by Martukanitz and coworkers for partial penetration welds. The weld had excellent microstructure but had porosity. MSFC Materials and Processes Laboratory is actively pursuing improved welding technology for Al-Li alloys. Areas of activity include weld modeling and reduction of stresses during welding to minimize cracking.

ALUMINUM-LITHIUM ALLOYS

E.A. Starke, Jr.* and C.P. Blankenship, Jr.**

*Department of Materials Science and Engineering

University of Virginia

Charlottesville, Virginia 22903

**General Electric Corporate Research and Development

Schenectady, New York 12301

I. Introduction

The interest in aluminum-lithium alloys derives from the large effect that lithium additions have on the modulus of aluminum, a six percent increase for every weight percent added, and the density, a three percent decrease for every weight percent added [1]. These changes are for lithium additions up to three weight percent. Recently, a second generation of aluminum-lithium alloys has been developed that has yield strengths as high as 700 MPa with strains to fracture of ten percent [2]. There is currently a wide variety of aluminum-lithium alloys available, Table 1.

This paper will review the relationships between the microstructure and properties of these new materials and will rely heavily on our recent research. It is a modification of a paper we presented at the 40th Sagamore Army Materials Research Conference in September, 1993. The large volume of papers on aluminum-lithium alloys prevents a complete comprehensive review of the literature.

II. Alloy Composition, Grain and Precipitate Structure

Composition: There are essentially two classes of aluminum-lithium alloys: those that contain copper additions and those that do not, e.g., 1420. All, however, have a number of things in common due to concern over the low fracture properties that plagued the early lithium-containing alloys, e.g., 2020. The presence of tramp elements, e.g., sodium, potassium, calcium, hydrogen and sulphur, has been shown to adversely affect fracture toughness [1] and the use of high purity lithium metal, fluxing and other specialized casting processes are employed to insure low levels of tramp elements in commercial alloys. Current users of Al-Li-X alloys normally require sodium levels below 0.002 wt.%. In addition, iron and silicon, which form coarse constituent particles when present in age-hardenable aluminum alloys, are kept to a minimum. Typical maximum specifications for iron and silicon are 0.2 and 0.1 weight percent, respectively. Producers aim for even lower levels and customers have been requiring levels as low as 0.15% Fe and 0.08% Si. Higher levels of Si have been shown to increase susceptibility to stress corrosion cracking [3].

TABLE 1. Current Al-Li Alloys and Compositions
Element in Weight %

Alloy	Li	Cu	Mg	Zr	Ag	Mn
1420	1.8-2.2	-	4.9-5.5	0.12	-	-
2090	1.9-2.6	2.4-3.0	-	0.08-0.15	-	-
2091	1.7-2.3	1.8-2.5	1.1-1.9	0.04-0.16	-	-
X2094	0.8-1.5	4.4-5.2	0.25-0.6	0.04-0.18	0.25-0.6	-
X2095	1.0-1.6	3.9-4.6	0.25-0.6	0.04-0.18	0.25-0.6	-
8090	2.2-2.7	1.0-1.6	0.6-1.3	0.04-0.16	-	-
8091	2.4-2.8	1.8-2.2	0.5-1.2	0.08-0.16	-	-
X8192	2.3-2.9	0.4-0.7	0.9-1.4	0.08-0.15	-	-
RX218	1.50	2.8	-	0.12	-	0.30
C255	1.50	2.86	-	0.11	-	0.30

Concern about the fracture properties also led to the use of zirconium as the dispersoid-forming element to control the grain structure in the aluminum-lithium alloys. Staley [4] has shown that the small, coherent Al_3Zr (δ') dispersoid particles have less of an adverse effect on fracture toughness than the coarser, incoherent Al_6Mn , $\text{Al}_{20}\text{Mn}_3\text{Cu}_2$ and $\text{Al}_{12}\text{Mg}_2\text{Cr}$ dispersoids that are employed in many commercial age-hardenable aluminum alloys. The presence of Al_3Zr makes it easier to produce unrecrystallized structures when they are desired in certain product forms. However, some of the newer aluminum-lithium alloys contain Mn in addition to Zr [5]. The Mn dispersoids may help to homogenize slip and minimize some problems associated with strain localization effects, which will be discussed later, and also make it easier to produce a recrystallized product when that is required.

Grain Structure and Texture: As a result of zirconium additions, all wrought Al-Li-X alloys possess a pancake grain structure and an intense deformation texture, although some sheet products may be processed to produce a recrystallized grain structure. Almost all Al-Li-X alloys have anisotropic mechanical properties resulting from the intense crystallographic textures, strengthening precipitates that nucleate on particular planes of the matrix, and mechanical fibering. Since most products do not undergo any recrystallization from the casting operation through final heat treatment, grain boundaries usually contain constituent particles and impurities, making them weaker than other boundaries. These features, combined with grain

boundary precipitation and strain localization effects, result in lower than desired toughness, especially in the S-L orientation of plate. Research is currently underway [6] to alter these detrimental effects by processing and chemistry modification.

Matrix Precipitates: The precipitates that form in Al-Li-X alloys are schematically represented in Figure 1 [7]. The primary ones used to strengthen the matrix are Al_3Li (δ'), Al_2Cu (θ'), Al_2CuLi (T_1), and Al_2CuMg (S'). A uniform distribution of spherical, coherent δ' particles is found in microstructures of most commercial alloys containing greater than approximately 1.5wt.% Li. The δ' particles are the dominate strengthening precipitates in Al-Li-Mg alloys and add strength to 2090- and 8090-type alloys. They have an ordered Li_2 structure and are sheared with relative ease when diameters are less than 50nm, which is always the case in normal tempers. The question of shearing versus bypassing is an important one, because the presence of shearable precipitates can lead to an inhomogeneous strain distribution during plastic deformation [8,9]. As will be discussed later, this can have an effect on a wide variety of properties.

The 2XXX and 8XXX Al-Li alloys contain copper for added strength since only medium strengths (370-430 MPa yield strength) can be obtained in Al-Li-Mg alloys. When sufficient copper and magnesium are present, orthorhombic S' may precipitate as rods or needles aligned along the $\langle 100 \rangle$ directions in the matrix. The S' is partially coherent with the matrix and shows a strong tendency to nucleate

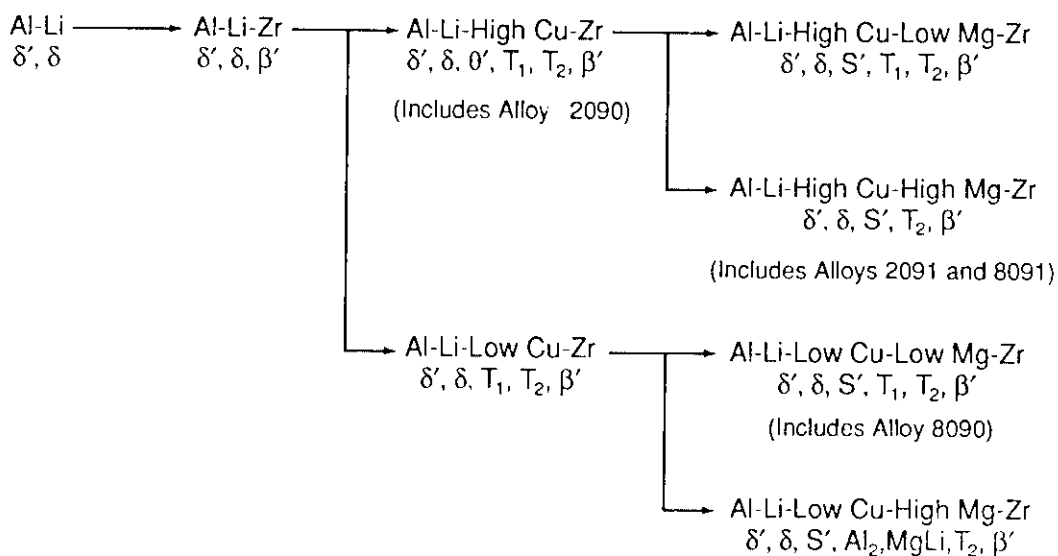


Figure 1. Schematic illustration of the precipitate phases that form in Al-Li-X alloys.

heterogeneously on matrix dislocations, low-angle boundaries and other structural inhomogeneities. The tetragonal Θ' precipitates as partially coherent plates on {100} planes of the aluminum matrix and also shows a strong tendency to nucleate on heterogeneities in the matrix. The critical diameter for the transition from shearing to looping for S' and Θ' range from 2-5nm. This number is scaled upward with the number of dislocations that pile-up at the matrix/particle interface [10]. The partially coherent hexagonal T_1 phase precipitates as platelets on {111} planes of the aluminum matrix. T_1 also has a tendency to nucleate on dislocations and low- and high-angle grain boundaries. The critical diameter for the transition from shearing to looping is 0.8nm which results in T_1 being a very potent strengthening precipitate [10].

A deformation step after quenching and prior to artificial aging, the T8 temper, is often used to accelerate aging, increase strength, and improve the strength/fracture toughness combination in commercial Al-Cu-Li-X alloys. The effectiveness of the T8 temper is related to the interfacial strains of the precipitates, being highly effective for precipitates having large interfacial strains e.g., S' , and Θ' , since the total strain present is minimized when the interfaces are associated with dislocations. The mechanism appears to be more complicated for T_1 . It seems that it is the creation of jogs and kinks during plastic deformation, rather than dislocations, by and in itself that provides conditions for increased nucleation of T_1 [11]. Consequently, plastic strains larger than normally used, e.g., for 2024, are needed to provide sufficient sites for rapid T_1 nucleation and growth in alloys such as 2090 [12]. The current practice is to stretch approximately 6% compared to the 2% used for 2024-T8.

Additions of minor alloying elements such as cadmium, indium, tin, silver and magnesium can significantly affect the nucleation of strengthening precipitates in Al-Cu-X alloys [13]. Although cadmium was used as a nucleating agent for Θ' in 2020, only 2095 currently uses nucleating agents, silver and magnesium, to aid in the precipitation of the strengthening phase, T_1 .

Grain Boundary Precipitates and Precipitate Free Zones: In addition to matrix precipitation during aging, heterogeneous precipitation of equilibrium phases occurs at grain boundaries. Depending on composition, the precipitates may be $AlLi$ (δ), Al_6CuLi_3 (T_2), Al_2Cu (Θ), Al_2CuMg (S), and a T_B phase of

unknown chemical composition. Although a stretch prior to aging has a significant effect on the aging kinetics, volume fraction and number density of matrix precipitates in Al-Cu-Li-X alloys, it has no effect on the size and volume fraction of grain boundary precipitates [14]. Nucleation and growth of equilibrium phases at grain boundaries deplete the adjacent region of solute resulting in a solute-depleted precipitate free zone (PFZ) adjacent to the grain boundaries. PFZ's may be minimized by lowering the aging temperature, which increases the solute supersaturation, and thus the driving force for homogeneous decomposition, and decreases diffusion rates, which decreases the nucleation and growth of the equilibrium precipitates.

III. Deformation and Fracture Behavior

Deformation in Al-Li-X alloys depends on the alloy composition and heat treatment and may be homogeneous or localized. Strain localization may result from the shearing of matrix precipitates or preferential deformation in softer PFZ's. When a precipitate is cut by a moving dislocation, the resistance that the precipitate offers to subsequent dislocation motion is reduced, resulting in a localization of slip. Duva et al. [15] have developed a model to quantify the slip intensity in deformed microstructures which is related to the number of dislocations expected in a slip band for particular volume fraction and particle size. The model takes into account the particular strengthening mechanism associated with the precipitate. The intense slip bands, which result from "slip plane softening" associated with shearable precipitates, may themselves be the regions of premature fracture, or they may impinge on grain boundaries and aid in intergranular fracture [16].

Jata and Starke [17] developed a model for transgranular fracture associated with shearable precipitates which was later modified by Roven [18]. The model relates the fracture toughness to slip band width, W_{SB} , and slip band spacing, S_{SB} . The slip band width decreases and the slip band spacing increases with increasing strain localization when particle shearing occurs, as predicted by Duva et al. [15]. The modified model is expressed by:

$$K_{IC} = (2S_{GB}W_{SB}\sigma_y E / M \tan \alpha S_{SB})^{1/2} \quad (1)$$

where K_{IC} is the plane strain fracture toughness for transgranular fracture, E is Young's modulus, α is the angle between the slip planes and the crack

plane, σ_y is the yield stress, S_{GB} is the spacing of the grain boundaries and M the Taylor crystallographic orientation factor. This equation applies to the case where strain localization occurs in the matrix and, therefore, for most underaged to peakaged Al-Li-X alloys.

Strain localization in the PFZ has a similar effect to that in the matrix and produces stress concentrations at grain boundary triple junctions. Grain boundary precipitates, which are the cause of the PFZ's, also have a major deleterious effect on fracture resistance since they are sites for microvoid nucleation [19]. Although a stretch prior to aging does not affect the kinetics of grain boundary precipitation and PFZ formation, it does accelerate matrix precipitation so that peak strength can be obtained in a shorter time than without a stretch. A stretch in combination with the lowest practical aging temperature, can produce the best strength/fracture toughness combination since grain boundary effects will be minimized. However, in peakaged and overaged conditions there is a high probability that deleterious grain boundary precipitates and associated PFZ's will be present. For these conditions, strain localization in the PFZ, microvoid nucleation at grain boundary precipitates, and intergranular fracture may occur and determine the fracture toughness of the material.

Hornbogen [20] used the critical strain to fracture concept of Hahn and Rosenfield [21] to develop a relationship between fracture toughness and strain localization in the PFZ similar to equation (1). For this case, crack initiation and propagation take place through the soft PFZ, and the fracture toughness is described by:

$$K_{ICi} = [CE\sigma_{ypfz}\epsilon_{pfz}(d_{pfz}/S_{GB})^{1/2}] \quad (2)$$

where d_{pfz} is the width of the PFZ and C is an empirical constant with the dimension of length.

Sugamata et al. [22] have examined the fracture toughness of an 8090 alloy as a function of age hardening. They also made quantitative measurements of microstructural, deformation, and fracture features for input into equations (1) and (2) to calculate fracture toughness as a function of age hardening. Equations (1) and (2) were weighted by the fraction of transgranular and intergranular fracture features determined on the fracture toughness samples by scanning electron microscopy, i.e., the calculated fracture toughness was determined by:

$$K_{IC} = F_t K_{ICi} + F_i K_{ICi} \quad (3)$$

where F_t and F_i are the fraction of transgranular and intergranular fracture, respectively. Figure 2 shows a comparison of predicted fracture toughness values with those measured experimentally. The fit is remarkably good, considering the possible sources of error.

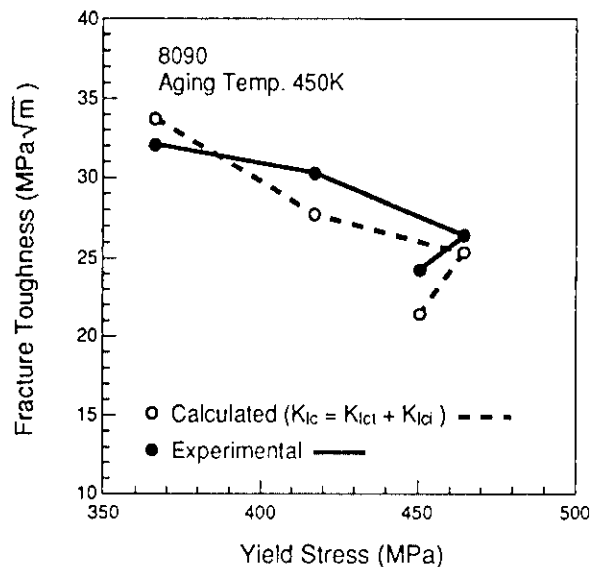


Figure 2. A comparison of predicted fracture toughness to those measured experimentally.

The problems associated with grain boundary precipitates and PFZ's may be minimized by a stretch and low temperature aging. The benefits of this approach were illustrated for Al-Li-X alloys by Ashton et al. [23] and Lewis et al. [3]. Blankenship and Starke [24] have recently shown that the fracture toughness of 2095 may be improved by 50%, with no deleterious effect on either the strength or fatigue resistance, by aging at 125°C instead of the conventional temperature of 165°C. The improvement was directly related to a reduced density of T_1 planes on subgrain boundaries and the related transition from intersubgranular fracture to transgranular dimpled rupture.

When low fracture toughness is associated with shearable precipitates, thermal treatments alone to improve this property are often impractical. Long time aging, i.e., overaging, may be accompanied by a transition from shearing to

looping of the strengthening precipitates and an improvement in the homogeneity of deformation. However, this is almost always accompanied by a significant penalty in strength and fracture toughness. Cassada et al. [9] showed that the addition of a non-shearable precipitate may homogenize deformation even when the major strengthening precipitate is shearable. They added germanium to a binary Al-Li alloy that normally exhibited coarse slip bands after deformation. Germanium rods 20nm in length effectively dispersed slip, and the fracture mode changed from low energy intergranular to high energy transgranular shear.

Gregson and Flower [25] studied the ability of T_1 plates and S' rods to homogenize slip. The authors concluded that T_1 failed to prevent strain localization. However, Blankenship et al. [10] have shown that the critical T_1 particle size for the transition from shearing to looping is 0.8nm, and that the thickness of T_1 in 2090 and 2095 is 2nm. As mentioned previously, the critical particle size scales with the number of dislocations that "pile-up" at the interface of the particle. If a shearable precipitate, e.g., δ' , and the spacing between the T_1 are large enough to accommodate a sufficient number of planar dislocations, T_1 may be sheared resulting in strain localization and planar deformation as normally observed in 2090-T8. On the other hand, when T_1 is the dominate strengthening phase, and little or no δ' is present, e.g., in 2095-T6 or 2095-T8, T_1 is not sheared and deformation is homogeneous.

Crooks and Starke [26] showed that deformation of Al-Cu-Li-X alloys can be homogeneous if a fine distribution of S' is present. Gregson and Flower [25] also concluded that the S' phase was an effective barrier to planar slip in microstructures where a uniform S' distribution was produced. The presence of S' does not guarantee homogeneous deformation, however, as illustrated by Blankenship et al. [10]. Analogous to the results described for T_1 , the shearability of S' depends on its size, spacing and the number of planar dislocations impinging on the particle interface.

Recent work by Lynch [27,28] has shown that short-term, high-temperature heat treatments followed by cold-water quenching increased toughness (as measured by double cantilever beam tests) by 180% with a 7% loss in strength. His explanation focused on solid-solution lithium atoms embrittling grain boundaries. He

speculated that a short, high-temperature exposure allowed grain boundary lithium atoms to diffuse rapidly to grain boundary precipitates. Since the treatment was short term, Lynch suspected matrix diffusion of lithium atoms was unable to replenish the depleted lithium solid solution on the boundary. Due to spatial resolution limitations and difficulties associated with detecting lithium atoms, secondary ion mass spectrometry and other techniques were unable to confirm or dispute the theory.

Blankenship and Starke [29] investigated double aging effects, similar to that conducted by Lynch, on deformation behavior and resulting fracture toughness in S-L and L-T orientations of 8090. Second step aging was performed in the 210-310°C range for 5-10 minutes. Dramatic increases in S-L toughness were observed while L-T toughness increased slightly. K_{IC} values, along with corresponding strengths, are listed in Table 2. Strained tensile bars were sectioned and examined by transmission electron microscopy to reveal the deformation mode of each heat treatment. The T8771 temper exhibited narrow, intense slip bands, while double aged samples exhibited homogeneous deformation. This behavior was attributed to a combination of δ' dissolution and growth of S' .

TABLE 2. AA8090 Strength and Toughness Values

Temper	Yield Strength (MPa)	K_{IC} (MPa \sqrt{m})
	S	S-L
T3	210	44*
T8771	360	13
210_5	340	16
210_10	350	20
210_15	345	22
230_5	340	22
230_10	340	27
250_5	330	24
300_5	260	45*
AF10		
AF15	300	31
AF25	275	34
100_145	385	14
	L	L-T
T8771	500	30
230_5	505	38

* K_{IC} values (insufficient sample thickness to maintain plane strain)

IV. Fatigue Crack Growth

Fatigue crack growth behavior may be divided into two categories: contributions by extrinsic crack tip shielding mechanisms and intrinsic crack growth resistance. Al-Li-Cu-X alloy microstructures may be altered to accommodate monotonic and cyclic strain either by intensely localized slip or by more homogeneous deformation. Important microstructural features affecting slip have been identified [1,8-10]; however, the relationships between intrinsic fatigue crack propagation rates, deformation, and cracking modes are not well understood. By virtue of their coarse planar deformation, 8090-T8771 and 2090-T8 are expected to exhibit extensive crack branching and deflection. This behavior should lead to higher degrees of closure than in 2095, which deforms homogeneously, and in conventional age-hardenable aluminum alloys that do not exhibit coarse planar slip.

Slavik et al. [30] recently investigated the influences of microstructure and deformation mode on inert environment intrinsic fatigue crack propagation for Al-Li-Cu-Mg alloys 2090, 8090, and 2095 compared to 2024. Their results are shown in Figure 3. The amount of shearable δ' precipitates and extent of localized planar slip deformation were reduced by composition (increased Cu/Li in 2095) and heat treatment (double aging of 8090). Intrinsic growth rates,

obtained at high constant K_{max} to minimize crack closure in vacuum and to eliminate any environmental effect, is alloy dependent; da/dN varies up to tenfold based on applied ΔK or $\Delta K/E$. When comparisons are based on a crack tip cyclic strain or opening displacement parameter ($\Delta K/(\sigma_{ys}E)^{1/2}$), growth rates are equivalent for all alloys except 2095-T8 which exhibits unique fatigue crack growth resistance. Tortuous fatigue crack profiles and large fracture surface facets occur for each Al-Li alloy independent of the precipitates present, particularly δ' , and the localized slip deformation structure. Reduced fatigue crack propagation rates for 2095 in vacuum can not be explained by either residual crack closure or slip reversibility arguments. The origin of the apparent slip band facets in a homogeneous slip alloy, such as 2095, is unclear. Further studies need to be conducted in order to understand crack tip damage accumulation and fracture surface facet crystallography for Al-Li alloys with varying slip localization.

V. Closure

In addition to those properties discussed above, there are certain other engineering properties of Al-Li-X alloys that are attractive in comparison to conventional baseline aluminum alloys. For example, most Al-Li-X alloys are amenable to superplastic forming [31], display moderate to good weldability [32], can be chemically milled, bonded, anodized, alclad, and

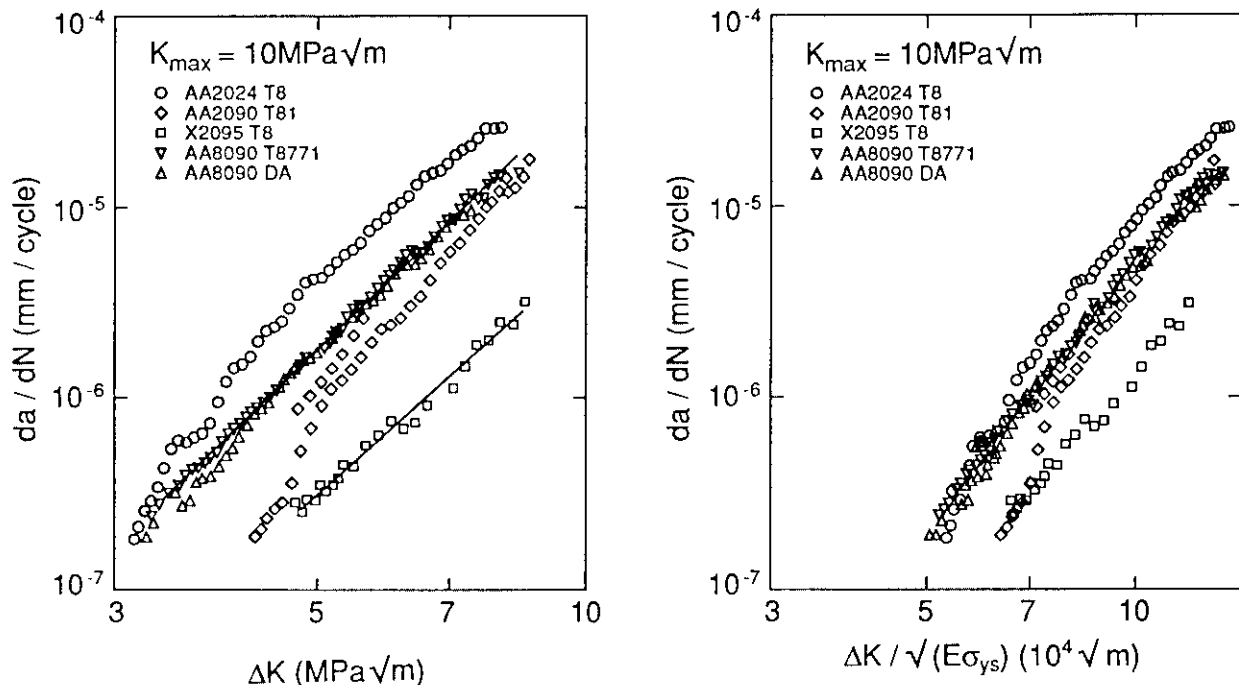


Figure 3. Intrinsic inert environment fatigue crack growth rates.

painted. On the debit side, as noted previously, Al-Li-X alloys often display considerable anisotropy in strength and ductility. They are somewhat more susceptible to surface oxidation at moderate temperatures and are prone to warping during quenching (mostly attributable to the relatively high quenching temperature). Diffusion of lithium can occur out to the surface during high temperature heat treatments which may lead to a lithium-depleted layer, and for sheet products a reduction in strength [33]. In addition, Al-Li-X alloys may suffer from low ductility and fracture toughness in the short transverse direction. These problems are due to a combination of grain structure, grain boundary precipitates, and segregation effects and may be minimized by improved processing. Most, if not all, problems associated with Al-Li-X alloys appear to be solvable by control of chemistry and intelligent processing methods. The advantages that the newer Al-Li-X alloys offer in density, modulus, and strength over conventional aluminum alloys should lead to an increase in their usage in aerospace systems.

Acknowledgements: The authors would like to thank the Office of Naval Research for providing funding under Contract No. N00014-91-J-1285, Dr. George R. Yoder, contract monitor.

References

1. Starke, E.A., Jr., Sanders, T.H., Jr., and Palmer, I.G., J. of Metals, **33**, p. 24, 1981.
2. Pickens, J.R., Heubaum, F.H., Langan, T.J., and Kramer, L.S., in Aluminum-Lithium V (T.H. Sanders, Jr. and E.A. Starke, Jr., eds.), MCE, Birmingham, England, p. 1397, 1989.
3. Lewis, R.E., Starke, E.A., Jr., Coons, W.C., Shiflet, G.J., Willner, E., Bjeletich, J.G., Mills, C.H., Harrington, R.M., and Petrakis, D.N., in Aluminum-Lithium IV, Journal de Physique, Colloque C3, p. 643, 1987.
4. Staley, J.T., ASTM STP 605, ASTM, Philadelphia, PA, p. 75, 1975.
5. Balmuth, E.S., Austin, K., Newman, J.M., Witters, J.J., and Chellman, D.J., "Low Density Al-Li Alloy Plate for Structural Applications," paper presented at Aeromat '93, Los Angeles, CA, 1993.
6. Hopkins, A.K., Isotropic Al-Li Wrought Products, WL-TR-93-4057, Materials Directorate, Wright Laboratory, Air Force Material Command, Wright-Patterson Air Force Base, OH 45433-7734.
7. Quist, W.E., and Narayanan, G.H., in Aluminum Alloys - Contemporary Research and Applications (A.K. Vasudevan and R.D. Doherty, eds.), Academic Press, Inc., San Diego, CA, p. 219, 1989.
8. Hornbogen, E., and Zum Gahr, K.H., Metallography, **8**, p. 181, 1975.
9. Cassada, W.A., Shiflet, G.J., and Starke, E.A., Jr., Acta Metall., **34**, p. 367, 1986.
10. Blankenship, C.P., Jr., Hornbogen, E., and Starke, E.A., Jr., "Predicting Slip Behavior in Alloys Containing Shearable and Strong Particles," Mater. Sci. Engr., **A169**, p. 33, 1993.
11. Cassada, W.A., Shiflet, G.J., and Starke, E.A., Jr., Metall. Trans. A, **22A**, p. 287, 1991.
12. Cassada, W.A., Shiflet, G.J., and Starke, E.A., Jr., Aluminum-Lithium IV, Journal de Physique, Colloque C3, 1987, p. 397; Metall. Trans. A, **22A**, p. 299, 1991.
13. Mukhopadhyay, A.K., Shiflet, G.J., and Starke, E.A., Jr., in Morris E. Fine Symposium (P.K. Liaw, J.R. Weertman, H.L. Marcus and J.S. Santer, eds.), TMS/AIME, Warrendale, PA, p. 283, 1990.
14. Ahrens, T., and Starke, E.A., Jr., in Aluminum-Lithium V (T.H. Sanders, Jr. and E.A. Starke, Jr., eds.), MCE Publications, Birmingham, England, p. 385, 1989.
15. Duva, J.M., Daeubler, M.A., Starke, E.A., Jr. and G. Lütjering, Acta Metall., **36**, p. 585, 1988.
16. Sanders, T.H., Jr., and Starke, E.A., Jr., Acta Metall., **30**, p. 927, 1982.
17. Jata, K.V., and Starke, E.A., Jr., Metall. Trans. A, **17A**, p. 1011, 1986.
18. Roven, H.J., Scripta Metall. Mater., **26**, p. 1383, 1992.
19. Vasudevan, A.K. and Doherty, R.D., Acta Metall., **35**, p. 1193, 1987.
20. E. Hornbogen, Z. Metallk., **66**, p. 511, 1975.
21. Hahn, G.T. and Rosenfield, A.R., ASTM STP 432, ASTM, Philadelphia, PA, p. 27, 1968.

22. Sugamata, M., Blankenship, C.P., Jr., and Starke, E.A., Jr., Mater. Sci. Engr., **A163**, p. 1, 1993.
23. Ashton, R.F., Thompson, D.S., Starke, E.A., Jr., and Lin, F.S., in Aluminum-Lithium III, (C. Baker, P.J. Gregson, S.J. Harris and C.J. Peel, eds.) The Institute of Metals, London, England, p. 66, 1986.
24. Blankenship, C.P., Jr., and Starke, E.A., Jr., Scripta Metall. et Mat., **26**, p. 1719, 1992.
25. Gregson, P.J., and Flower, H.M., Acta Metall., **33**, p. 527, 1985.
26. Crooks, R.E., and Starke, E.A., Jr., Metall. Trans. A, **15A**, p. 1387, 1984.
27. Lynch, S.P., Mater. Sci. Engr., **136**, p. 25, 1991.
28. Lynch, S.P., Byrness, R., and Nethercott, R.B., in Aluminum-Lithium VI (M. Peters and P.-J. Winkler, eds.), DGM Informationsgesellschaft mbH, Oberursel 1, Germany, p. 391, 1992.
29. Blankenship, C.P., Jr., and Starke, E.A., Jr., Metall. Trans. A, **24A**, p. 833, 1993.
30. Slavik, D.C., Blankenship, C.P., Jr., Starke, E.A., Jr., and Gangloff, R.P., Metall. Trans. A, **24A**, p. 1807, 1993.
31. Wadsworth, J., Hensahall, C.A., and Nieh, T.E., in Aluminum-Lithium II (C. Baker, P.J. Gregson, S.J. Harris and C.J. Peel, eds.), The Institute of Metals, London, England, p. 199, 1986.
32. Edwards, M.R., and Stoneham, V.E., in Aluminum-Lithium IV, Journal de Physique, Colloque C3, p. 293, 1987.
33. Papazian, J.M., Bott, G.G., and Shaw, P., in Proceedings of the 17th National SAMPE Conference, p. 688, 1985.

Aluminum-Lithium Alloys
Edgar A. Starke, Jr.

- Q: Vasu (Office of Naval Research in Washington, D.C.) Regarding the pileups have you seen whether the pileups are going into the boundary or whether they are just coming out of the boundary, in the T_1 ?
- A: Good question. Often when Al-Li alloys are fractured large slip steps or offsets are observed on the intergranular fracture surface. These are associated with dislocations egressing from the surface and indicate that dislocations were piled up at the grain boundary. Tom Sanders and I have observed this in underaged Al-Li alloys (which contain no grain boundary precipitates) as well as in peak aged samples. Although often intergranular fracture is associated with the presence of grain boundary precipitates, as you have shown in your excellent work on the subject, it may also be due to dislocation pileups at grain boundaries (the two processes may also work together).
- Q: There is one interesting plot you have shown which indicates that the number of particles in the boundary did not change with stretch.
- A: We conducted a series of experiments in which we collected quantitative data on the effect of stretch on the nucleation and growth of grain boundary precipitates. We found that the stretch, although greatly affecting the nucleation and growth of matrix precipitates, had no effect on the nucleation and growth of grain boundary precipitates. The stretch did accelerate the nucleation and growth of matrix precipitates so that the time to peak age was reduced. This resulted in a smaller volume fraction of grain boundary precipitates in the peak aged condition than would have been present if no stretch was given prior to aging to a similar strength level. A large stretch coupled with low temperature aging obviously results in a better strength-fracture toughness combination since this process results in a smaller volume fraction of grain boundary precipitates.
- Q: Since the solute is getting sucked away, you would expect to see some change in the production in grain boundary precipitates, therefore, something else is influencing it. There is a competition that creates the lack of solute in the grain boundary. The chemistry is the thing that really defines the event at the boundary.
- A: We also believe that we would see some effect on grain boundary production. However, the heterogeneous nucleation at the grain boundary must dominate the reaction as a function of time.
- Q: Is there a lot of solute bonded to the subgrain boundary; more than associated with T_1 ?

- A: We always observed precipitation on subgrain boundaries, with or without stretching prior to aging.
- Q: Does that remove the solute?
- A: Yes, again as you stretch you accelerate the kinetics of matrix precipitation so less time is required to reach peak strength and therefore less time to nucleate and grow subgrain and grain boundary precipitates.
- Q: Pickens (Martin Marietta) We see the same thing for 2195 alloys; i.e. less T_1 with more stretch, so the competition for solute while stretching reduces the particles on grain boundaries and subgrain boundaries as well.
- A: Not for the same aging time though Joe.
- Q: Same strength level.
- A: Yes, same strength level but you reach that strength in a much shorter time if a stretch is given prior to aging.
- Q: I am just agreeing with you.
- A: OK, we agree that you reach a given strength level in a shorter time with a stretch so you have less grain boundary precipitates and less T_1 on subgrain boundaries.
- Q: Vasudevan - The grain boundary precipitates lower your strength, that is the reason I asked the aging time.
- A: Yes, the aging time is the key, and the advantage of the stretch is to reduce the aging time which results in less grain boundary and subgrain boundary precipitates. That is why even for an alloy that contains nucleating agents like Mg and Ag (like in Joe's 2195) one is better off putting a stretch in the processing. This leads to a better strength-fracture toughness combination.
- Q: Troy Tack (Ashurst) In one of the slides you mentioned that for the sheet products a fine crystallized structure is better for fracture toughness. Do you feel that is true at cryogenic temperatures as well? I believe that Rob Ritchie showed the reverse trend was true with the recrystallized sheet. In other words, one would go from a mixed mode failure to ambient temperature to a higher strength with sheer fracture at lower temperatures.
- A: That may be true. The data that I was showed and the conclusions that I reached was based on work on 8090 that was conducted at ambient temperature. The results of that work indicated that at ambient temperature a recrystallized product was best for sheet

(plane stress) and an uncrystallized product was best for plate (plane strain).

Q: Roy Crooks (Navel Post Graduate School) I have a question on the nature of the grain boundary precipitates, that are considered bad. Is that more due to a large number of precipitates compared to other aluminum alloys or is it because the precipitates themselves have poor properties.

A: Well, I think it is the combination of both. The grain boundary precipitates that form in alloys like 2090 and 8090 seem to "snake" along the grain boundary' they do not appear in globular form like precipitates normally observed in 2024 and 7075. Consequently, I believe that the grain boundary precipitates in the Al-Li alloys are more detrimental to fracture properties because they cover a larger area of the grain boundary. However, the properties of the precipitates and/or the cohesive strength of the matrix might also be lower. I don't know what is the major contributing factor causing the grain boundary precipitates in Al-Li alloys to appear to have more of an adverse effect than those in other age hardenable aluminum alloys.

AL-LI ALLOY DEVELOPMENT AT REYNOLDS METALS COMPANY FOR AEROSPACE APPLICATIONS

A. Cho, R.E.Greene, M.H.Skillingberg and P.S.Fielding
Reynolds Metals Company
Richmond VA 23261

Abstract

For over a decade, the potential property advantages of Al-Li alloys led aircraft manufacturers and aluminum producers to invest enormous resources to develop Al-Li alloys primarily for aerospace applications. As a result, several Al-Li alloys have been commercially available for the last few years. However, utilization of these alloys is still limited, especially for durability and damage tolerant applications.

Recently, Reynolds Metals Company (RMC) has commercialized the Weldalite®049[1] family of Al-Li alloys with an emphasis on damage tolerant applications. These alloys include: 2195, for cryogenic tank applications on space launch systems; X2096, for replacement of 7075-T6 and 7050-T76 with 6% and 7% weight savings, respectively; and RX818/ML377, for elevated temperature applications. In addition, RMC has registered AA2197 which is an Al-Cu-Li-Mn alloy with excellent fatigue resistance, thermal stability and short transverse ductility. The unique property combination of AA2197 plate is most suitable for very thick gauge bulkhead applications.

This paper will discuss some of the critical properties of these alloys such as: fracture toughness, short transverse ductility, strength anisotropy, stress corrosion cracking resistance, and thermal stability.

I. Introduction

Li addition to Al alloys offers an attractive property combination of low density, high elastic modulus and high strength. This makes Al-Li alloys excellent candidate materials for aircraft structural applications. However, for Al-Li alloys with high Li content, some technical concerns exist in the area of fracture toughness, stress corrosion cracking resistance, thermal stability and/or short transverse ductility.

In order to develop commercially viable Al-Li alloys, RMC has avoided excessively low density or excessively high strength targets, and has maintained its emphasis on durability and damage tolerant applications. RMC demonstrated that, material properties of Al alloys could be improved with moderate Li additions. Therefore, the goal of the Al-Li alloy development program at RMC is to achieve material performance improvement by a moderate combination of mechanical property improvement and density reduction.

II. Selection of Alloy System

RMC's Al-Li alloy development efforts are based on three alloy systems; Al-Cu-Li-Mg-Ag system for high strength applications, Al-Cu-Mn system for thick plate bulkhead applications with improved fatigue resistance and reduced anisotropy, and Al-Mg-Li system for very low density applications. At present, RMC has commercialized

TABLE 1 - Al-Li alloys for Aerospace applications available from Reynolds Metals Company

<u>Al-Cu-Li-Mg-Ag system(Weldalite® 049)</u>	
AA2195 - .098 lbs./in ³ (2.72 g/cm ³)	High Strength/Cryogenic Fracture toughness
AAX2096-.095 lbs./in ³ (2.63 g/cm ³)	Low density/high strength/toughness 7050-T76, 7075-T6 replacement
RX818/ML377 - .097 lbs./in ³ (2.68 g/cm ³)	Elevated temperature applications 2618, 2519 replacement
<u>Al-Cu-Li-Mn system</u>	
AA2197 - .096 lbs./in ³ (2.66 g/cm ³)	2124-T, 7050-T74 Thick plate replacement

Al-Li alloys for aerospace applications based on the former two alloy systems. Table 1 shows the commercially available Al-Li alloys for aerospace applications.

III. Al-Cu-Li-Mg-Ag system

Al-Li alloys based on the Al-Cu-Li system are known for their high specific strengths due to the low density from Li addition and high strength from the very effective T_1 strengthening phase. These alloys can be further improved by controlling the Cu:Li ratio and adding Mg and Ag. The addition of small amounts of Mg and Ag lowers the solubility of Li in solid solution [2] and helps nucleation of T_1 precipitates [1]. The finer T_1 precipitates result in an improved fracture toughness for given strength levels. Small Ag additions significantly improves stress corrosion cracking resistance [4]. RMC has confirmed these attractive property combinations by conducting extensive evaluations of the Al-Cu-Li-Mg-Ag system (Weldalite® 049) for the last six years by both laboratory and commercial production scale activities. RMC has been successfully casting commercial scale rectangular ingots with a cross section as large as 16 inch (406 mm) thick by 60 inch (1524 mm) wide.

Among the Al-Cu-Li-Mg-Ag based alloys, 2195 and X2096 alloys are the most mature. RX818/ML377 alloys are still in the development stage under NASA-Langley Laboratory funding [6].

TABLE 2 - Registered Composition Limits of Al-Cu-Li-Mg-Ag (Weldalite® 049) and Al-Cu-Li-Mn Alloys

Elements	Weight %		
	AA2195	AA2096	AA2197
Cu	3.7 - 4.3	2.3 - 3.0	2.5 - 3.1
Li	.80 - 1.2	1.3 - 1.9	1.3 - 1.7
Mg	.25 - .80	.25 - .80	.25 max
Ag	.25 - .60	.25 - .60	- -
Zr	.08 - .16	.08 - .18	.08 - .15
Mn	.25 max	.25 max	.10 - .50
Zn	.25 max	.25 max	.05 max.
Fe	.15 max	.15 max	.10 max
Si	.12 max	.12 max	.10 max
Ti	.10 max	.10 max	.12 max
Other,ea.	.05 max	.05 max	.05 max
Other,total	.15 max.	.15 max.	.15 max
Al	Remain.	Remain.	Remain.

AA2195 is a high strength weldable alloy that is designed to replace AA2219 on welded cryogenic fuel tanks in space launch systems. AA2096 is a low density, high strength and high fracture toughness alloy designed to replace 7075-T6 and 7050-T76 for aircraft structure applications.

A. AA2195

AA2195 was developed to replace AA2219 for welded cryogenic fuel tanks. Compared to AA2219, AA2195 offers 40% higher strength and a 5% weight savings. The alloy was optimized to meet the Marshall Space Flight Center (MSFC) requirements for cryogenic fracture toughness and stress corrosion cracking (SCC) resistance. The required fracture toughness tests are conducted using surface crack tension test specimens shown in Figure 1. The MSFC specifications require that the fracture toughness values (K_{Ic}) at cryogenic temperatures be greater than or equal to the values at room temperature. The test location is at the T/2 plane for thin plate gore panels and ogive sections. Figure 2 shows the surface crack tension test results for 0.5" (13mm) thick 2195 -T8. The K_{Ic} values at

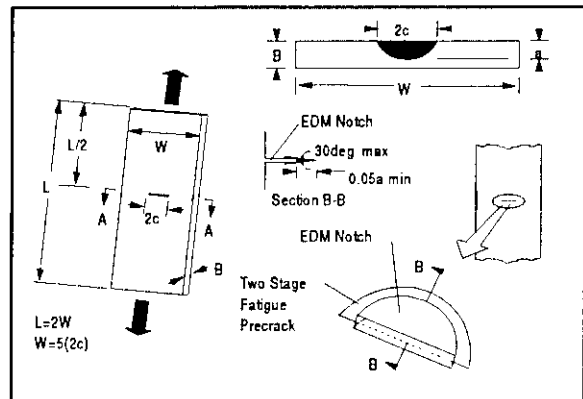


Figure 1 -- ASTM E740 Surface Crack Tension Test Specimen

T/2 plane at cryogenic temperatures of -320°F (-195°C) and -423°F (-253°C) are higher than those at room temperature. The test location for thick plate barrel panel sections is at the T/8 plane. Figure 3 shows the surface crack tension test results for 1.75" (44.5mm) thick 2195 -T8. Again, the K_{Ic} values at the T/8 plane at the cryogenic temperatures of -320°F (-195°C) and -423°F (-253°C) are higher than those at room temperature.

In most aerospace and aircraft applications, stress corrosion cracking (SCC) resistance is a

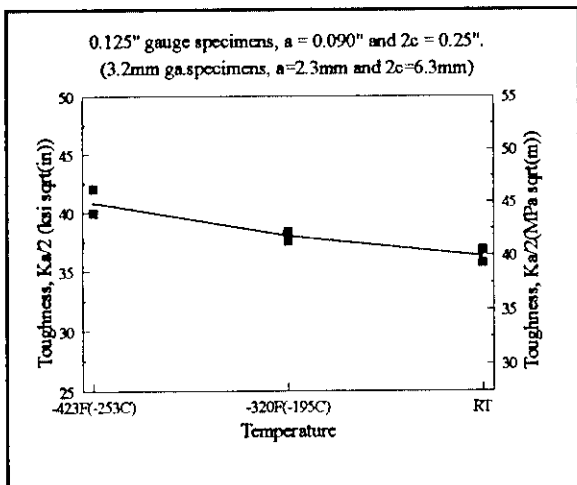


Figure 2 Surface crack tension results for 0.5" (13mm) gauge 2195-T8 plate at the T/2 plane.

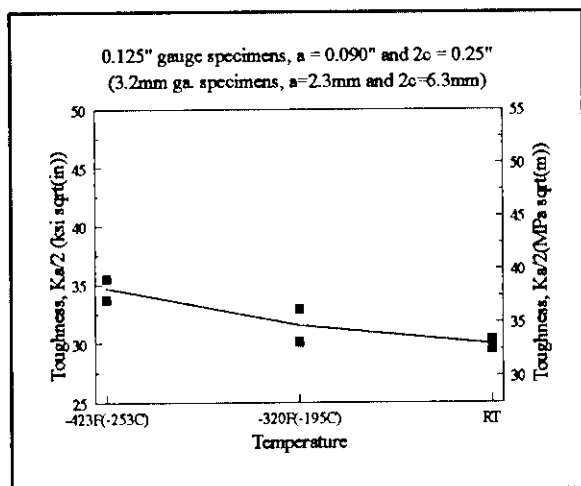


Figure 3 Surface crack tension results for 1.75" (44.5mm) gauge 2195-T8 plate at the T/8 plane.

critical property. The MSFC specification requires that the SCC threshold stress be more than 75% of the tensile yield stress in the test direction. SCC tests were conducted under applied stresses of up to 60 ksi (414 Mpa) to meet this requirement. Table 3 contains the SCC test results for 2195 plate in the short transverse direction. The data demonstrate the excellent SCC resistance of 2195 plate, a characteristic of all Reynolds' Al-Cu-Li-Mg-Ag alloys. In summary, 2195-T8 plate exhibits significant property improvement compared to alloy 2219, specifically good cryogenic fracture toughness and SCC resistance are obtained at 40% higher strength.

B. AA X2096

AAX2096 was developed to replace 7075-T6 and 7050-T76 for aircraft applications. Development of an alloy for aircraft structural applications requires maximizing weight savings while maintaining durability and damage tolerance requirements. To lower the density, lithium content was increased in X2096 compared to alloy 2195. However, to ensure good damage tolerance and durability, the Li:Cu atomic ratio was controlled to avoid δ' phase field [6]. As a result, X2096 exhibits an excellent combination of mechanical properties and corrosion resistance. Typical properties of thin gauge .75 inch (19mm) X2096-T8 temper plate are listed in Table 4. Both tensile properties and fracture toughness properties are sufficient to replace 7075-T6 and 7050-T76. Additional mechanical properties of X2096 wrought products are presented elsewhere [3].

C. RX818

Successful development of the high speed supersonic civil transport depends on the availability of high performance elevated temperature materials. Boeing Aircraft Company proposed several ambitious damage tolerance property goals for ingot metallurgy aluminum alloys. For such elevated temperature applications, RMC developed the RX818 alloy which utilizes a unique Cu:Li ratio to avoid grain boundary precipitates and δ' particles in the matrix. The nominal composition of RX818 alloy is Al-3.5% Cu-1.0% Li-4% Mg-4% Ag-13% Zr. Having grain boundaries free of precipitates, RX818-T8 plate showed very high ductility in the short transverse direction. The test results for 1.5" (38mm) gauge RX818-T8 plate in Table 5 show the average value for a 7.2% tensile elongation, which is unusually high for Li containing alloys in the short transverse direction.

Recent work on RX818 sheet gauge product at RMC indicates that RX818 alloy could meet Boeing's requirements for high combination of strength and fracture toughness during the long term elevated temperature service environment. Tensile yield stress vs. plane stress fracture toughness (K_{Ic}) values are plotted in Figure 4 along with properties of 7075-T6, 2024-T3 and 2090-T8 sheet. Note that the RX818 sheet properties shown

TABLE 3 -- Stress Corrosion Cracking
Resistance of 1.5 inch (38mm)
2195-T8R73 Plate

Applied Stress	Test Type/Dir.	Time to Failure
40ksi (276MPa)	Tensile/ST	NF,NF,NF
50ksi (345MPa)	Tensile/ST	NF,NF,NF
60ksi (414MPa)	Tensile/ST	NF,NF,NF
ASTM G47 and ASTM G44 for 30 days (3.5% NaCl Alternate Immersion)		

TABLE 4 -- Typical Mechanical Properties of 0.75 inch
(19mm) Gauge X2096-T8R70 Plate

Dir.	UTS ksi(MPa)	TYS ksi(MPa)	El. %	K_{IC} ksi \sqrt{in} (MPa \sqrt{m})
L	82.6(570)	79.1(546)	11.0	41.2(45.3)
LT	79.7(550)	74.9(517)	12.0	40.2(44.2)
45°	73.2(505)	67.0(462)	16.0	

All values are averaged from duplicates

simulate the effect of the thermal exposure during the service life of the high speed civil transport. The properties of the other alloys shown represent the properties without such exposures. The RX818 alloy sheet showed a marginal loss of fracture toughness after thermal exposure, however, it still maintained a superior combination of strength and fracture toughness compared with other alloys.

D. ML377

Laboratory scale experiments examining the

effect of recrystallization indicated that, after a thermal exposure, a recrystallized RX818 variant alloy(ML377) exhibited superior fracture toughness at a slightly reduced strength, compared with unrecrystallized RX818 alloy sheet. In order to confirm the effect of grain structure on the mechanical properties and thermal stability, both unrecrystallized (RX818) and recrystallized (ML377) sheet product have been fabricated from plant scale ingots. Figure 5 compares the tensile yield stresses of .090" (2.3mm) gauge RX818 and ML377 in T8 temper. ML377, which has a recrystallized microstructure, does not show the strength anisotropy of RX818. In Figure 6, ML377 sheet in T3 temper shows uniform ductility in all three directions indicating a better sheet forming capability than RX818. Figure 7 shows the combination of tensile yield stress and fracture toughness of RX818 and ML377 in the T8 temper condition. Again ML377 shows good fracture toughness values at a slightly lower strength than the RX818 alloy.

The current effort to further optimize the alloy composition and processing of RX818 alloy and its variants has been sponsored by NASA[5].

IV. Al-Cu-Li-Mn system

A. AA2197

Very thick gauge 2124-T851 plate has been the alloy of choice for very thick gauge plate applications for many years. However, the high fatigue crack growth rate of 2124-T851 plate has been a problem for aircraft bulkhead applications. As a result of a cooperative program[7], RX218-T851 alloy was developed with property goals based on Al alloy 2124-T851 plate. In 1993, RMC registered alloy RX218 as AA2197. The registered chemistry limits are listed in Table 2.

AA2197 is an Al-Cu-Li-Mn based alloy with a controlled Cu:Li ratio to avoid δ' particles in T8 temper condition. The addition of small amount of Mn to Al-Cu-Li alloys helps reduce strength anisotropy. A comprehensive test program involving static, cyclic, thermal and corrosion properties have been completed from 1.5"(38mm) gauge plate fabricated from a plant cast

TABLE 5 -- Tensile Properties of 1.5 inch (38mm) Gauge RX818-T8R73 Plate

Dir	UTS ksi(MPa)	TYS ksi(MPa)	El %
L	78.9(544)	77.2(533)	10.0
L.T	79.4(548)	73.6(508)	7.5
45	76.2(526)	70.7(488)	12.5
ST	77.5(535)	68.6(473)	7.2

All values are averaged from duplicates

12"(305mm) thick ingot[8]. In 1993, RMC was able to cast 12,000 lbs. ingots with a cross section of 16 inch (406 mm) thick x 60 inch (1524 mm) wide in order to fabricate very thick gauge plate product. RMC decided to fabricate 4 inch thick plate from the 16 inch thick ingot for additional evaluation. The mechanical properties of the 4 inch thick 2197-T851 plate are listed in Table 6. For comparison purposes, the property values from the required specification are listed also. Tensile properties showed isotropic behavior and met the specification requirement in all the test directions and test locations.

V. Conclusions

Al-Li alloys are very attractive candidate materials for aerospace and aircraft structural applications. The earlier generation Al-Li alloys offered significantly lower density and higher stiffness. However, higher Li content of those alloys caused property limitations related to damage tolerance and durability. RMC has introduced a new family of Al-Li alloys based on the Al-Cu-Li-Mg-Ag system and the Al-Cu-Li-Mn system that optimizes property improvement and weight savings by moderate addition of Li. These alloys include 2195, X2096, RX818, ML377 and 2197 alloys.

Acknowledgements

This activity was partially supported by NASA-Langley Grant NAG1-745. The authors are grateful to D. Bolstad from Martin Marietta Manned Space Systems for providing the surface crack tension test results for this publication.

TABLE 6 - Mechanical properties of plant produced 2197 -T851 plate

Test direc.	Test loc.	UTS ksi(MPa)	TYS ksi(MPa)	Elong. (%)
L	T/4	68.1(470)	65.6(453)	11.0
	T/2	69.4(479)	65.1(449)	10.8
property goal		62.0(428)	57.0(393)	5.0
LT	T/4	70.0(483)	65.5(452)	7.8
	T/2	68.2(471)	62.6(432)	7.0
property goal		63.0(435)	58.0(400)	4.0
45deg.	T/4	69.1(477)	64.0(442)	9.3
	T/2	65.5(452)	59.9(413)	9.0
property goal		NA	NA	NA
ST	T/2	65.9(455)	59.2(408)	4.7
property goal		59.0(407)	54.0(373)	1.5

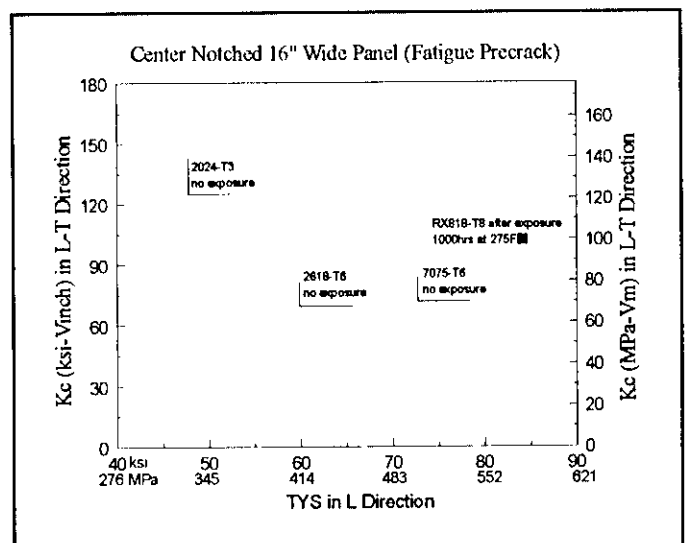


Figure 4 Fracture toughness of RX818 compared with conventional aluminum alloys.

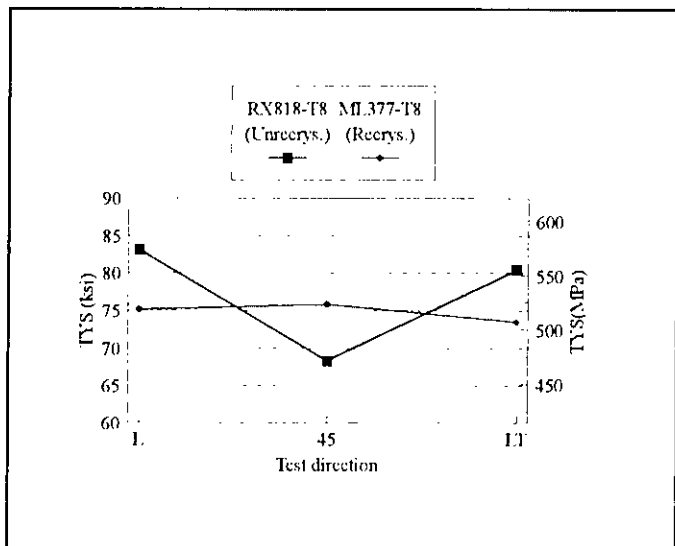


Figure 5 Strength anisotropy of 0.09"(2.3mm) gauge RX818 and ML377 in T8 temper.

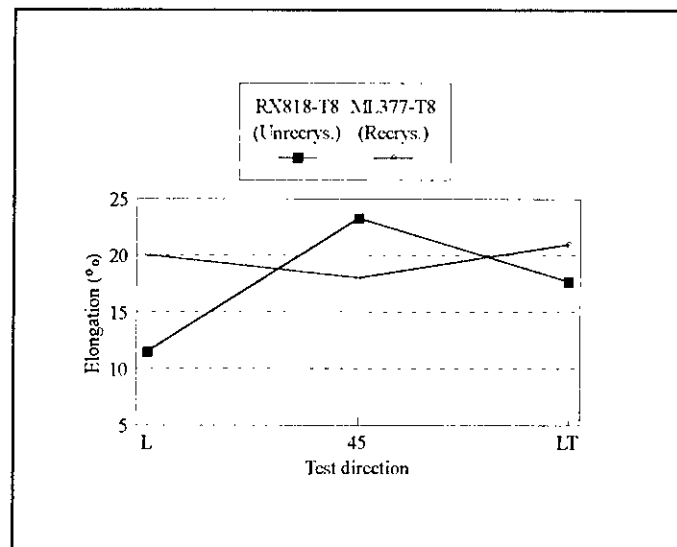


Figure 6 Tensile elongation of 0.09"(2.3mm) gauge RX 818 and ML 377 in T3 temper.

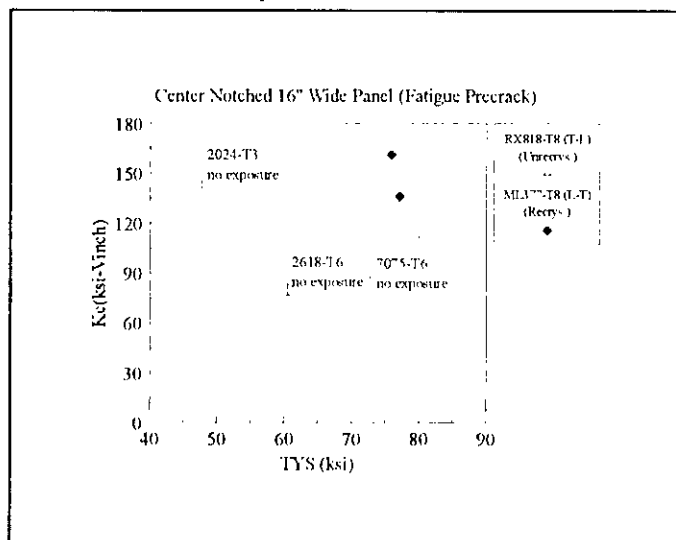


Figure 7 Fracture toughness of 0.09"(2.3mm) gauge RX818 and ML377 sheet in T8 temper.

References

1. J.R.Pickens, F.H.Heubaum, T.J.Langan, and L.S.Kramer, " Al-(4.5-6.3)Cu-1.3Li-.4Ag-.4Mg-.14Zr Alloy Weldalite 049", Proc. of the 5th Int. Al-Li Conf., Williamsburg, VA, Mar. 27-31, 1989.
2. S.F.Baumann and D.B.Williams, " The effect of ternary additions on the δ/α misfit and δ' solvus line in Al-Li alloys",Proc. of the 2nd Int. Al-Li Conference, Monterey,CA April 12-14, 1983.
3. A. Cho, R.E.Greene, M.H.Skillingberg, W.A.Cassada, H.M.Edwards and F.S.Fielding

"Status of High Strength Al-Li alloy Development at Reynolds Metals Company" Proc. of 40th Sagamore Army Materials Research Conference" Aug.30-Sept.2, 1993, Plymouth, MA

4. A. Cho, J.Beatty and D.H.Scott " Effect of temper on SCC Resistance of Al-Cu-Li-Mg-Ag alloys" TMS-AIME Mtg. Oct. 21-28, 1991

5. E.A.Stark, Jr. NASA Contractor Report 4517, "NASA-UVa Light Aerospace Alloy and Structure Technology Program Supplement: Aluminum-based Materials for High Speed Aircraft" Jan.1992.

6. A.Cho, R.E.Greene, M.H.Skillingberg, W.A.Cassada, H.M.Edwards and F.S.Fielding, "Status of Al-Li Program at Reynolds Metals Company", 6th Int. Al-Li Conf., Oct. 7-11, 1991

7. M.H.Skillingberg, E.S.Balmuth, D.J.Chellman, and R.A.Rainen. "Aluminum-Lithium Alloy Development for Parts Made from Thick Plate" , Proc.of TMS-AIME, New Orleans,LA, Feb. 1991.

8. D.J.Chellman, R.A.Rainen, S.B.Herner, E.S.Balmuth,R.C.Davis and K.R.Anderson, "Characterizationof a New Al-Li Alloy for Thick Plate" 6th Int. Al-Li Conf., Oct. 7-11, 1991

Al-Li Alloy Development at Reynolds Metals Company
for Aerospace Applications
A. Cho

Q: Kumar Jata (Air Force) You showed some data with increasing fracture toughness at cryogenic temperatures, was that 2095?

A: It was not 2095. It was 2195.

Q: Do you find the same trend?, do you find any isotropy at those low temperatures?

A: It depends on how you define "anisotropy." If you define anisotropy as "directionality", YES, fracture toughness values vary with testing direction at cryogenic temperatures the same way as at the room temperature, based on my experience with SCT specimens for 2195 as well as other Al alloys. If you test fracture toughness in L-T direction, you would have higher fracture toughness values than that tested in T-L.

Q: I just have on question about the HSCT applications. You know there has been some work done for Aluminum-Lithium alloys, I think. At warm temperatures, they found that some of the aluminum-lithium alloys, not commercial alloys but experimental materials, showed crack growth, both creep crack growth and also creep deformation at temperatures like 60 and 70 degrees C. Are you concerned about those kind of experiments for you material for HSCT applications?

A: We have been quite busy with UVA and NASA-Langley about HSCT alloy and process development and we did a lot of our stability tests in terms of strength, fracture toughness and precipitate particle coarsening behavior, and so on. As far as the creep test is concerned, we have planned it for 1994, so we have not done creep and creep related tests yet.

Q: Eui Lee (Navy) - I have a question. What makes the low temperature (cryogenic) fracture toughness improvement? Actually some people said that it is like homogeneous deformation and some people said that it is due to delamination, any comment on that?

A: About 3 or 4 years ago, there were a lot of debates going on between professors at University of California at Berkely, University of Arizona and University of Virginia. They proposed several different mechanisms regarding why fracture toughness values increase at the cryogenic temperatures. I think the answer is all of the above. Because when you look at the fractured surface of any kind of fracture toughness specimens, whether it's a Surface Crack Tension (SCT) specimen or Compact Tension (CT) specimens, you would see more delaminated features from the specimens tested at the cryogenic temperatures. In general, these alloys show higher

work hardening rate at the cryogenic temperatures which can be contributed to higher fracture toughness at the cryogenic temperatures.

One interesting observation is that, the commonly known metallurgical practices such as underaged temper, leaner solute alloy, etc, would increase the absolute value of fracture toughness value at the cryogenic temperatures to that of at the room temperature. This is an interesting observation because one of the MSFC's material specification requires such a ratio higher than 1.05.

Q: Mack Robert (Martin Marietta) - I just wondered, Alex, these newer alloys other than the 2195 that you talked about with the lower copper content, I wondered if any of those are weldable?

A: I am not quite sure of the definition of "weldability". GD space systems colleagues tried out for of those alloys, and I heard that they were about the same level of "weldability" with 2195 type composition alloy at that time. I was a welding trial in a very limited scope, no quantitative evaluation. O.K.? Reynolds did some limited efforts on comparing these alloys, actually all of those alloys including 2197, which is not a part of our Weldalite type alloys. All of them worked very well in according to our welders. So, what I think is that any aluminum-copper alloys and aluminum-lithium copper alloys are all essentially weldable. That is my understanding now.

Q: A number of years ago, Lockheed built a very large structure with 8090 and welded it, what were the welding tests that BD did?

A: I don't think they really conducted any kind of quantitative comparisons. My understanding is that they just conducted welding on a few plates.

Q: You gotta be very careful, you can lay two plates of 7075 on a table and weld them together but as soon as you tried to make something out of it and constrain it then it cracks. Your comment of aluminum-copper-lithium alloys are always weldable, should be modified; certain chemistries have very good weldability and others are very poor.

A: If you compare the ranking, which alloy weld better than the other, and which alloy is easier for repair welding, that is one thing. The other thing is that can you make a structure by welding regardless of how difficult it could be. Alloy 2014 is very bad for welding according to our welders, and Martin Marietta - Denver used that alloy and made a structure out of it. So, I did not mean to make any ranking of the alloys, but whether it is possible to weld. That was what I meant by "weldability."

Q: Alex I think your point is well taken, among various aluminum copper alloys weldabilities have been established to be varying and they can be ranked but until

more quantifiable tests are performed or standardized quantifiable tests are performed, you are really talking in a gray area of actual weldability rankings.

Q: If I hear what you are saying, you know that 2195 is very weldable, there is apparently not enough quantified work to really determinewhat you would consider weldable and what's not. Is that right?

A: Yes, I agree with you. I would like to tell you a story I heard from our marketing manager some time ago before his retirement. If he asks a welder would say, "I can." So much can be said about the "weldability."

ON THE YIELD STRESS ANISOTROPY OF AL-Li ALLOYS

A. K. Vasudevan, ONR Code-332, 800 N. Quincy St., VA. 22217
M. A. Przystupa, Dep. of Materials Sc. and Eng., UCLA, Los Angeles, CA.90024

Abstract

Commercial Al-Li base alloys exhibit strong yield strength anisotropy when compared to conventional 7XXX and 2XXX type aerospace alloys. This yield strength anisotropy is observed both in thicker products, such as plates, extrusions and forgings, and in the thinner products exemplified by sheets. In the thick section products this anisotropy manifests itself by the change of properties along the thickness direction. In thin products the change of properties takes place when moving away from the primary fabrication axis direction in the plane of the sheet. The observed anisotropic behavior seems to be due in part to the crystallographic texture developed during various fabrication processing stages and to the effects of the platelet precipitate formed during heat treatments. Several examples of the anisotropic behaviors of commercial Al-Li alloys are discussed in this note and supplemented with a brief mechanistic description of the sources of anisotropy in that family of alloys. It is also noted that the yield strength anisotropic behavior extends from room to cryogenic temperatures.

I. Introduction

Strength anisotropy in materials is generally attributed to the crystallographic texture which develops during fabrication steps transforming the material to its final product form. For example, the fabrication processes could consist of hot or cold rolling, or forging, that can give rise to different crystallographic grain orientations which results in the variations in the texture intensities. Superimposed on that will be a background of variations in grain sizes and shapes altered during fabrication. In addition to fabrication other factors can also influence texture. The most important ones are alloy composition and aging treatments which control which types of precipitates are present in the final microstructure. Among all possible types of precipitates the platelets seem to have the strongest effect on anisotropy. Since platelet precipitates are present in the Al-Li family of alloys, hence it is not surprising that both composition and aging seem to have strong influence on the yield stress anisotropy in this case. However,

the overall anisotropic behavior seems to be controlled by a complex interaction between the texture and the microstructure. The issue of the anisotropy of Al-Li alloys, and its source, have been debated since 1986 and results of the discussions can be found in several symposium proceedings [1,2].

II. Current Models

Most of the existing models describing anisotropic behavior of polycrystalline materials can be divided into two groups. The first group consists of models that deal purely with texture aspect of the problem, including grain shape and size effects. These are the so-called Taylor full constraint and relaxed constraint models. The second group of models deal with the role of oriented precipitates as well as their shapes and habit plane.

Based on the predictions from full and relaxed constraints models Przystupa et al [3] have pointed out that planar anisotropy in fcc alloys depends primarily on texture and the average number of available slip systems operating within each grain, Figure 1. Calculations were done by assuming that grains deform with five, four, three and one (Schmid model) slip systems. The trends are shown for five major fcc texture components, namely cube, goss, brass, copper and S. Cube and goss are the recrystallized textures, while brass, copper and S are textures that develop during deformation processing. The relative magnitudes of the Taylor factors (yield stresses, σ , normalized by a critical resolved shear stress, τ) vary with angle to the rolling direction. For cube, goss and brass components the anisotropy is the same for five, four and three operating slip systems and different for one slip system operating in a grain. However, copper and S components exhibit progressive change of anisotropy with the number of slip systems. If one superimposes the expected effects of the [100] or [111] platelet precipitates on texture anisotropy, Figure 1b, it would appear that [100] precipitates should decrease the anisotropy, while [111] precipitates should enhance it [3]. The models used for calculating these precipitations effects are addressed later in this section.

Yield strength anisotropy is also affected by grain shapes. When grains are equiaxed five slip systems are necessary to support any arbitrary deformation. However, when the grain aspect ratio begins to increase, the number of necessary slip systems begins to decrease and the effect on anisotropy are evident from results shown in Figure 1. The magnitudes of these effects are illustrated in Figure 2 for the case of pancake and lath shaped grains and for the hypothetical 50% copper + 50% S textures which are expected to give maximum grain shape effects. The grain shape effects for cube, goss or brass component will be smaller.

The precipitation anisotropy was first addressed by Hosford and Zeisloft (HZ)[4] and subsequently by Bates et al (BRW)[5]. In the HZ-model the yield stress is expressed as a sum of the contributions from the matrix and precipitates as:

$$\sigma = (1-f) \tau M + f \sigma_p [d\varepsilon_p/d\varepsilon] \quad (1)$$

where f is the precipitates volume fraction, M is Taylor factor, σ_p and ε_p are the precipitate effective stress and strain respectively. The HZ model assumes plastic matrix and constant stress intensity within the precipitate. The precipitation induced anisotropy comes from the term $d\varepsilon_p/d\varepsilon$, the index of anisotropy, which describes the differences between strains in the matrix and in the precipitate. The BRW model assumes elastic matrix, uniform strain in the precipitate and uses Eshelby's elastic approach to calculate the precipitate effective stress. This results in the following expression for yield strength:

$$\sigma = (1-f) \tau M + 2 f \mu \gamma \varepsilon^p \quad (2)$$

where μ is shear modulus, γ is Eshelby's accommodation factor and ε^p is the misfit strain. Note that both models contain adjustable parameters; in HZ-model the adjustable parameter is σ_p , while in BWR-model it is ε^p . The shape of the precipitate enter HZ-model through the strain ratio and in BWR approach it is incorporated in the accommodation factor. The size of the precipitates is introduced in both cases through the volume fraction f . Despite different assumptions both models give similar results [5].

III. Experimental Observations

The magnitudes and nature of texture and precipitation induced anisotropies in Al-Li alloys will be illustrated on examples taken from earlier work on 2090 alloys. These alloys exhibit strong anisotropy both in thick and thin products forms [6-8]. Their major precipitates, in the peak aged treatment, are spherical δ' and $[100] \theta'$ and $[111] T_1$ platelets.

In plate products the texture varies from surface to center. The degree of this variation depends on the alloy composition and the hot rolling processing parameters such as temperature, strain rate and amount of thickness reduction. Thick products from the Cu-containing aluminum alloys seems to develop strong textures. If Mg is also added, to bring about $[100] S'$ precipitates, the anisotropy is reduced. This trend can be observed in 2024 and 2020-type alloys where dominant precipitates are of the $[100]$ -type and where the background textures seem to be weaker than that in alloys containing $[111]$ type precipitates.

It was also reported that the longitudinal yield strength increased from low values at the surface of a 2090 alloy plate to a maximum value at the mid-thickness, Figure 3a. Associated texture intensities also had the same trend. Calculated from texture Taylor factors also increased from surface to center. By dissolving δ' precipitates using a reversion method, one can separate the contribution of T_1 to the anisotropy. Results are shown in Figure 3b clearly indicating that the total contribution to the anisotropic behavior comes from both texture and T_1 precipitate [6,7].

In the case of a sheet alloy, the background texture is constant, but the anisotropy varies with the aging treatment. The magnitude of the observed changes is shown in Figure 4a. Figure 4b schematically shows the reasons for changes and indicates five separate regions, from A to E, with different microstructural contribution to anisotropy in each region. Note that at short aging treatments (underaging) the anisotropic effects are strong and as the time progresses (overaging regions) the effects are minimized. These results seems to be consistent with the predictions of the texture and precipitation induced anisotropy models discussed above [8]. The same basic anisotropic behavior extends also to the cryogenic temperatures [9,10].

IV. Fabrication Effects

Composition plays a strong role in affecting development of textures both during hot and cold deformations. One of the most dramatic examples of the resulting changes is the evolution of texture in Al-Li alloys with varying Li/Cu ratio, as shown in Figure 5 using ODF plots. When the Li/Cu ratio increases the hot rolling texture components become strong, reaching a peak and then decrease with further increase in Li/Cu ratio. The controlling factor seems to be in this case the background amount of Li. This can be further illustrates by a series of the ODF $\Phi=0$ sections for different composition plotted on a Al-Li-Cu phase diagram, Figure 6.

Hirsch et al [12] have studied the development of cold rolling textures in 8090 alloy sheet, with varying starting initial textures and precipitates. They also observed that the relative amount of brass, S and copper textures varied strongly with the initial textures as well as with the grain shape and aging conditions.

V. Summary

- In the Al-Li family of alloys the development of crystallographic textures is controlled by the following parameters: alloy composition, initial texture, grain shapes and the heat-treating conditions. As a result, the optimization of textures have to be performed by choosing the controlling parameters within allowable limits and without sacrificing the resulting strength levels and other property combinations.
- Based on the experimental observations it is often suggested that textures affects not only the yield strength but that it also can strongly influence other properties such as fatigue (through crack nucleation and growth), fracture toughness, corrosion, sheet forming characteristics, superplastic behavior...etc. Such interpretations of the experimental data have to be carefully scrutinized. While the yield stress anisotropy is indeed affected by texture through the number of slip systems available for yielding at low strains, the same deformation mechanism need not hold for cases such as fatigue, fracture and corrosion where deformation path may be different than the one taking place during the tensile test. In case of room and/or at high temperatures forming and superplastic forming operations the texture can

also vary with deformation. Such texture evolution during forming operations can have implications on the final product integrity, and its dependence on the starting texture.

- Although strong textures do give rise to the anisotropic behavior, the anisotropy, as past experiences show, is not necessarily harmful. What is needed is a reexamination of the component design methodologies from the point of view of the best utilization of the anisotropic materials, or combinations of anisotropic and isotropic materials, to take advantage of their attributes. The integration of the component design and materials selection/design processes can lead to the low cost/advanced performance systems from the basically conventional materials.

References

1. Conference Proceedings on: Al-Li Alloys III, C. Baker et al. eds., Inst. of Metals, London, 1985; Al-Li Alloys IV, G. Champier et al. eds., J. de Physique, v. 48, 1987; Al-Li Alloys V, T. H. Sanders et al. eds., CPE Publications Ltd., Birmingham, UK, 1989.
2. Proceedings of: ICOTOM-8, J. S. Kallend and G. Gottstein eds., Metallurgical Society of AIME, Warrendale, PA, 1988; ICOTOM-9, Avignon, France, 1990; ICOTOM-10, Germany, 1993.
3. M. A. Przystupa, A. K. Vasudevan & W. G. Fricke, Jr, in J. S. Kallend and G. Gottstein eds., Proc. ICOTOM-8, Metallurgical Society of AIME, Warrendale, PA, p. 1051, 1988.
4. W. F. Hosford & R. H. Zeisloft, Met. Trans, vol.3, p. 113, 1972.
5. P. Bate, W. T. Roberts & D. V. Wilson, Acta. Metall., vol.29, p. 1797, 1981.
6. A. K. Vasudevan, W. G. Fricke, Jr, M. A. Przystupa & S. Panchanadeeswaran, in J. S. Kallend and G. Gottstein eds., Proc. ICOTOM-8, Metallurgical Society of AIME, Warrendale, PA, p. 1071, 1988.

7. A. K. Vasudevan, W. G. Fricke, Jr, R. C. Malcolm, R. J. Bucci, M. A. Przystupa & F. Barlat, *Met. Trans.* vol.19A, p. 731, 1988.
8. A. K. Vasudevan, M. A. Przystupa & W. G. Fricke, Jr, *Scripta Met.*, vol.24, p. 1429, 1990.
9. J. J. Ruschau and K.V. Jata, WL-TR-93-4096 Report, August 1993.
10. K. V. Jata and J. J. Ruschau, WRDC-TR-90-4013 Report, March 1990.
11. J. Hirsch, O. Engler, K. Lucke, M. Peters & K. Welpmann, 4th Al-Li Conf. Proc., 1987.

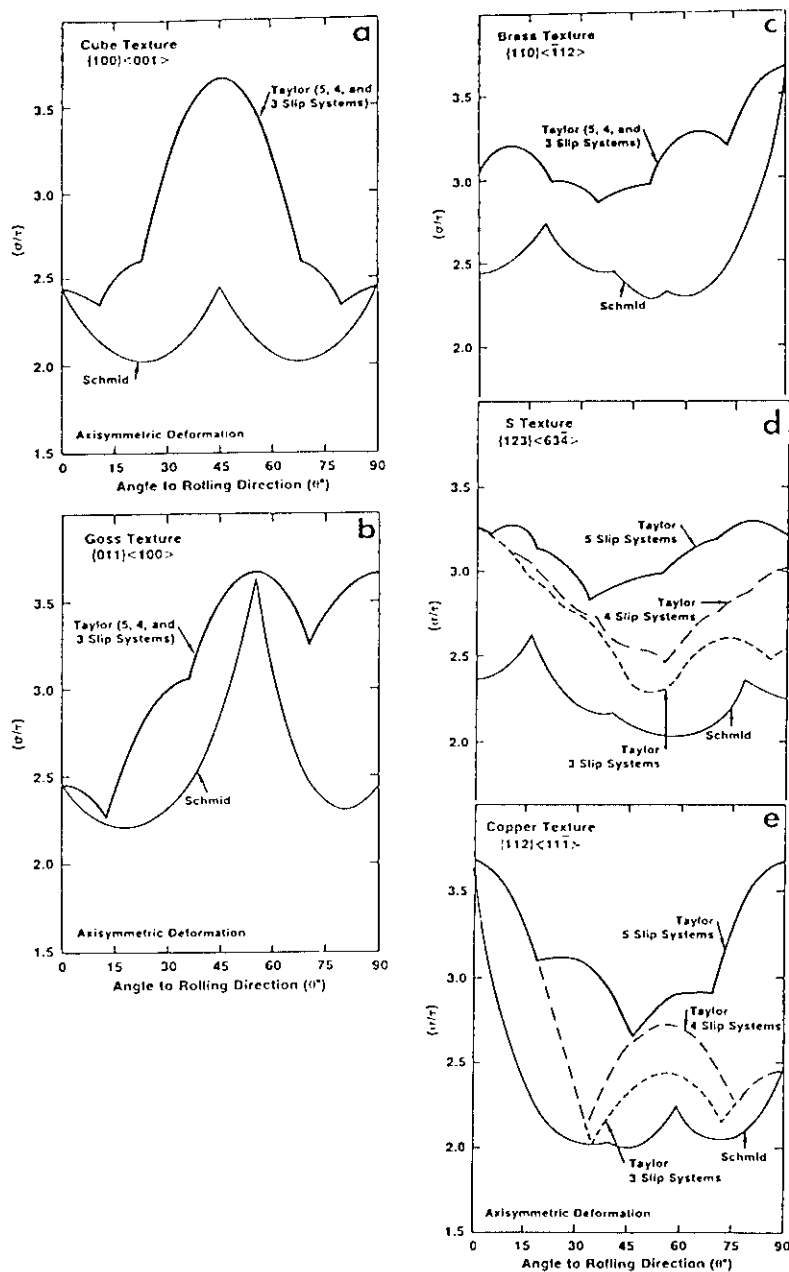


Figure 1a. Change of Taylor factors (normalized yield strength) with angle to the rolling directions for grains with ideal recrystallization (a) cube and (b) goss and rolling (c) brass, (d) S and (e) copper texture components deforming with five, four, three and one slip system.

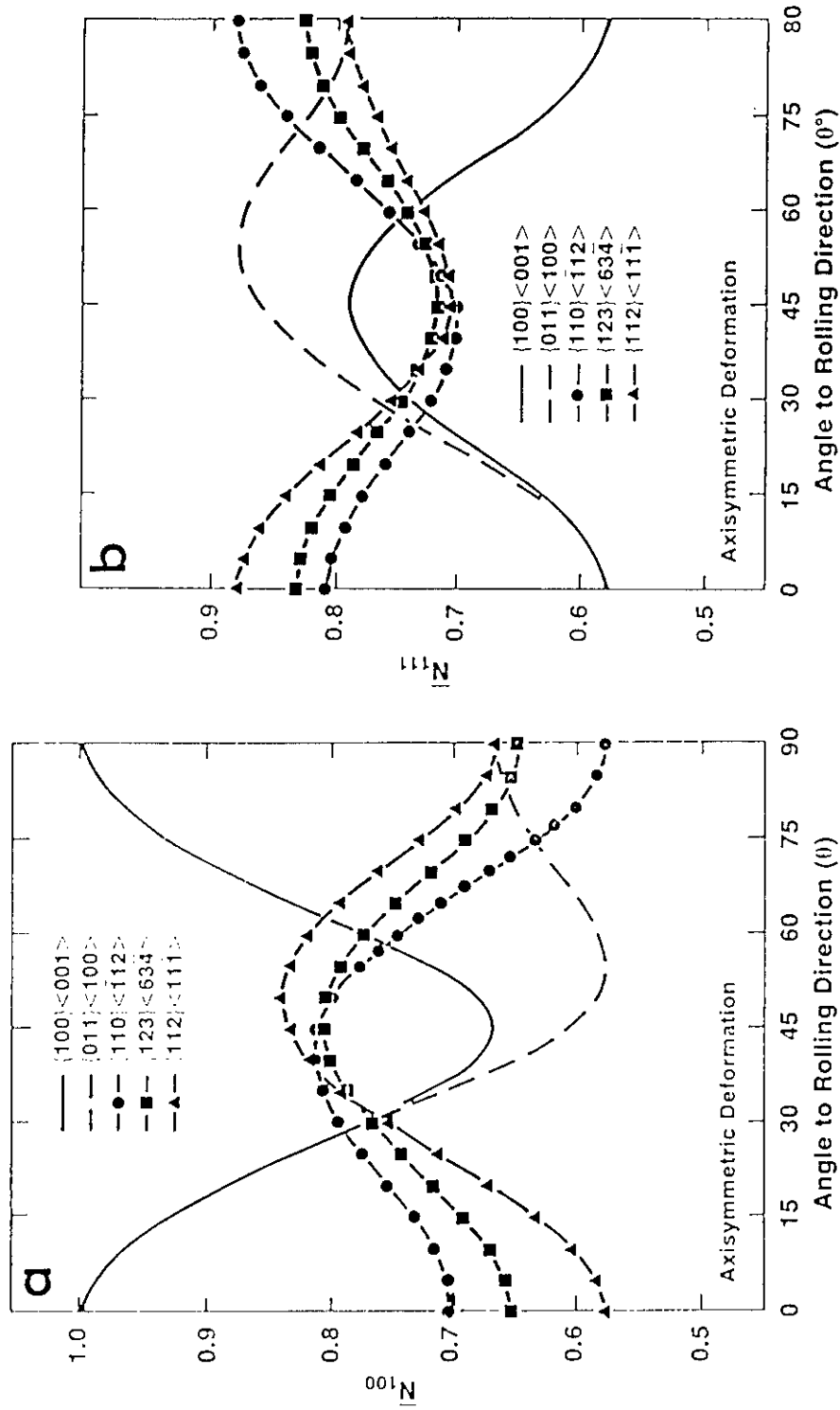


Figure 1b. Change of the precipitation anisotropy indexes $N=d\epsilon_p/d\epsilon$ with angle to rolling direction for Hosford-Zisloft model and (a) {100} and (b) {111} habit plane plate-like precipitates.

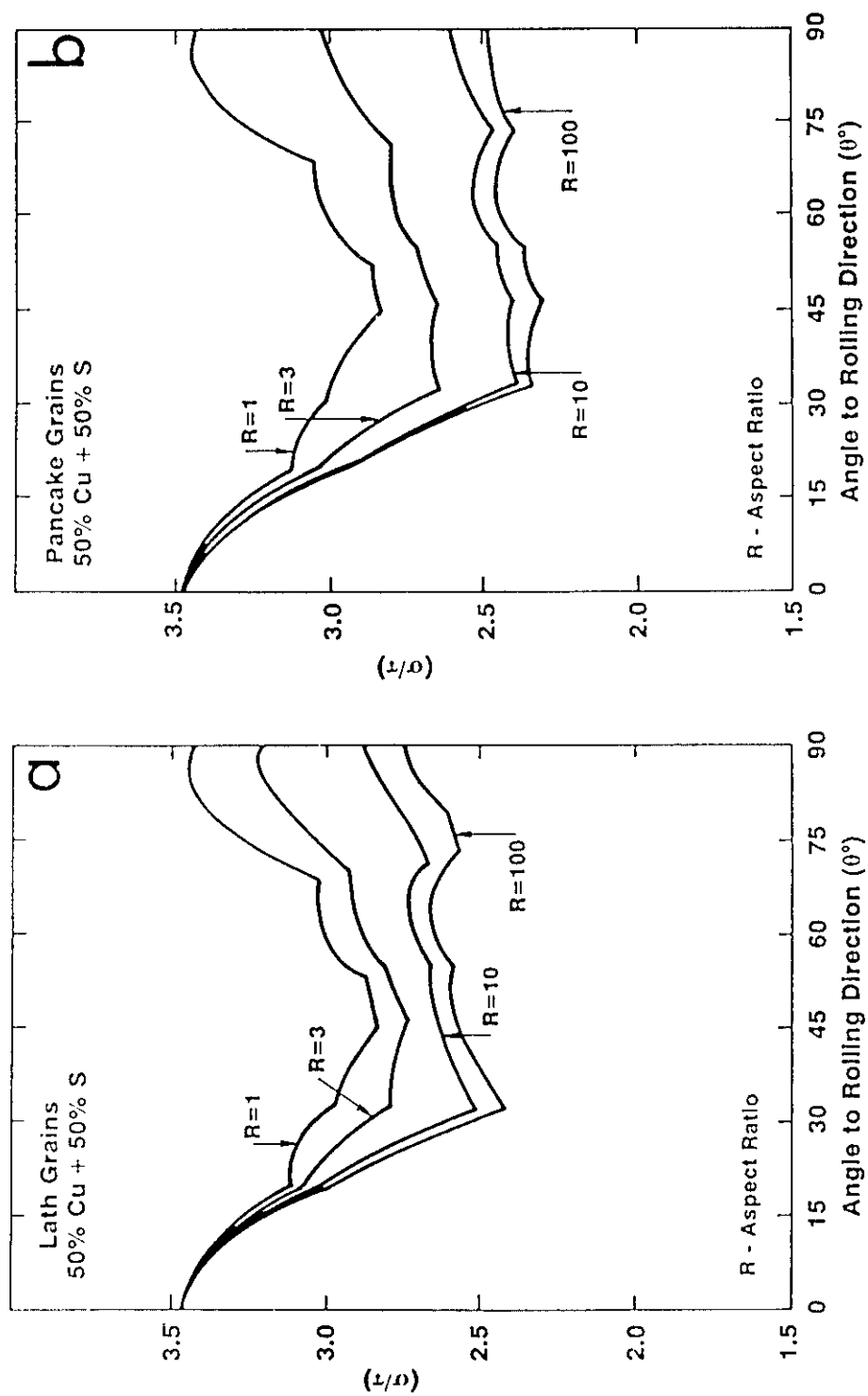


Figure 2. Effect of the aspect ratio of (a) lath and (b) pancake grains on the yield strength anisotropy for a hypothetical 50% copper + 50% S texture. Axisymmetric deformation, relaxed constraints model.

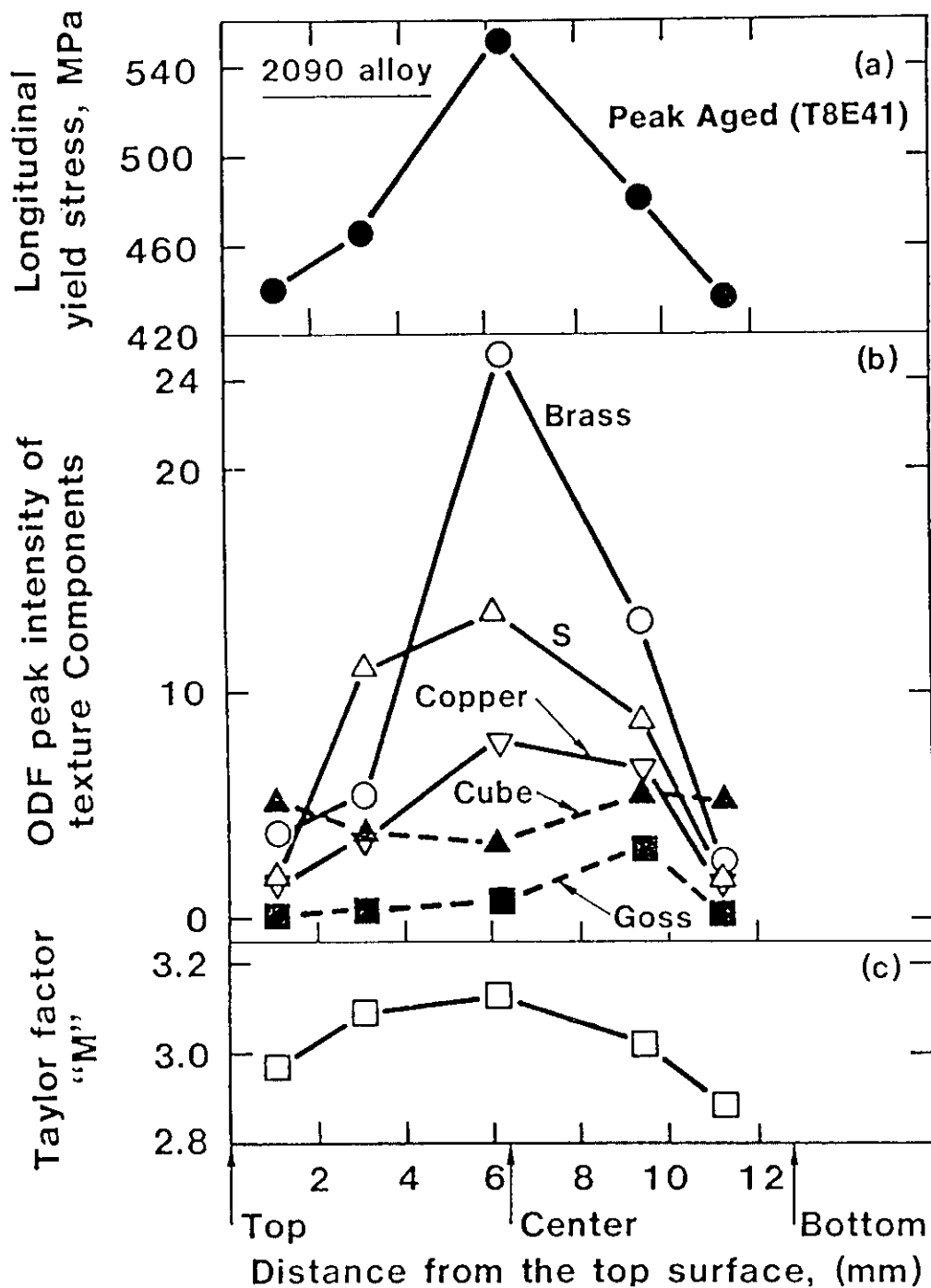


Figure 3a. Through-thickness variation of (a) longitudinal yield strength, (b) intensities of the major texture components and (c) Taylor factors, M , for 2090-T8E41 plate alloy.

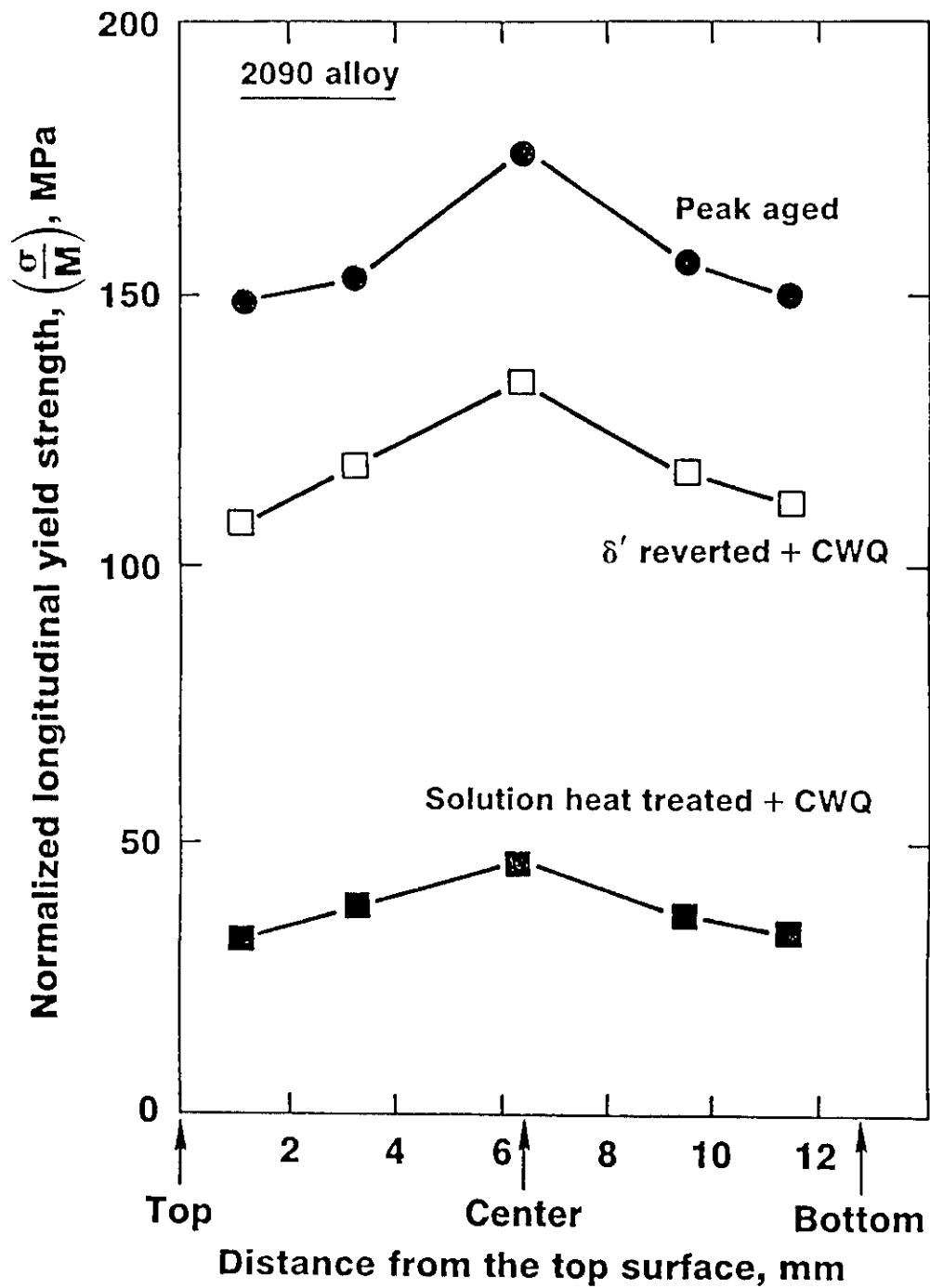


Figure 3b. Through-thickness yield strength gradients in 2090 plate alloy after solutionizing, peak-aging and δ' -reversion heat treatments.

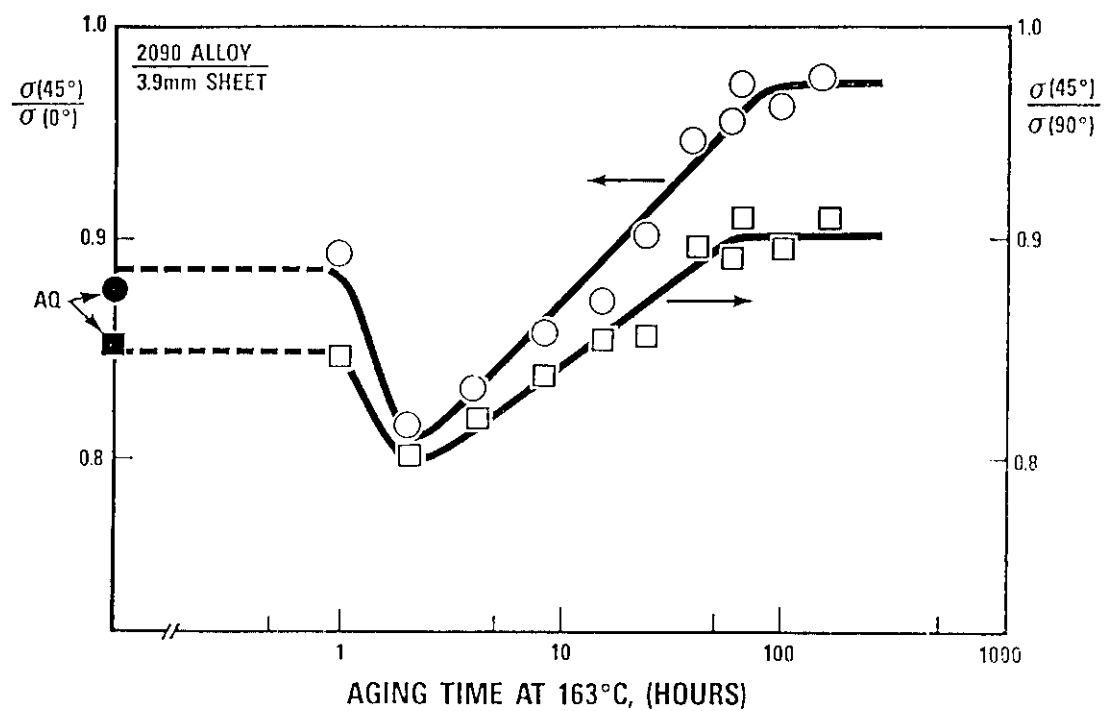


Figure 4a. Change of in-plane yield strength anisotropy of 2090 sheet alloy with aging time.

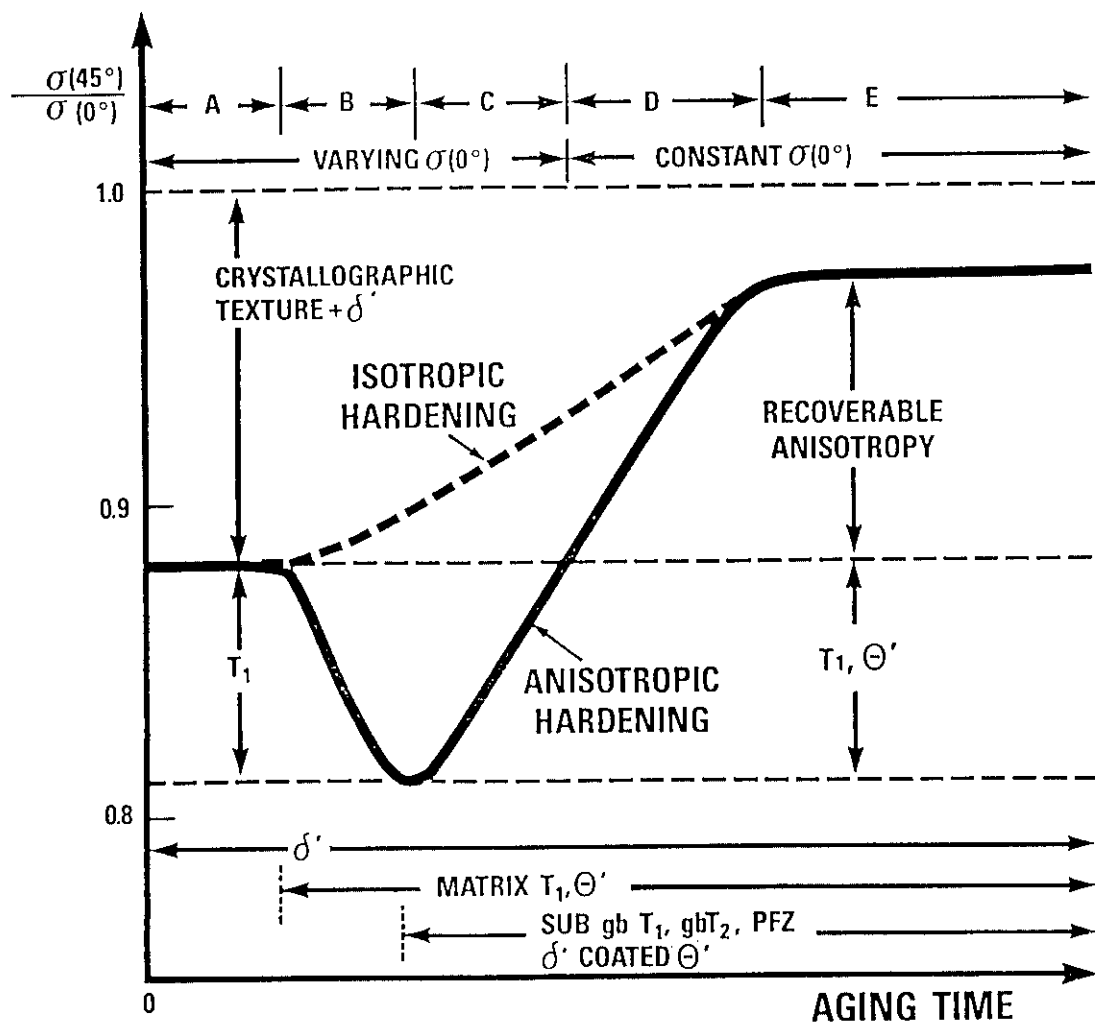


Figure 4b. Schematic showing interrelationships between yield strength anisotropy and microstructure in 2090 sheet alloys subject to different aging times.

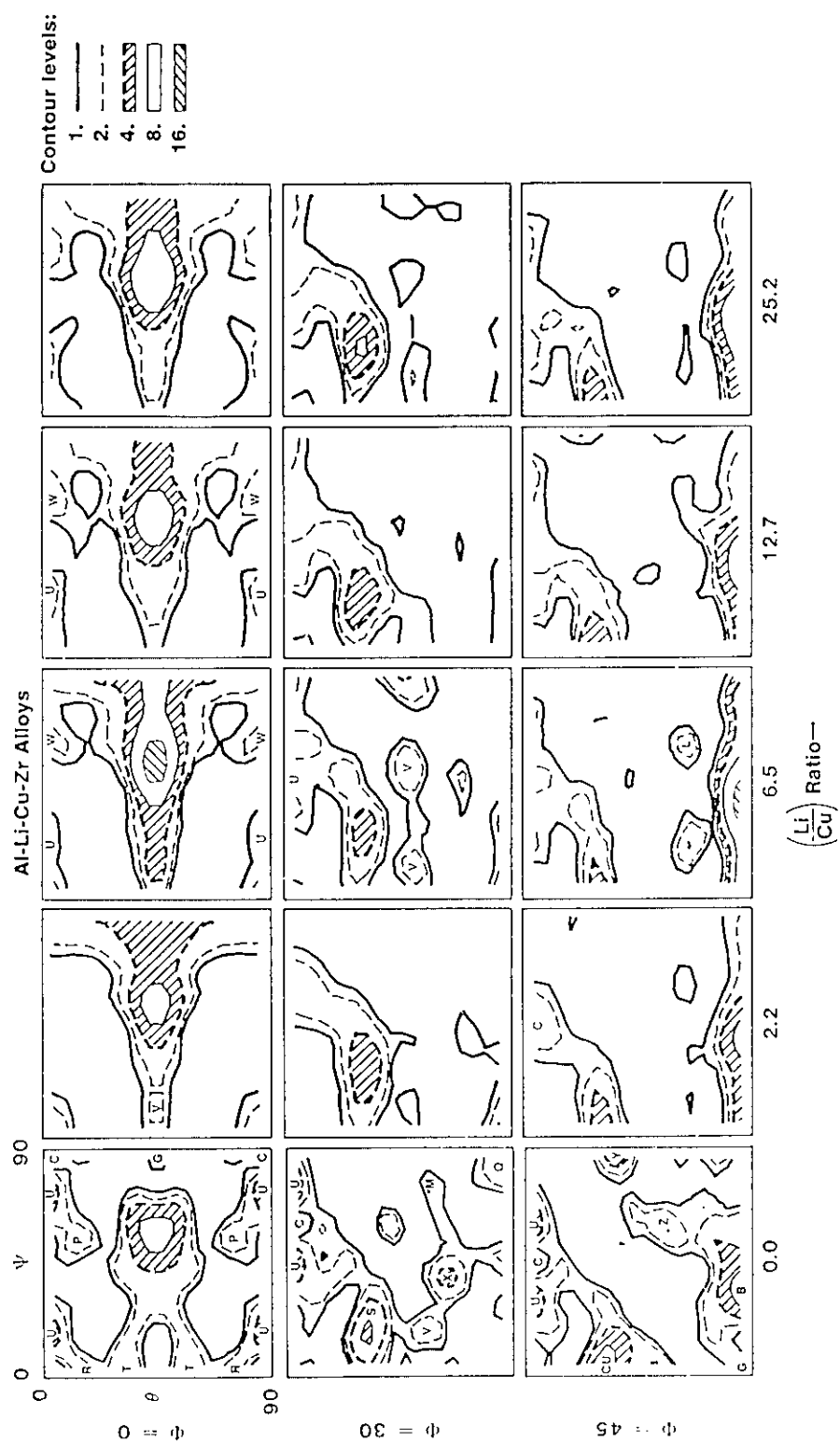


Figure 5. Change of the textures of Al-Cu-Li alloys with Li/Cu ratio. Positions of the major texture components are marked as B - brass, Cu - copper, C - cube, G - goss and S. Roe notation.

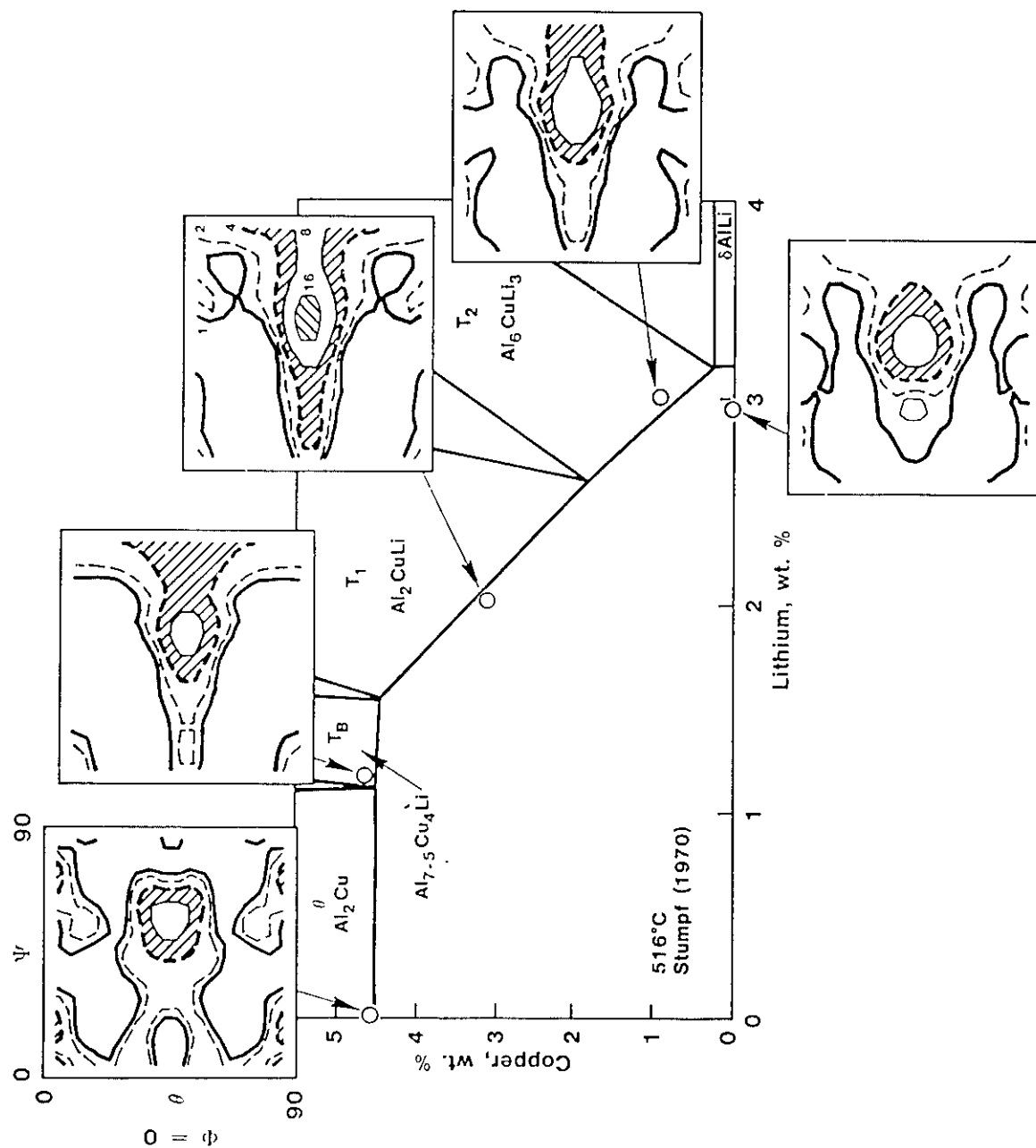


Figure 6. Change of the texture intensities on the ODF $\Phi = 0$ section with composition for ternary Al-Cu-Li alloys. Roe notation.

Crystallographic Texture and Anisotropy in Al-Li Alloys
A.K. Vasudevan

Q: Eui Lee (Navy) - That is a very good piece of work. If you stretch in the T-direction, there is a significant drop in anisotropy. They got really reduced anisotropic properties. I think that means that the T_1 is very important. Therefore, which direction will the material be stretched plays a significant role.

A: You mean stretching prior to aging.

Q: E.L. - Right, so that makes T_1 more resistant, like we are assuming that it has a strong texture. So that given more T_1 precipitates, stretch plays a major role.

A: That is very interesting. Do you have a paper on that stuff? I would like to get one because if I remember right, Roberto and we did one work where we pulled each tensile sample to 3%, along 0° , 22° , 45° , 67° , and 90° . We pulled each tensile sample before aging and we got exactly the same curve, as the one stretch in one direction only.

Q: We look in the TEM, and the dislocation distribution is different.

A: Can somebody comment on that? Can you do that in practice, can you stretch in the transverse direction? Dislocation distribution measurement has to be statistical to be relevant.

It is an interesting comment, and it alludes to the manufacturing problems. When we make a plate product process at 90° , it is difficult in the actual manufacture of plate and sheet products. For a secondary processor, where they blank parts to similar dimensions, it could be possible.

You may be able to do that in sheets, because in sheet, you have a thinner section. You might lose some edges, but you may lose about a foot in the edges, so then you have scraps coming in. But that is interesting, to see if it really does it.

Q: Alex Cho (Reynolds) You showed us about 1/3 of your slope about precipitates on (100) planes pushing the anisotropy in one direction and (111) in the other direction.

A: Yes, that is the observation, and as per Hosford's model prediction.

Q: A.C. - I was wondering how rigorously you did the calculation before you drew the conclusion like that?

A: It is a calculation based on certain assumptions. It is not rigorous.

- Q: A.C. - The reason I am saying this is because you really have to consider a little bit about what Dr. Lee mentioned. You really have to consider what variants of those (100) plane particles were (111) plane particles. You really have to make a distinction about those. I think we can make quite a difference in the results.
- A: Not necessarily. That is, σ_p in the Hosford relationship is an adjustable parameter but it takes into account the orientation of these precipitates. It takes into account every single variant. That is how the model considers the precipitation anisotropy.
- Q: One simple example is that if you have an alloy and temper conditions, you can produce T_1 particles and δ' particles, so that T_1 is sitting on (111) planes and the δ' on (100) planes. Actually, at one point in time I thought that if I could use both δ' and T_1 , it would help reduce anisotropy. The actual test results I got were the other way around. Now I was looking at different variant depending on stretching in one direction or another, or aging temperature conditions. You can control the partitioning between the different phases. It is not that simple having (100) or (111) participates now I am more dependant on what variant you could use; it's how many of variants you can produce?
- A: It is difficult to change the number of variants. You have to have four variants for T_1 , from physics in a polycrystalline material. You may bias the nucleation sites to increase some or decrease in density some variants.
- Q: The variant changes, depending on your stretching. Actually, in your presentation you produced different dislocation variants, because with a material like Al-Cu-Li (which is a highly textured material), stretched sheet has such a high level of stretch components. You really can control which variant you can produce, more than one variant or another. I had a discussion with Alan Ardell on how we can actually make some mild calculations for different ratios of T_1 or δ' particles. His response was, "At this point, we do not have a particular model to calculate the strengthening effect of these particles, following slip systems and variants; we cannot do it."
- A: That is true. The strengthening models are not comprehensive yet, but the thing is . .
- Q: No. It's a crystallographic orientation problem, because you have to follow each variant.
- A: I leave it to Ed to answer you
- A: Ed - I think what everybody said is correct because it depends on the number of density of the precipitates on different habit planes.
- A: Vasu - Please continue Ed.

- A: Ed - It depends on the shape of the grains, like you said, and on the number of slip systems. But whether you are having a plane of shearable precipitates, strain localization and homogenous also has an effect of the number of precipitates. It is very complex and it is a very difficult problem.
- A: Vasu - What you said is correct. That is why we did the three experiments, one is straight aging, one is only stretching uniaxially, and one was pre-fatigued, in a given textured alloy. No difference in yield anisotropy was observed.
- A: Ed - Yes, but you have to take into account that crystallographic texture, and in addition to that where the precipitates lie, which variant do the precipitates lie.
- A: Vasu - It is hard for me to conceive (from physics) that you can completely lose variants of precipitates.
- A: Ed - In addition to grain shapes, all three of those things are important and it is very complex. I don't think there is one simple model that explains it.
- A: Vasu - These models are good to give you guidelines about trends in the data. They are not perfect, as there are assumptions to develop models.
- A: Ed - And Bates model seems to apply better than Hosford.
- Q: Cho - I have a simple one. You showed about the Brass components lose intensity when you go from left to right on your viewgraph. I think on the X axis, the ratio is between Li over Cu. Was it?
- A: Yes. The Brass increases to a peak value and then it decreases. For the same hot rolling conditions.
- Q: Cho - You can have a ratio between Li and Cu or actually absolute amount of Li and Cu to play a role here. So, what kind of Li and Cu did you use?
- A: Those are nominal compositions of the alloy. These are actual compositions of the alloy, varied along the solvus line of the Al-Li-Cu phase diagram.
- Q: So you used 2090 and 2024?
- A: Yes, it is on the solvus periphery of Al-Li-Cu phase diagram.
- Q: So you have other alloying elements?
- A: Just the Zr.

- Q: Are these commercial alloys you are talking about, or experimental alloys?
- A: These are all experimental alloys, from Navair work.
- Q: So, three different ratios, but what about actual amount of Li or Cu?
- A: You mean actual amount it is a nominal composition?
- Q: What he is asking is did you keep the ratio constant?
- A: No. I showed the phase diagram, it is on the periphery of the phase diagram. We also have done one at a constant Li and it follows the same trend, but I did not bring the data. I mean, in a 2% Li alloy, we varied Cu.
- Q: I think what Alex is saying is . . .
- A: I understand, but the thing is, any (Li/Cu) ratio can be used to look at the data trends if it is systematic. It will follow the same curve if you plot it in terms of ratios.
- Q: For that particular stress component calculation. Was it done in Alcoa?
- A: Yes.
- Q: You talked about fatigue, that the high-cycle fatigue, low-cycle fatigue, and fatigue crack propagation at different angles.
- A: Yes.
- Q: We did high-cycle fatigue tests at 45° was the best, even though it showed the lowest strength with a best high-cycle fatigue. Low-cycle fatigue 45-60° were somewhat best. But fatigue crack propagation at 45° was the worst.
- A: I am not clear what this means, but one may want to rationalize in the following manner. In a multi-microstructured alloy like 2090 or 8090, the yield stretch anisotropy comes from (as we understand it) the texture/grain shape and T_1 . In the case of fatigue, the contribution need not be due to the same set of microstructures, but probably a subset. More importantly, the environment can play a larger role to alter the fatigue behavior under certain orientations. One has to analyze the problems carefully.
- Q: There were a lot of questions on Al-Li alloys, too, when we did fatigue crack growth rates and compared things, all the way up to when weldalite came out, even though we understood it. Then when we started to compare weldalite, it was always better and the crack profile was the same, although the deformation was homogenous. So it is very confusing.

- A: Probably it is. One has to dissect the observations carefully.
- Q: Troy Tack (Ashurst Corp.) - Just a brief question. I recall this morning in Cho's talk, he was showing data from 2197 Lockheed alloy with 2.7 Cu and 1.5 Li and the properties were very isotropic. Do you think that would be because of the low solute content, because it is much lower than the other alloys, or maybe because of the new dispersed system.
- A: Yes, I think there could be a cutoff in the amount of second phase hard particle in an alloy which can homogenize texture during high temperature deformation. For example, that is what happens in the MMC's. We see a strong texture in 8090, then it goes away with compositing. And texture is uniform through the thickness of a plate.
- Q: In the MMC's you have those hard particles at the temperatures you are deforming at.
- A: Yes, you tend to have nucleation for recrystallization coming in at the particle site. Plus you can also have some homogenization of deformations.
- A: I don't know if the people have seen the work on Ni-based alloys. I have been looking into Ni-base superalloys. Some of them do show very strong texture. When Thoria is dispersed into the alloys as a very fine dispersoid of the order of about a couple hundred Angstroms, the texture is homogenized. The texture components become nearly flat and weak. So, there are observations in other systems that people may want to look to see what they have done. And these are work done at NASA. They did this work about 20 years ago in Ni-base superalloy development. They show, I was surprised to see, textures in alloys that had the same type of pancake shape grains as in Al-Li alloys. When a little bit of Thoria was added, it minimized the texture. So, there are examples. It is essentially how we maintain the deformation to bring out the right type of texture. Ed made a good comment this morning. I think we should also learn how to really design with anisotropic materials. It is puzzling to me to sit in meetings where people would say, "I would rather use an advanced composite material which is highly anisotropic and expensive; but then come to about 15% difference in yield strength in Al-Li alloy, then say we cannot use this." They are willing to use the composites which are highly anisotropic. One needs to look at all issues. Look at design issues, apart from the material development, how we can apply this. That is one of the things I would like to see in programs on anisotropic materials. People do not seem to do innovative designs. Efforts seem to be more prevalent in alloy design.

AIR FORCE PROGRAM FOR DEVELOPING ISOTROPIC WROUGHT Al-Li ALLOYS

J. T. Morgan,¹ K. V. Jata,¹ V. K. Jain,² and A. K. Hopkins²

¹Air Force Wright Laboratory, Materials Directorate
Wright-Patterson Air Force Base, OH 45433

²University of Dayton, Research Institute
Dayton, OH 45469

Abstract

In the early 90's the Air Force assessed the needs of aluminum research technology through interviews with various government and industry representatives. It was concluded that the most pressing need in aluminum technology was to solve the anisotropic behavior of wrought Al-Li alloys. In order to significantly attack this problem, the Air Force initiated two programs. One program is being conducted in-house and is concentrating on novel processing techniques making use of process modeling. The other program, with the University of Dayton Research Institute (UDRI), is concentrating on more traditional approaches, besides making use of process modeling techniques. Four alloys have been chosen; two were synthesized by Kaiser based on 8090 composition, the remaining two by Alcoa based on 2090 composition but as experimental alloys. Of these two alloys, one was chosen by UDRI and the other by the Air Force for its in-house program. Described are the results of material behavior modeling conducted using compression testing. Results of the compression testing are used to develop constitutive equations for finite element modeling, to generate processing maps, and to predict microstructure and texture development during processing. Also presented are comparisons of compression testing with torsion testing performed on the UDRI program alloys by Concordia University.

1. Introduction

Since aluminum has become an affordable structural alloy, there have been three eras during which lithium was used as an alloying element. The first era was in the 1920's when a low Li (0.1%) alloy was developed and introduced. The material was called Scleron and obviously was not designed to take advantage of density reduction that can be obtained by Li additions. In the late 1950's and early 1960's both US and USSR introduced Li-containing aluminum alloys and used them in structures. ALCOA introduced X2020 in 1958 and produced

material for the RA-5C Vigilante aircraft. Special precautions were taken to ensure the low toughness of the material, which contained 1.1% Li, did not cause structural cracking. 2020 was withdrawn from production in 1974.

Much of the early history has been reviewed in papers presented at the first two International Conferences on Al-Li which were held in 1980 and 1983. Balmuth and Schmidt [1] provided a perspective and Quist et al., [2] an overview of the structural applications of Al-Li. The latter paper contained a chart depicting events on a timeline starting in 1924 and continuing through 1982. An update to that chart is shown in Figure 1, where recent alloy registrations are added to make the chart current. In the early 1980's the focus was on higher lithium content to lower density and raise specific strength and stiffness. At that time the economic and political environment was such that organic matrix composites (OMCs) were a threat to aluminum as the primary structural material on both military and commercial aircraft. Al-Li was seen as a way to neutralize some of the applications that were envisioned for OMCs. ALCOA, Alcan, Reynolds, Kaiser, and Pechiney all produced material similar to the current 8090 and 2090 alloys which contain more than 2% Li. Alloy 2090 was registered with the Aluminum Association in 1984, and 8090 in 1988. X2095 was registered in 1990 and was sold as a high strength weldable structural aluminum alloy. Currently there is interest in RX218 and C255 which contain 1.5% Li. The time frame from the introduction of 2090 in 1984 to the present represents the third era in Al-Li development.

In 1991 the Air Force Materials Directorate completed a study of the short- and long-term needs in aluminum technology for the Air Force. The motivation for the study was the radically changing international political climate. Since the fall of the Berlin Wall, it was apparent there would be fewer new Air Force Systems and existing aircraft would be kept in service longer. Air Force Commands,

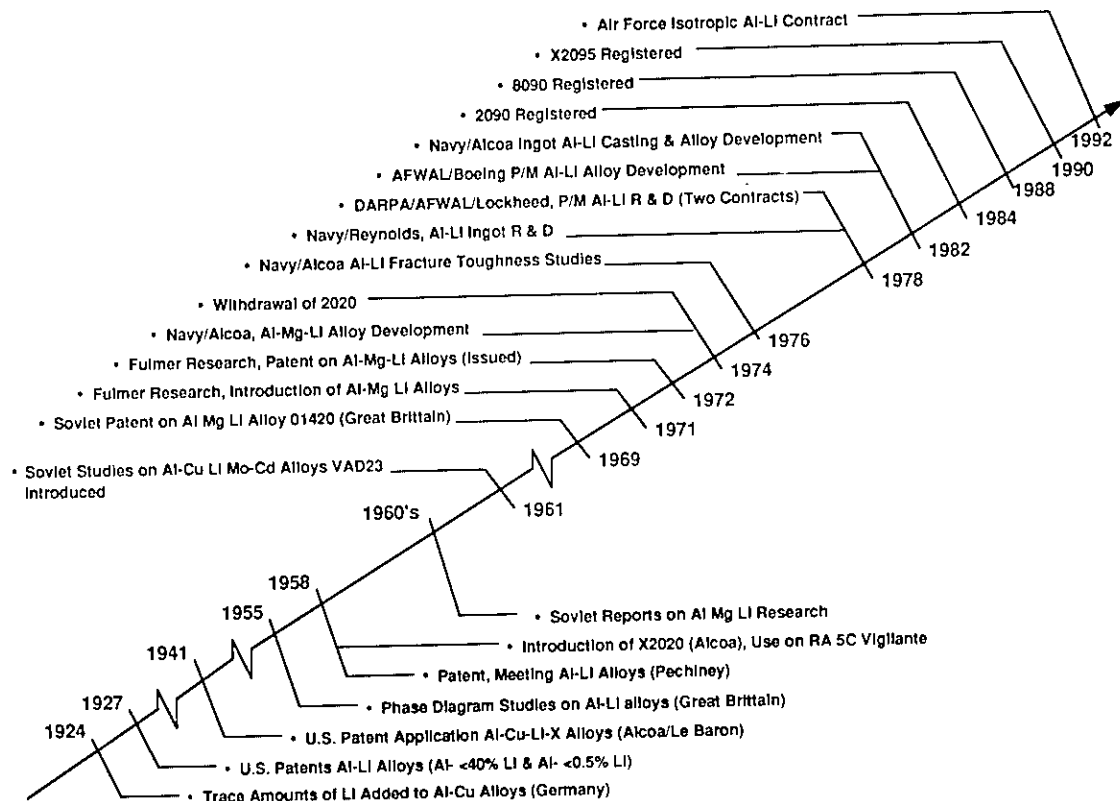


Figure 1. Historical perspective of Al-Li alloys [2].

System Program Offices, and industry were interviewed, and the highest identified need in aluminum alloys containing >2 w/o Li was to solve their anisotropy problem. As an example, the marginal short-transverse toughness was the reason for the recent announcement that a portion of the Al-Li products on the USAF C-17 cargo aircraft has been replaced by a non-Li aluminum. Since the introduction of the current Al-Li materials there have been only a few commitments to using Al-Li as "Bill of Material" for production systems [2]. The need to reduce anisotropy provided the impetus for the work reported in this paper.

Process modeling approaches are being used with the experimental alloys to design a process for the successful manufacturing of Al-Li wrought products with isotropic behavior. The process involves modeling of material behavior under actual manufacturing conditions, analytical modeling of the deformation processes, and physical modeling to verify the material behavior and analytical models. Two parallel efforts are ongoing: an Air Force (AF) in-house effort and an extramural effort with the

University of Dayton Research Institute (UDRI) serving as the prime contractor. The extramural effort is investigating the synergism of alloying and conventional processing technologies to solve the anisotropy in Al-Li alloys, whereas the in-house effort is concentrating on a series of novel processes. However, both efforts are making use of process modeling approaches.

The present work investigates the deformation behavior, microstructural evolution, and texture formation during hot compression and subsequent heat treatment of Al-Li alloys. Isothermal constant strain rate, compression tests were conducted, to simulate hot rolling of these alloys and their subsequent heat treatment, at various temperatures and strain rates. Flow stress data were used to develop processing maps and constitutive equations compatible with finite element modeling. The compressed specimens were examined under an optical microscope before and after heat treatment to study the evolution of microstructure. Pole figures and ODFs were obtained to determine the texture of the specimens.

II. Experimental Procedure

Material Selection

Four different Al-Li alloys were used for this work. In all the alloys the Li content was more than 2w/o. Of the four alloys, the AF investigated one and UDRI three alloys. Two alloys were purchased from ALCOA and two from Kaiser. The composition of the various alloys is given in Table I. The ALCOA ingots were cast in their R-330 research unit which simulates the casting of full size production ingots on a laboratory scale. The ingots were then homogenized at 538°C/24 hrs/slow cool and the peripheral 1.3 cm scalped to remove unwanted inclusions and alloy rich material. The material was characterized to reveal a dominant T_1 (Al_2CuLi) structure on the {111} octahedral plane and PFZs at the grain boundaries. X-ray mappings of the material showed the retention of Fe and Mn at the grain boundaries whereas Zn, Si, Cu and Mg tend to be dissolved into the grains. Since the ALCOA alloys are AF experimental, they will be referred to as AF(ML) and AF(UDRI).

Table I. Composition of Al-Li Alloys										
	Li	Cu	Mg	Zr	Fe	Mn	Zn	Si	Ti	Cr
Kaiser 8090/Zr	2.06	1.15	0.87	0.08	0.04	-	0.02	0.04	0.02	-
Kaiser 8090/Cr/Mn	2.01	1.10	0.88	0.02	0.04	0.52	0.02	0.05	0.03	0.14
AF(UDRI)	2.10	2.70	0.30	0.04	-	0.40	0.70	-	-	-
AF(ML)	2.10	2.70	0.40	0.05	-	0.40	0.75	-	-	-

Kaiser's two continuously-cast ingots were based on the 8090 composition. The size of each ingot was 16.5 cm x 16.5 cm x 90 cm. The ingots were homogenized at 538°C/16 hrs, air cooled, and the peripheral 1.6 cm scalped. One alloy contains 0.08% Zr and the other 0.02% Zr, 0.52% Mn and 0.14% Cr as dispersoid formers. These alloys will be referred to as 8090/Zr and 8090/Cr/Mn, respectively. The 8090/Zr composition was chosen to model the 8090 standard alloy which contains up to 0.11 w/o Zr. Zr was used at 0.08% because this is the threshold at which it manifests itself as a recrystallization inhibitor. The 8090/Cr/Mn was chosen because of earlier work of Dorward [3] which showed that using Mn and Cr in about a 4:1 ratio at 0.50 and 0.15 w/o level, recrystallization can be made to occur upon heat treatment of thermomechanically processed material. This recrystallization work was done on a

2090-based alloy modified to replace Zr with Mo and Cr. A minimal amount of Zr (0.02 w/o) is retained because of the high probability of occurrence of Zr at these levels in any commercial production where Zr is a residual "trash" element. It was thought that this low level of Zr would not interfere with recrystallization. All other constituent levels are typical for all three alloys bearing the 209X and 809X designations.

Measurement of Flow Stress

The flow stress database for these materials was generated using isothermal, constant-strain-rate compression testing. Test samples of 12.7 mm diameter and 19.10 mm height were machined from the cast, homogenized, and scalped ingots. A 25 kip MTS servo-hydraulic machine equipped with a microcomputer and a split radiant furnace was used. The dies and rams were machined from 17-4 PH stainless steel hardened to Rc45.

For the UDRI effort specimens were soaked at the test temperature for 15 minutes, a computer-generated, constant true strain control signal was triggered, and the specimen was compressed to a true strain of 1.4 (75% reduction in height) and water quenched. The Air Force in-house specimens were compressed to a true strain of about 0.7 (50% reduction in height) and allowed to air cool on a large steel test frame. The ram travel was controlled according to

$$y = \ell(1 - \exp(-\dot{\epsilon}t)) \quad (1)$$

where y is the ram displacement, ℓ the initial specimen height, $\dot{\epsilon}$ the strain rate, and t the time in seconds. The test matrix used for these materials is shown in Table II.

Table II. Test Matrix for the Compression Tests						
Strain Rate	Test Temperature °C					
	300	350	400	450	500	550
0.001	Y*	Y	Y	Y	Y	Y
0.01	Y	Y	Y	Y	Y	Y
0.05	X	X	X	X	X	-
0.10	X, Y	X, Y	X, Y	X, Y	X, Y	Y
0.50	X	X	X	X	X	-
1.00	X, Y	X, Y	X, Y	X, Y	X, Y	Y
5.00	X	X	X	X	X	-
10.00	X, Y	X, Y	X, Y	X, Y	X, Y	Y

*Y = AF, X = UDRI

From the load stroke data true stress versus true plastic strain plots were generated. The data were corrected for elastic deformation of the machine and deformation heating using the procedure outlined by Thomas & Srinivasan [4]. The microstructures of the deformed specimens were analyzed by polarized optical light microscopy.

Torsion Testing

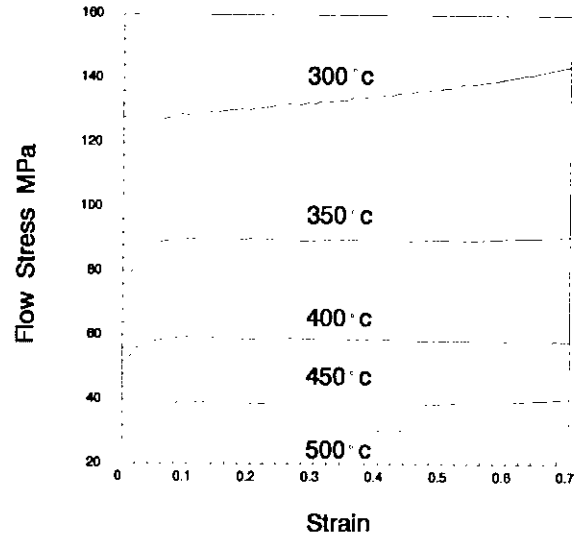
Hugh McQueen of Concordia University agreed to conduct torsion tests as an opportunity to compare, for the first time, both compression and torsion results on the same alloys with the same thermo-mechanical history. Accordingly, tests were conducted at temperatures of 300°C, 400°C, and 500°C and strain rates of 0.01, 0.1, 1.0, and 5.0/s. Relatively minor differences in flow stresses were observed between the two tests. Two papers will be presented at the ICAA4 describing the constitutive equation development [5] and the microstructure analysis [6].

III. Results and Discussion

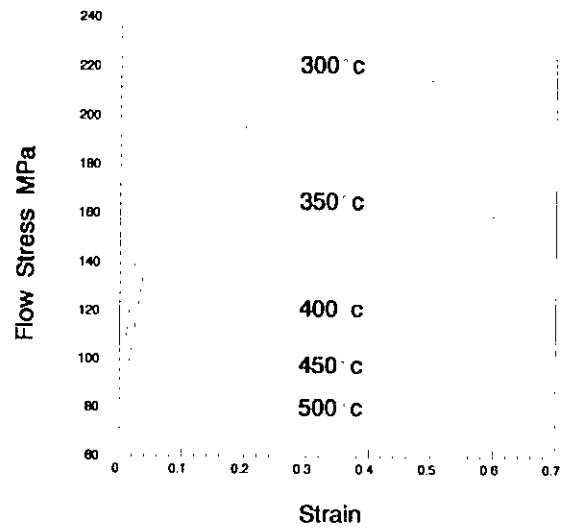
Figures 2a and b show the variation of flow stress with strain at various temperatures for strain rates of 0.05 and 10, respectively for the AF(UDRI) alloy. In both cases the stress increases with true plastic strain at 300°C temperature, indicating the dominance of strain hardening mechanism over strain softening. The flow curves at other temperatures show no effect of strain hardening and attain steady state at relatively low values of plastic strains. The flow stress decreases with increasing test temperature and decreasing strain rate. Although the flow stress curves have been corrected for the deformation heating effect, it should be borne in mind that the procedure used does not consider the distribution of strain and strain rate within the specimen volume. The finite element model DEFORM[®] was used to predict the strain and strain rate distribution in a compression specimen for various friction factors, m , at unit strain rate, and a nominal strain of 1.4. Figure 3 shows the strain distribution for $m=0.8$, the value realized for most of the compression test conditions. It may be noted that the strain varies from 0.043 to 2.55.

The flow stress variation exhibited by Figure 2 is typical to all the Al-Li alloys used in this program as exemplified by Figure 4. The figure shows a three dimensional carpet plot showing the variation of flow stress with $\ln(\dot{\epsilon})$ and $1000/T^{\circ}$, where T is the absolute test temperature in °K. As expected, the flow

stress increases with strain rate and decreases with temperature. Except for some minor discrepancies, the variation of flow stress satisfies the above rule. The stress values for the three alloys are comparable.



(a)



(b)

Figure 2. Variation of flow stress with strain at various temperatures, (a) $\dot{\epsilon} = 0.05 \text{ s}^{-1}$, (b) $\dot{\epsilon} = 10 \text{ s}^{-1}$.

A=0.043, B=0.357, C=0.670, D=0.984, E=1.297, F=1.611
G=1.924, H=2.238, I=2.551, J=2.551, Δ=.043

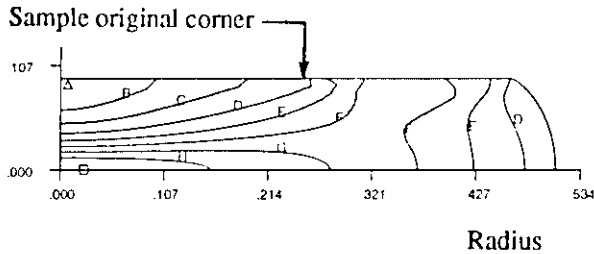


Figure 3. Strain distribution in a compression specimen for $m=0.8$ as predicted by DEFORM[®]. Processing conditions: $\dot{\epsilon} = 1 \text{ s}^{-1}$, $\epsilon = 1.4$.

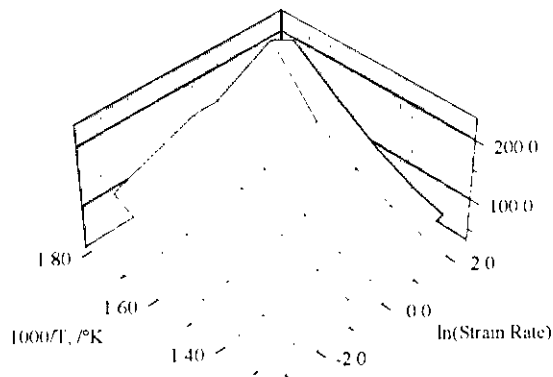


Figure 4. Stress carpet plot for AF(UDRI) for $\epsilon = 0.5$.

Constitutive Equation

The strain rate and temperature dependence of the flow stress during hot working can be described adequately using the phenomenological relationship developed for creep deformation:

$$A \sinh(\alpha \sigma_p)^n = \dot{\epsilon} \exp(Q/RT) = Z \quad (2)$$

where σ_p is the peak stress, $\dot{\epsilon}$ the strain rate, T the temperature, R the gas constant, and Z the Zener Hollomon parameter. A , α , and n are material constants and Q the apparent activation energy.

The peak flow stress data in the temperature range 300-500°C have been analyzed using the above

equation which contains four unknown parameters, namely Q , A , α , and n .

There is no standard technique available to determine these parameters from the flow stress data. For example, McQueen, et al. [8] plot $\log \sigma$ versus $\log \dot{\epsilon}$ data at each test temperature for various values of α (0.01-0.08 MPa^{-1}). A straight line is assumed to fit the data at each test temperature. An average value of the slopes n'_{av} is calculated for the set of straight lines for each value of α . Plots of $1/T$ versus $\log \sigma$ are then made at each strain rate, and average slope, s'_{av} is calculated for the set of straight lines for each value of α . Plots of α versus activation energy Q ($2.3 R n'_{av} s'_{av}$) are made. The steady state value Q is the required activation energy. The method is tedious and involves a large amount of computation. A different technique is therefore used in the present case.

The activation energy, Q , is defined by

$$Q = -R \left[\frac{\partial \ln(\dot{\epsilon})}{\partial (1/T)} \right]_{\sigma} \quad (3)$$

Plots of $\log \sigma$ versus $\log \dot{\epsilon}$ at different temperatures were made. From these plots, pairs of $\dot{\epsilon}$ and T data corresponding to a specific flow stress values were determined. Then plots of $\ln \dot{\epsilon}$ versus $1/T$ were developed and it was found that a straight line can be fitted to the data. In addition, the lines were found to be almost parallel. The values of activation energy were obtained corresponding to various stress levels. The average values of Q obtained for the various alloys are given in Table III.

Table III. Activation Energy Values	
Alloy	Q , kJ/mole
AF(UDRI)	189.1
8090/Cr/Mn	195.0
8090/Zr	195.0

The values of $\log(\sinh \alpha \sigma_p)$ were then plotted against $\log Z$, where $Z (= \dot{\epsilon} \exp(Q/RT))$ is the Zener Hollomon parameter. The parameter Z , for an alloy, was calculated using the above value of activation energy. Several values of α in the range of 0.01-0.05 were used. It was found that a straight line could be fitted to the data. Correlation coefficient for each regression line was obtained. As shown in Figure 5, the data were found to have the best fit for $\alpha = 0.01$.

The constitutive equations, which were obtained for the various alloys are given in Table IV.

Table IV. Constitutive Equations	
Alloy	Equation
AF(UDRI)	$Z = 4.8501 \times 10^{14} (\sinh 0.01 \sigma_p)^{6.3133}$
8090/Zr	$Z = 2.1069 \times 10^{15} (\sinh 0.01 \sigma_p)^{6.7305}$
8090/Cr/Mn	$Z = 1.4532 \times 10^{15} (\sinh 0.01 \sigma_p)^{7.6292}$

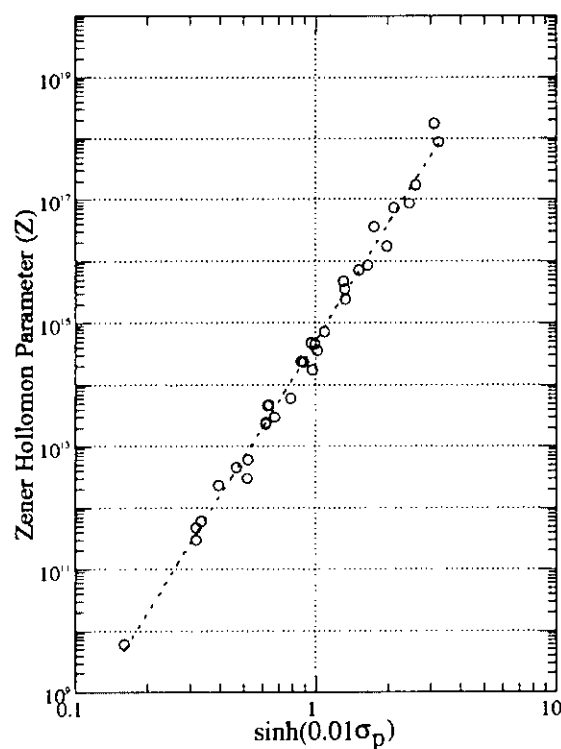


Figure 5. Plot of $\log(\sinh \alpha \dot{\epsilon})$ versus $\log(Z)$ for AF(UDRI).

Determination of Processing Maps

From the flow stress data, processing maps were produced using the approach of dynamic material modeling as described in References 9 through 13. Processing maps for all four alloys tested are shown in Figure 6. These maps show contours of efficiency of power dissipation. The efficiency term describes the portion of total power applied to a material system which is partitioned to metallurgical

processes. Variations in efficiency in temperature and strain rate space can show where processes such as dynamic recovery, dynamic recrystallization, wedge cracking, and phase transformations dominate. Favorable metallurgical processes as well as fracture processes are very efficient for power dissipation, therefore, care must be taken in evaluating these processing maps. Efficiency values for aluminum alloys such as 2024, 7091, and 6061 have been equated with metallurgical processes on a repeatable basis. The Al-Li efficiency values, however, do not correspond with the metallurgical processes on the above mentioned Al alloys. Additional microstructural work on these complex Al-Li alloys will be required to determine what processes dominate the various regions of the processing maps.

Also shown on the processing maps are shaded "Xed" regions indicating processing conditions which give rise to stable material flow. The stability of a material is determined using a Liapunov stability criterion which requires that a system lower its total energy continuously for stability. The "Xed" regions indicate that the material has satisfied several conditions for stability and is considered mechanically and thermodynamically stable in the shaded regions.

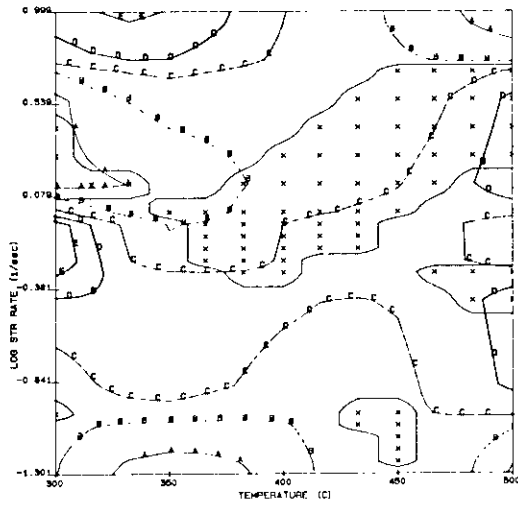
Microstructure

For the two Kaiser 8090 alloys, the as-homogenized structure consisted of nearly equiaxed grains with some residual dendritic growth from the casting process. The grains were relatively coarse, ranging from 100 μm to 300 μm . The 8090/Zr consisted of small δ' precipitates, ~ 50 nm, Al_3Zr with δ' shells, and an indistinctly formed second phase of ~ 200 nm plates. In the as-compressed condition, as well as after solution heat treatment, the grains here pancaked and did neither experience dynamic nor static recrystallization. Distinct subgrain boundaries remained at low angles ($< 10^\circ$) relative to the original grains. Additionally, the specimens remained heavily dislocated throughout the heat treatment process.

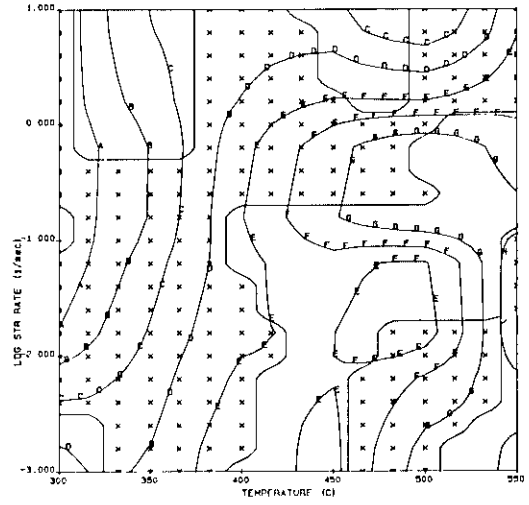
In the case of the 8090/Cr/Mn, the second phase consisted of 1-2 μm dispersoids and the third phase small δ' precipitates. Upon compression the grain structure likewise became pancaked. As in the case of 8090/Zr, there was little to modest evidence that recrystallization occurred after solution heat treatment. Any recrystallization occurring did so nonuniformly from the lowest temperature of deformation, 300°C, and at the higher strain rate

8090/Zr: A=12.5, B=18.4, C=24.2, D=30.1, E=35.9

AF(ML): A=18.2, B=20.4, C=2.7, D=24.9, E=27.1,
F=29.3, G=31.6, H=33.8, I=36.0



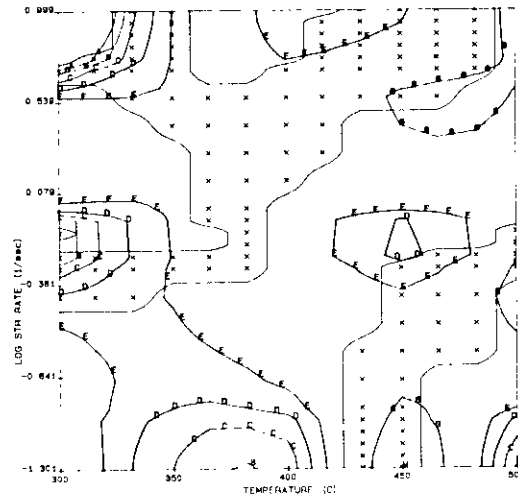
(a)



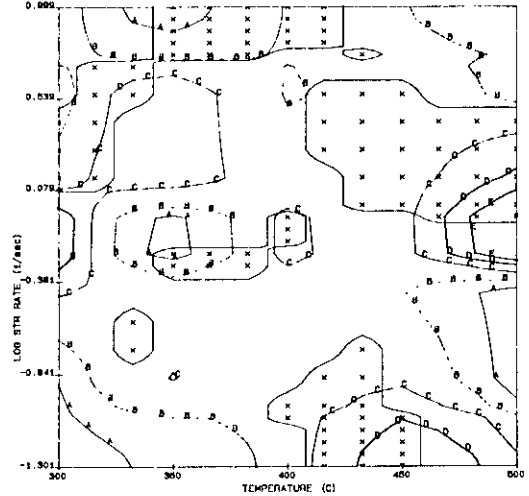
(b)

AF(UDRI): A=0.0, B=5.12, C=10.2, D=15.4,
E=20.4, F=25.6, G=30.7, H=35.9

8090/Cr/Mn: A=9.93, B=18.0, C=26.0, D=34.0,
E=42.1, F=50.1, G=58.1



(c)



(d)

Figure 6. Processing maps for $\epsilon = 0.5$ for the four alloys used in this work. Xed regions indicate the processing conditions for stable metal flow: (a) 8090Zr, (b) AF(ML), (c) AF(UDRI), and (d) 8090/Cr/Mn.

of 5/s. In the compression test there existed some friction between the dies and the specimen ends, $m = 0.2-0.8$, so that the deformation through the specimen was not uniform but varied by as much as $\pm 50\%$ through the thickness. The recrystallization only appeared in the most highly strained region, and even there only nonuniformly.

The Alcoa AF(UDRI) alloy, in the as-homogenized condition, showed very large grains, >1 mm. This coarseness caused problems with attempts to measure pole figures and resulting calculation of orientation distribution functions (ODFs) in both the as-homogenized and as-compressed conditions. Similar problems occurred with the 8090 alloys, but not to the degree observed here. The as-homogenized phase consisted of large, $5-10\text{ }\mu\text{m}$ θ_1 platelets dispersed throughout the structure on the octahedral planes. In the as-compressed condition, while these platelets broke up, there was no evidence of dynamic recrystallization, nor in the case of the 8090 alloys, and the predominant grain configurations were pancake in the highly strained regions and equiaxed in the relatively unstrained regions. Upon solution heat treatment, the AF(UDRI) underwent uniform recrystallization at all strain rates at $300-400^\circ\text{C}$, as evidenced by the development of dislocation free grains, and relatively uniform recrystallization at $450-500^\circ\text{C}$ and high strain rates ($\geq 5/\text{s}$).

The interesting feature of the AF(UDRI) alloy was that when uniform recrystallization occurred, it did so independently of degree of deformation ($\epsilon \geq 0.4$). As can be seen in Figure 3, the region adjacent to the platens did not undergo significant strain for the nominal value of $\epsilon = 1.4$. Figures 7 through 11 are collages of microstructure data consisting of photomicrographs of AF(UDRI) and AF(ML) in the as-homogenized, as compressed condition and after solution heat treatment.

The AF(ML) material behaved similar to the AF(UDRI) alloy under hot compression. Evidence of dynamic recovery was found in most specimens compressed at temperatures greater than 450°C . Figure 8 shows a photomicrograph of the center of a specimen compressed at 550°C and 0.01 s^{-1} . The amount of dynamic recovery increased with increasing temperature; however, at the higher temperature of 550°C , the recovered grains were larger than those at the lower temperatures. In addition, the amount of dynamic recovery was greater at strain rates of 0.01 s^{-1} to 0.1 s^{-1} . A large amount of

wedge cracking was also observed in the specimens tested at 550°C . Since the AF(ML) compression specimens were air cooled, it is not certain if the observed recovery occurred dynamically during deformation. Future compression testing followed by water quenching is planned for validation.

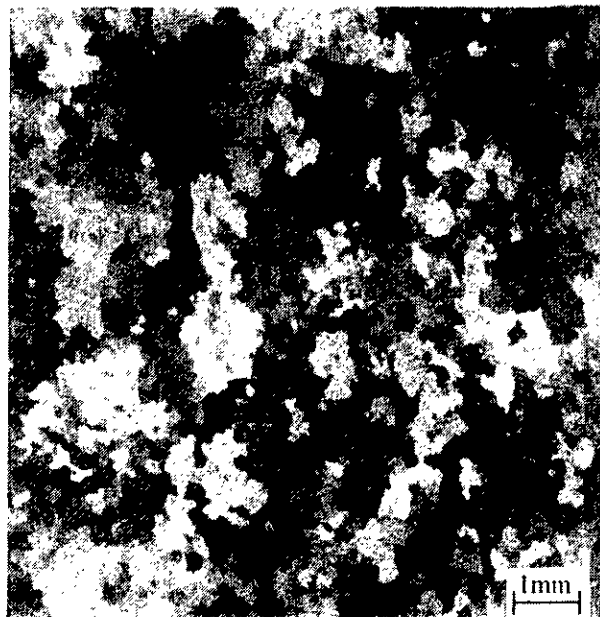


Figure 7. As-homogenized microstructure of the AF(UDRI) alloy.

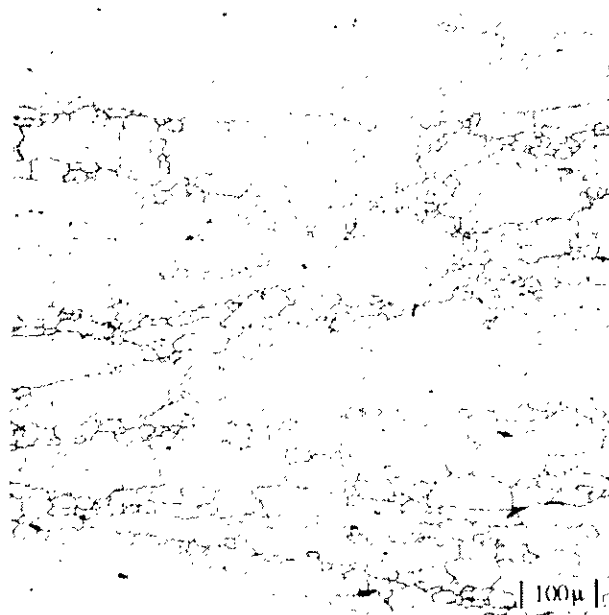


Figure 8. AF(ML) sample compressed at 550°C , 0.01 s^{-1} showing dynamically-recovered grain structure.

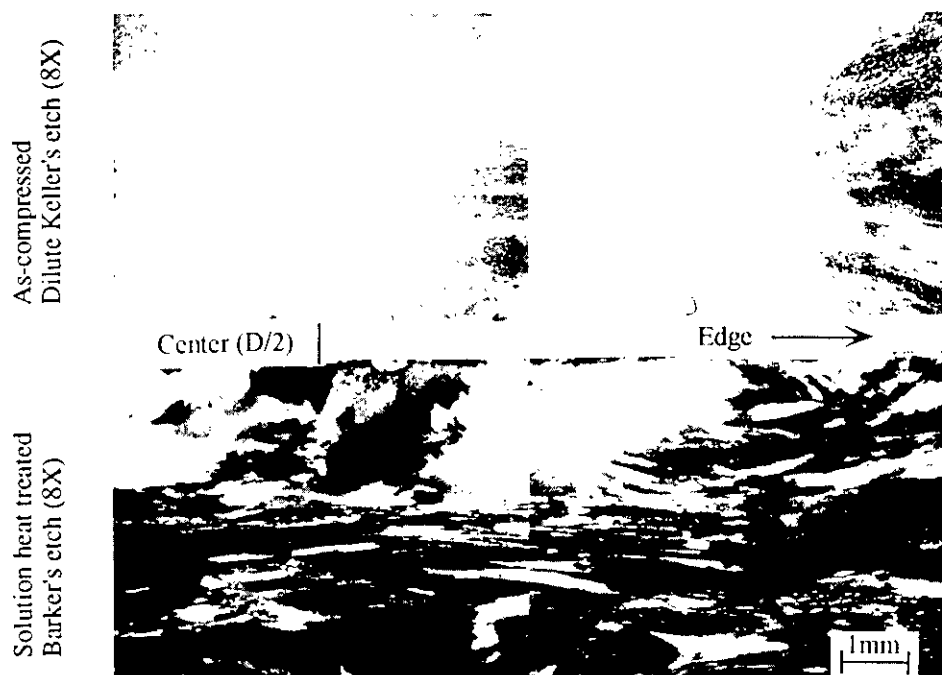


Figure 9. AF(UDRI) sample compressed at $500^{\circ}\text{C}/0.1\text{ s}^{-1}$. Top micrograph is in as-compressed condition and lower is after heat treatment with no recrystallization.

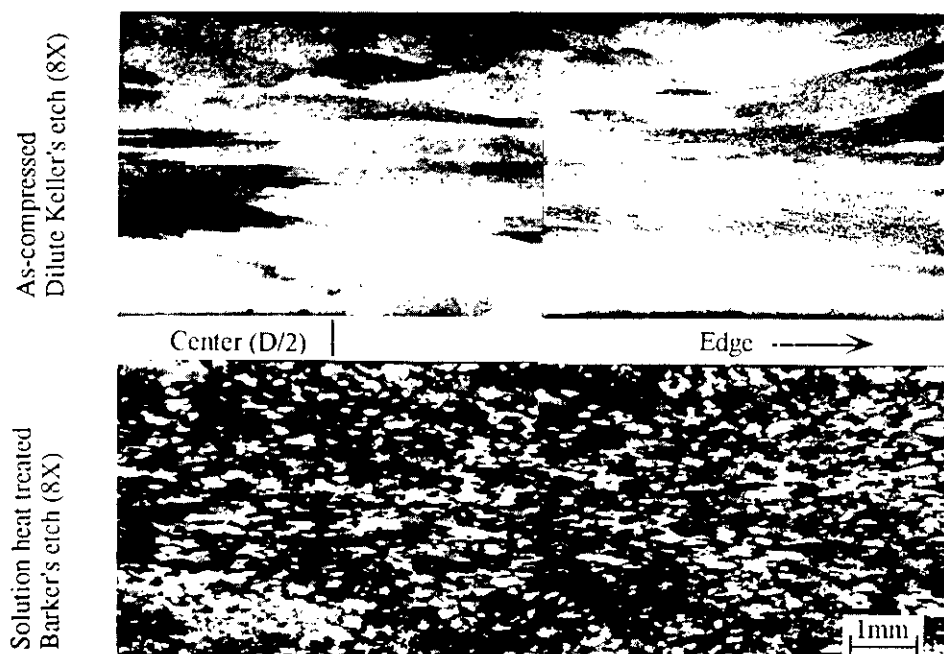


Figure 10. AF(UDRI) sample compressed at $300^{\circ}\text{C}/0.1\text{ s}^{-1}$. Top micrograph is in as-compressed condition and lower is after heat treatment with uniform recrystallization.

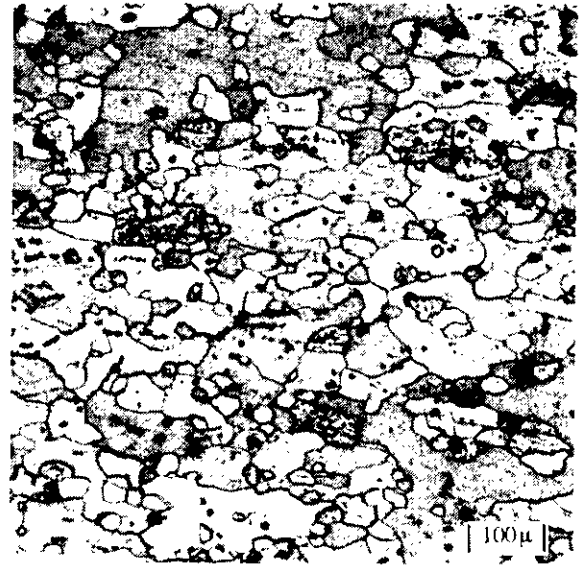
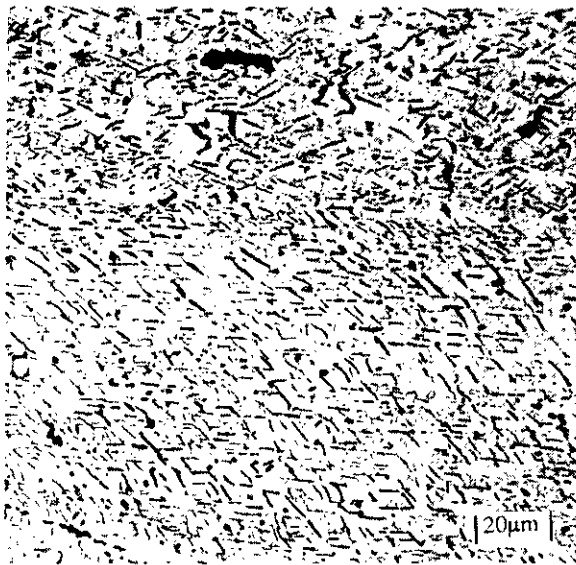


Figure 11. AF(ML) sample compressed at 350°C, 0.1 s⁻¹; left micrograph is in as-compressed condition and right is after heat treatment.

A solution heat treatment of 543°C for one hour and cooling by water quench was given to the AF(ML) compression specimens. The results on these specimens are very much like that of the AF(UDRI) alloy. Uniform recrystallization occurred in the specimens deformed at 300°C and 350°C with nonuniform recrystallization occurring in specimens deformed at 400°C and 450°C, and very little recrystallization in specimens deformed above 450°C. The smallest, most equiaxed recrystallized grains were observed in the specimens deformed at 350°C, resulting in a grain size of approximately 40 microns. Very little, if any, recrystallization was observed in specimens deformed above 450°C. It appears that the dynamically recovered grains discussed earlier have grown and/or consumed some of the smaller grains, thus resulting in a larger grain size of over 250 microns upon solution heat treatment. The strain rate at which the specimens were deformed had very little effect on the solution heat treatment results.

Pole Figures/ODF Calculations

Lambda Research performed pole figure and ODF analysis on all three UDRI alloys used in this effort. They first obtained three pole figures of the as-homogenized alloys. As expected, the pole figures showed a random texture for the 8090 alloys and the randomness ameliorated by the excessive coarse grains of the AF(UDRI) alloy. In the as-compressed condition, they measured the pole figures for the extreme points of the test array (300°C and 500°C,

and 0.05/s and 10/s, respectively) to bound the problem. The 8090 alloys showed some effects of grain coarseness which was reduced by 'turning' the data to impose orthorhombic symmetry on the system. In so doing, in most cases, the artifacts associated with individual grains were reduced and the classic {110} texture seen with uniaxial deformation emerged. The (111), (200), and (220) pole figures and the resulting ODF calculation showed sharpest texture occurring at the correct angles for these planes relative to the (110), i.e., the (110) planes lay parallel to the sample surface. In the case of the AF(UDRI) alloy, the pole figures did not clean up nearly as well as the 8090 alloys because of the severely dominant individual grain artifacts.

When the alloys were solution heat treated, the 8090 alloys retained much of their original texture, thus demonstrating lack of recrystallization, whereas the AF(UDRI) completely changed from a high-intensity, artifact-dominated structure to one of reduced-intensity of artifacts and greater number of low-intensity producing, randomly-oriented grains much like the as-homogenized 8090 alloys.

IV. Current Status

All testing and texture/microstructure analyses have been completed on the compression and torsion samples. Texture and microstructure evolution analysis via use of the viscoplastic finite element model DEFORM[®] using the relatively simple case

of uniaxial compression as a starting point before proceeding to the complex case of rolling, will be conducted.

Alcoa has shown that to achieve relative isotropy in the thermomechanically pressed C-155 with 1.85 w/o Li, they had to take the ingot through a two-step process. In the case of rolling, which the current program addresses, this meant breaking down and rolling the ingot to greater than 50% reduction using a process prescription which would promote recrystallization upon subsequent heat treatment. After this intermediate heat treatment, the plate is hot rolled further to final plate thickness using a prescription which would inhibit recrystallization upon subsequent heat treatment. Thus, a plate with unrecrystallized microstructure would be created which, because of its superior longitudinal properties, found application in those cases requiring this modest anisotropy. In our work in analyzing the behavior of the four alloys, we were not able to find a combination of strain rate and temperature in which recrystallization would occur uniformly and independently of degree of strain in either of the 8090 alloys. This was true even for the 8090/Cr/Mn in which the Zr content was suppressed to enhance recrystallization, and Cr and Mn were added to enhance it. Thus, we have abandoned further consideration of the 8090 alloys of the composition chosen for this effort, and we will continue along the original paths with the AF(UDRI) and AF(ML) alloys with 2.1 w/o Li.

V. Future Plans

UDRI Plans

Alcoa cast two 8.9 cm thick ingots of the 2.1 w/o Li under this effort. They will hot roll these ingots using the Alcoa Technical Center (ATC) reversing mill at the highest roll speed of 12 rpm and at a lay-on temperature of a maximum of 400°C, and take the ingot through enough passes (re-heating as necessary to keep the plate temperature above about 320°C) to an intermediate thickness of 3.2 cm. At this point, they will anneal the plate and quench it. We will take samples from the plate to make texture and microstructure measurements to assess the validity of our recrystallization assumptions. We will also rerun several compression tests on this recrystallized plate to assess any changes from the flow stress data generated on the as-homogenized material. We will also provide this texture and microstructure data to Scientific Forming Technology

Corporation, the process modelers using DEFORM® to begin their analysis of texture and microstructure evolution of the compression and rolling processes.

Alcoa will reheat the 3.2 cm plates and hot roll them to a final thickness of 1.12 cm. (These thicknesses were chosen to accurately model the two-step rolling operation of a 25.4 cm ingot to about 10.2 cm as an intermediate point and then to a final thickness of 3.2 cm, our original goal for subsequent mechanical property characterization.) One plate will be hot rolled to this final thickness (1.12 cm) using the same prescription as for the original ingot, and the second will be hot rolled using a prescription to prevent recrystallization. Texture and microstructure analyses will be performed on both plates.

Alcoa will cast two ingots of the original composition each measuring 40.6 cm x 101.6 cm x 127 cm. The peripheral 7.6 cm will be scalped, to remove inclusions and alloy-rich constituents, to leave a final as-homogenized ingot thickness of 25.4 cm. This latter thickness is the maximum that their ATC mill can handle. These ingots will be hot rolled using the same prescription and sequence as the ingots above, first to an intermediate thickness of 10.2 cm, heat treated, quenched, and re-heated to further hot roll to a final thickness of 3.2 cm along the two aforementioned paths.

Complete mechanical property characterization of both unrecrystallized and recrystallized plates will be performed. This will include tensile, fatigue (constant amplitude, and notch) plane strain fracture toughness (K_{Ic}), and J_{Ic} testing, as well as analysis of the failure mechanism.

AF Plans

Air Force in-house work will investigate texture development during various modes of deformation and subsequent heat treatments. The processing map and constitutive equations will be used to design experiments and analytically model the processes. A statistically designed rolling trial will be performed to determine which parameter, temperature, roll bite, or rolling direction is having the greatest effect on the development of textures. The rolling deformation-zone geometry will also be investigated to determine its effect on the formation of textures. Forge plus rolling and extrude plus rolling processing routes will also be investigated.

VI. Concluding Remarks

The work shows that 8090 alloys do not uniformly recrystallize at any combination of strain rate and temperature. The ALCOA's experimental alloys recrystallized on heat treatment after compression (low temperatures, all strain rates). Therefore these two alloys have been retained for future investigations.

Acknowledgments

Work performed at UDRI was supported by the Air Force Wright Laboratory, Materials Directorate, under Contract F33615-92-C-5914. The Air Force would like to acknowledge Tom Jones, Travis Brown, Joe Brown of Universal Energy Systems, and Bob Wilson, University of Dayton undergraduate student. UDRI would like to thank John Porter, Dennis Buchanan, George Hartman, and M. Vasantha for conducting the tests and developing the software.

References

1. Balmuth, E. S., and Schmidt, R., First International Al-Li Conference, 1980.
2. Quist, W. E., Narayanan, G. H., and Wingert, A. L., Second International Al-Li Conference, 1983.
3. Rioja, R. J., and Graham, R. H., *Advanced Materials and Processes*, Vol. 141, 1992.
4. Dorward, R. C., *Metall. Trans.*, Vol. 18A, October 1987.
5. Thomas, J. F., and Srinivasan, R., Jr. Computer Simulations in Materials Science (R. J. Arsenault, J. R. Beeler, & D. M. Esterling, eds.), ASM International, Metals Park, OH, 1986.
6. McQueen, H. J., Jain, V. K., Hopkins, A. K., Konopleva, G. V., and Sakaris, P., ICAA4, September 1994.
7. Avramovic-Cingara, G., McQueen, H. J., and Hopkins, A. K., ICAA4, September 1994.
8. McQueen, H. G., and Sakaris, P., Proceedings ICAA3, June 1992.
9. Prasad, Y. V. R. K., Gegel, H. L., Malas, J. C., Morgan, J. T., Lark, K. A., Doraivelu, S. M., and Barker, D. R., AFWAL-TR-84-4076 Air Force Wright Aeronautical Laboratories, Wright-Patterson Air Force Base, Ohio, 1984.
10. Gegel, H. L., Malas, J. C., Doraivelu, S. M., and Shende, V. A., *Forming and Forging*, Vol. 14, Metals Handbook (9th ed.), ASM International, Metals Park, Ohio, 1988.
11. Prasad, Y. V. R. K., Gegel, H. L., Doraivelu, S. M., Malas, J. C., Morgan, J. T., Lark, K. A., and Barker, D. R., *Metall. Trans.*, Vol. 15A, 1984.
12. Malas, J. C., "A Thermodynamic and Continuum Approach to the Design and Control of Precision Forging Processes. M.S. Thesis, Wright State University, Dayton, Ohio, 1985.
13. Gegel, H. L., Computer Simulations in Materials Science (R. J. Arsenault, J. R. Beeler, & D. M. Esterling, eds.), ASM International, Metals Park, Ohio, 1987.

Air Force Program for Developing Isotropic Wrought Al-Li Alloys
K. Jata

- Q: Alex Cho (Reynolds Metal Company) Those compression tests, were they uniaxially compression tests?
- A: Yes, they are.
- Q: A.C. - Have you really observed like strong stress component from those samples you have examined?
- A: I don't think so.
- Q: A.C. - I don't think so either. When you roll these alloys you are suppose to have a very strong stress component.
- A: That is right and you don't see that here.
- Q: A.C. - And I don't think you will be able to produce stress components out of the uniaxially compression test. These things don't connect, I don't know what you expect?
- A: I recognize that, yes.
- Q: Mack Roberts - You talked about modeling your process but it wasn't clear to me what kind of data you were collecting and what kind of model you ended up with? And how you analyzed that data to achieve the model?
- A: The rolling model incorporated a finite element code that has been developed by Scientific Forming Technology. Much of that was developed by the Air Force Materials Lab. It is just a finite element code, that's all, that can simulate any kind of working process; whether it is a forging, or an extrusion, or a rolling. Some codes only do 2D some do 3D. The one that has been used on this contract, is a 3D finite element code.
- Q: M.R. - Ok, so then your model was a mathematically derived?
- A: It is a finite element code that takes the thermomechanical history of the material. You just take the rolling mill parameters, you take your work piece parameters and you give the temperatures and some things like that, the flow stress per the compression test, you put all of this as an input and then the model will be able to predict the behavior for sure, but the texture probably not yet.
- Q: M.R. - So the model is a mathematically derived, not an empirically derived model.

- A: It is a mixture of both. It is mathematically derived that describes by finite element analysis the behavior of the part, but the input to the code you have to know what the flow stress versus temperature strain rate and the strain, so that is the empirical portion.
- Q: M.R. - I saw in one case you were showing a quadratic model, is that what you were saying?
- A: That is an equation to obtain the strain sensitivity m , ok, some people put a straight line, and some people put a 3rd degree polynomial.

HIGH STRENGTH Al-Cu-Li ALLOYS FOR LAUNCH SYSTEMS

Authors: Joseph R. Pickens¹

Wm. Troy Tack²

Frank W. Gayle³

Josephine R. Maisano¹

¹Martin Marietta Laboratories • Baltimore

1450 South Rolling Road

Baltimore, Maryland 21227-3898

²Ashurst Corporation

Denver, Colorado

³National Institute for Standards and Technology

Gaithersburg, Maryland 20899

I. Introduction

Aluminum-copper-lithium alloys can be viable candidates for launch systems because of higher strength and lower density compared with conventional aluminum copper alloys, if weldability is demonstrated [1,2]. The Weldalite® 049 family of Al-Cu-Li-Ag-Mg alloys has attained unprecedented strength levels [3-6] and weldability has been demonstrated by numerous welding techniques.[7-11] A major launch system component that could benefit from Al-Cu-Li alloys is the external tank of the space shuttle. This enormous structure houses liquid hydrogen and liquid oxygen thereby making cryogenic strength and fracture toughness primary alloy design criteria. Furthermore, it is critical for a candidate alloy to have higher strength and fracture toughness at cryogenic than at room temperature to obviate an expensive cryogenic proof test. That is, if strength and fracture toughness are higher at cryogenic than room temperature for both parent alloy and weldments, then the tank could be less expensively proof tested at room temperature with confidence that the tank would survive service at cryogenic temperatures.

The present work addresses compositional effects on cryogenic strength and fracture toughness in Al-Cu-Li-Ag-Mg structural alloys (as opposed to weldments). The extrusion product form was selected because process capabilities allow more careful control of thermomechanical processing than multistep rolling or forging. By studying composition effects via extrusions, differences in grain and sub-grain size and recrystallization effects can be minimized. The property targets selected by launch system design engineers in Martin Marietta Space Launch Systems (Denver) and Martin Marietta Manned Space Systems (Michoud, LA) under plane strain conditions are 585 MPa (85 ksi) longitudinal Yield Strength (YS) and 27.5 MPa√m (25 ksi√in) L-T K_{IC} at 25°C with no decrease in either at cryogenic temperatures. For the present study, cryogenic

testing will be performed at liquid nitrogen temperatures (-196°C) with lower temperature tests performed on relevant compositions in other studies at the aforementioned production facilities. Importantly, the present study is a precursor to narrow the composition ranges of interest for subsequent studies on larger extrusions and rolled product in all relevant orientations.

II. Experimental Plan

Experimental compositions of Al-Cu-Li-Ag-Mg Weldalite® alloys were selected based on previous alloy development studies [3-6]. The effect of Cu content on toughness will be reported in another communication. Based on unpublished work, and that of Tack et al.,[6] nominal Cu levels of 4 – 4.5 wt.% were selected for this study. The independent effect of Li content was assessed from 0.7 – 1.8 wt.% and Mg content was assessed from 0.2 – 0.6 wt.%. The amount of the nucleation aid, Ag, and grain refiner/recrystallization inhibitor, Zr, were nominally fixed at 0.4 and 0.14 wt.%, respectively. One available extrusion that has 0.23 wt%Ag and 0.24 wt%Mg was used to provide additional data in the lower Mg regime. The amounts of other alloying elements were held as closely as was possible to isolate Li content and Mg content as independent variables. The alloy compositions as measured by the inductively coupled plasma technique are in Table I.

Each alloy was cast under inert gas atmosphere into 16.5-cm (6.5-in) diameter cylindrical permanent molds at Martin Marietta Laboratories. The billets were homogenized at 454°C (850°F) for 16 h followed by 8 h at 504°C (940°F). They were then scalped to 15.6-cm diameter and extruded at International Light Metals to a 1.9 X 5.1-cm (0.75 X 2-in) rectangular bar at a ratio of 20.2:1. Extrusion parameters were very carefully controlled to minimize grain and sub-structural differences. That is,

extrusion was performed at a nominal preheat temperature of 370°C and a ram speed of 0.25 cm/s (0.1 in/s). Product speed was monitored to ensure fabrication at a constant strain rate.

Table I. Alloy Compositions (wt.%, Balance Aluminum)

Alloy No.	Cu	Li	Ag	Mg	Zr	Ti
1	4.23	0.73	0.40	0.34	0.15	0.02
2	4.28	0.84	0.36	0.41	0.14	0.03
3	3.95	1.03	0.39	0.37	0.14	0.03
4	4.19	1.21	0.37	0.38	0.14	0.04
5	4.00	1.41	0.38	0.37	0.14	0.03
6	3.78	1.81	0.40	0.34	0.15	0.03
7	4.04	0.86	0.38	0.24	0.14	0.03
8	4.28	0.84	0.36	0.38	0.14	0.03
9	4.31	0.80	0.36	0.38	0.14	0.03
10	4.04	0.85	0.38	0.60	0.15	0.03
11	4.38	1.04	0.38	0.38	0.14	0.03
12	3.89	0.87	0.23	0.24	0.14	0.02

Each extrusion was solution heat treated at a near-constant delta (4–7°C) below the solidus temperature for each composition as determined by earlier differential thermal analyses by Montoya et al.[12]. The 6.5-m long extrusions were water quenched to ~25°C within about 4s after removal from the vertical solutionizing furnace. Each extrusion was stretched 6% and artificial aging studies were performed at 143°C. Longitudinal (L) tensile tests were performed at 25 and -196°C according to ASTM E8 at several temperatures along the aging curve. Peak strength at 20°C will be noted when attained, and selected specimens were aged to a 25°C YS of approximately 625 MPa (90 ksi) to compare toughness at a near-constant strength level. Fracture toughness was measured from L-T, fatigue pre-cracked compact tension specimens according to ASTM E399 at 25 and -196°C. Selected microstructures were characterized by transmission electron microscopy (TEM) and fracture surfaces were observed by scanning electron microscopy (SEM).

III. Results

Each alloy extruded readily using the planned extrusion parameters thereby minimizing thermomechanical processing variations. Steady-state extrusion temperatures measured 1m from the die exit using a contact pyrometer were quite similar ranging from 435–445°C (815–835°F). Peak YS at 25°C ranged from a low of 613 MPa (88.9 ksi) for alloy 12 to a high of 703 MPa (102 ksi) for alloy 11 (See Table II). That is, every alloy could attain a 20°C YS of at least 612 MPa [9] which is 27 MPa above the target. Peak strength for the alloys with 0.4 wt% Mg

experiences a broad peak at 1 – 1.3 wt.% consistent with earlier results by Langan and Pickens[5] (See Figure 1). Peak strengths for several alloys not used in the present toughness study are included in Figure 1. The two alloys that contained 0.24 wt%Mg (7 and 12) were not as strong as similar alloys that have 0.4 wt%Mg.

Table II. Peak T8 Strengths For Selected Experimental Alloys

Alloy No.	YS		UTS		εl
	MPa	(ksi)	MPa	(ksi)	
1	613	88.9	629	91.2	9.6
2	676	98.1	683	99.1	8.6
3	669	97.0	674	97.8	8.9
4	690	100.1	696	101.0	7.1
5	663	96.1	665	96.5	2.3
6	645	93.5	649	94.2	2.1
7	631	91.5	649	94.2	8.5
8	672	97.5	684	99.2	10.0
9	679	98.5	686	99.5	9.5
10	662	96.0	668	96.9	8.2
11	703	102.0	705	102.2	8.8
12	612	88.8	631	91.5	8.1

Alloys 1 – 6 were aged to a nominal 20°C YS of 620 MPa to investigate the effect of Li content on toughness at 20 and -196°C. This strength level is underaged for most compositions. Strength at -196°C was typically 745 – 760 MPa (108 – 110 ksi). Toughness increased with decreasing Li content of this Al-4Cu-___Li-0.4Ag-0.4Mg-0.14Zr* alloy series from 1.81 down to 0.73 wt.% Li (Figure 2). The increase in toughness becomes less dramatic below about 1% Li. Toughness at 25°C is almost identical to that at -196°C for each alloy containing Li levels from 1.8 to 1.2 wt.%. Surprisingly, toughness at -196°C is greater than that at 25°C for alloys with Li contents below about 1 wt.%. In any event, each alloy with 1.2 wt.% Li or lower easily exceeded the 25°C strength-toughness goals (585 MPa YS, and 27.5 MPa√m K_{IC}). In fact, the alloys with ≤1.0 wt.% Li had 25°C K_{IC} values of 43 – 50 MPa√m at the 620 MPa YS level. The 1.4 wt.% Li containing alloy was approximately at the toughness goal, and the 1.8 wt.% Li containing alloy did not reach the toughness goal.

Alloys 7 – 10 were aged to the nominal 620 MPa (90 ksi) 25°C YS level to assess the effect of Mg content on toughness. The 0.4-0.6 wt.% Mg-containing alloys displayed 748 – 768 MPa (108.5 – 111.5 ksi) yield strength at -196°C with the 0.24

* wt.%

Al-(3.8-4.4)Cu-Li-0.4Ag-0.4Mg-0.14Zr
6% Stretch
T8 L-Orientation

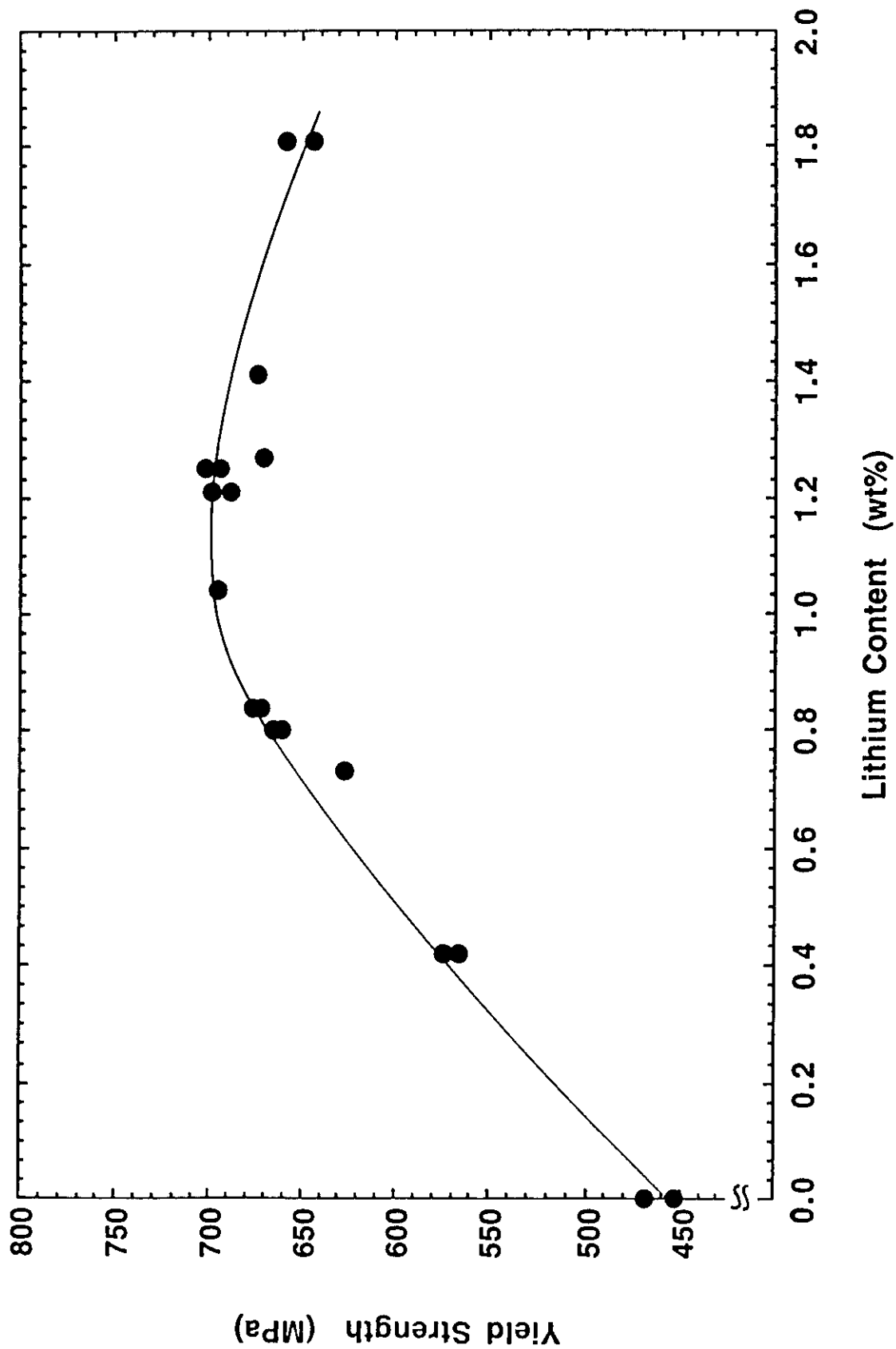


Figure 1. Peak strength of Al-(3.8-4.4)Cu-Li-0.4Ag-0.4Mg-0.14Zr alloys that were solutionized to a near constant delta below solidus temperature for each alloy.

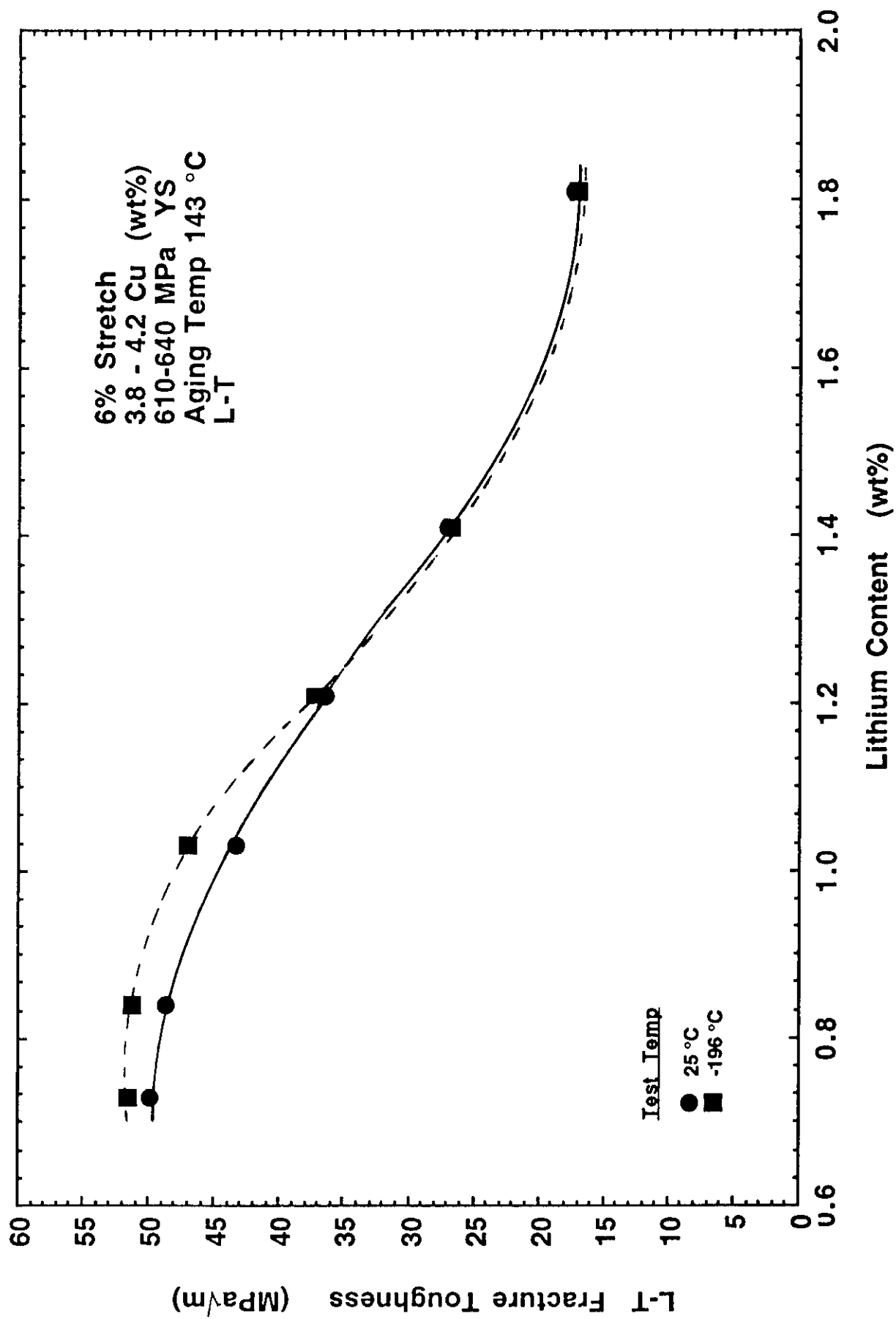


Figure 2. Fracture toughness of Al-4Cu-__Li-0.4Ag-0.4Mg-0.14Zr alloys at 25 and -196°C.

wt.% Mg-containing alloy lower at 726 MPa (105.3 ksi). Although data at ~0.2 wt.%Mg are limited, fracture toughness at 25°C for the alloys with Mg content from 0.34 – 0.6 wt.% are higher than those containing 0.24%Mg for these Al-4Cu-0.85Li-0.4Ag—Mg-0.14Zr alloys (Figure 3). To augment the data at lower Mg content, data for alloy 12, which contains 0.23 Ag and 0.24 Mg has been added to the figure. Note that the two 25°C fracture toughness values at a 0.34 wt%Mg are actually K_Q values, because the data failed the plasticity check. Although the data fall in a wide scatter band at -196°C, toughness is higher at -196°C than at 25°C at each Mg level. Furthermore, all alloys in this Mg study exceed the YS and K_{IC} goals (586 MPa and 27.5 MPa√m, respectively).

Alloys 3 and 11 have essentially the same composition except that alloy 11 has approximately an additional half weight percent Cu. The strength and toughness values at various high-strength aging conditions for these two alloys are compared in Table III. By comparing the data in Table III, it can be noted that the extra 0.43 wt.% Cu enables peak YS to be increased by about 5% (35 MPa or 5 ksi). However, toughness levels are very similar for the two alloys at comparable strength levels. The higher Cu-containing alloy (#11) actually shows essentially equivalent toughness at -196°C and 25°C when aged to the 679 MPa (98 ksi) 25°C YS level.

Table III. Strength-Toughness Combinations for Alloys 3 and 11 at High Strength Levels

	25°C				-196°C			
<u>Alloy 3 (Al-3.95Cu-1.03Li-0.39Ag-0.39Mg-0.14Zr)</u>								
Aging time (h) @ 143°C	YS (MPa)	UTS (MPa)	el (%)	K _{IC} (MPa√m)	YS (MPa)	UTS (MPa)	el %	K _{IC} (MPa√m)
12	585	613	11.8	48.1	711	767	12.3	55.7
13	613	634	10.5	44.5	720	772	9.2	51.2
14	627	645	10.8	43.7	758	802	9.7	47.4
21	651	660	8.8	40.4	794	824	8.5	41.8
60 (Peak)	669	674	8.9	n/a		n/a		
<u>Alloy 11 (Al-4.38Cu-1.04Li-0.38Ag-0.38Mg-0.14Zr)</u>								
Aging time (h) @ 143°C	YS (MPa)	UTS (MPa)	el (%)	K _{IC} (MPa√m)	YS (MPa)	UTS (MPa)	el %	K _{IC} (MPa√m)
8	592	638	11.1	47.2	720	779	14.3	48.7
11	641	663	10.8	37.8	786	817	11.1	44.8
16	679	683	9.0	38.5	772	813	12.2	37.6
24 (Peak)	703	705	9.7	31.2		n/a		

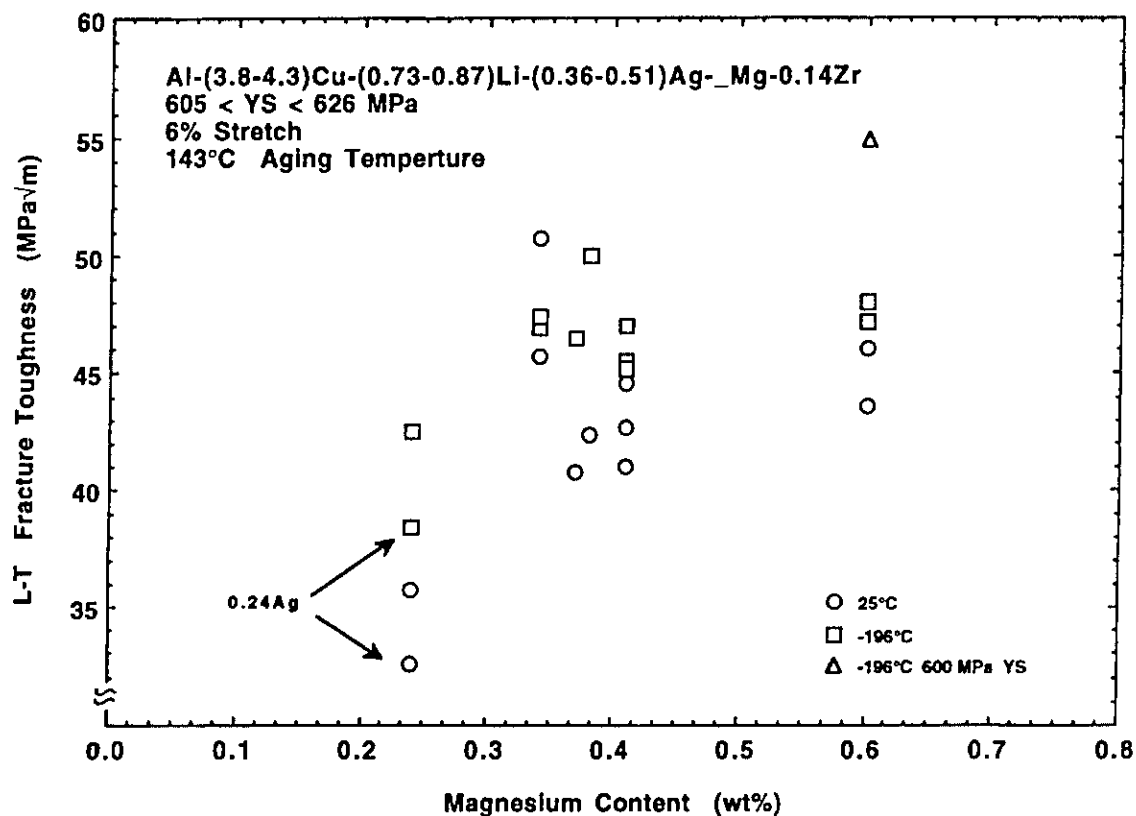


Figure 3. Fracture toughness of experimental alloys at 25 and 196°C as a function of Mg content.



Figure 4. Transmission electron micrograph of alloy 3 (3.95Cu-1.03Li) viewed down a cube axis of the fcc matrix. In this orientation Θ' platelets are oriented horizontally and vertically. S' is indicated by arrows. a) aged 12h at 143°C, b) aged 21h at 143°C.

TEM examination of Alloy 3 (Al-3.95Cu-1.03Li-0.39Ag-0.37Mg-0.14Zr) showed no significant difference in grain boundary precipitation in the two aging conditions. Matrix precipitation in this alloy contains T_1 , S', and θ' , (see Figure 4) as previously shown for this composition range [14, 16, 18]. The increased aging time from 12 to 21 hours resulted in significant increases in T_1 and especially S' precipitation. Perhaps the reduction in fracture toughness ratio (K_{IC} at -196°C + K_{IC} at 25°C ; FTR hereafter) that occurs with increased aging is associated with the increased precipitation of T_1 and S' at the expense of θ' .

Fractography was performed on the toughness specimens for alloy 3 that were tested at room and cryogenic temperature, in two aging conditions: 143°C for 12h (YS=585 MPa), and 143°C for 21h (YS=651 MPa). The room temperature fracture morphology, after aging for 12h (K_{IC} =48.1 MPa $\sqrt{\text{m}}$) consists of ductile microvoid coalescence, with some voids initiating at constituent particles (Figure 5a). There is a minor amount of intersubgranular fracture, e.g., a point A, Figure 5a.

For the same aging condition, tested at -196°C , (YS=711 MPa, K_{IC} =55.7 MPa $\sqrt{\text{m}}$) the failure mode becomes primarily ductile tearing at the grain and subgrain boundaries, with a greater amount of intersubgranular failure with some evidence of fine dimpling at subgrain interfaces (area B, Figure 5b). This suggests a tortuous crack path that is consistent with the high FTR (1.16) in this temper.

Fractography of the compact tension specimen, tested at 25°C , aged at 143°C for 21h (YS=651 MPa, K_{IC} =40.4 MPa $\sqrt{\text{m}}$) reveals a reduction in microvoid size (Figure 5c). At cryogenic temperatures, failure becomes primarily intersubgranular, with discrete areas of constituent particle pull out, and intersubgranular fracture of favorably oriented larger subgrains (Area C, Figure 5d).

Fractography of alloy 11 (Al-4.38Cu-1.04Li-0.38Ag-0.38Mg-0.14Zr aged at 143°C for 8h [YS=592 MPa]) was also performed at both room and cryogenic temperatures. The room temperature failure mode was predominately ductile microvoid coalescence, initiating at constituent particles (Figure 6a). The size, shape and areal fraction of microvoids was qualitatively similar to those seen for alloy 3 at a similar yield strength, which is consistent with the similar toughness values measured (48.1 MPa $\sqrt{\text{m}}$ for alloy 3, and 47.2 MPa $\sqrt{\text{m}}$ for alloy 11).

At -196°C , (YS=720 MPa, K_{IC} =48.7 MPa $\sqrt{\text{m}}$, Figure 6b) the fracture surface exhibits a significant amount of ductile intersubgranular failure, (area A). There also are areas of coarse constituent particle pull out (area B) and some featureless areas suggestive of low energy failure features (area C). Nevertheless, the toughness at -196°C is actually slightly higher than that at 25°C .

Perhaps the ductile intersubgranular features not seen for the 25°C fractures compensate for the lower energy regions.

IV Discussion

The increase in toughness with decreasing Li content for alloys of otherwise similar compositions that are aged at a constant strength level is expected from basic alloy design principles. However, it is interesting to note that most aluminum lithium alloy development after ~1980 involved relatively high Li contents (2 – 2.7 wt.%) so the density benefits accompanying high Li levels could be realized. This is somewhat unfortunate considering that alloy 2020, developed in the late 1950's, attained very high strength at albeit modest toughness levels with 1.1 wt.% Li. The development of Weldalite® 049-type alloys has typically emphasized the lower Li regime with compositions that benefited greatly from relatively small amounts of Ag+Mg as nucleation aids. As shown by Langan and Pickens [5] at higher Cu levels and seen in Figure 1 of the present work, the highest strengths in the Al-Cu-Li-Ag-Mg system are obtained at about 1-1.3wt%Li. Nevertheless, the 1 wt.% Li emphasized in this work is approximately 4 atomic % Li which is far greater than the atomic percentage of the other alloying elements.

The improvement in FTR at lower Li levels is unexpected. We presently do not have an explanation for the improvement seen below about 1.2 wt.%Li at the 620 MPa 25°C YS level. It is difficult to use any one mechanism to explain the fact that fracture toughness and yield strength both increase at cryogenic test temperatures. Tack et al. (6) reported fracture toughness increases at cryogenic temperatures for Weldalite® 049 variants with compositions of Al-4.0Cu-1.5Li-0.4Ag-0.40Mg-0.14Zr and Al-4.0Cu-1.0Li-0.40Ag-0.40Mg-0.14Zr. The higher Li variant (1.5% Li) displayed a fracture mode change from a transgranular shear/microvoid coalescence at ambient temperature to a transgranular shear/intersubgranular fracture at -196°C . However, the fact that fracture toughness is higher at cryogenic temperatures was attributed to the presence of discontinuous intergranular cracking parallel to the crack front. The intergranular cracking was attributed to the heavy grain boundary precipitation of T_1 (Al₂CuLi). The alloy most similar to the Al-4.0Cu-1.5Li-0.4Ag-0.4Mg-0.14Zr alloy in the present work is alloy 5, which with 1.41 w%Li showed no such cracking parallel to the crack front and displayed a flat cryogenic toughness trend. Tack et al.(6) also showed a 19% fracture toughness improvement at -196°C relative to ambient temperature fracture toughness for the Al-4.0Cu-

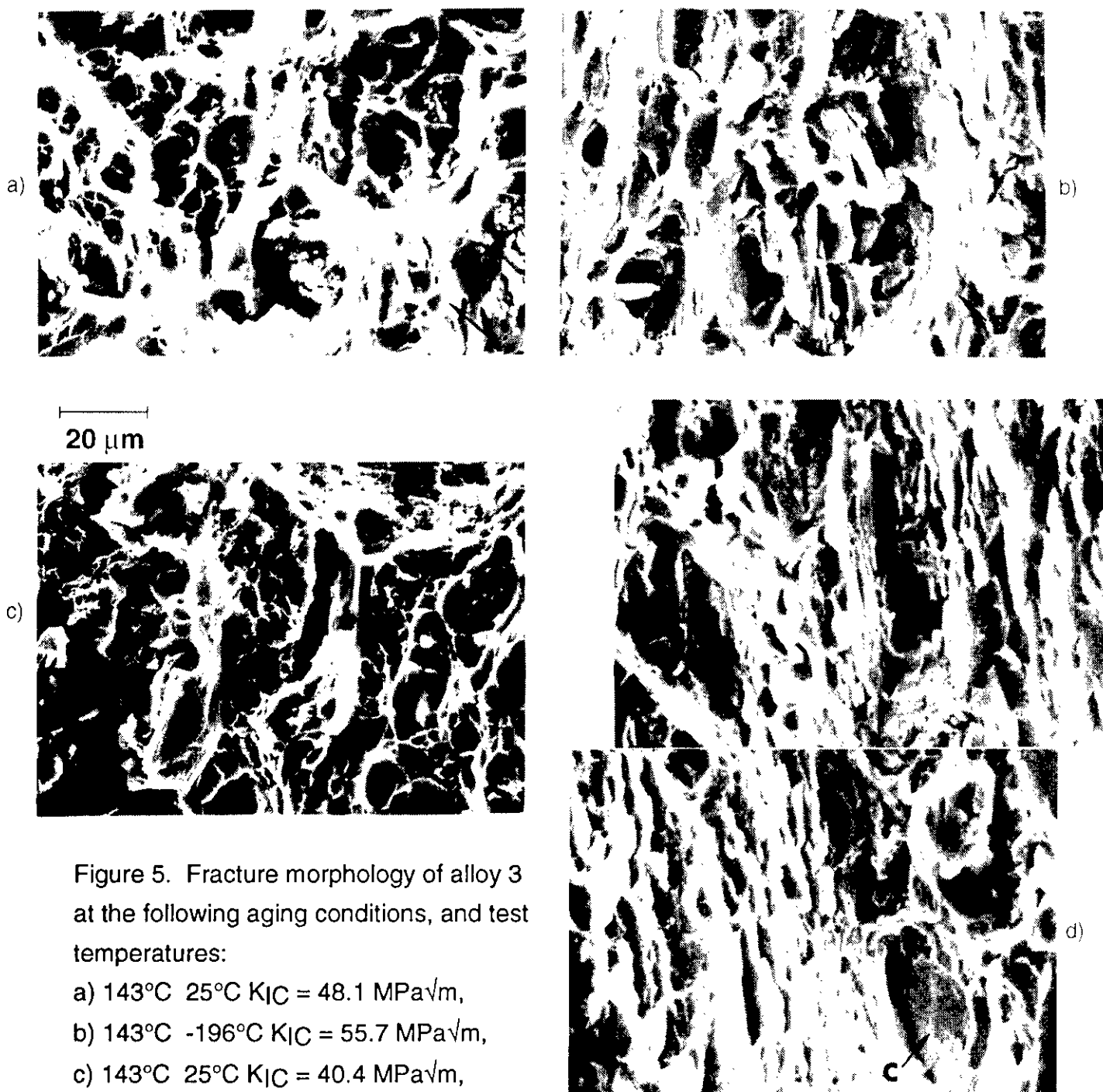


Figure 5. Fracture morphology of alloy 3 at the following aging conditions, and test temperatures:

- a) 143°C 25°C $K_{IC} = 48.1 \text{ MPa}\sqrt{\text{m}}$,
- b) 143°C -196°C $K_{IC} = 55.7 \text{ MPa}\sqrt{\text{m}}$,
- c) 143°C 25°C $K_{IC} = 40.4 \text{ MPa}\sqrt{\text{m}}$,
- d) 143°C -196°C $K_{IC} = 41.8 \text{ MPa}\sqrt{\text{m}}$.

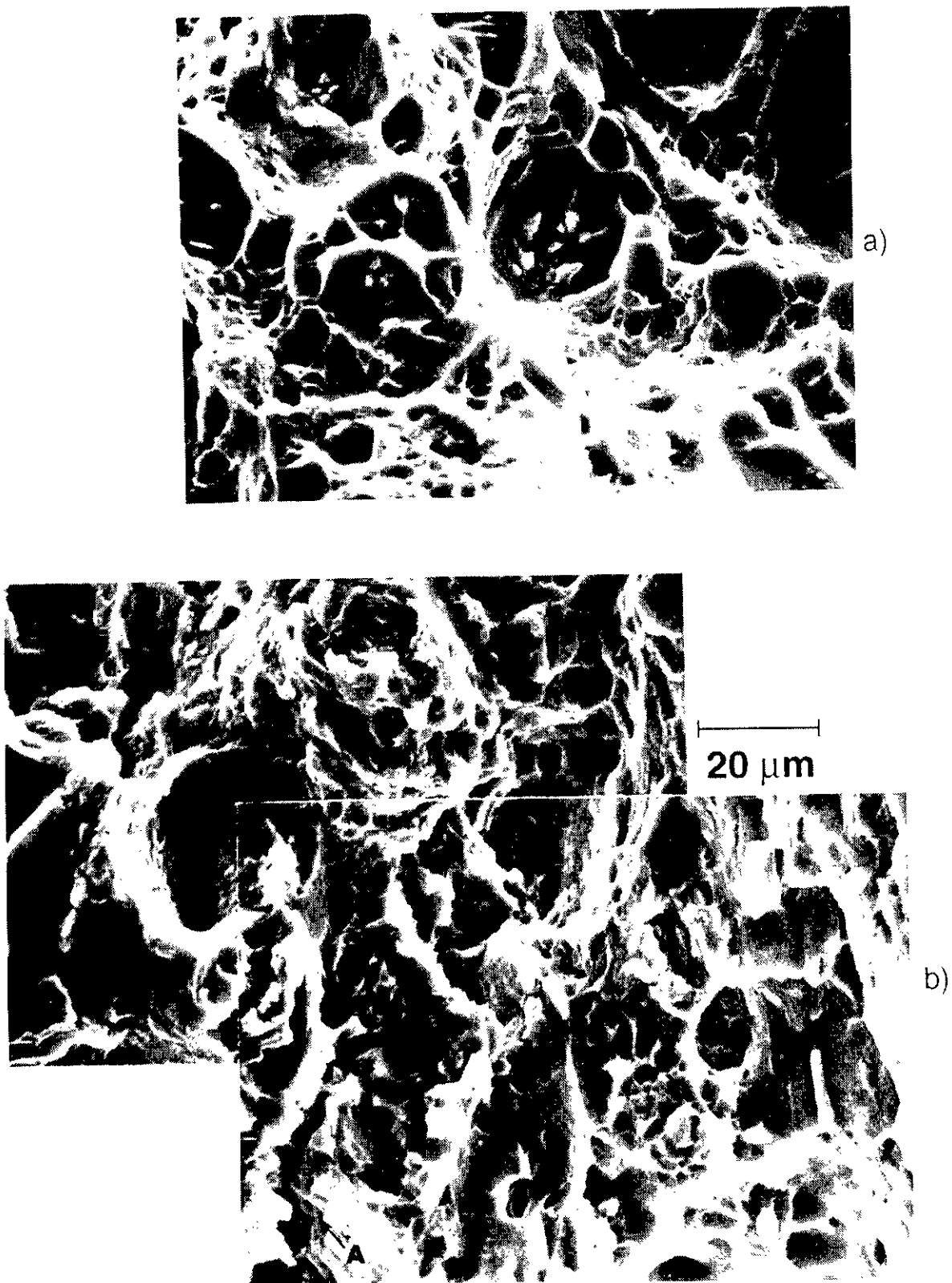


Figure 6. Fracture morphology of alloy 11 at the following aging conditions, and test temperatures: a) 143°C(8h) 25°C $K_{IC} = 47.2 \text{ MPa}\sqrt{\text{m}}$, and, b) 143°C(8h) -196°C $K_{IC} = 48.7 \text{ MPa}\sqrt{\text{m}}$.

1.0Li-0.4Ag-0.4Mg-0.14Zr alloy. This alloy retained a ductile microvoid coalescence fracture mode at -196°C. The alloy is very similar to alloy 3 in the present work, which showed a 14% increase in toughness at -196°C at the 613 MPa YS level. No evidence of "delamination toughening" was observed for this alloy indicating that its high FTR is intrinsic and likely to be realized in thin gage metals as well.

The toughness benefit at 25 or -196°C that accompanies lowering Li content becomes less dramatic as Li content is lowered (See Figure 2). For the 4-4.5 wt.% Cu level, 0.75 wt.% Li offers particularly attractive combinations of strength and toughness -- 620 MPa (89 ksi) YS and 50.6 MPa \sqrt{m} (47.7 ksi \sqrt{in}) K_{IC} at 25°C, which increases to 731 MPa (106 ksi) YS and 52.1 MPa \sqrt{m} (47.4 ksi \sqrt{in}) K_{IC} at -196°C. This Li level in the Weldalite® 049 alloy system offers particular promise for damage-tolerant applications. Although the elastic modulus was not precisely measured in this study, inspection of the stress strain curves for the 0.73 wt.% Li-containing alloy suggests values of Youngs modulus of about 74.5 – 75 GPa (10.8 – 10.9 Msi) and may result from the relatively high volume fraction of T_1 ; a phase whose modulus has been estimated to be 350 GPa.[13]

In parallel work [17], Li contents in the 0.4 – 0.5 wt.% regime have shown particular promise for warm temperature applications because of good toughness after elevated temperature exposure. In addition, strength-toughness combinations at 25 and -196°C are attractive. For example, an Al-4.24Cu-0.42Li-0.36Ag-0.36Mg-0.14Zr alloy attains a peak T8 YS at 25°C of 570 MPa (83 ksi) with K_{IC} of 46.4 mPa \sqrt{m} (42.2 ksi \sqrt{in}). This toughness is lower than the 25°C toughness of similar alloys with 0.7-0.8 wt% Li (Figure 2) at a 9% higher strength level, which underscores the potential of Weldalite® 049-type alloys at the 0.75 wt% Li level. The recommended Li level for cryogenic hardware could be between 0.75 and 1.05wt%, depending on product form and the toughness requirement for the specific subcomponent.

The increase in 25°C toughness at the 620 MPa YS level with increasing Mg content (See Figure 3) is a potentially useful result for damage-tolerant structures. Earlier work by Gayle et al. (14-15) observed S' (Al₂CuMg) precipitation in

similar underaged alloys at the 0.4wt% Mg level with increasing S' precipitation at higher Mg levels.(16) The microstructures of the extrusions in the present Mg study have not yet been characterized. Nevertheless, it is possible that the toughness increase results from increasing S' precipitation, which might homogenize slip. It is also possible that the additional Mg may effect more uniform overall matrix precipitation by increasing nucleation. In any event, weldability at the 0.4 wt%Mg level alloy has been demonstrated (with $\geq 4\%$ Cu) and constrained welding tests for the 0.6 wt%Mg-containing alloy must be demonstrated before this variant could be considered for cryogenic tankage.

The effect of Mg content on FTR is unclear because of insufficient data. Unfortunately, the nominal YS level of 620 MPa was not precisely attained. YS varied from a low of 605 to a high of 626 MPa and it may be difficult to discern small differences in FTR with even this slight variation in YS. The high -196°C toughness point at 0.6 w% Mg (Figure 3) was actually slightly out of this range (600 MPa) but its high value -- 55 MPa \sqrt{m} -- suggests that the higher Mg level warrants further study. In addition, the lower 20°C toughness at 0.24 wt% Mg could actually contribute to a higher FTR at this composition despite the fact that toughness may be lower. Additional data are currently being obtained. In any event, compositions at the 0.4wt% Mg level exceed target strength and toughness goals and, with extensive welding experience[10], is the recommended Mg level at this time for cryogenic tankage applications.

Many of the alloys investigated show particular promise for launch systems. In fact, all but alloy 6 is worthy of consideration. The strength-toughness combinations of alloys 3 and 11 are particularly noteworthy with metallurgical engineers in Martin Marietta plants showing great interest in alloy 3. It is important to realize that the data generated are longitudinal and L-T from extruded bar. The highly stressed orientation in cryogenic tankage is often LT and T-L. Consequently, the data obtained should be used to guide more extensive alloy development work. Additional ambient and cryogenic data on larger extrusions and rolled plate of various gages in L, LT, ST, 45° and L-T, T-L, and occasionally S-L should be generated. These data, coupled with extensive welding evaluations must be performed before an alloy can be used for cryogenic tankage.

V. Conclusions

1. The 25°C L-T fracture toughness of Al-4Cu-__Li-0.4Ag-0.4Mg-0.14Zr Weldalite® 049-type alloys increases with decreasing Li content from 1.8 to 0.7 wt.% at the 625 MPa (90 ksi) T8 yield strength level.
 - Fracture toughness values at 25°C and -196°C are approximately equivalent for each alloy from 1.8 to 1.2 wt.% Li.
 - Fracture toughness at -196°C is greater than that at 25°C for < 1.2 wt.% Li.
2. The 25°C L-T fracture toughness of Al-4Cu-(0.73-0.87)Li-0.4Ag-__Mg-0.14Zr Weldalite® 049-type alloys is higher with (nominally) 0.4-0.6% Mg than with 0.2% Mg at the nominal 625 MPa (90 ksi) T8 yield strength level.
 - Fracture toughness at -196°C is greater than that at 25°C for each Mg level.
3. Many compositions around the Al-4.0Cu-1.0Li-0.4Ag-0.4Mg-0.14Zr nominal composition are capable of displaying higher fracture toughness at -196°C than at 25°C.
4. As expected, all alloys displayed significantly higher strength at -196°C than at 25°C. Every alloy could be heat treated to >612 MPa (88.8 ksi) YS at 25°C.

Acknowledgements

The authors appreciate the technical input of Dr. F. H. Heubaum. This work was sponsored by the Martin Marietta Engineering Technologies Fund, with additional contributions from Dr. Gayle. Use of a trademark in this publication does not signify endorsement by NIST.

References

1. J.R. Pickens: "A Review of the Weldability of Lithium-Containing Aluminum Alloys," L. Mater. Sci., 1985, vol. 20, pp. 4247-4258.
2. J.R. Pickens, "Recent Developments in the Weldability of Lithium-Containing Aluminum Alloys," L. Mat. Science, vol. 25, no. 7, July 1990, pp. 3035-3047.
3. J.R. Pickens, F.H. Heubaum, T.J. Langan and L.S. Kramer, "Al-(4.5-6.3) Cu-- 1.3Li-0.4Ag--0.4Mg--0.14Zr Alloy Weldalite™ 049" Aluminum Lithium Alloys, T.H. Sanders and E.A. Starke, Jr., eds., Materials and Components Pub. Ltd. Birmingham, pp. 1397-1414.
4. J.R. Pickens, F.H. Heubaum, and T.J. Langan, "Design of an Ultra-High Strength Weldable Al-Cu-Li Alloy for Space Applications," Symposium on Airframe Materials in Proc. of 30th Annual CIM Conf. of Metallurgists, Ottawa, Canada, Aug 21, 1991, R.T. Holt and S. Lee Edts. pp 3-27.
5. T.J. Langan and J.R. Pickens, "Identification of Strengthening Phases in the Al-Cu-Li Alloy Weldalite™ 049," Op. Cit. ref. 3, pp. 691-700.
6. W.T. Tack, F.H. Heubaum, F.W. Gayle, and J.R. Pickens, "Weldalite™ 049: Effect of Compositions and Temper on Fracture Toughness Properties," Proc. of the Sixth Int. Conf. on Aluminum Lithium Alloy; Garmisch Partenkirchen, Oct 7-10, 1991, Vol. 1, pp. 409-414.
7. L.S. Kramer, F.H. Heubaum, and J.R. Pickens, "The Weldability of High Strength Al-Cu-Li Alloys," Op. Cit. ref. 3 pp. 1415-1424.
8. L.S. Kramer, C.E. Cross, J.R. Pickens, "The Effect of Compositions on the Weldability of Al-Cu-Li-Ag-Mg Alloys in the High Cu:Li Regime," Ibid, Vol. 2, pp. 1197-1202.
9. L. S. Kramer and J. R. Pickens, "Microstructure and Properties of a Welded Al-Cu-Li Alloy", Supplement to the Welding Journal, April 1992, pp.115-S-121-S.
10. J. R. Pickens, A. Szabo, L. S. Kramer, "Welding of Aluminum-Lithium Alloys", accepted for publication in the ASM Welding Handbook.
11. L. Loechel, et al. Final Report on National Launch System ADP #3106 "Development and Manufacture of Advanced Cryogenic Tank", May 28, 1993.
12. K.A. Montoya, F.H. Heubaum, K.S. Kumar, and J.R. Pickens, "Compositional Effects on the Solidus Temperature of an Al-Cu-Li-Ag-Mg Alloy," Scripta Metall. et Mater., vol 25, 1991, pp 1489-1494.
13. M. E. O'Dowd, W. Ruch, E. A. Starke Jr., "Dependence of Elastic Modulus on Microstructure of 2090-type Alloys" 4th International Aluminum Lithium Conference, G. Champier, B. Dubost, D. Miannay, L. Sabetay eds., Les Editions de Physique Pub, Cedex France, pp C3-565 ff.

14. F.W. Gayle, F.H. Heubaum, J.R. Pickens, "Structure and Properties During Aging of An Ultra-High Strength Al-Cu-Li-Ag-Mg Alloy," in Scripta Metallurgica et Materialia, vol. 24, 1990, pp. 79-84.
15. F.W. Gayle, F.H. Heubaum, J.R. Pickens, op. cit. ref. 3, pp. 701-710.
16. F. W. Gayle, Wm. T. Tack, G. Swanson, F. H. Heubaum, and J. R. Pickens, "Composition and Anisotropy in Al-Cu-Li-Ag-Mg Alloys", Scripta Metall. et Mater. Vol. 30, 1994, pp 761-766.
17. J. R. Pickens, Presentation at HSR Aluminum Base Alloys Workshop, March 9-11, 1994, NASA Langley Research Center, Langley, VA.
18. F.W. Gayle, W.T. Tack, F.H. Heubaum, and J.R. Pickens, "High Toughness, High Strength Aluminum Alloy: Design and Practice,"Op. Cit. ref. 6, Vol. 1, pp. 203-208.

High Strength Al-Cu-Li Alloys for Launch Systems
Joseph R. Pickens

Q: How do you control so accurate that you can control the composition variation?

A: Reynolds have done a very fine job in controlling the composition of most of the alloying elements. They have done a fine job in copper and lithium and I believe of late there were some variations in zirconium content but I think they have a good handle on that.

Q: What about the Mg.

A: Mg is important. We find that we get very good strength properties if you are above about .33 up to about .45; careful control of Mg content is really not a problem, because there is a fairly wide window. The concern that we have, and Attila and I have been trying to run the experiment, is to look at the higher magnesium levels and see if there is a weldability penalty as you go higher.

Q: Have you done any work concerning the high Mg content and the possibility of eliminating the silver?

A: Yes, we have done some studies eliminating the silver. As you know from the 3rd of a million dollars spent between Alcoa and Martin Marietta on that senseless patent battle, there are some very good Al-Cu-Li-Mg, weldalite alloys that do not have silver. They are patented, and Reynolds is licensed to produce them. I think there are some jewels just waiting to be developed but it is a matter of money. Basically, you can take any alloy I have here and come within 5 percent of the strength and toughness properties by taking the silver out. My comment earlier that the magnesium is more potent nucleation aid than the silver, is a manifestation of that, if you take some of these alloys and you take the silver out you will pay maybe a 5 percent hit in strength and then you will see a toughness hit that is about twice as big as I showed on that one slide. In fact, at the HSCT meeting a few months ago I did show some comparisons of silver versus no silver in Al-Cu-Li-Mg weldalite alloys. Silver containing alloys are tougher, it is worth paying the extra 20 cents a pound you pay for the silver. However, for specific applications there may be some winners among the Ag-free alloys.

Q: John Newman (Alcoa) I had a question about your composition. If you are looking at different plate gages, should you look at different zirconium levels?

A: I certainly would. I know that Reynolds is looking at that now because there has been some variation in properties in different plate gages and although, I have not been at all of the recent NASA-Martin Marietta-Reynolds meetings, I believe Reynolds are assessing the possibility of using different Zr levels for different gages of plate. I

have always argued in the past that we generally find better fracture toughness in a unrecrystallized microstructure. However it seems to me that with different orientations in service, what if you could introduce a controlled amount of 5 or 10 percent recrystallization to make the crack path more difficult? So there may be some gages where you might want to drop the Zr a hair to do just that. You'll likely get to the point where you need a very carefully controlled plant practice: but I think it is doable.

Q: Eui Lee (Navy) I have few short questions, first I think to use this alloy for a support skirt or like that extrudibility is very important; but extrudibility will not be as good as 6063. What kind of extrudibility do you expect?

A: That is a good question for the 2 applications, the bicycle tubes and hockey sticks, that Anodizing Inc. are pursuing. They were using low tech alloys such as 6061 and the key was that they were extruding through a ported die and the material would have to self-weld and form a good seam when it came out of the die. They were not piercing and extruding over a mandrel. They needed higher strength than you could attain through the conventional alloys. They tried 7178, which was probably the highest strength conventional aluminum alloy, as you might expect alloy 7178 would not self weld when it went through the die. Weldalite 2094 came around and the first time they got beautiful self welds. So that is why 2094, is of interest for ported-die, high strength extrusions.

Q: E.L. - The other one is anodizing is also important, what are the characteristics of anodizing?

A: I am glad you asked that. I made some M16 rifle receiver forgings from weldalite 2094 and went to a vendor who used the anodizing procedure actually developed by Martin Co. in the 50's. The vendor used the same parameters they use for 2014. The experienced technician turned the knob a little bit this way and a little bit that way; we got beautiful anodized surfaces on the receiver forgings.

Q: Eui Lee (Navy) The Navy used a lot of like investment castings for small parts. Have you considered using this alloy as for casting application?

A: Absolutely. You know the name weldalite*. I made up that name as a tongue-and-cheek joke because other Al-Li alloys not designed for weldability were called Alithalite*, Lital*, or Lockalite alloys. I made a casting variant and called it castalite A+ in an internal Martin Marietta meeting, I showed some really promising properties for some cast variants at about the 4 copper, 1 lithium levels and then I added analling elements to improve fluidity. Everyone in Martin Marietta who was looking at castings said, "where can I buy castalite; I would like to use some." Then I informed the potential users that they would have to pay money to develop castalite. Nobody wanted it that badly.

- Q: In the low lithium alloys, do you find delaminations in the high fracture toughness samples?
- A: No, that is what is so nice about these alloys. In the lower lithium regime you inherently get lower delamination tendency than in the higher regime but, in addition, I think the silver and the magnesium enables the solute to be grabbed by strengthening precipitates quicker than they might otherwise be; particularly with the 6 percent stretch. The Ag + Mg may be why we did not see delamination in the lower lithium levels.
- Q: So you get better fracture properties, without delamination?
- A: Yes, in fact as Troy Tack pointed out early on, the high toughness is intrinsic to the weldalite[®] alloy system if you make the material right. The toughening mechanism does not rely on delamination toughening.
- A: Troy Tack (Ashurst Corp.) We did do some weldalite alloy variations in a much larger study than this and found that in the higher lithium containing alloys. We could induce delamination toughening at cryogenic temperatures. In fact we have a paper in the Aluminum Lithium VI proceedings that shows that behavior. But what happens when you get to the thin gages use, for example, on the external tank, delamination toughening, will hurt fracture toughness. In fact, another paper in the proceedings, regarding 2090 fracture toughness shows that it is actually worse than 2219 in thin gages when you test wing surface crack tension geometry. Martin Marietta is now using the leaner Li-containing alloy because of the intrinsic toughness mechanism and that buys you better toughness in thick gages as well as thin gages.
- A: To amplify Troy's point, this composition right here at 1.5 weight % Li, showed high toughness when it delaminated, and lower toughness when it did not delaminate. I am not exactly sure what is different about how we made that alloy. By making the alloy "wrong", we can get the inflated toughness by delamination around a percent and a half lithium.
- Q: I think yield strength was about 100 ksi on that one.
- A: That too.
- Q: Po Chen (IITRI) I got a question regarding the previous viewgraph you put on. Could you put it on again. Lithium, when the lithium goes lower to 1.0 or 0.8 percent, can you relate the change in fracture toughness to microstructure in terms of like a volume fraction of precipitation, or the type of precipitate or something like that?
- A: Would love to but have not had the program to do it. I would like to do just that. I did my thesis on quantitative metallography, and I think there is some very interesting

work that could be done here but I have not yet done it.

Q: P.C. - So we have not gone through that stage?

A: Let me throw something out at you. If we go a little bit lower lithium, from the limited data I have, toughness seems to go down a little bit. Eventually, you decrease Li so much that you get to a point where you cannot reach the 90 ksi level and you also start to lower toughness.

Q: P.C - How about the ratio? The cryogenic toughness to ambient toughness ratio? Does the ratio go down or go up?

A: I can't comment on whether the ratio increases or decreases because I do not have enough data. Nevertheless, the ratio is still greater than one.

Q: John Meheilich (Commonwealth) When you reduce the lithium content you reduce the stiffness. How much of does this impact the design of the cryotank? Is the tank stiffness limited, yield strength limited, or both?

A: Well, that is a question for our designers. The modulus of these weldalite[®] alloys is still higher than you might think based on Li content because of the high volume fraction of T₁. In fact I went back and read some of Ed Starke's old papers because I thought this would come up. In my previous recollection of this paper. I thought the estimated modulus of T₁ was about 170 GPA but I went back and checked and I think Ed said it was 350 (in the work with Dowd and Wolfgang). So you seem to get more bang for your buck with T₁ than you do with delta prime so you do not quite have as bad of a modulus penalty at lower Li levels as you might otherwise. My guess is the modulus around here is about 10.8 or 10.9 Msi. In terms of the design question our guys were designing primarily to exploit the higher strength but these are quantifiable weight savings for increased stiffness.

ULTRA-LOW DENSITY, HIGH STIFFNESS Al-Li-X ALLOY FOR AEROSPACE STRUCTURAL APPLICATIONS

D.L. Yaney
Research and Development Division
Lockheed Missiles and Space Company, Inc.
Palo Alto, CA 94304

Abstract

An Al-Li alloy with nominal composition Al-5Li-0.2Zr (wt.%) has been successfully produced by spray casting and subsequently processed by forging, rolling and spinning operations into two 76 cm diameter domes (partial hemispheres). Prior to full scale processing, sub-scale metal working trials were performed in order to identify appropriate conditions for each thermomechanical processing step. Sub-scale processed material was also used to evaluate different aging treatments. Following full scale processing, the 76 cm diameter domes were solution heat treated at 843 K, glycol quenched, stabilized in liquid nitrogen, up-quenched using hot water and aged for 16 hrs. at 423 K. Optical microscopy was used to characterize the microstructure of the full scale domes. Tensile and short bar fracture toughness tests were performed in a variety of locations and orientations at both 296 and 77 K in order to provide a data base of key mechanical properties. The specific heat, thermal conductivity and thermal expansion coefficient of the heat treated domes were also measured over the temperature range of 77 to 296 K. The processed material was determined to be easily weldable using procedures previously developed for Al-Li alloy 8090.

1. Introduction

Because of their low density and high stiffness, Al-Li alloys are attractive materials for numerous aerospace applications. Currently, Al-Li alloys produced by conventional direct chill (DC) casting are limited to lithium contents of approximately 2.5 wt.%. Beyond this level, difficulties are encountered in producing sound, high quality ingots that do not contain coarse second phase particles at grain boundaries. As shown by Anyalebechi, Talbot and Granger [1], lithium dramatically increases the solubility of hydrogen in both liquid and solid aluminum. Thus, as lithium content increases, it becomes increasingly difficult to degas the melt so that the remaining hydrogen will not adversely affect the ductility and fracture toughness of the material. Because of the slow cooling rates associated with DC casting, the amount of zirconium

that can be successfully added to the melt to control grain size and retard recrystallization is limited to a maximum of 0.16 wt.% [2]. Above this amount, zirconium reacts with aluminum to produce large, needle-like particles of equilibrium tetragonal Al₃Zr rather than the fine spherical particles of metastable cubic Al₃Zr.

In order to overcome the problems associated with DC casting of Al-high Li alloys, some researchers [3-6] have turned to the use of Rapid Solidification Processing (RSP) to produce these materials. The high cooling rates associated with RSP suppress the formation of large particles along grain boundaries and refine the grain size. High cooling rates also permit higher zirconium concentrations to be used without the formation of tetragonal Al₃Zr [6]. Unlike Al₃Li (δ'), the primary strengthening phase in Al-Li alloys, cubic Al₃Zr is resistant to shear by dislocations [7]. In Al-Li alloys with high zirconium contents, the tendency toward planar slip is reduced leading to improved ductility [8].

Despite the advantages of producing Al-high Li alloys by RSP, numerous steps are typically involved in producing a consolidated product from RSP powders or ribbon. As a result, RSP materials are not economically competitive with similar materials produced by more direct methods such as DC casting. Another disadvantage of RSP, especially as applied to Al-Li alloys, is that the complex Al-Li oxides inevitably present on the surface of powders are often retained in the consolidated product as stringers or a semi-continuous network along prior particle boundaries [3,6]. The oxides serve as preferred sites for crack initiation resulting in an alloy with less than optimum ductility and fracture toughness. Also, because of the hydrated nature of the Al-Li oxide films, the hydrogen level of the alloy can be adversely increased [9].

In recent years, spray casting has been shown to be an effective method for producing Al-Li alloys with lithium contents in excess of 2.5 wt.% [9,10]. Spray casting combines many of the advantages of RSP and DC casting into a single technique. Cooling rates are

on the order of 10^2 to 10^4 K/s not as rapid as with RSP, but sufficient to produce significant microstructural refinement and to suppress the formation of some types of second phase particles. Oxide films are eliminated and the production rates are intermediate to those associated with RSP and DC casting.

To date, Al-Li alloys with lithium contents up to 4 percent have been successfully produced by spray casting [9]. In the present paper, it is demonstrated that an alloy with nominal composition Al-5Li-0.2Zr can be successfully produced by spray casting and subsequently processed by forging, rolling and spinning operations into an end dome typical of those used in 200 liter space flight dewars. Following heat treatment, such a dome is shown to exhibit an acceptable combination of mechanical properties including strength, ductility and fracture toughness. The alloy investigated, with a density of 2.35 g/cm^3 and an elastic modulus of 86.2 GPa, is 17 percent less dense and 17 percent stiffer than aluminum alloy 2219.

II. Experimental

A. Material and Processing

Two spray cast Al-Li alloys, both produced by the COSPRAY Products Division of Alcan International, were investigated: (a) Al-4.99 wt.%Li-0.08 wt.%Zr and (b) Al-5.11 wt.%Li-0.17 wt.%Zr. Hot isostatic pressing (HIPping), when performed on the Al-5.11Li-0.17Zr alloy, consisted of heating for 6 hours at 823 K and 103 MPa. For the Al-4.99Li-0.08Zr alloy, a HIP cycle of 6 hours at 843 K and 103 MPa was used. All sub-scale metal working trials were performed on 44.5 mm dia. x 114 mm L. cylinders machined from the HIPped Al-4.99Li-0.08Zr alloy. A list of sub-scale processing steps is given below.

- (1) uniaxially forge, 63% reduction at 773 K
- (2) round roll ($0^\circ, 90^\circ, 45^\circ, 135^\circ, 0^\circ, 90^\circ \dots$), 63% reduction at 773 K
- (3) single rolling pass, 10% reduction, at 673 K

A portion of the sub-scale processed material was solution heat treated at 848 K, water quenched, and aged for either 16 or 96 hours at 423 K.

Two full scale (76 cm dia.) end domes were fabricated from the as-spray cast Al-5.11Li-0.17Zr alloy. The steps involved in full scale processing are given below.

- (1) Cut 159 mm thick x 277 mm dia. section from trimmed billet
- (2) 3-axis forge at temperatures between 673 and 773 K to yield 406 x 406 x 57 mm plate
- (3) Cross roll at temperatures between 673 and 773 K to yield 787 x 787 x 16 mm plate
- (4) Cut 762 mm diameter disc from plate and spin form to final configuration at temperatures ranging from 673 to 773 K.

Following spin forming, the domes were solution heat treated at 843 K, glycol quenched, immersed in liquid nitrogen, upquenched using near 373 K water and then aged for 16 hours at 423 K.

B. Testing and Evaluation

In order to provide a basis for subsequent evaluation of thermomechanically processed material, tensile tests were performed on HIPped sections of the Al-5.11Li-0.17Zr alloy that had been solution heat treated at 848 K, water quenched and aged for 16 hours at 423 K. A strain rate of $1 \times 10^{-4} \text{ s}^{-1}$ was used for all tests. Radial, circumferential and longitudinal orientations were evaluated.

Tensile tests ($\dot{\epsilon} = 1 \times 10^{-4} \text{ s}^{-1}$) and short bar fracture toughness tests were used to evaluate sub-scale processed material. Tests at 77 and 296 K were performed on as-processed material as well as on materials that had been solution heat treated and aged. Both radial and circumferential orientations were used for the tensile tests. For the short bar fracture toughness tests, LC and LR orientations were evaluated.

Tensile tests ($\dot{\epsilon} = 1 \times 10^{-4} \text{ s}^{-1}$) and short bar fracture toughness tests were also used to evaluate one of the heat treated domes. Radial and circumferential orientations were used for the tensile specimens. In one set of tests, the radial and circumferential directions were each parallel to one of the two rolling directions. In a second set of tests, the radial and circumferential directions were at an angle of 45 degrees with respect to the two rolling directions. Short bar fracture toughness tests were conducted in the LC, LR, RC, and CR orientations. Radial and circumferential directions were each parallel to one of the two rolling directions.

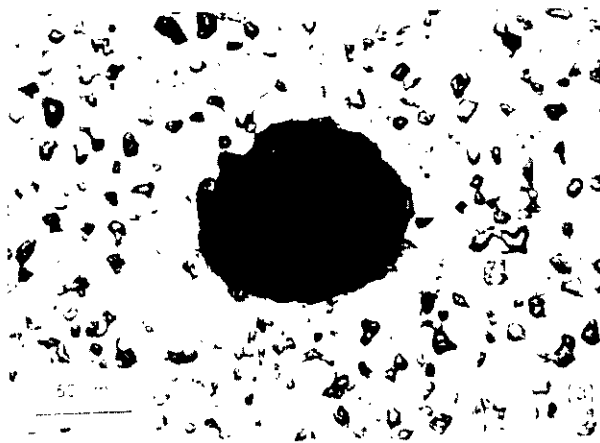
Thermal properties of the heat treated domes including coefficient of thermal expansion, specific heat and thermal conductivity were measured over the temperature range of 296 to 77K. All measurements were made at the Thermophysical Properties Research Laboratory at Purdue University.

In order to evaluate the weldability of the heat treated domes, test panels (102 x 102 x 95 mm) with a double J-groove weld joint design were gas tungsten arc welded using NG61 + 0.15 Zr filler metal. Sub-scale Charpy specimens (55 x 10 x 0.7 mm) were cut from the welded test panels and impact toughness was measured as a function of position with respect to the weld centerline. Charpy impact tests were performed at both 77 and 296 K.

III. Results

A. As-Spray Cast and Hipped Materials

An optical micrograph (longitudinal cross-section) of the as-spray cast Al-5.11Li-0.17Zr alloy is shown in Figure 1(a). Spray cast materials typically contain from 1 to 3 percent residual porosity. Pores vary in size with the largest having diameters of approximately 100 μ m. An optical micrograph of the same alloy after hipping for 6 hours at 823 K and 103 MPa is shown in Figure 1(b). Porosity is completely eliminated and some of the equilibrium δ phase (AlLi), originally present almost exclusively at grain boundaries, has re-precipitated as small particles within the grains. HIPing retains the fine uniform grain structure characteristic of spray cast materials. Both materials have a grain size of approximately 50 μ m.



The microstructural uniformity inherent in spray cast materials is further illustrated by the fact that the tensile properties of a hipped, solution heat treated and aged Al-5.11Li-0.17Zr alloy do not vary appreciably with respect to orientation within the original billet (Table I).

B. Sub-Scale Metal Working Trials

As discussed in the Introduction, one of the primary goals of this investigation was to demonstrate that an end dome for a typical 200 liter cryogenic tank can be successfully fabricated from a spray cast Al-Li alloy with nominal composition: Al-5Li-0.2Zr. However, in order to provide a better initial understanding of the alloy's elevated temperature deformation behavior, sub-scale processing trials were performed. A complete description of the steps involved in the sub-scale processing trials was given previously in the Experimental section. It should be noted that the purpose of the final 10 percent rolling pass at 673 K was to simulate the type of reduction expected during spin forming of the full scale dome. No problems were encountered with any of the sub-scale metal working operations. Portions of the sub-scale processed material were subsequently solution heat treated at 848 K, water quenched and then aged at either 16 or 96 hours at 423 K in order to evaluate the effect of aging time on selected mechanical properties.

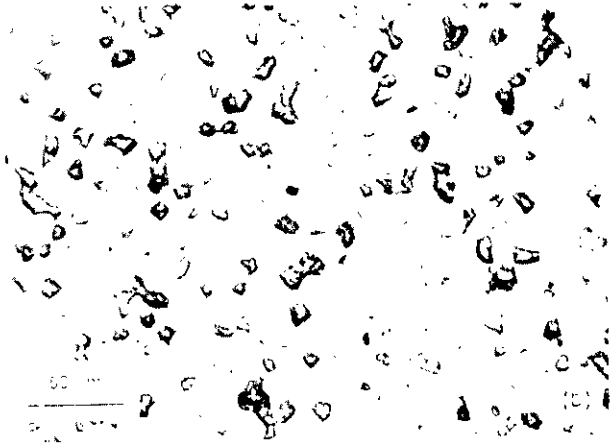


Fig. 1. Optical micrographs of polished and etched, longitudinal cross-sections of: (a) as-spray cast and (b) HIPped (6hrs. at 823 K and 103 MPa) Al-5.11Zr-0.17Zr alloy. Note large pore in center of as-spray cast structure. Dark etching phase is the equilibrium δ phase, AlLi.

Table I. Tensile Properties of an Al-5.11Li-0.17Zr Alloy Following HIPping (823 K, 6 hrs., 103 MPa), Solution Heat Treatment (848 K), Water Quenching and Aging (16 hrs. at 423 K).			
Orientation	Yield Strength (KSI)	Ultimate Strength (KSI)	Percent Elongation
Radial	35.4	40.6	1.8
Circumferential	36.4	40.4	1.6
Longitudinal	37.0	41.0	1.2

At first glance, it might be thought that a higher aging temperature, with its associated shorter aging time, might be preferred on the basis of lower production costs. However, Palmer [11] has shown that for equivalent yield strength values in an Al-4Li-0.2Zr alloy, aging at 423 K instead of 443 K results in higher ductilities (approx. 1%) and ultimate tensile strengths (3-25 MPa). Since it was anticipated that an Al-5Li-0.2Zr alloy would have a similar response, an aging temperature of 423 K was used throughout this study.

The results of room temperature tensile tests are shown in Figure 2(a). The data points for zero aging time correspond to thermomechanically processed material prior to solution heat treatment and aging. Despite the relatively low aging temperature, strength initially increases quite rapidly with increasing aging

time. However, beyond 16 hours, little change is observed. As expected, the observed increase in strength with increasing aging time is accompanied by a simultaneous decrease in ductility.

In Figure 2(b) apparent fracture toughness is plotted as a function of aging time at 423 K. Despite its high ductility, the as-processed material, prior to solution heat treatment and aging, displays the lowest fracture toughness. In this condition, however, the yield strength of the alloy is also quite low. Crack initiation in the short bar specimens is associated with extensive crack tip plasticity. Thus, as can be seen in Figure 2(b) increasing the strength of the matrix by aging, is able to increase the apparent fracture toughness of the material.

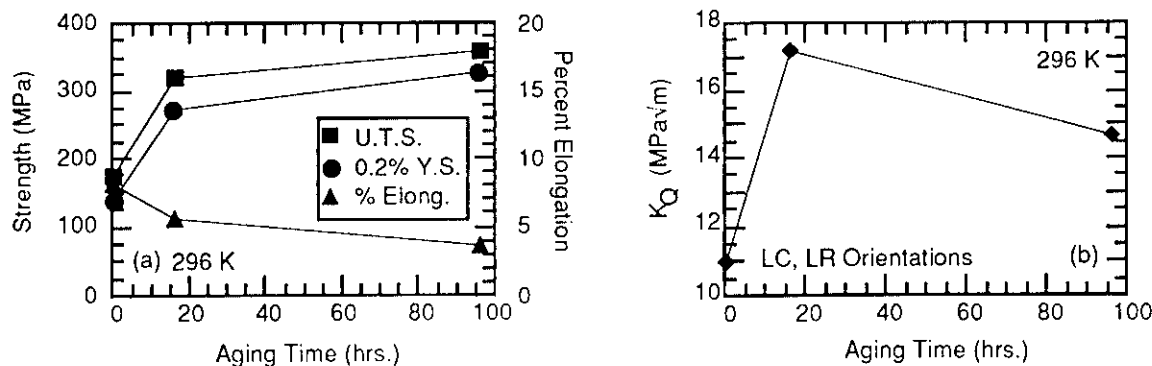


Fig. 2. (a) 0.2% offset yield strength, ultimate tensile strength and percent elongation to failure and (b) apparent fracture toughness (average of LC and LR orientations) as a function of aging time at 423 K for sub-scale processed Al-4.99Li-0.08Zr alloy following solution heat treatment at 848 K and water quenching. Room temperature data. Note that data points at zero aging time correspond to thermomechanically processed material prior to solution heat treatment and aging.

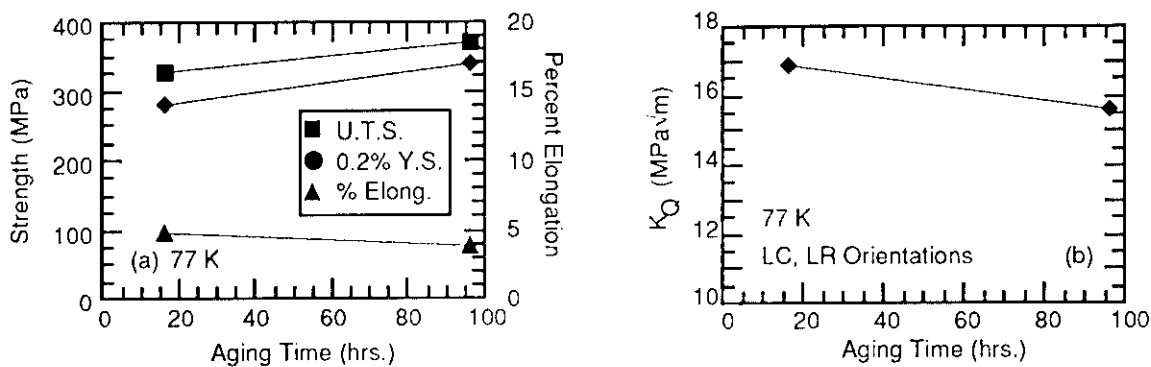


Fig. 3. (a) 0.2% offset yield strength, ultimate tensile strength and percent elongation to failure and (b) apparent fracture toughness (average of LC and LR orientations) as a function of aging time at 423 K for sub-scale processed Al-4.99Li-0.08Zr alloy following solution heat treatment at 848 K and water quenching. 77 K data. Note that data points at zero aging time correspond to thermomechanically processed material prior to solution heat treatment and aging.

In addition to the room temperature tests described above, tensile and short bar fracture toughness tests were also performed at 77 K (Figure 3). Yield and ultimate tensile strengths for both aging times increase slightly with decreasing temperature. For samples aged 16 hours at 423 K, this increase in strength is accompanied by a slight decrease in ductility. Little change is observed in the ductility of specimens subjected to the 96 hour aging treatment. With respect to fracture toughness, very little change is observed with temperature in specimens receiving the 16 hour aging treatment. For peak aged, 96 hour specimens, the apparent fracture toughness is observed to increase slightly at the lower test temperature. Although a reduction in test temperature does produce some changes in deformation behavior, the major trends observed at room temperature continue to hold at 77K. Aging for relatively short times, such as 16 hours at 423 K, appears to give an alloy with the best overall combination of strength, ductility and fracture toughness. Thus, for the full scale dome (discussed below), an aging treatment of 16 hours at 423 K was selected.

C. Full Scale Fabrication

Upon successful completion of the sub-scale metal working trials, two 76 cm diameter end domes (partial hemispheres) were fabricated. A complete description of the fabrication process was given

previously. Both domes were solution heat treated at 843 K, glycol quenched, and then immersed in liquid nitrogen. Once the domes had come to thermal equilibrium, they were removed from the cryogenic bath and up-quenched by spraying with jets of near 373 K water. The purpose of this upquenching procedure was to relieve, at least in part, the residual stresses present in the dome following quenching from the solution heat treat temperature. The aging treatment, as identified in the sub-scale processing trials consisted of heating for 16 hours at 423 K. Following heat treatment, one of the domes was sectioned and extensively characterized.

Since the amount of deformation associated with the spinning process is relatively small compared to that incurred during cross-rolling, care was taken to keep track of the two rolling directions during spin forming. Three dimensional optical micrographs taken near the center and near the outer edge of one of the domes are shown in Figures 4(a) and 4(b), respectively. In both Figures, the radial and circumferential directions are parallel to one of the two cross-rolling directions. The thickness of the dome near its center is roughly 16 mm while the thickness near the edge is nearly 11 mm. The increased deformation at the edge of the dome, results in a modest refinement of the microstructure in this region (Figure 4). However, this refinement is not sufficient to produce any noticeable variation in tensile or fracture toughness properties. As a result, for the

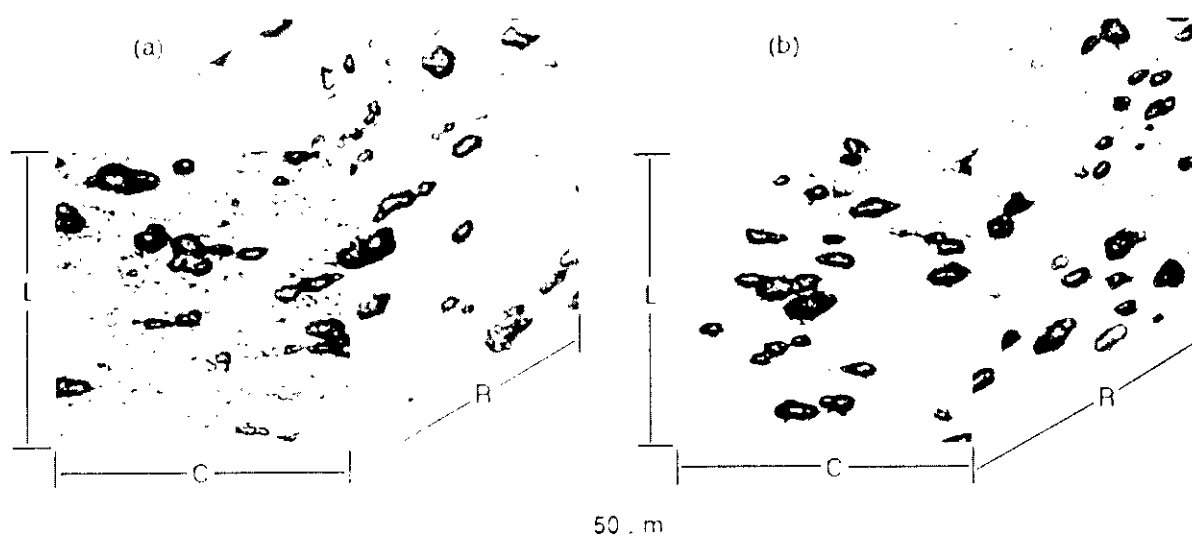


Fig. 4. 'Three-dimensional' optical micrographs of 76 cm diameter dome following solution heat treatment at 843 K, glycol quenching, liquid nitrogen immersion, upquenching and aging at 423 K for 16 hours. (a) near center and (b) outer edge location.

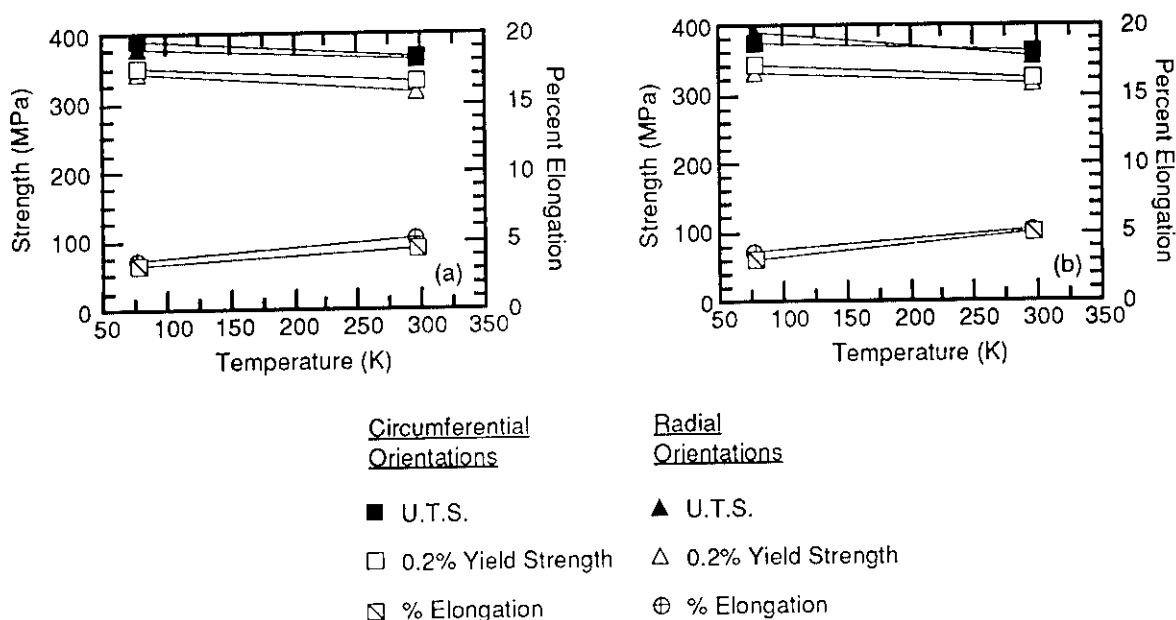


Fig. 5. 0.2% offset yield strength, ultimate tensile strength and percent elongation to failure in both radial and circumferential orientations of an Al-5.11Li-0.17Zr alloy dome following solution heat treatment at 843 K, glycol quenching, liquid nitrogen immersion, upquenching and aging at 423 K for 16 hours. (a) radial and circumferential directions parallel to cross-rolling directions. (b) radial and circumferential directions at an angle of 45 degrees with respect to the cross-rolling directions.

tensile data reported in Fig. 5, each data point represents the average of three measurements taken from near center, middle and outer edge locations of the dome.

The results of tensile tests performed at 296 and 77 K are summarized in Figure 5. For the data shown in Figure 5(a), the tensile axes of the radial specimens are parallel to one of the two rolling directions while the tensile axes of the circumferential specimens are parallel to the other rolling direction. In Figure 5(b), the radial and circumferential orientations are once again orthogonal to one another. However, the tensile axes of the specimens are at an angle of 45 degrees with respect to the rolling directions. In comparing the two Figures, it is clear that the tensile properties of the dome are fairly isotropic. Also, the differences observed between radial and circumferential orientations is small, perhaps as a result of the limited deformation associated with spin forming.

Short bar fracture toughness specimens were used to measure apparent fracture toughness in the LC, LR, RC and CR orientations as a function of test temperature. For the data shown in Figure 6, the radial and circumferential orientations are each parallel to one of the two rolling directions. As implied in the Figure, no difference was observed between LC and LR orientations and between RC and CR orientations.

Also, no variation in fracture toughness with respect to position (center to edge) within the dome was found. As a result, each LC,LR data point is an average of

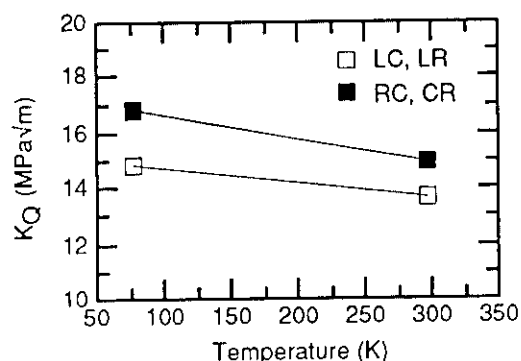


Fig. 6. Apparent short bar fracture toughness as a function of test temperature for the Al-5.11Li-0.17Zr alloy dome following solution heat treatment at 843 K, glycol quenching, liquid nitrogen immersion, upquenching and aging at 423 K for 16 hours. Radial and circumferential directions are parallel to cross-rolling directions.

eight measurements while each RC, CR data point is an average of four measurements. Fracture toughness is slightly less for specimens in which the fracture plane is the rolling plane. This is not surprising in view of the texture effects and alignment of the δ phase seen in

Figure 4. Regardless of orientation, however, apparent fracture toughness increases with decreasing test temperature.

In comparing the results of tensile and short bar fracture toughness tests performed on full scale processed material with those performed on the sub-scale processed material, noticeable differences are seen. The full scale processed material exhibits consistently higher yield strength, higher ultimate tensile strength and lower ductility. Although the precise reason for these variations is not known, it is likely that the somewhat higher lithium and zirconium contents of the full scale processed material play an important role.

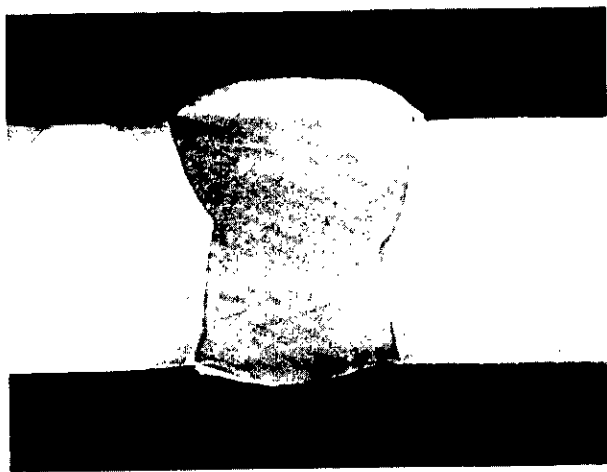


Fig. 7. Polished and etched cross-section of weld in Al-5.11Li-0.17Zr alloy dome material.

Because of the importance of welding in the fabrication of many structures, welding trials were performed on sections taken from one of the Al-Li domes. The Al-5.11Li-0.17Zr alloy can be easily welded using procedures previously developed for AlLi alloy 8090. Radiographic inspection was used to verify the overall quality of the welds. An optical photograph of a polished and etched section of one of the is shown in Figure 7. The results of room temperature Charpy impact tests performed at various locations with respect to the weld centerline are shown in Figure 8. As can be seen, impact resistance decreases with increasing distance from the weld centerline.

Results of thermal property measurements made on one of the heat treated domes are summarized in Figure 9. Data from 2219 and 8090 are included for comparison. As-expected, the mean coefficient of thermal expansion (Figure 9(a)) is quite similar to that

of other non-lithium containing alloys such as 2219. Because of the high lithium content, the thermal

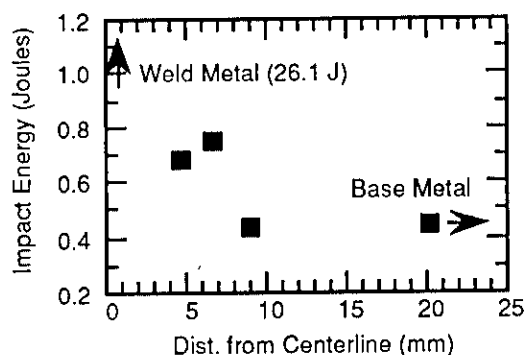


Fig. 8. Impact energy as a function of distance from weld centerline for gas tungsten arc weldment in heat treated Al-5.11Li-0.17Zr dome. NG61+0.15Zr filler metal.

conductivity of the Al-5.11Li-0.2Zr alloy is roughly a factor of two lower than 2219 at a temperature of 77 K. However, the difference between 8090 and the Al-5.11Li-0.2Zr alloy is quite small despite a factor of two difference in lithium concentration. Specific heat of the 5 wt.%Li alloy also exceeds that of 2219 and 8090 although the difference disappears at cryogenic temperatures.

IV. Discussion

In an early investigation of Al-high Li alloys, Meschter, Lederich and O'Neal [3] used RSP to produce both an Al-3.95Li-0.2Zr and an Al-4.7Li-0.2Zr alloy. For the near 5 wt.%Li alloy, extruded (19:1) at 673 K, solution heat treated at 861K and then peak aged at 433 K, ductilities in the range of 0.8 to 4 percent were reported. As noted by these authors, solution heat treatment, even at temperatures as high as 861 K, cannot reduce the volume fraction of δ phase in Al-5wt.%Li alloys below 10 percent. Because the δ phase is reportedly brittle at room temperature, the low ductility values observed were attributed entirely to the presence of too much δ phase. Other authors have since made this claim [4]. However, numerous factors, not just δ phase content, have been shown to affect the ductility of Al-high Li alloys. For example, as discussed previously, Palmer [11] has shown that in an Al-4Li alloy, aging at 443 K rather than at 423 K decreases the ductility of the alloy by roughly 1% for equivalent values of yield strength. Increasing the volume fraction of the δ' phase has a similar effect. As shown in Figure 2, increasing the volume fraction of the δ' phase in an Al-4.99Li-0.08Zr alloy (without changing the percentage of δ phase) by increasing the aging time at 423 K from 16 to 96 hours, lowers the ductility by

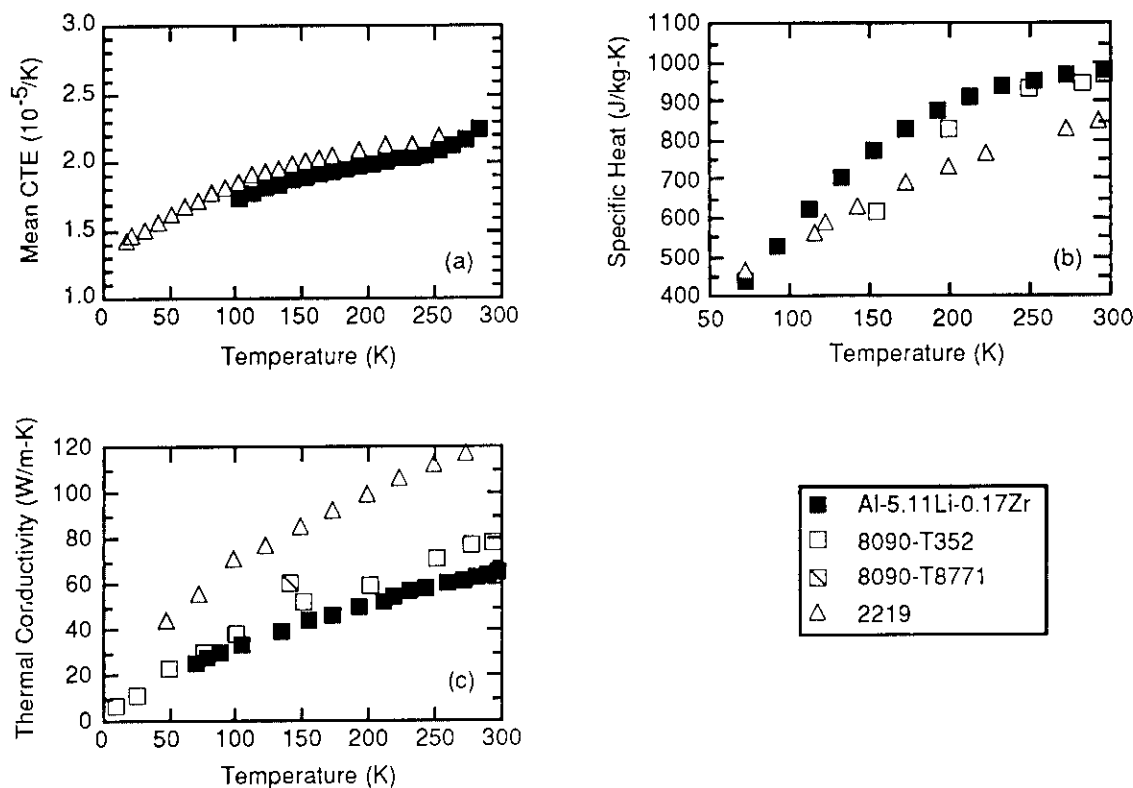


Fig. 9. (a) Mean coefficient of thermal expansion, (b) specific heat and (c) thermal conductivity of full scale processed Al-5.11Li-0.17Zr dome following solution heat treatment at 843 K, glycol quenching, liquid nitrogen immersion, upquenching and aging at 423 K for 16 hours. Data for 8090 Al-Li alloy and 2219 are included for comparison. 8090 and 2219 data from Ref. 12.

roughly 2%. Also, no mention is made with respect to the 5 wt.%Li alloy as to the effect of Al-Li oxide stringers on ductility. In addition to these considerations, the distribution of the δ phase is also important. Consider, for example, the Al-5.11Li-0.17Zr alloy in the HIPped, solution heat treated (848 K) and aged condition (16 hours at 423 K). The δ phase is present, to a large extent, as blocky particles at grain boundaries and triple junctions. As recorded in Table I, both the strength and ductility of the alloy in this condition are fairly low. However, when the same alloy is subjected to extensive thermomechanical processing followed by virtually the same heat treatment, both strength and ductility increase dramatically (Figure 5). In the thermomechanically processed material (Figure 4), the grain size is greatly reduced and numerous sub-grain boundaries are undoubtedly present. Both factors contribute to the observed increase in strength. The percentage of grain boundary area covered by the δ phase is lower and thus crack initiation and propagation promoted by the δ phase is more difficult.

Although the percentage of δ phase is a consideration in Al-high Li alloys, other factors are also important. By avoiding the formation of unwanted oxide particles through the use of spray casting instead of RSP, and by using appropriate thermomechanical processing and heat treatment procedures, it is possible to produce an Al-5Li-0.2Zr alloy which combines intermediate strength with acceptable values of ductility and fracture toughness. Such an alloy is 17% less dense and 17% stiffer than non-lithium bearing alloy 2219 and represents an attractive alternative to existing alloys for use in numerous room and cryogenic temperature aerospace applications.

V. Summary

Spray casting has been successfully used to produce an Al-Li alloy with nominal composition Al-5Li-0.2Zr. With a density of 2.35 g/cm^3 and a stiffness of 86.2 GPa the alloy is 17 percent less dense and 17 percent stiffer than non-lithium containing 2219. The alloy has been successfully processed by a series of forging, rolling and spinning operations to produce two

76 cm diameter end domes typical of those required for use in 200 liter cryogenic dewars. Extensive thermomechanical working and appropriate heat treatment have been shown to be important in producing an alloy with an acceptable combination of strength, ductility and fracture toughness. The alloy is easily weldable using procedures previously developed for Al-Li alloy 8090.

Acknowledgment

This work was supported by the Lockheed Independent Research and Development Program.

References

1. P.N. Anyalebechi, D.E.J. Talbot and D.A. Granger, in *Light-Weight Alloys for Aerospace Applications*, (E.W. Lee, E.H. Chia and N.J. Kim eds.), pp. 249-270, The Minerals, Metals and Materials Society, Warrendale, PA, 1989.
2. R.S. James, in *Metals Handbook*, 10th ed., Vol. 2, pp. 178-99, ASM International, Materials Park, OH, 1990.
3. P.J. Meschter, F.J. Lederich and J.E. O'Neal, in *Proceedings of the Third International Aluminium-Lithium Conference*, (C. Baker, P.J. Gregson, S.J. Harris and C.J. Peel, eds.), pp. 85-96, July 8-11, 1985, University of Oxford, The Institute of Metals, London, 1986.
4. H.B. McShane, M.S. Mahmoud and T. Sheppard, in *Proceedings of the Fifth International Aluminum-Lithium Conference*, (T.H. Sanders, Jr. and E.A. Starke, Jr., eds.), pp. 287-303, March 27-31, 1989, Williamsburg, VA, MCE Publications, Birmingham, UK, 1989.
5. I.N. Fridlyander, Y.A. Gorbunov and M.G. Stepanova, in *Proceedings of the Sixth International Aluminium-Lithium Conference*, (M. Peters and P.J. Winkler, eds.), pp. 387-89, October 7-11, 1991, Garmisch-Partenkirchen, Germany, DGM Informationsgesellschaft mbH, Oberursel, Germany, 1992.
6. N.J. Kim, *Mat. Sci. and Eng.*, **A158**, pp. 103-110, 1992.
7. N. Ryum, *Acta Metall.*, **17**, pp. 269-278, 1969.
8. N.J. Kim and S.K. Das, **20**, pp. 1107-1110, 1986.
9. I.G. Palmer, D.J. Chellman and J. White, to be published in *Proceedings of the Second International Conference on Spray Forming (ICSF-2)*, September 13-15, 1993, Swansea, UK.
10. K.A. Kojima, R.E. Lewis and M.J. Kaufman, in *Proceedings of the Fifth International Aluminum-Lithium Conference*, (T.H. Sanders, Jr. and E.A. Starke, Jr., eds.), pp. 85-94, March 27-31, 1989, Williamsburg, VA, MCE Publications, Birmingham, UK, 1989.
11. I.G. Palmer, private communication.
12. N.J. Simon, E.S. Drexler and R.P. Reed, "Review of Cryogenic Mechanical and Thermal Properties of Al-Li Alloys and 2219", AL-TR-90-064, September, 1990.

Ultra-Low Density, High Stiffness Al-Li-X Alloy for
Aerospace Applications
D.L. Yaney

Q: Joe Pickens - With all that delta in the matrix are you concerned about corrosion, stress corrosion?

A: Early on we did some stress corrosion cracking trials on this material and it gave surprisingly good results, I mean better than anything we have seen from 8090 for example.

Q: J.P. - The strength is lower, but the actual general corrosion having the delta particles in the matrix, have you done any standard immersion tests?

A: We have performed standard alternate immersion tests in 3.5 percent sodium chloride solution and been generally pleased with the results.

Q: Mack Roberts (Martin Marietta) Where would the applications be where the stiffness of this material would make it a better application than for instance 2195 weldalite 049?

A: Like 6061 and 8090, UL50 is an intermediate strength alloy, but because of its low density and high stiffness, UL50 is a more attractive replacement for these materials than Weldalite. Over the past 10 years, Lockheed Missiles and Space Company has used large amounts of 8090 for various applications. For these applications, low density and high stiffness were more important parameters than high strength in terms of reducing structural weight.

Q: Bob DiTolla (Martin Marietta) Given the amount of data that you presented I have a bunch of questions, but let me just ask you one. In the type of applications of these type of dome structures that we have, we have to fasten to usually weld them to rings and inherent in that type of structure you get quite a lot of deformation and nonlinear discontinuities and with that of course you get a lot of deformation. I was a little bit scared on your low elongation values and wanted to know if you could comment on that. Is that a problem, what can you do to raise those?

A: You are saying that when you weld to a ring structure you're getting deformation not in the weld metal but in the base metal, is that what you're concerned about?

Q: B.D. - When I pressurize the tank.

A: This particular application is a non-pressurized application. For a highly pressurized application, you would probably want to use a high strength rather than an intermediate strength alloy.

- Q: Eui Lee (Navy) Your alloy is looking alot like a high Li content and also your solution temperature is very high at 575 C, so have you checked lithium surface loss?
- A: Yes, you do get a lithium loss from the surface; approximately 5 mils in the domes after processing and heat treatment.
- Q: ? (Applied Research Lab) Do you seen any volitization of lithium in the spray casting process?
- A: Naturally ther is some lithium loss associated with the spray casting process. However, the material producer did not share with us the details of the spray casting process so I don't know the exact amount of lithium loss.
- Q: One further question, I assume your Charpy impact data with fusion zone represented magnesium bearing filler metal?
- A: That's correct.

HIGH FRACTURE TOUGHNESS IN AL-LI ALLOYS - THE RESULT OF VACUUM REFINING TO EFFECT ALKALI METAL IMPURITY REMOVAL

J.L. Mihelich
Commonwealth Aluminum Technologies
Louisville, Kentucky, USA
C.G. Bennett
Comalco Aluminium Limited
Melbourne, Victoria, Australia
E.D. Sweet and I. Musulin
Comalco Research Centre
Melbourne, Victoria, Australia

Abstract

Low short transverse (S-L) fracture toughness in aluminium-lithium alloys has been attributed to a number of causes including embrittlement arising from the presence of alkali metal impurities (AMI's). Vacuum refining of Al-Li alloys to achieve low AMI contents, ie <1 ppm each of Na, K, Cs, and Rb prevents the formation of alkali-rich grain boundary phases that can be liquid at room temperature. In addition to the removal of AMI's, vacuum refining removes hydrogen from the melt allowing for residual hydrogen contents of <0.2 ppm in the wrought products. The resulting 'low-AMI' alloys demonstrate significant improvements in S-L fracture toughness when compared with those with AMI contents of 5 to 10 ppm which are obtained commercially by conventional melting and casting techniques.

Results are presented from a recent program aimed at quantifying the contributions of Na and K to the embrittlement of 2090 alloy with a range of AMI contents. A correlation exists between the AMI content, proportion of the fracture surface occupied by intergranular brittle 'islands' and the short transverse (S-L) fracture toughness of Al-Li based alloys.

I. Introduction

The current generation of commercially available Al-Li based alloys are capable of delivering expected improvements in stiffness and weight savings. However, the commercial acceptance of these alloys is being inhibited by several factors, namely (i) their tendency for low-energy intergranular fracture, resulting in low fracture toughness in the short-transverse (S-L) orientation, (ii) their variability of properties from batch to batch and (iii) their relatively high material cost.

Commercially available Al-Li based alloys typically have alkali metal impurity contents within the range 3-10 ppm of Na + K and hydrogen contents within the range 0.3-0.6 ppm. Vacuum refining technology developed by Comalco Aluminium Limited, Melbourne, Australia⁽¹⁾ has enabled the production of Al-Li based alloys with very low alkali metal impurities (AMI) and hydrogen contents, ie. < 1 ppm each of Na, K, Cs, Rb and < 0.2 ppm H₂. The resulting products, manufactured in the United States and marketed as VACLITETM Al-Li alloy products, exhibit significant improvements in fracture toughness, stress corrosion resistance and ease of fabrication by extrusion, forging, rolling, welding and other means. The vacuum refining technology is not specific to any one lithium containing alloy series but is 'generic' to any lithium containing alloy.

II. Experimental Details

An experimentally designed program involved the casting of some ninety 127 mm diameter ingots of 2090 alloy with nominal compositional details are shown in Table I and cover a range of AMI contents.

Table I			
Compositional Details			
Element	Wt%	ppm	Method
Li	2.0		ICP
Cu	2.4		ICP
Zr	0.1		ICP
Na		<0.5 to 20	GDMS
K		<0.5 to 20	GDMS
H ₂		0.1 to 0.3	Inert Gas Fusion

Homogenisation, extrusion, solution-treatment, stretch and age processing was performed under controlled and reproducible conditions.

All mechanical testing was performed on specimens in the T8 condition that were machined from the center location of 60 mm x 14 mm rectangular-section extrusion. Short transverse (S-L) fracture toughness was determined at 20°C using chevron-notch short bar testing (ASTM E 1304). Yield strength was determined for the longitudinal direction.

III. Results

To enable a meaningful comparison of fracture toughness data for extrusions with varying AMI content, a comparison is ideally made at constant levels of yield strength.

In Figures 1(a) - (c), S-L fracture toughness data are presented for samples with AMI contents over the range 1 - 40 ppm (Na + K) for yield strength levels of 440 MPa, 476 MPa and 492 MPa, respectively. At each level of yield strength, the fracture toughness for samples with 1-2 ppm (Na + K) is significantly higher than the fracture toughness of samples with > 5 ppm (Na + K) AMI content and this improvement increases at lower yield strength levels.

By using two ageing treatments for each extrusion, variations in yield strength levels were achieved, so that by assuming linearity, the fracture toughness could be normalised to a constant longitudinal yield strength of 455 MPa, Figure 2. There is a dramatic increase in toughness as the AMI content is reduced below 3-5 ppm (Na + K). Statistical analysis of the data suggests a logarithmic relationship between fracture toughness and AMI content, as presented in Figures 3 and 4.

SEM observations of the fracture surfaces of S-L specimens identify a change in the proportions of the brittle regions or 'islands' as AMI content is reduced. Fractographs of extrusion samples identified in Figure 1(a) are presented in Figures 3 and 4:

- Sample A with 21 ppm Na, 10 ppm K, 0.2 ppm H₂ has $K_V = 20 \text{ MPa m}^{1/2}$. The fracture surface exhibits cleavage-like and intergranular brittle 'islands' that have coalesced (Area of brittle 'islands' 80-90%).
- Sample B with 0.7 ppm Na, 10 ppm K, 0.3 ppm H₂ has $K_V = 23 \text{ MPa m}^{1/2}$. The fracture surface exhibits brittle intergranular 'islands' surrounded by dimpled areas (Area of brittle 'islands' 10-20%).
- Sample C with 3.7 ppm Na, 1.9 ppm K, 0.2 ppm H₂ has $K_V = 27 \text{ MPa m}^{1/2}$. The fracture surface exhibits brittle intergranular 'islands' surrounded by dimpled areas (Area of brittle 'islands' 5-10%).
- Sample D with 0.92 ppm Na, 0.04 ppm K, 0.2 ppm H₂ has $K_V = 35 \text{ MPa m}^{1/2}$. The fracture surface exhibits a mixed transgranular/intergranular dimpled appearance (Area of brittle 'islands' < 1%).
- Sample E with 7.2 ppm Na, 0.25 ppm K, 0.2 ppm H₂.
- Sample B with 0.7 ppm Na, 10 ppm K, 0.3 ppm H₂.

IV. Discussion

Various researchers^(2, 3, 4, 5, 6) have considered the possible influence of alkali metal impurities and hydrogen on the mechanical properties of Al-Li based alloys. A consensus of opinion has been that, provided the alkali metal impurities were at the 5-10 ppm level as achieved by the conventional manufacturing route for Al-Li based alloys, alkali metal impurities would not contribute to the low-energy intergranular fracture problem nor the variability of property response of these alloys.

Webster^(7, 8) proposed that these alkali metal impurities were present in grain boundary locations as a liquid eutectic phase at room temperature and that these grain boundary particles lowered the surface energy and promoted intergranular weakness. Webster showed that in Al-Li based alloys with alkali metal impurity levels considerably higher than present in commercial alloys, liquid sodium-rich grain boundary phases exist and that these phases are sites of high hydrogen concentrations.

Work by Lynch⁽⁹⁾ and others has shown that AMI can facilitate crack growth and result in the formation of distinctive brittle intergranular 'islands' (and occasional cleavage-like 'islands') centered on inclusions. Recently Lynch⁽¹⁰⁾ has used SIMS to identify concentrations of AMI on the brittle 'islands' seen on fracture surfaces produced by creep cracking

of commercial Al-Li based alloys with AMI contents of 8 ppm (Na + K).

The brittle intergranular 'islands' (Figures 4 and 5) are similar to those observed previously by Lynch and others and shown to be associated with the presence of Na + K rich liquid phases.

The proposed mechanism for the formation of these brittle 'islands' involves the transport of Na and K atoms to crack tips and adsorption induced weakening of interatomic bonds at crack tips. Transport occurs by capillary flow of liquid and, at low crack velocities, can also occur by surface diffusion.

A transition to more ductile crack growth occurs when the supply of embrittling atoms is exhausted or when transport processes cannot keep up with crack growth. Cracks run out of embrittling AMI liquid sooner, and the brittle islands are smaller, when the volume of liquid phases is smaller and when crack velocities are higher. The proposed embrittlement mechanism is schematically presented in Figure 6.

The increase in the quantity of liquid present at higher AMI levels explains the observed variation in the percentage of brittle 'islands' seen as a function of Na + K content (Figures 3 and 4). In addition, 10-20% of the fracture surface is occupied by 'islands' at an AMI level of approximately 10 ppm regardless of whether the predominant AMI is Na or K (Figure 5). This demonstrates that both Na and K contribute to reduced toughness.

Thus, a correlation exists between the AMI content, proportion of the fracture surface occupied by intergranular brittle 'islands' and the short transverse (S-L) fracture toughness of Al-Li based alloys.

Other factors beside AMI levels undoubtedly influence fracture toughness. However, it is suggested that the presence of such impurities dominates fracture toughness properties at levels as low as 3-5 ppm (Na + K). It may be that only now, with the availability of VACLITETM low-impurity Al-Li alloy products, will the inherent strength and toughness relationships be developed for Al-Li based alloy series.

V. Conclusions

1. Vacuum refining Al-Li based alloys to very low alkali metal impurity contents (< 1.0 ppm each of Na, K, Cs, Rb) and hydrogen content (< 0.2 ppm H₂) significantly improves S-L fracture toughness.

- 2090 alloy extrusions of 14 mm section thickness in the T8 temper are characterised by :

- $K_V = 34-37 \text{ MPa m}^{1/2}$ @ longitudinal
YS = $440 \pm 12 \text{ MPa}$
- $K_V = 24-28 \text{ MPa m}^{1/2}$ @ longitudinal
YS = $476 \pm 12 \text{ MPa}$
- $K_V = 22-26 \text{ MPa m}^{1/2}$ @ longitudinal
YS = $492 \pm 12 \text{ MPa}$.

2. Fracture surfaces of material with low AMI content are characterized by a predominantly dimpled, higher energy, failure mode with an absence of the alkali metal induced brittle intergranular 'islands' observed in Al-Li alloys with higher Na + K contents.
3. A correlation exists between the alkali metal impurity content, proportion of the fracture surface occupied by intergranular brittle 'islands' and the short transverse (S-L) fracture toughness of Al-Li based alloys.
4. An embrittlement mechanism, involving the presence of a liquid alkali phase at grain boundaries is proposed as the failure mechanism producing significantly reduced fracture toughness for Al-Li based alloys. It is suggested that the presence of such impurities dominates the fracture toughness properties at levels as low as 3-5 ppm (Na + K).

Acknowledgment

The authors wish to acknowledge the excellent fractography and its interpretation provided by Dr. S.P. Lynch, Aeronautical Research Laboratory of the Australian Government's Defence Science & Technology Organisation, Melbourne, Australia.

References

1. US Patent 5 085 830.
2. A.K. Vasudévan, A.C. Miller and M.M. Kersker, Aluminium-Lithium Alloys II, Proc. 2nd Int. Conf. on Aluminium-Lithium Alloys, Metallurgical Society of AIME, Warrendale, PA, 1984, pp 181-199.
3. D.N. Fager, M.V. Hyatt and H.T. Diep,

- SCRIPTA METALLURGICA, Vol. 20,
1986, pp 1159-1164.
4. W.S. Miller, M.P. Thomas and J. White,
SCRIPTA METALLURGICA, Vol. 21,
1987, pp 663-668.
 5. C.D. Buscemi and E.S.C. Chin,
MICROSTRUCTURAL SCIENCE, Vol. 16,
1988, pp 221-230.
 6. J.J. Lewandowski and N.J.H. Holroyd,
MATERIALS SCIENCE AND
ENGINEERING, A123, 1990, pp 219-227.
 7. D. Webster,
Aluminium-Lithium Alloys III, Proc. 3rd Int.
Conf. on Aluminium-Lithium Alloys, Institute
of Metals, London, 1986, pp 602-609.
 8. D. Webster,
METALLURGICAL TRANSACTIONS,
Vol. 18A, Dec 1987, pp 2181-2193.
 9. S.P. Lynch,
MATERIALS SCIENCE AND
ENGINEERING, A136, 1991, pp 45-57.
 10. S.P. Lynch,
MATERIALS SCIENCE &
TECHNOLOGY, Vol. 8, Jan 1992, pp 34-42.

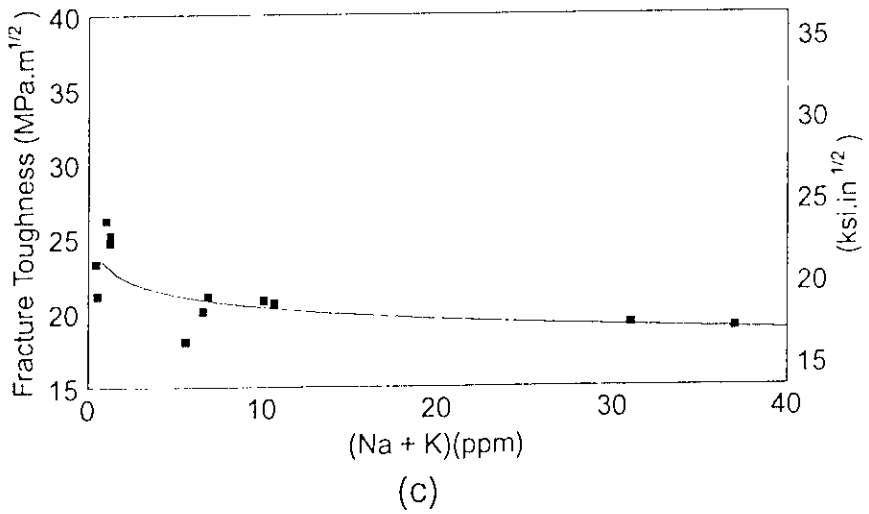
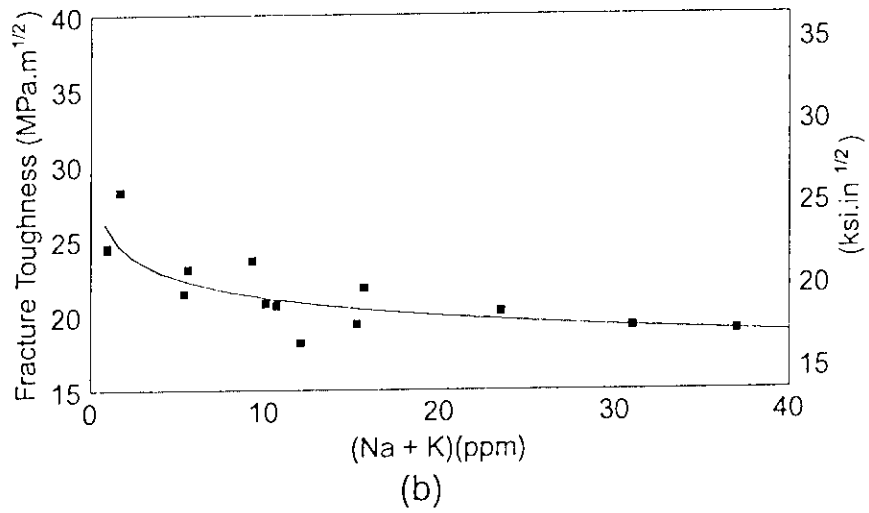
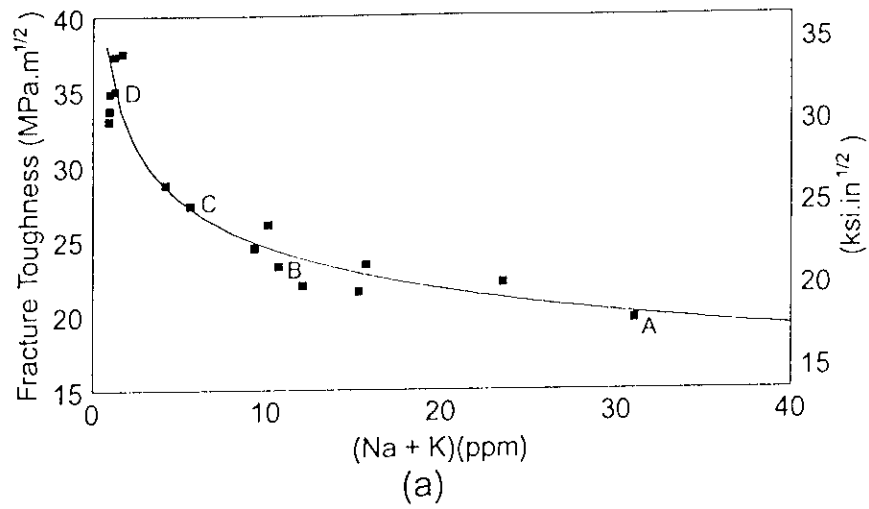


Figure 1: S-L Fracture Toughness versus AMI content for yield strengths of (a) 440 ± 12 MPa (64 ± 2 ksi); (b) 476 ± 12 MPa (69 ± 2 ksi); (c) 492 ± 12 MPa (71 ± 2 ksi)..

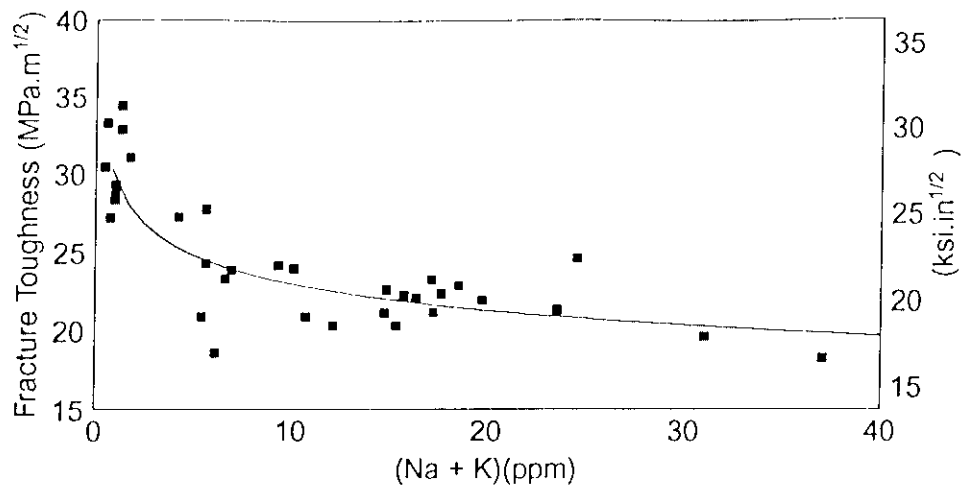


Figure 2: S-L Fracture Toughness versus AMI content normalised at 455 MPa (66 ksi)



Figure 3: SEM of sample D with < 1 ppm Na+K showing a predominantly transgranular dimpled fracture surface.

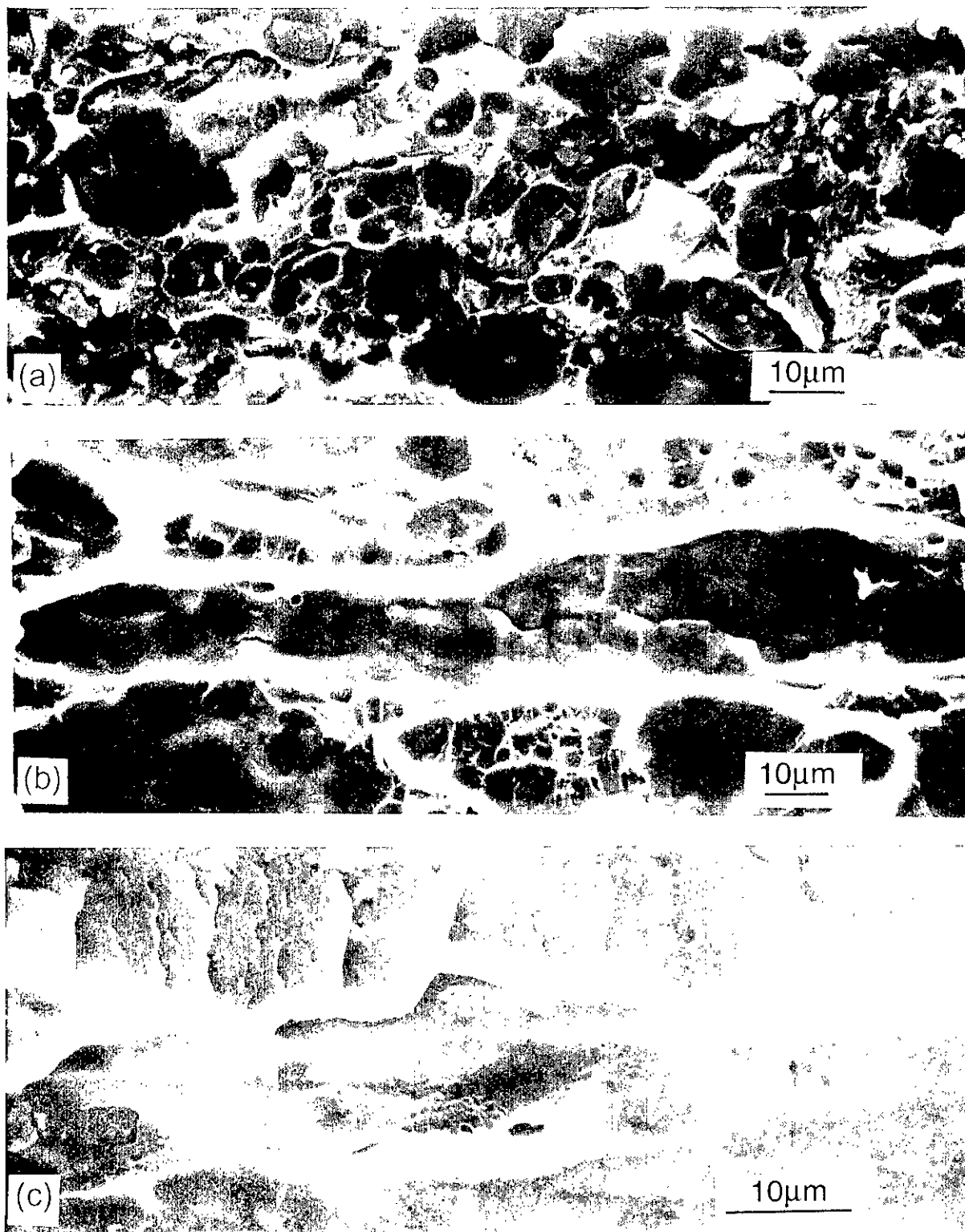


Figure 4: SEM of fracture surfaces of material with (a) C: 5.6 ppm Na+K, (b) B: 11 ppm Na+K, (c) A: 31 ppm Na+K, showing a decreasing proportion of the fracture surface covered by brittle 'islands' with decreasing Na+K content.

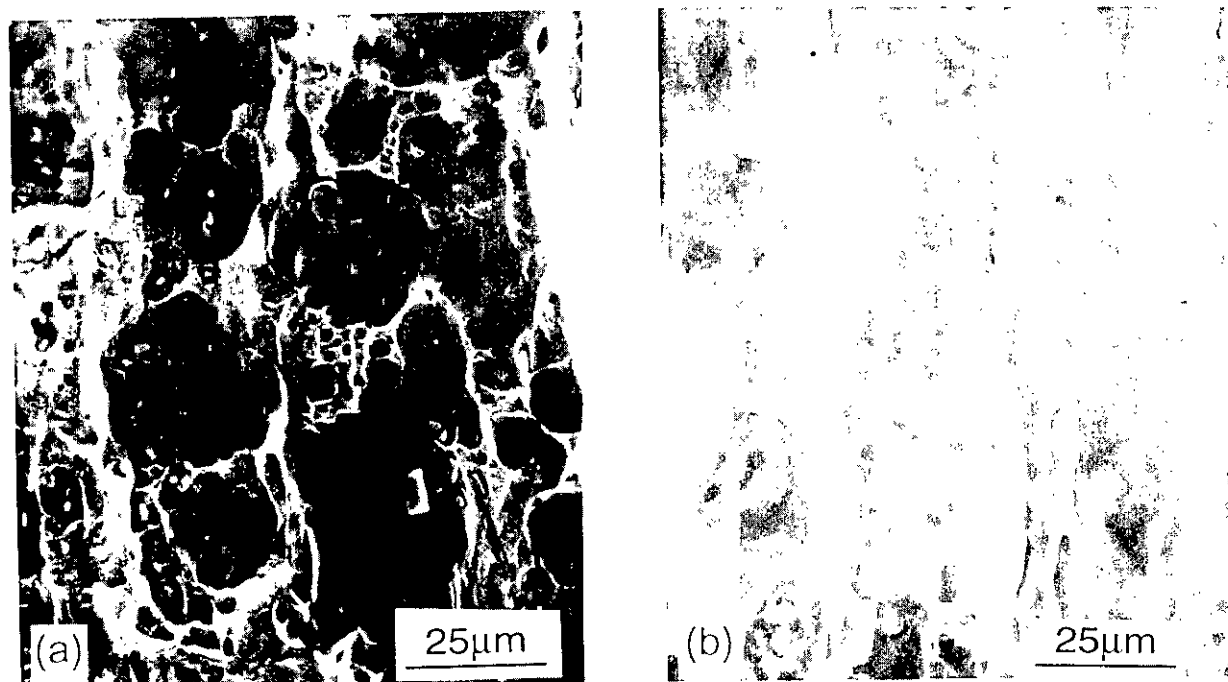


Figure 5 : SEM of fracture surfaces of specimens with (a) E: 7.2 ppm Na and 0.25 ppm K, and (b) B: 0.7 ppm Na and 10 ppm K, showing a similar extent of brittle 'islands' (10-20%) for specimens with predominantly one AMI type at a level of ~ 10 ppm.

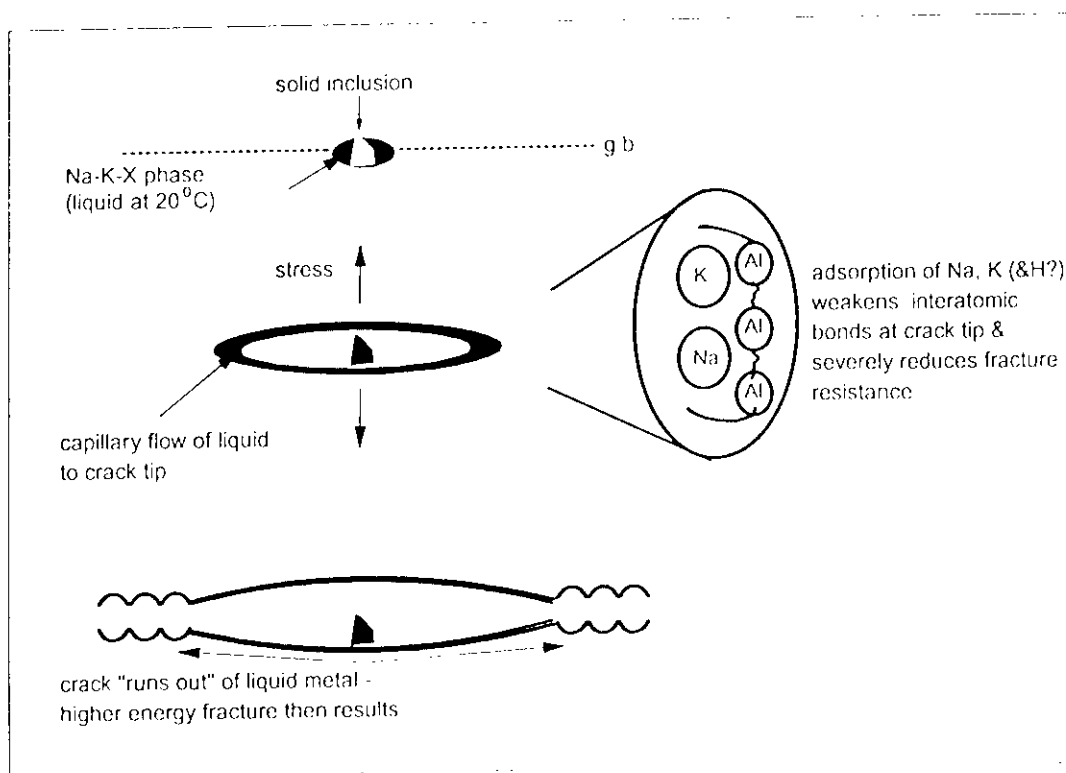


Figure 6 : Schematic diagram of embrittlement of Al-Li alloys by alkali metal impurities.

High Fracture Toughness in Al-Li Alloys - The Result of Vacuum
Refining to Effect Alkali Metal Impurity Removal
J.L. Mihelich

Q: Lee (Navy) Will you tell me a little bit about your vacuum process, is it like argon degassing kind of just put in the vacuum or what?

A: The technique that we have used involves a vacuum induction melting system where the furnace is in a tank which is evacuated. The material is charged into the furnace and the material is melted down under vacuum. Additional material can be added or alloy can be added through a vacuum lock so the vacuum is not broken. You are talking about 10 microns type of pressure for refining and again temperature control is very important here.

Q: E.L. - Argon or chlorine degassing?

A: No, with this pores you are pulling off the atmosphere above the molten metal; any gases which are intrapped will come off from the metal. So you have no need to degas with chlorine to remove hydrogen because you are pulling it off with the vacuum. And in fact you can get very low levels (say 0.1 ppm or less) because you have reduced the pressure below atmospheric.

Q: E.L. - So what is the difference between your vacuum processing and vacuum refining?

A: Vacuum refining, as we practice it, means better vacuum levels (lower pressures) and control of the temperature to effect removal of the undesirable trace elements. A controlled method. There are all different types of vacuum, you can have a vacuum cleaner but this would not remove much dissolved gas or alkali metals. A very high quality vacuum is needed to effect removal of the alkali metal impurities.

Q: Do you use a vacuum induction furnace?

A: Yes, it is a vacuum induction furnace. It is the easiest to use in our process; it is based on superalloy technology. It was developed in the 1950's. It is very commonly practiced throughout the world.

Q: Whats so big about the patent?

A: The patent in fact features the control of the alkali metal impurities to very low levels. We have one patent issued which indicates control of the alkali metals below 1 ppm. We also have another one that has been granted but not issued yet which indicates that there are benefits to be had in the range up to about 5 ppm of sodium and potassium and this is what is unique. We are in fact controlling the composition

by processing to get improved quality so described in the paper.

- A: To make the product do you have to like patent it?
- Q: The technique of producing the very low levels of alkali metals and hydrogen and the low levels of the alkali metals are patented.
- Q: Tim Langan (Martin Marietta) Have you looked at the effect of temperature on toughness; have you gone down to cryogenic temperatures, if it is an LME effect you would think that may be diminished and your curve may flatten out a little bit.
- A: There has been work done in this area looking at the more conventional levels of alkali metals in these alloys. Don Webster, who consults for us, has done work in this area. You do see this effect of dropping the temperature down and getting rid of the liquid metal embrittlement.
- Q: Have you looked at going to higher temperatures to get more liquid?
- A: When you are talking about eutectic which is liquid at room temperature; the liquid already exists so if you go up in temperature it will not make any difference.
- Q: No. If you go to higher temperature it will be in liquid form.
- A: It is in liquid form at room temperature already.
- Q: If you go to higher temperature more should be in liquid form.
- A: Where is it going to come from if the liquid eutectic is already there at room temperature?
- Q: Did you lose more copper if you go to higher temperatures?
- A: Because of changing the fluidity of the liquid or something like that?
- Q: Covering more grain boundary?
- A: We have not looked at this effect but certainly that is something that could be done, but we have not looked at it.
- Q: I could tell you whether you have a liquid metal or not.
- A: Well, I think the same point that Tim made about dropping the temperature down to freeze the liquid and we have seen that. We have seen that behavior so it kind of convinces us that this is liquid metal embrittlement. We have not gone up in

temperatre however.

Q: When you go to higher levels do you see intergranular failure at low temperatures, the eutectic would still be there but in a frozen brittle phase.

A: Yes but it has very little effect and you do not see a big pattern on the fracture surface.

Q: Joe Pickens (Martin Marietta) I think it is very interesting that Tim and I were thinking on the similar lines. One experiment is to go lower and see if your toughness increases to see whether it is actually an absorption metal embrittlement phenomenon or it is just a brittle phase. You can get solid metal and induce embrittlement to about 75 percent of the absolute melting point. You may want to see if you get any inflection point in your ductility as you go lower in temperature; alternatively in this experiment, it is a little more complicated to run, but you do go to higher temperatures you do wind up loosing the susceptibility to absorption metal embrittlement with a desorption effects. Of course there could be other things that screw up your toughness at the higher temperatures but I think there can be some very interesting mechanistic work done on this material.

A: Well, we are open to that. The idea that COMALCO has at this point is not to keep this technology exclusively to ourselves although we are in the process of selling and marketing billet. We think there may be some interest by other people who are in the aluminum lithium business and we are open to talk about licensing our technology.

Q: Bill Bhat (Marshall) Have you looked at weldability or can you speculate on that?

A: There was some work done, again we have not done too much on weldability. Carl Cross at Colorado School of Mines did some Vareststraint tests a few years ago and indicated, with the low AMI levels that weldability of 2090 for example, the alloy we looked at here, and also experimental 8090, looked to be better than the conventional Al-Li alloys.

Q: Sodium and potassium are both in the alkali family, are they both volitized?

A: Yes, it turns out that they are. One question I was prepared to answer wasn't asked so I will ask it myself; how much lithium do you lose when you vacuum refine? We do not loose anymore than 5 percent and we are going down to some pretty low vacuum levels. We are pulling off the sodium, potassium, and hydrogen, but we are not removing the lithium.

CHARACTERIZATION OF LITHIUM DISTRIBUTION IN ALUMINUM-LITHIUM MATERIALS

K. K. Soni¹, D. B. Williams², J. M. Chabala¹, R. Levi-Setti¹, and D. E. Newbury³

1. The Enrico Fermi Institute
The University of Chicago
Chicago, IL 60637.

2. Department of Materials Science and Engineering
Lehigh University
Bethlehem, PA 18015.

3. National Institute of Standards and Technology
Gaithersburg, MD 20899.

Abstract

Secondary ion mass spectrometry (SIMS) is particularly suited to the mapping of Li distribution in Al-Li alloys and composites. Scanning ion microprobe and direct-imaging ion microscope instruments have been utilized to study the chemical microstructures of Al-Li alloys. Case studies are described here to illustrate the application of SIMS in the imaging microanalysis of Al-Li alloys: (a) elemental distributions in Al-Li-Cu alloys, (b) interfacial reactions in Al-Li/SiC composite, and (c) quantitative profiling of subsurface depletion of Li and Mg in oxidized alloys.

Introduction

The microstructure of Al-Li alloys has been extensively investigated by transmission electron microscopy [1]. In contrast, relatively little attention has been devoted to the phase compositions and alloy microchemistry. Knowledge of Li distribution in these alloys is critical to alloy development and in the evaluation of processing methods. This objective can be best accomplished by secondary ion mass spectrometry (SIMS) due to its extremely high sensitivity for Li, in contrast to virtual inability of other microanalytical techniques. The high secondary ion signal for Li (approaching few MHz) means that probe size-limited resolution can be obtained in SIMS maps, enabling detection of fine detail in Li distribution with good resolution in a short times. Using imaging-SIMS, we have explored Li distribution to understand microstructures, phase equilibria, and oxidation behavior of Al-Li base alloys [2-8]. We illustrate the analytical power of SIMS with selected case studies.

SIMS methodologies

Ion microscope and scanning ion microscope are the two basic tools for imaging SIMS microanalysis (For more details, see ref. [9]). In the ion microscope, an image of the distribution of a particular element is obtained by illuminating all points of a surface area with a primary ion beam, and by collecting the emitted secondary ions with an image-forming, stigmatic mas-selective ion optical system. In the scanning ion microprobe, a finely focused primary ion probe is rastered over a surface, while the sputtered secondary ion signal is synchronously detected and mass-analyzed to form an image pixel-by-pixel. Additionally, in the SIM, the total ion-induced secondary ion signal (ISI) signal can be used to construct topographic images of the scanned surface area. In the ion microscope, all points of the bombarded surface contribute to the final image simultaneously; whereas, in the SIM, each pixel is recorded in sequence.

The lateral resolution with an ion probe, formed using a liquid metal ion source such as Ga, is nearly equal to the probe diameter (50-100 nm) provided the signal is strong. The SIM instruments offer significantly better resolution than that of the ion microscope. However, the ion microprobe is unsuitable for obtaining deep depth profiles because of its slow erosion rate, whereas the ion microscope can be used to perform depth profiling up to a depth of ~10 μm .

High Resolution Compositional Imaging with SIMS

We have demonstrated that quantitative imaging with the high resolution Scanning Ion Microprobe developed at The University of Chicago

(UC SIM), while a relatively recent technological advance, has matured to the state where it can be favorably compared in many respects with the much better known technique of x-ray imaging/microanalysis in the Electron Probe Micro-Analyzer (EPMA) – a most common and versatile materials characterization technique [10, 11]. Both techniques use bulk samples, which require relatively little preparation prior to examination. The advantages of the SIMS approach compared to EPMA, in terms of the combined performances of the UC-SIM and the ion microscope are:

(a) A 10X-50X increase in spatial resolution: In the UC SIM compositional images display 50-100 nm resolution compared with 1-2 μm in the EPMA.

(b) SIM/SIMS can detect the full elemental range as well as different isotopic species of all elements. EPMA cannot detect elements below about Be (such as Li which is the focus of this research), is increasingly insensitive to elements below about Na, and cannot detect isotopic species.

(c) The signal intensity in SIM/SIMS is significantly higher than in x-ray detection in the EPMA due to high ion yields, efficient signal collection and the absence of any significant background signal. Typical peak to background ratios in the SIM/SIMS are 10^3 - 10^6 , compared with 10^2 - 10^4 in the EPMA. Because of this, the time needed to accumulate a 512 x 512 map of a single element is a few seconds to a few minutes in the UC SIM compared to minutes/hours for the EPMA. Furthermore, the analytical sensitivity of the SIMS method (e.g. for the CAMECA IMS-4F, at the 1 μm lateral resolution level) ranges from ppb to ppm, while in the EPMA the range is ppm-1%.

(d) The SIM/SIMS can carry out depth profiling at the same time as spatial mapping is being performed to give three-dimensional elemental distributions. Each map originates from a surface layer at most a few nanometers deep. The EPMA samples the composition to a depth of several micrometers but cannot easily give any real depth distribution information.

(e) The SIM/SIMS can handle signals from samples with rough surfaces. The EPMA requires a smooth polished surface.

Of course the SIM/SIMS technique also has drawbacks compared to EPMA:

(a) The sample surface condition is critical and pre-cleaning with an argon ion gun in the pre-pump chamber is essential.

(b) Quantification of the secondary ion signal can be complicated by the matrix effects, and occasional un-resolvable mass overlaps. In this investigation we have successfully used the empirical technique of relative sensitivity factors determined on multi-element standards similar in nature to the unknown material. Relative errors of the order of 10% have been achieved by this method.

(c) The analytical sensitivity in high lateral resolution SIMS maps is limited due to the unavoidable trade-off between sensitivity and resolution.

(d) The ion beam destroys the sample layers that have been scanned, so once examined, the same sample layers cannot be re-analyzed.

On the whole, however, it can be said that the advantages of the SIM/SIMS approach to imaging microanalysis of Li in Al far outweigh its drawbacks. The chief advantage of compositional imaging becomes evident in the analysis of unknowns about which little prior information is available. This technique uniformly samples every point in an image matrix without bias, which unfortunately is not the case when an analyst is selecting locations for point analyses. As a result of this unbiased sampling, compositional imaging is often able to reveal unusual and unexpected phenomena which might be overlooked in conventional analysis. The combination of images supported by quantitative concentration values at every picture element in the image gives a comprehensive view of the chemical microstructure, often revealing hitherto-unpredicted effects.

Examples of Applications

A. Al-Li-Cu alloys

Most Al-Li base commercial alloys contain Cu, often with the addition of Mg. The Al-Li-Cu phase diagram is crucial to the understanding of the constitution of commercial alloys. However, relatively little work has been done regarding the phase equilibria in this system since the seminal study performed by Hardy and Silcock [12]. They identified the ternary phases and determined isothermal sections at 350 and 500°C using metallography and x-

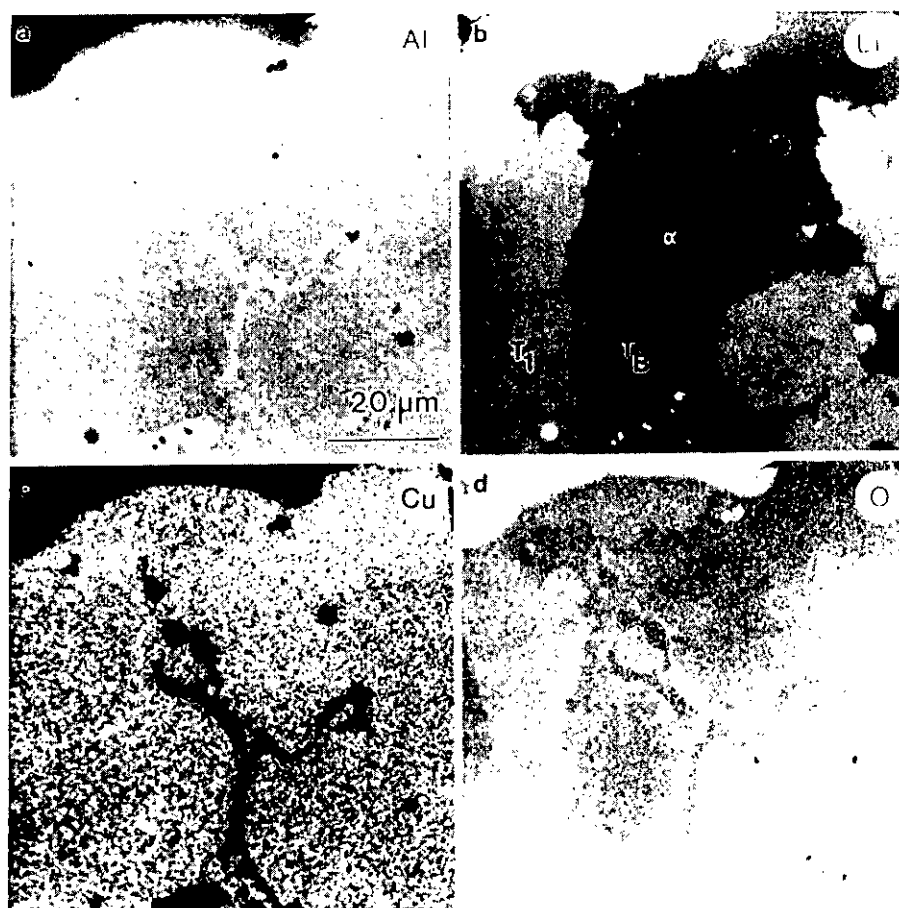


Fig. 1. Correlative UC SIM maps of an Al-23.4 at.% Li-27.1 at.% Cu alloy, showing the distribution of primary T_1 and phase mixture of T_B and α : (a) Al^+ , (b) Li^+ , (c) Cu^+ and (d) O^- . These images are displayed with a logarithmic gray scale to enhance brightness in low intensity areas.

ray diffraction work on a large number of alloys. In the Al-Li-Cu system, two phases of major importance are T_1 and T_2 , with nominal compositions of Al_2LiCu and Al_6Li_3Cu , respectively. In commercial alloys, containing ~2 wt Cu, T_1 develops a plate-like structure with a thickness <2 nm and contributes to the alloy strength by dispersion of planar slip. However, it cannot be analyzed in this form by the available microanalytical techniques. The Al-Li-Cu phase equilibria were studied by casting Al alloys with high contents of Li and Cu [4, 13].

An Al-23.4 at Li-27.1 at% Cu alloy was cast close to the stoichiometry of the T_1 phase to have phases large enough to microanalyze by imaging SIMS. The alloys was heat treated at 500°C for 7 days. Specimen for SIMS analysis was prepared using conventional metallographic procedures with final stages of preparation including polishing with 1 μ m diamond paste and 0.3 μ m Al_2O_3 suspension in ethylene glycol. Specimen contact with water was avoided as it may alter the surface chemistry by leaching out Li.

Figs. 1(a-d) show Al^+ , Li^+ , Cu^+ and O^- distribution maps of the same specimen area of the ternary alloy. The individual phases are marked on the Li map. It is evident that α (aluminum solid-solution) dominates in the Al^+ image, but it contains the least amounts of Li and Cu, as expected. T_1 can be identified as the phase richest in Li. T_1 and T_B contain roughly equal amounts of Al and Cu and therefore cannot be discerned from each other in Al and Cu maps. It must be mentioned here that these images represent the distributions of secondary ion intensities, and not of true concentrations. The conversion of secondary ion intensities to corresponding concentrations requires empirical calibration to account for the well known matrix-effects and instrumental factors [9]. Nevertheless, the secondary ion images are useful in demonstrating the relative trends in elemental distributions. The feature in the top-left corner is Li-oxide formed during the polishing process. The O^- image (Fig.3d) displays the same distribution as in the Li^+ map (Fig. 3b). This similarity suggests that the oxygen segregation is directly related to the Li content of the individual phases. The traces of oxygen are assumed to arise from the oxidation of the liquid alloy during casting, reaction of Li with oxygen in the specimen chamber or surface oxidation during specimen preparation and storage. The last two factors are unlikely as the specimens were sputter-cleaned with an Ar^+ gun prior

to the acquisition of images in UHV environment.

Note a subtle effect in the Li map. There is a gradient in the Li distribution within the T_B phase: the T_B precipitates are deficient in Li in the central region compared to the particle periphery. A possible explanation for this phenomenon is that the T_B phase forms by a peritectic reaction between liquid and T_1 , which involves solute diffusion through the growing solid and consequently does not reach equilibrium state. Formation of T_B by a peritectic reaction was also discussed by Dubost *et al.* [14], who characterized the phase equilibria in the Al-Li-Cu system.

B. Al-Li/SiC_p composite

Figures 2(a-d) show SIMS images of an Al-2.1 wt% Li alloy/SiC_p composite. This MMC was prepared by spray atomization, coinjection, and deposition as described by Gupta *et al.* [15]. Application of imaging SIMS in the study of composite materials has been discussed by Soni *et al.* [16]. Fig. 2a is an ISI image displaying topographic contrast of the scanned area. Shadowing is pronounced in this image because the channeltron detector that collects the ISI signal looks at the scanned area at a shallow angle. Consequently, the relief at the interface is enhanced and the particles appear to be sticking out of the matrix. The secondary ion signal for mass discrimination, however, is collected normal to the specimen surface so that shadowing and edge effects are minimized in the SIMS maps. The Al-Li surfaces are invariably covered with Li-rich oxide which can complicate surface analysis. SIMS maps shown in Figure 2 were recorded after sputter-cleaning the surface with an auxiliary Ar^+ beam in the prepump chamber of the UC SIM. The main feature in the SIMS maps is the presence of a Li-rich oxide at the interface and also at some other locations in the matrix, which may have formed during fabrication. This reaction depletes the alloy matrix of useful Li and is, therefore, undesirable because Li is added to strengthen the matrix. The SiC particles dominate the Si-image, as expected. Enhanced emission of Si from the edges of the particles suggests that an SiO_2 layer envelopes the SiC particles. There is no detectable Li or Al diffusion into the SiC phase.

Obviously, there is chemical interaction between the Al-Li matrix and the SiC particles during fabrication which is manifest as oxide formation at the interface. The SiC particles are known to be covered with a thin layer of SiO_2 and may be partly

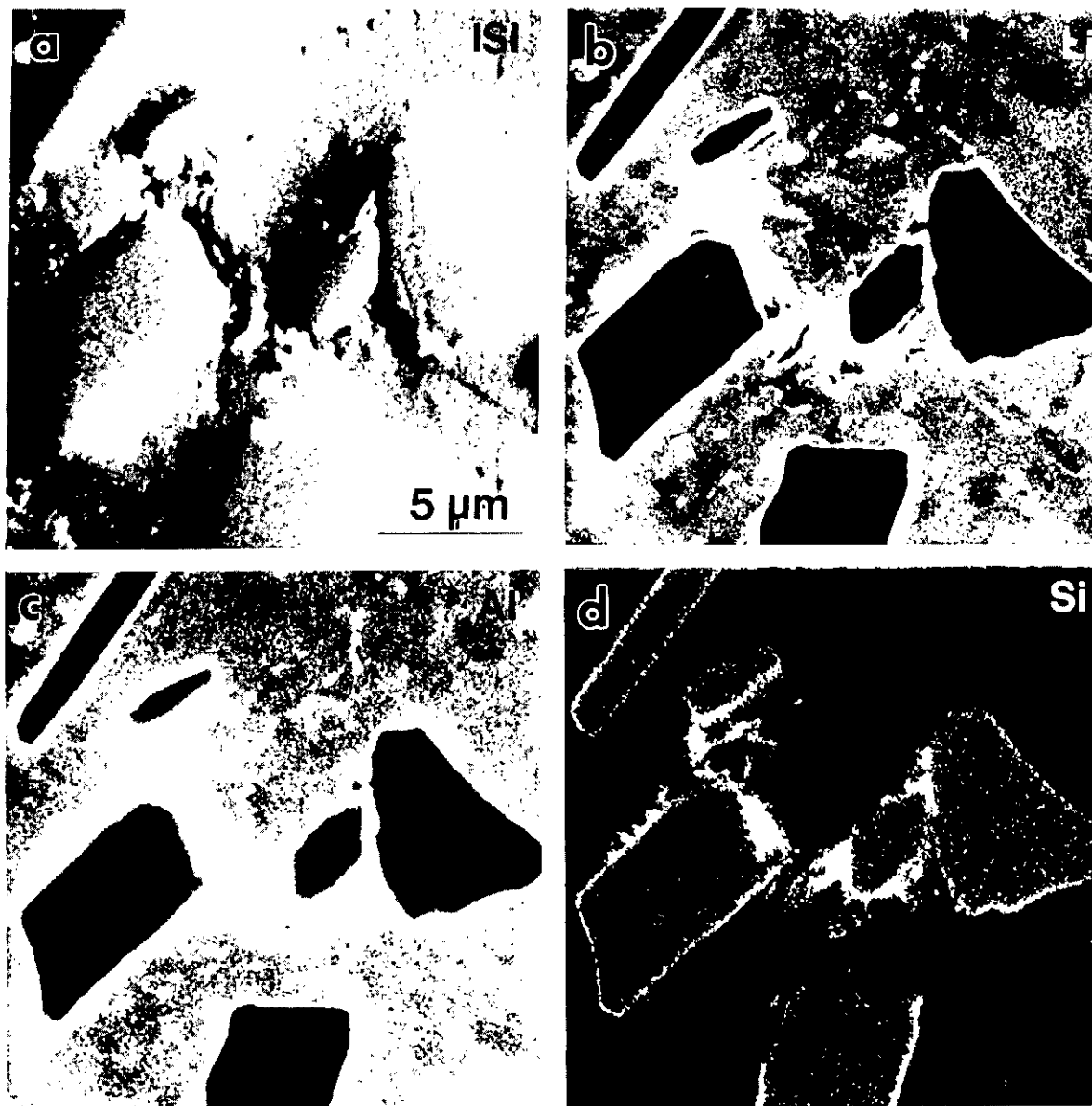


Fig 2. UC SIM maps of one area of an Al-2.1 wt.% Li alloy reinforced with SiC in as-fabricated condition. The specimen was sputter-cleaned with an auxiliary Ar beam in the ante-chamber of the UC SIM. (a) ISI (topography), (b) Li⁺, (c) Al⁺, (d) Si⁺. Note oxidation at the fiber/matrix interface.

responsible for this oxidation. Consequently, Li is drained from the matrix, altering the microstructure and the aging response. These factors must be taken into consideration when designing or modeling such composite systems. However, the reaction is limited to the interface and the SiC particles are not attacked by Li or Al. It is expected that these chemical interactions will be more severe if the MMC is subjected to solutionizing and aging treatments.

C. Quantitative profiling of Li and Mg loss caused by oxidation

Al-Li-Mg-Cu alloys undergo surface loss of both Li and Mg following high temperature treatments in air because of the preferential oxidation of these elements [8]. Soni *et al.* established systematically the depletion behavior of Li and Mg using imaging-SIMS and neutron depth profiling (NDP) [7, 8]. An example is illustrated here to describe the procedure employed in the quantitative imaging and profiling of surface depletion with the ion microscope.

A polished specimen of an Al-2 wt% Li-3.1 wt% Mg-1 wt% Cu alloy was oxidized in air at 530°C for 1 h and then water quenched to remove most of the oxide layer. The compositional changes occurring in a direction normal to this surface were of interest. Specimens were mounted in epoxy with the originally polished surface normal to the mount surface. Two similar specimens were mounted together, with the oxidized surfaces abutting each other, in order to have a sufficiently large area for examination around the oxide/alloy interface and to avoid sampling of the epoxy with the ion beam. This mount was ground, polished, and coated with Au for SIMS examination. Fig. 3 shows maps of Al⁺, Cu⁺, Li⁺, and Mg⁺ SIMS maps of this specimen. Note the presence of oxide residue at the interface of the abutting specimens. These images show qualitatively that the alloy adjacent to the oxide has lost both Li and Mg, whereas Al and Cu are nearly unchanged. SIMS signal intensity profiles in a direction normal to the interface, were obtained by retrospective analysis of the digital SIMS maps. Intensity ratios of Li, Mg, and Cu with respect to Al were calculated at each pixel. Quantification was performed by using the unaffected specimen area as an internal standard. This procedure is discussed in detail by Soni *et al.* [8]. Fig. 4 shows quantitative concentration profiles of Li, Mg and Cu in the near-surface area of this specimen. The solid lines through Li and Mg data points were obtained by the least-squares fit of a diffusion

equation that describes the depletion process. The solute concentration C at a distance x from the oxide/alloy interface can be expressed as:

$$\frac{C - C_I}{C_B - C_I} = \text{erf}\left(\frac{x}{2\sqrt{Dt}}\right) \quad [1]$$

where C_I is the solute concentration at the oxide/alloy interface, C_B that in the bulk alloy, and D is the interdiffusion coefficient of the alloy at the oxidation temperature. This curve-fitting procedure can be used to obtain the value for D . Note that the value of C_I is non-zero for both Li and Mg.

Acknowledgments

This material is based on work sponsored by the National Science Foundation under grants DMR 9015868 and 9111839. We thank Prof. E. J. Lavernaia (University of California, Irvine) for providing the Al-Li MMC sample.

References

1. Williams, D. B., and Howell, P. R., "The Microstructure of Aluminum-Lithium Base Alloys," in *Aluminum Alloys-Contemporary Research and Applications*, Eds: A. K. Vasudevan, R. D. Doherty, Academic Press, San Diego, 365-388, 1989.
2. Williams, D. B., Levi-Setti, R., Chabala, J. M., and Newbury, D. E., "High Spatial Resolution Secondary Ion Imaging and Secondary Ion Mass Spectrometry of Aluminium-lithium Alloys," *J. Microsc.*, **148**, 241-252, 1987.
3. Williams, D. B., Levi-Setti, R., Chabala, J. M., and Newbury, D. E., "Microanalysis of Precipitates in Aluminum-Lithium Alloys with a Scanning Ion Microprobe," *Appl. Surf. Sci.*, **37**, 78-94, 1989.
4. Soni, K. K., Chabala, J. M., Levi-Setti, R., Williams, D. B., Newbury, D. E., Bright, D. S., "Phase Equilibria in the Al-Li-Cu System Determined by Secondary Ion Mass Spectrometry," *Microbeam Analysis*, **2**, 13-21, 1993.
5. Soni, K. K., "Characterization of Phase Equilibria and Oxidation Behavior of

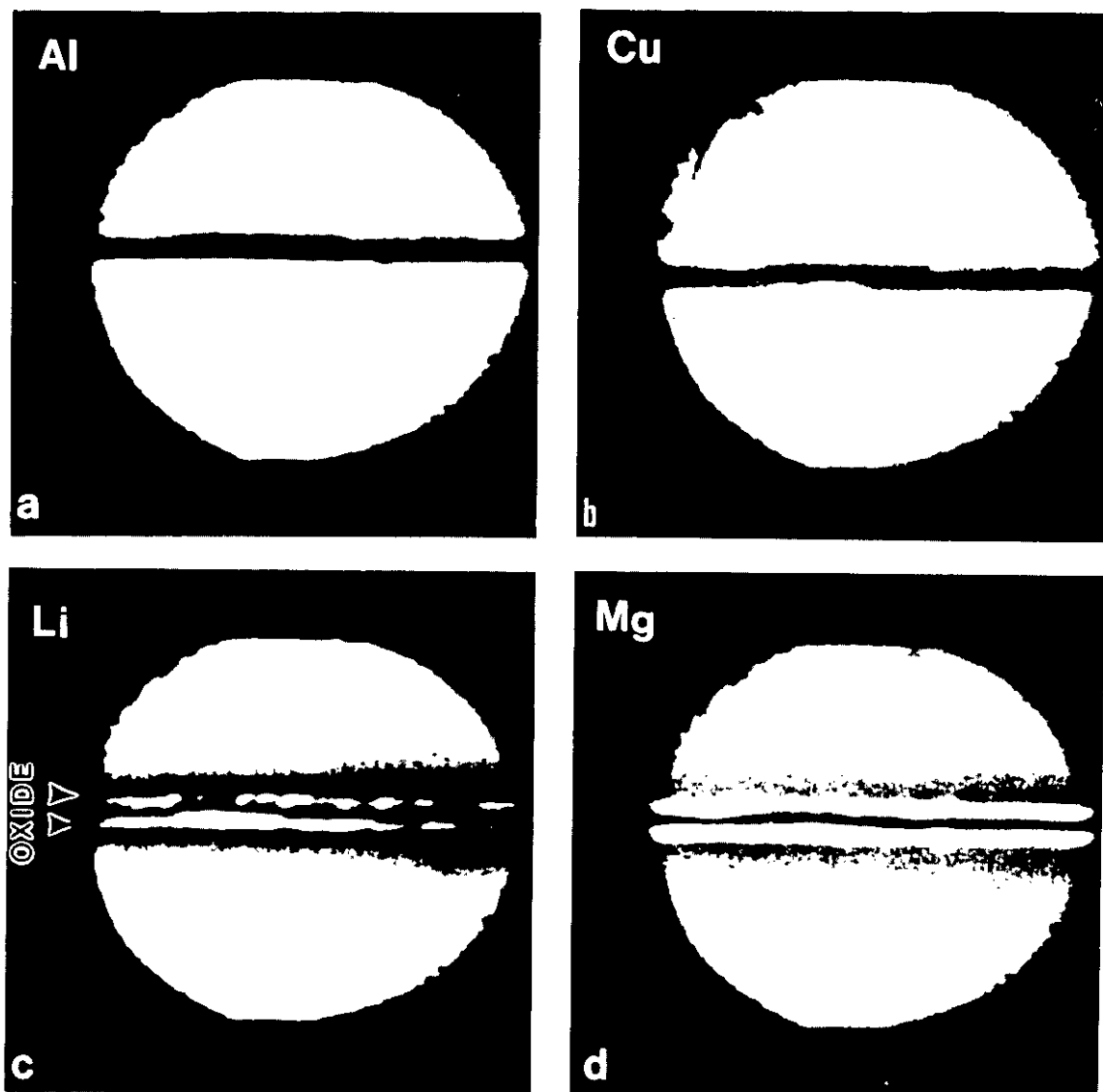


Fig. 3. SIMS maps of an Al-2 wt.% Li-3.1 wt.% Mg-1 wt.% Cu alloy heat treated in air at 530°C for 1 hr: (a) Al^+ , (b) Cu^+ , (c) Li^+ , and (d) Mg^+ . Field of view $\sim 150\ \mu\text{m}$ in diameter. Note depletion in Li and Mg, whereas Al and Cu distributions are uniform. Quantitative profiles extracted from these digital images are shown in Fig. 4.

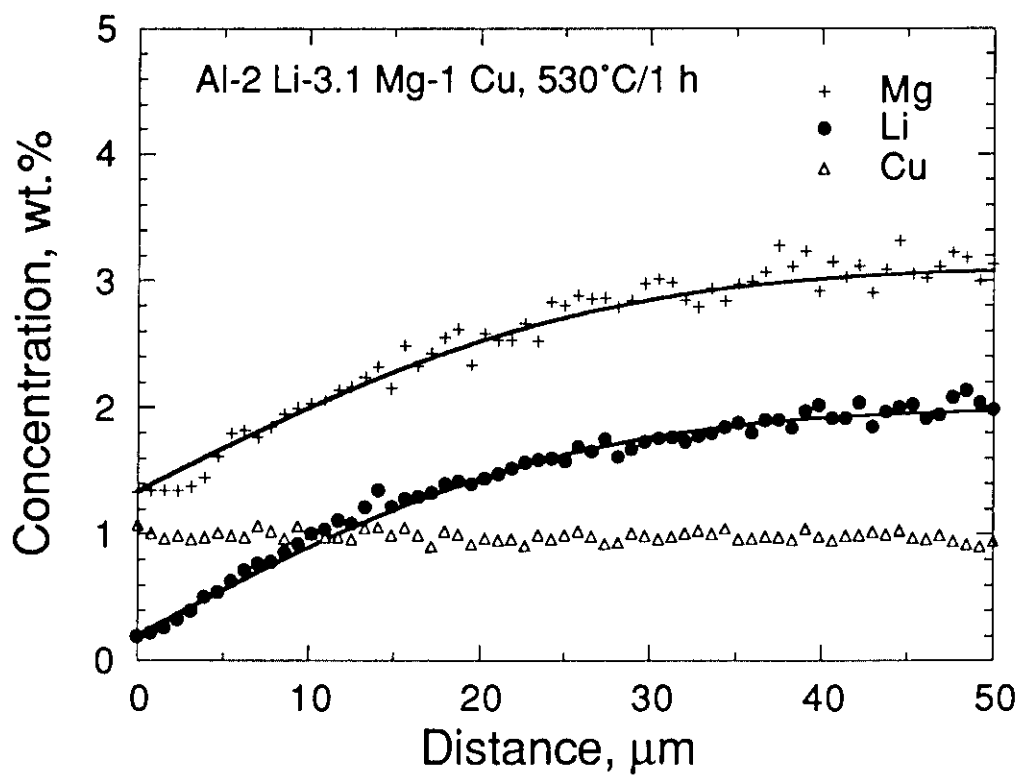


Fig. 4. SIMS lateral profiles of an Al-2 Li-3.1 Mg-1 Cu (wt%) alloy oxidized at 530°C/1 h showing depletion of both Li and Mg. The solid lines are the least-squares fit of a diffusion equation that describes the depletion process.

- Aluminum-Lithium Alloys by Electron, Ion, and Neutron Beams," Ph.D. dissertation, Lehigh University, Bethlehem, PA, 1991.
6. Soni, K. K., Williams, D. B., Chabala, J. M., Levi-Setti, R., and Newbury, D. E., "Morphological and Microchemical Phenomena in the High Temperature Oxidation of Binary Al-Li Alloys," *Oxidation of Metals*, **36**, 361-378, 1991.
 7. Soni, K. K., Williams, D. B., Newbury, D. E., Chi, P., Downing, R. G., and Lamaze, G., "Depth-Distribution of Li in Oxidized Al-Li Alloys Determined by Secondary Ion Mass Spectrometry and Neutron Depth Profiling," *Corrosion*, **49**, 31-41, 1993.
 8. Soni, K. K., Williams, D. B., Newbury, D. E., Chi, P., Gillen, G., and Bright D. S., "Compositional Changes in Aluminum-Lithium-Base Alloys Caused by Oxidation," *Metallurgical Transactions*, **24 A**, 2279-88, 1993.
 9. Benninghoven, A., Rudenauer, F. G., and Werner, H. W., "Secondary Ion Mass Spectrometry: Basic Concepts, Instrumental Aspects and Trends," John Wiley, New York, 1987.
 10. Levi-Setti, R., "Critical issues in the application of a gallium probe to high resolution secondary ion imaging," *Surf. Sci.*, **246**, 94-106, 1991.
 11. Levi-Setti, R., Chabala, J. M., Gavrilov, K. L., Mogilevsky, R., and Soni, K. K., "Imaging-SIMS Studies of Advanced Materials," *Scanning Microscopy*, **7**, 1161-1172, 1994.
 12. Hardy, H. K., and Silcock, J. M., "The phase sections at 500°C and 350°C of aluminium-rich Aluminium-Copper-Lithium alloys," *J. Inst. Metals*, **84**, 423-428, 1955-56.
 13. Vecchio, K. S. and Williams, D. B., "Convergent beam electron diffraction analysis of the T₁ (Al₂CuLi) phase in Al-Li-Cu alloys," *Metall. Trans.* **19A**, 2885-91, 1988.
 14. Dubost, B., Colinet, C., and Ansara, I., "An experimental and thermodynamic study of the Al-Li-Cu equilibrium phase diagram," *Proc. 5th Inter. Aluminum-Lithium Conf.*, Williamsburg, VA. Eds.: T.H. Sanders and E.A. Starke, M.A.C.E., Birmingham, U.K., 623-632, 1989.
 15. Gupta, M., Ibrahim, I. A., Mohamed, F. A., and Lavernia, E. J., "Wetting and Interfacial Reactions in Al-Li-SiC Metal Matrix Composites Processed by Spray Atomization and Deposition," *J. Mater. Sci.*, **26**, 6673-84, 1991.
 16. Soni, K. K., Chabala, J. M., Mogilevsky, R., Levi-Setti, R., Tseng, M. W., and Williams, D. B., "Ion Microprobe Investigations of Interfacial Phenomena in Composites," *JOM (Journal of The Minerals, Metals, and Materials Society)*, **45**, 29-33, 1993.

Characterization of Lithium Distribution in
Aluminum-Lithium Materials
K.K. Soni

No questions.

STRESS - ASSISTED δ' PRECIPITATION ON DISLOCATIONS IN AN Al-Li ALLOY

Z. M. Wang and G.J. Shiflet

Department of Materials Science and Engineering, University of Virginia, Charlottesville, VA 22903.

Abstract

The morphology and growth behavior of δ' precipitates nucleating on dislocations in an Al-Li alloy were investigated by TEM. Attention was focused on the effect of short circuit diffusion paths on the development of precipitate morphology. The study was conducted on a binary aluminum alloy containing 2.27 wt% Li which was cold rolled to a 50% reduction in area. The δ' particle size was measured as a function of time and temperature in samples isothermally aged in the temperature range between 210°C and 250°C. These experimental results on growth were compared with theoretical calculations which demonstrated that fast diffusion paths become increasingly important as temperature is lowered.

I. Introduction

It is widely known that dislocations significantly affect mechanical properties of metal alloys. Dislocations can also modify several processes of the precipitation phenomena in crystalline materials including nucleation and growth of new phases. The dilute Al-Li binary alloy, in contrast to the complicated and competitive precipitation kinetics of the commercial systems, has a simple precipitation sequence with δ' precipitation at temperatures below 300°C. Therefore, it provides a good opportunity to study coherent heterogeneous nucleation and growth kinetics on dislocations.

In this system the δ' nucleus interface is fully coherent with the aluminum matrix, thus the nucleation process is termed "coherent". The assistance which a dislocation affords coherent nucleation has been investigated several times [1-4]. For a coherent nucleus, the catalytic action of the dislocation is a results of the interaction energy between the dislocation and the nucleus. If the nucleus has the same elastic properties as the matrix, the interaction energy arises entirely from the work done by the stress field of the dislocation in helping to produce the displacement associated with the constrained shape and volume change of the nucleus. During δ' growth on dislocations, dislocations can

affect the process in two ways: first, the stress field associated with the dislocation can exert an attractive force on solute atoms which have a different volume from the matrix, and second, the dislocation itself serves as a high diffusivity path for the flow of solute. Both mechanisms will tend to enhance the growth kinetics of δ' attached to the dislocation line.

There is an increasing tendency to employ alloys at higher temperature service where processes such as coarsening, PFZ formation, and phase transformations towards the, often, less desirable equilibrium phase, becomes a concern. As all these processes depends on diffusion in some fashion, interest has predominately been associated with volume diffusion, however, at moderate temperatures short circuit diffusion paths can be a contributor to deleterious changes in microstructure. In the present work, experiments were performed to study the heterogeneous precipitation kinetics of δ' at dislocations. Particular attention was paid to δ' growth kinetics as well as its growth morphology so that a comparison between related theories [5-7] and quantitative experimental studies can be made. The relative effects of volume diffusion and pipe diffusion is discussed in the context of how important short circuit diffusion is in alloy aging.

II. Experimental Procedure

A single binary alloy of Al - 2.27 wt% Li was prepared by the Reynolds Metals metallurgical laboratory where high purity materials were induction melted and cast in an argon atmosphere. In order to get sufficient dislocation structure and sub-boundaries the alloy was cold rolled to 50% reduction in area prior to heat treatment. Samples of the thin sheet material encapsulated in an Ar environment were solution heat treated for 15 minutes at 550°C in a high temperature salt bath, and isothermally transformed at four different aging temperatures for several aging time sequences. Table 1 gives the heat treatment conditions. Samples were prepared for transmission electron microscopy (TEM) using standard techniques and examined using 120 keV. Direct counting was the method used to determine the number of precipitates per unit

Table I. Heat treatment conditions for Al - 2.27 wt% Li alloy.

Aging temperature (°C)	Aging time (min)
210	1, 2, 5, 10, 30, 60, 120, 180
230	5, 15, 30, 60, 90, 120, 180
240	15, 35, 45, 60, 90, 120, 155, 180
250	45, 60, 90, 120, 150, 180

length of dislocations. Where necessary, δ' particle diameters, d , were measured on centered dark-field micrographs imaged from δ' superlattice reflections. The diameter was measured on an average of 200 particles for each aging time, t , and temperature T .

III. Results

Nucleation and Morphological Development

The shape of δ' particles which form during aging in association with dislocations differs considerably from the highly spherical morphology normally produced by homogeneous nucleation. Most of the δ' particles associated with dislocations have a kidney bean shaped morphology. It was previously determined [8] that the δ' precipitates are always observed to be distributed to a single side of the parent dislocation. As the aging time is increased from 0.5 to 3 hr. a large increase in the number of δ' is observed and the average size increases to approximately 2000-2500 Å [8]. The particle shape also evolves considerably, a very deep cusp is

produced as individual δ' particles grow around the parent dislocation [Fig. 1]. Small particles of the equilibrium phase δ are also visible on the dislocations in figure 1 (arrow), where the thin δ precipitates have produced the Moiré contrast fringes associated with the dislocations. The latter is another example of heterogeneous nucleation of a precipitate. The evolution of the δ' precipitate morphology is summarized in figure 2 where δ' centered dark field images of specimens aged for times 0.5, 3 and 9 hours at 533 K (260 °C) are shown. These micrographs along with schematic drawings illustrate the evolution of δ' with respect to the catalyzing edge dislocation. Although several attempts were made to observe δ' at shorter times they were unsuccessful. Heterogeneous precipitation of δ' occurs at edge dislocations or dislocations with strong edge character and a kidney shaped particle results (Figs. 2b,c). In this case the Burgers vector is $\frac{1}{2}\langle 110 \rangle$ type.

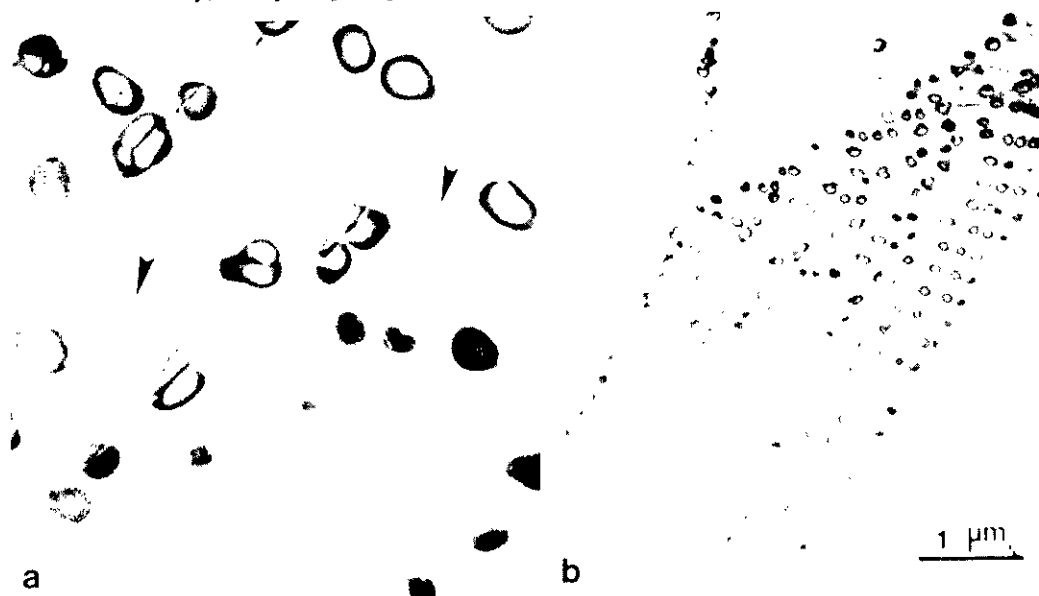


Fig. 1. Co-precipitation of δ and δ' on a dislocation sub-boundary. Aged 260 °C for 3 hours.

An example of δ' nucleation on the edge component of a dislocation is shown in figure 3. Note from the dislocation weak-beam dark-field image (Fig. 3c) that δ' precipitation does not destroy the dislocation structure. As growth progresses, a deep cusp is developed as the particle envelops the dislocation (Fig. 2c). This is followed by elimination of the cusp and loss of coherency with the matrix (Fig. 2d).

The position which the nucleus takes in the dislocation strain field will be just that which relieves the largest proportion of the dilatational transformation strain. All of the theories of

nucleation on dislocations attempt to model the reduction in the nucleation free energy barrier due to the presence of a dislocation. The approach uniformly taken is one that assumes that a dislocation can act as a reaction catalyst because of the free energy stored in its large strain field. The reduction in this free energy because of a local relaxation (either total, for an incoherent particle, or at least partial, for a coherent particle) because of the formation of a second phase particle, is expected to be the primary reason for the catalytic effect.

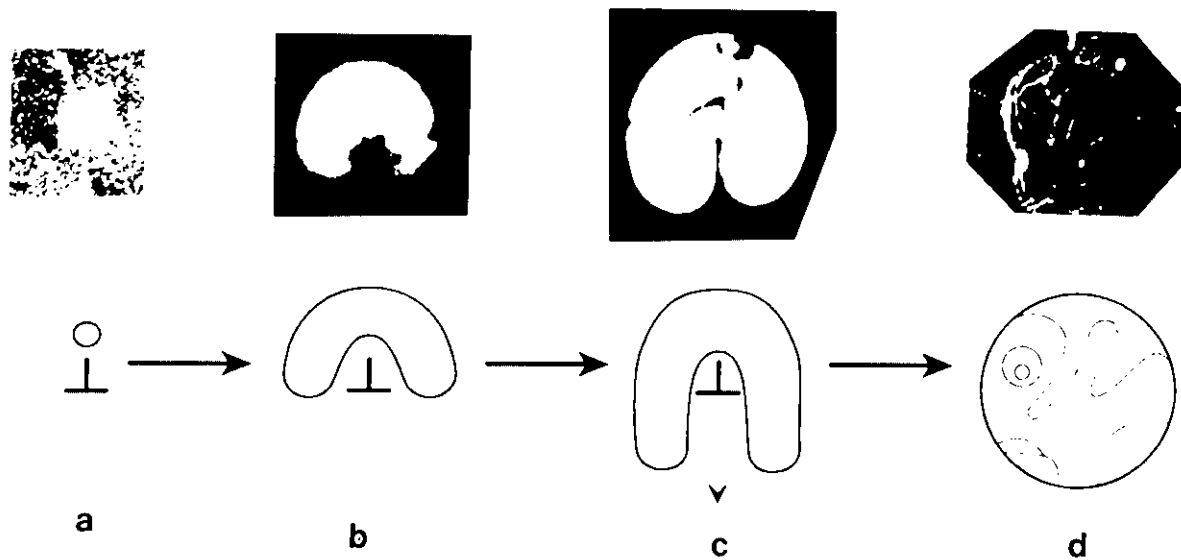


Fig. 2. The evolution of the δ' morphology with aging time at 260 °C shown by δ' - CDF image. The corresponding mechanism is represented by a sequence of sketches.

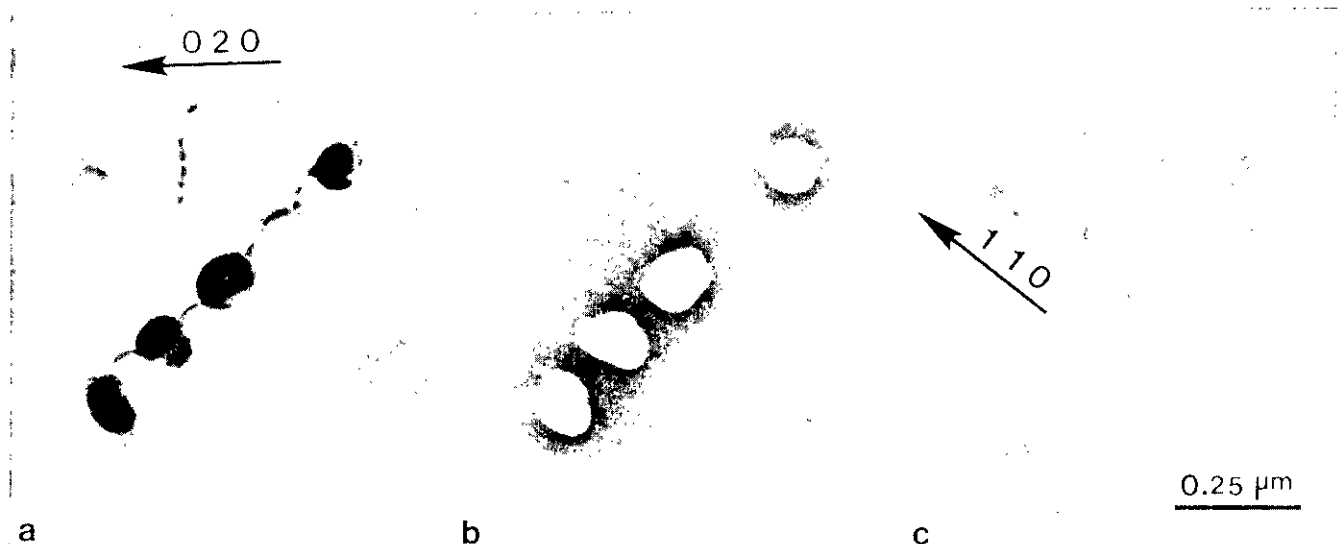


Fig. 3. δ' - nucleation at the edge component of a dislocation. Aged at 260 °C for 1 hour.

δ' Growth Kinetics on Dislocations

Table 2. The linear regression results of $\log(d)$ vs. $\log(t)$ at different temperatures.

aging temperature ($^{\circ}\text{C}$)	index n	R (chi - square)	α_{exp} ($\text{\AA}/\text{sec}^{1/2}$)
210	0.566	0.99	4.81
230	0.551	0.98	6.91
240	0.537	0.99	7.65
250	0.511	0.98	7.36

The results from the measurement of δ' diameter, d , vs. time, t , and temperature, T , are given in figure 4. These results were analyzed using several approaches. The first approach is to plot the relationship between $\log(d)$ and $\log(t)$, which is linear. Good agreement is found (chi-squared, Table 2) between the experimental points and a linear regression fitted curve suggests a relationship of the form

$$d = \alpha_{\text{exp}} t^n \quad (1)$$

where n is in the range from 0.51 to 0.56, and with an average value of 0.54. These indices, n , are close to the parabolic value of 0.50. Determination of the experimental parabolic growth rate constant, α_{exp} , employing eq. (1) is listed in Table 2.

The calculated volume fraction of δ' per unit length of dislocation shows that δ' is still in the growth stage for the heat treatment conditions used in the present work. The theory of diffusion-controlled growth predicts that a spherical particle follows a parabolic growth law. The plot of mean particle radius r vs. square root of time, $t^{1/2}$, is given in Fig. 4. The rate constant α_{exp} can then be obtained from the slope of each curve at different temperatures and is plotted in Fig. 5. For spherical precipitate growth, an analytical solution has been given as [7]:

$$\frac{(C_{\delta'/a} - C_o)}{(C_{\delta'/a} - C_{a/\delta'})} = \frac{(\alpha_{\text{th}}^2/2D_v)\{1 - \alpha_{\text{th}}/2 \sqrt{\pi}/D_v \exp(\alpha_{\text{th}}^2/4D_v) [1 - \text{erf}(\alpha_{\text{th}}/(2D_v))]\}}{2} \quad (2)$$

where $C_{\delta'/a}$ and $C_{a/\delta'}$ are phase boundary compositions, C_o is the corresponding bulk composition, D_v is bulk or volume diffusivity, and α_{th} has same meaning as the rate constant shown in eq. (1). A theoretical α_{th} can be obtained by solving eq. (2) for each temperature. The comparison between these values and the experimental parabolic growth rate constant, α_{exp} is given in Fig. 5. The plot shows that there is a discrepancy between the experimental and theoretical results. Taking into account

the temperature effect, the gradient of α_{th} from eq. (2) is larger than that determined by the experimental data. This can be further investigated by noting that the rate constant α is proportional to the square root of the diffusion coefficient, i.e., $D_v^{1/2}$. Hence, if we assume that δ' growth on dislocations in this work is primarily controlled by volume diffusion of Li, the related activation energy for Li diffusion can be obtained by making the plot of $\ln(\alpha)$ vs. $1/T$ (Fig. 6) since $D_v = D_{v0} \exp(-Q/kT)$, where kT has its usual meaning. The slope of the curve $\ln(\alpha)$ vs. $1/T$ times $2k$ gives an activation energy value of 0.504 eV. Table 3 lists the comparison with related documented activation data.

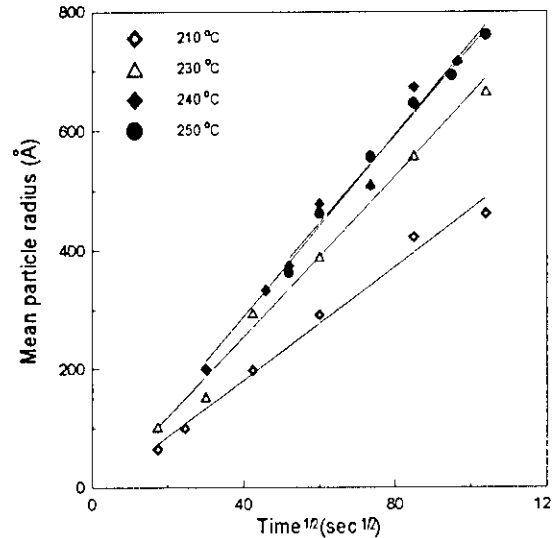


Fig. 4. Mean particle radius r vs the square root of time $t^{1/2}$ plot for different temperatures.

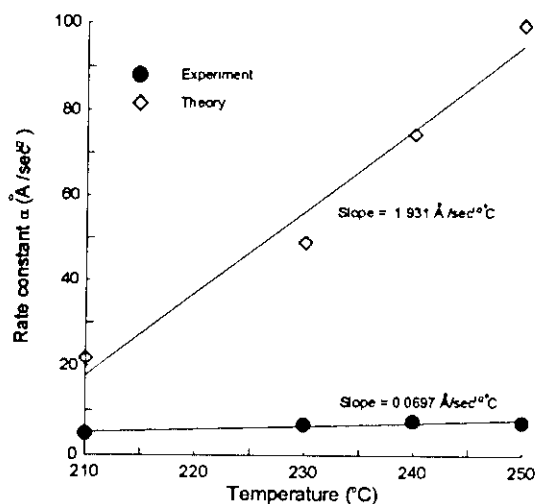


Fig. 5. The rate constant α vs temperature, T .

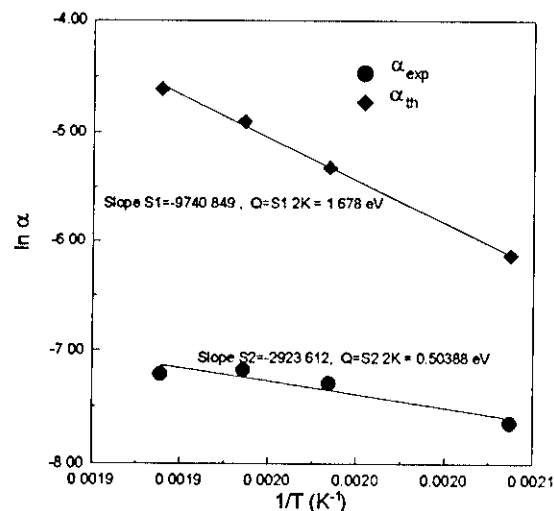


Fig. 6. $\ln \alpha$ vs $1/T$.

Table 3. The comparison of activation energy for Li diffusion in Al.

Agent	Activation Energy (eV)	Reference
Volume	1.25±0.176	Williams & Edington ^[9]
dislocation pipe	0.525±0.173	Kirshnal, Vyboyshechik & Sudnik ^[10]
δ' growth on dislocations	0.504	Present work

The value obtained by experimental data is significantly smaller than the reported value of 1.25 eV, i.e. activation energy for Li volume diffusion in Al matrix. The discrepancy between the experimental results and the parabolic growth theory shown above raises two questions: 1) Is the volume diffusion of Li the only mechanism during the δ' growth on dislocations in the temperature range applied in this work? 2) What role do dislocations have during δ' growth?

IV. Discussion

In order to understand and explain the experimental results, related theories developed previously were examined. The earliest treatment of the effect of dislocations on precipitation was given by Cottrell and Bilby [5] in an attempt to explain the strain-aging of steel. Taking into account the coupling between concentration gradients and the

drift flux which is due to the interaction between solute atoms and dislocations is a complication difficult to treat mathematically. As a simplification, Cottrell and Bilby [5] chose to limit their consideration to systems of initially uniform concentration of solute, aged for only short times. In this case, particle growth kinetics on dislocations of the form $d \propto t^{0.22}$ would be expected. In the present work, the measured value of exponent index associated with time (see Table 2) is higher than 0.22. This indicates that δ' growth kinetics obtained in this experiment are faster than that predicted by a drift flux assumption. Later, Ham [6] developed a model employing a more sophisticated mathematical treatment and obtained a solution which contains an initial transient corresponding to the one given by Cottrell and Bilby but tends to a higher growth rate at longer times, specifically, $d \propto t^{0.26}$. However, the present data obtained for δ' still cannot be explained by Ham's solution.

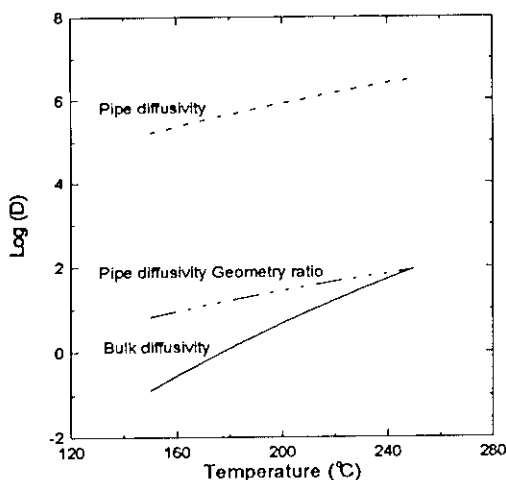


Fig. 7. The comparison between pipe diffusivity D_p and bulk diffusivity D_v .

Calculations utilizing volume and pipe diffusivities for Li in Al alloys based on the data given in Table 3 have been made and are shown in figure 7. The plot demonstrates that pipe diffusion is much faster than volume diffusion. However, the effective region of the dislocation pipe available for mass transport is very small compared to bulk so that volume diffusion becomes more compatible with pipe diffusion if this limitation is considered. This is certainly true with increasing temperature. At high temperatures (240 C), consider a growing spherical precipitate of δ' associated with a dislocation, the growth rate depends on the total number of Li atoms arriving at the surface of the particle from the bulk plus the number arriving from the dislocation pipe region. The contribution from the dislocation pipe can be estimated from the various models that have been developed to study short circuit diffusion. A well known one is Fisher's approach to understand high diffusion paths along grain boundaries [11]. Based on this, a Fisher-type treatment for a cylindrical pipe was developed by Smoluchowski [12]. These ideas were applied to calculate the flux of solute atoms to the δ' precipitates on dislocations directly from dislocation pipes. An average dislocation pipe radius of 10Å and experimental measured δ' radius were used in the calculations. Figure 8 shows the ratio of Li atom fluxes resulting from volume and dislocation pipe diffusivities. The plot indicates that volume diffusion of Li becomes more dominant at higher temperatures and longer aging times. Conversely, as temperature is lowered, diffusion limited phenomena such as growth and coarsening, whose kinetics may be thought to be

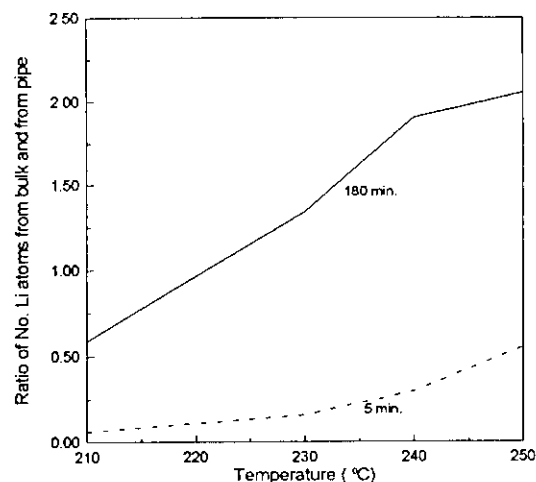


Fig. 8. The ratio of calculated number of Li atoms joined into a δ' particle per second from bulk and from dislocation pipe.

limited by volume diffusion through the matrix phase, can have higher kinetics due to short circuit effects. Pipe diffusion through a dislocation can accelerate the growth of precipitates beyond what would normally be determined employing volume diffusivities exclusively.

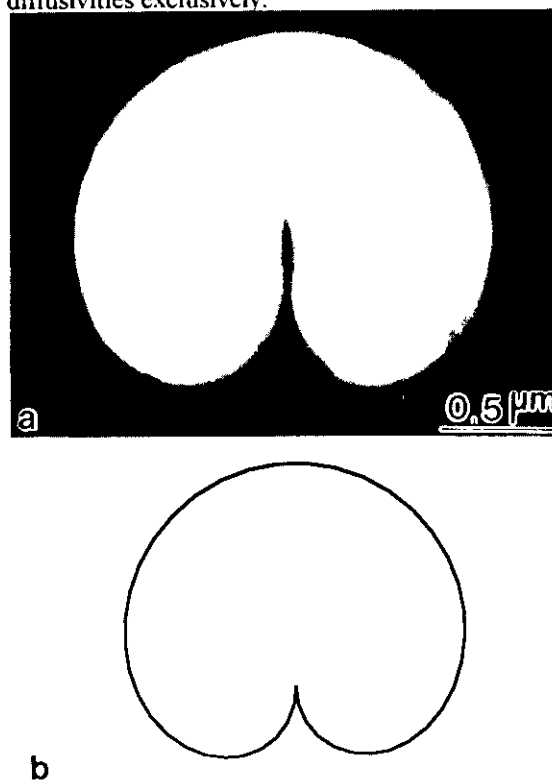


Fig. 9. (a) δ' - CDF image shows a typical δ' morphology, which can be compared with the calculated profile of solute atoms depleted region associated with an edge dislocation.

Finally one can examine how the dislocation strain field affects the δ' growth morphology at very short times when the Li concentration has not build up as described by Cottrell and Bilby. Figure 9(a) is a TEM micrograph showing the δ' shape associated with an edge dislocation core. This shape can be compared with the Li depleted region profile (Fig. 9(b)) calculated from theory [5]. Therefore, at the initial growth stage of δ' the kidney shape was formed and then developed with time as described in the previous section and figure 2.

V. Conclusions

The modeling of δ' growth kinetics cannot be accounted for by volume diffusion of Li alone. Short circuit diffusion of Li atoms in dislocation pipes must be combined with normal diffusion considerations. A fictitious activation energy calculated for the growth kinetics of δ' precipitates actually incorporates both the activation energies of volume and pipe diffusion, but does demonstrate a value less than the reported activation energy of Li volume diffusion alone. Experiments of δ' growth at still lower temperatures will need to be done to extract an activation energy for Li diffusion in dislocation pipes.

Acknowledgments

The authors are grateful to the Department of Energy, Office of Basic Sciences under grant No DE-FG05-89ER45389. Reynolds Metals company is thanked for providing the alloy.

References

1. C.C. Dollins, Acta. Met., vol. 18, 1209 (1970).
2. D.M. Barnett, Scripta Met., vol. 5, 261 (1971).
3. F.C. Larche, "Dislocations in Solids", (edited by F.R.N. Nabarro) vol. 4, p. 137, North - Holland Co.(1979).
4. J.W. Cahn, Acta. Metall., vol. 5, 169 (1975).
5. A.H. Cottrell and B.A. Bilby, Proc. Phys. Soc. (London), vol. A62, 49 (1949).
6. F.S. Ham, J. Appl. Phys., vol. 30, 915 (1959).
7. F.C. Frank, Proc. Roy. Soc. London, vol. 201A, 586 (1950).
8. W.A. Cassada, G.J. Shiflet and W.A. Jesser, Acta Metall., vol. 40, 2101 (1992).
9. D.B. Williams and J.W. Edington, Metal Sci., vol. 9, p. 529 (1975).
10. M.A. Krishtal, M.A. Vyboyshechik and V.A. Sudnik, Fiz. Metal. Metalloved., vol. 36, 1103 (1973).
11. J.C. Fisher, J. Appl. Phys., vol. 22, 74 (1951).
12. R. Smoluchowski, Phys. Rev., vol. 87, 482 (1952).

**Stress-Assisted δ' Precipitation on Dislocations
in an Al-Li Alloy
Z. M. Wang**

- Q: Gary, it is a very nice piece of work as usual. Subgrain boundaries is very interesting, you are getting the formation of the delta prime and since the diffusion has to be greater just to the dislocation pipe compared to the bulk concentration for it to have the nucleation sites. Do you see any PFC at all?
- A: Yes, in fact some of the work we are doing right now is examining the effects of grain boundary misorientation on diffusivity, and because the instrumentation is so good now we can measure PFC's versus grain boundary misorientation and use these data to back-calculate diffusion coefficients in grain boundaries and their possible implication on such phenomena as, for instance, PFC's or texture.
- Q: Do you see a difference between the precipitate location and the high angle boundary misorientation?
- A: Yes, absolutely. However, we did this work on Al-Cu alloys and I did not bring that data here.
- Q: You are talking about the diffusivity as a function of angle of misorientation, what is kind of the ratio between, let's say an average grain boundary misorientation diffusivity in that grain boundary versus that in the dislocation pipe?
- A: The grain boundary diffusion is greater because it delivers more solute along its plane rather than along a line, as with a dislocation. The effect of temperature is very potent.
- Q: I have a question, you talked about coarsening behavior and so forth, but isn't the dislocation lost at some point and will there be a discontinuity then in coarsening behavior?
- A: Yes, I think that it will depend upon coarsening associated with what defect. If the dislocations associated with the delta prime particles move out of the matrix (say to the interphase or grain boundary) the kinetics should change. What I showed is that as time went on an interesting phenomenon occurs (Fig. 2 of our paper). This dislocation actually climbs out of the precipitate cusp and is lost to the interphase boundary, the reason it climbs out is that at some point the growing equilibrium delta requires the lithium from the metastable delta prime precipitate. Because lithium atoms are substitutional with aluminum, vacancies are required. The process of diffusion from the delta prime precipitate to the dislocation and ultimately to the delta particle results in the climb of the dislocation out of the delta prime cusp. The cusp closes because it no longer has the anti-phase boundary. Finally the dislocation wraps

around the delta prime resulting in a loss of coherency, and a change in kinetics.

Q: Well sometimes you get the small delta prime precipitates growing together and when they coalesce you get an anti-phase boundary.

A: Yes, that is true too, 50/50.

Q: Joseph Pickens (Martin Marietta) Where does the delta prime nucleate homogeneously coming very well annealed for this dislocation density? Is it vacancy clusters?

A: If it is homogeneous nucleation it can't be at any matrix defect, it has to be in a perfect lattice. There are only two examples I can think of with homogeneous nucleation. A key in determining whether it is homogeneous is a high particle density. It is homogeneous if the precipitate density is 10^{17} particles per cubic centimeter. There are not that many heterogeneous nucleation sites in the matrix. Besides Al-Li the other one is cobalt particles in the Cu-Co system that seems to be homogeneous nucleation.

Q: Are you going to comment on the parabolic behavior when you would have expected it to be the $\frac{1}{3}$ power?

A: Another thing you have to be aware of is coarsening is a process of constant volume fraction and if you have another subsequent precipitation reaction like delta (in our case), the volume fraction of delta prime is changed. The particles may be getting bigger but the volume fraction of the delta prime is going down, so that is not pure coarsening. What the problem is, and I glossed over, is how come the parabolic growth kinetics from the theory were higher than the growth kinetics of the stress assisted delta prime particles associated with dislocations? Because you have the volume diffusion plus the pipe diffusion, the particles on dislocations should have higher kinetics. The answer is, in part, because of the competition for Li solute. A much higher precipitate density forms on the dislocation leading to increased competition for each Li solute atom.

ALUMINUM-LITHIUM ALLOY 2195 REVERSION AGING STUDY

I. K. Hall¹, D. B. Sisk²,

¹Advanced Systems and Technology
Martin Marietta Astronautics
San Diego, CA 92123

²Advanced Systems and Technology
Martin Marietta Astronautics
Huntsville, AL 35806

Abstract

Reversion aging is of interest to the aerospace industry as a means of improving producibility and reducing cost for aluminum-lithium structural components. Reversion aging of aluminum-lithium alloys after solution heat treatment and quench (SHT&Q) delays the natural aging process creating a stable low strength, high elongation condition ideal for forming. The room temperature stability of the reversion temper eliminates the need for expensive or operationally cumbersome low temperature (dry ice) storage after SHT&Q. This paper describes an investigation into the reversion aging characteristics of the 2195 aluminum-lithium alloy.

A stable low strength, high elongation condition was induced in 2195 aluminum-lithium using a variety of reversion aging practices. The strength attained in the reverted condition was dependent upon the peak temperature reached during reversion aging. Strength and ductility in the reverted condition were not influenced by the time delay between SHT&Q and the reversion aging treatment. Furthermore, after forming or cold working, the reverted temper material responded normally to artificial aging, achieving T8 properties comparable to non-reversion aged material.

I. Introduction

Performance requirements for aircraft and aerospace vehicles have fueled the development of high strength aluminum-lithium alloys for primary structural components. Manufacturing considerations for these same structural components are best satisfied by a material with low strength and high ductility. To accommodate these opposing requirements (low strength/high ductility for forming, high strength in service), forming of an aluminum-lithium part is often accomplished immediately after solution heat treatment and quench (SHT&Q) when the material is in an unstable but low strength as-quenched condition. The part is then artificially aged up to the high strength temper to meet the service requirements.

If forming cannot be accomplished within hours of solution heat treatment, the part is routinely packed in dry ice or refrigerated to delay the natural aging process until the forming operation can be scheduled. Low temperature preservation of large parts for extended periods, however, can be cumbersome and expensive.

For aluminum-lithium alloys, a potentially attractive alternative to low temperature (dry ice) storage is reversion aging. In reversion aging a component is briefly exposed to an elevated temperature. Temperatures up to 390°F for a period of 30 minutes were evaluated in this study. The effect of this brief elevated temperature excursion is to significantly slow the natural aging process, stabilizing the material in the low strength and high ductility condition.

Previous studies, i.e. Gayle et al. [1], have shown that reversion aging of Weldalite™ 049 is caused by the dissolution of δ' and the fine GP zones. Over an extended period of time (>1000 hours at ambient temperature), δ' and the fine GP zones eventually re-precipitate and the strength climbs to the naturally aged T4 level. However, this significant slowing of the natural aging process creates a generous window during which forming operations can be accomplished.

The 2195 aluminum-lithium alloy is of interest to the aerospace industry for use in launch vehicle propellant tanks and adapter structures. This alloy falls within the Weldalite™ system but has a different composition than the Weldalite™ 049 evaluated by Gayle et al.. The same metallurgical phenomena are at work in 2195 so it is reasonable to assume that the 2195 alloy will respond to reversion aging treatments in a very similar manner. However, there is little information in the open literature specifically regarding the reversion aging response of the 2195 composition.

This paper describes the results of a study performed by Martin Marietta Astronautics to address

the 2195 reversion aging information void. The purpose of this study was not to further the metallurgical understanding of reversion aging, but rather, to quantify the reverted response of 2195 and develop a reversion aging practice for 2195 components taking producibility considerations into account (i.e. practical heat up and cool down cycles for large parts, time delays between SHT&Q and reversion aging, etc.).

II. Study Objective

The objectives of this study were to, 1) establish a baseline 2195 ambient temperature natural aging curve, 2) establish a baseline 2195 dry ice storage aging curve, 3) evaluate the effect of heat input on reverted temper yield strength and elongation, 4) evaluate the effect that the time interval between SHT&Q and reversion aging has on reverted temper yield strength and elongation, 5) define the duration of the reverted temper window, at least over the study test period, and 6) evaluate the affect of reversion aging on final 2195-T8 properties.

III. Approach

Test Specimens

Room temperature tensile properties were generated using ASTM standard 4-inch-long "dog bone" specimens, 0.380-inch-wide at the grips, with a reduced gage section of 0.250-inch, and a thickness of 0.200-inch. The specimens were machined in the LT orientation, from 0.375-inch-thick 2195-T8 Al-Li plate. All specimens were solution heat treated at 940 to 955°F for 2.0 hours and cold water quenched to room temperature within 15 seconds.

Aging Practices

Immediately following SHT&Q, the tensile specimens were divided into eight groups and maintained under controlled conditions. Tensile testing was performed at time intervals of 15 minutes, 1, 2, 5, 8, 24, 48, 72, and 144 hours after SHT&Q, reversion aging, or an incubation period. A summary of the eight test groups evaluated in this study is presented in Table 1 and discussed in the following paragraphs.

After SHT&Q, Group 1 specimens were allowed to naturally age at ambient temperature until tensile testing was performed.

The Group 2 specimens were placed in dry ice immediately after SHT&Q and were only warmed to room temperature a few minutes prior to testing.

Table 1. Summary description of the eight test groups included in the reversion aging study.

GROUP	REVERSION AGING STUDY
	DESCRIPTION
1	NATURAL AGING RESPONSE CURVE
2	DRY ICE STORAGE AGING RESPONSE CURVE
3	290°F REVERSION AGING RESPONSE CURVE (1 DAY AFTER SHT&Q, FIGURE 1 PROFILE)
4	390°F REVERSION AGING RESPONSE CURVE (1 DAY AFTER SHT&Q, FIGURE 2 PROFILE)
5	290°F REVERSION AGING TREATMENTS COMPARISON (FIGURE 3 PROFILE)
6	EFFECT OF THE TIME INTERVAL BETWEEN SHT&Q AND REVERSION AGING (1 HOUR VERSES 24 HOURS)
7	EFFECT OF INCREASING PEAK REVERSION TEMPERATURE ON REVERTED TEMPER PROPERTIES.
8	EFFECT OF REVERSION AGING ON FINAL T8 PROPERTIES (AFTER STRETCH AND ARTIFICIAL AGE)

Groups 3 and 4 specimens were allowed to naturally age for approximately one day after SHT&Q before being reversion aged at 290°F and 390°F respectively. The 290°F treatment followed a ramp-hold-ramp temperature profile (Figure 1).

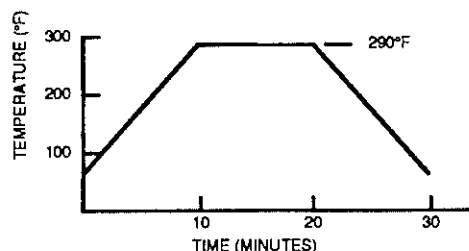


Figure 1. 290°F reversion aging treatment temperature profile (ramp-hold-ramp).

The 390°F treatment followed a ramp-quench profile as illustrated in Figure 2. Total reversion time (exposure to temperatures above ambient) for both treatments was 30 minutes.

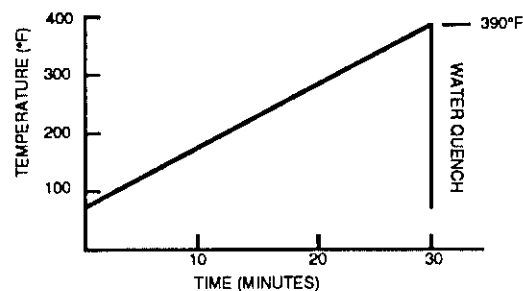


Figure 2. 390°F reversion aging treatment temperature profile (ramp-quench).

Group 5 specimens received a 290°F ramp-quench reversion aging treatment. This reversion treatment temperature profile, shown in Figure 3, was included for comparison with Group 3 to evaluate the effect of heat input for a constant time on reverted temper properties.

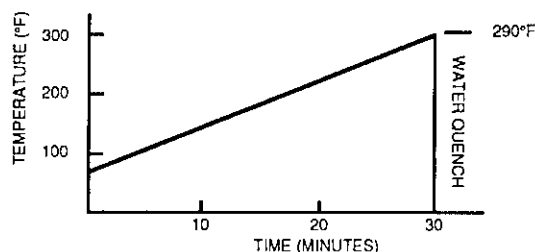


Figure 3. 290°F reversion aging treatment temperature profile (ramp-quench).

Specimens in Groups 6 were identical to Group 3 and 4 specimens except that they were reversion aged one hour instead of 24 hours after SHT&Q. These specimens were included in the study to determine if the strength of reversion aged 2195 was a function of the time between SHT&Q and the reversion treatment.

Group 7 specimens were included in the study to further evaluate the effect of peak reversion temperature on reverted temper properties. Reversion aging treatments at both 230°F and 365°F, with ramp-quench temperature profiles identical those in Figures 1 and 3 were used.

Finally, the Group 8 specimens were included in the study to determine if the various reversion aging practices effected the final T8 properties. After receiving 290°F or 390°F reversion aging treatments at various time intervals following SHT&Q (one hour, 24 hours, and 144 hours), followed by room temperature incubation periods of varying durations up to 144 hours, the specimens in this test group were then stretched 4 to 5% and artificially aged at 290°F for 26 hours to achieve the T8 condition. Non-reversion aged specimens were included in this group as a control.

Test Method

Testing was performed at room temperature on an Instron Model 1125 Electromechanical Universal Test System in the Martin Marietta Mechanical

Properties Test Lab in San Diego, CA. One inch gage marks were placed on each specimen prior to testing. To generate load versus deflection (strain) charts a one inch strain gage extensometer was used. The test machine cross-head travel rate was 0.05 inch per minute through yield at which time the extensometer was removed to preclude damaging it. The cross-head rate was then increased to 0.1 inch per minute until specimen failure occurred. After failure, each specimen was held firmly back together and the distance between gage marks was re-measured. The resulting elongation value was calculated and recorded. All specimens failed normally within the gage section.

IV. Results and Discussion

Aging Response Curves

The tensile test data from the various specimen test groups was used to generate aging response curves for the 2195 alloy. A graph of time versus ultimate tensile strength for the first four test groups is presented in Figure 4. Similar graphs depicting time versus tensile yield strength and time versus elongation are shown in Figures 5 and 6 respectively.

Strength

As can be observed in Figures 4 and 5, the tensile ultimate and yield graphs are essentially identical in shape, with the ultimate strength generally being 25 to 30 ksi higher. For the purposes of the following discussions we will refer to the yield strength data, Figure 5, to illustrate various points.

In Figure 5, the tensile yield strength versus time plot for the Group 1 specimens (natural aging baseline shown with solid circles) shows that the yield strength does not increase significantly within the first hour after SHT&Q. This data indicates that if cold working is to be performed following heat treatment, it should be done as soon as possible. As expected, a significant increase in yield strength was observed soon thereafter. The yield strength rose from 20.5 ksi immediately after SHT&Q to 36.3 ksi within the first 8 hours. After 8 hours the strength increase rate slowed with a value of 40.2 ksi recorded at hour 24. By hour 72 the yield strength only rose to 42.6 ksi., and after 2,518 hours, the yield strength had reached approximately 50 ksi.

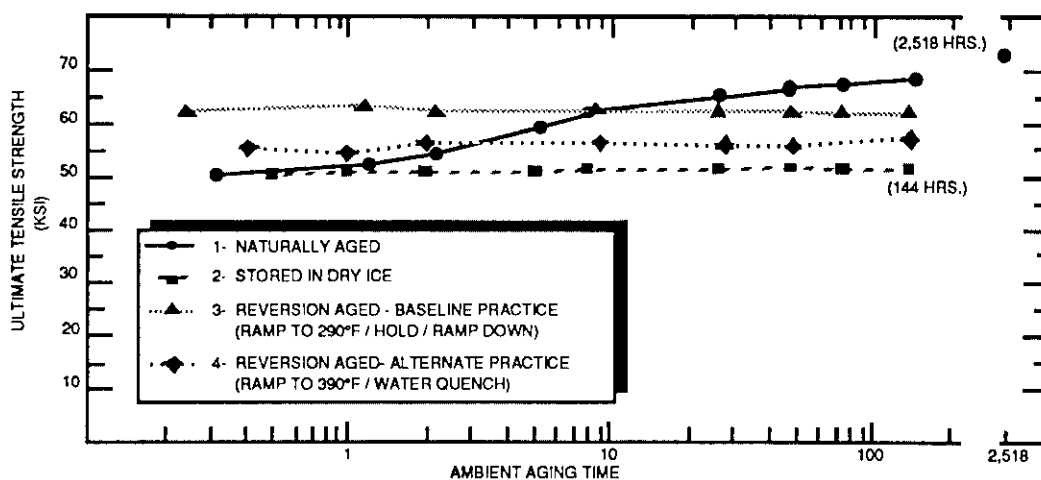


Figure 4. Ultimate tensile strength verses time curves for 2195 Al-Li.

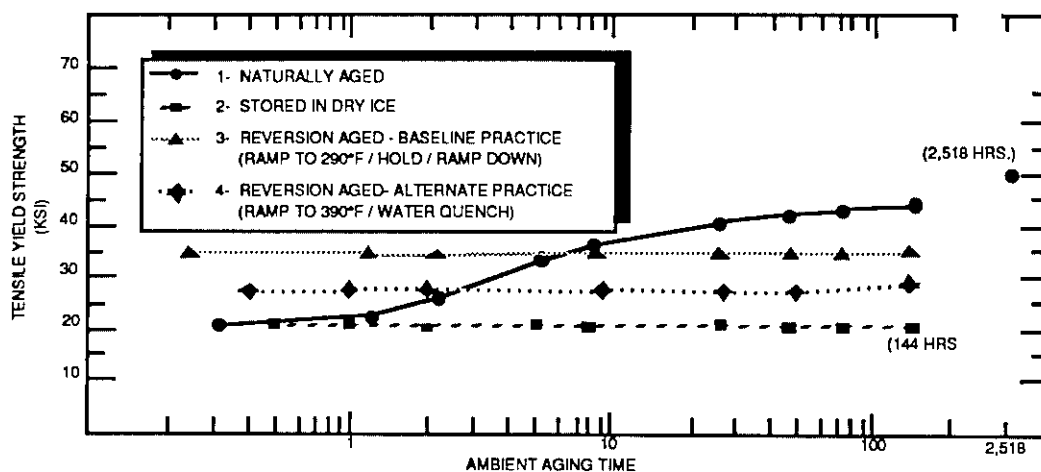


Figure 5. Tensile yield strength verses time curves for 2195 Al-Li.

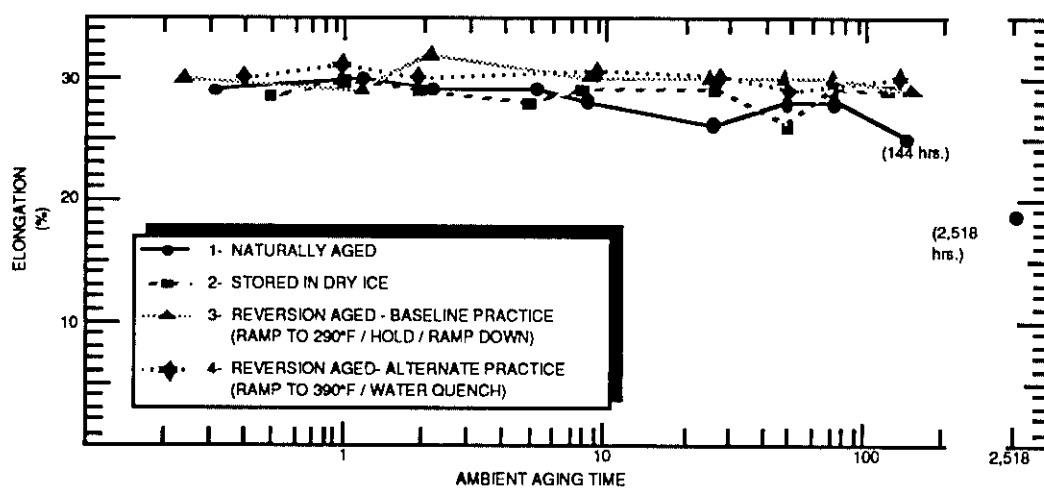


Figure 6. Elongation percentage verses time curves for 2195 Al-Li.

The Group 2 tensile yield plot (solid squares) in Figure 5 is essentially flat. This clearly shows that the dry ice storage effectively retarded any natural aging response over the 144 hour test period. The typical yield strength of dry ice stored specimens was 20.8 ksi.

The data further shows that the 390°F reversion aging treatment was more effective than the 290°F treatment in lowering the yield strength of the reverted temper. A typical yield strength of 27.5 ksi was observed after the 390°F treatment while the specimens treated at 290°F had typical values of 34.6 ksi.

It should be noted that the properties achieved in the reverted temper are a function of both temperature and time. As indicated, the lowest yield strength in this experiment was associated with the 390°F reversion practice performed over a fixed 30 minute heating cycle. As previously noted, the 30 minute cycle was selected based on practical handling considerations for large parts. However, it is recognized that a complete study, including time as a variable, should be performed.

As can be seen in Figures 4 through 6, a significant incubation period, or cold forming window, occurs after both the 290°F and 390°F reversion aging treatments. Based on the flatness of the strength vs. time curves it appears that the low strength/high elongation state will continue far beyond the 144 hours. The 144 hour limit was selected for this evaluation because it was believed to be a reasonable time frame during which a large part could be moved and set-up for stretching or forming operations. One of our recommendations for future work is to extend these curves out to significantly longer times.

Elongation

As shown in Figure 6, and as might be expected, the Group 1 elongation values decayed as the 2195 samples naturally aged. However, the elongation values in general did not change drastically over time for any of the four test groups and conditions. This data suggests that reversion aging is effective in maintaining a highly ductile condition. Elongation, therefore, need not be a concern when performing subsequent forming operations in the reverted temper.

290°F Ramp-Quench Comparison (Group 5)

Table 2 shows a comparison of the tensile test results from Group 5. After being allowed to

naturally age for 24 hours following SHT&Q, some of the specimens were reversion aged using the 290°F ramp-hold-ramp treatment and some were reversion aged using the 290°F ramp-quench treatment. Tensile tests were performed both immediately after reversion aging and after a 144 hour incubation period.

Table 2. A comparison of tensile properties from two different 290°F reversion aging treatments performed at two different times.

290°F REVERSION AGING TREATMENT COMPARISON (30 MINUTE EXPOSURE)						
SEQUENCE OF EVENTS	RAMP-UP HOLD RAMP-DOWN			RAMP-UP QUENCH		
	FTU (KSI)	FTY (KSI)	E (%)	FTU (KSI)	FTY (KSI)	E (%)
SHT&Q NATURAL AGE 24 HRS REVERSION AGE TEST	61.88	34.60	30.00	63.48	36.26	28.00
SHT&Q NATURAL AGE 24 HRS REVERSION AGE INCUBATE 144 HRS TEST	62.50	35.40	29.00	64.87	37.82	27.50

The data suggests that the ramp-hold-ramp reversion treatment and the ramp-quench treatment are very close to each other in terms of achieving the reverted condition. The ramp-quench treatment is considered more desirable from a practical manufacturing standpoint. Both treatments were effective in maintaining the reverted temper over the 144 hour incubation period.

Time To Perform Reversion Age (Group 6)

Table 3 shows a comparison of the tensile test results from test Groups 6 and Group 3. The Group 6 specimens were reversion aged immediately after SHT&Q (within one hour). The Group 3 specimens were allowed to naturally age for 24 hours prior to reversion aging.

The small variation in the data indicates that it really doesn't matter if the reversion aging treatment is performed immediately after SHT&Q or after a one day delay. Data recorded during cold stretching of some of the Group 8 specimens, which were reversion aged 144 hours after SHT&Q, also indicated no noticeable difference in yield strength as a function of time before reversion treatment.

Although the 290°F reversion aging treatment was the focus of the above discussion, it should be noted that the same trend holds true with respect to the 390°F reversion age treatment.

Table 3. A comparison of Groups 6 and 3 reverted properties.

COMPARISON OF WHEN 290°F REVERSION AGING IS PERFORMED AFTER SHT&Q			
SEQUENCE OF EVENTS	RAMP-UP HOLD RAMP-DOWN		
	FTU (KSI)	FTY (KSI)	E (%)
SHT&Q REVERSION AGE TEST	65.23	33.81	25.00
SHT&Q NATURAL AGE 24 HRS REVERSION AGE TEST	62.82	35.16	28.00

Effect of Reversion Temperature (Group 7)

Tensile yield strength data from the Group 7 specimens, reversion aged at 230°F and 265°F (ramp-quench profile), is plotted on the graph in Figure 7 along with the 290°F and 390°F data. The plotted data illustrates the effect that increasing reversion aging temperature has on decreasing the reverted tensile yield strength of the 2195 alloy.

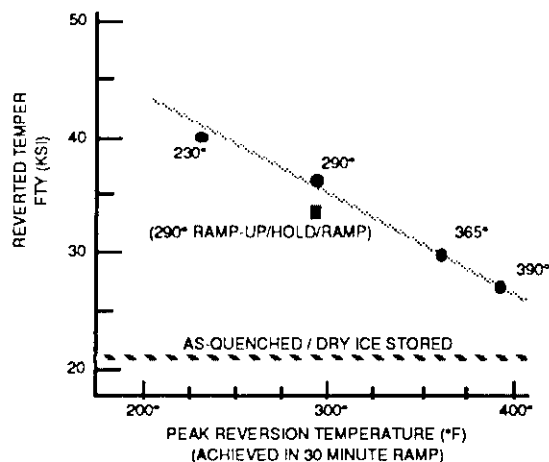


Figure 7. Reverted yield strength decreases with increasing peak reversion aging temperature.

At least over the temperature range used in this study, a linear relationship exists between peak reversion aging temperature and the resulting yield strength (temperature profile and exposure time were held constant). As the reversion aging temperature increases, the yield strength decreases. The trend indicates that a follow on study should include reversion temperature profiles above 390°F.

Reversion Aging Effect on T8 Properties (Group 8)

Figure 8 is a bar chart comparing typical tensile ultimate, yield, and elongation values of 290°F and 390°F reversion aged specimens that were cold stretched 4-6%, then artificially aged to the T8 condition. The natural aging times of these specimens before reversion aging, and the incubation times after reversion aging all varied. Changes in these processing variables had a very small influence on the final properties.

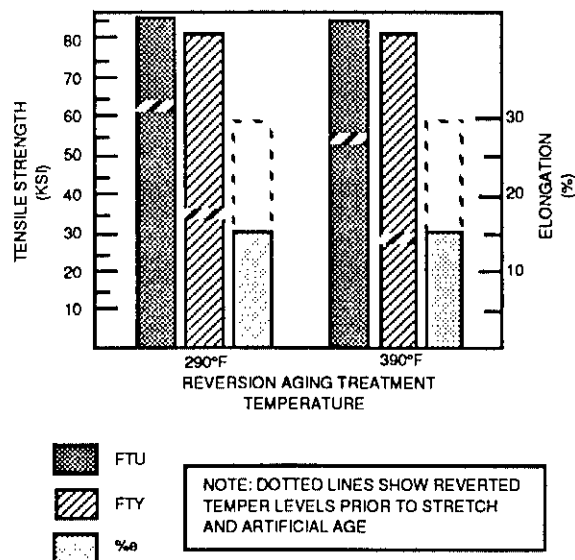


Figure 8. Ftu, Fty, and elongation for alloy 2195 reversion aged then stretched and artificially aged to the T8 temper.

The dotted lines in the histogram chart in Figure 8 identify the properties in the reverted condition. The fully shaded bars represent the properties of the final T8 temper. As can be seen, from the figure, similar T8 properties were achieved after both reversion aging treatments. Since the 390°F reversion aging treatment produced the lowest reverted temper strength levels, it shows the largest increase with stretching and artificial aging. Non-reversion aged T8 properties were within the scatter of the Figure 8 results.

V. Conclusions

1. Reversion aging halts the natural aging process, creating a stable low strength, high elongation condition in Al-Li alloy 2195.

2. The yield strength in the reverted temper is inversely proportional to the peak temperature achieved during the 30 minute reversion aging process used in this study.
3. Within the limits of this investigation, the yield strength of reversion aged alloy 2195 was not found to be a function of the time between SHT&Q and when the reversion treatment was performed.
4. Reversion aging had no measurable influence on the final peak aged strength of 2195 after stretch and artificial aging.

VI. Recommendations

1. Further reversion aging investigations should be performed considering time as a variable.
2. A future study should investigate the effect of reversion aging on fracture properties.
3. Temperatures above 390°F should be investigated to determine if reversion temper yield strengths can be brought down closer to the values obtained with dry ice stored specimens.
4. The incubation period after reversion aging should be investigated beyond 144 hours.
5. Further studies should also be directed at confirming the metallurgical processes behind the reversion effect in 2195 aluminum-lithium.

Acknowledgment

Work performed by the authors was supported under the Martin Marietta Astronautics, Cryogenic Tank Technology Program.

References

Sources Cited

1. Gayle, F.W., Heubaum, F.H., and Pickens, J.R., "Natural Aging and Reversion Behavior of Al-Cu-Li-Ag-Mg Alloy Weldalite™ 049.", ALUMINUM-LITHIUM 5, p. 701-710.

Sources Referenced

1. Sisk, D.B. to Hall, I.K., memo, "Aging Optimization Test Program for 2195", November 30, 1993.
2. Eisenreich, T.J., Test Lab Engineering Report, "Tensile Test Results Generated During the Reversion Age Study of 2195 Aluminum-Lithium Alloy", TJE: SMP 94-003.
3. Hall, I.K., Advanced Systems Engineering Report, "Aluminum-Lithium Alloy 2195 Reversion Aging Study", January 27, 1994.
4. Hall, I.K., Advanced Systems Engineering Report, "Aluminum-Lithium Alloy 2195 Reversion Aging Follow-on Study", April 12, 1994

Aluminum-Lithium Alloy 2195 Reversion Aging Study
I.K. Hall

- Q: Joe Pickens (Martin Marietta) What was the initial amount of stretch in the T8 temper?
- A: 4-6 percent.
- Q: Mack Roberts (Martin Marietta) I just wanted to comment, the work that you did there would be a real good application for a designed experiment. You would probably get more information with less testing. You might want to consider that for the add-on, the additional work you are going to do. I would be glad to help you set that up.
- A: We would be glad to have your assistance. We have worked with designed experiments on our rolled ring forging and our near-net forging programs. But, what happened in this case was that we started out doing a onesy-towsy experiment, then it grew and it grew with follow-on experiments. We have talked about using a DOE and we would like to get with you guys, especially if you have some good experiences with designed experiments. We have worked a little with Taguchi methods, but would appreciate your help.
- Q: Ed Starke - I assume that what you are after is to not have to ship in dry ice.
- A: Yes. We can ship, but we can not guarantee, even with insulated containers, that the dry ice would not sublime during a prolonged shipment, allowing natural aging and the associated tensile strength increase to occur.

CRITICAL ELECTROCHEMICAL POTENTIALS RELATING TO THE RAPID ENVIRONMENTALLY ASSISTED CRACKING OF ADVANCED ALUMINUM ALLOYS

F.D. Wall, G.E. Stoner
Center for Electrochemical Sciences and Engineering
Department of Materials Science and Engineering
University of Virginia
Charlottesville, Virginia 22902

Abstract

The contribution of an active pathway to the environmentally assisted cracking of several Al-Li-Cu alloys is discussed in terms of the electrochemical behavior of the tempered alloys and modelled boundary features. Scratching electrode experiments have revealed regions of applied electrochemical potential in which solutionized Al-Li-Cu alloys passivate spontaneously whereas copper depleted aluminum and the T_1 phase undergo active dissolution. In-situ constant load testing and slow extension rate testing of tempered alloys have revealed transitions in time-to-failure and in mechanical behavior corresponding to small changes in applied potential. Correlations based on these critical potentials have been drawn between the behavior of the T_1 phase, copper depleted aluminum and the behavior of the tempered alloys.

I. Introduction

A possible mechanism for environmentally assisted cracking (EAC) in aluminum-lithium-copper alloys is the preferential dissolution of an active phase or region combined with the effects of mechanical stress to result in crack growth. The critical components of such a mechanism are the solution chemistry necessary for crack growth and the electrochemical behavior of the alloy on the microstructural scale.

An initial insight into the necessary components of the solution chemistry was made by Holroyd^[1] and Craig^[2] in their investigations of alloy 8090 (Al-Li-Cu-Mg). They found that axially stressed, smooth bar tensile samples of peak-aged 8090 would not fail under conditions of constant immersion in 3.5 w/o NaCl solution but rapidly failed upon removal to laboratory air. Samples were pre-exposed to the aqueous chloride environment for up to fifty days then removed to non-aqueous environments varying in terms of relative humidity and the presence or absence of atmospheric CO_2 . Rapid failures did not correlate with a specific value of relative humidity but

were found to strongly correlate with the presence of CO_2 . Samples which were removed to a CO_2 -free environment did not exhibit failures.

A possible explanation for the change in material response upon removal from the aqueous environment is the development of a new local solution chemistry. Al-Li-Cu samples exposed to NaCl solution tend to undergo pitting attack and upon removal of specimens from a bulk aqueous environment the pits may retain solution and thus become isolated, occluded cells. Holroyd attempted to simulate the occluded chemistry by creating a system of high surface area to solution volume ratio and determining the resultant solution chemistry^[1]. When shavings of material were exposed to aqueous chloride environments the generated solutions were found to be alkaline (pH of 8 to 10) and to contain lithium ions in the millimolar concentration range determined via atomic absorption spectroscopy. Based on the factors of CO_2 , alkaline solution chemistry and the presence of lithium ions, Craig proposed the following to account for the pre-exposure embrittlement phenomenon^[2]: (1) The NaCl environment is highly aggressive towards the alloy and under conditions of constant immersion depassivates the grain boundaries not allowing crack initiation, (2) Removing a sample from the bulk environment allows the local chemistries to become alkaline and active, (3) Absorption of CO_2 promotes passivation by $LiAlO_2$ and allows for a borderline active/passive condition under which anodic dissolution crack initiation and propagation is possible.

Pre-exposure embrittlement was also found to apply to alloy 2090 (Al-Li-Cu) as determined by Moran^[3,4] using the experimental approach of Craig and Holroyd^[1,2]. Moran modified the model proposed by Craig for environmental cracking by rejecting $LiAlO_2$ as the critical passivating species since it should precipitate independent of the presence of CO_2 ^[4]. Moran's model predicted a more direct role for the dissolved CO_2 in the formation of the passivating species, possibly leading directly to the precipitation of Li_2CO_3 . X-ray diffraction studies performed by Buchheit^[5,6] indicated that passivation is

due to the formation of hydrotalcite-type films on the material surface.

Moran also suggested that the heterogeneous precipitation of the T_1 (Al_2LiCu) phase influenced the EAC behavior of these alloys^[3] by providing an active pathway along subgrain boundaries. Buchheit^[6,9] provided an argument for a critical role for the T_1 phase based on quantification of corrosion rates of microstructural features in a model crevice environment. Buchheit synthesized a bulk ingot intended to simulate the behavior of the T_1 phase and determined the electrochemical behavior in aqueous solutions using potentiodynamic polarization experiments. His results indicated that the modeled phase was highly active compared to the surrounding matrix material^[6]. These findings were in agreement with the observed pre-exposure embrittlement phenomenon: in an occluded environment crack propagation could occur due to dissolution of the active phase along subgrain boundaries while the matrix remained passive due to a precipitation reaction based upon lithium ions and dissolved carbonate ions; however, in the presence of a bulk electrolyte, the environment would be depassivating towards the crack walls and a sharp crack could not be maintained.

By characterizing the electrochemistry of the microstructural features and the bulk alloy in the same environmental conditions, Buchheit was able to demonstrate a correlation between the EAC behavior of the bulk alloy and the electrochemical parameters of the individual microstructural phases. His experiments revealed that in a simulated crevice environment such as 0.6M NaCl + 0.1M Li_2CO_3 the breakdown potential (E_{br}) of the matrix phase ($\alpha-Al$) is shifted to a more noble potential than that of the T_1 phase^[9,10]. Thus the two E_{br} values define a potential range in which the matrix phase is passivated while the T_1 phase is highly active. It was shown that potentiostatically polarizing a mechanically stressed smooth tensile sample within this potential range resulted in rapid material failure (less than one day). Samples polarized cathodic to the E_{br} value of the T_1 phase did not exhibit failures nor were any indications of localized attack apparent after five days of testing.

The results of Buchheit^[6-10] and Moran^[3,4] suggest a mechanism of EAC in Al-Li-Cu alloys controlled by the presence of an active subgrain boundary phase and the development of a passivating crevice environment. The critical potential associated with rapid EAC failures shows correlation with the breakdown potential of the T_1 phase as determined by a bulk casting. The model based upon dissolution of the T_1 phase fails to predict crack propagation along

regions of the sub-boundaries separating the precipitate particles. The current research re-examines critical potentials for rapid environmentally assisted cracking of Al-Li-Cu alloys with particular attention to possible contributions from a copper depleted region along grain or sub-grain boundaries.

II. Experimental Procedures

Materials

The primary alloys used in this research effort are aluminum alloys 2090 (Al-2 Li-2.5 Cu-0.1 Zr) and 2095 (Al-4 Cu-1 Li-0.25 Mg-0.25 Ag-0.1 Zr). Both alloys were received in the form of stretched and aged 3.8 cm thick plate. 2095 was studied in two as-received tempers and in the solutionized and quenched condition (SHT + CWQ). 2090 was studied in the as-received T8 condition, SHT + CWQ, and in several under aged tempers. All aging conditions and designations to be used for reference to the various alloy/temper combinations are given in Table 1. Aluminum alloy 2124 (Al-4 Cu-1.5 Mg-0.25 Zn-0.2 Zr) was used in the T8 condition for comparisons with a non-lithium containing alloy. To model copper depleted material 99.99 Al was used as well as three Al-Cu binaries (Al-0.1 Cu, Al-1.0 Cu, Al-3.96 Cu).

Test Environments

An aqueous environment containing 0.6 M NaCl + 0.1 M Li_2CO_3 is used to simulate a possible occluded cell chemistry based on lithium ions from the corroding material and carbonate due to dissolved CO_2 from ambient air. Previous research has shown that a potential range exists in this environment where stressed tensile samples undergo rapid dissolution-assisted cracking^[10]. Aqueous 0.1M NaCl + 0.1M Na_2CrO_4 has been observed to produce the same general material response as the lithium carbonate environment but with less experimental variability and for that reason has been used as a complimentary environment for many of the experiments in this research.

Constant Load Experiments

The EAC behavior of short transverse, smooth bar tensile samples was assessed using a constant load/time-to-failure experiment. Samples were wet polished to a 1200 grit finish with silicon carbide grinding paper followed by ultrasonic cleaning in acetone then deionized water. The tensile samples were mounted in an environmental cell via grips extending into the test cell. The grips and ends of the samples were painted with an insulating coating leaving only the gauge length of the sample exposed.

Table 1. Aging conditions and designations for materials discussed in this paper.

Designation	SHT	Quench	Stretch	Aging	Comments
2090-T8	1 hr/545°C	cold water	3.5%	14 hrs/160°C	peak-aged
2090-A	1 hr/545°C	cold water	none	1.5 hrs/160°C	under-aged
2090-B	1 hr/545°C	cold water	none	3.0 hrs/160°C	under-aged
2090-C	1 hr/545°C	cold water	none	7.0 hrs/160°C	under-aged
2090-SHT	1 hr/545°C	cold water	none	none	model for α -Al
2095-A	1 hr/505°C	cold water	6.5%	20 hrs/143°C	under-aged
2095-B	1 hr/505°C	cold water	6 %	30 hrs/143°C	peak-aged
2095-SHT	1 hr/505°C	cold water	none	none	model for α -Al

The experimental procedure began with loading the sample to 60% of the material yield stress (YS). Solution was added until the gauge section of the sample was completely submerged. The solution was aerated with laboratory air using a fish tank air pump. A Stonehart BC 1200 potentiostat was used to potentiostatically hold the specimen at a prescribed potential using a three electrode arrangement incorporating a saturated calomel reference and platinized niobium counter electrode. After the potential was applied, the specimen potential, current and applied load was monitored as a function of time until the termination of the experiment. The end of the experiment was determined by either the failure of the specimen or the passage of five days time without evidence of localized corrosion (both visual observation and assessment of corrosion current were used for this determination). TTF and failure/no failure were recorded as a function of applied potential for each combination of material and environment.

A variation of the basic constant load experiment was also performed in which the sample surface was mechanically destabilized by scratching with a glass rod in an attempt to expose bare material to the environment/potential combination. The scratch was performed after a stable corrosion current had been obtained at the applied potential. Upon

scratching a transient in the corrosion current was observed. After the transient the current either returned to the pre-scratched value, indicating repassivation, or increased in magnitude over time reflecting material corrosion. In cases where the sample did not repassivate sample failure occurred within 24 hours. If the sample did repassivate the applied potential was increased to a more anodic value and the process was repeated until a potential was reached which resulted in sample failure.

Slow Extension Rate Experiments

The EAC behavior of the research alloys in the experimental environments was further assessed by slowly straining specimens under conditions of constant applied potential. Specimens were prepared according to the description given under constant load experiments. After samples were mounted in the test cell and the solution added, they were slowly strained at an initial strain rate of 10^{-6} /sec until failure occurred. Load, potential and corrosion current were monitored as a function of time for the duration of the experiment.

Straining Electrode Experiments

These experiments were used to assess the response of material to combinations of potential and environment under conditions of plastic deformation.

Smooth round tensile specimens were mounted in a cell in a three electrode configuration with a saturated calomel reference electrode and a platinized niobium mesh counter electrode. Sample ends and grips were coated with an insulating material such that only the gauge length was exposed. Once the sample was mounted in a screw driven table-top load frame, the test solution was added, the sample was potentiostatically polarized then strained to failure at an initial strain rate of approximately 10^{-4} /sec. Corrosion current, potential and applied load were monitored as a function of time for the duration of the experiment.

Scratching electrode experiments

These experiments were used to assess the electrochemical response of unstrained specimens to various combinations of environment and applied potential. An electrical connection was made to specimens by spot welding nickel ribbon wire to one face of a 1 cm^2 flat specimen. The specimen was then mounted in epoxy so that the opposite face was exposed. The exposed face was polished to a 600 grit finish with SiC grinding paper. Specimens were exposed to test solution under an applied potential. Once a stable corrosion current was observed, the sample surface was scratched with a glass rod. If the specimen spontaneously repassivated (based on corrosion current measurements) then the applied potential was increased by 10mV to a more anodic value and the process repeated.

III. Experimental Results

Constant Load Experiments

Samples of 2095-A,B and 2090-T8 polarized to $-475\text{mV}_{\text{SCE}}$ in the chloride/chromate environment all failed in less than 24 hours; however, polarization to $-550\text{mV}_{\text{SCE}}$ did not result in any perceptible signs of localized corrosion after five days of exposure. Similar results were obtained for samples in the chloride/lithium carbonate environment at potentials of $-700\text{mV}_{\text{SCE}}$ and $-750\text{mV}_{\text{SCE}}$ respectively.

When the scratching electrode technique was used in conjunction with these tests, it was found that samples would fail at potentials where they had previously appeared to be stable. The potential where a transition from repassivation to material failure is observed has been denoted the critical potential. All reported critical potentials are from scratching electrode experiments. Figure 1 shows the critical potentials for 2095-A, 2095-B, 2090-T8 and 2124-T8 in the $0.6\text{M NaCl} + 0.1\text{M Li}_2\text{CO}_3$ environment. The scatter in the data and the lack of distinction in

critical potentials in this environment make it difficult to establish any trends in the data.

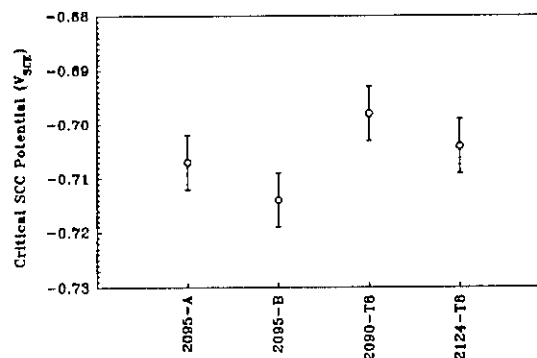


Figure 1. Critical EAC potentials for ST samples loaded to 60%YS in $0.6\text{M NaCl} + 0.1\text{M Li}_2\text{CO}_3$.

More extensive characterization has been performed in the $0.1\text{M NaCl} + 0.1\text{M Na}_2\text{CrO}_4$ environment since it has been possible to distinguish between critical potentials for various materials in this environment. Figure 2 contains the data for various materials. The easily identifiable differences in critical potentials make it possible to use this parameter to distinguish various materials and tempers.

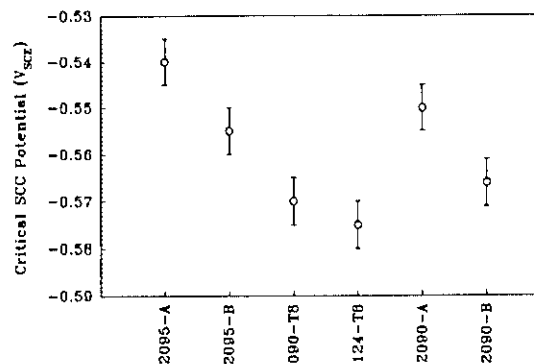


Figure 2. Critical EAC potentials for ST samples loaded to 60%YS in $0.1\text{M NaCl} + 0.1\text{M Na}_2\text{CrO}_4$.

A significant difference exists in the corrosion currents recorded for the scratching electrode/constant load tests for under aged 2090 compared to 2090-T8 and the tempers of 2095 investigated. Figures 3 and 4 show the applied tensile load, corrosion current, and applied potential for under-aged and peak-aged 2090 respectively. Under-aged material exhibits a very brief period of corrosion (approximately 20 minutes) between the failure inducing scratch and material failure and during this period the corrosion currents only reach 30-50 μA . In

contrast are the results for the peak-aged material (Figure 4) in which the sample corrodes for approximately 24 hours before failure with corrosion currents in the 100 μ A range.

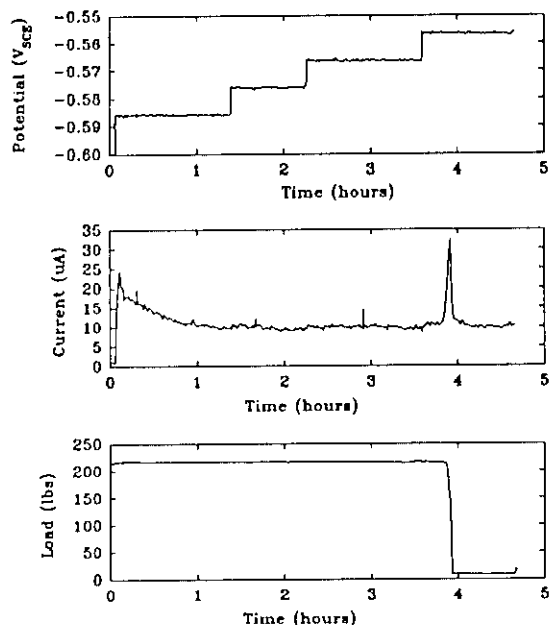


Figure 3. Underaged 2090-A loaded to 60%YS in 0.1M NaCl + 0.1M Na₂CrO₄.

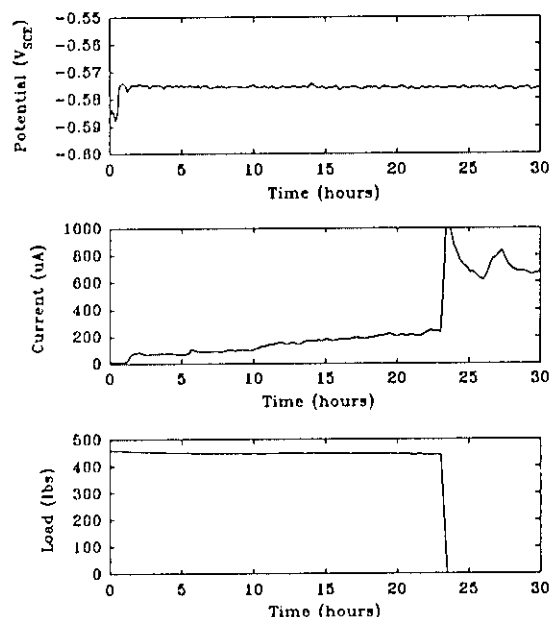


Figure 4. 2090-T8 loaded to 60%YS in 0.1M NaCl + 0.1M Na₂CrO₄

Slow Extension Rate Experiments

At this time only one sample for each of the temper/potential/environment combinations has been tested; therefore, the data presented for these experiments is intended to indicate trends in material behavior and not reflect absolute values of the measured parameter.

The reduction in elongation to failure compared to straining in air was determined for 2095-A and 2095-B in the 0.1M NaCl + 0.1M Na₂CrO₄ environment as a function of applied potential. The resulting data is shown in Table 2. For the open circuit experiments there was essentially no change in elongation compared to the specimens pulled in air and no evidence of significant corrosion. At -540mV_{SCE} there was a noticeable decrease in elongation to failure. For this potential no evidence of localized corrosion was evident during elastic deformation while the onset of plastic deformation coincided with large increases in corrosion current and the appearance of visible localized corrosion sites. At the most anodic potentials investigated (-475mV_{SCE}) large corrosion currents were observed from the outset of the test and the specimens suffered complete loss of material properties before the yield strength of the material was achieved.

Table 2. Reduction in elongation to failure for 2095-A and 2095-B strained in 0.1M NaCl + 0.1M Na₂CrO₄ at 10⁻⁶/sec.

Potential (V _{SCE})	2095-A ($e_{f,air}-e_{t,env}$)/ $e_{f,air}$	2095-B ($e_{f,air}-e_{t,env}$)/ $e_{f,air}$
open circuit (approx -0.7)	0.01	0.01
-0.540	0.5	0.8
-0.475	1	1

Straining Electrode Experiments

Straining electrode experiments were performed on SHT+CWQ 2090 and 99.99 Al; the former to simulate the behavior of grain interiors and the latter to simulate the worst case of copper depletion along a boundary. Results from these experiments are given in Figure 5 for the NaCl/Na₂CrO₄ environment at an applied potential of -550mV_{SCE} and Figure 6 for the NaCl/Li₂CO₃ environment at an applied potential of -700mV_{SCE}. Applied electrochemical potentials were chosen from regions where the constant load specimens were observed to fail after scratching experiments were performed. Straining of the 99.99 Al under the prescribed conditions resulted in large corrosion currents at the onset of plastic deformation. Plastic

deformation of the SHT+CWQ 2090, however, resulted in spontaneous repassivation for each potential/environment combination.

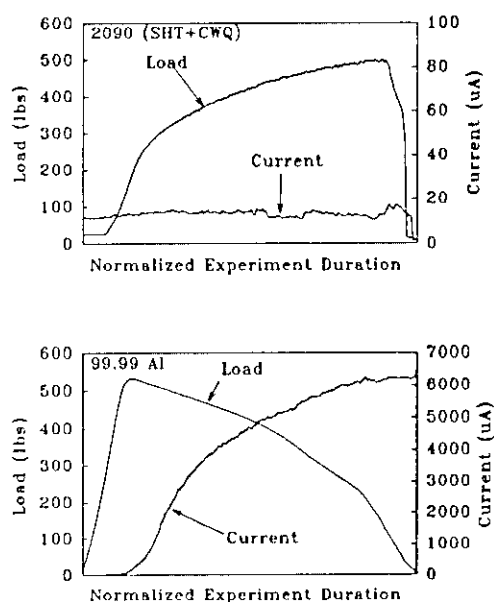


Figure 5. Current responses for plastically deformed SHT 2090 and 99.99 Al polarized to $-550\text{mV}_{\text{SCE}}$ in $0.1\text{M NaCl} + 0.1\text{M Na}_2\text{CrO}_4$.

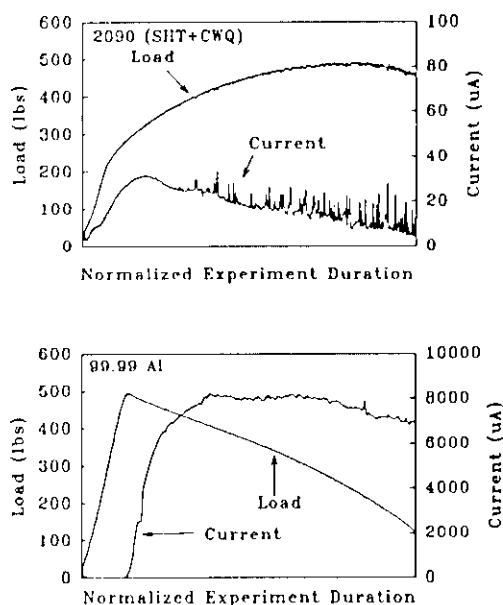


Figure 6. Current responses for plastically deformed SHT 2090 and 99.99 Al polarized to $-700\text{mV}_{\text{SCE}}$ in $0.6\text{M NaCl} + 0.1\text{M Li}_2\text{CO}_3$.

Scratching Electrode Experiments

Scratching electrode experiments were performed to assess the potentials at which various materials would no longer spontaneously repassivate in the test environments. Figure 7 contains representative current vs time plots from scratching electrode experiments performed on 2095-A and 2095-B in $0.1\text{M NaCl} + 0.1\text{M Na}_2\text{CrO}_4$. The first two graphs are for experiments performed at $-550\text{mV}_{\text{SCE}}$. At this potential scratching the surface of 2095-A results in current transients followed by material repassivation whereas scratching the 2095-B surface results in sustained corrosion. Increasing the potential to $-525\text{mV}_{\text{SCE}}$ and repeating the experiment on the 2095-A temper results in sustained corrosion. These experiments demonstrate a difference in critical potential based upon material temper. The peak-aged 2095-B has a more cathodic critical potential than the under-aged 2095-A.

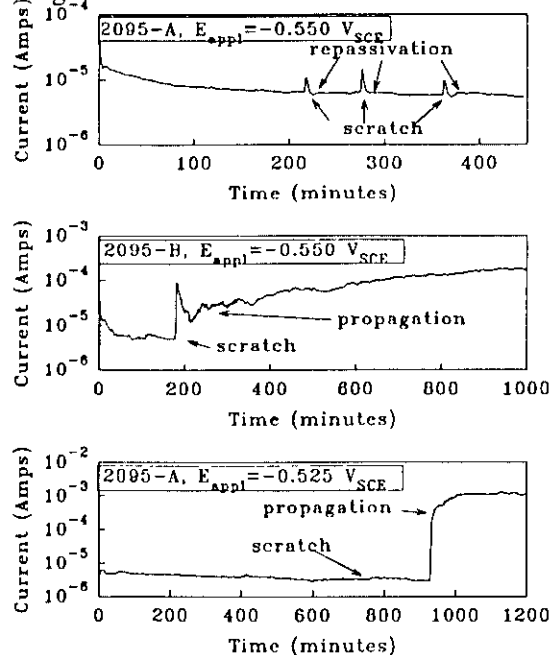


Figure 7. Current responses of two 2095 tempers in $0.1\text{M NaCl} + 0.1\text{M Na}_2\text{CrO}_4$ after scratching with a glass rod.

Figure 8 contains data for scratching electrode experiments performed on SHT+CWQ 2095 and 99.99 Al. These data indicate that the critical potential for the 99.99 Al occurs around $-600\text{mV}_{\text{SCE}}$ and the critical potential for the solutionized material occurs around $-500\text{mV}_{\text{SCE}}$. Since SHT+CWQ 2095 contains approximately 4 w/o copper, this experiment indicates the bounds of critical potentials for aluminum containing between 0 w/o and 4 w/o copper. In order to verify the relationship between

copper content and critical potential scratching electrode experiments were performed on three Al-Cu binarics ranging from 0.1 to 3.96 w/o copper. The results of these experiments are shown in Figure 9 as a plot of critical potential vs copper content.

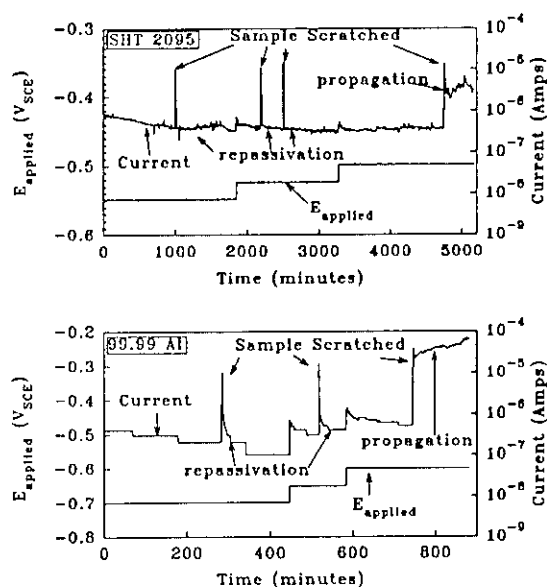


Figure 8. Data for scratching electrode experiment performed on SHT 2095 and 99.99 Al in 0.1M NaCl + 0.1M Na₂CrO₄.

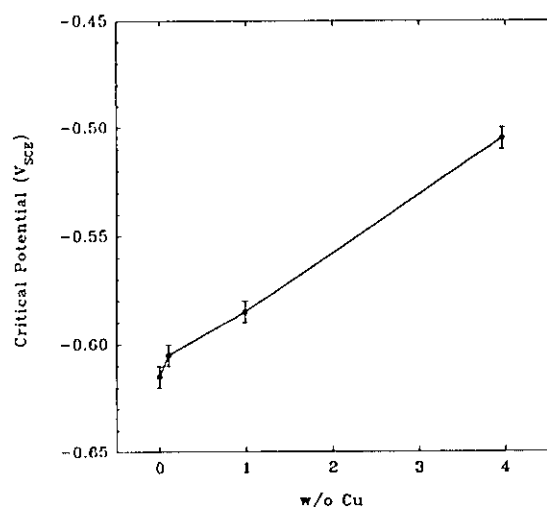


Figure 9. Critical potentials determined as a function of copper content in 0.1M NaCl + 0.1M Na₂CrO₄.

IV. Discussion

A transition from spontaneous repassivation to propagation of corrosion and material failure occurs at a characteristic applied potential for a given material/temper/environment combination (Figures 1 and 2). A similar transition in material behavior has been reported by Buchheit^[9,10] for the environments under consideration. His data indicated that materials would not fail when polarized cathodically with respect to the breakdown potential of the T₁ phase as determined by electrochemical characterization of a bulk casting of the phase^[8]. A criteria for rapid EAC failure was proposed as follows: Samples polarized cathodic to the E_{br} value for the T₁ phase will not fail and samples polarized between the E_{br} values of the T₁ phase and the grain interiors will rapidly fail due to intersubgranular corrosion^[9,10].

The results of this investigation suggest an amendment to the criterion for rapid failure. Since failures have been observed in the chloride/chromate environment at potentials cathodic to -550mV_{SCE} and the reported value for the T₁ E_{br} value in this environment is approximately -510mV_{SCE}⁷, it appears that failures can occur below the critical potential associated with the T₁ breakdown potential. Rapid EAC failures occur in the investigated environments when a critical potential is exceeded, and if localized attack is responsible for the failures, then the critical potential should correspond to the electrochemical behavior of a microstructural feature or features. Likely candidates include the highly active T₁ phase and a region of copper depletion caused by precipitation of Cu-rich phases, or perhaps a combination of both features.

Evidence of a Cu-depleted region along both sub-grain and grain boundaries in an Al-Li-Cu alloy has been reported by Kumai et al.^[11] in the form of scanning transmission electron microscopy/electron dispersive x-ray data. Profiles across sub-grain and grain boundaries indicate a region of decreased Al and increased Cu content bordered by regions of heightened Al content and decreased Cu content. The authors proposed that the solute depleted zones were due to the formation of copper rich phases along the boundaries. Both 2090^[12] and 2095^[13] are known to be strengthened by T₁ (Al₂CuLi) precipitation which occurs preferentially along sub-grain boundaries and, therefore, it is suspected that similar copper depletion occurs along boundaries in these alloys as was observed by Kumai.

In this investigation the worst case of Cu-depletion has been modelled with 99.99 Al and the undepleted case with solutionized and quenched alloy

material. The straining and scratching electrode experiments were performed to determine if the electrochemical behavior of these materials could be linked to the behavior of the bulk alloy.

The straining electrode experiments give an indication of material electrochemical behavior under conditions of plastic strain for a given environment and imposed potential. The data (Figures 5 and 6) show that at $-550\text{mV}_{\text{SCE}}$ in the chloride/chromate environment the 99.99 Al is highly active while the SHT+CWQ alloy spontaneously repassivates upon being plastically deformed. Thus, at a growing crack tip under these conditions plastic deformation would result in a highly active Cu-depleted region and a spontaneously passivating matrix. This behaviour accurately predicts the EAC failures observed for the tempered alloys in the constant load experiments.

Results from the straining electrode experiments only describe the electrochemical behavior for two extreme cases of solid solution copper levels in an aluminum matrix. To evaluate the relationship between copper content and critical potential, scratch testing was performed on several aluminum-copper binary alloys. Figure 9 shows the resulting data for alloys of 0, 0.10, 1.0, and 3.96 w/o copper. These data indicate significant increases (more anodic) in the critical potential for copper additions in the 0.1 to 3.96 w/o range. This data parallels that reported by Gavele^[14] for pitting potentials of Al-Cu binary alloys in a sodium chloride environment. He found that varying the copper content from 0 to 4 w/o resulted in an anodic shift of the pitting potential on the order of 150 mV.

If the critical potentials associated with rapid EAC failures reflect the electrochemical behavior of a copper depleted region, then the dependence of critical potential on copper content (discussed above) predicts a variability in the critical potentials for alloys with a different extent of copper depletion along the boundaries. A variability in extent of copper depletion is governed by the initial copper level in the alloy and by the thermal treatment. Thus, according to this reasoning, the critical potentials determined by the constant load testing should vary as a function of alloy and temper.

Inspection of the data in Figures 1 and 2 reveals that alloys 2090 and 2095 do exhibit different critical potentials and that different tempers of the same alloy also have differing critical potentials. The only easily distinguishable trend in the data is identified by examining critical potentials for different aging times for a given alloy at a fixed temperature. According to this criterion, the potentials for the under-aged (2095-A) and peak-aged (2095-B) may be

compared to one another and the under-aged tempers of 2090 may be compared. The 2090-T8 may not be compared to the under-aged tempers since only the material in the T8 condition underwent a 3.5% stretch prior to aging (see Table 1). The critical potential for the 2095-B temper is found to be cathodic to the value for the 2095-A temper. According to the model for copper depletion, this difference corresponds to a greater extent of depletion in the B temper. If the extent of copper depletion begins at no depletion for a solutionized and quenched material and progresses towards a greater extent of depletion with tempering, then the critical potentials of the depleted boundaries should become more cathodic as the extent of aging increases. From this reasoning it appears that the copper depletion model for critical potentials in tempered alloys is able to correctly predict the observed trend. The scratch testing on unstressed 2095-A and 2095-B confirms these results (Figure 7). Also the same trend is observed for underaged 2090 tempers although the potentials are not as well defined as for the 2095 tempers.

There is a significant difference in the constant load experiments for the extremely underaged tempers of 2090 compared to the other materials/tempers investigated. For 2090-T8, 2095-A and 2095-B failure in the constant load testing only occurs after high corrosion currents ($100\text{ }\mu\text{A}$ - 10 mA) have been sustained for extended lengths of time (10-30 hours) - see Figure 4. Contrastingly, in the under-aged tempers of 2090 failures have occurred after brief periods (20-40 minutes) of less severe corrosion ($20\text{-}50\text{ }\mu\text{A}$). Thus the total charge passed before failure in the severely under-aged materials is orders of magnitude less than that in the peak-aged or near peak-aged materials. This extreme contrast suggests a significant change in the mechanism of crack propagation for the different tempers. At this time insufficient data has been collected to explain this profound change in behavior. Although these differences exist, the similarity in critical potentials still links the behavior all of the tempers to a common microstructural feature.

If observed critical potentials for tempered alloys are due to the formation of a copper depleted region along sub-grain or grain boundaries and are not due to the precipitation of T_1 , then similar critical potentials should be observed in other Al-Cu alloys which do not contain the T_1 phase. Figures 1 and 2 reveal that critical potentials for alloy 2124 exist in both the $\text{NaCl}/\text{Na}_2\text{CrO}_4$ and $\text{NaCl}/\text{Li}_2\text{CO}_3$ environments in potential ranges similar to those observed for alloys 2090 and 2095. The similarity in potentials can be rationalized by the existence of

copper depleted regions in all three alloys; however, electrochemical parameters of the T_1 phase cannot explain this similarity between alloys since 2124 contains no lithium and hence no T_1 .

Two likely pathways for dissolution based EAC in Al-Li-Cu alloys are copper depleted regions and sub-boundaries decorated with the active T_1 phase. The temper dependance of the critical potential and the observation of a critical potential in alloy 2124 similar to those of 2090 and 2095 are facts more easily explained by copper depletion being the dominating feature. However, the role of the T_1 phase in the EAC behavior cannot be dismissed on the basis of this data. As reported by Buchheit⁷, the T_1 phase exhibits a breakdown potential at a potential of about $-510\text{mV}_{\text{SCE}}$ in the chloride/chromate environment, but is still highly active at potentials cathodic to this value. Over the range in potential covering all of the critical potentials determined in this research, the T_1 phase is reported to have a corrosion current density greater than 10^{-5} amps/cm². The highly active nature of the T_1 phase suggests that it contributes to crack propagation during EAC of these alloys. However, the presence of this phase may not be sufficient to cause rapid EAC failures. Further research is required to separate the roles of copper depleted regions and the T_1 phase.

Some additional insight into the possible roles of T_1 and a copper depleted region is gained by examining the reduction in elongation to failure data from the SSRT testing performed on 2095-A and 2095-B in the NaCl/Na₂CrO₄ environment (Table 2).

At the open circuit potential the reduction in elongation to failure is essentially zero, indicating an absence of EAC. Additionally, no significant corrosion current was recorded for the duration of this experiment. The open circuit potential for these alloys in the chloride/chromate environment is approximately $-700\text{mV}_{\text{SCE}}$. Scratching electrode experiments (Figure 9) place this potential below the critical potential for aluminum containing 0 w/o copper; therefore, even during plastic deformation, when bare material is exposed to the test environment, a region of depleted copper should spontaneously repassivate. Under these same conditions the T_1 phase should have a corrosion current density of approximately 10^{-5} amps/cm². Therefore, the condition of T_1 active and the copper depleted region spontaneously repassivating results in no observable environmental effects.

Increasing the potential to $-540\text{mV}_{\text{SCE}}$ results in significant reductions in elongation to failure for both 2095 tempers. During the test the corrosion current remained at a low value (μA range) until the

onset of plastic deformation at which time currents rose to the mA range. The scratching electrode data places this potential in the region where a copper depleted zone will not repassivate after bare material has been exposed to the solution and the polarization data for the T_1 phase indicates a corrosion current density of approximately 10^{-5} amps/cm² at this potential. These experiments predict the onset of plastic deformation will trigger rapid EAC cracking for the case of T_1 active and the copper depleted region not spontaneously repassivating.

At the most anodic potential tested, $-475\text{mV}_{\text{SCE}}$, both tempers of 2095 exhibited complete loss of mechanical properties before the yield point of the material was reached. Corrosion currents approached the milliamp range soon after the sample was potentiostatically polarized. At this potential the copper depleted region will not repassivate and the T_1 phase will corrode at a current density greater than 10^{-4} amps/cm². Thus for the case of T_1 highly active and copper depleted region not repassivating, this experiment predicts extreme EAC initiating well before plastic deformation of the material has occurred.

These experiments show that for the T_1 phase being highly active plastic deformation is not required for initiation of EAC, whereas when the T_1 phase is still active but to a lesser extent, plastic deformation is required to initiate EAC. These results indicate that T_1 may play a critical role in the initiation of cracking. The reduction in elongation to failure at potentials correlating to critical potentials predicted for a copper depleted region suggests that the activity of a copper depleted region may control rapid EAC in these alloys for the investigated environmental conditions.

V. Conclusions

1. Scratching electrode experiments performed on various aluminum-copper binary alloys in conjunction with constant load experiments on tempered Al-Li-Cu alloys suggests critical potentials for EAC correlate to the electrochemical behavior of a copper depleted region.
2. The temper dependance of critical potentials in alloys 2090 and 2095 can be rationalized by a crack propagation model based on dissolution of a copper depleted pathway.
3. The similarity in critical EAC potentials for alloys 2124, 2090 and 2095 can not be explained by the presence of the T_1 phase since it does not occur in

alloy 2124; however, a copper depleted region could occur in each of these materials and could account for the similarity in behavior.

4. Differences in total charge passed and times-to-failure for extremely under-aged tempers of 2090 compared to peak-aged material suggest a change in crack propagation mechanism with tempering.

References

1. N.J.H Holroyd, A. Gray, G.M. Scamans, R. Hermann, Aluminum Lithium Alloys III, C. Baker, P.J. Gregson, S.J. Harris, C.J. Peel, eds. (The Institute of Metals, London, 1986) p 310.
2. J.G. Craig, R.C. Newman, M.R. Jarret, N.J. Holroyd, *J. de Physique*, 48, C3 (1987): p.825.
3. J.P. Moran, Ph.D. Dissertation, University of Virginia, 1990.
4. J.P. Moran, G.E. Stoner, Aluminum Lithium Alloys V, T.H. Sanders, Jr., E.A. Starke, Jr., eds. (MCE Publications Ltd., Birmingham, UK, 1989), p.1187.
5. R.G. Buchheit, M.D. Bode, G.E. Stoner, *Corrosion*, 50, 3 (1994): pp.205-214.
6. R.G. Buchheit, Ph.D. Dissertation, University of Virginia, 1991.
7. R.G. Buchheit, G.E. Stoner, Aluminum Lithium Alloys V, T.H. Sanders, Jr., E.A. Starke, Jr., eds. (MCE Publications Ltd., Birmingham, UK, 1989), p. 1347.
8. R.G. Buchheit, Jr., J.P. Moran, G.E. Stoner, *Corrosion*, 46, 8 (1990): p.610.
9. R.G. Buchheit, Jr., F.D. Wall, Jr., G.E. Stoner, "The Effect of Applied Potential in Static Load SCC Testing of 2090 in Cl⁻ and Cl⁻/CrO₄²⁻ Environments," Proceedings of the Electrochemical Society - Environmentally Enhanced Fracture Symposium, Fall Meeting 1990 (Pennington, NJ, 1991).
10. R.G. Buchheit, Jr., F.D. Wall, Jr., G.E. Stoner, "Stress Corrosion Cracking of Al-Li-Cu-Zr Alloy 2090 in Aqueous Cl⁻ and Mixed Cl⁻/CO₃²⁻ Environments," *Corrosion*/91, Paper no. 99, (Houston, TX: NACE, 1991).
11. C. Kumai, J. Kusinski, G. Thomas, T.M. Devine, *Corrosion*, 45, 4 (1989): p. 294.
12. M.K. Tosten, A.K. Vesudevan, P.R. Howell, Aluminum Lithium Alloys III, C. Baker Editor (The Institute of Metals, London, 1986), p.490.
13. T.J. Langan, J.R. Pickens, Aluminum Lithium Alloys V, T.H. Sanders, Jr., E.A. Starke, Jr., eds. (MCE Publications Ltd., Birmingham, UK, 1989), p. 691.
14. J.R. Gavele, S.M. de Micheli, I.L. Muller, S.B. de Wexler, I.L. Alanis, "Critical Potentials for Localized Corrosion of Aluminum Alloys," Localized Corrosion, (Houston, TX: NACE, 1972), pp. 580-599.

**Critical Electrochemical Potentials Relating to the Rapid Environmentally
Assisted Cracking of Advanced Aluminum Alloys
F. D. Wall**

- Q: Alex Cho (Reynolds) One of your conclusion about using 2124 aluminum in reference alloy, but 2124 does not have T1 base; however it could have another active phase?
- A: Yes, I should have mentioned that there is a possibility that 2124 contains an active phase that could result in the same type of failure as a T1 based mechanism would cause in the lithium containing alloys. However, the similarity in the transition potentials for the two materials drives us to consider that the mechanism may be due to a common microstructural feature and not two different active phases which just happen to have the same electrochemical characteristics. but you have a completely legitimate argument and that is something I should have addressed when I brought up the data.
- Q: Timothy Langan (Martin Marietta) You used the solutionized and quenched 2095 as your matrix, that would really be the matrix in the very under aged type temper. If your trying to compare the difference between the grain and the subgrain boundary it is better to look at single crystals.
- A: That is true, that would be the ideal case. What I have done originally was intended to simulate the two worst case extremes of copper concentration, represented by the solutionized material and pure aluminum. Those are the outer bounds used to establish a trend. You are right that the outer bound should actually be the copper concentration of the matrix for the temper used in the electrochemical experiments.

ENVIRONMENTALLY ASSISTED CRACKING AND LOCALIZED CORROSION SUSCEPTIBILITY OF ALUMINUM ALLOYS 2195 AND 2219

Timothy J. Langan , Patrick E. McCubbin and Joseph R. Pickens

Martin Marietta Laboratories
1450 S. Rolling Rd.
Baltimore, Maryland 21227

ABSTRACT

The Al-Cu-Li-Ag-Mg alloy Weldalite® 2195 has been proposed as the main structural alloy for the liquid hydrogen and liquid oxygen tanks for the next generation of launch systems. Based on the prior performance of other high strength aluminum alloys, a head-to-head study of corrosion and stress-corrosion cracking (SCC) was performed to determine the susceptibility of 2195 relative to 2219. Corrosion and SCC specimens were machined from 1.8-in thick 2195 T8 and 2-in thick 2219 T87 plate. No SCC was observed for either alloy tested under alternate immersion in an aqueous 3.5% NaCl solution. Although no SCC was observed, extensive linear pitting was present for both alloys. Potentiodynamic polarization studies showed that both alloys pit at the corrosion potential (ECORR) in an aerated aqueous 3.5% NaCl solution. In addition, very similar values of ECORR were measured for 2219 and 2195 in the aerated solution (~0.720 volts vs. SCE). Based on this preliminary evaluation, it appears that replacing 2219 with 2195 will not result in an increase in susceptibility to corrosion or SCC. Further work is required to relate results from this accelerated testing with susceptibility in actual service environments.

1.0 INTRODUCTION

The weight savings associated with the high strength, low density and increased modulus of the Al-Cu-Li-Ag-Mg-Zr Weldalite® alloy 2195(1-5) make it a superior candidate for replacing the conventional Al-Cu alloys currently used for cryotankage on launch systems. Historically, susceptibility to stress-corrosion cracking (SCC) has limited the usefulness of high-strength, age-hardenable aluminum alloys(6). In addition the electrochemically

active nature of lithium has raised concerns as to its effect on corrosion susceptibility as an alloying element in alloys such as 2195. However, previous work by Langan(7) and coworkers(8-9) showed no SCC susceptibility for Al-Cu-Li-Ag-Mg Weldalite® alloys 2094 and 2095. A degradation in both tensile strength and elongation resulting from directional, non-stress-assisted pitting, was observed in specimens exposed stressed and unstressed under alternate immersion (AI) in a 3.5% NaCl aqueous solution. The directional pitting occurred on stressed and unstressed specimens for all tempers investigated, with extensive intersubgranular corrosion in the severely underaged tempers.

The work reported in this paper was performed to provide a head-to-head comparison of the resistance to corrosion and SCC for 2195 T8 plate vs. 2219 T87 plate. Corrosion potentials (ECORR) were measured for both alloys in aerated and deaerated aqueous 3.5% NaCl solutions and in an ASTM test solution (formulated to ensure that corrosion is not limited by cathodic reactant) to assess the possibility of galvanic corrosion problems associated with replacing 2219 with 2195.

Electrochemical potentiodynamic scans were conducted to provide an assessment of pitting susceptibility in aqueous saline environments for both alloys. The breakaway potentials (EB) were used to define relative pitting susceptibility of the two alloys. The role of localized attack in the degradation of mechanical properties for both alloys was also determined. In addition, SCC testing was performed for both alloys in accordance with ASTM G47 and ASTM G 64.

2.0 MATERIALS AND EXPERIMENTAL PROCEDURES

2.1 Materials

The 2195 specimens were machined from 4.6-cm (1.8-in) thick plate, which was cast and rolled by Reynolds Metals Co. (lot #913U881-A-1B) at their plant in McCook, IL. All testing was performed in the as-received T8 temper (SHT, water quenched, stretched 6% and aged for 36h at 143°C). Tensile strengths of 581 MPa (84.2 ksi) and 585 MPa (84.8 ksi) and tensile yield strength of 556 MPa (80.7 ksi) and 538 MPa (78.0 ksi) were measured by Martin Marietta Manned Space Systems for this plate in the L and LT orientations, respectively. The lot number and mechanical properties for the 5.1-cm (2-in.) thick 2219-T87 plate were not available. The chemical composition of the 2195 plate as measured by the inductively coupled plasma technique is given in Table 1. The nominal composition of 2219 is also presented in Table 1.

face of each plate at the half thickness ($t/2$) location. The specimens were mounted in either Buehler EPO-KWIK fast cure epoxy or Struers Citofix acrylic mounting resin and the L-LT face was polished using 1000 grit SiC paper. The specimen edges were masked with MICROSTOP to avoid crevice corrosion at the interface between the metal and the mount.

ECORR values were measured and anodic potentiodynamic scans were performed for both alloys in a 3.5% NaCl aqueous solution under aerated and deaerated conditions. In addition, cathodic potentiodynamic scans were performed for both alloys in the 3.5% NaCl solution under aerated conditions. Solutions were aerated or deaerated by bubbling either lab air or N₂ through a glass stone. Potentiodynamic scans were performed at a scan rate of 0.1 mV/s.

Table 1 Chemical Composition of Alloys
(wt%, balance Aluminum)

	Cu	Li	Ag	Mg	Zr	Mn	V	Ti
Weldalite® 2195	4.00	0.89	0.40	0.41	n/a	--	--	n/a
2219 (nominal)	6.30	--	--	--	0.18	0.30	0.10	0.06

2.2 Electrochemistry

The corrosion potentials (ECORR) were measured for 2195 T8 and 2219 T87 according to the ASTM Standard Practice for Measurement of Corrosion Potentials of Aluminum Alloys (G69-81). In this practice, ECORR is measured in an aqueous solution with 58.5 g of NaCl and 9 ml of 30% H₂O₂ per liter of water. The H₂O₂ is present in the solution to ensure that the electrochemical reactions are not limited by cathodic reactant. Measurements were made vs. a saturated calomel electrode (SCE) using a PAR Model 373 Potentiostat/Gavanostat. A standard three electrode system was used for all measurements with a graphite counter electrode. Test specimens were sectioned from the L-LT

2.3 Environmentally assisted cracking testing

Resistance to environmentally assisted fracture was evaluated for both alloys using 0.125-in diameter direct tensile specimens. Window-frame-type loading fixtures (ASTM Standard Practice G 49) were used for testing. The stress was applied using a specially designed loading device (see ASTM Standard Practice G 49) and was calculated based on displacement in the gage section using Hooke's law. Specimens were loaded to 75% of the measured short transverse (ST) yield strength and exposed under AI in a 3.5% NaCl solution for either 1 or 10 days. Unstressed specimens were also exposed under AI in a 3.5% NaCl aqueous solution for 1 or 10 days. After testing, surviving specimens

were either loaded to failure on an Instron test frame or sectioned and examined metallographically.

3.0 RESULTS

ECORR values measured for 2219 and 2195 in accordance with ASTM G69 showed little variation during the 2-h exposure. The naturally aerated aqueous solution with NaCl and H₂O₂ used for these measurements induced pitting for both alloys. Similar ECORR values were measured for 2219 and 2195: -0.717 V and -0.712 V respectively (Table 2). To provide a baseline for the testing, ECORR values were also

$\sim 10^{-6}$ A/cm² is maintained (Figure 1) on polarizing in the anodic direction from ECORR up to the breakaway potential (E_B), with breakaway occurring at essentially the same potential for both alloys; -0.683 V for 2219 and -0.661 V for 2195. In the aerated solution no passive region is observed for either alloy (Figure 2). The cathodic polarization behavior in the aerated solution is similar for 2195 and 2219, with both alloys reaching a limiting current of $\sim 2.3 \times 10^{-5}$ A/cm².

No failures were observed for 2219 and 2195 specimens loaded to 75% of their respective ST yield strengths (σ_y) and exposed

Table 2 ECORR and E_B measured for 2219 and 2195 in aerated and deaerated solutions

Alloy	ECORR ASTM Test Solution	ECORR Aerated 3.5 wt% NaCl Solution	ECORR Deaerated 3.5 wt% NaCl Solution	E _B Deaerated 3.5 wt% NaCl Solution
2195 T8		-0.720 -0.721	-1.132 -1.130 -1.073	-0.661 -0.660 -0.661
<i>mean</i>	-0.717	-0.720	-1.111	-0.661
2219 T87		-0.720 -0.716 -0.718	-0.977 -0.942	-0.687 -0.679
<i>mean</i>	-0.721	-0.718	-0.960	-0.683
3003	-0.742			

measured for the Al-Mn alloy 3003.

ECORR values were measured for 2219 and 2195 in deaerated and aerated aqueous solutions containing 3.5 wt% NaCl (Table 2). The ECORR measured in the aqueous 3.5% NaCl solution were essentially the same for 2219 and 2195 under the aerated conditions, but the 2219 was more noble than the 2195 under deaerated conditions. Potentiodynamic scans performed to evaluate the anodic polarization behavior for both alloys in the deaerated solutions show that a passive current (I_{pass}) of

for 10 days under AI in an aqueous 3.5 wt% NaCl solution (Table 3). After the 10 day test the specimens were removed and either loaded to failure in air or cross sectioned for metallographic evaluation. Cross sections of the 2195 and 2219 specimens exposed unstressed for 10 days showed extensive localized corrosion (Figure 3). The localized attack is blunt in nature and penetrates to approximately the same depth in the 2195 and 2219 specimens, but the sites are more numerous on 2219 than 2195. Localized attack was also observed for the 2195 and 2219 specimens that were exposed for 10 days stressed

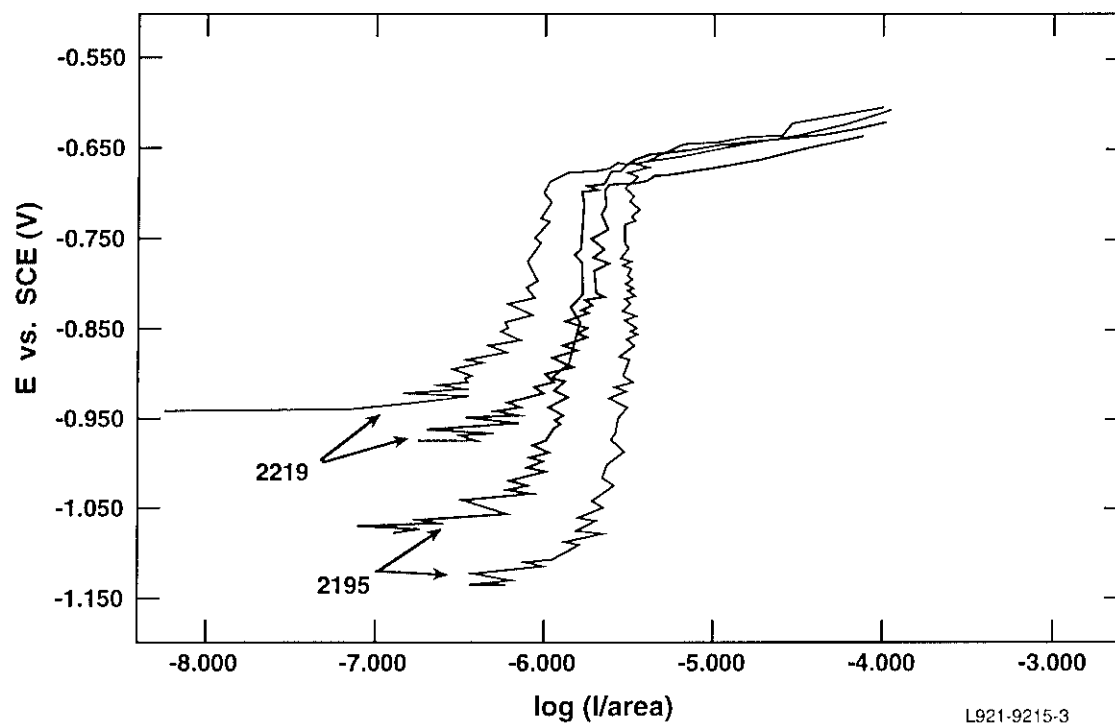


Figure 1 Anodic branch of the polarization scan for 2219 and 2195 in a deaerated aqueous 3.5% NaCl solution.

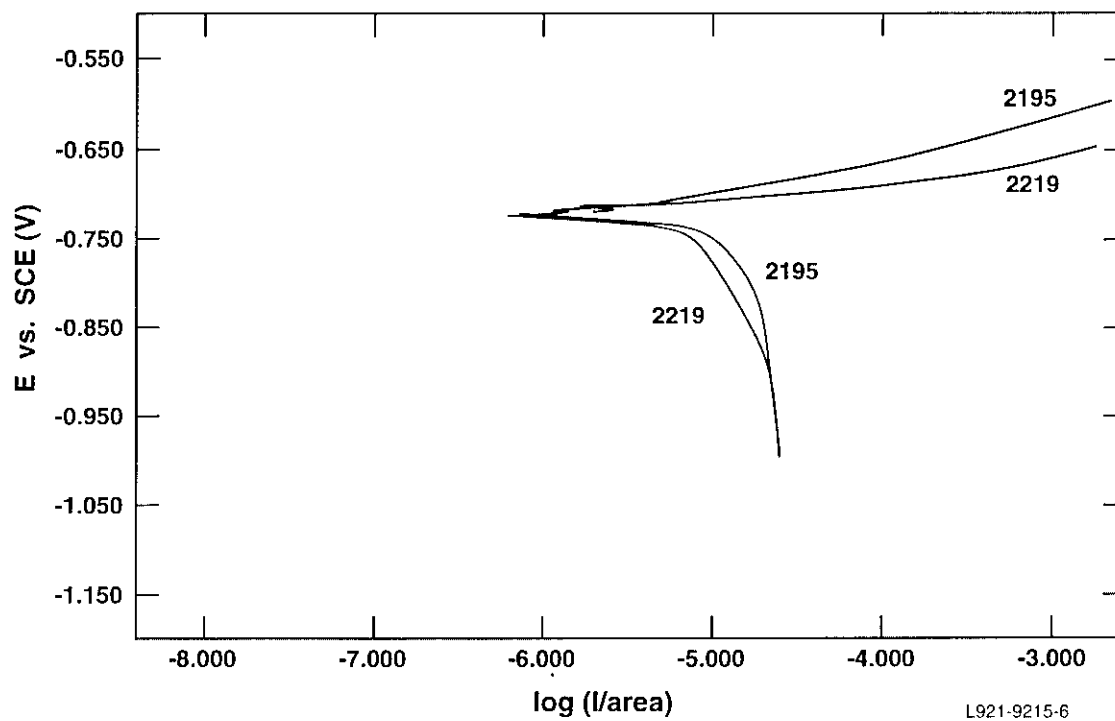


Figure 2 Anodic and cathodic branches of the polarization scans for 2219 and 2195 in an aerated aqueous 3.5% NaCl solution.

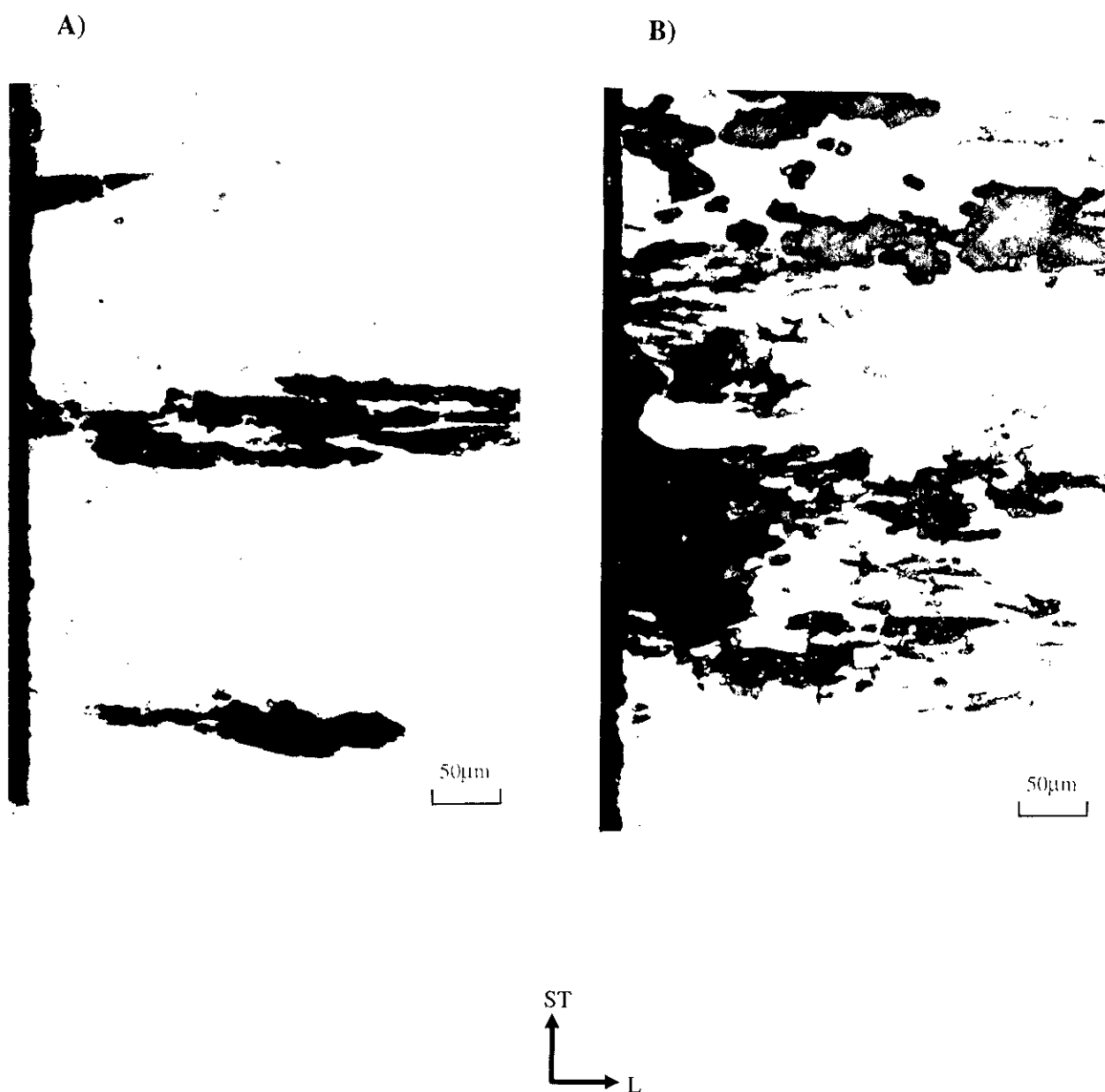


Figure 3 Micrograph of a cross section taken from a 2195 specimen (a) and 2219 specimen (b) exposed unstressed for 10 days under AI in an aqueous 3.5% NaCl solution.

at 75% of the ST σ_y (Figure 4). Qualitatively the depth of penetration for the localized attack was less after the stressed (Figure 4) than the

the test duration and test conditions were selected based on the standard test methods used for 2xxx alloys defined in ASTM standards G47^(a) and

Table 3 Results of SCC Testing for 2219 and 2195

Alloy/Temper	Applied Stress MPa (ksi)	Time-to-Failure
2195 T8	380 (55)	NF, NF, NF
2219 T87	296 (43)	NF, NF, NF

unstressed exposure.

Load-to-failure was measured for representative 2195 and 2219 specimens exposed for 10 days stressed. In addition, load-to-failure was measured for specimens removed after a 1 day exposure in the solution and after no exposure to the solution. Load-to-Failure values after exposure were normalized with non-exposed values to determine the effect of exposure on fracture load (Figure 5). This value is expressed as the fracture load ratio (FLR):

$$\text{Fracture Load Ratio (FLR)} = \frac{\text{Load - to - failure after exposure}}{\text{Load - to - failure no exposure}}$$

The FLR for 2219 and 2195 specimens exposed for 1 day stressed and unstressed were ~ 1 , which indicates that the exposure did not reduce the fracture load. FLR values of 0.81 and 0.85 were measured for 2219 and 2195, respectively, after a 10 day exposure stressed at 75% ST σ_y . The specimens exposed unstressed for 10 days showed a lower FLR than that observed for the stressed specimens: ratios of 0.73 and 0.78 for 2219 and 2195, respectively. This is strong evidence that the pitting corrosion observed is not stress assisted.

4.0 DISCUSSION

The observed SCC resistance is very promising for alloy 2195, but two uncertainties about the SCC test suggest caution about over-generalizing the results. Since no standard test has been developed to specifically determine SCC susceptibility of aluminum-lithium alloys,

G64^(b). Both of these standards point out that the test duration selected for the various aluminum alloy systems are long enough to detect SCC without introducing excessive pitting. The 10 day test duration was selected based on 1) early work by Moore et al (9), which showed that Al-Cu-Li-Mg-Ag-Zr Weldalite[®] alloys can be susceptible to pitting induced failures during long-term exposures and, 2) on the fact that 2195 has a copper content similar to that present in the high strength 2xxx alloys. Atmospheric testing is required to confirm that testing for 10 days properly ranks the SCC resistance of 2195.

The other critical issue associated with testing aluminum-lithium alloys is the unique solution chemistry that develops in crack-tips and occluded cells. Holroyd et al.⁽¹⁰⁾ showed that Li ions increase the solution pH within occluded cells for aluminum-lithium alloys. This is opposite of the acidification observed for occluded cells in conventional high strength aluminum alloys. They⁽¹⁰⁾ proposed that the localized chemistry in corrosion fissures controls SCC, with crack initiation only occurring when conditions are met to form a specific local environment. This mechanism was used to explain the discrepancy observed for SCC testing of Al-Cu-Li-Mg-Zr alloy 8090 under constant immersion vs alternate immersion. Craig et al.

^(a) ASTM Standard Test Method for Determining Susceptibility to Stress-Corrosion Cracking of High Strength Aluminum Alloy Products

^(b) ASTM Standard Classification of the Resistance to Stress-Corrosion Cracking of High Strength Aluminum Alloys

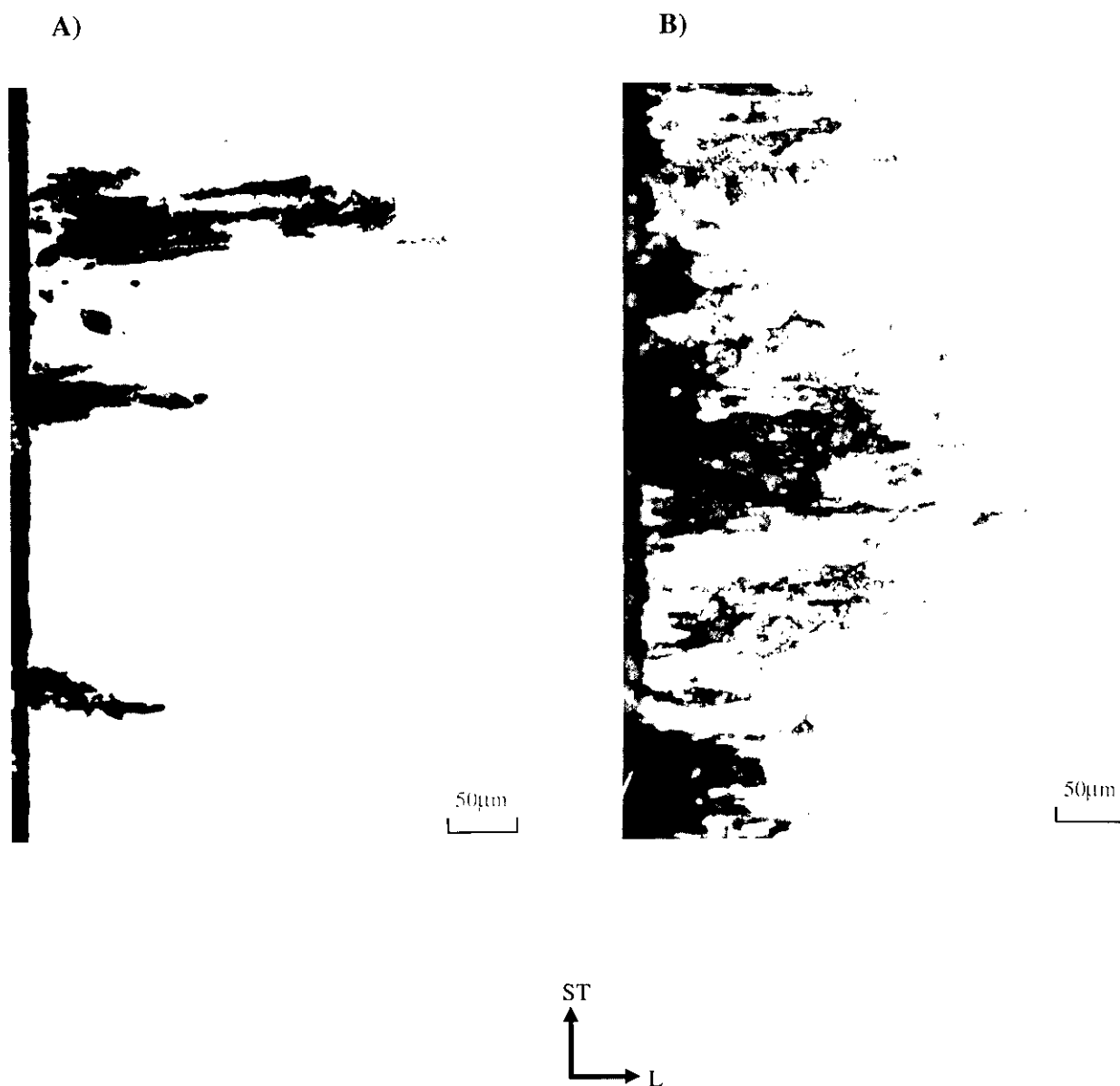


Figure 4 Micrograph of a cross section taken from a 2195 specimen (a) and 2219 specimen (b) after a 10 day exposure under AI in an aqueous 3.5% NaCl solution stressed to 75% of the ST σ_y .

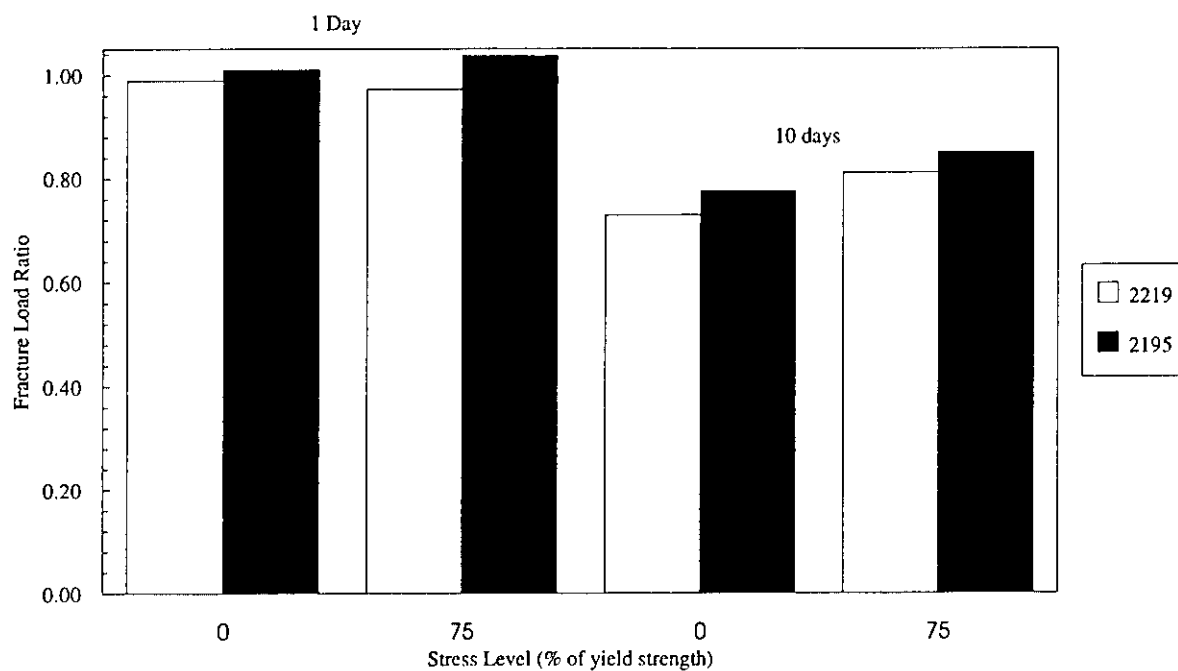


Figure 5 Fracture load ratio measured for 2219 and 2195 tensile specimens after stressed and unstressed exposures under alternate immersion in a 3.5% NaCl solution for 1 or 10 days.

(11-12) showed that the carbonate/bicarbonate reactions that occur as CO_2 is absorbed into the electrolyte play a key role in developing the local environment necessary for crack initiation to occur. In the absence of these reactions the crack walls do not passivate and SCC crack initiation does not occur. Recent work at the University of Virginia has shown a similar behavior for the Al-Cu-Li-Zr alloy 2090⁽¹³⁻¹⁶⁾. In addition, preliminary unpublished work by Moore et al⁽¹⁷⁾ showed that an alkaline pH also develops in simulated pits for Al-Cu-Li Weldalite[®] alloys. Thus, it is clear that further work is required to determine if the test conditions defined in ASTM G44 are optimum for predicting the SCC resistance of aluminum-lithium alloys in service.

Keeping these two testing uncertainties in mind, it is important to note that no failures were observed for either alloy in the tempers evaluated. This result was expected for 2219 which is resistant to SCC in the peakaged T87 temper. Additionally, both alloys showed about the same susceptibility to localized corrosion during both stressed and unstressed testing. The attack observed on cross sections taken for exposed specimens is similar to that observed by Langan⁽⁷⁾ for extrusions and plates of alloy 2095 in near peakaged and overaged tempers. This attack results from the dissolution of copper-rich constituent phase particles in the microstructure and it is not intergranular in nature. None of the intersubgranular attack observed in severely underaged tempers of 2095 was present on the 2195 specimens. Temper development is required to ensure that this type of attack does not occur in underaged tempers designed to optimize toughness at both room and cryogenic temperatures. Furthermore, we emphasize that testing must be performed on each product form before service.

Although the E_{CORR} values measured in the aerated solution were similar for 2219 and 2195, the more active nature of 2195 in the deaerated solution suggests that localized corrosion cells may setup between the alloys under certain conditions. The more active E_{CORR} observed for 2195 in the deaerated solution probably results from the lower copper content and the presence of lithium in the alloy. The similar values of E_B and E_{CORR} measured for both alloys in the aerated solution illustrates

the important role of copper in pitting. It is also important to note that the E_B in the deaerated solution corresponds with the E_{CORR} values measured in the aerated solution. Thus both alloys are susceptible to pitting corrosion in aerated saline solutions at E_{CORR} .

5.0 CONCLUSIONS

- No SCC susceptibility was observed for 2195 specimens stressed to 75% of the yield strength in the ST direction.
- The localized attack observed on the 2195 T8 SCC specimens is similar to that observed for 2219 T87 specimens.
- 2195 T8 and 2219 T87 plate have essentially the same open circuit potential (E_{CORR}) in the ASTM solution.
- 2195 T8 and 2219 T87 plate have essentially the same breakaway potential (pitting potential) in an aerated 3.5% NaCl solution.

6.0 ACKNOWLEDGMENTS

The authors wish to thank Harry Oppenhauser for his help with SCC testing and metallographic evaluations. This work was supported by Martin Marietta Manned Space Systems IRAD M40D. The preparation of this manuscript was supported under Martin Marietta Laboratories IRAD.

7.0 REFERENCE

1. J.R. Pickens, F.H. Heubaum, L.S. Kramer and K.S. Kumar, "Ultra-High-Strength Weldable Aluminum-Lithium Alloys," US Patent #5,032,359 (1991)
2. J.R. Pickens, F.H. Heubaum, T.J. Langan and L.S. Kramer, "Al-4.5-6.3Cu-1.3Li-0.4Ag-0.14Zr Alloy WeldaliteTM 049," in Proc. of the Fifth Int. Conf. on Aluminum Lithium Alloys,

- E.A. Starke Jr. and T.H. Sanders Jr., eds., Mater. Comp. Eng. Pub., Warley, England, pp. 1397-1414 (1989)
3. J.R. Pickens, F.H. Heubaum, and T.J. Langan, "Design of an Ultra-High Strength Weldable Al-Cu-Li Alloy for Space Applications," in Proc. of the 30th Annual CIM Conf. of Metallurgists, Ottawa, Canada, pp. 3-25 (1991)
4. J.R. Pickens, W.T. Tack, F.W. Gayle and J.R. Maisano, "High Strength Al-Cu-Li Alloys for Launch Systems," in Proc. of the Earth to Orbit Conf., MSFC, Huntsville, Al., (1994)
5. W.T. Tack and L.W. Loechel, "Weldalite™ 049: Applicability of a New High Strength Weldable Al-Cu-Li Alloy," Op. Cit. ref.2, pp. 1457-1467
6. M.O. Speidel, "Stress Corrosion Cracking of Aluminum Alloys," Metall. Trans. A, vol. 6A, pp. 631-651 (1975)
7. T.J. Langan, "Environmentally Assisted Cracking of Al-Cu-Li Alloys," Ph.D. Thesis, The Johns Hopkins University, Baltimore, MD. (1991)
8. T.J. Langan, K. Sieradzki and J.R. Pickens, "Effect of Artificial Aging on Environmentally Assisted Cracking of Al-Cu-Li Alloy X2095 Plate," in the Proceeding of the Tri-Services Conference on Corrosion, Plymouth, Massachusetts, May 12-14, 1992
9. K. Moore, T.J. Langan, F.H. Heubaum, and J. R. Pickens, "Effect of Cu Content on the Corrosion and Stress Corrosion Behavior of Al-C-Li Weldalite™ Alloys," Op. Cit. ref.2, pp. 1281-1291
10. N.J.H. Holroyd, A. Gray, G.M. Seamans, and R. Herman: "Environment-Sensitive Fracture of Al-Li-Cu-Mg Alloys," in Proc. of the Third Int. Aluminum-Lithium Conf., C. Baker, P.J. Gregson, S.J. Harris and P.J. Peel, eds., The Inst. of Metals, London, England, pp. 310-320 (1986)
11. J.G. Craig, R.C. Newman, M.R. Jarrett, and N.J.H. Holroyd. "Stress-Corrosion Cracking and Pre-Exposure Effects in Al-Li-Cu-Mg Alloy 8090," Environmental Degradation of Engineering Materials III, M.R. Louthan, R.P. McNitt and R.D. Sisson, eds., Pennsylvania State University, p. 313.(1987)
12. J.G. Craig, R.C. Newman, M.R. Jarrett, and N.J.H. Holroyd: "Local Chemistry of Stress-Corrosion in Al-Li-Cu-Mg Alloys," Aluminum-Lithium Alloys IV, G. Champier, B. Dubost, D. Miannay, and L. Sabetay, eds., Les Editions de Physique, Paris, pp. C3-825-833 (1987)
13. J.P. Moran and G.E. Stoner, "Solution Chemistry Effects on the Stress Corrosion Behavior of Alloy 2090 (Al-Li-Cu) and Alloy 2024 (Al-Cu-Mg)," in Proc of the Fifth Int. Conf. on Aluminum Lithium Alloys, E.A. Starke Jr. and T.H. Sanders Jr., eds., Mater. Comp. Eng. Pub., Warley, England, pp 1187-1196 (1989)
14. R.G. Buchheit, J.P. Moran and G.E. Stoner, "Localized Corrosion Behavior of 2090 -- The Role of Microstructural Heterogeneity," Corrosion, vol. 46, no. 8, pp. 610-617 (1990)
15. J.P. Moran, "Mechanisms of Localized Corrosion and Stress Corrosion of an Al-Li-Cu Alloy 2090," Ph.D. Thesis, Univ. of Va. (1990)
16. R.G. Buchheit, F.D. Wall G.E. Stoner, and J.P. Moran, "An Anodic Dissolution-Based Mechanism for the rapid Cracking, Pre-Exposure Phenomenon Demonstrated by Al-Li-Cu Alloys," Paper No. 623, Corrosion 94, NACE International (1994)
17. K. Moore, T.J. Langan, and J.R. Pickens, Unpublished Results, (1987)

**Environmentally Assisted Cracking and Localized Corrosion
Susceptibility of Aluminum Alloys 2195 and 2219
T. J. Langan**

- Q: Larry Foremen (Materials Lab) What percent of yield strength did you test at?
- A: For the head to head comparison between 2219 and 2195 the specimens were loaded to 75% of the short transverse yield strength.
- Q: L.F. - Did you run any of the specimens for longer than 10 days and if so, how long did they last?
- A: No. We did not. All specimens were removed after 10 days and tensile tested to measure residual strength. I am concerned about how the 10 day test will correlate with service, but since there is no ASTM standard specifically for the Al-Li alloys, we went with the standard for the 2000 series alloys, which is ten days. We are trying to simulate the actual service with an accelerated test and one of the problems with this test is that it induces extensive pitting. The test specimen is very small, 1/8" diameter specimen, and once you initiate a pit it can fail. So, I think increasing the time over that specified in the standard, may give conflicting information.
- Q: L.F. - I agree.
- Q: It appears that the corrosion performance of 2195 is very age dependent?
- A: Yes, in the severely underaged temper alloy 2095, which is close in composition to the 2195 alloy tested here, showed extensive non-stress assisted intersubgranular corrosion. This type of corrosion was not obscured in near peak and overaged tempers.
- Q: Alex Cho - Do you have a measure of the fracture toughnesses of the plates that you used?
- A: No. I do not. Well, let's see, on these particular plates it has been measured. I do not have the numbers right here with me.
- A: Joseph Pickens - There were some unrecrystallized areas on the plate and some recrystallized regions, in the good regions we were getting K_{IC} of approximately 30-34 ksi-(inch^{3/2}) at the 80 to 85 ksi yield strength per level in the LT direction.

STRESS CORROSION CRACKING AND MICROSTRUCTURAL EVALUATIONS OF ALUMINUM LITHIUM ALLOY 2195-RT 70 VARIABLE POLARITY PLASMA ARC (VPPA) WELDMENTS

R. M. Diwan¹, P. D. Torres², and T. Malone²

¹Department of Mechanical Engineering
Southern University
Baton Rouge, LA 70813

²Materials and Processes Laboratory
National Aeronautics and Space Administration/MFSC
Marshall Space Flight Center, AL 35812

Abstract

This study presents the evaluations of stress corrosion cracking (SCC) resistance of advanced aluminum lithium alloy 2195-RT70 variable polarity plasma arc (VPPA) weldments and their related microstructural effects. Beam type test specimens, 1 inch wide by 0.200 inch thickness of the single pass and double pass VPPA weldments of 2195 aluminum lithium alloys using 2319 filler material, with bead on and bead off configurations are tested for their stress corrosion cracking resistance and their microstructural behavior. Evaluations are carried out as per ASTM G44-88 and NASA TM X- 53483 test procedures at the stress values corresponding to 50, 75, and 90 % of the yield strength values. The stress corrosion cracking (SCC) resistance of the aluminum lithium alloy weldments is analyzed and related to the microstructural effects of selected single pass and double pass weld specimens. The aluminum lithium welded specimens are evaluated in effort to understand the welding behavior and characteristics of these aluminum lithium alloys. The microstructural characterizations of test specimens and stress corrosion behavior of the aluminum lithium alloy system are discussed to show and present new applications of the advanced light weight aluminum lithium 2195 alloys.

1. Introduction

Stress corrosion cracking (SCC) evaluations using standardized procedures as per ASTM G44-88 and NASA TM X-53483 (1,2) are carried out for analysis of the behavior of selected variable polarity plasma arc (VPPA)

weldments of aluminum lithium 2195 alloys and their SCC resistance and microstructural behavior. This study provides information on the tensile mechanical properties, stress corrosion resistance and metallurgical behavior of these new developing family of structural aluminum lithium alloys. Much of the work on the aluminum lithium alloy system and microstructural properties is beginning to indicate the production viability and applicability of these aluminum lithium alloys for welded aerospace applications. These aluminum lithium alloys are promising as replacement of the conventional aluminum alloys as they can provide a 5-10 percent lower density, a 20-30 percent increase in strength and about a 10 percent increase in elastic modulus, with good weldability and improved cryogenic properties. There have been previous studies on the aluminum lithium alloys (3-9) which have been carried out on the liquid oxygen compatibility and mechanical behavior of these alloys at cryogenic temperatures, on the effects of low melting point impurities, and the weldability of these alloys. A broad range of variables, however, could be affecting the weldability and the SCC resistance of weldments of these alloys under production conditions of this alloy system. While the weld metal and heat affected zone metallographic characterizations have been carried out and no macroscopic and microscopic cracking has been seen under the present test method conditions, it must be realized that the resistance of the alloys is related to the weld thermal cycle, consistency in weld preparation methods, control on composition and all associated parameters.

The stress corrosion cracking and microstructural and fractographic evaluations of

the selected single pass and double pass variable polarity plasma arc weldments of aluminum lithium alloy about 1 inch wide by .200 inch thick 2195-RT 70 specimens with 2319 filler material produced under controlled conditions have been carried out to evaluate the stress corrosion resistance of these alloys. The stress corrosion tests are carried out of the single pass and double pass weld specimens of two configurations (a) with bead off / root off for unstressed specimens and for specimens at loads corresponding to 50, 75 and 90 % of yield strength values and (b) with bead on / root off for specimens at loads corresponding to 90% of yield strength values of the specimens. The SCC test specimens under the bead on / root off 90 % yield stress loading would provide the maximum load condition and include the geometry effect associated with extra weld metal thickness from the crown build up. The data obtained from externally loaded stress corrosion tests of the specific test materials would help to identify the behavior of the selected 2195 series of the aluminum lithium alloys and their stress corrosion resistance. Robotic variable polarity plasma arc (VPPA) processes are being developed, however, the nature of gas metal reactions in the plasma arc welding of aluminum lithium alloys with effects of lithium depletion, migration and segregation and any porosity effects are not clearly understood. A recent study (10) on the microstructural characteristics and weldability of double pass VPPA fusion welds of 2195 aluminum lithium alloys with the conventional 2219 alloys has been carried out that has typified the wide range of microstructures and weldability of these alloys, along with the physical processes and weldability of these alloys.

II. Experimental Procedures

The compositions of the 2195-RT70 materials employed in this investigation for the variable polarity plasma arc VPPA weldments are shown in Table I. The heat treatment and temper conditions of this material are specified as solution heat treatment (SHT) at 502-513C (935-955F) with 6% cold work and aging at 143C (290F) for 30 hours. Test weld panels of the 2195-RT 70 aluminum lithium with 2319 filler material were fabricated using the VPPA welding process under controlled conditions at Marshall Space Flight Center, NASA and

evaluated for their mechanical properties. Evaluations of mechanical properties of selected

Table I Test Weld Material Composition and Filler Material Composition used in the VPPA welding process.

Test Material 2195	Filler Material 2319
Copper 3.7-4.3	Copper 5.8-6.8
Lithium 0.8-1.2	Magnesium 0.02
Magnesium 0.25-0.8	Manganese 0.20-0.40
Silver 0.25-0.6	Silicon 0.20
Zirconium 0.08-0.16	Iron 0.30
Manganese 0.25 max	Titanium 0.02-0.10
Silicon 0.12 max	Zinc 0.10
Iron 0.15 max	Others, each 0.05 max
Titanium 0.10 max	Others, total 0.15 max
Others, each 0.05 max	Aluminum Remainder
Aluminum Remainder	

beam type test specimens of dimensions as shown in Figure 1 were carried out. These specimens were machined from 6 weld panels. Three panels were manufactured using 1 weld pass; and the other three were constructed using 2 passes. For evaluation of base mechanical properties, the root and crown of the weld specimens were removed before performing tensile tests.

Stress corrosion cracking (SCC) resistance evaluations were carried out of the 1 pass and 2 pass weld specimens in selected bead off / root off and bead on / root off for unstressed specimens and at load values corresponding to 50, 75 and 90% of yield strength values as per the ASTM G44-88 and NASA TM X-53483 test procedures. The test specimens of the two configurations were stressed in pairs against each other using "H"-type fixtures and half cylinders, and bolting together the ends of the beams. The bent beam stress assembly with a typical bead on / root off configuration is shown in Figure 2. Passivated 316 stainless steel threaded rods of 5/16-inch diameter nuts and washers were used. The other parts of the assembly were made of aluminum alloy 6061-T6. These long duration tests were conducted at Marshall Space Flight Center and the length of the exposure was 90 days. Details of the test procedures are as given in NASA TM X-53483.

The centers of the duplicate specimens were placed across the top and bottom of the "H" fixture with the bead side of the specimens in the outside (tension side). The desired change in the distance between the plates along the longitudinal axis of the bolts were obtained corresponding to selected stress levels. The threaded rods, nuts, washers, half cylinders, and ends of the specimens were coated with West-Coat Maskant number 2 to prevent galvanic action. A small amount of Conoco HD - 2 calcium grease was added where the maskant ended and salt entrapment was possible. The weld area and the heat affected zones of the specimens were cleaned with acetone and ethyl alcohol. The specimens were placed in a 3.5% NaCl alternate immersion environment per ASTM G44-88. The stressed specimens were tested in sextuplicate (6) and the unstressed specimens were tested in duplicate (2). Evaluations were carried after the stress corrosion cracking tests as indicated in the described environment.

An analysis of the mechanical properties along with the microstructure and microhardness of the weld zone, heat affected zone and the base metal structure was carried out of the typical VPPA weldment specimens. The specimens were further evaluated after long duration stress corrosion testing after an

exposure period of 90 days for the specified stress levels. Further to the stress corrosion cracking (SCC) resistance evaluations, and upon no failure indication, 18 representative test weld specimens were selected and notched and tested to failure to produce weld region fractures. These specimens were notched for nick-break test and machine cut on sides approximately 1/8 inch or 3.17 mm. deep to produce weld region fractures as per API standard 1104 (11). Microstructural characteristics and fracture surfaces were examined and the fracture surfaces were evaluated using the AMRAY scanning electron microscope and microprobe facility. Metallographic sections of the weld specimen regions after SCC testing and notch tensile testing to failure were carefully prepared using diamond saw slow cutting procedures to include the base metal, heat affected zone and weld metal areas. Standard metallographic techniques of mechanical polishing and specimen preparation were used for analysis of microstructure of the test weld regions. After polishing, the specimens were etched to reveal microstructural features with a standard solution of Keller's reagent for about 10 seconds. The induced fracture surfaces of selected test specimens were examined using stereomicroscope technique with oblique views of the fracture surfaces and standard electron microscopy techniques.

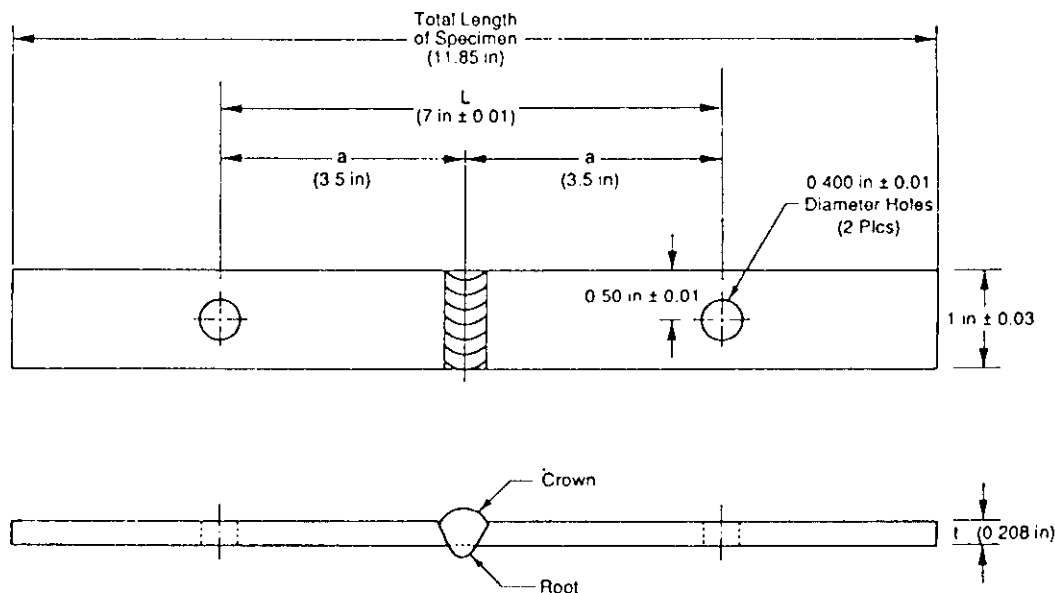


Figure 1. Bent-Beam Stress Corrosion Specimen.

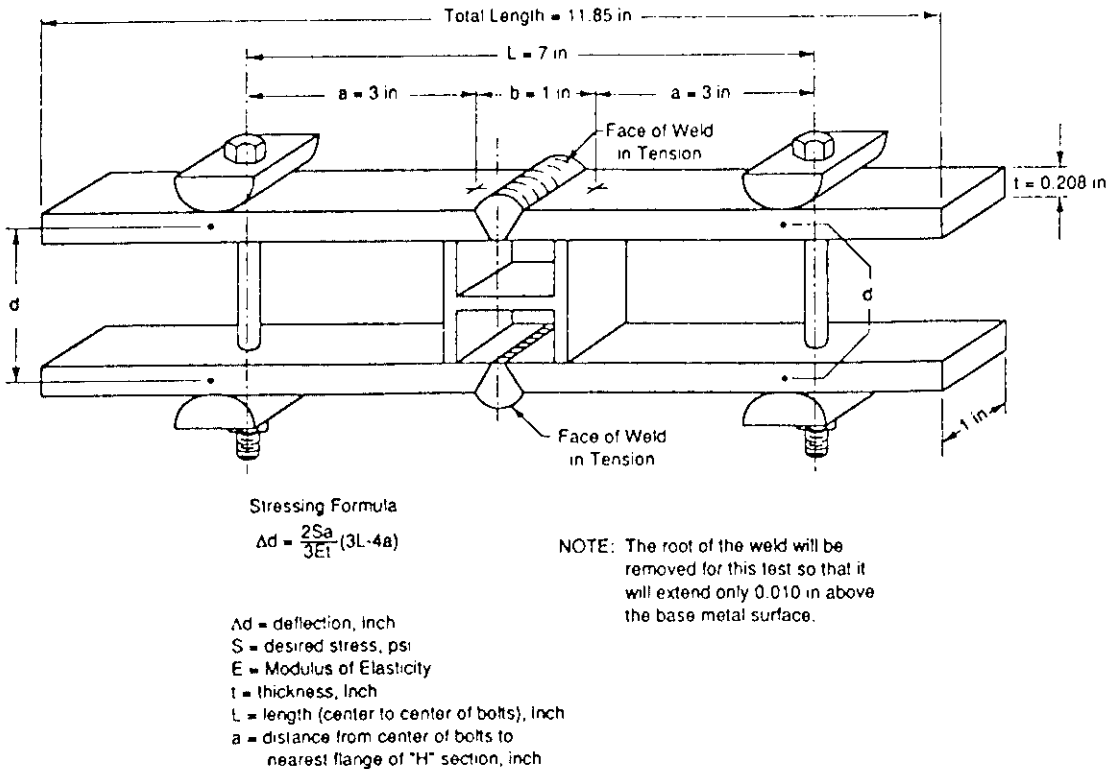


Figure 2. Bent-Beam Stress Corrosion Assembly with a Typical Bead on / Root off VPPA Test Weld Specimen. Testing is done as per NASA TM X-53483.

III. Results and Discussions

The room temperature tensile properties of the single pass and double pass VPPA test welds of the selected 2195-RT 70 Al-Li alloys are shown in Table II. In the square butt groove test weld specimens tensile tested to failure in bead off / root off configuration with a representative specimen from each weld test panel, it is observed that a larger variation in properties is present in the case of double pass test welds as compared to the single pass test welds. In case of the double pass test welds, the ultimate tensile strength properties are seen to range from 39.7 - 49.8 ksi, and 0.2 % yield strength values range from 30.1 - 33.5 ksi with per cent elongation values ranging from 1.3 - 3.4 % in 1-inch gage length and from 1.8 - 6.5 % in 2-inch gage length and values ranging from 4.76 - 10.36 % for per cent reduction of area values. This can be attributed to welding microstructural variations and effects of second pass on subsequent microstructural evolution.

Typical representative macrographs of the test weld failure areas as seen for single pass specimen 1-1 and double pass specimen 2-1 exhibited failures in the weld metal regions. Metallographic examination and evaluation of the polished and etched test weld specimens showed typical pan cake type parent metal structure with heat affected zone and weld metal solidification structures. The microhardness values as measured by the Micromet I microhardness tester are seen to range from 81.7 - 142 HVN values for the double pass test weld specimens compared to 95.0 - 138.0 HVN values for the single pass test weld specimens. Larger variations are seen in the double pass weld specimens compared to the single pass weld specimens, with values increasing from the center weld region towards the heat affected zone to the parent metal structure areas. These variations could be related to the weld metal solidification microstructures and variations in the heat affected zones as affected by the more

complex thermal history of the double pass weld test specimens.

Of all the specimens that underwent the stress corrosion evaluations of the Al-Li alloy 2195-RT 70 VPPA welds using NASA stress corrosion bent test specimens as per NASA TM X-53483, none of the specimens tested in this program failed. Out of these tested specimens, 18 representative test weld specimens were further notched and tensile tested to failure to produce weld region failures. The notched failure stress of these specimens after the SCC resistance tests are given in Table III.

The stress corrosion resistance of the test weld materials indicates the efficacy of the VPPA weld process in providing a cleaner weld due to the "keyhole" effect and more heat of the VPPA process. No porosity or hot tear cracking or lack of penetration is observed in the test weld specimens.

Results of the metallurgical evaluations and analysis of the notch tensile VPPA weld test specimens carried out to represent each weld configuration and load level of the specimens, indicated failure due to possible over loads, with some pitting as a result of extensive stress corrosion testing under externally loaded specimen test conditions.

An assessment of weldability behavior of Al-Li 2195 alloy test welds related to microstructural development (11) with beads intact had shown the failure closer to the weld metal solidification interface inside the weld

metal region. The SEM fractography of the weld specimens tensile tested to failure had shown crack initiation near the corner of the root pass and progression in different locations in several weld areas.

Depending on the test weld specimen condition, microstructural characteristics in welds could be analyzed with resulting columnar, dendritic or equiaxed weld microstructures. It should be realized that the grain structure of the weld metal would depend on the composition of the weld region, the solidification parameter given by the ratio of the temperature gradient and the weld pool solidification rate, and the shape of the weld pool as affected by the welding speed and the heat input rate.

Figures 3 and 4 represent the stereomicrographic results of fracture surfaces of typical VPPA single pass and double pass weldment specimens notch tensile tested after SCC evaluations under loads corresponding to 90% of the yield strength values with bead on / root off and bead off / root off configurations showing fracture and pitting near the fracture interfaces. Onset of cracking and some severe pitting along fracture side surfaces is seen as demonstrated in case of the bead off / root off configuration test specimens. The failure in all cases appear to be due to ductile over loads with fibrous structure seen in some cases which could be microfissuring with in the weld failure area in the notched failed specimens.

Specimen Identification	UTS ksi	0.2 % YS ksi	TE in 1-in Gage %	TE in 2-in Gage %	RA %
Single Pass Specimens					
1-1 (007-12)	48.7	31.1	2.55	5.2	7.47
1-2 (011-12)	47.6	31.3	4.30	7.0	7.64
1-3 (012-10)	48.7	34.5	4.00	7.2	9.67
Double Pass Specimens					
2-1 (004-10)	48.7	30.1	2.45	6.5	10.36
2-2(005-11)	49.8	31.1	3.40	6.5	9.63
2-3 (014-10)	39.7	33.5	1.30	1.8	4.76

Table III Notched Weldments Tensile Test Results of the VPPA Single Pass and Double Pass 0.200-inch thick Specimens After SCC Evaluations and Testing.

A. Single Pass VPPA Weld Specimens After SCC Testing

Specimen	Load (% of 0.2% YS Value)	Weld Configuration	Notched Failure Stress psi.
1S-1 (011-9)	0	Bead off / Root off	36004.4
1S-2 (012-2)	50	Bead off / Root off	37918.7
1S-3 (012-9)	50	Bead off / Root off	38361.8
1S-4 (007-3)	75	Bead off / Root off	39918.9
1S-5 (007-4)	75	Bead off / Root off	44048.2
1S-6 (012-5)	90	Bead off / Root Off	41818.2
1S-7 (012-6)	90	Bead off / Root off	38980.7
1S-8 (007-7)	90	Bead on / Root off	36007.2
1S-9 (007-8)	90	Bead on / Root off	36897.3

B. Double Pass VPPA Weld Specimens After SCC Testing

1D-1 (005-9)	0	Bead off / Root off	42300.8
1D-2 (004-1)	50	Bead off / Root off	37025.8
1D-3 (004-2)	50	Bead off / Root off	39437.7
1D-4 (014-3)	75	Bead off / Root off	41660.6
1D-5 (014-4)	75	Bead off / Root off	38781.9
1D-6 (005-5)	90	Bead off / Root off	39773.8
1D-7 (005-6)	90	Bead off / Root off	40708.3
1D-8 (014-7)	90	Bead on / Root off	40143.5
1D-9 (014-8)	90	Bead on / Root off	34155.6

The metallographic characteristics of the VPPA test weld specimens after SCC testing and notch tensile testing to failure under all loading conditions are analyzed. The microstructural evolution during welding solidification would depend on undercooling, thermal history of the VPPA welding process and this could be susceptible to any effects of the stress corrosion cracking resistance testing during loading in selected environment for the extended duration of the tests. The typical microstructures of the welded specimens show the heat affected zone, onset of pitting leading to

cracking in some cases at the surface and the typical pancake interior grains in the matrix of the aluminum lithium alloys. Figure 5 shows the double pass VPPA weld specimens microstructures after the SCC test and the notch tensile testing to failure showing the weld metal, heat affected zone and parent metal structure. Similar effects are seen for the single pass VPPA weld specimens.

The SEM fractographic evaluations in most VPPA weld test specimens indicate dimples and ductile overload failures of



Figure 3 Bead on / Root off weld notch test specimen fracture surface of specimen tensile tested to failure after SCC test under load corresponding to 90 % of the yield strength value.



Figure 4 Bead off / Root off weld notch test specimen fracture surface of specimen tensile tested to failure after SCC testing under load corresponding to 90 % of the yield strength value showing onset of cracking and some pitting along fracture side surfaces.

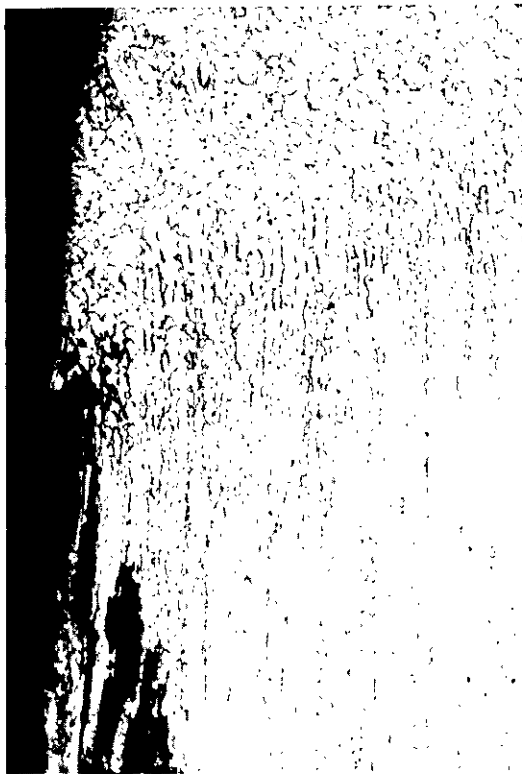


Figure 5 VPPA double pass weld specimen microstructure near weld failure zone after SCC testing under loads corresponding to 0, 50, 75 and 90 % of yield stress values and notch tensile testing to failure.

specimens notch tensile tested to failure after the SCC tests with no characteristic stress corrosion effects of the environment. Figure 6 reveals the typical ductile overloads shearing effects as mostly seen in failures with no lack of fusion. Some rubbing or wear effects could be possible due to bending loads in the SCC testing and a possible delamination and slag inclusion and porosity effect leading to tearing in case of the

90 % bead off / root off load SCC tested specimen notch tensile tested to failure. In all other cases, the welds appear to be sound and failure after the SCC testing appear to be due to presence of ductile overloading on notch tensile testing to failure.

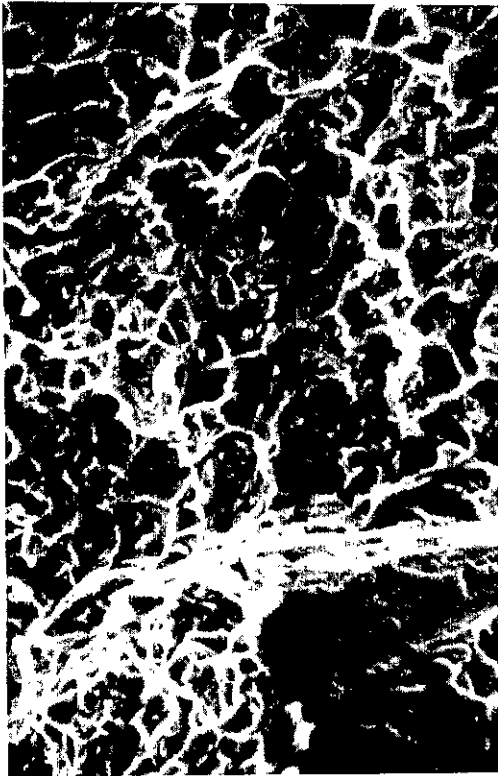


Figure 6 SEM fractograph of VPPA weld test specimens after SCC testing and notch tensile test to failure for single pass VPPA weld at 0 % load for SCC testing and for double pass VPPA weld at 90 % load for SCC testing.

IV. Concluding Remarks

The stress corrosion cracking evaluations of the VPPA single pass and double pass weldments of 0.200-inch thick specimens as carried out per NASA TM X-53483 did not fail in the test program. The metallurgical evaluations were further carried out and SCC test weld specimens were notch tensile tested to failure and predominantly the failures as examined with the metallographic characterizations and the SEM fractography revealed narrow heat affected zones with typical microstructures for the aluminum lithium alloy welds which failed in tensile ductile overloading

conditions showing typical dimple fracture characteristics, with some pitting and onset of cracking, and a possible tearing effect which could be due to hydrogen effects and porosity possibly causing fracture characteristics as seen in the 90 % load double pass VPPA weldment specimen. In all cases other than as indicated, all VPPA test welds appear to be sound and clean showing good integrity of the welding process. Some studies need to be further carried out on the possible lithium effects and porosity build up which are still not clear.

Acknowledgment

This work was supported by NASA/Marshall Space Flight Center Grant NAG 8-252.

References

1. Humphries, T.S., "Procedures for Externally Loading and Corrosion Testing Stress Corrosion Specimens", NASA/Marshall Space Flight Center, TM X-53483, 1966.
2. American Society For Testing and Materials , Standard ASTM G44-88, "Standard Practice for Evaluating Stress Corrosion Stress Cracking Resistance of Metals and Alloys by Alternate Immersion in 3.5% Sodium Chloride Solution", 1988.
3. Pickens, J.R., "The Weldability of Lithium-containing Aluminum Alloys", Journal of Materials Science, 20, pp. 4247-4258, 1985.
4. Cross, C.E., Tack, W.T. , Locchel and Kramer, L.S. , "Aluminum Weldability and Hot Tearing Theory "Proceedings of Materials Weldability Symposium, Materials Week, ASM International, Detroit, October, 1990.
5. Molan, P.A. and Srivatsan, T.S. "Laser Beam Weld Microstructures and Properties of Aluminum Lithium Alloy 2090", Materials Letters, Vol. 9, Number 7.8, pp. 245-251.
6. Martukanitz, R.P., Natalie , C.A. and Knoefel, J.O., "The Weldability of 2090 (an Al-Li-Cu Alloy), Journal of Metals, pp. 38-42, November 1987.
7. Nunes Jr., A.C., Bayless E.O. Jr. and Wilson, W.A., "The Variable Polarity Plasma Arc Welding Process:its Application to the Shuttle External Tank-Second Interim Report, NASA TM-86842, November 1984.
8. Cross, C.E. and Olson D.L., "Hot Tearing Model to Assess Aluminum Weldability" Proceedings of the Third Intl. Al-Li Conference, pp. 1869-1875, 1986.
9. Diwan, R.M., "Liquid Oxygen LOX Compatibility Evaluations of Aluminum Lithium (Al-Li) Alloys: Investigations of the Alcoa 2090 and MMC Weldalite 049 Alloys", NASA , NGT-01-08-021, 1989.
10. Diwan, R.M., " Quantitative Microstructural Analysis and Weldability Study of Aluminum Lithium Alloys", Proceedings, International Metallographic Society Conference, 1993.
11. American Petroleum Institute Standard , API 1104, "Welding of Pipelines and Related Facilities", 1989.
12. Srivatsan, T.S. and Sudarshan, T.S., "Welding of Lightweight Aluminum LithiumAlloys", Welding Journal, Welding Research Supplement, P. 173-s, July 1991.
13. Papazian, J.M., Schulte, R.L. and Adler, P.N., "Lithium Depletion during Heat Treatment of Aluminum Lithium Alloys" Met. Trans A, Vol. 17A,pp. 635-643, April 1986..
14. Lin, W., Lippold, J.C. and Baeslack, W.A. , "An Evaluation of Heat-Affected Zone Liquation Cracking Susceptibility, Part I: Development of a Method for Quantification", Welding Journal, Welding Research Supplement, p. 135-s, April 1993

Stress Corrosion Cracking and Microstructural Evaluation of Aluminum
Lithium Alloy 2195-RT 70 Variable Polarity Plasma ARC (VPPA) Weldments
Diwan

- Q: Aldridge (Martin Marietta) The last fracture, was it at the fusion line?
- A: No. It is in the weld metal. In the weld metal, it is not on the interface.
- Q: Someone else - That looks to me like that grain boundary situation, did you consider that possibility?
- A: Well, it is kind of open, you can make a model, but my suspicion is that it could be some kind of porosity or hydrogen effects and so on.
- Q: How do you know what the load is on your specimen?
- A: The load was calculated, I think if you remember the slides, there is a formula in that test procedure that we used that ASTM G4488, give you some of the test procedure and the loading formula, you should look at the standard TMX53483, NASA uses that.
- Q: Have you checked that out with the strain gages?
- A: No. We did not use the strain gages but based on that particular formula we used the calculated delta D, the deflection with the S value which is related to the yield stress that we tested from the base mechanical properties and from that we applied the loading. We think that formula gives us the actual loading of the 50, 75, or 90 percent yield strength.
- Q: How about relaxation
- A: Good question.
- Q: As we try to improve our understanding of basic welding metallurgy materials, you probably should not refer to the heat affected zone by optical-visual observation, the microstructural modification should be a little more quantifiable.
- A: Well several people in the field, for steels have given different variations as to how it could be related to the temperature between the liquid and the solidus. And you are right in that sense. But when you look at the optical micrograph it is a clear distinct reading you can measure to the microns like if it was 100 or 500 microns.
- Q: Reduction in properties would far surpass any visual observations?

A: That is possible, yes.

DETERMINING THE CRIPPLING STRENGTH OF ALUMINUM LITHIUM SKIN/STRINGER STRUCTURES

Robert Di Tolla
General Dynamics
Space Systems Division (GDSS)
San Diego, CA 92138

Abstract

Aluminum lithium alloys have been used in aerospace applications to produce lighter and stronger structural components. However, structural analysis methods for semi-monocoque (skin/stringer) structures are predicated on semi-empirical solutions which have not been validated for aluminum lithium materials. As a supplement to an existing analytical approach, short column crippling tests have been used to determine allowable cross-sectional crippling strengths of an extruded and a formed aluminum lithium skin/stringer design.

I. Introduction

Launch vehicles often use riveted skin/stringer designs for adapters, fairings and inter-tank structures. In this type of construction, the stringers ideally react all of the applied axial load and the skin panels react all of the applied shear load. The GDSS Centaur equipment module and type D payload adapter are skin/stringer structures which function as the attachment for spacecraft and the mounting for avionics and guidance packages on the Atlas launch vehicle (Figure 1).

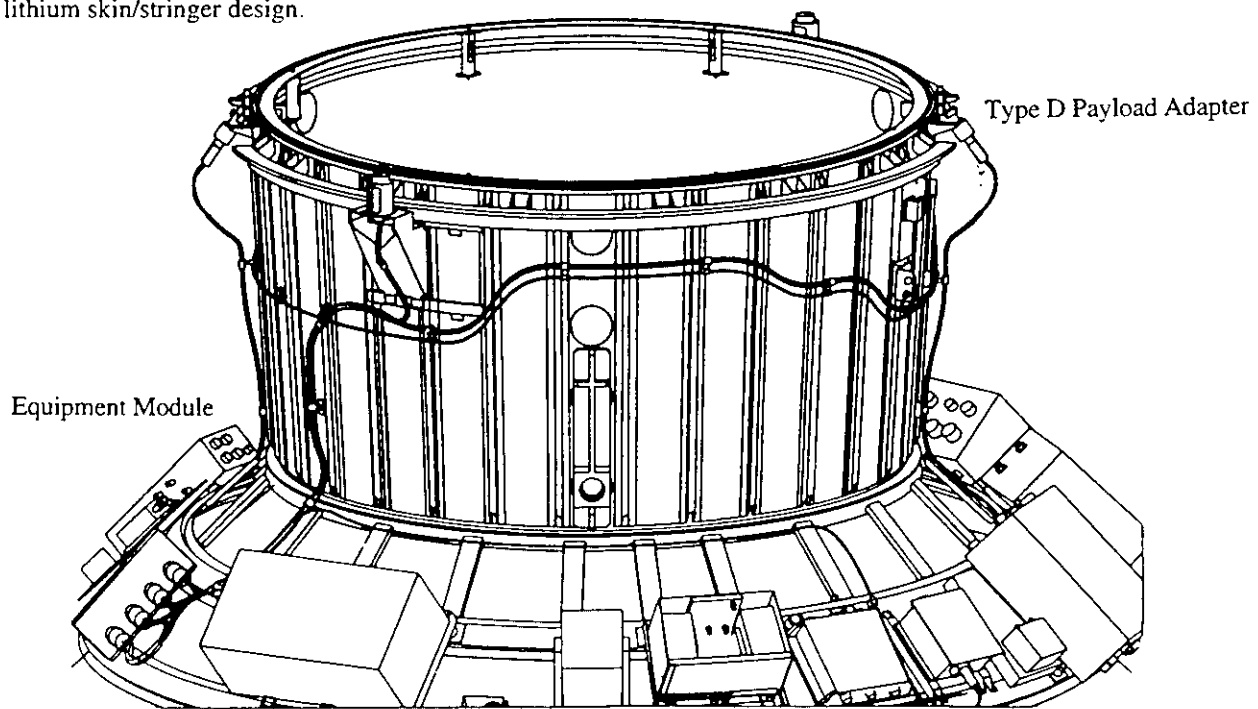


Figure 1: GDSS Equipment Module and Type D Payload Adapter

	sheet			extrusion	
	2090 [2]	2024 [2]	2024 [2]	2090 [3]	2024 [2]
temper	T83	T81	T861	T86	T8511
F _{tu} (ksi)	77	68	71	77	64
F _{cy} (ksi)	67	61	63	70	57
F _{cy} @ 45° (ksi)	58	61	63	n/a	n/a
E _c (msi)	11.8	10.7	10.7	11.8	11.0
ω (lb/in ³)	0.093	0.101	0.101	0.093	0.101

Table 1: 2090 and 2024 Specification Material Properties

To accommodate heavier spacecraft, aluminum lithium (2090) was proposed as a material substitution for the skins, stringers, and mid frames for both of these structures. A comparison of 2090 specification material properties with conventional aluminum (2024) properties demonstrates that the 2090 alloy is up to 23% stronger in its longitudinal grain direction, 7% stiffer and 92% of the density of the 2024 alloy at a comparative temper (Table 1).

II. Analytical Methodology for Skin/Stringer

Crippling Analysis

Although its strength and stiffness properties are well documented, the use of thin gage aluminum lithium in skin/stringer structures requires that additional strength parameters be determined. In particular, allowable structural design loads are a function of the skin/stringer cross-sectional crippling strength (F_{cc}). Crippling of the cross-section occurs with permanent inelastic deformation of thin flange and web elements in their own planes such that no further compressive axial load can be reacted. An analytical method is available for calculating the cross-sectional crippling strength of both extruded and formed skin/stringer designs and involves the

following procedure:

1) Determine the cross-sectional crippling strength of the stringer area, A_s excluding attached skin. The Needham Method [1] for formed sections and the Gerard Method [1] for extruded sections are both semi-empirical methods for crippling analysis which are widely used. Both methods have been derived from extensive data bases of common aerospace materials and cross-sections.

2) Although thin skin panels usually buckle under the combination of compression and shear loads, some effective skin reacts compressive loads with the stringer cross-section. The width of this effective skin (w_d) can be calculated as:

$$w_d = 1.90 t (E_c/F_{cc})^{1/2} \quad (1)$$

where: t = skin thickness

E_c = compressive Young's Modulus.

3) Thin skin acting with the stringer cross-section cannot always react compressive load at the same stress level as the stringer. It is conservatively assumed that once the effective skin reaches its limit

of linear behavior (F_{lin}), all additional compressive load is reacted by the stringer. Linear capability of the skin is most often defined by either its inter-rivet buckling strength (F_{irb}) or the proportional limit of the material (F_p). The effective skin width calculated in (1) is thereby modified to reflect its lower strength capability by :

$$w_r = w_d (F_{lin} / F_{cc}) \quad (2)$$

4) Section properties are calculated for the composite cross-section which includes the stringer area A_s , and

skin with effective width, w_r . The total area, $A_s + w_r t$ has the allowable cross-sectional crippling strength F_{cc} , as calculated in step 1.

Three particulars of aluminum lithium skin/stringer designs make the prediction of crippling strength by purely analytical means somewhat unreliable. First, aluminum lithium is an anisotropic material for which there is no documented crippling test data for extruded or formed sections. Second, analytical determination of inter-rivet buckling strength is highly dependent on identification of the

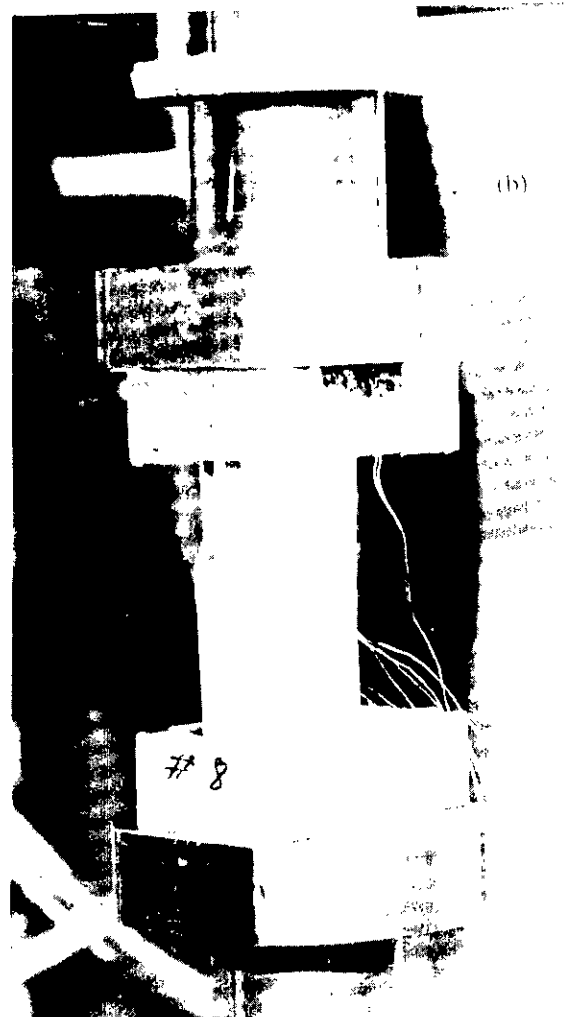
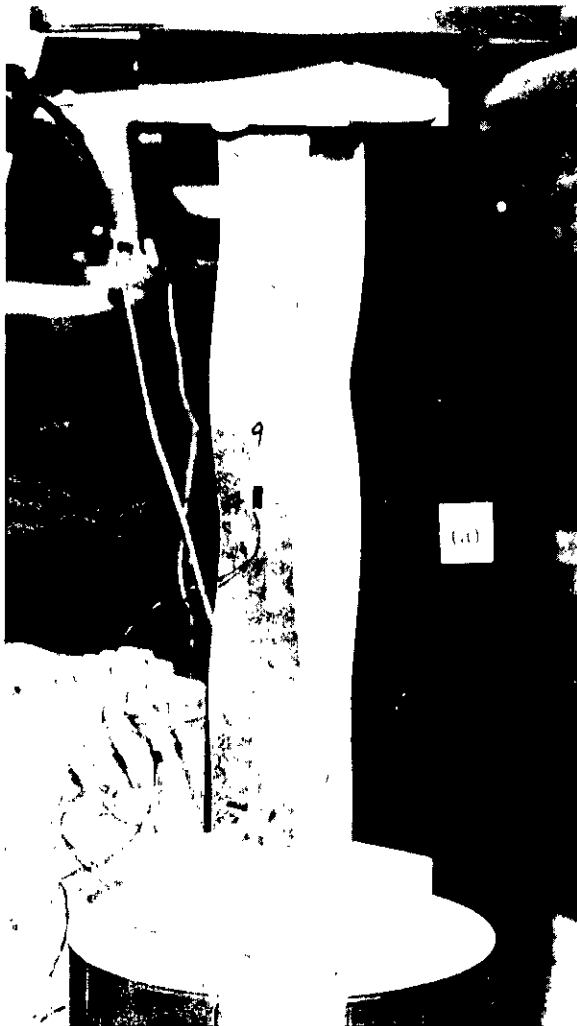


Figure 2: Extruded (a) and Formed (b) Stringer Short Column Crippling Tests

end fixity conditions. End fixity of the skin varies with the type of stringer to which it is fastened and the type of rivets which are used. Available analytical methods are not detailed enough to always properly account for these variables. Finally, in the fabrication of conical structures, complications arise when the material grain orientations of the skin and stringers are not parallel.

III. Short Column Crippling Test Procedure

To aid in the implementation of the previously described analytical procedure to aluminum lithium structures, short column crippling

tests were performed. The purpose of the tests was to determine the cross-sectional crippling strength and the limit of elastic skin behavior for both a formed and an extruded aluminum lithium skin/stringer design. Extruded and formed stringer specimens were tested separately, but with similar test procedures and configurations (Figure 2). Geometry of the tested stringer cross-sections is shown in Figure 3.

To ensure that end effects did not influence crippling modes [4] specimen lengths were calculated such that the column slenderness ratios (L' / ρ) were

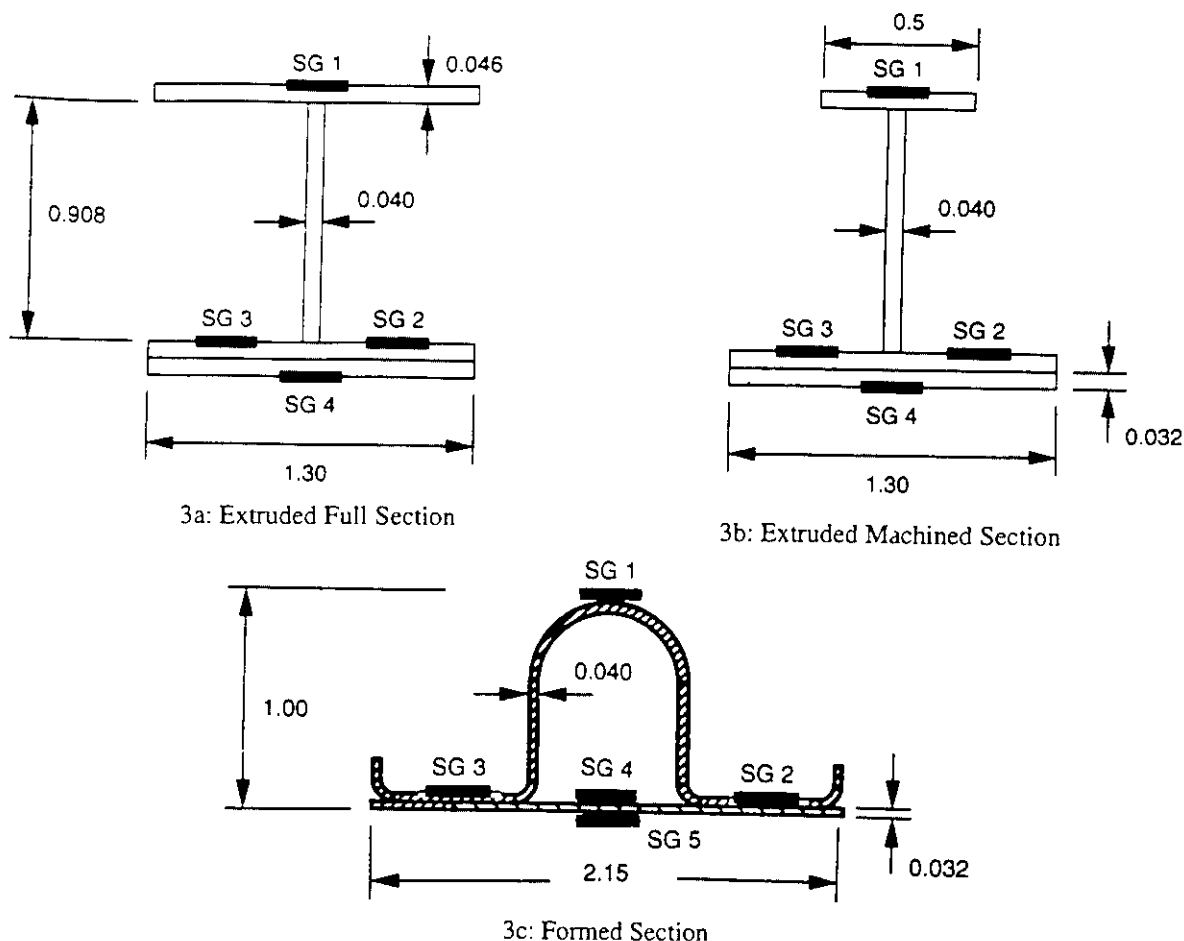


Figure 3: Short Column Crippling Test Specimen Cross-Sections

greater than 12. A uniform axial load distribution through the cross-sections was obtained by potting the ends with a plaster compound and capping them with steel angles. As a control, stringers of both 2090 and 2024 alloys were tested. Properties of the tested materials were also determined and are summarized in Table 2.

IV. Extruded (I-Section) Stringer Crippling Test Results

Eight extruded stringer specimens without skin were loaded to their maximum axial capability in order to determine crippling strength (Table 3). Stringer grain orientation was parallel to the axial load direction for the extruded 2090 sections.

	sheet				extrusion	
	2090		2024		2090	2024
structure	E/M	PLA	E/M	PLA	E/M	E/M
temper	T83	T83	T861	T81	T86	T8511
F_{tu} (ksi)	79.9	79.6	71.0	68.7	83.9	68.3
F_{tu} @ 45° (ksi)	67.0	69.4	n/a	n/a	n/a	n/a
F_{cy} (ksi)	72.9	74.9	63.0	62.0	77.9	62.5
F_{cy} @ 45° (ksi)	59.6	62.0	n/a	n/a	n/a	n/a

Table 2: Actual Material Properties for Short Column Crippling Tests

	full section (A=0.159 in ²)		machined section (A=0.122 in ²)	
	2090	2024	2090	2024
1	8850	7575	6720	5610
2	8850		6615	
3	8895		6465	
P_{ave} (lbs)	8865	7575	6600	5610
Test F_{cc} (ksi)	55.7	47.6	54.0	45.9
Gerard F_{cc} (ksi)	55.1	45.6	54.8	45.3

Table 3: Cross-Sectional Crippling Stresses (Extruded Stringer without Skin)

The limits of linear skin behavior were determined from short column compression tests of the composite sections (Table 4). When cutting out the skin pattern of the conical equipment module from a flat sheet, the skin grain orientation will not always be parallel to the applied axial load direction. Therefore, a conservative 45 degree grain orientation was chosen for the skin in the extruded specimens. Inter-rivet skin buckling was not observed in any of the extruded stringer tests. Linear strength capabilities of the skins were derived from axial load versus strain plots similar to those shown in Figure 4.

V. Formed (Hat-Section) Stringer Crippling Test Results

Five 2090 stringer specimens without skin were also loaded to their maximum axial load capability (Table 5). Stringer grain orientations were at 45 degrees to the axial load direction for the formed 2090 sections. The 45 degree orientation was chosen because the amount of control of the grain direction was not known at the time of the initial forming and assembly of the first type D payload adapter. Unfortunately, no 2024 sections were tested.

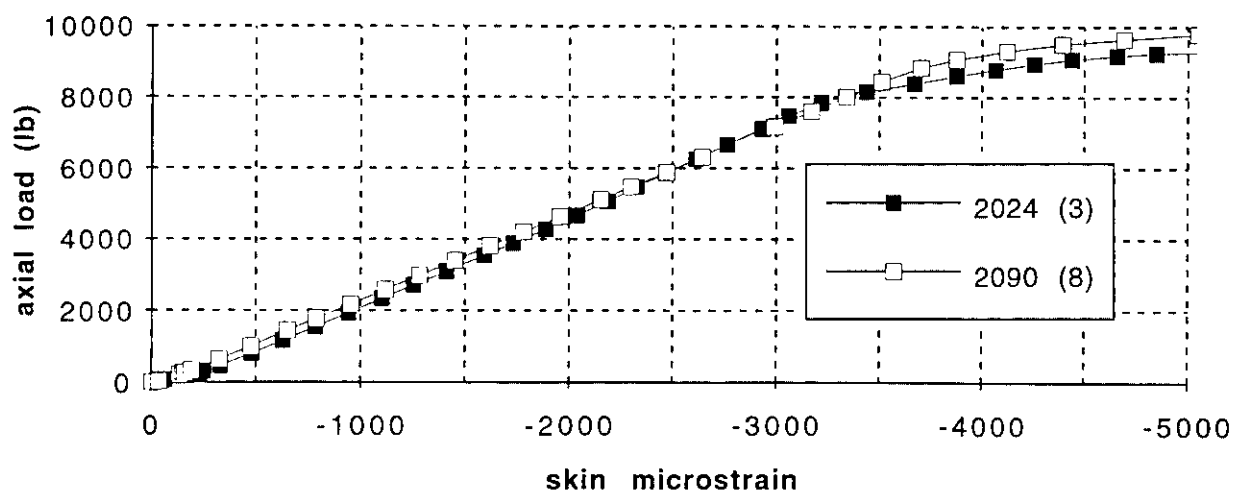


Figure 4: Skin Strain vs Axial Load (Extruded Stringer Specimens)

	full section		machined section	
	2090	2024	2090	2024
1	3451	3401	4005	3846
2	3507	3697	3867	4045
3	3405	3216	3991	3899
4	n/a		3995	
5	3434		4025	
6	3449		3983	
average μ strain	3450	3440	3980	3930
F_{lin} (ksi)	39.3	36.8	46.5	42.1

Table 4: Skin Linear Capabilities (Extruded Stringer)

	section w/out skin (A=0.146in ²)
1	9810
2	9794
3	9908
4	9808
5	9804
P_{ave} (lbs)	9825
Test F_{cc} (ksi)	67.3
Needham F_{cc} (ksi)	57.6

The limits of linear skin behavior for the formed stringer sections were determined from short column compression tests of composite sections (Table 6). Skin and stringer grain orientations were at 45 degrees to the axial load direction. Inter-rivet buckling of the skins was observed in all of the tested formed stringer specimens. Inter-rivet buckling strengths were determined from axial load versus strain plots similar to those shown in Figure 5.

Table 5: Formed Stringer Crippling Stresses

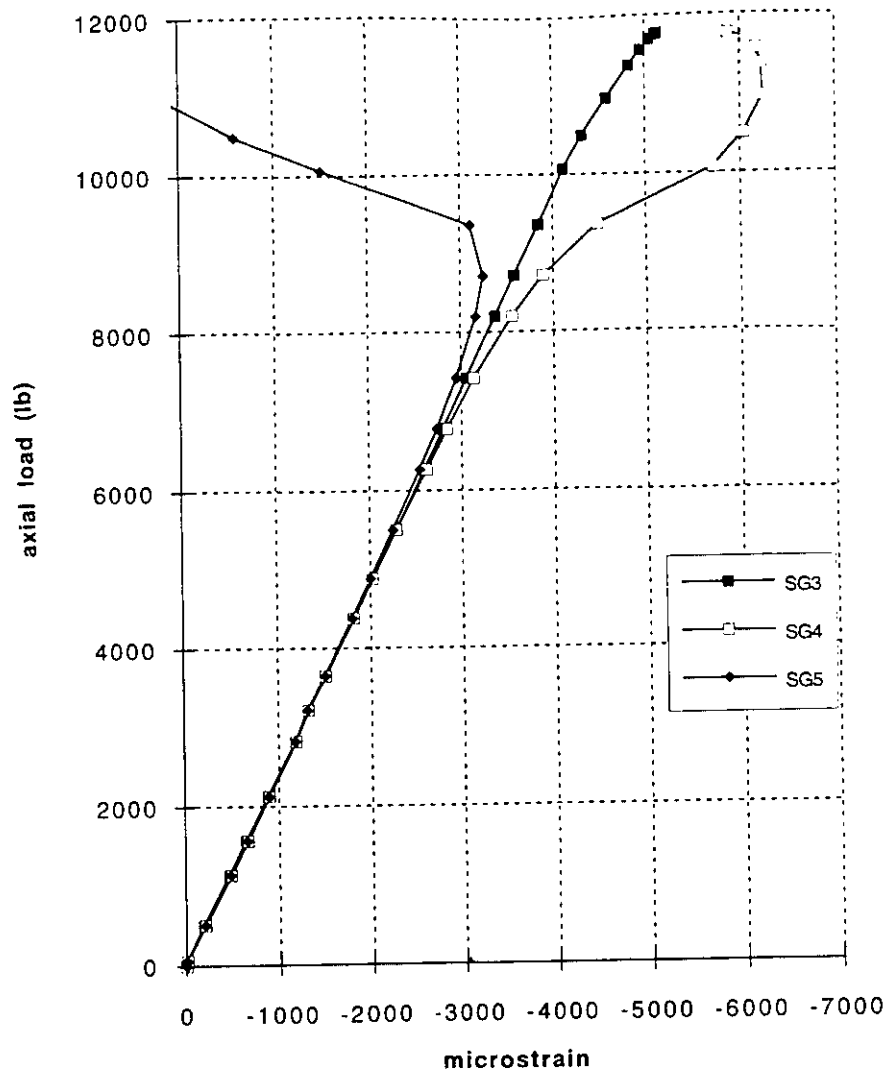


Figure 5: Skin Strain vs Axial Load (Formed Stringer Specimens)

Inter-rivet buckling strength (F_{irb}) is often analytically determined by equation 3 which was derived from the Euler column buckling equation [1].

$$F_{irb} = K_c \frac{\pi^2 E}{\left(\frac{p}{0.29 t}\right)^2} \quad (3)$$

where: K_c = constant reflecting end conditions,
 E = material tangent modulus,
 p = rivet pitch,
 t = skin thickness.

Prediction of inter-rivet buckling strength using equation 3 is highly dependent upon the proper identification of the degree of fixity provided at the support points. Textbook recommended values for K_c range from 4.0 for a fixed-end support provided by flat-head rivets to 1.0 for a pin-ended support provided by countersunk rivets [1]. Using the test-derived skin buckling stresses from Table 6, equation 3 is satisfied for values of $K_c = 2.0$ for both the 2090 and 2024 formed sections which were tested.

	skin thickness = 0.032 in	
	2090	2024
1	3649	3512
2	4104	3415
3	3835	3465
4	4090	3352
5	3890	
6	3605	
average μ strain	3860	3440
F_{irb} (ksi)	44.0	36.8

Table 6: Test-Derived Inter-Rivet Buckling Stresses

VI. Concluding Remarks

Results of the short column crippling tests indicated that the analytical method for determining cross-sectional crippling strength which was described in Section II can be applied to aluminum lithium skin/stringer designs with the following recommendations:

- 1) The Gerard Method demonstrated analytical prediction of the crippling strengths of all four of the extruded cross-sections without skins within 4%. For the machined cross-sections, in which buckling of the web precipitated buckling of either of the flanges, it is recommended that the web thickness be used in the Gerard equation. For the full cross-sections, thickness of the flanges should be used.
- 2) For the extruded cross-sections, in which no inter-rivet skin buckling was observed, the limits of linear strain in the skin were independent of material type. However, the geometry of the stringer cross-section did have an effect on the linear limit. Short column crippling tests have been the most reliable method for determining the limit of linear skin behavior.
- 3) For sections with skin which does not buckle between the rivets prior to cross-sectional crippling, elastic-perfectly plastic behavior of the skin has been assumed. Naturally, this assumption in limiting the linear skin capability to the proportional limit of the material is conservative.
- 4) The Needham Method demonstrated analytical prediction of the formed cross-sectional crippling strength at 86% of the tested value. The test-derived

crippling strength equaled $1.10 F_{cy}$. The Needham Method is recognized as a conservative approach, and greater cross-sectional crippling strengths can usually be demonstrated in short column tests.

5) Analytical prediction of inter-rivet skin buckling strength is highly dependent upon an accurate representation of the degree of fixity provided by the stringer and the rivets. It is recommended that additional short column test data be used to support the application of equation (3) for the analytical prediction of inter-rivet buckling strength.

References

1. Bruhn, E.F., Analysis and Design of Flight Vehicle Structures, Tri-State Offset, 1973.
2. Military Handbook for Metallic Materials and Elements for Aerospace Vehicle Structures, Version 5F, 15 December 1992.
3. Aerospace Material Specification, Society of Automotive Engineers, 4232, 1 January 1990.
4. Perry, D. and Azar, J., Aircraft Structures, McGraw-Hill, 1982.

Determining the Crippling Strength of Aluminum-Lithium
Skin/Stringer Structure
Robert Di Tolla

- Q: John Mahelic (Commonwealth Aluminum) The joining of the skin to your hat sections, you said by riveting, is there any adhesives or anything like that because I think that would tend to change the way that would cripple.
- A: Absolutely. The reason of course we get away from any type of adhesive are manufacturing type problems, inspection and so forth. We have done some studies on welding structures, welding skins and stringers together. But only studies, manufacturing and inspection of course would have many problems.
- Q: Did you do any compression testing with clamped edges or fixtures on the edge of the compression sample?
- A: How do you mean? These are all compression tested.
- Q: But I find in your photograph that there was no fixtures on the edge of the sample to simulate the constraint that you would see in the actual structure.
- A: In the actual structure. What we are doing is simulating the behavior of the structure between the ends, ok, and that behavior occurs over a very finite distance. We use that information in a column crippling type equation to determine the overall behavior. However, we do have concerns about the effects of the boundary conditions because we do introduce bending moments at the end. And one of the development programs that we are doing on this new equipment module structure we actually are doing some tests with the end rings to determine what those end effects are.
- Q: Tom Bales (NASA-Langley) Also I was a little bit confused with your data with the test you have of the actual part. Did you obtain a higher stress level than what you had projected is that correct?
- A: In the formed cross sections we are trying to correlate the semi-empirical methods that have been available for decades with the tested values and the tested values came out to be 10-15 percent higher which kind of confirms our feelings that the semi-empirical methods are conservative. They are conservative and been used in the past; however, when we are actually designing the structure if we have done these tests we can use the higher allowables.
- Q: Tom Bales - What I guess I was looking for if you are getting stress levels that were higher and would be projected from the off axis properties under a bi-axial test conditions?

- A: We are testing the sections in the short column tests with the 45 degree grain orientation. In the actual structure this grain depending on the angle of the cone this grain orientation can be anywhere from of course 0 up to 45 so this is another conservatism that we are introducing.
- Q: Ed Starke - Did you orient the grains of the 2024 in the same way you did the aluminum lithium alloys?
- A: I do not think we are able to determine effectively what the grain orientation in the 2024 is. I wish Keith were here. He is the one that did the tests for me. But I do not believe we did that comparison. I know when we are manufacturing the structure for 2024 we do not call out any grain direction.
- Q: Joe Pickens (Martin Marietta) One thing you may want to consider that our colleagues in Denver and Mashoo have considered but in fact back burnered is the use of weldalite 2094 rivets, we can give you some rivet material that can be fairly soft and as quench condition and naturally aged to yield strengths of 57-68 ksi, with ultimates in the 80's and seems to me that if your shaving ounces out of a space structure that maybe worth considering by down sizing the rivets. So, I can give you a piece of it if you would like to play with it.
- A: Yes. I would appreciate that, sounds good, thanks.

TESTING OF ALUMINUM LITHIUM (Al-Li) ALLOY 2095-T8

Hideo Taketani
Material & Process Engineering
McDonnell Douglas Aerospace
5301 Bolsa Avenue
Huntington Beach, CA 92647-2099

Abstract

Alloy 2095-T8 (Weldalite) was designed as a high-strength, weldable, cryogenic Al-Li alloy for space applications. Copper was added to increase strength, and small quantities of silver and magnesium were added to stimulate precipitation during aging. Zirconium was added as a grain refiner and, finally, titanium as a cell size refiner.

Tensile, bearing, compression, and fatigue tests were conducted on 1/2-inch-thick plate at room temperature. Both longitudinal and long transverse grain directions were evaluated.

Ultimate tensile strength ranged from 80.5 to 84.0 ksi, compression yield strength from 68.1 to 73.2 ksi, ultimate tensile bearing strength from 120 to 122 ksi at $e/D = 1.5$ and 155 to 159 ksi at $e/D = 2.0$. These values exceeded the values for conventional high-strength aluminum alloy 7075-T73 and Al-Li alloy 2091-T3.

Fatigue tests were conducted for the first time on this alloy. The endurance limit was found to be around 43 ksi for smooth unnotched specimens and 12 ksi for notched ($K_t = 3.0$) specimens based upon $R = 0.1$, stress cycle = 20 MHz, and limiting cycle = 1,000,000. The endurance value for the smooth specimen exceeded the value for 7075-T73, but the notched values did not.

I. Introduction

To expedite implementation of new materials, including Aluminum Lithium alloys, to take advantage of their lower density and higher modulus, the Air Force has initiated a cooperative test program with industry. The Air Force supplies the new material free, and some 34 aerospace companies test these materials at their cost to obtain a large body of test data quickly so that design engineers will have in-depth material data for incorporation into new design or for material substitution into existing design.

As a part of this cooperative test program, aluminum lithium alloy (Weldalite) 2095-T8 plate was tested.

II. Material and Procedure

The 2095-T8 plate, measuring 1/2 by 24 by 48 inches, was carefully laid out to ensure that all the test specimens required, including the correct grain orientation, could be obtained. To prevent loss of identity, the test specimens were labeled with an indentation stamp.

Chemistry was performed using wet analysis, and tension, compression, and bearing tests were conducted according to American Society for Testing and Materials (ASTM) requirements. The fatigue tests were conducted in accordance with ASTM E466 except that each test specimen's reduced section was radiused to prevent failure outside of the gage length (Figure 1). Such failures occurred in the past with other new materials.

Microstructure was determined in the three orthogonal directions. Specimens were ground through to 60 grit silicon carbide paper followed by polishing with

H42017

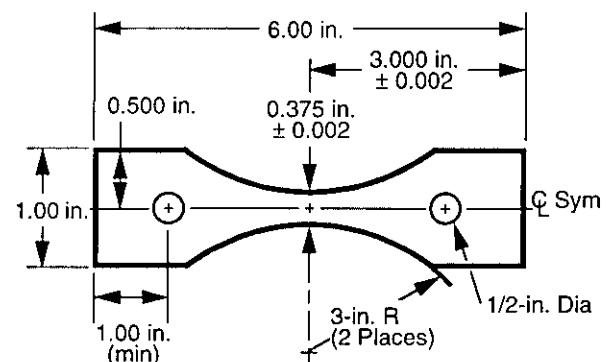


Figure 1. Smooth fatigue ($K_t = 1$) specimen with radiused reduced section

6 μm diamond paste and 0.05 μm Al_2O_3 slurry and etching with Keller's etch.

III. Results and Discussion

The chemistry values are shown in Table 1. The results agreed with the literature values (the Aluminum Association, Inc.) with the exception of the lithium content, which varied widely.

The microstructure of this alloy resembled the typical "plywood structure" of Al-Li alloys, although the grain size was much finer as compared to Al-Li alloy 2091-T3 (Figure 2).

The tensile, compression, and bearing results are shown in Tables 2–5, respectively, together with values for other alloys for comparison purposes. Although not measured, comparisons of density, modulus, and fracture toughness values are shown in Table 6. The results for alloy 2095-T8 exceeded the values for alloys 2091-T3 and 7075-T73.

The fatigue results are plotted in Figures 2–6. Alloy 2095-T8, as compared to alloys 2091-T3 and

Element	Composition (Wt%)	
	Specification ⁽¹⁾	Analysis
Si	0.12 Max	0.02
Fe	0.15 Max	0.14
Cu	3.9–4.6	4.18
Mn	0.10 Max	<0.01
Mg	0.25–0.6	0.37
Zn	0.25 Max	0.03
Ag	0.25–0.6	0.55
Li	1.0–1.6	2.21, 1.63, 1.28, 1.93
Zr	0.04–0.18	0.14
Ti	0.10 Max	0.01
Others, each	0.05 Max	—
Others, total	0.15 Max	—
Al	Remainder	Remainder

Reference: (1) The Aluminum Association, et al.

11

7075-T73, had slightly superior smooth fatigue properties in both the longitudinal and long transverse directions. However, the notched fatigue strengths were

H42025.1

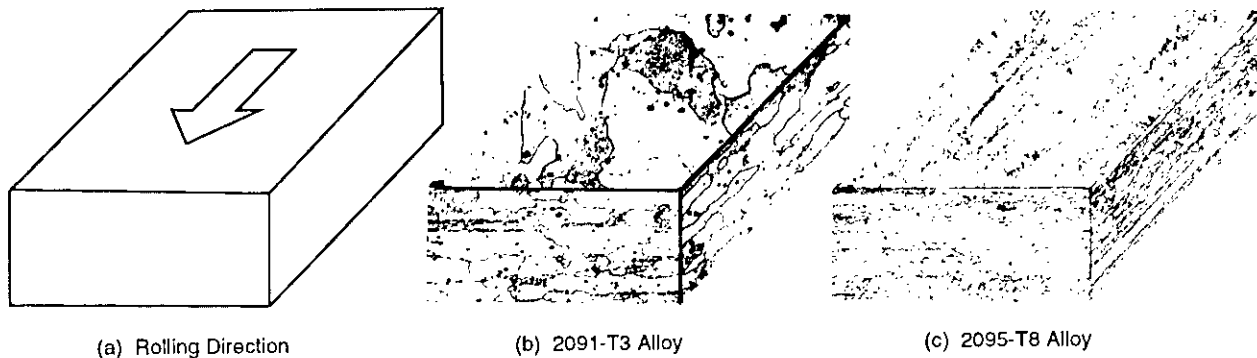


Figure 2. Microstructure comparison

Table 2. Tensile results and comparisons

Alloy	Grain Direction	YS (ksi)	UTS (ksi)	Elongation (%)
2095-T8	Longitudinal	77.0	83.1	11.7
2091-T3 ⁽²⁾		49.5	59.6	20.4
7075-T73 ⁽³⁾		63.0	73.0	13.0
2095-T8	Long Transverse	71.9	81.2	14.3
2091-T3		46.6	64.8	13.3
7075-T73		63.0	73.0	13.0

References: (2) Maryann Phillips, et al.
(3) P.L. Mehr, et al.

12

Table 3. Compression results and comparisons

Alloy	Grain Direction	YS (ksi)	Modulus (Msi)
2095-T8	Longitudinal	68.9	11.4
2091-T3		40.8	11.5
7075-T73		56.0	10.6
2095-T8	Long Transverse	72.8	13.7
2091-T3		49.1	11.4
7075-T73		56.0	10.6

13

**Table 4. Bearing results and comparisons
(e/D = 1.5)**

Alloy	Grain Direction	YS (ksi)	UTS (ksi)
2095-T8	Longitudinal	102	121
2091-T3		74.6	95.4
7075-T73		86.0	106
2095-T8	Long Transverse	98.6	122
2091-T3		75.7	97.9
7075-T73		86.0	106

14

**Table 5. Bearing results and comparisons
(e/D = 2.0)**

Alloy	Grain Direction	YS (ksi)	UTS (ksi)
2095-T8	Longitudinal	121	157
2091-T3		86.0	120
7075-T73		104	137
2095-T8	Long Transverse	123	157
2091-T3		89.1	122
7075-T73		104	137

15

Table 6. Published property values comparisons

Alloy	Density (lb/in ³)	Elastic Modulus (Msi)	K _c ksi √ in.
2095-T8	0.098	11.3	60
2091-T3 ⁴⁾	0.094	11.2	138
7075-T6	0.101	10.3	80

Reference: (4) R.J. Rioja, et al.

16

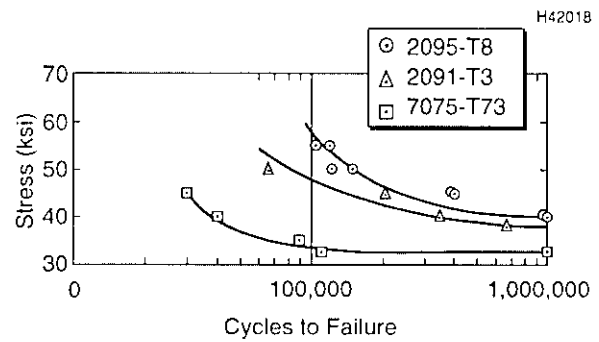


Figure 3. Longitudinal smooth ($K_t = 1.0$) S/N results

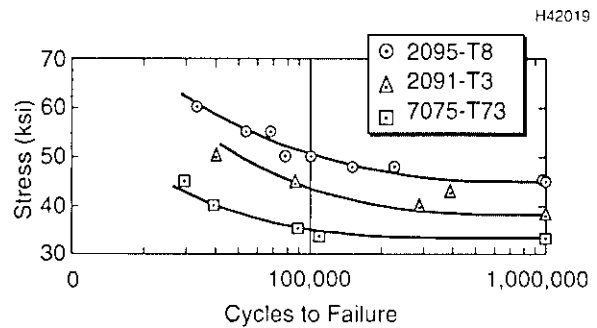


Figure 4. Long transverse smooth ($K_t = 1.0$) S/N results

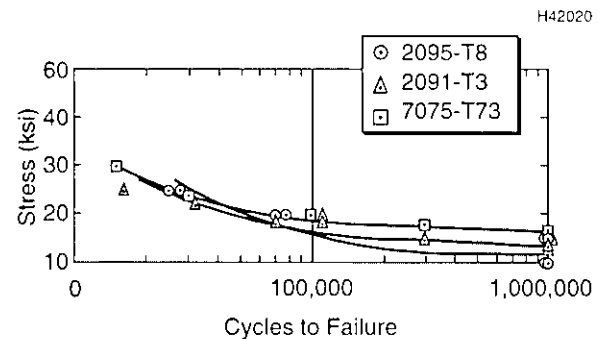


Figure 5. Longitudinal notched ($K_t = 3.0$) S/N results

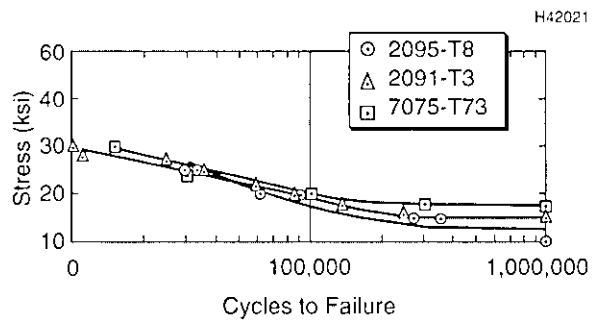


Figure 6. Transverse notched ($K_t = 3.0$) S/N results

lower, as given in Table 7, which illustrates the notch sensitivity of alloy 2095-T8.

The microstructure comparison of this alloy with alloy 2091-T3 is shown in Figure 7 where the fine grain structure of alloy 2095-T8 can be seen. The tensile overload feature of this alloy, as shown in Figure 8, is atypical with deep-stretched dimple features. However, the fatigue features are typical as shown in Figure 9.

Table 7. Fatigue comparison

Alloy	Threshold Fatigue Stress (ksi)		
	Smooth	Notched	Difference
2095-T8	43.0	12.0	31.0
2091-T3	31.0	14.0	17.0
7075-T73	33.0	17.0	16.0

17:

IV. Conclusion

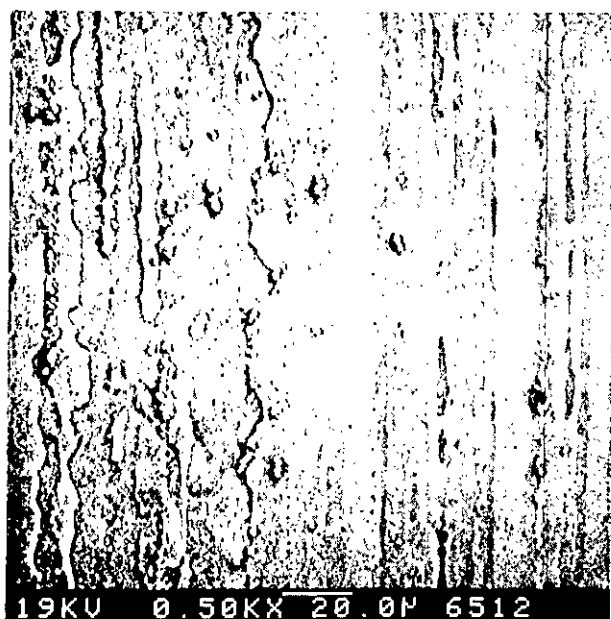
Alloy 2095-T8 is a high-strength, somewhat low-density aluminum lithium alloy. Its mechanical

properties, compression strength, and bearing values are greater than those of alloys 2091-T3 and 7075-T73. The smooth fatigue strength is also better, but its notched fatigue strength is lower.

References

1. The Aluminum Association, Inc., "Registered Composition Limits of 2095," Washington, D.C.
2. Maryann Phillips and Steven R. Thompson, "The Mechanical Property Data Base From An Air Force/ Industry Cooperative Test Program on Advanced Aluminum Alloy (2091 Sheet, Plate, and 8090 Extrusion)," WL-TR-93-4078, June 1993.
3. P.L. Mehr, E.H. Spuhler, and L.W. Mayer, "Alcoa Alloy 7075-T73" (Alcoa Green Letter), Pittsburgh, PA, September 1971.
4. R.J. Rioja, J.M. Newman, and A.K. Govada, "Al-Li Damage Tolerant Sheet for Fuselage Skin Applications," Sixth International Aluminum-Lithium Conference, 1991, Garmisch-Partenkirchen (FRG), ISBN 3-88355-180-5, 1992.

H42022.1



2095-T8



2091-T3

Figure 7. Microstructure comparison between 2095-T8 and 2091-T3 at 500X

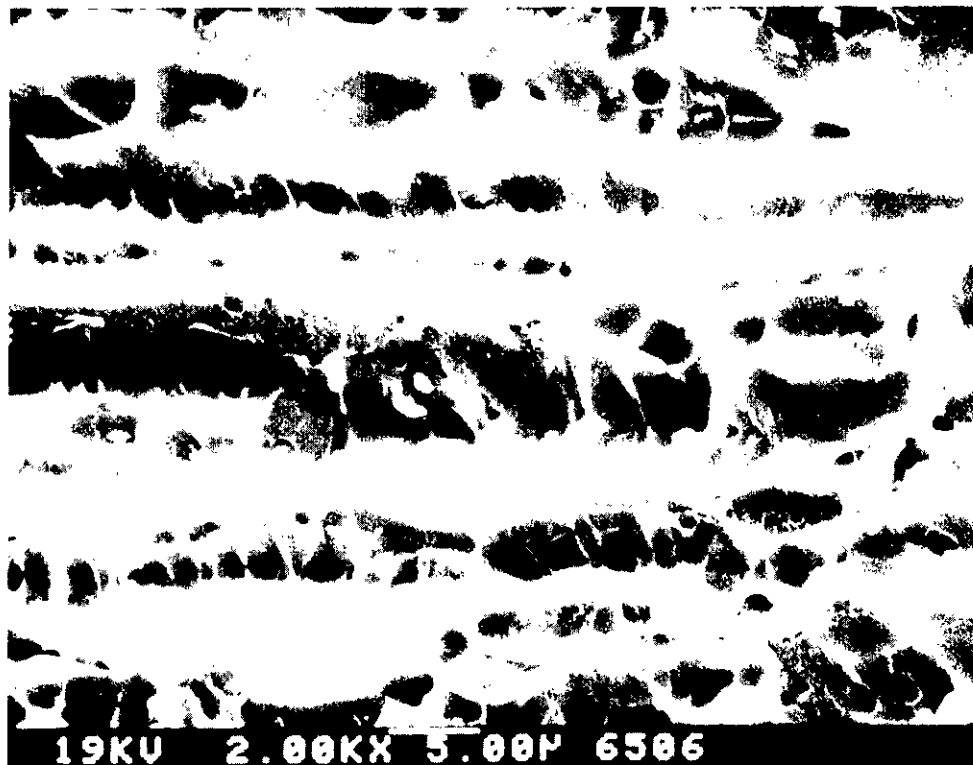
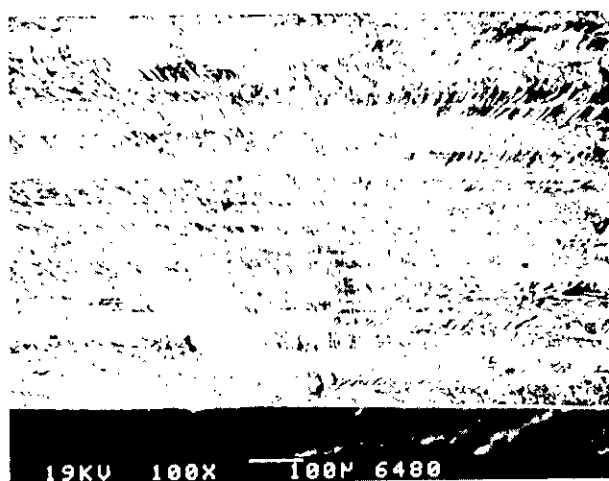


Figure 8. Somewhat atypical tensile overload feature of Al-Li Alloy 2095-T8 consisting of deep-stretched dimples (2000X)



(a) Fatigue Feature at 100X



(b) Striated Fatigue Feature at 2000X

Figure 9. Typical microstructural fatigue features of Al-Li Alloy 2095-T8 (100X)

Testing of Aluminum Lithium (Al-Li) Alloy 2095-T8
H. Taketani

- Q: Lee (Navy) Are your isogrid component age formed or not?
- A: No. We form it in the T6 temper and we put on the brake press and then we brake form it.
- Q: E.L. - What is the major concern in that part that you used 7075 T73 instead of T6?
- A: We were worried about the corrosion.
- Q: E.L. - Corrosion, is it one shot deal?
- A: I know but it sits around at the seacoast atmosphere and we are having corrosion already on hardware that just sits waiting for the payload to be integrated consequently we went to 7075 T73.
- Q: E.L. - I see, but you have not compared the corrosion properties of 7075-T73 and the 2095?
- A: No we have not.
- Q: Tom Bales (NASA-Langley) You say this was part of a round robin program with the Air Force?
- A: Yes with Wright Patterson Air Force Base.
- Q: T.B. - Has this information been published somewhere?
- A: It is being printed right now, they are having a publication printed on the 8090.
- Q: T.B. - I was aware of the 2090 and 8090 test program but I did not know they were doing a 2095 also.
- A: I believe it is being printed right now. They tell me, the results of all the testing are being published.
- Q: Have you checked the effect of spring back?
- A: Yes, the spring back and I am sure the Martin Marietta people know this, is much worse on aluminum lithium alloys. In a previous paper we formed 2090. I made an isogrid cylinder 8 feet in diameter and 10 feet high and the springback was pretty bad. I have talked with the Martin Marietta people they are also having problem with

springback. Basically when you form a long cylinder, you get a transverse curvature which we call anticlastic curvature which is a saddle shape, you get a coke bottle. When you get two of these to line up to make the longitudinal weld, you get a mismatch and you have a very difficult time making that seam weld so the anticlastic curvature is worse on aluminum lithium alloys because I guess of the higher modulus.

Q: Troy Tack (Ashurst Corp.) I wanted to ask you that with single stage to orbit will the fatigue considerations become much more important as compared to the expendable launch vehicles and that will apply to cryogenic design as well.

A: Yes, that is right. They were interested in the fatigue testing of aluminum lithium alloys. We did not run it to 10 million cycles because that is more or less for commercial airplanes or fighter airplanes. For aerospace application 1 million cycles, we felt, would be sufficient.

Q: T.T.- What about single stage to orbit, how many cycles will you design it for?

A: I do not know what the plan is right now. We are still in the preliminary stages of trying to layout the test program for single stage to orbit application.

Q: ? (Wright Patterson Air Force Base) In your talk you were comparing some results of -T3 versus T8, is there any reason for that?

A: Only because that is what I could find in the literature.

Q: ? (WPAF) - Because alot of your conclusions were based upon 2095 being superior to the other which was in the -T8 temper. I wonder if it is naturally superior?

A: Yes, I apologize. The only reason for that comparison was because in the literature that is the temper they tested and the other alloys were tested in the -T3 and -T73 temper. That is a good point.

Q: ? - Have you considered high speed machining?

A: Yes, for the isogrid it would be a natural since we remove so much metal. But my understanding is that when we ran the tests we did not get good results because the ribs would bend over, and we could not hold the tolerances.

Q: ? - So you mean the aluminum lithium?

A: Not only Al-Li but also the conventional aluminum alloys. We tried running some high speed machining but were unsuccessful.

MICROSTRUCTURE-CRYOGENIC FRACTURE CORRELATIONS IN WELDALITE™ WELDMENTS

R. Crooks*, J. S. Sedlak**, A. Szabo¹ and M. R. Mitchell^{1†}

* Naval Postgraduate School, Monterey, CA

**U.S. Coast Guard, Washington, D.C.

¹Martin Marietta Manned Space Systems, New Orleans, LA

[†]Rockwell International Science Center, Thousand Oaks, CA

ABSTRACT

Welded panels representing three composition variations of the Al-Cu-Li alloy Weldalite™ (2094, 2095 and 2195) and one of 2219 were provided by Martin Marietta Manned Space Systems, after welding by Variable Polarity Plasma Arc (VPPA) technique with 2319 filler. Slow three-point bend tests were performed on these welds at 77 K and interrupted at the onset of fracture. Metallographic sections were then used to establish crack paths in the cryogenically tested material. Fracture of the Al-Cu-Li alloys was intergranular and associated with grain boundary phases. Second phase material formed nearly continuous layers around individual grains of an equiaxed grain zone (EZ) at the fusion zone boundary and similar material was observed to extend laterally into the heat affected zone (HAZ) in some instances. Delamination during bending was observed in the EZ (2094), the HAZ (2094 and 2095) and the fusion zone (2095, 2195 and 2219). The amount of second phase in the EZ and the tendency for low ductility fracture through this region appear to decrease as the Cu + Li content decreases. The crystal structure of the second phase was also found to vary with alloy content. The Weldalite™ samples with the lowest copper and lithium contents, nominally Al-4.0Cu-1.0Li (2195), exhibited better cryogenic strength and ductility than 2219.

1. INTRODUCTION

Aluminum-Copper-Lithium (Al-Cu-Li) alloys offer low densities, high strengths, and exceptional cryogenic properties. One of the most promising types of Al-Cu-Li alloys, Weldalite™, is being evaluated for use in the Space Shuttle External Tank, a large, welded, cryogenic structure. The use of thinner plate sections of the higher strength Weldalite™ alloy would result in appreciable weight savings over the currently-used Aluminum-Copper alloy 2219 and allow a greater payload.

There has been recent interest in Al-Cu-Li alloys for aerospace applications, particularly for cryogenic

tankage [1-3]. Research efforts at Martin Marietta and Reynolds Aluminum have resulted in the development of a series of weldable Al-Cu-Li alloys, termed Weldalite™ [2-6]. Several studies have been conducted on the cryogenic properties of Weldalite™ 049 and related Al-Cu-Li alloys. Pickens et al. showed that 5.0 % Cu Weldalite™ 049 extrusions, in various tempers, exhibited better tensile strengths at cryogenic temperatures (77K) than at room temperature with out any loss of ductility [2]. This increase in strength at cryogenic temperatures has been observed for other Al-Cu-Li alloys, Glazer and Morris, for instance, demonstrated similar behavior for 2090-T81 and 2091-T8 plate [1]. Kerr and Merino compared the cryogenic properties of welded 2090 with welded 2219 and reported that the 2090 coupons exhibited superior tensile properties and reasonably good ductility [7].

An alloy is considered to have good weldability if it can be joined by conventional welding processes with a minimum of welding defects. Welding defects can be divided into four categories: 1) hot tears [or hot cracking] in the weld metal or heat-affected zone, 2) porosity or inclusions in the weld metal, 3) lack of fusion or incomplete penetration of the weld metal, and 4) softening in the heat-affected zone [8]. Hot cracking has been cited as a concern in the welding of the new, commercial Al-Cu-Li alloys. Zacharia, et al. [9] reported that Alloy 2090 and 2091 weldments, for instance, are susceptible to hot cracking. Small differences in base metal composition have been shown to affect hot cracking behavior [3]. Weldalite™, which has a lower lithium content and a greater copper to lithium ratio than Alloy 2090 and 2091, is reported to have good weldability without hot cracking [5].

Weldalite™ responds well to Variable Polarity Plasma Arc welding (VPPA) and VPPA has been used for several evaluation studies of Weldalite™. The welding of high strength, age hardened alloys results in a variation of microstructures and properties in and near the weld region. The goal of this study is to correlate the microstructures of VPPA welded

specimens with their fracture behavior when subjected to three-point bending at cryogenic temperatures. The stress state in three point bending ranges from maximum tension at the outer radius of curvature to compression at the inner radius of curvature. Cracks from the outer radius advance into a diminishing stress field, which is often adequate to stop the fracture process. Partially cracked samples allow the examination of crack paths and therefore the identification of weak or undesirable microstructural features

II. EXPERIMENTAL PROCEDURE

Specimens evaluated here include welded coupons fabricated from three Weldalite™ chemistries and one chemistry of the conventional Al-Cu alloy 2219. The samples were tested in slow, monotonic, three-point bending at 77 K. Interrupted cracks were examined metallographically and compared to the microstructures of undeformed samples. Microstructural features important in the fracture process were studied in detail by scanning and transmission electron microscopy.

A. Materials

Alloy designations and nominal compositions are shown in Table 1. Each sample was received in the as-welded condition after welding by a two-pass, backside-shielded, Variable Polarity Plasma Arc (VPPA) process using 2319 filler. The weld direction was parallel to the rolling direction of the 8mm thick plate. Prior to welding, the plate was given a T6 temper. Sample dimensions were 25 x 152 x 8 mm, with the weld bead across the width of the sample.

Table 1. Alloy Compositions	
Alloy	Nominal Composition, wt%
2094	Al-4.7Cu-1.3Li-0.4Ag-0.14Zr
2095	Al-4.5Cu-1.0Li-0.4Ag-0.14Zr
2195	Al-4.0Cu-1.0Li-0.4Ag-0.14Zr
2219	Al-6.3Cu-0.3Mn-0.14Zr-0.06Ti
2319 (filler)	Al-6.3Cu-0.3Mn-0.15Ti-0.14Zr

B. Bend Testing

The intent of the bend testing procedure was to

initiate cracks in the specimens and interrupt the crack before total failure, or through thickness cracking, occurred. This was done by monitoring the load cell output, detecting a slight load drop, and terminating the test. Testing was performed on an Instron Model 6027 programmed for compression testing at a crosshead speed of 1 mm/min. An Instron 10 kN load cell was used to obtain load data. A schematic of the three-point bend testing fixture is shown in Fig. 1, with a sample mounted for testing. The lower two-point support used one fixed

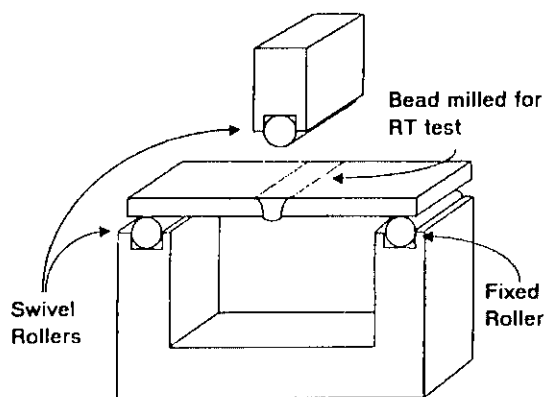


Fig. 1 Schematic of three-point bend fixture with milled sample mounted for RT test.

and one swivel base roller with a 140 mm span between the rollers. This lower support was attached to the moveable crosshead. The upper support used a swivel roller to provide the third contact point for bend testing. A liquid-tight dewar was constructed from styrofoam and a commercially available sprayable foam to fit securely around the test fixture and mount on the Instron crosshead. Sample and fixture temperatures were brought to 77K by addition of liquid nitrogen to the dewar, monitored during testing and maintained at 77 K. Two tests were performed on each alloy, one with the weld face in tension (face tension or FT) and one with the weld root in tension (root tension or RT). For FT tests the root weld bead was milled smooth prior to testing. Similarly the face weld bead was removed for RT tests. This was done to provide a smooth contact surface for the upper roller of the test fixture.

C. Microscopy

Specimens were examined by optical, scanning electron and transmission electron microscopy. Samples were prepared for optical examination by

standard metallographic practice. Mechanically polished samples were anodized in a room temperature solution of 5.5 ml HBF_4 and 95 ml H_2O with an addition of 7 grams Boric acid at 14.5 volts for 60 to 70 seconds. Micrographs were recorded on 35 mm film with a Zeiss Photomicroscope.

The Scanning Electron Microscope (SEM), was used to view the grain structure and second phase particles in the samples provided. Samples were prepared as for metallographic examination, but with the substitution of electropolishing for anodizing. Micrographs were obtained using backscattered electron images. A Cambridge S200 was used at an accelerating voltage of 20 kV.

The Transmission Electron Microscope was used for collecting diffraction data. Thin foils were prepared from equiaxed grain regions of the 2095 and 2195 alloys and diffraction patterns were obtained for the identification of second phase particles. Thin sections of the welded sample were cut parallel to the fusion line to produce a section containing equiaxed grains. Each section was lightly etched to locate the equiaxed grains; 3.0 mm diameter thin foils were then prepared from these regions. A 30% nitric acid, 70% methanol electrolyte solution chilled to -20°C was used to electropolish the foils. Micrographs and selected area diffraction data were obtained with a JEOL JEM 100CX operated at 120 kV.

III. Results

Three Point Bending and Fracture

The results from the bend tests conducted at cryogenic temperature are presented in Table 2, which lists the alloys, bend test orientation (root tension (RT) or face tension (FT)), the failure modes observed in the samples after metallographic examination, the values for maximum load at test termination (F_{\max}), and the maximum deflection at test termination (y_{\max}). Failure modes were characterized by the crack path location in one of three microstructural regions: the fusion zone (FZ), the heat-affected zone (HAZ) or in an equiaxed grain zone along the FZ/HAZ interface (EZ). An example of HAZ cracking is shown for the 2095 RT sample in Fig. 2. All HAZ failures were found within 300 μm of the EZ.

Undeformed Microstructures

A typical optical micrograph is shown in Fig. 3.

Table 2. Failure Modes in Cryogenic Bending

Alloy	Test	Failure Mode	F_{\max} , kN	y_{\max} , mm
2094	RT	EZ	6.73	4.1
2094	FT	HAZ	6.70	7.4
2095	RT	HAZ	6.00	4.3
2095	FT	HAZ	7.01	10.1
2195	RT	FZ	7.06	12.2
2195	FT	HAZ	6.62	17.3
2219	RT	FZ	4.91	12.7
2219	FT	FZ	4.96	7.6

This illustrates the key features of the weld microstructure: the equiaxed grains bordering the fusion zone, the elongated grains of the base alloy and the large second phase particles present in the fusion zone and in parts of the heat affected zone.

Equiaxed Zone.

Backscattered electron images of the EZ in the 2094 and 2195 alloys compared in Fig. 4 show a significant decrease in the amount of grain boundary phase in the leaner alloy.

Electron Diffraction Studies

Several thin foils were made of the equiaxed grain region in the fusion zone of the 2095 and 2195 alloys for examination in the Transmission Electron Microscope (TEM). Grain boundaries were more aggressively attacked during foil preparation than the matrix, making the preparation of foils difficult. This behavior was more severe for the 2094 alloy, from which no useful thin foils were produced.

Two types of grain boundary particle morphologies were observed. The first type of particle was found at grain boundary triple junctions and was fairly equiaxed. The second type of particle was distinguished by a long and continuous shape along grain boundaries. Selected area diffraction patterns were obtained for both types of particles in alloys 2095 and 2195. The results from the analysis of these patterns are summarized in Table 3.

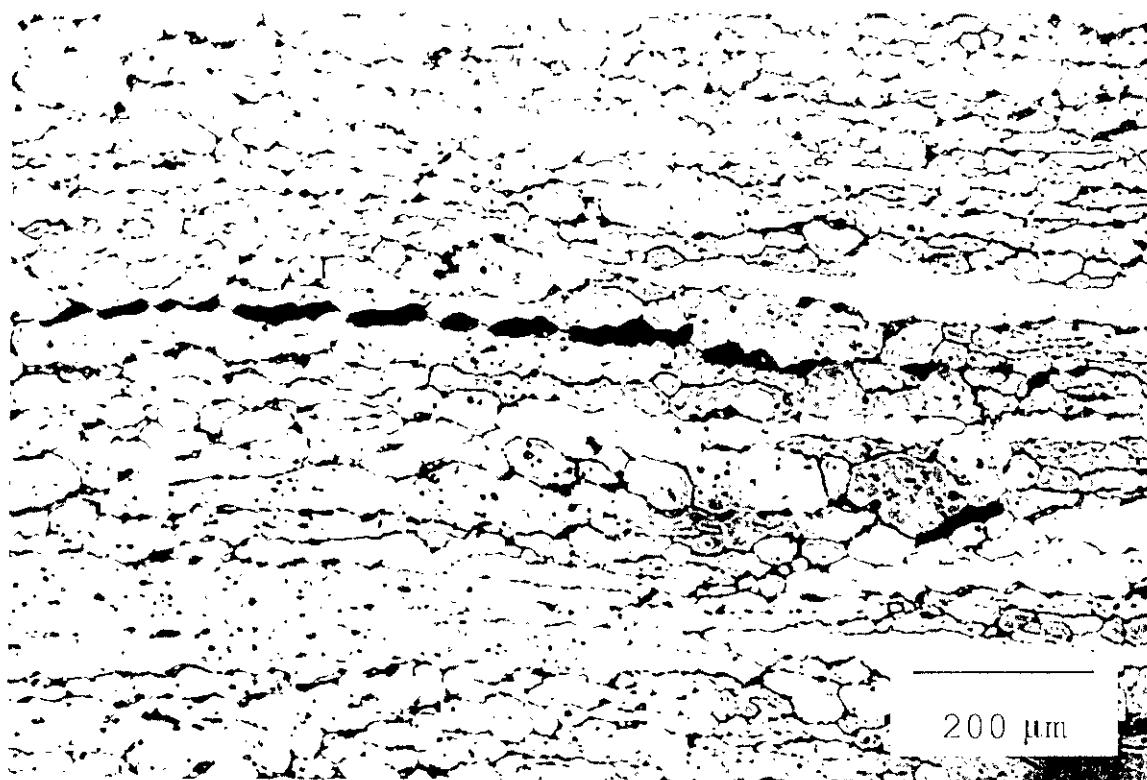


Fig. 2. HAZ delamination, 2095, 77K RT bend test. ST plane, anodized, polarized light.

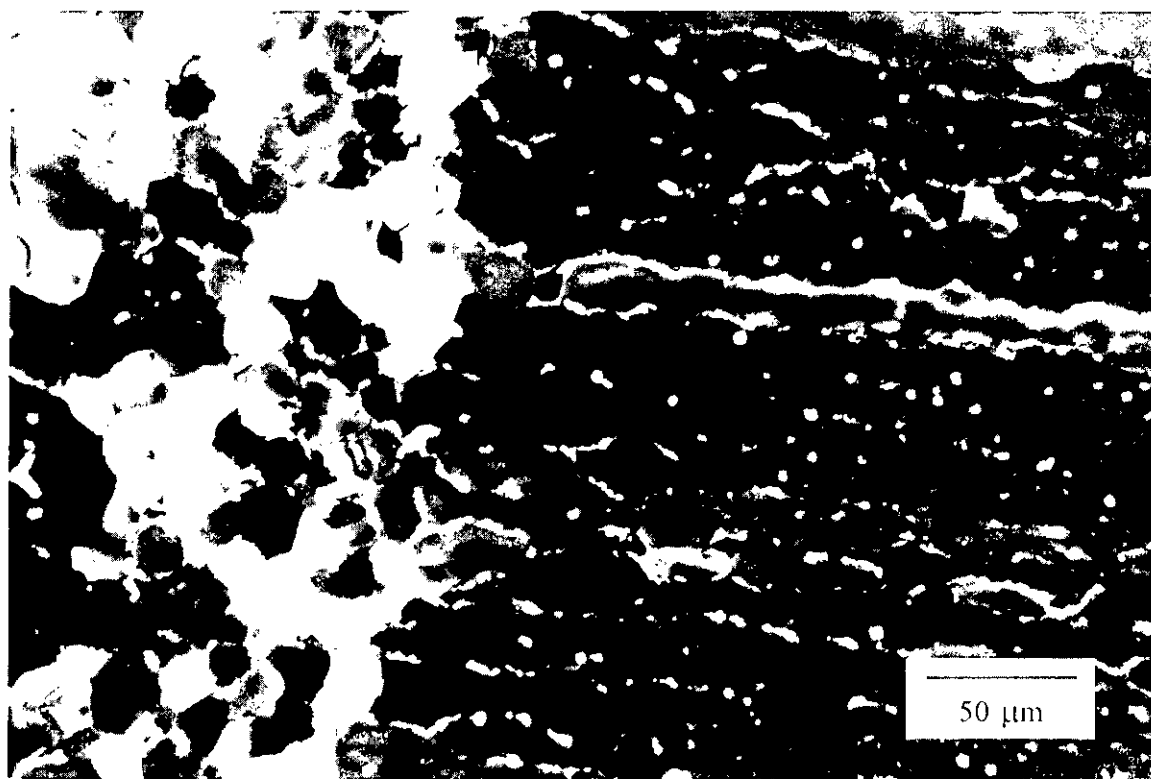


Fig. 3. Typical microstructure of welded 2094. ST Plane, anodized, polarized light.

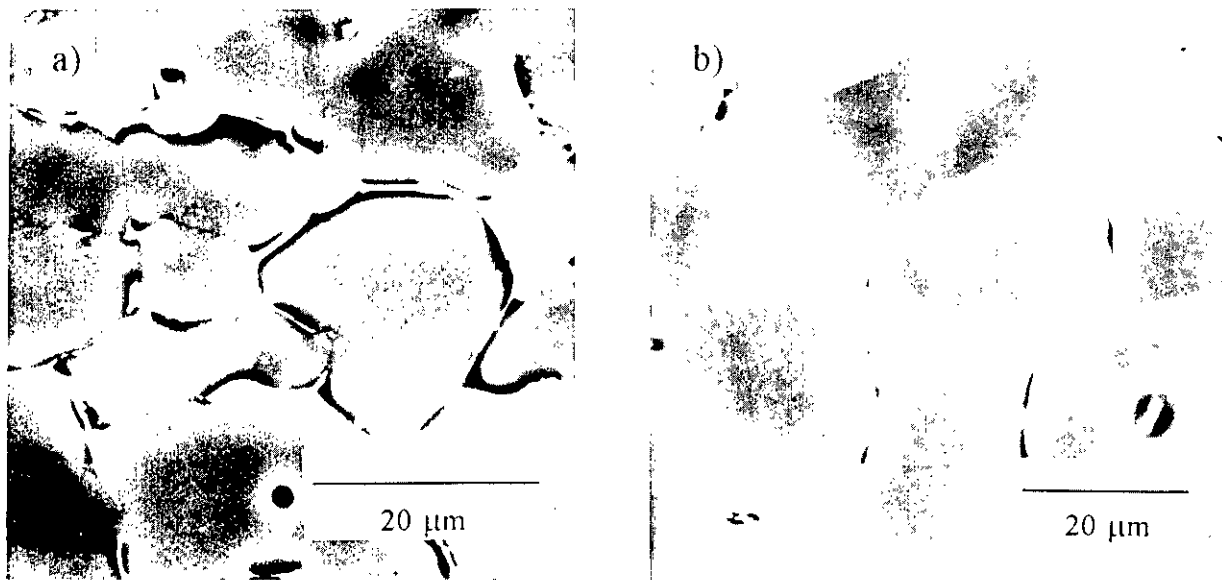


Fig. 4. Scanning electron micrographs of EZ grains, backscattered electron images: a) 2094; b) 2195.

Table 3. Summary of Diffraction Data from EZ Phases

Alloy	Particle Location	d, Å	hkl	Lattice Parameter
2095	Triple Junctions	4.33	200	$a = 8.67\text{Å}$
		2.47	002	$c = 4.94\text{Å}$
		2.14	202	tetragonal
2095	G.B.'s	4.30	002	$a = 8.60\text{Å}$
		3.84	021	cubic
		2.38	023	
		2.15	004	
2195	Triple Junctions	3.37	111	$a = 5.83\text{Å}$
		2.07	220	cubic, T_B
		1.76	311	28-12
2195	G.B.'s	4.23	010	$a = 4.96\text{Å}$
		1.60	120	$c = 8.51\text{Å}$
		1.50	130	hexagonal 40-1285 ?

IV. Discussion

The mechanical testing method was chosen with two purposes: to simulate crack initiation environments which may occur in service and to prepare interrupted crack samples for metallographic study. In both cases material in the weld bead may

play a role, and the weld beads were incorporated in the testing on the tension side of the bend test sample. The mechanical test data is therefore only qualitative, since the bend samples were not machined to precise dimensions, and because of the notch effect of the bead itself. The weld root bead had a smaller radius in all cases, and the resulting greater notch effect is evident in the lower maximum deflection of the RT vs. FT values for the Al-Cu-Li alloys. From a qualitative standpoint, it appears that the ductility (indicated by the maximum deflection in bending) increases with leaner alloys in the order 2094 to 2095 to 2195. This corresponds to a change in failure mode from EZ to HAZ to FZ. In the absence of notch effects or significant microstructural and property inhomogeneities, FZ fracture is expected, since that is the location of the greatest stresses in bending. It is noteworthy that both the 2195 and the conventional material, 2219, fractured in the FZ. The strength benefit of the 2195 alloy is evident in the cryogenic bend testing: it shows similar or better maximum deflection to 2219 at an approximately 40% greater load.

Microstructural examination of the EZ reveals a reason for the fracture mode differences between alloys. The amount of second phase appears much greater at EZ grain boundaries in 2094 than in 2195 (Fig. 4). The properties of the grain boundary phases can be expected to change from one alloy to another as well, since diffraction studies show different phases in the two alloys examined.

Analysis of electron diffraction patterns of the grain boundary particles in the EZ of alloy 2095 yielded crystal structure data not listed in the JCPDS data files [10]. The presence of non-equilibrium phases in this region would be consistent with rapid freezing of a liquated phase. Since the grain boundary phase is relatively thin ($\sim 0.5\mu\text{m}$ or less), and since the samples were not given subsequent heat-treatments, rapid solidification effects may have been retained. The grain boundary phase particle in the 2095 alloy was indexed as cubic with $a = 8.60\text{\AA}$. The triple junction phase in the 2095 alloy had a tetragonal crystal structure with $a = 8.67\text{\AA}$ and $c = 4.96\text{\AA}$. Neither structure matched any of the common Al-Cu-Li phases eg. T_1 or T_B [11]. The grain boundary particle in the 2195 alloy yielded diffraction data reported in JCPDS 40-1285. In a study by Shen et al. [12] this phase was produced by melt spinning and exhibited icosahedral symmetry. Our diffraction patterns indexed as hexagonal with $a = 4.96\text{\AA}$ and $c = 8.51\text{\AA}$. This may be similar to T_1 , but with a distortion of the "c" lattice parameter from the usual value of 9.35\AA . The triple junction particle found in the 2195 alloy had a cubic crystal structure with $a = 5.83\text{\AA}$, and was identified as T_B .

V. Conclusions

A comparison of weldments of three Weldalite™ alloys showed the following effects of decreasing the Cu + Li content:

1. The amount of liquated second phase in an equiaxed grain zone at the fusion zone boundary (the EZ) decreased.
2. The crystal structure of the grain boundary phases in the EZ changed.
3. The tendency for fracture in the EZ decreased.
4. The cryogenic ductility (the amount of deflection in three point bending) increased.

The Al-Cu-Li alloy with the lowest Cu + Li content, 2195, exhibited better cryogenic ductility and significantly greater strength than the conventional cryogenic tank alloy 2219.

Acknowledgements

This work was conducted under a Cooperative Research and Development Agreement with Martin Marietta Manned Space Systems, who provided the sample material, technical support and funding for this program. We gratefully acknowledge their assistance. Conversations with Prof. A. Fox of NPGS on diffraction analysis were helpful.

References

1. Glazer, J., and Morris, J.W., Jr., "The Strength-Toughness Relationship at Cryogenic Temperatures in Aluminum-Lithium Alloy Plate", Aluminum-Lithium Alloys V, Conference Proceedings, MCE Publications, Ltd., Birmingham, U.K., edited by Sanders, T.H., Jr. and Starke, E.A., Jr., pp. 1471-1480, 1989
2. Pickens, J.R., Heubaum, F.H., Langan, T.J. and Kramer, L.S., "Al-(4.5-6.3)Cu-1.3Li-0.4Ag-0.4Mg-0.14Zr Alloy Weldalite™ 049", Aluminum-Lithium Alloys V, Conference Proceedings, MCE Publications, Ltd., Birmingham, U.K., edited by Sanders, T.H., Jr. and Starke, E.A., Jr., pp.1397-1414, 1989
3. Tack, W.T. and Loechel, L.W., "Weldalite™ 049: Applicability of a New High Strength, Weldable Al-Cu-Li Alloy", Aluminum-Lithium Alloys V, Conference Proceedings, MCE Publications, Ltd., Birmingham, U.K., edited by Sanders, T.H. Jr. and Starke, E.A., Jr., pp. 1457-1467, 1989
4. Cho, A., Ashton, R.F., Steele, G.W., Kirby, J.L., "Status of Weldable Al-Li Alloy (Weldalite 049™) Development at Reynolds Metals Company", Aluminum-Lithium Alloys V, Conference Proceedings, MCE Publications, Ltd., Birmingham, U.K., edited by Sanders, T.H. Jr. and Starke, E.A., Jr., pp. 1377-1386, 1989
5. Kramer, L.S., Heubaum, F.H., and Pickens, J.R., "The Weldability of Al-Cu-Li Alloys", Aluminum-Lithium Alloys V, Conference Proceedings, MCE Publications, Ltd., Birmingham, U.K., edited by Sanders, T.H., Jr. and Starke, E.A., Jr., pp. 1415-1424, 1989
6. Kramer, L.S., and Pickens, J.R., "Microstructure and Properties of a Welded Al-Cu-Li Alloy", *Welding Journal*, pp. 115-s - 121-s, April 1992.
7. Kerr, J.R. and Merino, R.E., "Cryogenic Properties of VPPA Welded Aluminum-Lithium Alloys", Aluminum-Lithium Alloys V, Conference Proceedings, MCE Publications, Ltd., Birmingham, U.K., edited by Sanders, T.H., Jr. and Starke, E.A., Jr., pp. 1491-1500, , 1989
8. Cross, C.E. and Edwards, G.R., "Welding of Aluminum Alloys", *Treatise on Materials Science*

- and Technology, Vol. 31, Academic Press, Inc., San Diego, CA, 1989
9. Zacharia, T., David, S.A., Vitek, J.M., and Martukanitz, R.P., "Weldability and Microstructural Characterization of Al-Li Alloys", Aluminum-Lithium Alloys V, Conference Proceedings, MCE Publications, Ltd., Birmingham, U.K., edited by Sanders, T.H., Jr. and Starke, E.A., Jr., pp.1387-1396, 1989
 10. Joint Committee on Powder Diffraction Standards, JCPDS Data Set 41 and earlier.
 11. Hardy, H.K., and Silcock, J.M., "The Phase Sections at 500° and 350° C of Aluminum-Rich Aluminum-Copper-Lithium Alloys", Journal of the Institute of Metals, Vol.84, pp.423-428, 1955/6.
 12. Shen, Y., Poon, S., Dmowski, W., Egami, T., Shiflet, G., *Phys. Rev. Lett.*, 58, 1440, 1987.

Microstructure-Cryogenic Fracture Correlations in Weldalite Weldments
R. Crooks

Q: Do you use the residual stress is all removed from these things if I understand?

A: No, there as the material as welded the residual stress is from rolling I think the material is given a stretch prior to aging.

Q: Within the weld you are pretty sure there is no residual stress, I am wondering whether those deflections the changes in deflection has anything to do with the residual stress changes and how much of that is very sensitive the deflection changes in a three point bend test.

A: We had not considered that.

Q: In other words if you look at the constant crack open displacement of determining your maximum deflection and then compare only four compositions you might get a better view for the stuff.

A: I do not know.

Q: Mack Roberts (Martin Marietta) Both of those papers seem to have concluded that the grain boundary liquation is the problem and I am wondering what the vintage of those welds is, what is the date that they were made.

A: We received them approximately 2 years ago Szabo could comment on that.

Q: M.R. - And I assume that is the case with the other welds, the reason I ask the question is that those older vintage welds were the higher heat input slower travel speed route pass which was that was one of the problems with that welding procedure that produced that grain boundary liquation it would be interesting to see what some of the newer welding procedure welds look like.

A: We would be happy to do that.

Q: Roberto Ria (Alcoa) I think to have some difference in opinion on approach with the composition of weldalite from a fracture toughness standpoint through the years we aim towards leaner composition lower copper, lower lithium to get rid of the second phase particles, but from a welding standpoint we were always told the higher the copper the better weldability; however your results indicate that the leaner alloy has better elongations better strength and I am wondering am I missing something is it possible that the more weldable alloys the one with the better fracture toughness and performance of current temperatures are the ones with the leaner copper. So I am confused.

- A: I will defer to Martin Marietta. I think the initial comment I think was the higher copper contents typically were added to reduce solidification cracking. Since then it's been found that some of the leaner compositions have improved or decreased the delta prime precipitate instead of see you want to move toward the leader of copper and lithium contents from that standpoint which alternately affects the toughness and so on so the higher copper certainly helps cracks sensitivity but in other instances it is a detractor so we are at this point optimizing composition.
- Q: Joe Pickens (Martin Marietta) I agree with what you said except there was never any delta prime in these alloys we stayed out of the phase field where you would get delta prime, right there is something you are missing. We did a study I guess it was 1988 or so where we made weldlite alloys with copper levels from 6.3 down to 4.0 and we did real weld constrain welding test at manned space systems and that time we felt we could not weld at 4.5 percent copper and below as it turns out when we got a little smarter and did the tests properly that was not the case and we could weld down to 4.0 so at that point in time that is why you see the 4.7 in some of the earlier 2094 is because a Attila colleague found that we could not weld at 4.5 generally speaking we did find that the higher copper gives better high cracking resistance and of course no surprises to any metallurgist you lower the solute particularly when you are above the solubility limit the fracture toughness goes up. And we got down to the point where we looked at the alloys that gave really good cryogenic fracture toughness and they fell in two schools one school of around 4.0 copper with lithium levels in the 1 percent regime and others with about 4.5 copper with 1 to 1.1 percent lithium that is the 2020 regime of lithium and we did some comparisons and manned spaced systems and the 4.0 /1.0 turned out to give the best combination of properties. I will talk a little bit about those factors in my talk but one factor missing is we had difficulty welding at 4.5 copper at one point. And just get smarter the more you weld.
- Q: Mac Roberts (Martin Marietta) I agree with what you both say, but I believe the far more significant factor in the quality in the weld and the weldability is the welding procedure used to weld the alloy and with the proper welding procedure you can get good welds with any of the chemistries and I am going to talk a little more about that this afternoon.
- Q: Tim Langan (Martin Marietta) Mack the one thing is we are characterizing some of the new things that came out of the DOE under the DOE study and the fine equiax zone is still present. Some of the liquation back into the parent metal is disappearing with the faster travel speed so we are currently looking at those higher travel speed welds.

MECHANICAL TESTING OF 0.5-INCH WELDED ALUMINUM-LITHIUM ALLOY

R. Bond¹ and T.W. Malone²

¹IIT Research Institute/Metallurgy Research Facility

George C. Marshall Space Flight Center

Marshall Space Flight Center, Alabama 35812

²Metallurgical Engineering Branch

National Aeronautics and Space Administration

George C. Marshall Space Flight Center

Marshall Space Flight Center, Alabama 35812

ABSTRACT

This paper describes a study of the tensile properties of welded aluminum (Al) and aluminum-lithium (Al-Li) fabricated plates (Alloys 2219 and 2195, respectively). Alloy 2195 is the proposed replacement material for the Super Light Weight Tank (SLWT), a lighter version of the Space Shuttle's external fuel tank which is manufactured from Alloy 2219. The SLWT will be used to enhance the Shuttle's ability to support deployment of Space Station "Alpha."

Eight types of samples, prepared from 0.5-inch (1.27-cm) thick plates of Alloys 2219 and 2195, comprised the following:

- flat downhand (1G) weld orientations:
 - 2219/2219
 - 2219/2195
 - 2195/2195
- vertical up (3G) weld orientations:
 - 2219/2219
 - 2219/2195
 - 2195/2195
- longitudinal unwelded 2195 plate
- transverse unwelded 2195 plate

Three-pass weld schedules were used for the (1G) orientations, while two-pass weld schedules were used for the (3G) weld orientations. All welds used 2319 Al spooled filler wire 0.062-inch (0.158-cm) in diameter. Testing was conducted in air at 75 °F (24 °C), liquid nitrogen (LN₂) at -320 °F (-196 °C), and liquid hydrogen (LH₂) at -423 °F (-253 °C).

Strain gauges were applied in unique configurations to measure localized strain in all welded sample type and test environment combinations. Results showed that the mechanical properties of welded 2195/2195 exceed those of welded 2219/2219 and 2195/2219. Data analysis results indicate that if Alloy 2195 plate weld schedules can be optimized, they can produce higher strength welds with lower rejection rates.

I. INTRODUCTION

Russia experimented for many years with Al-Li alloys before the United States aerospace community became aware of the alloys potential. During this time, it was discovered that the weight of components constructed from Al can be greatly reduced, without losing strength or ductility, by adding up to 1.2% Li. Recently, a task was initiated to take advantage of "materials enhanced performance" by constructing a highly visible, high performance flight article (i.e.: the Space Shuttle external fuel tank).

II. BACKGROUND

A report published by the Advisory Committee on the Redesign of the Space Station, Vest, *et al.* [1], dated June 10, 1993, concludes that an Al-Li external fuel tank is required to reach high inclination orbits.

As directed by NASA Headquarters, Marshall Space Flight Center (MSFC) is developing the Super Light Weight Tank (SLWT), a third-generation tank which is lighter than the current external fuel tank. The SLWT is scheduled to be delivered in early 1997, with a first element launch scheduled for later that year.

III. GENERAL PREPARATIONS

Martin Marietta procured 0.5-inch (1.27-cm) thick plates of Alloy 2195 in the T8 condition (solution heat treated, cold worked, then artificially aged) from Reynolds Aluminum. NASA provided program stock of 0.5-inch thick plates of commercial Alloy 2219 in the T87 condition (solution heat treated, cold worked, artificially aged, then stabilized by overaging to resist stress corrosion cracking). All plates were machined to 6-inch (15.24-cm) by 24-inch (60.96-cm) samples to fit a weld qualification jig.

Plate Preparation

Different joint configurations were used for the two weld orientations. The flat downhand (1G) weld orientation used a modified U-groove butt joint configuration, with five flats (which made up the curved portion of the U-groove) whose overall dimensions had an 0.18-inch (0.457-cm) depth by a 0.38-inch (0.965-cm) width. The vertical up (3G) weld orientation used a square butt joint configuration.

All weld surfaces were cleaned and deburred by machining, chemical degreasing/etching, and/or vigorous wire brushing immediately before and between successive variable pulsed plasma arc (VPPA) passes.

Weld Setup

Machined and cleaned test plates were placed in a unique weld qualification jig. The long edges were held together with full-length bar clamps to ensure proper alignment, and an inert helium gas chamber was used to keep gas pressure on the root side of the weld joint to prevent oxidation.

Weld Procedures

The plates were held in the jig during direct current (DC) straight polarity Gas Tungsten Arc (GTA) tack welding. Tack welds were applied by hand to the torch side of the plates (without adding filler wire) to control warpage during successive autonomous weld passes. GTA welds prevent the first pass autogenous welds from becoming contaminated with filler wire remelt.

All autonomous welding was done with a CYBER TIG II 300-amp variable polarity power supply (manufactured by Hobart), an AVC cyclomatic voltage controller, and a B&B 300-amp water-cooled plasma torch using a 2% thoriaated tungsten electrode. A General Digital Industries computer-controlled 3-axis manipulator was used to exactly position the torch head.

The plates were cooled to room temperature between each weld pass and before being removed from the jig (air cooled from the weld torch side and helium purge cooled from the weld root side). The 2319 filler wire was kept in a continuous purge inert gas dispensing drum during all phases of the welding program.

Optimized (1993) weld parameters are shown in the Appendix which were adjusted to accommodate variations in materials and weld joint configurations (e.g.; modified U-groove butt joints versus square butt joints).

Weld Inspection

Three nondestructive inspection methods (visual, X-ray, and dye penetrant) were used to identify weld plates which met established standards for the External Tank. All welding was performed in NASA's Developmental Processes Laboratory at MSFC.

Tensile Sample Preparation

Standard tensile ("dogbone") samples were prepared from 0.5-inch plates. Unwelded 2195 base material was sectioned in longitudinal and transverse orientations. The other samples were prepared with (1G) and (3G) weld orientations from 2219 welded to 2219 (2219/2219), 2219 welded to 2195 (2219/2195), and 2195 welded to 2195 (2195/2195). Three-pass schedules were used for the (1G) weld orientation, and two-pass weld schedules were used for the (3G) weld orientations. All welds were made using spooled 2319 filler wire with a 0.062-inch (0.158-cm) diameter.

A Bridgeport mill was used to machine the standard pin-loaded "dogbone" design with a gauge of 2.25 inches (5.72 cm) and a length of 8 inches (20.32 cm). (See Figure 1.)



Fig. 1. Standard pin-loaded "dogbone" sample fabricated from 0.5-inch (1.27-cm) plate.

Strain Gauge Application

Depending on the weld orientation, either five or six strain gauges were attached to each of the 18 types weld samples. Continuous deformation was measured using two sizes of cryogenic precision strain gauges (manufactured by Micro-Measurements Group, Inc. as Models WK-13-125AD-350 and WK-13-062AP-350) with respective gauge lengths of 0.125 inch (0.32 cm) and 0.062 inch (0.16 cm). These lengths provided: (1) a larger averaging region for the parent metal measurements, and (2) maximum sensitivity in the weld bead and HAZ regions.

IV. RESULTS

Strain Gauge Placement

Twenty two of the 135 samples tested had strain gauges attached to them. Nine, three-pass (1G) weld orientation samples had five strain gauges attached to the gauge section edges, symmetrically centered about the weld bead, across the thickness plane of the plate.

A tenth 1G weld sample had six strain gauges attached to the gauge section edges. Two were centered within the root and double crown pass, and four symmetrically spaced about the weld bead. (This was used to measure the differences in the strain levels of the autogenous fusion metal and the filler wire metal during uniform tensile loading.)

Five two-pass (3G) weld orientation samples had six strain gauges attached to the gauge section edges, as previously described for the (1G) orientation.

The seven remaining (3G) weld samples had five strain gauges attached to the gauge section edges, symmetrically spaced about the weld bead, across the thickness plane of the plate. (See Figures 2 and 3 for strain gauge placements of the six-gauge samples.)

For each sample, deformation information was obtained for both parent materials, HAZs, and the weld bead. (See Figure 4.)

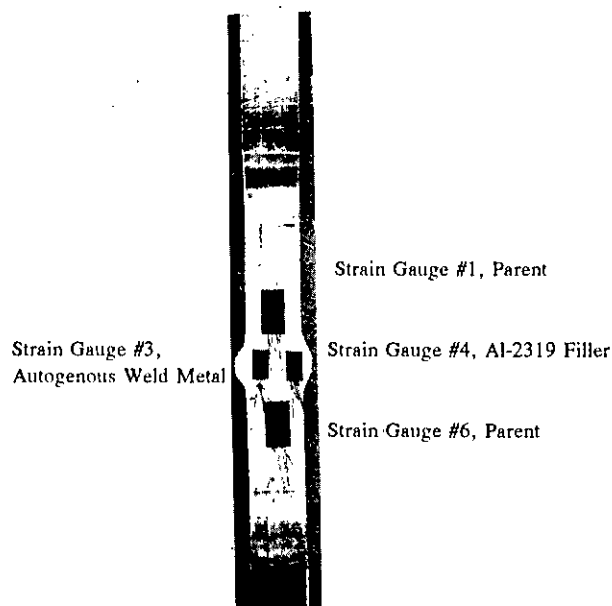


Fig. 2. Strain gauge placement on vertical up (3G) two-pass weld sample, side 1.

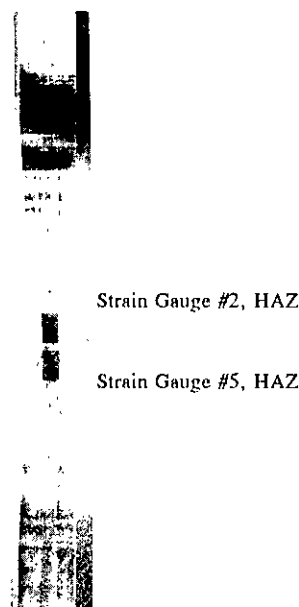


Fig. 3. Strain gauge placement on vertical up (3G) two-pass weld sample, side 2.

Figure 4 depicts some interesting weld regions: (1) parent 2195, (2) 2195 HAZ, (3) weld bead root formed from the first autogenous weld pass, (4) recrystallized fusion zone between weld passes, (5) weld bead crown formed by the second weld pass, (6) 2195 HAZ, and (7) parent 2195.

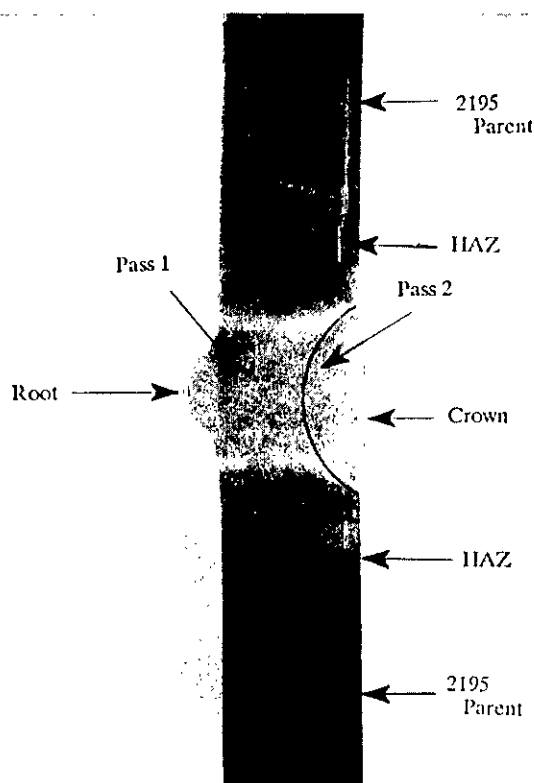


Fig. 4. Macroetch photograph of vertical up (3G) two-pass weld sample of 2195/2195.

Computerized Data Acquisition

An OMEGA ACRO-900 computerized data acquisition system was used to collect load and 2-inch (5.08-cm) extensometer information, as well as either five or six strain gauge channels at a sampling rate of two readings per second. This data was collected until the strain gauges delaminated and/or the sample failed.

Tensile Testing

All tensile testing was conducted at NASA's Cryogenic Test Facility or Materials and Processes Laboratory at MSFC. Tensile testing was conducted in LH_2 at -423°F (-253°C), LN_2 at -320°F (-196°C), and air at 75°F (24°C). Stroke control mode testing was conducted at a standardized rate of 0.05-inch (0.127-cm) crosshead displacement per minute.

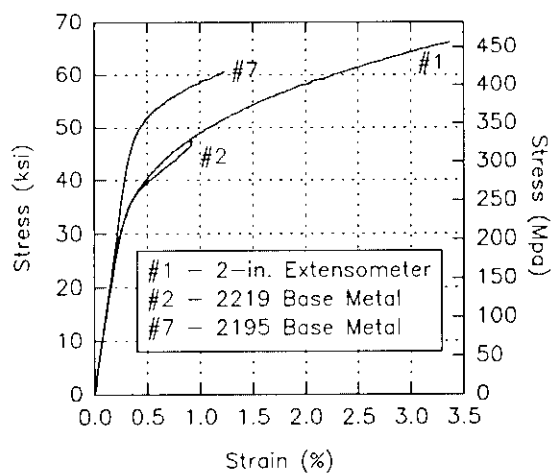
Two test machines were used to obtain the various test conditions. Cryogenic tests were performed on a 60,000 lb (27,211 Kg) Riehle load frame, using a 5-gallon (18.9-liter) closed vacuum-jacketed cryostat that allows test samples to be submerged in liquid test media. Sample deformation was recorded with a 1-inch (2.54-cm) cryogenic-rated short arm extensometer (MTS Model 632.11 E-21) attached to a 1-inch (2.54-cm) extension adapter (MTS Model 632.15B-30, Option 001). This combination provided a 2-inch (5.08-cm) cryogenic short arm extensometer with a 0.2-inch (0.508-cm) full scale extension calibration of 10%.

Air tests were performed under the same parameters as the cryogenic tests using a 20,000 lb (9,070 Kg) MTS load frame with MTS 448 servo-control electronics.

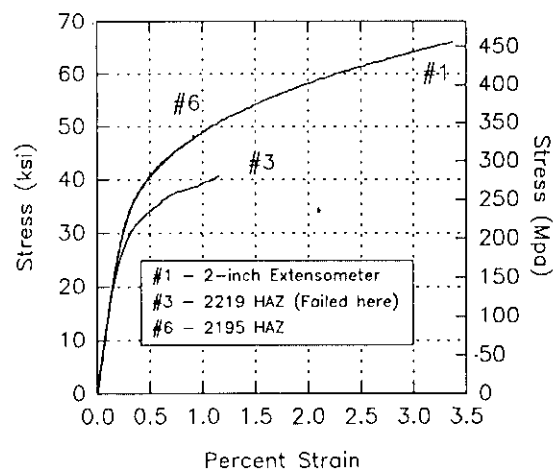
V. DISCUSSION OF RESULTS

Strain Gauge Testing

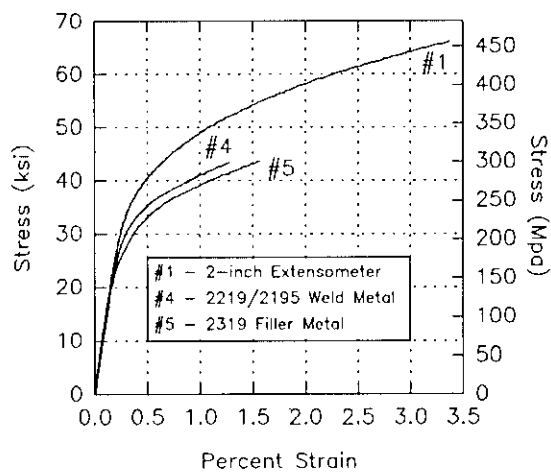
Representative data is provide for the 2219/2195 vertical up (3G) two-pass welded sample (which was submerged in LH_2 for 15 minutes before tensile testing) in Figures 5A through C. All figures show the highly localized continuous strain data in the (A) base metal (gauges #2 and #7), (B) HAZ (gauges #3 and #6), and (C) weld bead (gauges #4 and #5), respectively. In all figures, trace #1 shows the standard 2-inch (5.08-cm) extensometer stress versus strain deformation data normally collected during tensile testing. (See Table I for strain gauged sample data summary.) Note that both weld metal regions and the 2219 HAZ show lower yield strengths than the extensometer offset yield strength.



(A)



(B)



(C)

Fig. 5. Continuous strain gauge and extensometer data for (A) base metal, (B) HAZ, and (C) weld bead of 2219/2195 vertical up (3G) two-pass weld sample tested in LH_2 .

TABLE I. Strain Gauge Sample Data Summary									
Test Media (°F)	Plate Number	Material A & B (Weld Orient.)	Strain Gauge Placement 0.2 % Yield Strength (ksi)						UTS (ksi)
			2" Ext.	Parent (A Side)	HAZ (A Side)	Weld	HAZ (B Side)	Parent (B Side)	
Air (72)	612-BTS-5	2219-2219 (3G)	23.7		26.4	16.1	25.0 *		37.5
	613-ATS-1	2195-2219 (3G)	29.1		36.8	22.3	25.7 *		42.4
	613-ATS-4		34.3		--	28.4	31.9 *		54.2
	614-KTS-43	2195-2195 (3G)	33.1		33.1 *	25.1	35.9		51.2
	615-FTS-22	2219-2219 (1G)	N/A		32.7	--	31.8 *		41.4
	615-ATS-3		25.1	29.1	16.6 *	15.5	17.3	--	42.9
	616-BTS-8	2195-2219 (1G)	30.0		33.7	24.8	--, *		47.2
	617-CTS-10	2195-2195 (1G)	34.3		34.2 *	27.5	36.7		45.7
LN ₂ (-320)	612-ETS-19	2219-2219 (3G)	27.6	37.2	22.2 *	21.2	22.2	33.6	49.3
	613-ATS-3	2219-2195 (3G)	35.2		27.9 *	25.0	40.5	--	56.0
	Two -Pass Weld Schedules: 2319 (Filler Wire) XXXX (Fusion Material)**								
	613-DTS-14	2219-2195 (3G)	35.0	36.3	29.8 *	28.8 29.4	32.2	43.2	55.3
	614-ITS-36	2195-2195 (3G)	38.6	48.0	34.6	30.0 29.8	32.1 *	43.1	57.0
	615-ETS-20	2219-2219 (1G)	30.0	48.2	27.4 *	19.9	25.5	43.8	53.9
	616-BTS-5	2195-2219 (1G)	34.9	42.1	30.9 *	27.5	43.1	50.0	57.0
	617-CTS-12	2195-2195 (1G)	35.2		39.6 *	28.9	36.9		45.7
LH ₂ (-423)	612-FTS-21	2219-2219 (3G)	34.4	39.9	30.0	25.4 27.1	30.0 *	40.1	59.7
	613-BTS-8	2219-2195 (3G)	41.8		36.1 *	34.0	46.0		58.1
	613-FTS-22		40.2	39.0	32.7 *	31.8 34.8	40.2	52.6	66.2
	614-JTS-39	2195-2195 (3G)	47.3	52.0	42.8	41.9 35.9	42.6 *	52.0	62.8
	615-CTS-10	2219-2219 (1G)	34.0	41.9	28.5 *	28.7	29.8	46.2	61.1
	616-ATS-4	2219-2195 (1G)	42.6	41.9	36.0 *	37.5	43.2	51.9	69.6
	Three -Pass Weld Schedule: 2319 (Filler Wire) XXXX (Fusion Material)***								
	617-BTS-8	2195-2195 (1G)	50.1	54.9	46.5	45.9 37.5	45.9 *	54.0	60.3

Notes:

- N/A = No Extensometer Data
- = Strain Gauge Failed Before Reaching 0.2% YS
- * = Fracture Location
- ** = Single-Pass Filler Wire (Crown) | Autogenous Fusion Material (Root Pass)
- *** = Double-Pass Filler Wire (Crown) | Autogenous Fusion Material (Root Pass)

Tensile Testing

Tensile test data for the three environment parameters confirm that 2195/2195 welded with 2319 filler wire in the (1G) and (3G) weld orientations is consistently as strong as either 2219/2219 or 2219/2195. Note that the unwelded base results are almost twice as strong as the welded samples. (See Figures 6 and 7.) Samples tested in air, LN_2 , and LH_2 met the minimum UTS requirements of 38.0, 49.0, and 54.0 ksi, respectively.

No differences were detected in longitudinal and transverse unwelded base data, therefore, the ultimate tensile and 0.2% offset yield strengths were pooled.

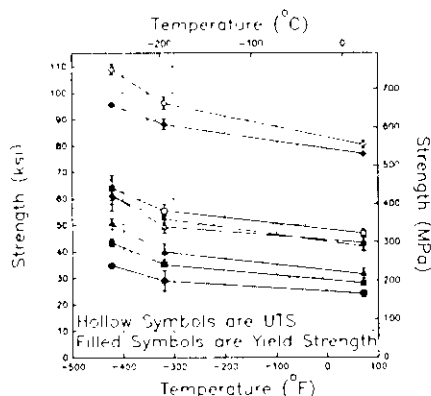


Fig. 6. 0.2% yield and ultimate tensile strength versus testing temperature for flat downhand (1G) samples.

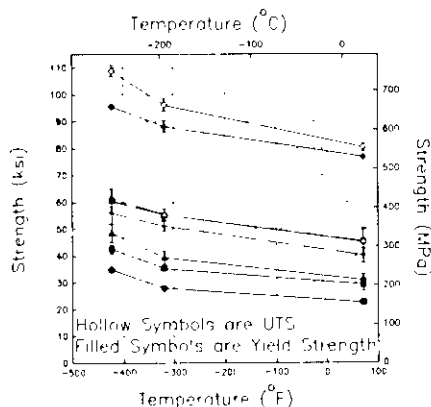


Fig. 7. 0.2% yield and ultimate tensile strength versus testing temperature for vertical up (3G) samples.

Ductility measurements for the unwelded orientation were also pooled. Figures 8 and 9 show ductility expressed in the form of % elongation data for each weld orientation. Results indicate that 2195 in the welded condition surpasses established material design criteria for manufacturing the SLWT.

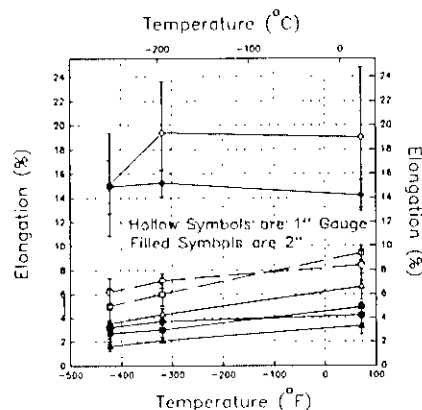
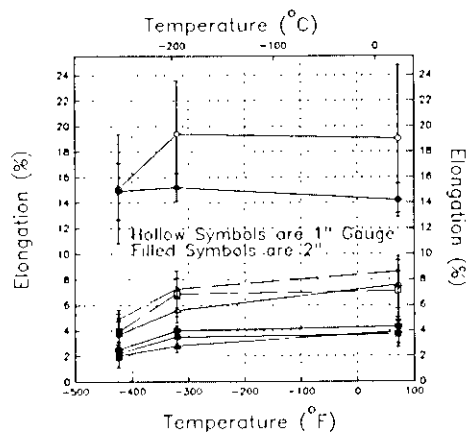


Fig. 8. Elongation versus testing temperature for flat downhand (1G) samples.



Key to Symbols in Figures 6-9.

- Al 2219 - Al 2219
- Al 2219 - Al-Li 2195 MIXED
- ▲ Al-Li 2195 - Al-Li 2195
- ◆ Al-Li 2195 UNWELDED BASE

Note: Error Bars are 1 SD

Fig. 9. Elongation versus testing temperature for vertical up (3G) samples.

Fracture Analysis

Most mixed mode failures occurred on the 2219 side of the weld. Closer analysis revealed that all failures initiated at the root corners of the weld bead, with most following the fusion line between the weld bead and the HAZ slightly edging inward toward the weld bead nugget but then veering back to the fusion line. The rest arced around the first pass fusion line, juttied through the weld bead, and followed the fusion line on the other side of the weld bead until failure. (Figure 10 shows a typical fracture path.)



Fig. 10. Macrograph of a typical fracture path.

Closer examination of the failed root corners revealed microporosity, microporosity coalescence, and microcracking at the fracture initiation sites. These conditions combined with the weld bead root geometry with respect to the plate surface, forming a high stress concentration riser which is an excellent fracture initiator. Figure 11 shows representative root corner micropores and micropore coalescence, and Figure 12 shows the root corner microcracks in a broken sample.

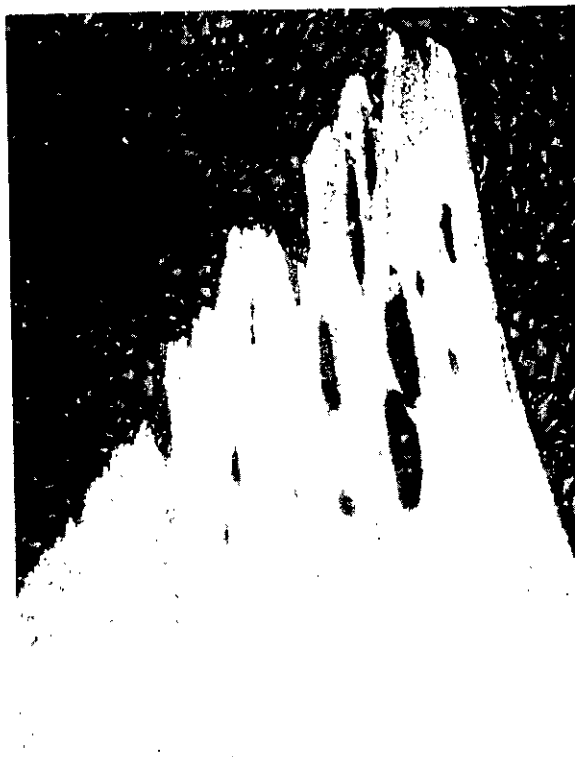


Fig. 11. Root corner micropores and micropore coalescence.

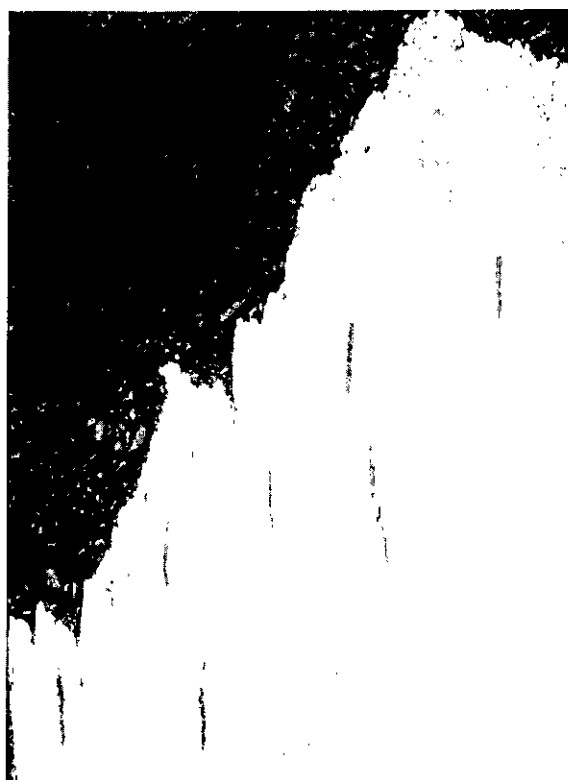


Fig. 12. Root corner microcracks.

ACKNOWLEDGMENT

The development task was a joint effort by NASA, Martin Marietta Corporation (MMC), and IIT Research Institute (IITRI) at Marshall Space Flight Center (MSFC). NASA managed the program; MMC acquired the material, welded test panels, and machined test specimens; IITRI performed all tensile tests, data collection, and data analysis, and compiled the final data report.

Daniel J. Rybicki, Senior Welding Engineer of MMC, developed the optimized weld schedule and performed the weld work. MMC is supported by NASA/MSFC Contract NAS8-36200, Technical Directive 3.6.2.1-725 R, DO 91.

Robert W. Bond, Jeffrey H. Sanders, and Craig Stafford of IITRI performed the primary work with editing and layout by Denise McCool and Susan Hessler. IITRI is supported by NASA/MSFC Contract NAS8-38258, DO 89, Task Project Code P06150-P623.

REFERENCES

1. Vest, Charles M., *et al.*, "Final Report to the President: Committee on the Redesign of the Space Station," Massachusetts Institute of Technology, Cambridge, MA, 1993.

APPENDIX

VPPA Weld Schedule Parameters for 1993 Panel Series 612 and 615 (2219/2319/2219)					
Weld Parameters	Panel Series 612 (1993) Vertical Up (3G) Weld Orientation		Panel Series 615 (1993) Flat Downhand (1G) Weld Orientation		
	1st Pass	2nd Pass	1st Pass	2nd Pass	3rd Pass
Current (Amps)	270.0	185.0	180.0	195.0	185.0
Voltage (Volts)	28.5	24.5	29.5	26.0	26.0
Travel Speed (IPM)	9.0	8.0	8.0	8.0	7.5
Filler Wire Feed Rate (IPM)	20.0	50.0	0	100.0	70.0
Total Plasma Gas Flow (CFH Argon)	6.0	2.0	4.0	2.0	2.0
Torch Shield Gas Flow (CFH Helium)	80.0	80.0	70.0	70.0	70.0
Root Side Purge Gas Flow (CFH Helium)	0	0	N/A	N/A	N/A

VPPA Weld Schedule Parameters for 1993 Panel Series 613 and 616 (2195/2319/2219)					
Weld Parameters	Panel Series 613 (1993) Vertical Up (3G) Weld Orientation		Panel Series 616 (1993) Flat Downhand (1G) Weld Orientation		
	1st Pass	2nd Pass	1st Pass	2nd Pass	3rd Pass
Current (Amps)	260.0	180.0	169.0	195.0	175.0
Voltage (Volts)	26.5	24.0	29.4	25.8	25.5
Travel Speed (IPM)	7.0	6.0	6.1	8.0	6.5
Filler Wire Feed Rate (IPM)	0	60.0	0	70.0	80.0
Total Plasma Gas Flow (CFH Argon)	5.5	1.5	4.0	2.0	2.0
Torch Shield Gas Flow (CFH Helium)	80.0	80.0	60.0	80.0	80.0
Root Side Purge Gas Flow (CFH Helium)	170.0	150.0	95.0	95.0	0

VPPA Weld Schedule Parameters for 1993 Panel Series 614 and 617 (2195/2319/2195)					
Weld Parameters	Panel Series 614 (1993) Vertical Up (3G) Weld Orientation		Panel Series 617 (1993) Flat Downhand (1G) Weld Orientation		
	1st Pass	2nd Pass	1st Pass	2nd Pass	3rd Pass
Current (Amps)	245.0	180.0	164.0	195.0	168.0
Voltage (Volts)	27.0	23.0	28.5	25.0	24.8
Travel Speed (IPM)	6.5	5.0	6.3	8.0	6.5
Filler Wire Feed Rate (IPM)	0	50.0	0	100.0	52.0
Total Plasma Gas Flow (CFH Argon)	5.3	1.5	4.0	2.0	2.0
Torch Shield Gas Flow (CFH Helium)	80.0	80.0	60.0	95.0	95.0
Root Side Purge Gas Flow (CFH Helium)	170.0	150.0	95.0	95.0	0

Mechanical Testing of 0.5-inch Welded Aluminum-Lithium Alloy
R. Bond

No questions.

FRACTURE PROPERTIES OF 0.5-INCH WELDED ALUMINUM-LITHIUM ALLOY

P. McGill¹, M. Watwood², and B. Malone²

¹Materials and Processes Laboratory
National Aeronautics and Space Administration
George C. Marshall Space Flight Center
Marshall Space Flight Center, Alabama 35812
²ITT Research Institute/Metallurgy Research Facility
George C. Marshall Space Flight Center
Marshall Space Flight Center, Alabama 35812

ABSTRACT

This report addresses the fracture behavior of welded aluminum-lithium (Al-Li) plate in air and liquid hydrogen (LH₂), based on a study of surface-flawed panels fabricated from aluminum (Al) 2219 and Al-Li 2195. Test panels were prepared from 0.5-inch plates by welding 2219 to 2219 (2219/2219), 2219 to 2195 (2219/2195), and 2195 to 2195 (2195/2195), all using Al 2319 filler wire.

After semi-elliptical surface flaws with aspect ratios ($a/2c$) from 0.14 to 1.0 were introduced at weld fusion lines, the panels were precracked and loaded to failure in tension in ambient air (75 °F) and LH₂ (-424 °F). Fracture criteria were derived from surface flaw and tensile data using Newman's Two-Parameter Failure Criterion.

Test results indicated that welded 0.5-inch 2195 plate has superior fracture properties to those of welded 0.5-inch 2219. In all configurations, small flaws had greater fracture properties at cryogenic temperature than at ambient temperature.

I. INTRODUCTION

The Space Shuttle now uses an external fuel tank fabricated from Al 2219. NASA intends to replace this tank with the Super Light Weight Tank (SLWT), a third-generation tank fabricated from Al-Li 2195 that will be approximately 8,000 pounds lighter. The SLWT will allow heavier payloads to be deployed into low-earth orbit, as well as permitting higher orbits at higher inclinations that will facilitate rendezvous with the Russian space station Mir.

II. MATERIAL

Test specimens were machined from 2195 manufactured by Reynolds Metal Company (RMC) as lot #922T078A/Plate 1A, 1B, and 1C/Drop 1380-8. After being heat treated to the RT70 temper, this

material received a 6% stretch and was aged at 290 °F for 24 hours. (See compositional breakdown in Table 1.) The 2219 material was heat treated to the T87 condition. All welds used 0.063-inch Al 2319 filler wire.^[1]

TABLE 1. Composition of Al-Li 2195

Element	Weight %
Si	0.03
Fe	0.03
Cu	3.85
Mg	0.37
Ni	0.01
Zn	0.03
Ti	0.01
Li	0.96
Ag	0.34
Zr	0.14
Al	Balance

III. WELDING

Test panels were prepared by Martin Marietta at Marshall Space Flight Center (MSFC) Materials and Processes Laboratory. First, 0.5-inch thick material was cut into 6- by 24-inch plates. The plates were welded together to form 12- by 24-inch panels, which were radiographically inspected.

Six panel series were prepared, using three material configurations and two weld orientations. The material configurations were 2219-T87 welded to 2219-T87 (2219/2219), 2219-T87 welded to 2195-RT70 (2219/2195), and 2195-RT70 welded to 2195-RT70 (2195/2195). The weld orientations were 1G downhand (using a modified U groove-butt joint

and a three-pass schedule) and 3G vertical up (using a square-butt joint and a two-pass schedule). The panels were machined before welding and then chemically etched or wire-brushed between passes. To control alignment, hand-placed tack welds were applied to the panels before initial welding.

All panels were joined via Variable Polarity Plasma Arc (VPPA) welding,^[2] using an automated system (i.e.: Hobar CYBER TIG II 300 Amp capacity variable power supply, AVC cyclomatic voltage controller, water-cooled 350-amp B & B plasma torch with a 2% thoriated tungsten electrode). Torch head position was maintained with a computer-controlled General Digital 3-axis manipulator.

IV. TESTING

All tests were conducted at the MSFC Hydrogen Test Facility, using standard surface-crack tension specimens, per American Society for Testing and Materials (ASTM) standard E740. The weld beads were machined flush, and a starter notch was electro-discharge machined (EDM'ed) at the fusion line on the crown side of each weld. (See Figure 1.)

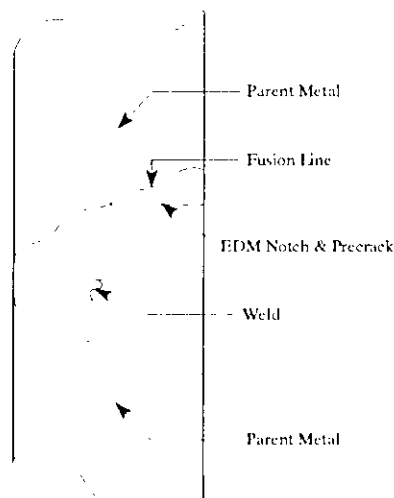


Fig. 1. EDM Notch.

Tensile data indicated that the fusion line was the weakest part of the weld.^[2] For 2219/2195, the starter notch was placed on the 2219 side of the weld for air tests and on the 2195 side for LH₂ tests. This decision was based on failure patterns observed in tensile test specimens.^[2] (See tensile data summary in Appendix A.)

Semi-elliptical starter notches were EDM'ed into the sample, and precracking was initiated in air. Tension precracking was performed at a frequency of 40 Hz, using a sine function and an R ratio of 0.1. Precracking continued until the starter notch had grown a minimum of 0.010 inches. Precrack loads were kept below 60% of the projected failure load.

All testing was performed in displacement (stroke) control with a test speed of 0.05 in/min. The samples were tested in ambient air (75 °F) or LH₂ (-423 °F), and they remained completely submerged during LH₂ testing.

V. DATA ANALYSIS

Net section stresses for each test specimen were calculated using Equation 1:

$$S_n = \frac{P_{max}}{A_{net}} \quad (1)$$

where:

S_n = Net Section Stress
 P_{max} = Maximum Test Load
 A_{net} = Net Section Area

The normalized crack length for each specimen was calculated using Equation 2:

$$a_{norm} = \frac{aF_n^2}{Q} \quad (2)$$

where:

a_{norm} = Normalized Crack Length
 a = Crack Depth
 F_n = Boundary Correction Factor
 Q = Shape Factor for Ellipse

This normalized flaw length represents the half length of a through flaw in an infinite plate, producing a stress intensity factor equal to that of a surface flaw. The geometric correction factor (F_n) is based on finite element solutions by Newman and Raju.^[3] Since stress intensity varies around the surface flaw perimeter, a reference point was chosen at a depth of $a/2$ from the specimen surface. (See Figure 2.)

The $a/2$ depth corresponds to a parametric angle of 30° from the surface of the specimen. At this point, a good correlation exists between stress intensity and fracture strength, as indicated by Newman's data.^[4]

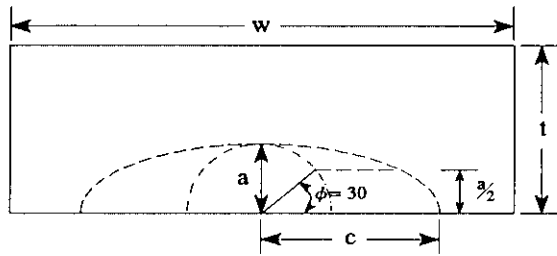


Fig. 2. Semi-Elliptical Notch Detail.

The stress intensity (K_{Ic}) at $a/2$ can be calculated from Equation 3:

$$K_{Ic} = S_{net} \sqrt{\pi a_{norm}} \quad (3)$$

where:

K_{Ic} = Stress Intensity Factor

Net section failure stresses were compared to normalized flaw length for all welds. (See Figures 3, 4, and 5, which combine data for vertical and downhand welds.)

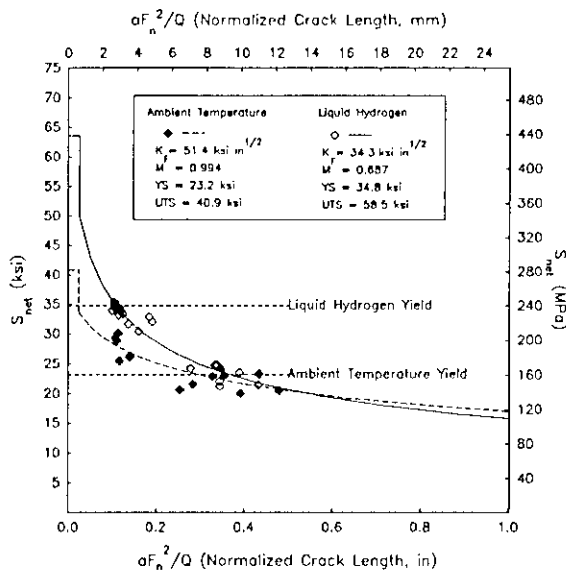


Fig. 3. Net Section Failure Stress for 2219/2219 As A Function of Normalized Flaw Size.

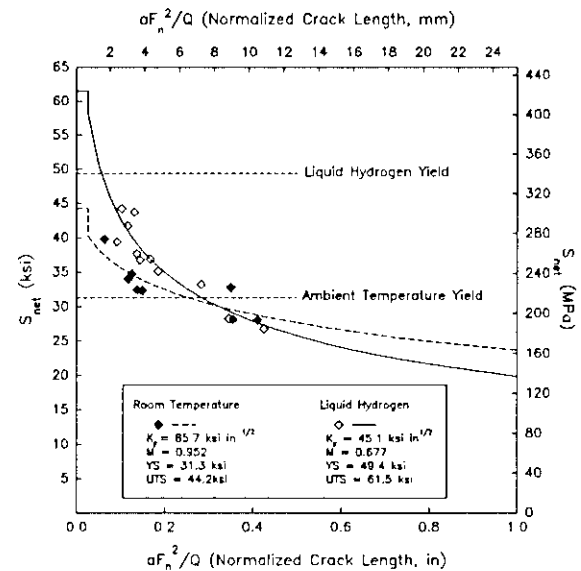


Fig. 4. Net Section Failure Stress for 2219/2195 As A Function of Normalized Flaw Size.

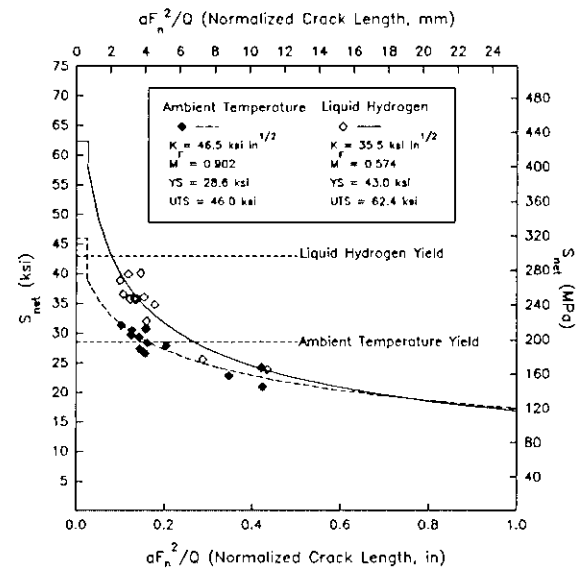


Fig. 5. Net Section Failure Stress for 2195/2195 As A Function of Normalized Flaw Size.

The fracture data was modelled using Newman's two-parameter fracture criterion.^[5] This method allows the determination of two parameters (K_I and m) to describe the fracture strength of a material as a function of crack size and shape. The parameters are developed from a combination of

linear elastic fracture mechanics and Neuber's rule to describe the plastic stress state in the vicinity of a notch. K_t is a toughness parameter measured in $\text{ksi}\sqrt{\text{in}}$, while m is a nondimensional parameter that basically serves to fit the data. The m parameter helps to account for plasticity and residual stresses in the vicinity of the notch. Fracture parameters vary with material thickness, process, and temperature.

Once K_t and m are known for a material, the net section failure stress failure stress for a given flaw size can be determined from Equation 4:

$$S_u = \frac{K_t}{\sqrt{\pi a_{\text{norm}}}} \frac{K_t m}{\sigma_u} \quad (4)$$

where:

K_t, m = Toughness Parameters
 σ_u = Ultimate Tensile Strength

Table 2 presents a summary of the curve fit and strength parameters for each weld configuration. (Note that these properties are all average values. See Appendix B for a tabular listing of the test data.)

TABLE 2. Summary of Curve Fit and Strength Parameters					
Weld	Temp (°F)	YS (ksi)	US (ksi)	K_t (ksi $\text{in}^{1/2}$)	M
2219/2219	70	23.2	40.9	51.4	0.994
	-423	34.8	58.5	34.3	0.687
2219/2195	70	28.6	46.0	46.5	0.902
	-423	43.0	62.4	35.5	0.574
2195/2195	70	31.3	44.2	85.7	0.952
	-423	49.4	61.5	45.1	0.677

VI. RESULTS

No variations in weld strength appeared to be associated with the two weld orientations. At cryogenic temperature, all failures occurred at net section stresses below the yield stress of the material, which indicates that toughness is the controlling parameter. At ambient temperature, weld behavior is driven by toughness for large flaws and strength for small flaws.

Another important generic trend is the intersection of the cryogenic and ambient temperature failure curves. This "crossover" in net section failure stresses affects the requirements for proof-testing cryo-tankage, demonstrating the need for adequate nondestructive evaluation (NDE) to screen for flaws beyond the crossover point.

At both cryogenic and ambient temperatures, the fracture toughness ratio (FTR) drops at large flaws. This phenomenon minimizes the effectiveness of proof-testing to screen for large flaws. The FTR is greater than one for small flaws at or near the NDE detectable limit. (Table 3 summarizes FTR values, based on curve fit parameters.)

Table 3. Fracture Toughness Ratios for Various Normalized Flaw Lengths			
a_{norm}	K_{Ic} at $a/2$ (ksi $\sqrt{\text{in}}$)		FTR
	Cryogenic	Ambient	
2219/2219			
0.1	19.96	15.92	1.25
0.2	22.74	19.95	1.14
0.3	24.24	22.48	1.08
0.4	25.23	24.31	1.04
2195/2195			
0.1	23.92	19.96	1.20
0.2	27.73	25.75	1.08
0.3	29.84	29.54	1.01
0.4	31.26	32.38	0.97

Figures 6 and 7 show composites of net section strength versus normalized flaw size curves for each temperature. Weld strength for 2195/2195 exceeds that of 2219/2219 by 20% or more, while weld strength for 2219/2195 falls between the two. (Table 4 summarizes net section failure strengths, based on curve fit parameters.) Net section strength values at normalized flaw sizes of 1 inch were extrapolated from the curve fit. (See Appendix C for fractography of representative failure surfaces.)

Table 4. Summary of Net Section Strengths Values						
a_{norm}	S_{net} (ksi)					
	Cryogenic			Ambient		
	2195/2195	2219/2219	Strength Ratio	2195/2195	2219/2219	Strength Ratio
0.1	42.67	35.61	1.20	35.61	28.40	1.25
0.3	30.74	24.97	1.23	30.43	23.15	1.31
1.0	19.88	15.77	1.26	23.69	17.01	1.39

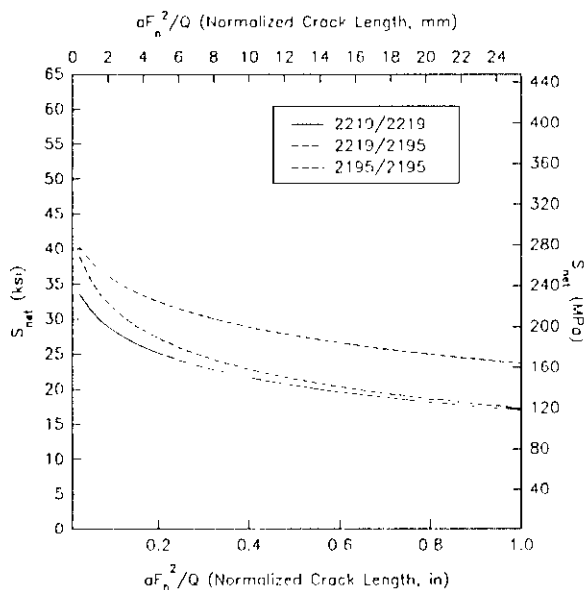


Fig. 6. Ambient Net Section Failure Stresses As A Function of Normalized Flaw Size.

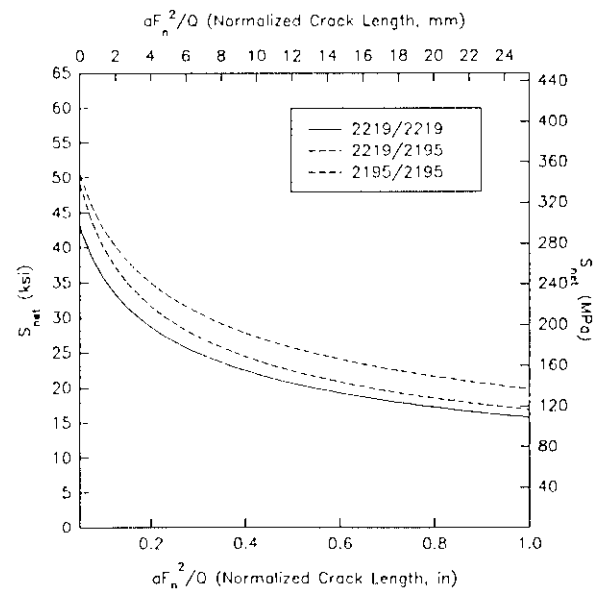


Fig. 7. Cryogenic Net Section Failure Stresses As A Function of Normalized Flaw Size.

CONCLUSIONS

Surface crack tension tests were performed on 0.5-inch welded plates of Al-Li 2195 and Al 2219 which contained semi-elliptical surface cracks at the fusion line of the weld. At both ambient and cryogenic temperatures, 2195 exhibited 20% higher fracture strength than conventional 2219-T87 with flaws of similar size. The 2195 plate had a fracture toughness ratio greater than 1.0 for normalized flawlengths in excess of approximately 0.3-inch. (This "crossover" flaw size emphasizes the need for NDE screening.)

At cryogenic temperature, all failures occurred below net section yield stresses, indicating behavior controlled by toughness. At ambient temperature, small flaws were driven by strength and large flaws were driven by toughness.

ACKNOWLEDGEMENTS

This study was supported by NASA/Marshall Space Flight Center Contract NAS8-38258. The authors wish to thank C. Stafford for test assistance.

REFERENCES

1. Rybicki, D.J. and Ezell, K.G., "High Performance Aluminum Lithium External Tank Study," Technical Directive 3.6.2.1 - 725 R4, September 1993.
2. Bond, R., Malone, T.W., and Rybicki, D.J., "Mechanical Testing of 0.5-Inch Welded Aluminum-Lithium Alloy," Proceedings of the 1994 Conference on Advanced Earth to Orbit Propulsion Technology, Marshall Space Flight Center, AL, May 17 - 19, 1994.
3. Newman, Jr., J.C. and Raju, I.S., "Stress-Intensity Factor Equations for Cracks in Three-Dimensional Finite Bodies Subjected to Tension and Bending Loads," *First Series, Computational Methods in Mechanics, Vol. 2: Computational Methods in the Mechanics of Fracture*, edited by S.N. Atluri, NY: Elsevier Science Publishing Co, 1986, pp. 311 - 334.
4. Birt, M.J., Hafley, R.A., Newman, Jr., J.C., "Application of the Two-Parameter Fracture Criterion to Aluminum-Lithium Alloys," NASA Technical Memorandum 109126.
5. Newman, Jr., J.C., "Fracture Analysis of Surface- and Through-Cracked Sheets and Plates," *Engineering Fracture Mechanics*, Vol. 5, UK: Pergamon Press, 1973, pp. 667 - 689.

APPENDIX A--Summary of Tensile Data¹²

Panel Series	Environment	Yield (ksi)	UTS (ksi)	Modulus (Msi)	EI (%)	RA (%)
612 (2219/2219) Vertical	Air	22.6	40.0	10.7	8.6	4.3
	LH ₂	34.8	56.1	12.5	4.9	2.5
615 (2219/2219) Downhand	Air	24.0	41.8	10.8	8.4	4.2
	LH ₂	34.7	60.9	11.7	6.2	3.2
613 (2219/2195) Vertical	Air	29.2	45.2	11.0	7.1	3.7
	LH ₂	42.5	60.6	12.7	3.9	2.2
616 (2219/2195) Downhand	Air	28.0	46.7	12.0	9.4	4.9
	LH ₂	43.4	64.1	12.0	5.0	2.7
614 (2195/2195) Vertical	Air	31.0	45.3	10.5	7.6	3.9
	LH ₂	48.4	61.6	12.2	3.7	2.0
617 (2195/2195) Downhand	Air	31.5	43.1	11.1	6.6	3.3
	LH ₂	50.4	61.3	13.3	3.5	1.6

APPENDIX B-- Raw Data

2219/2219 Vertical (Panel Series 612)					
Temp. (°F)	Width (in.)	Thickness (in.)	P _{max} (lbs)	a (in.)	2c (in.)
Amb.	3.005	0.519	12,680	0.412	2.412
	3.005	0.510	13,990	0.426	2.787
	3.003	0.533	16,380	0.447	2.530
	3.004	0.517	16,660	0.428	2.506
	3.008	0.542	19,060	0.419	2.424
	3.010	0.529	37,050	0.410	0.548
	3.005	0.490	39,900	0.220	0.521
	3.010	0.505	42,090	0.212	0.507
-423	3.003	0.541	13,760	0.452	2.772
	3.007	0.525	16,310	0.429	2.494
	3.008	0.543	16,576	0.442	2.677
	3.007	0.551	21,250	0.409	2.491
	3.004	0.505	41,000	0.414	0.831
	3.009	0.546	43,380	0.413	0.854
	3.003	0.507	49,000	0.247	0.507
	3.004	0.530	49,340	0.270	0.538
	3.009	0.540	51,490	0.253	0.515
	3.008	0.513	51,7700	0.221	0.462
	3.007	0.534	52,550	0.213	0.497

2219/2219 Downhand (Panel Series 615)					
Temp. (°F)	Width (in.)	Thickness (in.)	P _{max} (lbs)	a (in.)	2c (in.)
Amb.	3.007	0.531	14,680	0.399	2.763
	3.004	0.526	17,500	0.444	2.481
	3.006	0.548	21,510	0.404	2.061
	3.008	0.548	22,820	0.351	1.970
	3.006	0.517	36,430	0.382	0.557
	3.005	0.546	39,250	0.250	0.519
	3.010	0.495	42,030	0.224	0.535
	3.006	0.537	11,110	0.425	2.908
-423	3.006	0.517	15,780	0.409	2.528
	3.005	0.535	19,871	0.410	2.403
	3.007	0.534	23,790	0.387	2.055
	3.006	0.530	45,240	0.394	0.535
	3.008	0.531	42,500	0.375	0.683
	3.007	0.519	50,660	0.215	0.503
	3.009	0.536	51,140	0.241	0.555
	3.007	0.546	51,260	0.237	0.529
	3.009	0.531	51,610	0.193	0.515
	3.008	0.518	51,740	0.218	0.493
	3.008	0.528	52,680	0.217	0.476

2195/2195 Vertical (Panel Series 614)					
Temp. (°F)	Width (in.)	Thickness (in.)	P _{max} (lbs)	a (in.)	2c (in.)
Amb.	2.995	0.530	19,040	0.419	2.760
	2.997	0.525	19,850	0.436	2.534
	2.999	0.514	20,790	0.460	2.510
	2.998	0.522	27,650	0.438	2.043
	2.996	0.524	44,670	0.400	0.600
	3.001	0.581	49,970	0.273	0.541
	2.995	0.524	61,030	0.114	0.389
-423	2.995	0.531	18,575	0.401	2.844
	2.995	0.539	22,250	0.418	3.520
	2.996	0.519	29,940	0.414	2.008
	2.996	0.524	51,550	0.365	0.584
	2.996	0.521	60,960	0.249	0.507
	2.996	0.538	67,800	0.205	0.485

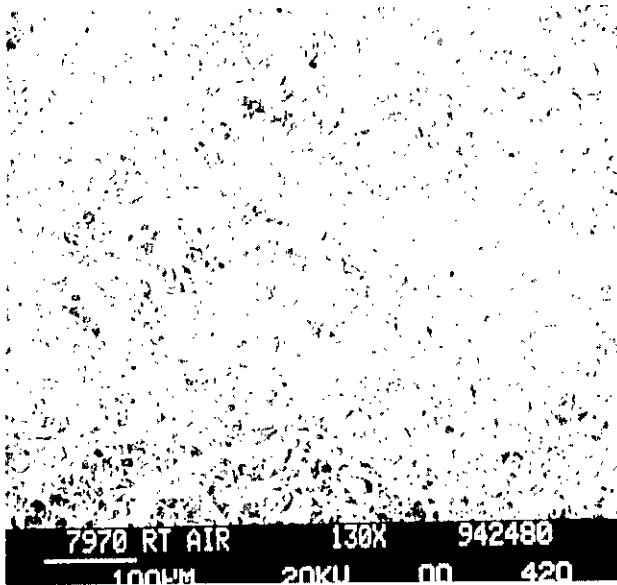
2195/2195 Downhand (Panel Series 617)					
Temp. (°F)	Width (in.)	Thickness (in.)	P _{max} (lbs)	a (in.)	2c (in.)
Amb.	3.009	0.537	47,540	0.345	0.550
	3.009	0.548	42,580	0.244	0.533
-423	3.009	0.532	47,100	0.370	0.896
	3.010	0.517	49,340	0.381	0.729
	3.008	0.550	57,100	0.278	0.638
	3.007	0.542	61,590	0.177	0.472
	3.010	0.527	62,790	0.374	0.510

2219/2195 Vertica (Panel Series 613)					
Temp. (°F)	Width (in.)	Thickness (in.)	P _{max} (lbs)	a (in.)	2c (in.)
Amb.	2.995	0.519	15,940	0.408	2.796
	2.996	0.529	39,070	0.386	0.685
	2.996	0.511	40,770	0.394	0.667
	2.997	0.533	41,770	0.394	0.565
	2.998	0.527	43,600	0.270	0.538
	2.994	0.527	44,510	0.265	0.568
-423	2.993	0.532	15,550	0.428	2.799
	2.993	0.533	23,608	0.421	2.083
	2.996	0.527	44,070	0.386	0.670
	2.995	0.528	46,400	0.394	0.800
	2.993	0.519	50,540	0.301	0.565
	2.996	0.539	52,170	0.370	0.548
	2.995	0.532	53,080	0.258	0.538
	2.999	0.530	58,530	0.201	0.466

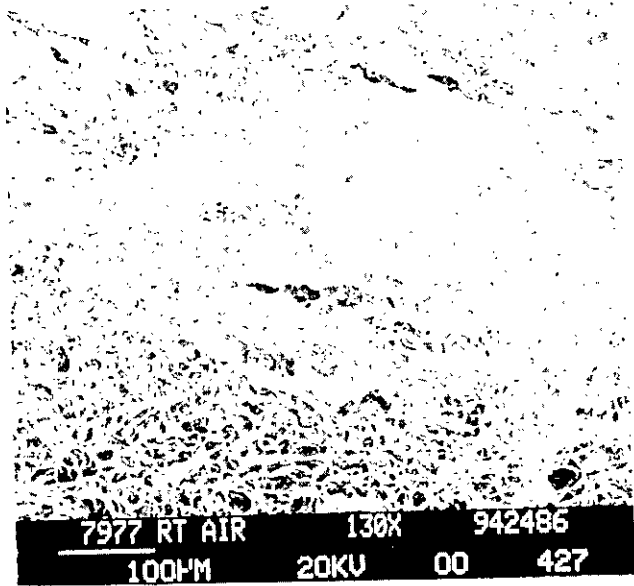
2219/2195 Downhand (Panel Series 616)					
Temp. (°F)	Width (in.)	Thickness (in.)	P _{max} (lbs)	a (in.)	2c (in.)
Amb.	2.995	0.509	13,200	0.409	2.786
	2.995	0.529	17,080	0.424	2.509
	2.996	0.514	34,130	0.366	1.104
	2.996	0.533	37,630	0.308	0.751
	2.996	0.531	38,670	0.403	0.573
	2.995	0.525	42,370	0.366	0.671
	2.998	0.529	47,260	0.203	0.488
-423	2.996	0.526	30,000	0.400	2.011
	2.999	0.531	50,450	0.387	0.636
	2.996	0.529	52,090	0.323	0.532
	2.999	0.528	54,690	0.206	0.535
	2.997	0.514	54,910	0.366	0.596
	2.995	0.532	59,450	0.228	0.582

2195 Parent Material					
Temp. (°F)	Width (in.)	Thickness (in.)	P _{max} (lbs)	a (in.)	2c (in.)
Amb.	2.997	0.511	28,375	0.510	2.605
	2.999	0.514	31,800	0.455	2.554
	2.995	0.521	35,125	0.425	2.821
	2.186	0.515	69,600	0.420	0.528
	2.191	0.511	73,400	0.252	0.508
	2.187	0.506	75,600	0.286	0.516
	2.188	0.506	76,000	0.307	0.542
	2.187	0.488	77,100	0.212	0.533
	2.187	0.514	78,100	0.220	0.525
-423	2.995	0.515	23,325	0.432	2.907
	2.998	0.509	29,783	0.148	2.668
	1.599	0.519	49,380	0.332	0.541
	2.188	0.501	75,600	0.328	0.574
	2.996	0.518	78,700	0.488	0.725
	2.993	0.510	95,130	0.295	0.688
	2.994	0.522	105,200	0.420	0.528

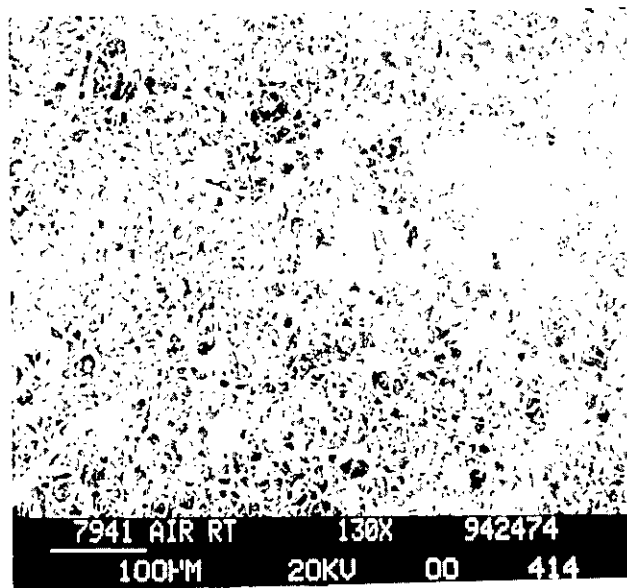
APPENDIX C—Fractographies of Representative Failure Surfaces



2219/2195

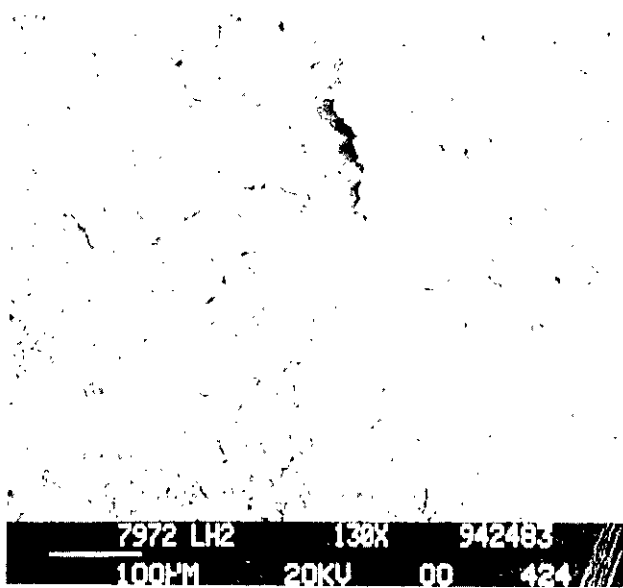


2195/2195

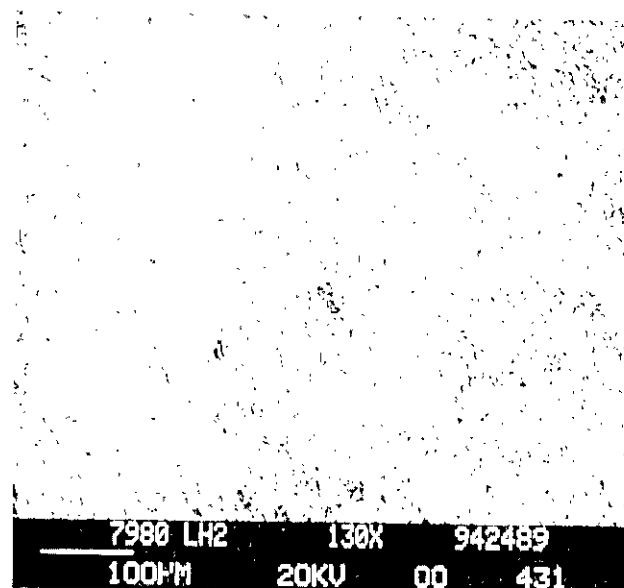


2219/2219

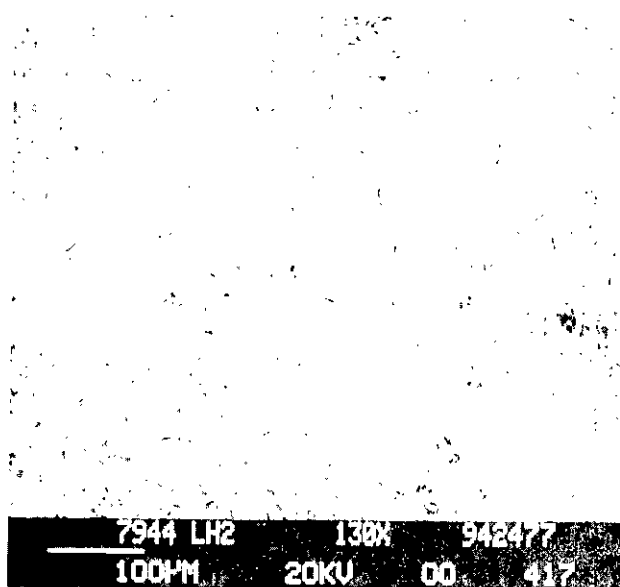
Fig. 1. Fracture Surface for Samples Tested in Ambient Air



2219/2195



2195/2195



2219/2219

Fig. 2. Fracture Surface for Samples Tested in LH_2

Fracture Properties of 0.5-inch Welded Aluminum-Lithium Alloy
P. McGill

Q: When you mentioned weld bead shaving, what was that?

A: Yes, we just took the beads off the front and the back mostly to facilitate notching and test measurements.

ANALYSIS OF THE 2195 ALUMINUM-LITHIUM ALLOY WELD MICROSTRUCTURE AND FRACTURE BEHAVIOR

by

P.C. Bastias¹, M. Diehm², G. T. Hahn¹, K-Y. Kim², M. Kral², S. R. Shah³, J. E. Wittig²

Abstract

This paper describes macro- and microstructural examinations and local strain measurements on variable polarity plasma arc (VPPA) butt welds of Al-Cu-Li alloys 2195/2195 and 2219/2195. The examinations were conducted on tensile specimens of downhand and vertical-up welds tested at RT, -196 °C (-320 °F), and -253 °C (-423 °F). The study sought the connection between configuration and microstructure of the welds, and their mechanical strength and toughness. Macro- and fractographic examinations reveal that most of the fractures in the 2195/2195 welds originated at the root corner in the equiaxed grain zone (EQZ) or partially melted zone (PMZ). The fractures either extend diagonally into the first-pass fusion zone or along the edge of the first-pass fusion zone in the EQZ or PMZ. All the 2195/2219 type of welds failed on the 2219 side at the edge of the fusion zone in the PMZ. The 2219/2219 specimens failed in the same way. The strain distribution in 2195 welds is similar to that observed in lower strength 2219 welds. In both cases large local ductility values, 14-17% elongation, are sustained within the narrow, shearing, cross-over regions. The fractures nucleate at the root and crown corners in the heavily strained material. The 2195 welds display about the same high, local ductilities, e.g. ~15%, at -196 °C (-320 °F) and -253 °C (-423 °F) as the 2219 welds. However the strain concentrations in the root and crown corners of the 2195 welds are about 2x larger than in the 2219 welds and the 2-in gage length elongation values of 2195 are correspondingly smaller. Metallographic analyses of the 2195 welds revealed a significant reduction in the amount of equiaxed grain microstructure at the edge of the fusion zone, and in the amount of intermetallic precipitates in these grains, compared to the first generation of Weldalite weldments. The transmission electron microscope study indicates that this intermetallic phases are the same as those previously reported for Weldalite welds, i.e. a face centered tetragonal Al₂Cu-phase, a hexagonal Al-Cu-Fe phase, and a face centered cubic Al-Cu phase was detected occasionally. Finally, coarse precipitates that resemble the overaged precipitates in the base material were detected within the equiaxed grains along the first fusion zone pass, raising questions about origins of this microstructure.

Introduction

The potential application of aluminum-lithium alloys have been investigated for almost a decade [1-3]. Weldalite™ 049 was designed using the widely used alloy 2219 (Al-6.3% Cu) as a starting point [4]. The strength of Weldalite depends on the Li content, with a maximum occurring between 1.1 to 1.4% Li [5], and independent of the amount of Cu, for concentrations between 4.6-6.3%. The ductility is higher for lower percentages of Cu. Nucleation aids like Ag and Mg [6] are used in limited amounts and Zr was used as a grain refiner. The relatively high Cu and low Li of Weldalite is in part responsible for high volume fractions of T₁ precipitates in this alloy [7]. The contribution to strengthening from precipitation is through order hardening and modulus hardening [8-10]. The volume fraction and mean diameter of precipitates control the overall strength. The contribution of grain size to the yield strength is negligible. In Al-Cu-Li alloys, Cu eases the bypassing of δ' , thus facilitating homogeneous deformation, and promotes the formation of θ' and T₁, which act as unshearable obstacles increasing the yield strength. Weldalite derives its strength from ultrafine T₁ plates. The T₁ phase has been shown to be a more potent strengthener than δ' [11,12]. No propensity to hot cracking is observed, while welding

¹ Mechanical Engineering Department, Vanderbilt University, Nashville, TN, 37235, USA.

² Materials Science and Engineering Department, Vanderbilt University.

³ Currently with Martin Marietta Manned Space Systems, New Orleans, LO, USA.

similarly to 2219. VPPA welds of Weldalite to Weldalite filler display a mean tensile strength 36% higher than 2219/2319 welds.

Extensive studies of the mechanical properties and microstructure of base metal and butt welded plates of Weldalite have been performed [13-16]. Welds made with this alloy are stronger than those produced with the more conventional 2219, Al-Cu alloy, plates. When Weldalite is joined to 2219, the butt weld fails on the weaker, 2219 side. Microstructural and fractographic examinations performed by Shah et al. [13,14] reveal that the Weldalite/Wedalite welds fracture within a narrow region at the edge of the fusion zone. This region consists of fine equiaxed grains with intermetallic phases at the grain boundaries. The "equiaxed zone" (EQZ) does not mix with the weld wire, and is not found in 2219-T87. As a result of these studies the Li and Cu contents of the alloy were reduced; Cu was decreased from 4.75 % in Weldalite to 4.0% in 2195, and Li from 1.26% to 0.97% in Weldalite and 2195 respectively. This paper describes microstructural, fractographic and strain distribution studies performed on VPPA-welds of 2195.

Materials and Experimental Procedure

The study reported here was performed on plate welded by Martin Marietta Manned Space Systems. The welds were fabricated from 6.35 mm (0.25 in) , 8.13 mm (0.32 in), and 9.53 (0.375 in) thick plates of 2195 welded either to the same material or to 2219 plates. The composition of the 2195 plates, derived from 5 heats, were in the following ranges (in wt%): Cu (3.90-4.09), Li (0.94-1.02), Mg (0.30-0.39), Ag (0.38-0.40), Zr (0.13-0.14), Fe (0.03-0.05), and Si (0.02-0.003). The plates were in the T8-condition: solution treated 2 hours at 510 °C (950 °F), stretched (either 3% or 6%) and aged 20 to 36 hours at 143 °C (290 °F). The welds were joined by both "vertical-up" and "dow-hand", 2-pass VPPA welds using 2319 filler wire.

Samples of the plates, cut transverse to the weld were tested to fracture at room temperature, -196 °C (-320 °F), and -253 °C (-423 °F) by Secar, Arvidson and Arvidson (17). The fracture surfaces and weld cross sections of 27 broken 2195/2195 and 8 broken 2195/2219 weld tests bars were examined by optical, scanning- (SEM), and transmission-electron (TEM) microscopy and are the subject of this paper. Metallographic samples for optical and SEM examination were prepared by conventional grinding, electropolishing in 90:10 ethanol:perchloric acid, and etching with Keller's reagent. Samples for transmission electron microscopy were reduced to 50 μ m by dimple grinding and then thinned to electron transparency by ion milling.

Prior to tensile testing, a fine grid of 1.27 mm (0.050 in) diameter circles was applied to some of the specimens on the crown side of the weld by a photo deposition process. After testing, photographs were taken of the deformed grid. The photodeposited layer did not show signs of peeling or debonding. Magnified prints were used to determine the distribution of longitudinal strain in the weld along the test bar centerline. More details of the experimental procedure can be found in [18].

Results

Macro-Examinations and Fractography

Low magnification fractography, as in Figure 1, reveals the general location of the fractures with respect to the fusion zone (FZ). The higher magnification fractographs make it possible to place the fracture in either the dendritic FZ or 2 narrow transition regions, the equiaxed zone and partially melted zone. These 2 zones form between the FZ and the heat affected zone. The fracture surfaces in Figure 2 illustrate the distinguishing features of the zones: (i) The fusion zone displays the outlines of the larger dendritic grains and a finer texture than the EQZ (Figure 2a), (ii) The EQZ displays the exposed, rough, equiaxed grain boundary facets with intermetallic particles, (iii) The partially melted zone (PMZ) displays features of the EQZ along with remnants of the directionality of the unmelted, as rolled grain structure.

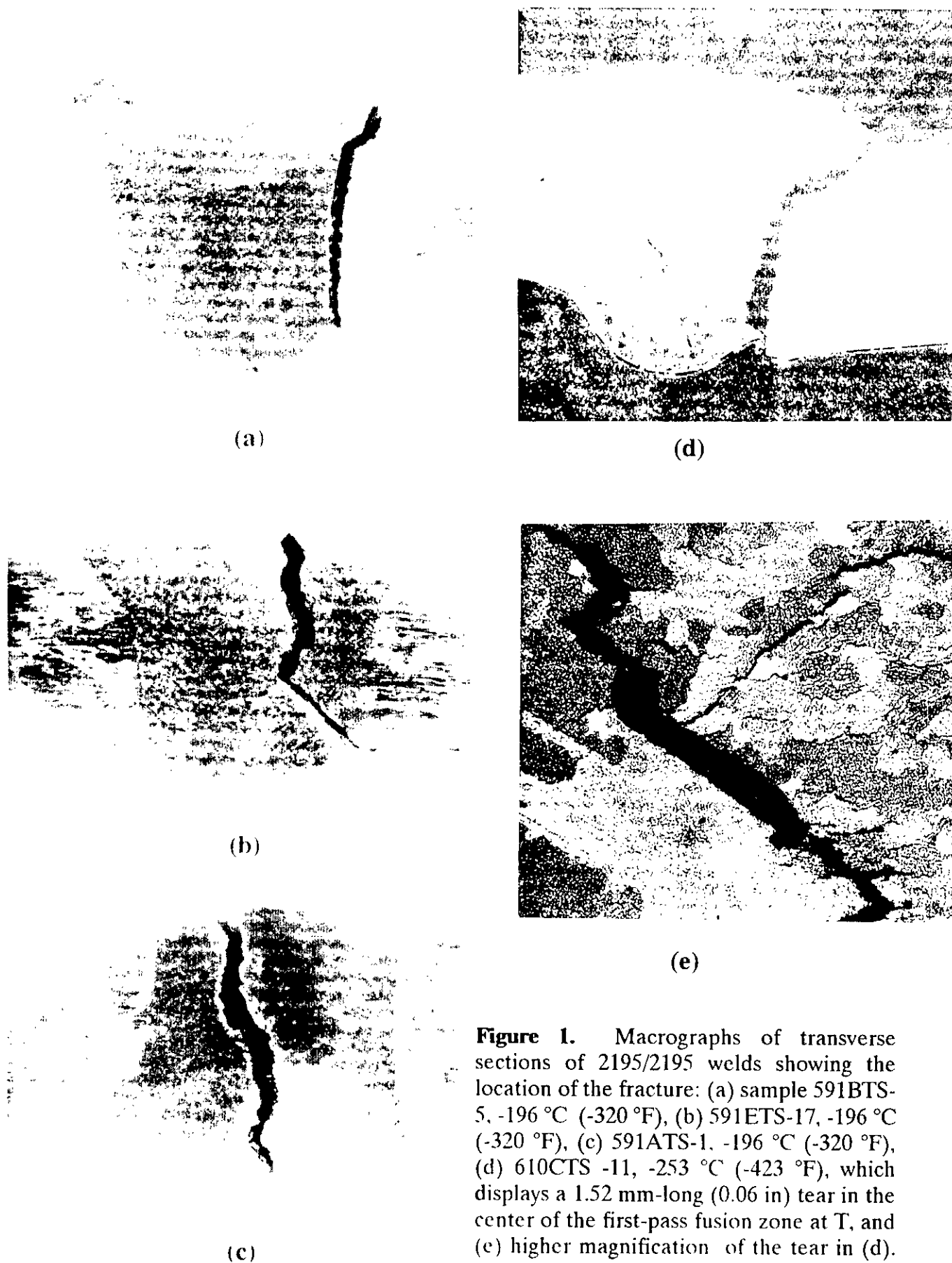


Figure 1. Macrographs of transverse sections of 2195/2195 welds showing the location of the fracture: (a) sample 591BTS-5, -196°C (-320°F), (b) 591ETS-17, -196°C (-320°F), (c) 591ATS-1, -196°C (-320°F), (d) 610CTS -11, -253°C (-423°F), which displays a 1.52 mm-long (0.06 in) tear in the center of the first-pass fusion zone at T, and (e) higher magnification of the tear in (d).

Insight into the locations of the fracture origin was derived from observations of incipient cracking at an unbroken root corner in the absence of such cracking at the opposite, unbroken crown corner. These observations and the fact, that 24 out of 25, 2195/2195 weld fractures involved one of the root corners, indicate that nearly all of the fractures of these welds originate in the EQZ or PMZ at a reinforcement corner, usually a root corner. The fractures then extend from the root corner in 3 ways: (1) Along the edge of the FZ with the EQZ or PMZ of the first pass and second pass (11 out of 24 samples), (2) Through the center of the FZ (11 out of 24 samples) and (3) Diagonally from the root corner into the middle of the first pass fusion zone and then through the second pass FZ (2 out of 25 samples). Examples are shown in Figure 2.

One sample out of the 25 examined, fractured across the center of the first and second pass FZ (Figure 1c). No obvious defects that could account for the nucleation of this fracture in the FZ were found. However, 2 welds which broke along the edge of the FZ did display about 1.52 mm (0.06 in)-long interdendritic tears in the center of the fusion zone (see Figures 2b and 2c). The 2195/2219 welds fractured on the weaker 2219 side. These fractures also appear to originate close to the root corner.

Equiaxed Zone Microstructural Characterization

Figure 3 shows the development of the EQZ from the first pass of a 2195/2195, 8.13 mm (0.32 in) weld. The elongated grains of the rolled base material first coarsen, then form an equiaxed morphology, before transforming into the dendritic fusion zone. Table 1 summarizes the semi-quantitative results describing the width of the equiaxed zone for the various weld conditions. Compared to the extensive amount of the EQZ reported previously in the Weldalite/Wedalite welds, the EQZ of the 2195/2195, 8.13 mm (0.32 in) weld is considerably less pronounced. Occurrence of the EQZ is further reduced in the 6.35 mm (0.25 in) thick 2195/2195 welds. The width of the equiaxed microstructure varied from 0 to 90 μm in the first pass and 0 to 60 μm in the second pass. In some locations the region was only one grain size thick and it seemed that the PMZ evolved directly into the dendritic FZ. The 2195/2219 welds have the least amount of equiaxed grains compared to the other weld types. The equiaxed grains are present on the 2195 side only, irrespective of the thickness of the plate.

Table 1 Range of the width of the equiaxed grain zone in decreasing order as observed in several weld samples.

Weld ID	Thickness mm (in)	1 st Pass μm	2 nd Pass μm
Weldalite/Wedalite	9.52 (0.375)	550 to 750	250 to 350
2195/2195	8.13 (0.32)	20 to 550	0 to 100
2195/2195	6.35 (0.25)	0 to 90	0 to 60
2195/2219, 2195 side	8.13 (0.32)	0 to 100	0 to 60

Both the equiaxed grain size and the amount of intermetallic phases present on the EQZ grain boundaries are also considerably different for the 2195/2195 welds compared to the Weldalite/Wedalite welds. Figures 4 a and b show representative SEM images from the EQZ of a Weldalite/Wedalite weld and the first pass of a 2195/2195, 8.13 mm (0.32 in) weld. The average equiaxed grain size for Weldalite is $11 \mu\text{m} \pm 1.2 \mu\text{m}$ and for the 2195/2195, 8.13 (0.32 in) welds is $17 \mu\text{m} \pm 5.5 \mu\text{m}$. The grain boundary

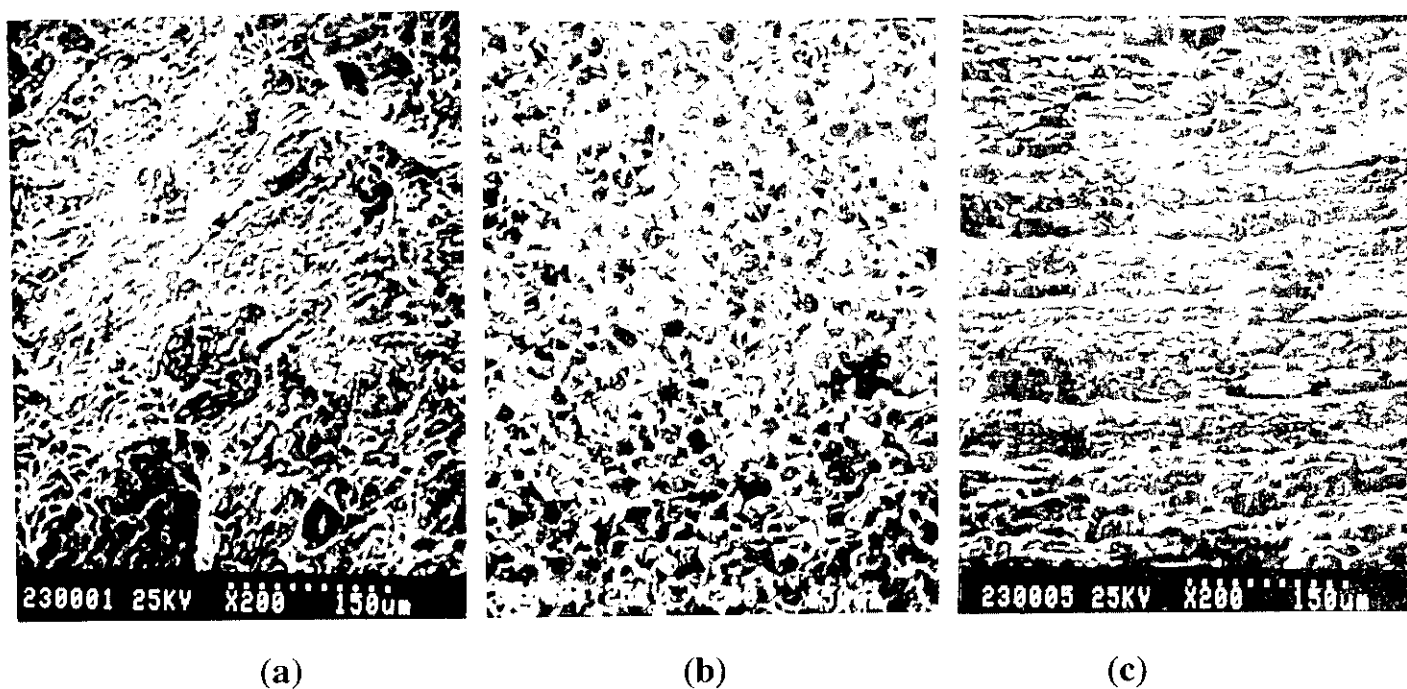


Figure 2 Fractographs of 2195/2195 welds showing the characteristic fracture appearance of (a) the fusion zone (sample 607CTS-11), -253 °C (-423 °F), (b) the equiaxed zone (598BTS-5), -196 °C (320 °F), and (c) the partially melted zone (607CTS-11), -253 °C (-423 °F).

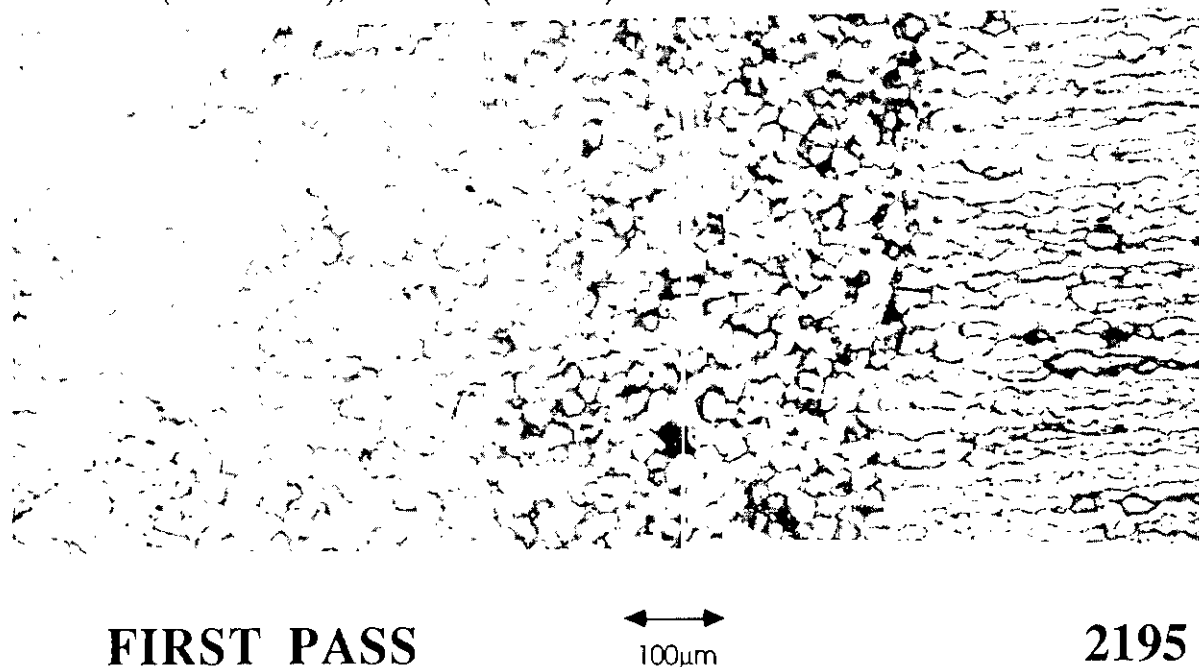


Figure 3 Representative range of widths of the equiaxed grain region as observed in several welds of 2195/2195, 8.13 mm (0.32 in). The extreme left shows the first pass, the extreme right is the 2195 base material. Magnification: x160.

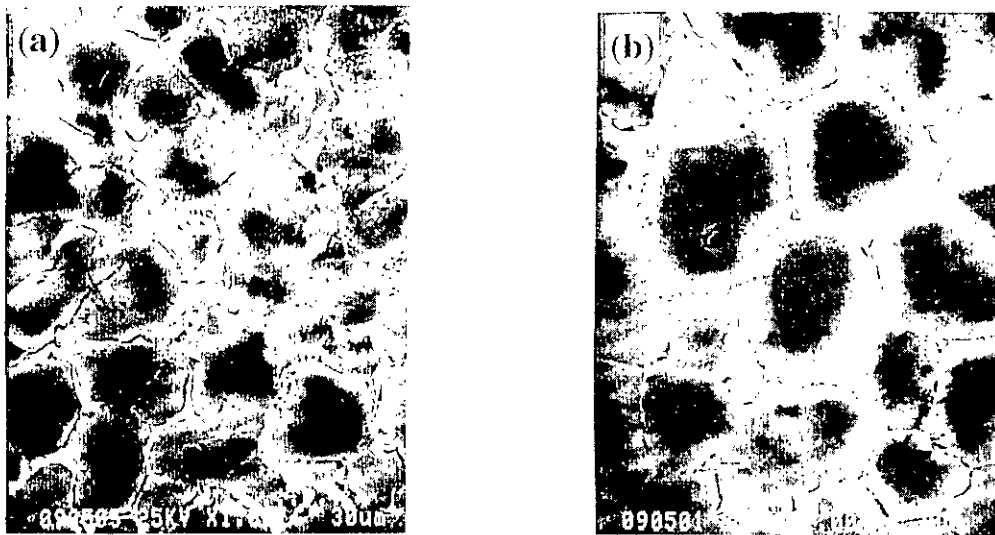
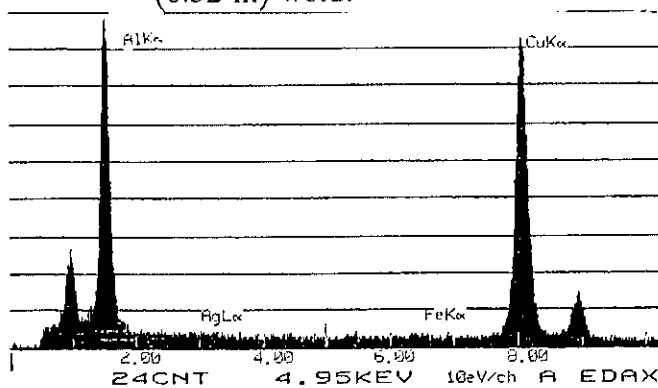
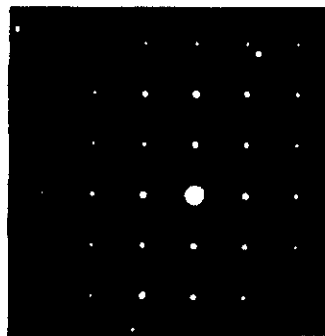


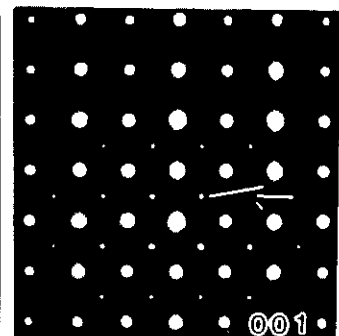
Figure 4 Equiaxed grains from the root corner of transverse sections of fractured: (a) Weldalite/Weldalite, 9.53 mm (0.375 in) (b) 2195/2195, 8.13 mm (0.32 in) weld.



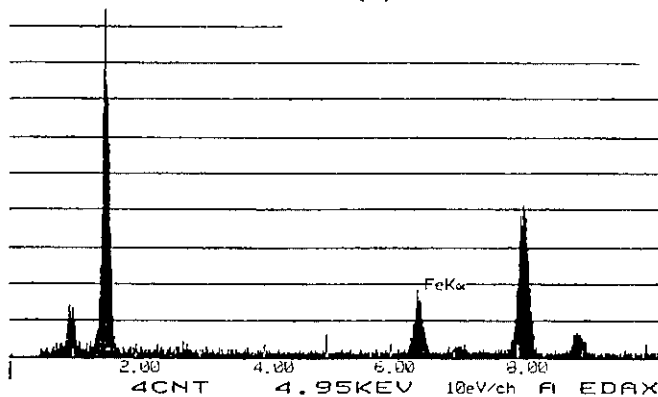
(a)



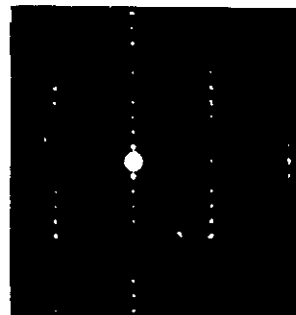
(b)



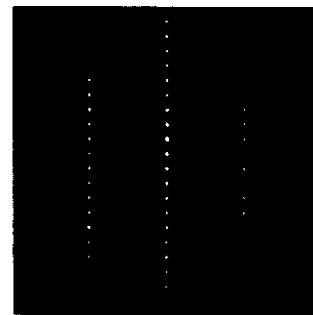
(c)



(d)



(e)



(f)

Figure 5 (a) EDS spectrum of a Al-Cu type grain boundary precipitate found in equiaxed grain region of 2195/2195, 8.13 mm (0.32 in), (b) The [001] SAD ZAP. Phase is Al_2Cu with face centered tetragonal structure ($a=0.43$ nm, $c=0.61$ nm), (c) The [001] ZAP of the grain boundary precipitates present in Weldalite/Weldalite (The forbidden reflections at the $\frac{1}{2}$ positions might be due to the change in the structure factor by the addition of Li), (d) EDS spectrum of Al-Cu-Fe intermetallic found in 2195/2195 and 2195/2219 welds, (e) and (f) SAD ZAP from precipitate.

coverage of intermetallic compounds is $45\% \pm 6.7\%$ and $38\% \pm 5.5\%$ for Weldalite and 2195 respectively. The combination of a larger grain size with lower percent intermetallic coverage for the 2195/2195 equiaxed grains requires that the equiaxed grain boundary second phase content is greatly reduced in the 2195 welds compared to Weldalite. TEM analyses of thin foils was used to investigate the intermetallic phases at the grain boundaries of the 2195/2195 equiaxed microstructure. The results were similar to those previously reported for the Weldalite/Weldalite welds [13] with a few notable exceptions. Consistent with the Weldalite/Weldalite results, the precipitation at the grain boundaries was mainly Al-Cu and Al-Cu-Fe rich phases. Figure 5 (a) shows an energy dispersive spectrum (EDS) and a selected area diffraction pattern (SAD) from a precipitate having the Al_2Cu face centered tetragonal structure ($a=0.43$ nm and $c=0.61$ nm). However, this [001] zone axis pattern (ZAP) does not contain the forbidden reflections that were observed previously from precipitates in the Weldalite/Weldalite welds. A [001] ZAP containing these extra spots, which have been attributed to Li incorporation in the Al_2Cu structure, is included in Figure 5 (b) for comparison. The lack of these extra reflections was observed for precipitates in both the 2195/2195 and the 2195/2219 welds.

In addition to the Al_2Cu intermetallic phase, the same Al-Cu-Fe precipitate found in the Weldalite/Weldalite welds was frequently detected on the equiaxed grain boundaries of both the 2195/2195 and 2195/2219 welds. These Fe rich precipitates were often as large as the Al_2Cu Type. Figures 5 a and b show representative EDS spectrum and SAD patterns. The angle of tilt between the identical ZAP's in Figures 5 b and c is 60° which indicates that this crystal structure has a hexagonal Bravais lattice. This structure is not consistent with reported equilibrium phases and is believed to be formed by the rejection of Fe during solidification. Finally, a second type of Al-Cu phase was occasionally detected on the 2195/2195 grain boundaries. This face centered cubic (FCC) structure with a $a=0.60$ nm may be the Al-Cu-Li, T_B phase (FCC with $a=0.58$ nm), which is an equilibrium phase in over aged Al-Li alloys. However, observation of this precipitate is rather rare in comparison to the other two types.

Local Strain Measurements

The variations of the longitudinal strain component at the centerline of three different type of welds, as a function of the distance from the center of the weld are presented in Figure 6. The areas under the strain distribution curves were integrated over a 25.4 mm (1 in) length in order to evaluate the percent elongation for this gage length. Figure 7 compares the calculated elongations, with the measured values. There is a reasonable agreement considering the coarseness of the grid used. The axial elongation is attended by a lateral contraction, and by a through the thickness or out-of-plane plastic deformation. The lateral contraction is significant, contributing up to 25% of the elongation displayed by the specimens. Table 2 indicates the resulting 1 in and 2 in gage lengths percent elongations and the peak percent lateral contraction for selected specimens. The peak strains measured at the crown (and root) corners are about 3 to 8 times larger than the elongation measured over a 2 inches gage length. This strain concentration factor (SCF) is calculated as \approx (peak local strain / elongation over a 2 inches gage length). At low temperatures the 2219/2219 and 2195/2195 welds displayed peak strains of, on average, 15% compared with 12% for the 2219/2195. However the SCF displayed by 2195/2195 welds at low temperatures is $\text{SCF} \approx 8.0$, compared with $\text{SCF} \approx 4.2$ and 5.0 for the 2219/2219 and 2195/2219 welds respectively. In every case the strain concentrations are higher at low temperature than at room temperature.

Discussion

The macro examinations and the higher magnification fractographs indicate that the failures of the 2195 welds tend to initiate in the EQZ and PMZ at the root corner. In about one half of the 2195 welds, the fracture extends in either the EQZ or PMZ along the edge of the FZ, in the other half the fracture penetrated into and traversed the FZ. In contrast, all of the weldalite weld failures were confined to the EQZ. Also, the failures of 2195/2219 welds always occurred on the weaker 2219 side. The small, 1.52 mm-long (0.06 in) tears observed in the FZ of 2195 welds in isolated cases do not appear to be of

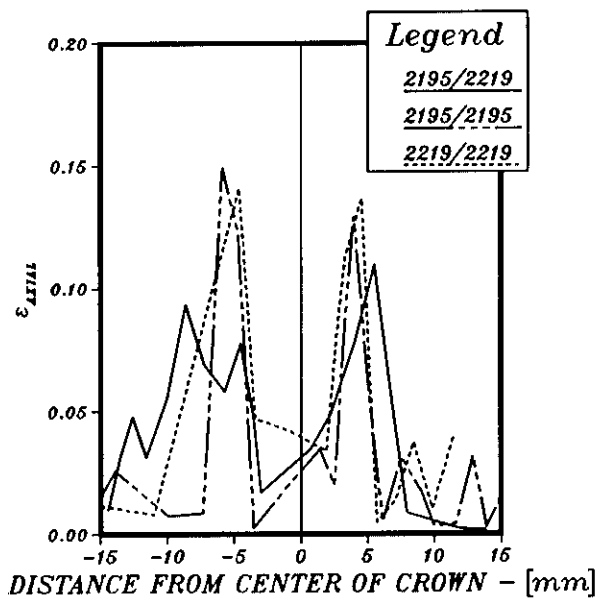


Figure 6 Strain distribution measured from the distorted grid at center of specimen after testing at -253 °C (-423 °C). (a) 2195/2219, (b) 2195/2195, (c) 2219/2219.

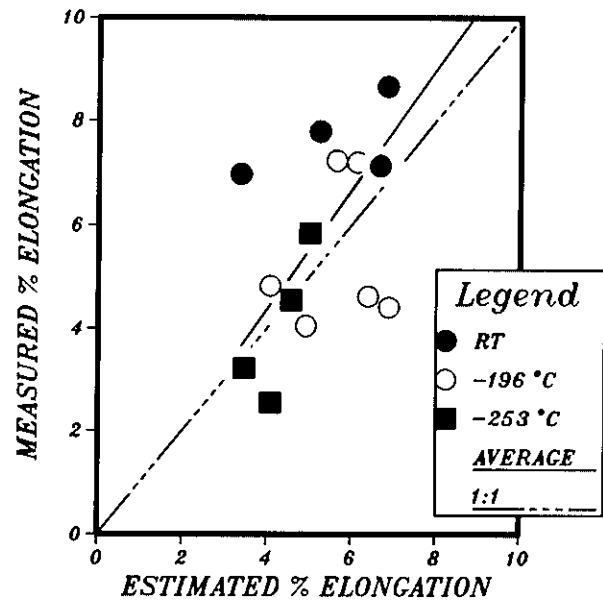


Figure 7 Estimated versus measured percent elongation for different type of welds. The key indicates the testing temperatures.

Table 2 Results from Tensile tests [16]

Sample ID	Mater. ID	Test. Temp. °C(°F)	σ_{UTS} MPa (ksi)	% Elongation		% Later. Contr.	Max. Strain (%)	Strain Conc. Fact.
				1"	2"			
591-IITS-32	2195/2195	RT	333.5 (48.4)	6.9	3.0	1.7	17	5.6
592-IITS-22	2219/2219		308.0(44.7)	11.4	5.4	6.5	19	3.5
594-AITS-4	2195/2219		318.3(46.2)	7.2	3.9	4.6	15	3.8
591-GTS-25	2195/2195	-196 (-320)	421.0(61.1)	4.9	1.4	0.8	11.5	8.2
592-BITS-5	2219/2219		340.4(49.4)	7.3	3.2	4.1	15.5	4.8
594-DTS-16	2195/2219		364.5(52.9)	4.1	2.3	1.9	18	7.8
591-FITS-23	2195/2195	-253 (-423)	472.7(68.6)	2.6	1.6	0.9	12.5	7.8
592-IITS-31	2219/2219		432.0(62.7)	5.1	3.1	2.9	11.5	3.7
594-GTS-28	2195/2219		410.0(59.5)	3.3	2.2	1.9	10.5	4.7

immediate concern. While estimates of the FZ fracture toughness at -196 °C (-320 °F) suggests that the critical flaw size at this temperature is about 5x the size of the tear. The nature of these defects and their possible presence prior to testing deserves more attention.

The new 2195/2195 welds show a significant reduction in the amount of equiaxed microstructure at the edge of the fusion zone compared with Weldalite welds. The origin of this equiaxed zone is still uncertain. Recent experimental observations would indicate that it may be related to partially melted base material. This would be supported by the observation of over aged precipitates in the equiaxed grains, and by similar crystallographic relationships.

The grain boundary precipitates in the EQZ of the 2195/2195 welds are similar to those previously observed in the Weldalite/Weldalite welds. However, reducing the Li and Cu content from the original Weldalite composition has decreased the grain boundary coverage and volume fraction of the intermetallic compounds in the EQZ of the 2195/2195 welds. Both the reduction in intermetallic phases at the grain boundaries and the decreased size of this EQZ may be responsible for the change in the fracture path for the 2195/2195 tensile samples. The standard fracture path of the previous Weldalite/Weldalite tensile samples remained exclusively along the fusion line within the EQZ. Although the 2195/2195 fractures may initiate at the root corners, in about 50% of the fractures the path deviates from the fusion line into the FZ. This indicates that the EQZ is no longer the weakest link that dictates the fracture behavior of the 2195/2195 welds.

The strain distribution in 2195 is similar to the one observed in the lower strength 2219 welds. The strain is concentrated in a narrow shear bands which traverse the weld from a corner of the crown to the opposite far corner of the root [19-21]. The fractures nucleate at the root corner in the heavily strained material. At low temperatures the strain concentration in 2195/2195 welds is almost 2x as large as those in 2219/2219 welds. This may be due to the larger strain gradients resulting from a higher strength base material. The laterally unconstrained tensile test specimens overstate the ductility of the specimens by 25%, and understate the flow strength by about 5% [21].

Conclusions

- (1) The bulk of the 2195/2195 specimens fracture originated at the root corner in either the equiaxed grain zone (EQZ) or partially melted zone (PMZ), and either extended diagonally into the fusion zone or along the edge of the fusion zone with the EQZ or PMZ. Small, 1.52 mm-long, interdendritic tears accompanied by many microfractures were observed in 2 welds. These defects do not appear to have been involved in any of the failures.
- (2) All of the 2195/2219 weld failures originated at the root corner and extended along the edge of the FZ in the partially melted zone.
- (3) The amount of equiaxed grains in the fusion zone of the new generation 2195 Al-Cu-Li based alloys has been greatly reduced. The coverage of intermetallic phases at the equiaxed grain boundaries has also been reduced by lowering the content of Cu and Li.
- (4) The local strain distribution in 2195/2195 welds is similar to the one in 2219/2219. While both type of welds display the same high local ductility at low temperatures, e.g. 15%. The strain concentrations in the 2195 welds are about 2x larger as those in 2219. This results in smaller % elongation.

Acknowledgments

The authors are grateful for the financial support provided by Martin Marietta Manned Space Systems. The authors wish to acknowledge the efforts of Messrs D. Bolstad, J. Hunt, D. Wistrand and

D. Rybicki for providing the material used in this study. They are grateful to E. Suarez for making available samples of electron-beam welds, and a weld of a thicker section. Messrs. R. McReynolds, J. Du, assisted with specimen preparation and measurements.

References

- 1 Sanders Jr., T. H., and Starke Jr., E. A., Editors, "Al-Li Alloys," TMS-AIME, Warrendale, PA. 1981.
- 2 Sanders Jr., T. H., and Starke Jr., E. A., Editors, "Al-Li Alloys II," TMS-AIME, Warrendale, PA. 1983.
- 3 Baker, C., Gregson, P. J., Harris, S. J., and Peel C. J., Editors, "Al-Li Alloys III," Institute of Metal, London, UK, 1986.
- 4 Pickens, J. R., Heubaum, F. H., Langan, T. J., and Kramer, L. S., "Proceedings of the Fifth International Aluminum-Lithium Conference," T. H. Sanders Jr., and E. A. Starke Jr., Eds., MCE Publications Ltd., Birmingham, U.K., p. 1397, 1989.
- 5 Langan, T. J., and Pickens, J. R., "Proceedings of the Fifth International Aluminum-Lithium Conference," T. H. Sanders Jr., and E. A. Starke Jr., Eds., MCE Publications Ltd., Birmingham, U.K., p. 691, 1989.
- 6 Polmear, I. J., Trans. Met. Soc., AIME, Vol. 230, 1964, pp. 1331-1339.
- 7 Hardy, H. K., and Silcock, J. M., Journal of the Institute of Metals, Vol. 84, 1955, pp. 423-428.
- 8 Noble, B., Harris, S. J., and Dinsdale, K., Met. Sci., Vol. 16, 1982, p. 425.
- 9 Jensrud, O., "Al-Li Alloys III," Baker, C., Gregson, P. J., Harris, S. J., and Peel C. J., Editors, Institute of Metal, London, UK, 1986.
- 10 Miura, Y., Miura, A., Furukawa, M., Nemento, M., "Al-Li Alloys III," Baker, C., Gregson, P. J., Harris, S. J., and Peel C. J., Editors, Institute of Metal, London, UK, 1986.
- 11 Huang, J. C., and Ardell, A. J., Acta Metall., Vol. 36, 1988, pp. 2995-3006.
- 12 Huang, J. C., and Ardell, A. J., "Aluminum Technology 86", T. Sheppard, Ed., Institute of Metals, London 1986, pp. 434-441.
- 13 Shah, S. R., Wittig, J. E., and Hahn, G. T., "Microstructural Analysis of a High Strength Al-Cu-Li (Weldalite™ 049) Alloy Weld", Conf. on Trends in Welding Research, June 1992, Gatlinburg, TN, USA.
- 14 Shah, S. R., "Microstructural Analysis of the Failure Mode in Al-Cu and Al-Cu-Li Alloy VPPA Welds", Ph.D. Dissertation, Materials Science and Engineering Department, Vanderbilt University, Nashville, TN, USA, 1993.
- 15 Diehm, M., "A Microstructural Analysis of Fractured Al-Cu-Si Weldments", Master Thesis, Materials Science and Engineering Department, Vanderbilt University, Nashville, TN, USA, 1993.
- 16 "High Performance Al-Li Alloy External Tank Study", NASA Document #MMC-ETSE05-431.
- 17 Seckar, C. J., Arvidson, R. E., Arvidson, J. M., "Analysis of a New Aluminum-Lithium Alloy Weld Tensile and Fracture Mechanics Properties of 72 °F, -320 °F, and -423 °F. Final Report to Martin Marietta Manned Space System, August 1992.
- 18 Bastias, P. C., Diehm, M., Hahn, G. T., Kim, K-Y, Kral, M., Shah, S.R., and Wittig J. E., "Iterim report to Martin Marietta Manned Space System, Sept. 4, 1992.
- 19 Smith, R. R., "Finite Element Analysis of the Deformation and Strength of GTA and VPPA welds of 2219-T87 Aluminum Plates," Master's Thesis, Vanderbilt University, Dec. 1986.
- 20 McClearen, V. B., "Analysis of the Stress-Strain Characteristics of VPPA Weldments of 2219-T87 Aluminum Plate," Master's Thesis, Vanderbilt University, May 1988.
- 21 Bastias, P. C., Nunes, A. C., Hahn, G. T., Kim, K. Y., and Rubin, C. A., "Contributions of Weld Geometry to the Strengths of Aluminum Alloy Butt Welds", Conf. on Trends in Welding Research, June 1992, Gatlinburg, TN, USA.

Analysis of the 2195 Aluminum-Lithium Alloy Weld
Microstructure and Fracture Behavior
P. Bastias

No presentation.

OPTIMIZATION OF THE VPPA WELDING PROCESS FOR 2195 ALUMINUM-LITHIUM ALLOY USING RESPONSE SURFACE TECHNIQUES

M. O. Roberts¹, E. F. Scholz¹, L. W. Loechel¹, and K. Lawless²

¹Martin Marietta Astronautics

P. O. Box 179, MS-T330, Denver, CO 80201

²Materials and Processes Laboratory

National Aeronautics and Space Administration/MSFC

Marshall Space Flight Center, AL 35812

Abstract

This paper presents the results of a designed experiment using the Response Surface approach to optimize and improve the Variable Polarity Plasma Arc Welding (VPPAW) process for 0.200 inch thick 2195 aluminum-lithium alloy, and to collect welding sensor data. Data are presented which show response surface correlations between the welding variables investigated and weld mechanical properties. Optimum welding variable sets are presented and the resulting improvement in mechanical properties are discussed. Weld microstructure improvements are discussed. Conclusions are drawn regarding the success of this experiment, and the applicability of the Response Surface Design of Experiments (DOE) approach to this type of work. In addition a short discussion on the mechanics of this method is presented.

I. Introduction and Background

The (DOE) approach had been extensively applied to optimization and improvement of welding processes for aluminum-lithium alloys under Advanced Launch System and National Launch System funding. (References 1, 2, 3, and 4). Initially the Taguchi DOE method was used and recently the Response Surface DOE method has

been applied with improved results. In every case, when using the welding processes which have been developed and optimized by traditional methods, as a starting point, significant process improvements and optimizations have been achieved.

Previous work for the VPPAW process included a pathfinder Taguchi designed experiment using 2219 aluminum alloy, two Taguchi designs using 2094 aluminum-lithium alloy, and a Response Surface design using 2094 alloy. See compositions Table 1.

An additional objective of this work was to further develop the application of intelligent sensor technology. This technology working in concert with robust, optimized processes will be applied to launch vehicle propellant tank manufacturing in a Statistical Process Control (SPC) environment. A variety of sensors will be integral with the weld process control for seam tracking, molten puddle imaging, solidified weld bead profiling, and penetration control. The goal in the application of weld process sensor and control technology is to combine the use of robust processes having low variability, developed using DOE techniques, with SPC to eliminate off-line weld inspection.

Table 1 - Nominal Compositions

Element	Cu	Mg	Mn	Li	Ag	Zr	Ti	V	Al
2219 Aluminum 0.350 Inch Thick Plate	6.3		0.30			0.15	0.06	0.10	Bal.
2094 Aluminum - Lithium 0.350 Inch Thick Plate	4.75	0.40		1.25	0.40	0.15	0.02		Bal.
2195 Aluminum - Lithium 0.200 Inch Thick Plate	4.00	0.40		1.00	0.40	0.15			Bal.
2319 Aluminum 0.062 " Dia. Filler Wire	6.3		0.30			0.15	0.08	0.10	Bal.

In a step toward achieving these benefits, a close relationship was maintained, and a team approach was used between the user (NASA/MSFC), producer (Martin Marietta Astronautics, MMA), and the sensor subsystem supplier (Applied Research and Engineering Group of Science Applications International Corporation, SAIC) during the experiment design, execution, and data analysis reported in this paper.

II. Experimental Procedure - Materials - Equipment

The designed experiment was performed using the VPPAW process. The material welded was 0.200 inch nominal thickness aluminum-lithium alloy 2195 plate in the T87 temper, using a square butt weld joint. Table 1 lists the nominal 2195 alloy composition.

The material preparation consisted of cutting the 48 inch by 120 inch rolled plate into the 6 inch by 24 inch weld test plate size, with the long grain direction either transverse or parallel to the 24 inch welding direction; milling the plates to proper thickness (0.180 inch, 0.200 inch, or 0.220 inch); milling the edges to be welded to remove a minimum of 0.010 inch; chemically etching the plates in a sodium hydroxide solution; spray coating with AC Products, AC-910 protective coating; wrapping in brown paper; shipping from MMA, Denver, to the welding location at MSFC/NASA; and storing prior to welding. Just prior to welding the plates, the paper was removed, the coating peeled off, the edges solvent wiped, the weld joint abutting edges draw filed, the adjacent surfaces scraped with a scraping tool, the plates tacked welded together using the manual gas tungsten arc process, the run-on and run-off tabs attached with tack welds, and punch marks placed on the plates per Figure 1 for weld shrinkage measurements. The test plates were prepared with varying grain directions and thicknesses because these were two of the test matrix variables. Reference Tables 2 and 3.

The equipment used to accomplish the welding at NASA/MSFC consisted of 3 major systems elements, all interfaced together for command and control, and data exchanging capability. The three major systems are; 1)

Weld sensor system, 2) HAWCS II weld control system, and 3) Cincinnati Milacron 6-axis robot. The HAWCS II and sensor system are interfaced with a parallel bus-level interface for data exchange at bus speeds. Through this interface, the HAWCS II can control the operation of the sensor system and give the sensors access to real time weld information. Real time sensor information is displayed on the sensor user interface display terminal and weld information is displayed on the sensor user interface on the HAWCS II user interface display terminal. All sensor set-ups and weld schedule modifications are performed using these terminals. The HAWCS II also communicates to the robot through a digital interface for position and control signals. Through this interface, the HAWCS II can issue move commands and get information indicative of robot end-effector position. A schematic of the communications / control architecture is shown in Figure 2.

The experiment design and analyses were accomplished using Echip, Inc. software. The experiment design selected was a linear with center point design. This type of design was chosen because it allows the screening of a maximum number of variables with a minimum number of test welds. This designed experiment screens the variables to determine the relative significance of the variable effects on the responses. In addition, the linearity or curvature and the degree of fit of the process models generated is estimated. From this information the necessity for further experimentation and model augmentation and refinements can be determined. With further experimental trials the linear models can be augmented to higher order models (interaction, quadratic, cubic), so that a greater degree of fit of can be achieved, the process can be more accurately modeled, and greater predictive accuracy is obtained.

The starting point variables and the variable level sets are shown in the preliminary design test matrix, Table 2. These starting point variables and variable levels were determined by a team of welding engineers and welding technicians, using engineering judgment and practical experience. The variables and levels were then adjusted and

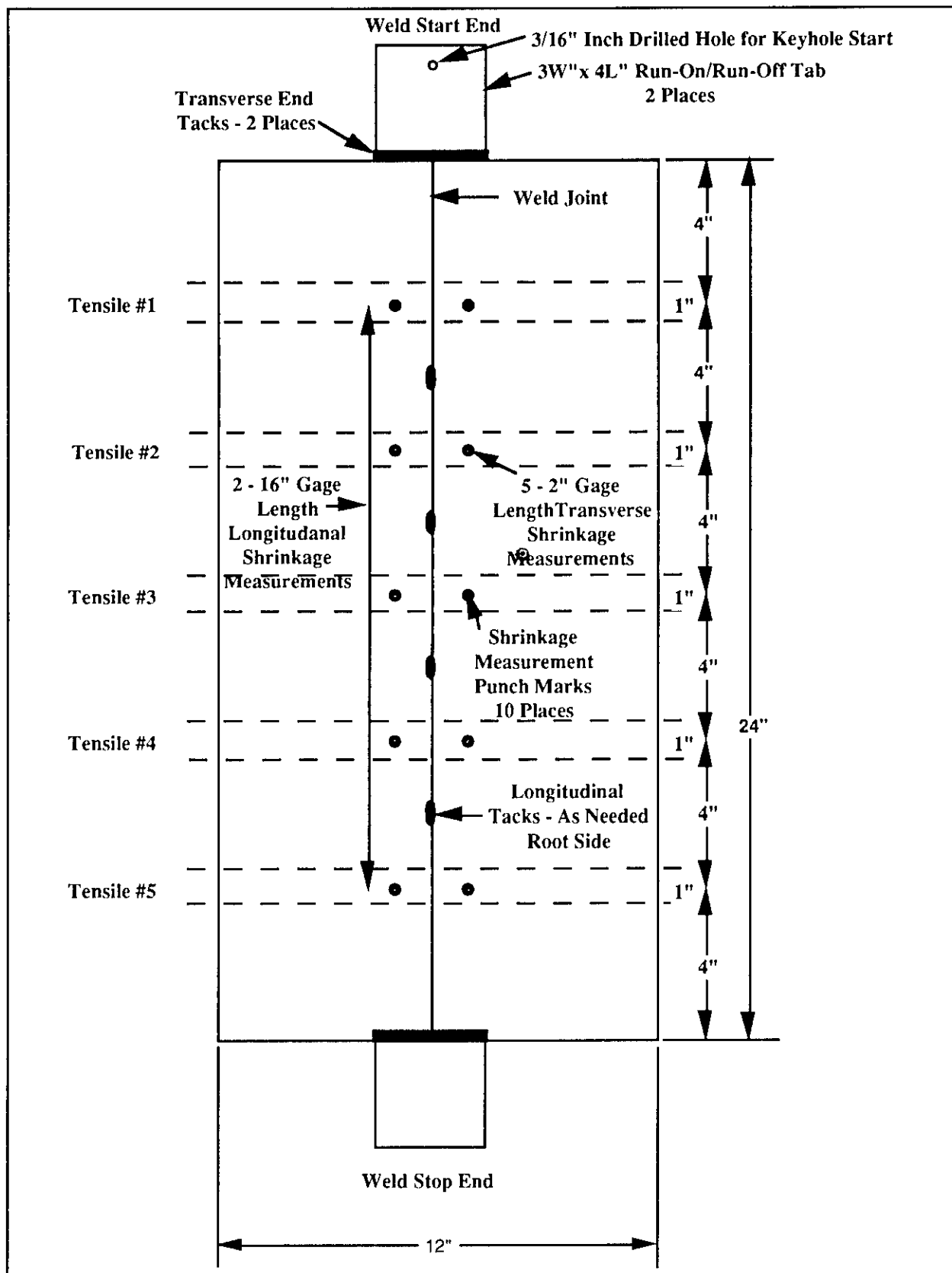


Figure 1 - Test Plates Prepared for Welding.

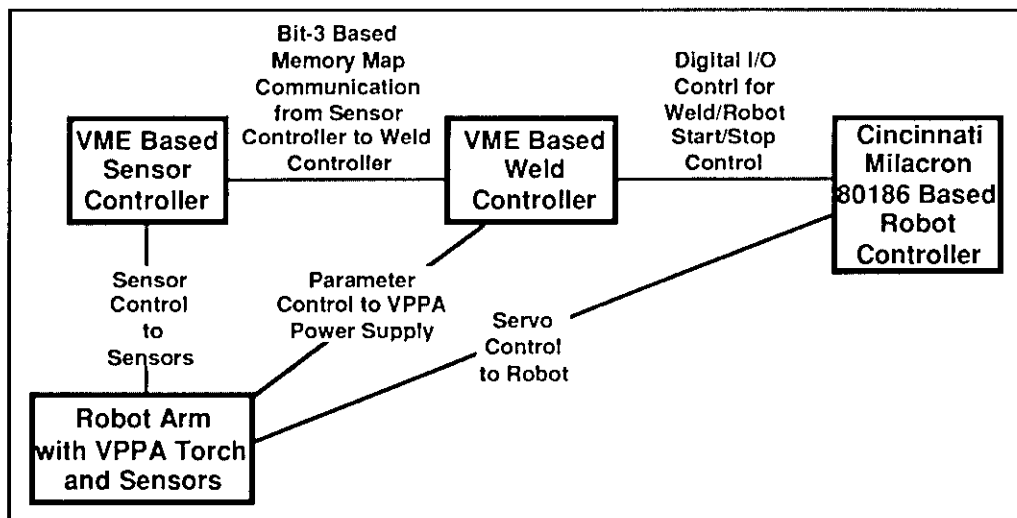


Figure 2 - Schematic of the Communications / Control Architecture for the MSFC Welding Robot with Weld Sensors.

Table 2 - Preliminary Linear with Center Point Design Test Matrix-Random Order

Weld Letter	Pen Pass Curr. Amps	Pen Pass Travel In/Min	Fill Pass Stand Off In	Fill Pass Travel In/Min	Fill Pass Wire In/Min	Rev. Amps Time Mil-Sec	Torch % He Bal. Argon	Plate Thick Inch	Grain Dir. Degree 0=Long	Gap Inch	Mis-match Inch	Seam Track Inch
A	100	6	0.125	6	20	2	50	0.180	0	0	0	-0.030
B	130	6	0.250	10	20	6	50	0.180	0	0.040	0.040	-0.030
C	100	6	0.250	6	60	6	100	0.180	0	0	0.040	0.030
D	130	10	0.125	10	20	2	50	0.220	180	0.040	0	-0.030
E	130	6	0.125	6	60	2	50	0.220	0	0.040	0.040	0.030
F	100	10	0.125	6	60	2	100	0.220	180	0	0	0.030
G	115	8	0.1875	8	40	4	75	0.200	90	0.020	0.020	0
H	100	10	0.250	10	20	6	100	0.180	180	0	0	-0.030
I	130	10	0.125	10	60	2	100	0.180	0	0	0.040	-0.030
J	130	6	0.250	6	20	2	100	0.220	180	0	0.040	-0.030
K	100	10	0.125	10	60	6	50	0.180	0	0.040	0	0.030
L	100	10	0.125	6	20	6	100	0.220	0	0.040	0.040	-0.030
M	100	6	0.250	10	60	2	100	0.220	0	0.040	0	-0.030
N	100	6	0.250	6	20	6	50	0.220	180	0.040	0	0.030
O	130	10	0.250	6	60	6	50	0.220	0	0	0	-0.030
P	100	10	0.250	6	60	2	50	0.180	180	0.040	0.040	-0.030
Q	130	10	0.125	10	20	2	50	0.220	180	0.040	0	-0.030
R	100	10	0.125	10	60	6	50	0.180	0	0.040	0	0.030
S	130	6	0.125	6	60	6	100	0.180	180	0.040	0	-0.030
T	130	6	0.250	6	20	2	100	0.220	180	0	0.040	-0.030
U	100	6	0.250	6	60	6	100	0.180	0	0	0.040	0.030
V	130	10	0.250	10	20	2	100	0.180	180	0.040	0.040	0.030
W	130	6	0.125	10	20	6	100	0.220	0	0	0	0.030
X	100	6	0.125	10	60	6	50	0.220	180	0	0.040	-0.030
Y	100	10	0.250	6	60	2	50	0.180	180	0.040	0.040	-0.030

finalized based on extensive preliminary testing. The objective of the DOE approach is to select the variables, the number of variables, and the variable ranges, so that the variable sets dictated by the test matrix result in a wide variation in responses (results or outputs), so that a large part of the operable process space can be empirically modeled. If the number of variables and/or the variable ranges is too large, variable level sets will occur in the test matrix which are outside of the operable process area, i.e., in this case no weld occurs, or the weld is so marginal that meaningful test results cannot be achieved.

To determine if the number of variables and their ranges resulted in a design entirely within the operable process area, 25 pre-test matrix test welds were made using worst case variable level combinations. As a result of this extensive pre-test matrix work, a final test matrix was evolved and is shown in Table 3. Note that the number of variables was reduced from 12 to 8 and that the range of the levels was changed for 5 variables. Plate thickness and grain direction could not be changed, since all of the test plates were prepared prior to testing.

Even with the extensive preliminary testing, it was necessary to adjust one of the variable levels, after test welding had started. The fill pass travel speed had to be increased from 6 to 7 inches per minute to obtain a weld for test matrix weld number 10, Table 3. This is termed "repairing a broken design", and can be done with the software without comprising the integrity of the experiment.

The 20 test welds were then made with the variable level combinations and in the random order listed in the test matrix, Table 3. Other welding parameters which were held constant for all welds are shown in Table 4.

The test welds were then visually inspected, radiographed, machined for tensile testing and metallographic examination, and measured for mismatch and peaking. Figure 1 shows the tensile specimen location. Tensile specimens were one inch constant width with the weld reinforcements intact. After a 30 day minimum room temperature natural aging period the welds were tensile tested and the ultimate tensile strength (UTS) and percent elongation in 2 inches were recorded.

Table 3 - Final Design Test Matrix - Random Order

Weld No.	Pen Pass Curr. Amps	Pen Pass Travel In/Min	Fill Pass Stand Off In	Fill Pass Travel In/Min	Fill Pass Wire In/Min	Plate Thick Inch	Grain Dir. Degree 0=Long	Fill Seam Track Inch
12	135	8	0.175	10	20	0.220	180	0
14	115	10	0.250	6	20	0.220	0	0.040
9	115	10	0.175	10	20	0.220	0	0.040
1	115	8	0.175	6	20	0.180	0	0
5	115	8	0.250	10	20	0.180	180	0.040
10	135	8	0.250	7	40	0.180	180	0
11	115	10	0.175	10	40	0.180	180	0
2	135	10	0.250	10	40	0.220	180	0.040
8	135	10	0.175	6	20	0.180	180	0.040
4	135	10	0.250	10	20	0.180	0	0
3	115	8	0.175	6	40	0.220	180	0.040
7	115	8	0.250	10	40	0.220	0	0
6	135	10	0.175	6	40	0.220	0	0
15	125	9	0.213	8	30	0.200	90	0.020
2	135	10	0.250	10	40	0.220	180	0.040
3	115	8	0.175	6	40	0.220	180	0.040
13	135	8	0.175	10	40	0.180	0	0.040
4	135	10	0.250	10	20	0.180	0	0
1	115	8	0.175	6	20	0.180	0	0
14	115	10	0.250	6	20	0.220	0	0.040

Table 4 - Constant Welding Parameters

Parameter	Value
Base Metal	Weldalite® 2195-T8
Weld Joint Prep. / Cleaning	Dry Machine to Thickness, Square Butt Joint, Chemical Clean, Coat,Remove Coating Solvent Wipe, File Edges, Scrape Adjacent Surfaces.
Welding Passes	Two
Welding Position	Vertical Up
Welding Equipment	Hobart / HAWCS Controller / Cincinnati Milacron at MSFC
Welding Torch	B&B, Plasma
Welding Torch Angle	3° Leading
Electrode Composition	2% Thoriated Tungsten
Electrode Configuration	5/32 Inch Dia., Flat Ground Edge
Electrode Position	Recessed 0.045 in. into Orifice
Penetration Pass Torch Gas Flow Rate	31.4 CFH; 25 psi Ar, 25 psi He Viri 75Ar/25He Mixer
Fill Pass Torch Gas	100 % He, 70 CFH
Orifice Diameter	1/8 in.
Orifice Gas Composition	100% Argon
Orifice Gas Flow Rate	5.0 CFH - Penetration Pass 2.0 CFH - Fill Pass 2.0 CFH - Pilot Arc
Root Shielding Gas Penetration Pass Only	75% Helium / 25% Argon @170CFH; 30 psi Ar, 30 psi He Viri 75He/25Ar Mixer
Root Shielding Gas Shoe Stand-off	0.188 inch
Filler Wire Diameter	0.062 in.
Filler Wire Alloy	2319 Aluminum
Penetration Pass Stand-off Distance	0.150 In.
Penetration Pass Wire Feed Rate	0 In./min.
Fill Pass Current	88 Amps
Current Polarity Ratio (Both Passes)	19 milliseconds DCEN 4 milliseconds DCEP
Additional Reverse Polarity Current (Both Passes)	60 Amps
Fixture and Weldment Temperature	Room Temperature (80) +/- 5 °F

The data was then analyzed, the relative effects of the test variables on the responses was determined, and response surface relationship models were generated between the welding variables and the responses. From these response surface relationships optimum variable level sets were selected which were predicted to yield maximum UTS, maximum percent elongation, and minimum variability as measured by standard deviation. In addition the model fit was determined from the standard deviation of the data points from the best fitted linear model and the linear fit of the center point.

A response surface is a 3 dimensional pictorial model which shows the relationship between any 2 variables and any response measured. Since only 2 variables can be pictured at a time the off axis variables can be set at any value, so that the predicted response for any combination of variables can be obtained from the response surface model.

After the optimum variable level sets were selected from within the experimental space (interpolated) and outside the experimental space (extrapolated), confirmation test welds were made and tested using the same welding and testing procedures to confirm the predicted results.

III. Results and Discussion

Figure 3 is the Pareto chart showing the relative significance of the test variables on the mean UTS. The degree of significance is shown in the summary of results list, Table 5. and is indicated by the number of asterisks, one to three, listed for each variable. No asterisks means that a variable is relatively insignificant.

Next a two dimensional contour plot, Figure 4, was generated which shows the relationship between the two most significant variables and the mean UTS. This plot shows the optimum level of the on-axis and off-axis variables as selected by the software, the predicted UTS with this variable level set, and the 3 x standard deviation limits on the predicted UTS. This standard deviation is calculated from the residual standard deviation of the linear model fit to the data points.

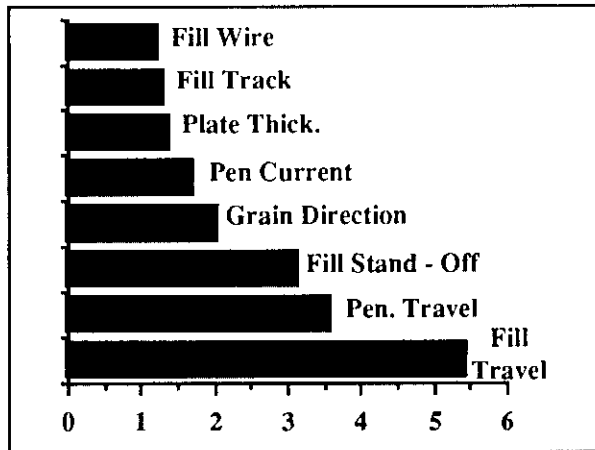


Figure 3 - Relative Effects of Variables on Mean UTS.

Table 5 - Significant Variables	
Summary of Results UTS_Mean	
	1 Pen_Amps
**	2 Pen_Travel
*	3 Fill_Stand-off
**	4 Fill_Travel
	5 Fill_Wire
	6 Plate_Thick
	7 Grain_Dir
	8 Fill_Track

Figure 5 is the same information and data as plotted in Figure 4 except that a 3 dimensional response surface is shown for easy visualization of the relationship. Mathematically the relationship between all of the experimental variables and any response can be determined from the data. The relationship between any two variables and any response can be plotted as 2 dimensional contour plots and 3 dimensional response surfaces. Other plots were generated and examined. The most meaningful and useful plots are those which relate the most significant variables to the most important response as shown here. The off-axis variables can be set at any level and the cursor on the computer screen can be moved to any on-axis variable location, interpolated or extrapolated, to obtain real time predictions.

The linear model fit for mean UTS is good as indicated by the ratio low ratio of the residual standard deviation (model error) to the

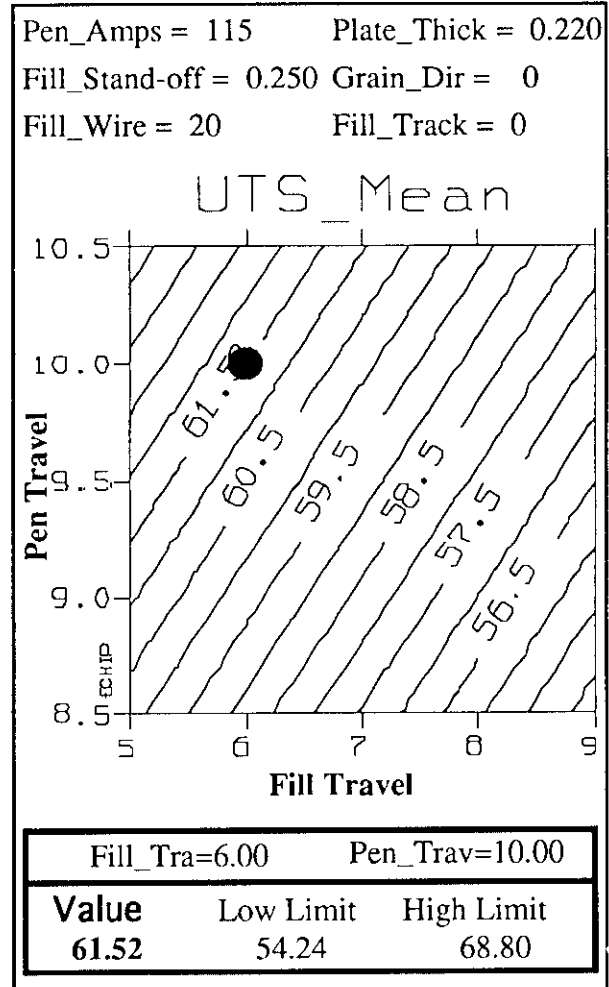


Figure 4 - Two Dimensional Contour Plot.

repetition standard deviation (pure error), $2.7/1.6=1.6$, and the good fit of the center point linear model prediction, 55.0 ksi to the actual tested value, 53.6 ksi.

After analysis and examination of the data, welding variable level combinations, Table 6, were selected for test welds to confirm the predicted optimum weld results.

The results from the confirmation welds are shown in Table 7. Note the significant improvement which occurred from the starting point weld schedules to the DOE optimized weld schedules, and the accuracy of the prediction for the interpolated optimum weld schedule. As expected the predictability of the extrapolated weld schedules was poor, however, some of these welds have features

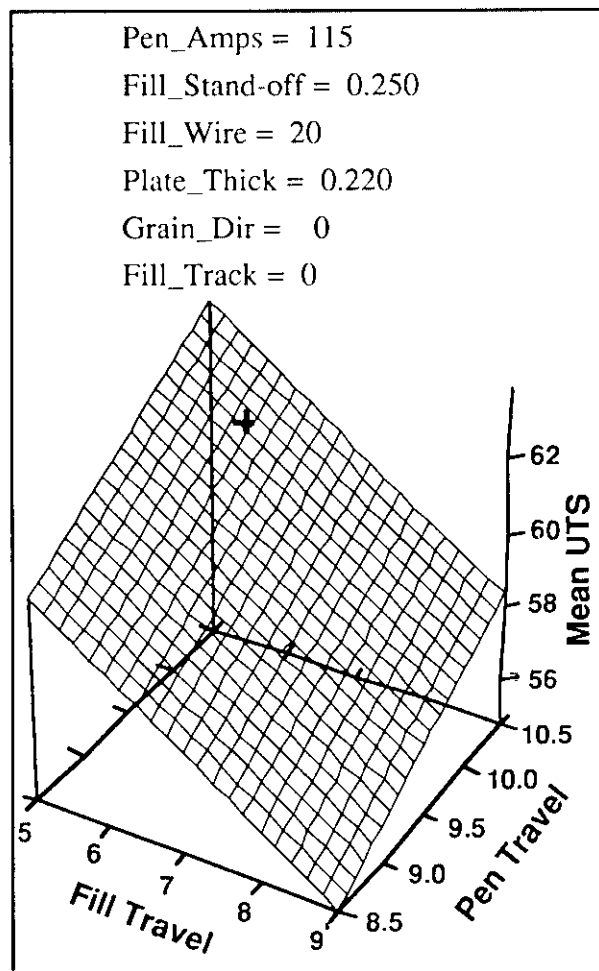


Figure 5 - Response Surface Relationship

which are more robust for production implementation. The more robust features are a wider penetration pass fusion zone and increased root reinforcement which result in greater tolerance to torch tracking, part fit up, and process penetration variations. Although the mean UTS is somewhat lower, the reduced variability (standard deviation) and increased robustness, without sacrificing the desirable microstructure, make these good changes for production implementation.

Figures 6 and 7 show the marked improvement in the weld microstructure as a result of the DOE optimized welds. Previous weld schedules resulted in welds with columnar dendritic and fine equiaxed grains in both the penetration and fill passes. Some grain boundary liquation at the fusion line is present and the large root reinforcement results in lower UTS due to a notch effect. The DOE optimized weld, Figure 7, shows the fine equiaxed dendritic microstructure throughout, which is indicative of lower effective heat input. The lower heat input also results in less microsegregation of alloying elements, minimizes grain boundary liquation at the fusion line, and improves mechanical properties. The reduced weld root reinforcement also reduces the notch effect and improves mechanical properties.

Even though tensile fractures of the DOE optimized welds occurred in the weld fusion zone, at the fusion line, and the heat affected zone, the strengths were high and consistent.

Table 6 - Confirmation Test Weld Schedules

Weld Schedule	Pen Pass Curr. Amps	Pen Pass Travel In/Min	Fill Pass Stand Off In	Fill Pass Travel In/Min	Fill Pass Wire In/Min	Plate Thick Inch	Grain Dir. Degree 0=Long	Fill Seam Track Inch
Optimum Interpolated	115	10	0.250	6	20	0.220	0 (Long)	0
Optimum Extrapolated Root Pass	158	14	0.250	6	20	0.220	0 (Long)	0
Optimum Extrapolated Fill Pass	125	10	0.250	5	15	0.220	0 (Long)	0
Optimum Extrapolated Both Passes	158	14	0.250	5	15	0.220	0 (Long)	0

Table 7 - Confirmation Test Results				
Weld Schedule	Predicted Mean UTS ksi	Actual Mean UTS ksi	Stand. Dev. ksi	Mean Elong 2 inch %
Optimum Interpolated	61.5	61.5	1.1	5.9
Optimum Extrapolated Root Pass	65.0	60.7	0.9	6.0
Optimum Extrapolated Fill Pass	63.2	58.7	0.4	5.8
Optimum Extrapolated Both Passes	66.7	60.1	1.2	6.2
Original	52.2	49.7	3.0	2.2

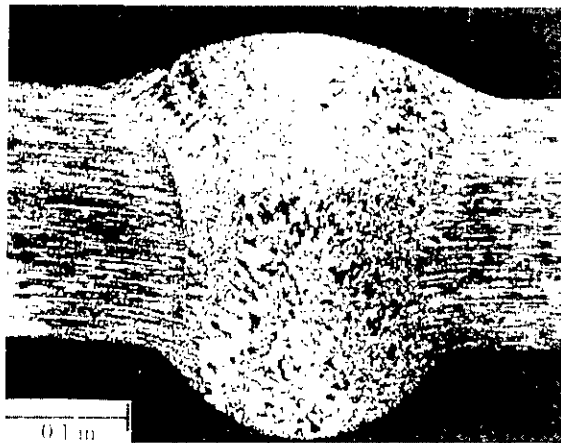


Figure 6 - Typical Previous Weld Microstructure.

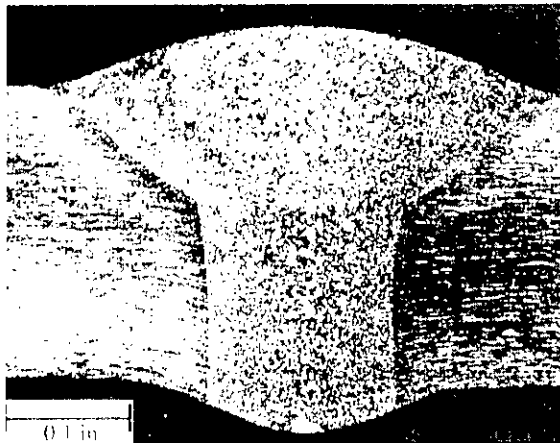


Figure 7 - Typical DOE Optimized Weld Microstructure.

IV. Conclusions

The value of the DOE method for optimizing and improving welding processes was again demonstrated.

Significant improvements were made in mechanical properties, weld fusion zone shape, microstructure, variability, and robustness of the process. Strengths across the width of weld and parent metal HAZ, were consistent and equalized, regardless of fracture location.

The welding microstructure described should be a good baseline for eliminating cracking which has occurred during repair welding of this alloy.

The pre-test matrix testing was again shown to be just as important as the actual test matrix testing, to the success of the designed experiment. Additional resources are required to conduct the preliminary testing, however, the value added is very pertinent to the success of the experiment.

V. Acknowledgments

The authors acknowledge the work and support given by welding technicians Sam Clark, NASA/MSFC, and Ray Zibilich, MMA; Carolyn Russell and Chip Jones NASA management; Jim Odom, Larry Kennedy, Brad Powell and Wayne Goode, SAIC; NDE and mechanical testing support work at MSFC; NDE and metallographic support work at MMA, and Martin Marietta management, technical, and engineering support at MSFC.

VI. References

1. Mack Roberts, et. al., Martin Marietta Astronautics, Denver, Colorado "Development and Manufacture of Advanced Cryogenic Tank, National Launch System Advanced Development Program #3106", May 28, 1993.
2. Mack Roberts and Larry Loechel, Martin Marietta Astronautics, Denver, Colorado "Welding Process Procedure Development and Optimization Using Design of Experiments", paper presented at 74th annual American Welding Society Convention, Houston Texas, April 1993.

3. E. F. Scholz, et. al., Martin Marietta Astronautics, Denver Colorado, "Advanced Cryogenic Tank Development Status", paper presented at AIAA 29th Joint Propulsion Conference, Monterey, California, June, 1993.
4. Mack Roberts, et. al., Martin Marietta Astronautics, Denver Colorado, "Advanced Cryogenic Tank Development Status", paper presented at AIAA 28th Joint Propulsion Conference, Nashville, Tennessee, July, 1992.

Optimization of the VPPA Welding Process for 2195 Aluminum-Lithium
Alloy using Response Surface Techniques
M.O. Roberts

- Q: Joe Pickens - I must commend you on a very intriguing study, your numbers look exceptional with a 61.5 ksi high temperature weld strength. If you were to do the design allowables based on your 61.5 ksi UTS and 1.1 standard deviation would you us a plus and minus 3 sigma?
- A: Yes. That is an allowable estimation.
- Q: I was wondering did you alter the microstructure, and how do you prove that it solved the cracking problem and how did it do on repairs?
- A: There has been some repair welding done on that using the DOE optimum as the initial weld schedule. Attila and the guys down here have done a follow on DOE to find the best initial weld schedule for repairing, so they are continuing to work in that direction. But, in answer to your question which was how did we prove that was a good microstructure for eliminating cracking, we actually run some tests welds where we E-stopped and you could not make it crack. We also did some repairs and we got to R5 on those repairs. And I think the paper that was presented this morning when the gentleman showed the welds where they had welded 4 hot passes one on top of another to make that crack in that area, I would like to try that, but I do not believe you could make the initial crack in this area with that procedure either.
- Comment: Just as a point of reference Joe the DOE that Kirby Lawless and I drew up basically we took the speeds even higher to 18 inches and the travel speed on the keyhole pass and the results were extremely comparable. I think we averaged 61 ksi with about a .5 ksi standard deviation and again the failure moved out of the weld and away from the fusion line on a majority of the tensile specimens. It is repeatable.
- Q: The Taugchi method is always very impressive, some of these monotonic properties and it has its place but what happens when you come to the next generation of alloys like Joe was talking about 21 different alloys that he wants to come up with, say the next optimization give you a variation in a composition so do you have to go through the whole routine.
- A: No, I do not think so because for welding of the alloys we used 2094 in the early experiments and 2195 in these later ones and essentially we found that the same parameters are significant regardless of which alloy you are welding you might have to adjust the level of the variables, but the same significant variables could be used for the follow on DOE.

- Q: How many iterations do you have to do, you had a fairly large numbers of variations you had to go through for that alloy. Do you have to repeat the same thing for the new set of alloys with a different lithium to copper ratio copper to mag ratio?
- A: No, I do not believe so I believe you could just take the variables that we found to be significant-you could take those variables and with a very small experiment determine what is the optimum level of those 3 variables.
- Q: Would the same optimization work, with minor change in chemistry?
- A: As I have said we have done that on actually about 4 variances of weldalite the last one being 2195. We started out very early in the game with actually 2219 and the same variables were significant on 2219 as were significant on 2195.
- Q: Does this method have any bearing to suggest to the alloy designers what they should do to make your life a little better?
- A: In what respect from alloy development?
- Q: Designing alloys, you are designing in order to press optimum welding, can you tell them how they could do to help you out? Because you have your problems, they have their problems.
- A: Yes I understand your question. You know actually as I said this morning I think we could take any of the alloy variances, of course the lower copper should be harder to weld, but I think we could take any of the alloy variances and come up with a process that we could weld it with without getting the undesirable grain boundary liquation and that sort of thing.
- A: Someone else - I think if I could answer that I think that this particular DOE was aimed primarily at the process parameter optimization.
- Q: But can you tell them how they could improve an alloy for welding to help you out?
- A: Well, you are suggesting that we use alloy chemistry as a variable, we did not use it as a variable in any of these experiments, so the answer to your question is if you want to know what alloy chemistry is the best for welding you make that one of the variables or several of the variables, you look at whatever element you want to look at in your DOE.
- Q: Jeff Sanders (IITRI) All the data was on 0.200 inch thick, so for you to scale it up to 0.5 inch, do you know enough to say if it would have the same two main variables?
- A: Well, the last experiment was 0.200 the previous ones were 0.350 most of them and I

think there again you would do the same thing as he was asking about alloy chemistry. We found that the same variables were significant regardless of thickness so you would just have to do a small experiment to find the best, you would have to adjust those significant parameters as well as the others to compensate for the thickness but it is not as big a problem as doing the initial experiment or not as much work.

BACKSIDE SHIELDING DEVICE FOR ALUMINUM-LITHIUM VPPA WELDING

Gerald Bjorkman
Advanced Systems and Technology
Martin Marietta Astronautics
Huntsville, Al. 35806

Abstract

Backside shielding using an inert gas is required for variable polarity plasma arc (VPPA) welding of aluminum-lithium alloys to shield the molten and cooling weld metal from gaseous contaminants in the air. Stationary and traveling backside purge chambers, or boxes, are used to perform this shielding task; however, problems arise with these devices for both lab and production welding environment. Therefore, an open faced backside shielding device was developed. It was tested and evaluated with three device configurations on 0.200-inch-thick 2195 aluminum-lithium with positive results using both argon and helium shield gas. Part of the testing consisted of a Taguchi design of experiment where acceptable visual, dye penetrant, metallographic and radiographic results were achieved. All testing was performed at NASA/MSFC Productivity Enhancement Complex (PEC).

1. Introduction

In aluminum-lithium alloys, the lithium addition increases tensile strength and modulus of elasticity with a decrease in density, which is an improvement over conventional aluminum alloys. As a result, aluminum lithium alloys have been under evaluation for cryogenic propellant tank application on advanced launch vehicles to enhanced performance. The 2195 alloy, one of the most popular, has been selected for application on NASA's "Super Light Weight" External Tank Program for the Space Shuttle. For these advanced aluminum-lithium cryogenic propellant tanks, the variable polarity plasma arc (VPPA) welding process has been baselined in most cases. The process, which is shown Figure 1, is typically performed in the vertical welding position.

The unique characteristics of the VPPA welding process is the keyhole weld technique and variable polarity action. The keyhole technique allows greater weld penetration compared with gas tungsten arc (GTA) welding, reducing the number of passes required to complete a weld. Furthermore, it

promotes gaseous weld contaminants to escape out the backside of the weld. The variable polarity produces cathodic cleaning action that improves weld quality.

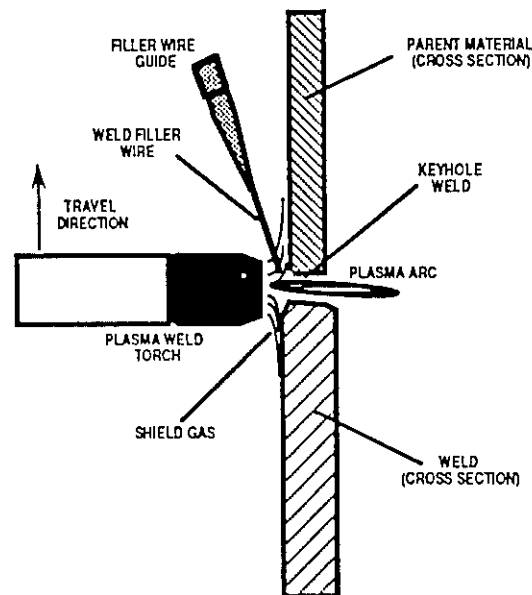


Fig. 1. VPPA Weld Process.

With VPPA welding conventional aluminum alloys, no backside shielding is required during the VPPA welding process; however, inert gas shielding is required for lithium containing alloys on the weld backside. If no shielding on the weld backside is used, the molten weld metal reacts with gaseous contaminants in the air causing unacceptable oxide formation. This oxide can disrupt the formation and solidification of the weld puddle as shown in Figure 2. In addition, the weld metal will contain unacceptable pores on the root side of the weld. In Figure 3, these pores can be seen at the toe of the weld.

Two methods typically used to shield the weld backside are the backside purge box and traveling shoe. The backside purge box, which is shown in Figure 4, consists of a box that is fixed to the backside of the welding fixture. It contains the entire length of the weld. The box has inlets and

outlets for purging the contained volume with shield gas. As a added convenience, view sights are typically built in so that the weld operator can see the backside of the weld during welding operation. Generally, the purge box will have an oxygen sensor to verify the purge and a pressure gauge so that the box has a minimum amount of gas pressure. Too much gas pressure in the box will cause the weld to be pushed out towards the torch disrupting the weld formation.



Fig. 2. Unshielded VPPA Weld Backside.

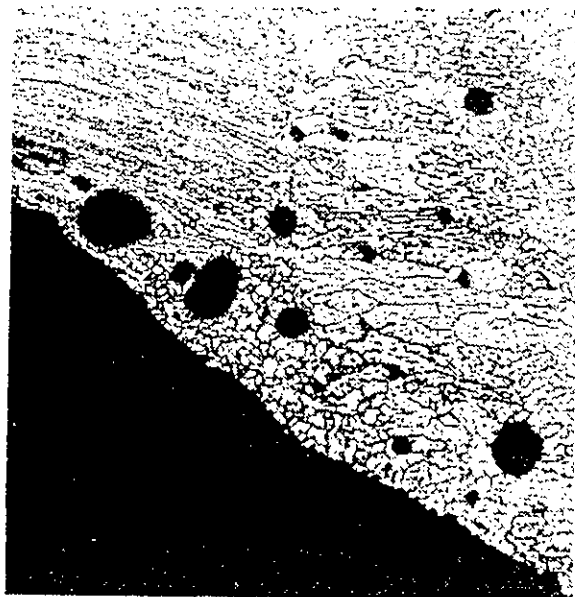


Fig. 3. Unshielded VPPA Weld, Root side Micrograph (50X).

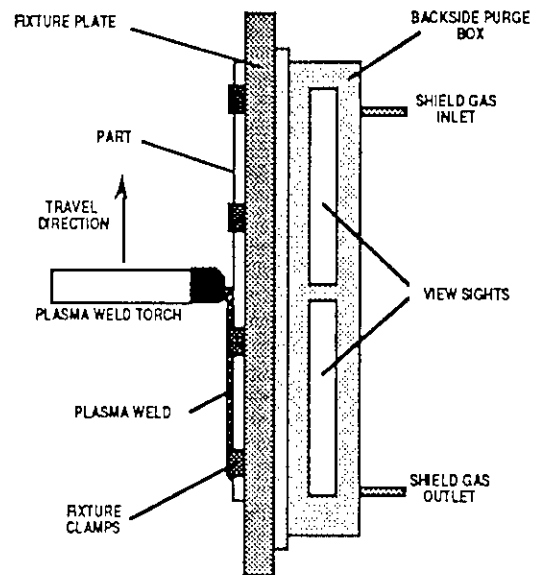


Fig. 4. Purge Box.

The traveling shoe, in Figure 5, is a derivative of the purge box producing the same shielding action; however, it is fastened to a travel mechanism that moves synchronously with the plasma weld torch. The shoe typically consists of a box type configuration with one end open where the shield gas exits and the plasma arc enters.

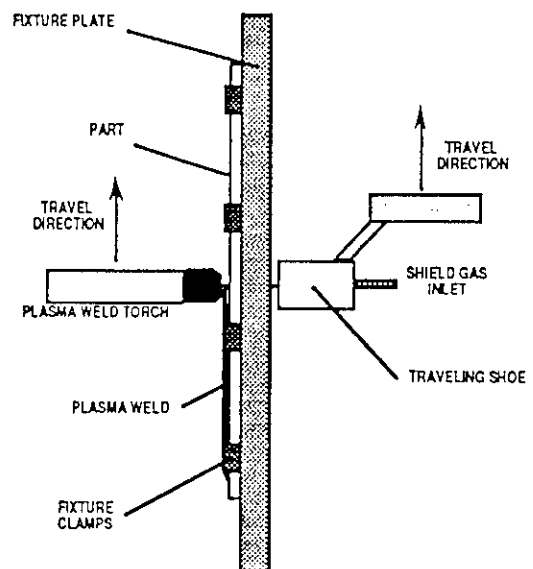


Fig. 5. Traveling Shoe.

Problems with these devices arise for both lab and production environments that are either related to issues of visibility, required monitoring equipment or weld tool size. Therefore, an effort was

made to reduce or eliminate these problems by developing a new backside shield device.

II. Concept

To meet the above requirements an open type shield device was conceived. Its basic principle consisted of blanketing the molten weld metal with a layer of shield gas while opened to the air. In concept, the shield gas enters the device through inlet tubes and is diffused as it exits. Then the gas collides into the part being welded a layer of shield gas is formed. This gas layer then moves outward and inward in relation to the weld area, as shown in Figure 6. The outward movement inhibits air from reaching the weld, and the inward movement shields the weld with a blanket of gas. Then, the center opening allows the plasma gas and shield to pass through the device without causing pressure effects on the weld and excessive heating of the device.

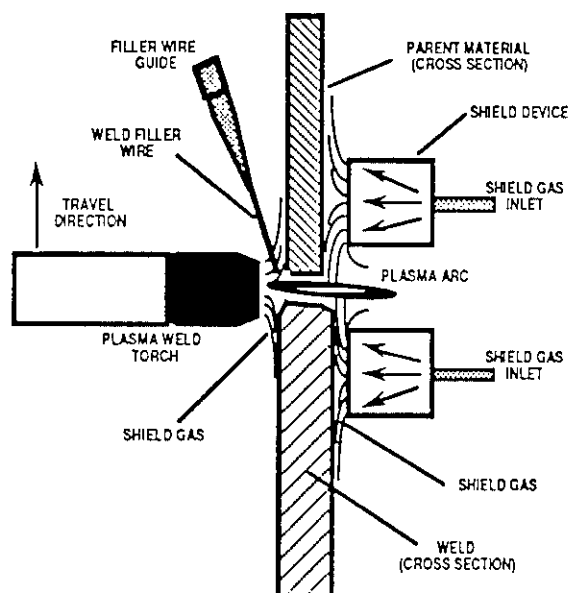


Fig. 6. Backside Shielding Concept.

III. Construction

The prototype device consisted of a circular shape construction so that the shield gas would surround and blanket the weld. It was produced out of stainless steel with a three inch outside diameter and a one inch inside diameter hole for the plasma arc passage. The shield gas entered the device through inlet tubes. The inlet tubes connect to a internal ring which distributes the shield gas throughout the circular shaped device. Steel wool was packed into the cavity of the device to further diffuse the shield gas. The gas was then forced through a perforated stainless steel sheet and out against the part being

welded forming the shield gas layer. Figures 7 and 8 are photographs of the device.

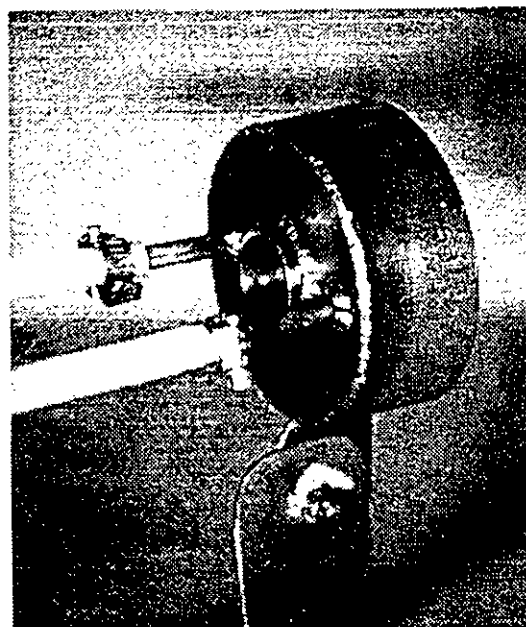


Fig. 7. Circular Backside Shield.

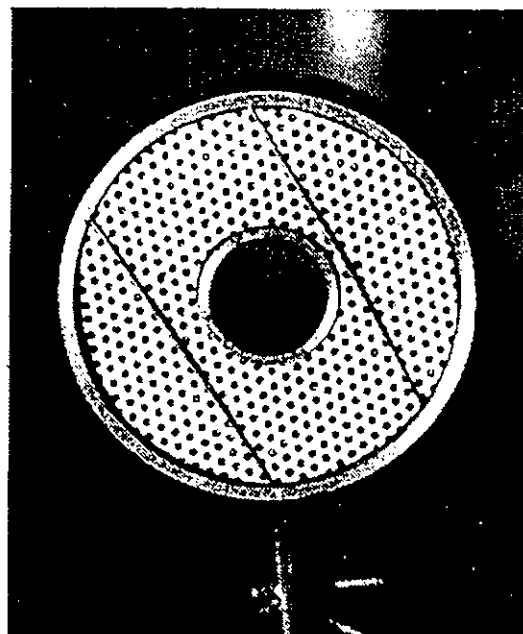


Fig. 8. Circular Backside Shield, Front.

Two additional prototypes constructed and tested. The first, made from stainless steel, was produced to evaluate whether the center opening could be enlarged from one to two inches in diameter without losing shielding. The second was made from hard coated aluminum with a one inch inside and three inch outside diameter.

A second configuration of the backside shield device was constructed to accommodate the vertical weld tool in building #4705 at NASA's Productivity Enhancement Complex (PEC). This version was constructed rectangular in shape to fit between the two inch wide gap of the weld fixture backup bars as depicted in Figure 9.

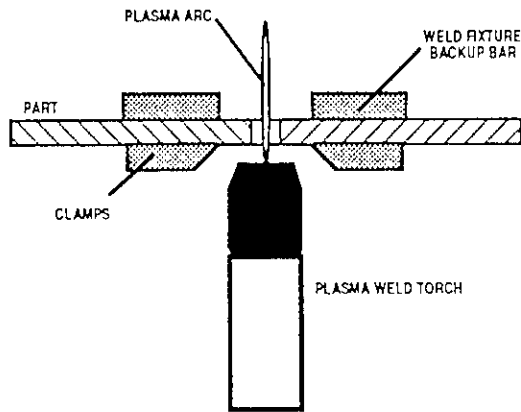


Fig. 9. Vertical Weld Tool, Top View.

The device was constructed out of stainless steel sheet with the same steel wool/stainless steel perforated sheet shield gas diffusion method as in the circular version. The center opening was rectangular in shape as like the outside perimeter, which was designed to allow the use of a laser vision system to observe and track the weld during operation. Figures 10, 11 and 12 are photographs of this rectangular configuration.



Fig. 10. Rectangular Backside Shield

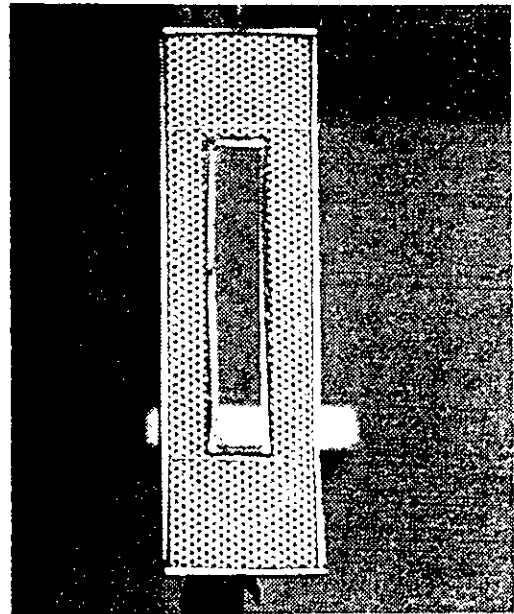


Fig. 11. Rectangular Backside Shield, Front.

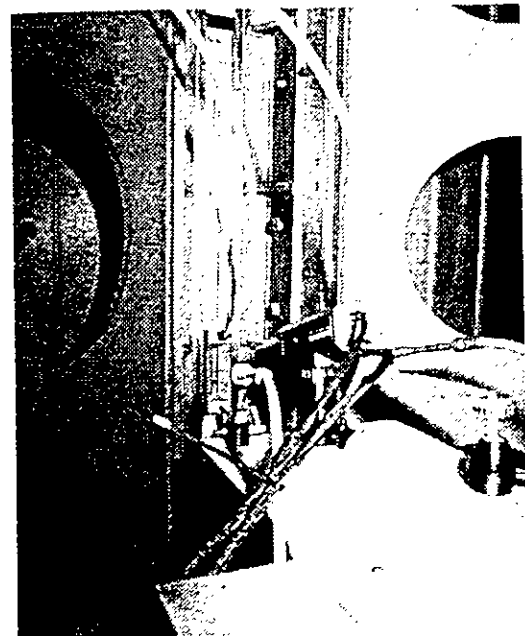


Fig. 12. Rectangular Backside Shield with Laser System.

The third configuration constructed was designed for weld fixtures with one inch wide backup bar gaps, specifically called "Picture Frame" weld fixtures. This time the design was slightly different.

The shield gas was not diffused and distributed about the perimeter of the molten weld metal. In this case, due to the narrow gap between the backup bars, gas outlets trailing and leading the weld puddle were only allowed, as shown in Figure 13. This version was also constructed of stainless steel sheet with the steel wool and stainless steel perforated sheet diffusion.

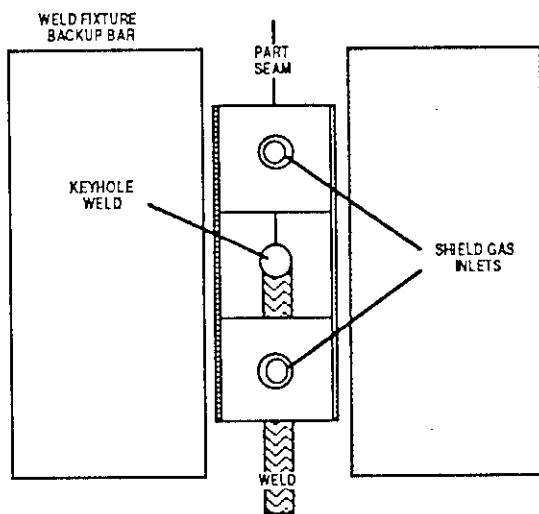


Fig. 13. Back View of Shield.

IV. Testing

The testing of these backside shielding devices were performed using GDI/ Hobart VPPA welding equipment with the B&B plasma weld torch. A standard flow of 160 cfm for shield gas and a .2 inch device-to-part stand off distance was used for both argon and helium. Testing took place at NASA/MSFC in the Productivity Enhancement Complex (PEC). The stainless steel circular shaped prototypes were tested on 0.200" 2195-T8R70 aluminum lithium material using 2319 filler wire with both argon and helium shield gas. Testing on the hard coated aluminum circular shape configuration was used in a Taguchi design of experiment on 0.200-inch-thick 2195-RT70 using 2319 filler wire with helium shield gas. On the vertical weld tool in building #4705 at NASA's Productivity Enhancement Complex (PEC), the rectangular version was tested incorporating the use of a laser vision system. Welding was performed on 0.200" 2195 T8R70 aluminum lithium material 2319 filler wire. The narrow gap backside shield was tested on alternate filler wire studies for 2195 aluminum lithium on 0.200-inch-thick material 1100 and 4047 filler wires. All welds were radiographically and metallurgically inspected. However, the Taguchi design of experiment specimens were radiographically, metallographically and dye penetrant inspected.

V. Results

The stainless steel prototype, having the one inch diameter center opening, shielded the weld producing radiographically and metallurgically acceptable welds with both argon and helium shield gases. However, arcing occurred from the plasma arc to the backside shield device. In an attempt to eliminate the arcing, the device was insulated from the electrical ground of the weld system; however, this did not correct the problem. The two inch diameter stainless steel prototype was tested eliminating the arcing; however, the weld was not adequately shielded by the device. The weld formed, but it had a unacceptable thick oxidation on its surface. This was due to the larger inside diameter hole, which caused the shield gas layer to break down before reaching the weld area allowing air contamination.

The hard coated aluminum backside shield used in the Taguchi design of experiment was successfully tested, and due to the hard coat aluminum, it eliminated the arcing that was occurring between the torch and device. Radiographic, metallurgical and dye penetrant acceptable results were achieved. Figure 14 shows the shielded backside of a specimen from the experiment, and Figure 15 is a metallograph from the shielded weld.



Fig. 14. Photo of Weld Back Side Shielded.

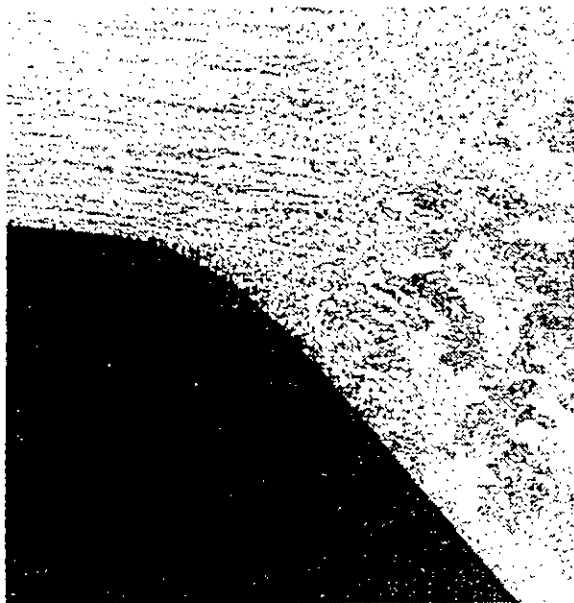


Fig. 15. Shielded VPPA Weld, Root side
Micrograph (50X).

The second configuration, or rectangular version, also produced radiographically and metallurgically acceptable welds. Even though the device was constructed out of stainless steel there was no arcing observed. This was attributed to the rectangular center opening, which did not allow the plasma arc to make contact with the device. In addition, the device allowed the laser vision system to access the backside and view the weld during the welding operation.

Results from the third configuration, or narrow gap backside shield for the "picture frame" weld fixture produced radiographically and metallurgically acceptable welds. No arcing was experienced even though it was constructed out of stainless steel. There was satisfactory clearance between the weld torch and the device to avoid plasma arc contact with the device.

VI. Concluding Remarks

A backside shielding concept was successfully proven through the construction and test of three shield device configurations. Complete weld visibility, oxygen/pressure equipment elimination and size reduction were achieved. Acceptable welds per radiographic, metallographic and dye penetrant inspection were produced, and successful shielding with either helium or argon of the weld backside was performed.

As a result of this work, a United States Patent Application has been filed for this backside shielding device

VII. Acknowledgment

Work performed by the author was sponsored by Martin Marietta Astronautics Group Independent Research and Development efforts and the "Cryogenic Tank Technology Program." a Cooperative Independent Research and Development Program between Martin Marietta Astronautics Group and NASA-MSFC. Special thanks to Sam Clark and Carolyn Russell of MSFC for welding support during the effort.

VIII. References

1. American Welding Society, "Welding Handbook", Vol. 2, American Welding Society, Miami, Fl.
2. Nunes, A.C., et. al., "Variable Polarity Plasma Arc Welding on the Space Shuttle External Tank", Welding Journal, Vol. 63, 27-35, Sept., 1984.
3. Tomsic, M., and Barhorst, S., "Keyhole Plasma Arc Welding of Aluminum with Variable Polarity Power". Welding Journal, Vol. 63, 25-32, February, 1984.

Backside Shielding Device for Aluminum-Lithium VPPA Welding
Gerald Bjorkman

- Q: Mack Roberts - I think that is an excellent way to do it, as you know we use the solid back side shield on our welds which was a rectangular shoe and one of the big problems we had during our welding was you cannot see anything from the backside until it is gone 3 or 4 inches and comes out from underneath the shoe and you cannot see alot from the front side because you got the torch and sensor bank there in front. That should be a big help because you can tell more watching the weld backside. I was wondering if that will fit on the tools down at the MAF? Can you get that down narrow enough where it would fit in there?
- A: Yes, the third version made for a "picture frame" weld fixture was 3/4 of an inch wide, which should be adequate for weld tools at MAF. However, if a weld tool has a smaller gap between the weld backup bars, a device could be designed to fit at least a 1/2 inch wide gap. this is as long as there is a leading and trailing shield media incorporated inthe actual shield device. As long as you have the leading and tailing shiled media incorporated, you could design a device for even a smaller opening.
- Q: MR - So it doesn't have to go all the way around it?
- A: Yes, the third version proved that if you have adequate backup bars, you can still properly purge the weld area with a shield gaas layer
- Q: MR - I sure would like to try that next time we do some.
- A: Now that we work for the same company I guess we will.
- Q: Tim Vaughn - What factors and variables are you using in the DOE?
- A: We have three control factors incorporated in the DOE, parent material chemistry, weld passes quantity and weld heat input. The different parent material chemistries are 2195, 2195 with only 0.69% lithium and 2195 with 3.62% copper and 0.78% lithium. There are single and double pass welds along with low and high weld heat input settings. In the manufacturin process it may be very desirable to have 62 Ksi two pass welds for max weld joint strength; however, two pass welds can double your changes for having weld defects which is one reason for analyzing the single pass weld. Furthermore, weld time can be reduced in half going from a double pass to a single pass weld. These are all producibility issues to be looked at.
- Q: TV - But you are not looking at like gas combinations?
- A: No, because the Taguchi experiment selected we could not incorporate the shield gas a factor. It would have taken away one of the interaction columns which we needed

to analyze. If we selected to run a response surface methodology, we could have included it. However, for this experiment we were concerned with screening material chemistry, weld passes and weld heat input. I will say results so far from the various chemistries tested there was no appreciable difference in weld strength. It would be interesting to evaluate these chemistries using Mack Roberst high strength. It would be interesting to evaluate these chemistries using Mack Roberts high strength weld schedule. However, I cannot discuss what we will be doing next.

LASER BEAM WELDING OF ALUMINUM-LITHIUM STRUCTURES

R. P. Martukanitz¹, K. G. Lysher¹, and P. R. Howell²

¹ Applied Research Laboratory
The Pennsylvania State University
State College, PA 16804

² Materials Science and Engineering Department
The Pennsylvania State University
State College, PA 16802

Abstract

Laser beam welding is being evaluated as a candidate joining process for fabricating structures from aluminum-lithium alloys. The primary objective of this evaluation was to determine joint quality and critical properties associated with laser beam welds of lap joints representing 2095-T6 stiffeners welded to 2095-T8 skin and 8090-T6 stiffeners welded to 2090-T83 skin; however, preliminary trials were also conducted to determine the applicability of laser beam welding for producing butt welds on alloy 2195-T8. Due to the concentrated heat source and high processing speeds, laser beam welding of these alloys results in minimal degradation within the heat affected zone and a fine solidification structure within the fusion zone. Although laser beam welding is anticipated to result in improved joint properties, the ability of the process to produce porosity-free welds must be assessed.

I. Introduction

NASA and industry studies have shown that low density aluminum-lithium alloy technology can aid in improving performance and increasing payload of launch vehicles (Refs. 1-3). Components that have been targeted for implementation of these new alloys are cryogenic tanks and dry bay structures. Components, such as the cryogenic tanks that carry liquid hydrogen and liquid oxygen, are fabricated from stiffened panels. Stiffeners are necessary along the length of the panels in order to prevent longitudinal buckling during dynamic loading of the tank.

NASA has proposed the use of "built-up" structures for panels which would be fabricated into tanks. This concept, shown in Figure 1, is vastly different from the current panel design requiring considerable machining in order to produce the stiffened structure and results in accumulation of costly aluminum-lithium scrap. The proposed joint between

SUPERPLASTICALLY FORMED (SPF), EXTRUDED, OR
ROLL-FORMED STIFFENERS

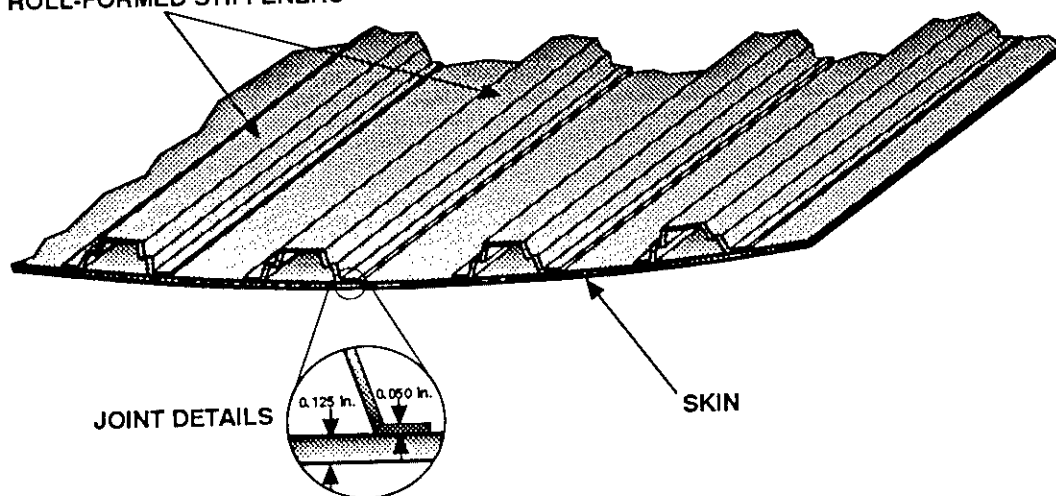


Figure 1. Illustration of Stiffened Panel Proposed for Built-Up Structures.

the stiffener and the skin will experience two primary, loading conditions. Compressive stress along the length of the panels will result in a shear stress along the stiffener to skin welds, and hoop stress due to internal pressure will result in transverse tensile stress across the partial penetration weld in the skin-sheet.

Longitudinal stiffeners, in the form of superplastically formed (SPF) parts, extrusions, or roll-formed sheet would be joined to skin-sheet that had been roll-formed to the radius of the tank in order to produce the panels. After fabrication, the panels would be welded together to form tank and dry bay structures. Prospective aluminum-lithium alloys include 8090-T6, 2095-T6, or 2195-T6 for stiffeners, and 2090-T83, 2095-T8, or 2195-T8 for skin-sheet. The nominal compositions for these alloys are shown in Table I (Refs. 4 and 5).

Table I. Nominal Compositions of Aluminum-Lithium Alloys of Interest (Refs. 4 and 5)				
wt%	8090	2090	2095	2195
Li	2.5	2.2	1.0	1.0
Cu	1.0	2.7	4.0	4.0
Mg	1.0	0.2	0.4	0.4
Zr	0.10	0.12	0.14	0.12
Ag	0.0	0.0	0.4	0.4

Methods being considered for joining stiffeners to the skin are resistance spot welding, resistance seam welding, and laser beam welding. Laser beam welding for this application possesses several advantages over resistance spot and seam welding. In order to optimize structural integrity during load transfer, it is desirable to produce welds as close to the corner of the vertical member of the stiffener as possible. Laser beam welding provides a continuous weld along the length of the stiffener, extremely close to the corner of the vertical member. This provides efficient load transfer capabilities and avoids unnecessary weight penalty due to excessive stiffener flange requirements. Laser welding also offers other potential benefits such as higher production rates, minimal heat affected zones, low thermal distortion, and the potential for process automation.

The current processes utilized for butt welding of panels and gore sections are gas tungsten arc (GTA) welding with direct current-electrode negative and variable polarity plasma arc (VPPA) welding. Although the GTA and VPPA welding processes are

capable of exceptional weld quality, they also result in low processing speeds and high heat input.

II. Evaluation

The evaluation primarily involved the establishment of process parameters for producing laser beam lap welds for mechanical property and metallurgical characterization. Processing parameters, such as beam power, travel speed, and shielding gas arrangement were identified for producing lap welds on alloy combinations of 8090-T6 to 2090-T83 and 2095-T6 to 2095-T8. Material thicknesses of interest included 0.050 in. thick sheet representing stiffeners and 0.095 in. thick and 0.120 in. thick skin-sheet. Surface pretreatments were also evaluated for minimizing porosity associated with the surface condition of the sheet. Once established, these processing parameters would be used to produce test specimens for ascertaining the viability of laser beam welding for this application. Critical mechanical properties required for characterization of the lap joints included transverse tensile strength of the partial penetration weld of the skin-sheet and tension shear strength transverse to the interface of the lap joint.

Process parameters were developed utilizing the Laser Articulating Robotic System (LARS) supported by a United Technologies Model SM21, 14 kW, CO₂ laser. The beam mode of this laser is represented by TEM 01*, and focusing is accomplished through the use of a f10 spherical mirror that provides a spot size at focus of 0.030 inches in diameter. This results in attainable power densities at focus of $7.07 \times 10^6 \text{ W/in.}^2$ at 5.0 kW to $1.99 \times 10^7 \text{ W/in.}^2$ at 14 kW output power. The optical arrangement utilized for LARS is shown in Figure 2.

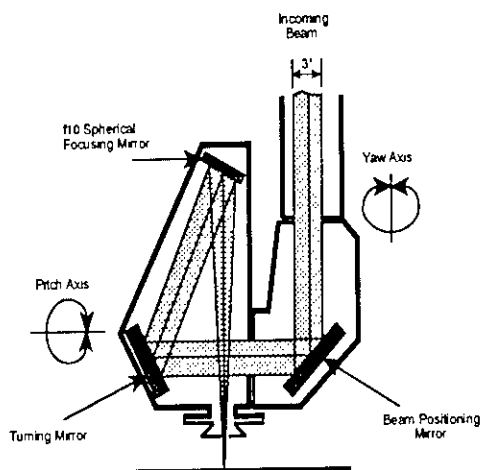


Figure 2. Optical Arrangement Used for the Laser Articulating Robotic System (LARS).

A. Process Development

Processing power and travel speed were identified for producing autogenous laser beam lap welds having full penetration of the sheet representing the stiffeners and partial penetration into the skin for both alloy combinations. Constraints imposed on the process required that these parameters produce between 40 and 60 percent penetration into the skin-sheet at processing speeds applicable to high production rates. Table II list the range of laser beam welding parameters established during process development, and Figure 3 is a macrograph of a lap weld of 0.050 in. thick 8090-T6 to 0.120 in. thick 2090-T83 produced using the parameters of Table II.

Table II. Range of Welding Parameters Identified During Process Development	
Beam Power	5 to 7 kW at Source
Processing Speed	150 to 160 IPM
Gas for Shielding and Plasma Suppression	200 CFH Helium
Gas Arrangement	Front of Weld with 0.375 in. Dia. Nozzle
Optical Parameters	f10 Spherical Mirror
Stand-off Distance	6.0 in. From Work-piece to Welding Head



Figure 3. Laser Beam Lap Weld of 0.050 in. Thick 8090-T6 to 0.120 in. Thick 2090-T83 (Kellers Etch).

B. Surface Pretreating

Evaluations conducted during process parameter development indicated that porosity formed within the fusion zone during laser beam welding. This occurred with various pretreatments, which included wire brushing, solvent degreasing, and mild NaOH etching. It was believed that a hydrogen enriched layer, specifically the formation of LiH, near the surface of the base metal was responsible for gas porosity during welding (Refs. 6 and 7). To determine if the hydrogen enriched layer was the source of porosity, aggressive pretreatments were evaluated.

Chemical milling in a 32% NaOH aqueous solution at 210°F was utilized to remove 0.001, 0.005, and 0.010 inch per side for each alloy prior to welding. After welding, the top-sheet representing the stiffener was removed exposing the top surface of the partial penetration welds of the skin. The degree of porosity present at this surface, which represents the lap weld interface, was quantified by visually determining the number of pores per linear inch of weld at 10X magnification. Shown in Figure 4 are levels of weld porosity produced by the various pretreatments for both alloy combinations. Flame emission atomic absorption for lithium concentration of chemical milling solutions was also conducted to quantify the depth of LiH formation near the surface.

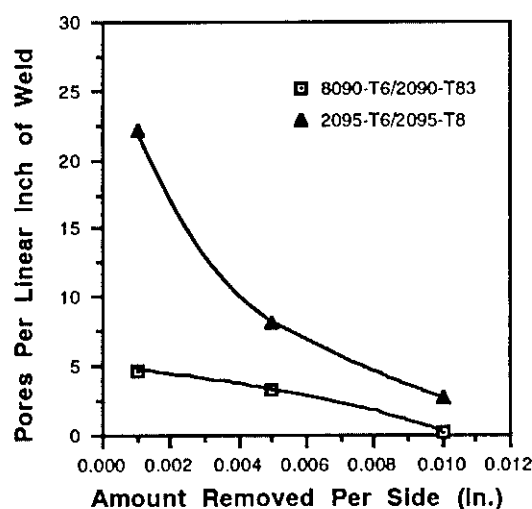


Figure 4. Laser Beam Weld Porosity at Interface of Lap Welds for Aluminum-Lithium Alloys That Were Chemical Milled to Various Thicknesses.

C. Mechanical Property Characterization

Mechanical property characterization included tensile tests across the partial penetration welds of the skin-sheet and tension shear tests to ascertain shear

strength at the lap weld interface. These properties were considered critical in determining the viability of laser beam welding for producing stiffened panels for tank structures. Tensile tests across the partial penetration welds of the skin would provide an indication of the response of the panel to internal pressurization, and tension shear tests would be used to measure joint strength at the interface.

Tensile strengths of the partial penetration welds of the face-sheet materials were determined on weld specimens produced using established process parameters and aggressive chemical milling (0.010 in. removed per side) prior to welding. Laser beam welds were produced on fully overlapped specimens representing 8090-T6 to 2090-T83 and 2095-T6 to 2095-T8. After welding, the top sheet was carefully removed and subsize tensile specimens having a 0.50 in. width at the reduced section and 1.0 inch gage length were obtained transverse to the partial penetration welds. A minimum period of 220 hours between welding and testing was allowed to elapse to ensure sufficient room-temperature precipitation strengthening (natural aging) in the fusion and heat affected zone had occurred. The results of tensile tests for the partial penetration welds and unwelded base-metal are shown in Table III. The mean and standard deviations shown in the table are derived from three specimens for base metal and five specimens for the partial penetration welds.

Table III. Results of Tensile Tests for Base Metal and Partial Penetration Welds of Skin-Sheet				
Alloy and Temper	Statistic	UTS (KSI)	YS (KSI)	Elong. (%)
2090-T83 Base Metal	Mean	80.4	74.7	6.7
	Std. Dev.	0.18	0.33	0.6
2090-T83 Weld ^b	Mean	61.6	a	0.0
	Std. Dev.	3.31	a	0.0
2095-T8 Base Metal	Mean	89.9	84.2	10.3
	Std. Dev.	0.36	0.39	0.6
2095-T8 Weld ^c	Mean	58.8	54.7	0.8
	Std. dev.	3.28	2.78	0.4

- a. Failed before reaching 0.2 percent offset.
b. Average weld penetration of 40 percent.
c. Average weld penetration of 60 percent.

Microhardness measurements transverse to the partial penetration welds of the skin-sheet were also obtained at 4, 24, 72, and 220 hours after welding. These measurements would be used to determine the degree of degradation within the heat affected zone and the ability of the weld to naturally age after welding. Microhardness profiles across the fusion zone (FZ) and heat affected zone (HAZ) of the partial penetration welds of 2090-T83 and 2095-T8 are shown in Figure 5 and Figure 6, respectively.

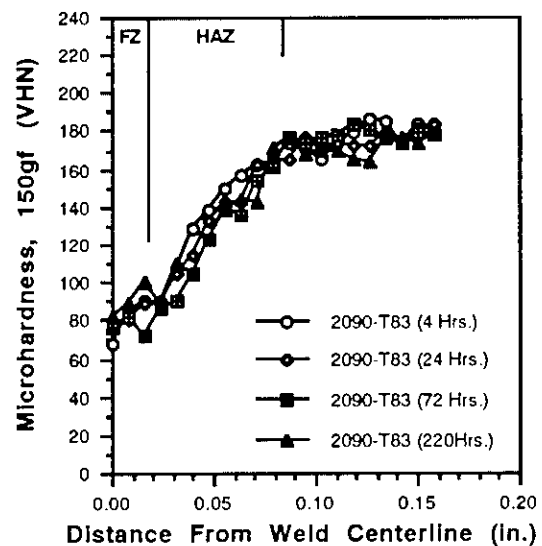


Figure 5. Microhardness Measurements Across Partial Penetration Weld of 2090-T83 Obtained at Various Times After Welding.

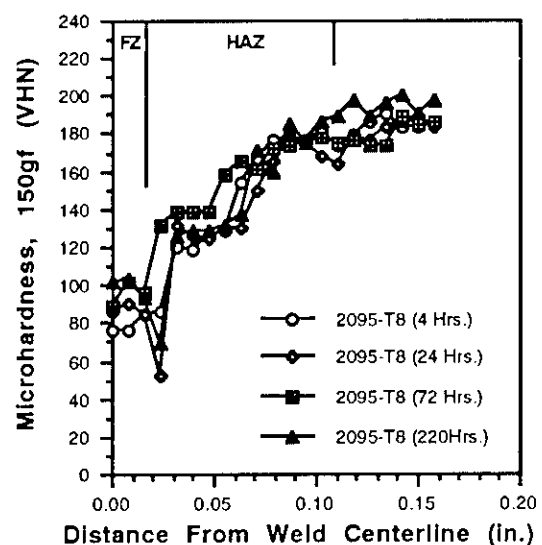


Figure 6. Microhardness Measurements Across Partial Penetration Weld of 2095-T8 Obtained at Various Times After Welding.

Weld tension shear specimens for both alloy combinations were produced on material that had been chemically milled 0.001, 0.005, and 0.010 in. per side to ascertain the effect of porosity on weld shear strength. Specimens were obtained by laser beam welding along the center of a 4.0 inch overlap. Shear specimens being 0.750 in. wide and 8.0 in. long were then removed from the welded samples. Shims, having a thickness of the sheet, were utilized during testing to maintain axial loading. A minimum period of 220 hours between welding and testing was allowed to elapse to ensure sufficient natural aging of the welds had occurred. Tables IV and V list the results of tension shear tests for the alloy combinations 8090-T6 welded to 2090-T83 and 2095-T6 welded to 2095-T8, respectively. In all cases, the mean and standard deviations are based on five specimens.

Table IV. Results of Tension Shear Tests of 8090-T6 Welded to 2090-T83				
Removed per Side (in.)	Statistic	Weld Area (sq. in.)	Shear Load (lb.)	Shear Strength (KSI)
0.001	Mean	0.065	803	12.4
	Std. Dev.			0.95
0.005	Mean	0.081	909	11.3
	Std. Dev.			1.01
0.010	Mean	0.069	776	11.3
	Std. Dev.			1.21

Table V. Results of Tension Shear Tests of 2095-T6 Welded to 2095-T8				
Removed per Side (in.)	Statistic	Weld Area (sq. in.)	Shear Load (lb.)	Shear Strength (KSI)
0.001	Mean	0.048	955	20.1
	Std. Dev.			0.71
0.005	Mean	0.050	931	18.5
	Std. Dev.			2.09
0.010	Mean	0.049	940	19.3
	Std. Dev.			1.45

III. Discussion

Although the results of the investigation have reinforced the potential advantages of laser beam welding for producing structures of aluminum-lithium alloys, limitations concerning current processing were also identified. Aggressive pretreatment in the form of chemical milling in a 32% NaOH aqueous solution at 210°F was found to be necessary to reduce porosity at the weld interface. This required removal of 0.010 in. per side by chemical milling prior to welding and is believed due to the presence of a hydrogen-enriched layer near the surface. Prior investigations have shown that thermal processing of aluminum-lithium alloys results in surface reactions between the metal and water vapor to form diatomic hydrogen (Refs. 8-11). Hydrogen is subsequently absorbed into the surface and may be available to form lithium hydride. These reactions result in lithium depletion near the surface and is believed to be accompanied by hydrogen enrichment.

Shown in Figure 7 is the concentration of lithium by atomic absorption measurements of NaOH solutions used to chemically mill 0.120 inch thick 2090-T83 and 2095-T8 specimens. (Refs. 12). The lithium content of the figure has been calibrated to be proportional to the lithium content within the material removed by chemical milling. Lithium depletion at the surface is evident for both alloys. The depleted zone for alloy 2090 is approximately 0.005 in. in depth; whereas, depletion of lithium for alloy 2095 appears to extend to the maximum milling depth of 0.010 in. obtained during this experiment.

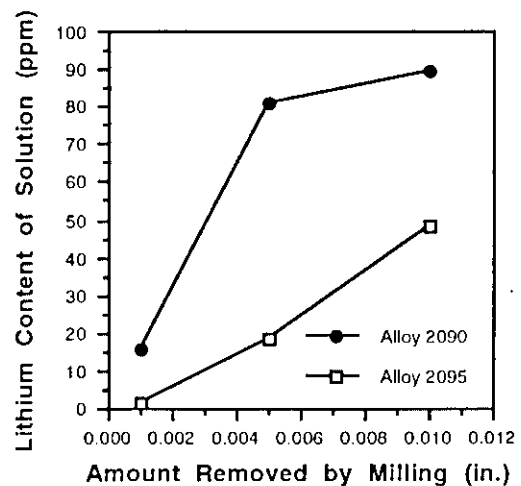


Figure 7. Results of Atomic Absorption Measurements for Lithium Content of NaOH Solutions Used to Chemically Mill Alloys 2090 and 2095 to Various Depths (Ref. 10).

Although it was also observed that porosity near the interface could be decreased by aggressive chemical milling, large porosity within the root of the partial penetration weld of the skin-sheet continued to be present. Unlike the porosity found near the interface, many times the larger pores found within the weld root were irregular in shape and dark in color. These observations may indicate that this porosity is due to instability of the vapor cavity formed during laser beam welding.

Upon establishment of the vapor cavity, or keyhole, during laser beam welding, the fluid forces present in the molten pool are balanced by the vaporization pressure within the cavity. Lithium and magnesium are known to exert a significantly greater vapor pressure than aluminum in the liquid state (Ref. 13) and these large differences may lead to periodic venting and collapse of the vapor cavity. The high velocity of the solidification front associated with the process could then result in periodic formation of voids or pores.

Although direct comparison to lap joints produced by other processes were not performed, the mechanical property data indicates that laser beam welding is capable of producing ample joint strengths for these applications. The values for ultimate tensile strength of the partial penetration welds of the skin represent a joint efficiency of 77 percent for 2090-T83 and 65 percent for 2095-T8; however, comparison of joint efficiencies should not be made between the two alloys based on these values. The strength across the partial penetration welds of the 2090-T83 represented a penetration of 40 percent of the thickness; whereas, the partial penetration of the 2095-T8 exhibited 60 percent penetration. Valid comparisons would require similar penetration since the fusion and heat affected zones of these alloys represent vastly different microstructures, and strengths. It is also noted that the tensile elongation values of the partial penetration welds appear low; however, aluminum alloys containing appreciable levels of copper typically exhibit low elongations across the weld and may not adequately represent weld ductility. The relationship between weld ductility and toughness of these alloys is of substantial consequence and is currently under separate investigation.

Results of tension shear tests indicate appreciably higher shear strengths are achieved with lap welds of 2095-T6 to 2095-T8 when compared to the 8090-T6 to 2090-T83 alloy combination. Regression analysis at a 90 percent probability showed no discernible differences in shear strength of the lap welds that could be attributed to the amount of material removed by chemical milling for either alloy combination. The high shear strength displayed by the

2095-T6 to 2095-T8 combination is believed to be attributed to the ability of this alloy to naturally age after welding. This phenomena is illustrated by the hardness profiles of Figure 6.

The laser beam welding process has also been used to produce butt welds on alloy 2195-T8 for comparison to the VPPA process. Initial results indicate that laser beam welding may yield significant improvements in joint properties; however, weld porosity associated with the process must be addressed. Figure 8 represents hardness measurements across the fusion and heat affected zone for 0.200 in. thick 2195-T8 produced by the VPPA and laser beam welding processes. The differences in the extent of the heat affected zones for both processes is readily apparent.

The degree of degradation within the heat affected zone for both welding processes is also illustrated in the micrographs of Figure 9. The fusion zone is shown to the right of the interface in the micrographs. The fine solidification structure of the laser beam weld is evident, as well as several small pores near the interface. Although the microstructures within the heat affected zone near the interface appear dramatically different for the two processes, microstructural transformations responsible for loss of strength in this region, i.e. dissolution of strengthening precipitate, may not be resolved optically. Transmission electron microscopy is planned to further characterize this region. The role in which microstructural modification of the heat affected zone effect weld ductility and toughness of these alloys is of particular interest.

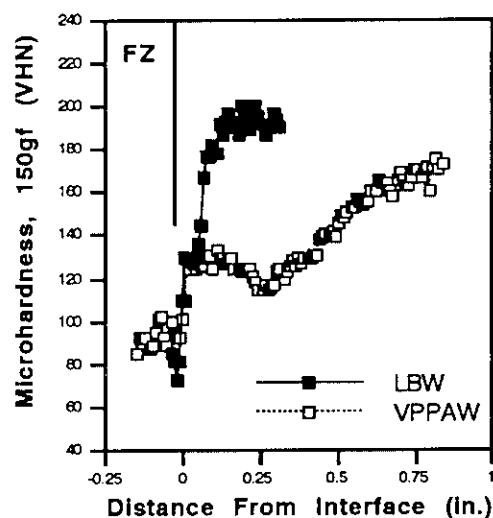


Figure 8. Microhardness Measurements Across Welds Produced by the VPPA and Laser Beam Welding Processes.

IV. Summary

An investigation has been performed to determine the applicability of laser beam welding for producing aluminum-lithium structures. Tensile tests across the partial penetration welds of skin sheet representing alloys 2090-T83 and 2095-T8 indicate that laser beam welding is capable of producing ample joint strength for these applications. Results of tension shear tests show appreciably higher shear strengths are achieved with lap welds of 2095-T6 welded to 2095-T8 when compared to the 8090-T6 to 2090-T83 alloy combination. The high shear strength displayed by the 2095-T6 to 2095-T8 combination is believed to be attributed to the ability of this alloy to naturally age after welding.

Although laser beam welding results in a fine solidification structure and minimal heat affected zones, weld porosity is typically observed. Chemical milling to remove 0.010 in. per side prior to welding was utilized to eliminate porosity near the interface of the lap weld; however, porosity continued to be present at the weld root. Observations indicate that this porosity may be due to instability of the weld vapor cavity.

Acknowledgment

Work performed during this investigation was funded by NASA Langley Research Center under P.O. L-4409D. The technical contributions of C. L. Lach, the Contract Monitor, are also greatly appreciated.

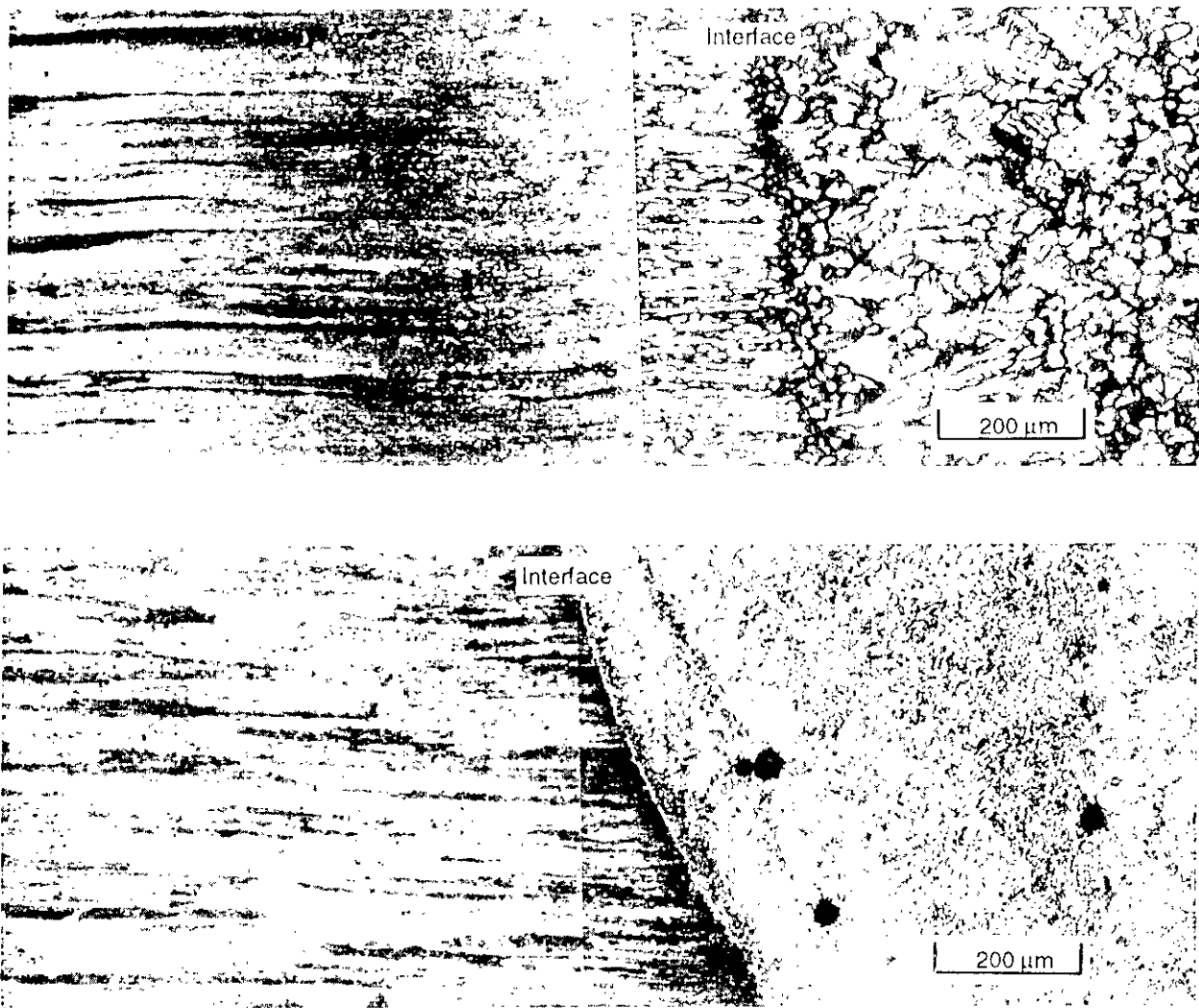


Figure 9. Microstructures Within the Heat Affected Zone for 0.200 in. Thick 2195-T8: Top Micrograph Represents VPPA Weld and Bottom Micrograph Represents Laser Beam Weld (Concentrated Kellers Etch).

References

1. NASA Langley Research Center, Advanced Aluminum Technology for Cryogenic Tank Application Workshop, Hampton, VA, 1987.
2. General Dynamics Space Systems, "Space Transportation Architecture Study", Report GDSS-STAS-87-002, 1987.
3. Tack, W. T. and Loechel, L. W., "Weldalite 049: Applicability of a New High Strength, Weldable Al-Li-Cu Alloy", Aluminum-Lithium Alloys, Volume III, Proceedings of the Fifth International Aluminum-Lithium Conference, Materials and Component Engineering Publication Ltd., Birmingham, UK, 1989, p. 1462.
4. Cross, C. E., Tack, W. T., Loechel, L. W., and Kramer, L. S., "Aluminum Weldability and Hot Tearing Theory", Weldability of Materials, American Society for Metals, 1990, p. 279.
5. Cho, A., Greene, R. E., Skillingberg, M. H., Cassada, W. A., Edwards, H. M., and Fielding, P. S., "Status of High Strength Al-Li Alloy Development at Reynolds Metals Company", Presented at the 40th Sagamore Army Materials Research Conference, 1993.
6. Martukanitz, R. P., Natalic, C. A., and Knoefel, J. O., "The Weldability of 2090 (An Al-Li-Cu Alloy)", Journal of Metals, (11), 1987, p. 38.
7. Pickens, J. R., "The Weldability of Lithium-Containing Aluminum Alloys", Journal of Material Science, Vol. 20, 1985, p. 4247.
8. Dickenson, R. C., Wefers, K., and Lawless, K. R., "Internal Lithium Hydride Precipitation in Al-Li alloys", Proceedings of the Fifth International Aluminum-Lithium Conference, Materials and Component Engineering Publications Ltd., Birmingham (UK), 1989, p. 1337.
9. Bavarian, B., Becker, J., Parikh, S. N., and Zamanzadeh, M., "Localized Corrosion of 2090 and 2091 Al-Li Alloys", Proceedings of the Fifth International Aluminum-Lithium Conference, Materials and Component Engineering Publications Ltd., Birmingham (UK), 1989, p. 1231.
10. Fridlyander, I. N., Metal Oved. Term. Obrab. Met., (4), 1970, p. 44.
11. Wefers, K and Mozelewski, F. A., "Surface Chemistry of Al-Li-Cu Alloys", Proceedings of the 8th International Light Metals Conference, 1987.
12. Hardy, D. J. and P. R. Howell, Unpublished Research, Materials Science and Engineering Department, The Pennsylvania State University, University Park, Pa., 1993.
13. Iida, T. and R. I. L. Guthrie, The Physical Properties of Liquid Metals, Clarendon Press, Oxford, 1993, p. 88 (Original data from Kubaschewski and Alcock, 1979).

Laser Beam Welding of Aluminum Lithium Structures
R.P. Martukanitz

- Q: Attila Szabo (Martin Marietta) A couple of years ago I had the opportunity to work with Penn State with the LAR system and we ran a series of 2219 test panels square butt joints 1/4", 3/8", and 1/2" thicknesses and just a point of reference the 1/4" thicknesses we got beautiful welds which tested very well in tension and were essentially X-ray clear; however the 3/8 and 1/2" thicknesses we had extreme difficulties with large voids like the ones you showed in your photographs. They were fairly common throughout these thicknesses, so I would be interested in the how your process optimization can resolve that?
- A: As I pointed out, porosity formed at the root of laser beam welds in aluminum alloys typically caused by instability between the hydrodynamic forces of the pool and vapor pressures within the keyhole or vapor cavity. As the depth of the vapor cavity is increased, the likelihood of instability is increased. Welding velocity also plays an important role in improving stability of the pool and vapor cavity. I suspect that the process parameters utilized during these earlier experiment, in which I was not involved, provided greater pool stability at the lower powers utilized for welding of the 1/4 inch material. We have recently shown that higher powers with a defocused beam may be used to control vapor cavity depth, and hence, reduce process related porosity.

ANALYSIS OF WELD HOT CRACKS IN AL-LI ALLOY 2195

By

Raymond G Thompson
University of Alabama at Birmingham

SUMMARY

Autogenous welds in an alloy 2195 plate were supplied by Carolyn Russell of MSFC. The plate was welded with an initial through thickness pass and subsequent overlays of up to 3 additional passes. The weld had several visible cracks that extended from weld metal through the HAZ. Upon further metallographic examination, *cracks were typically found below the overlay welds in both the weld metal and the HAZ.*

All cracks found were hot cracks formed from liquid films along the interfaces of dendrites and grain boundaries. These cracks were examined in the SEM and the Scanning Auger Microprobe (SAM). Little new information was found in SEM examination. The SAM examination revealed the probable source of the hot cracking. Specimen were cut from the welds and fractured in the ultrahigh vacuum of the SAM system. The fracture exposed fresh, internal hot cracks for chemical analysis of the surface atom layers in the SAM. It was found that the hot crack surfaces were highly concentrated in Li and Cu in the HAZ and Li in the fusion zone; with various surfaces also containing excesses of Si and Sn. Ar sputtering, which removes the top few layers of atoms from the specimen surface, easily removed the excess concentration of these elements with the exception of Cu. This showed that the high concentrations of Li, Sn, and Si were concentrated in a very thin hot crack liquid film. Cu, however, was not concentrated in the surface.

It was concluded that the low melting eutectic films were due to different mechanisms in the HAZ and fusion zone. Segregation of Li in the fusion zone to the final liquid layers reduced the eutectic temperature of liquid surrounding the dendrites. Liquation of Cu and Li rich precipitates in the HAZ caused Cu rich intergranular liquid. This liquid, when associated with Li segregation, produced HAZ liquid films with eutectic temperatures similar to the recrystallization

temperature.. These effects were accentuated on some surfaces by excess Si and Sn. Although SAM is not quantitative, certain techniques make it possible to estimate surface concentrations. Using one such technique it was found that the HAZ hot crack surface contained 15%atomic Li and 12atomic% Cu while the average alloy concentration for these elements is 4atomic% and 2atomic% respectively.

SAMPLE DESCRIPTION AND WELD MICROSTRUCTURE

A welded plate supplied by Carolyn Russell, shown in Figure 1, was examined for its hot cracking behavior. The plate was welded with an initial through thickness pass and subsequent overlay passes to simulate repair welds. Microstructural analysis from these welds showed that cracking was prevalent at many locations in both the fusion zone and the HAZ, Figure 2.

The microstructure consisted of a cold rolled base metal, a recrystallized HAZ, and a dendritic fusion zone. *Hot cracks were found in each of these zones.* A telling observation was that hot cracks penetrated into the cold rolled base metal. This indicated that the liquid films associated with hot cracking were stable below the recrystallization temperature for this alloy. If a recrystallization temperature of about 500C is assumed for the 2195 alloy, then *the liquid film is stable around 450C.*

FAILURE ANALYSIS

Figure 2 shows typical cracks found in the fusion and HAZ zones. *The cracks are found at interfaces of dendrites in the fusion zone, at grain boundaries in the recrystallized HAZ, and along grain boundaries in the cold rolled base metal.* Thus the cracks are not limited to a single microstructure or weld zone.

A sample was broken from the cracked area of Figure 3. The sample was broken by hand and observed in the SEM. Figure 4 shows the fracture surface to be composed of an intergranular fracture. The higher magnification photographs of this surface shows that the fracture was along a hot crack which contained a liquid layer at fracture. The hot crack spanned an area from the dendritic fusion zone, Figure 4.B, to the recrystallized HAZ, Figure 4.C. X-ray chemical analysis of the fracture surfaces (Figures 4.A and 4.B) did not indicate anything suspicious about the liquid film chemistry. It should be born in mind that x-ray analysis samples the

chemistry to a depth of about 200 to 500 atom layers. Any chemical species segregated to the outer layers of the liquid film would be overwhelmed by the chemistry of the bulk and thus "invisible" in the x-ray analysis. Also Li is not found in the x-ray analysis because of its low atomic number (3).

It was concluded that the hot cracks found in alloy 2195 welds are due to low melting liquid films. These films form on interfaces of dendrites and grain boundaries in the fusion zone, the HAZ and even the base plate (low temperature portion of HAZ). *These liquid films may be stable to about 450C* since they are observed at temperatures below the recrystallization temperature of the base plate.

ANALYSIS OF THE HOT CRACK LIQUID FILM

A SAM with internal fracture stage was used to analyze the chemistry of the liquid film found to cause hot cracking in alloy 2195 welds. The Auger technique excites chemical analysis only from the top 2 to 3 atom layers at the surface of the specimen. This makes it the most effective technique for analyzing the surface chemistry of metals and ceramics. It also is effective at exciting chemistry from all elements except H and He. *Thus it is good for finding low atomic number elements like Li, B, C, O, N etc.* SAM samples were cut from the weld zone as shown in Figure 3. Samples were fractured in vacuum, typically 2×10^{-7} torr, and immediately examined for their surface chemistry. Since the SAM is also an excellent SEM, the analysis is also a good failure analysis tool. Table 1 contains the semiquantitative analysis of surfaces observed in the SAM. Appendix A-D contain the Auger spectra from some representative surfaces. The surfaces from which the spectra were taken are shown on attached photographs.

It was found that Li segregated during the solidification of the fusion zone to the liquid film surrounding dendrites and concentrated there in amounts 5 times greater than its average atomic concentration in the bulk alloy. It was found that Cu-rich liquid films formed in the HAZ and that Li segregated to the surface of these films. It was also found that Si, Ag and Sn segregated to some surfaces. The SAM is equipped with an Ar sputter gun which allows the top layers of atoms to be stripped away so that chemical depth profiling is possible. Such profiling allows you to determine if the elements at the surface are concentrated in a very thin layer or if they are part of a larger bulk phase. Removal of the top layers of atoms eliminated the strong concentrations of all of the above elements except Cu. This showed Cu was not concentrated in the surface but was enriched in the HAZ liquid

but not in the fusion zone liquid. However, Li, Si and Sn were concentrated in a very thin layer at the interface of the hot cracks. Nitrogen was found in the liquid film after sputtering the surface layers.

Summary Auger Data

(data may be normalized to the matrix composition from the matrix fracture surface or sputtered surface, ie, Li concentration computed directly from Auger peak heights is factor of 2 to 3 times too large)

Atomic %	Matrix	Grain Hot Crack	Sputter	Dendrite Hot Crack	Sputter	Dendrite Not Hot Crack	Prec.
Li	14	24	8	34	8	18	22
Cu	1	10	10	2	4	17	9
Al	71	26	43	24	45	42	42
O	13	31	14	39	25	22	24

Although the SAM specimens were fractured in vacuum, most hot cracks observed had already been exposed to air because they were connected to the external surface of the weld when they were formed. Thus most hot cracks observed in the SAM had large concentrations of oxygen on the surface. However, one set of hot cracks were found that were indeed removed from the external surface of the weld and gave an excellent characterization of the internal liquid layer. These surfaces and their Auger spectra are found in Appendix B.1 and B.2. Appendix A contains an analysis of a freshly fractured matrix. This matrix spectrum gives a standard of the bulk 2195 material for comparison to the hot crack surfaces. Several precipitates were analyzed and these are given in Appendix D. Dendritic hot cracks which were exposed to air prior to fracture in the SAM are given in Appendix C.

It was concluded from the SAM study that Li and Si and, to a lesser extent, Ag and Sn segregated to the liquid film surface in the HAZ during welding. These elements concentrated in the film and were found in the top few layers of the interface. Based on a semiquantitative technique, it was found that *the surface layers of hot crack liquid films in both the HAZ and fusion zone typically contained about 15atomic% and 20atomic% Li respectively. Cu-rich precipitates appeared to liquate in the HAZ and produce Cu-rich liquid films with about*

12atomic% Cu. The semiquantitative technique used does not allow a calculation of Si. Thus it is probable that thin liquid films containing well over 50atomic% Li, Cu, Si, Sn and Ag existed along dendrite and grain boundary interfaces in the microstructure during welding.

THEORY OF HOT CRACK PROBLEM

A study of binary phase diagrams for combinations of Al, Li, Cu, Si, Ag, Sn, O, and N revealed some interesting information. Most binary combinations of these elements give eutectic liquids in the temperature range of 600C to 550C. This temperature range is not low enough to cause the observed hot cracking. Ternary reactions are known to depress the eutectic temperature some, but not to the extent observed in these welds. However, binary combinations of *Li, Cu and Sn do produce eutectic reactions in the 200C range.* Given the observation of large concentrations of Li and Cu on all hot crack surfaces, it seems justified to suggest that *the combination of Li and Cu in the interface liquid depresses the eutectic temperature of the liquid and is responsible for the hot cracking problem.* The segregation of Sn would aggravate the problem but does not appear to be required for the observed hot cracking. This conclusion is consistent with the penetration of hot cracks into the un-recrystallized portion of the alloy 2195 base metal.

It is important to consider the probability that the cause of the Cu-Li films are different for the HAZ and fusion zone. By observing the chemistry of liquid films in both regions it was apparent that Cu enrichment occurred primarily in the HAZ. Thus a source of Cu is necessary for the liquid. This source is likely precipitates rich in Cu and possibly Li such as those identified in fracture surfaces of the SAM study. However, in the fusion zone the problem is partitioning of Li to the liquid phase during solidification. Cu was found to partition into this liquid only slightly compared to the bulk. Thus different approaches may be needed to solve these problems.

RECOMMENDATIONS

The hot crack problem in alloy 2195 has been linked to the intentional alloy additions, Li and Cu. Li partitions into the liquid phase of the weld metal as it solidifies and supports a eutectic liquid film stable around 450C. A Cu and Li enriched liquid film which is also stable around 450C coats the HAZ grain

boundaries. Cracking occurs when stress from thermal contraction and other constraints develop when the weld zone is in the 400C to 500C range.

One solution would be to *dilute the Li concentration in the fusion zone eutectic film* by adding elements to the weld metal that are insoluble in Al. These would then partition to the liquid and could (if chosen correctly) be made to raise the eutectic temperature of the film. The HAZ part of the problem could be addressed through *heat treatment which eliminates the detrimental precipitates* from the microstructure. These two actions taken together would protect the base metal and remove the problem from the weld metal.

Another solution is to *weld with a filler metal that does not contain Li*. The HAZ part of the problem could be addressed through *heat treatment which eliminates the detrimental precipitates* from the microstructure. These two actions taken together would protect the base metal and remove the problem from the weld metal.

Solutions such as trying to design a weld procedure so that shrinkage stress does not develop in the weld until the eutectic film is solidified are difficult to obtain. This solution seems improbable because of the eutectic temperature of the film.

Table 1
Liquid Film Surface Chemistry*
(Scanning Auger Microprobe)

Freshly Fractured Matrix Surface									
	Li	C	N	O	Al	Cu	Ag	Sn	Si**
2BC	14%	0%	0%	13%	71%	1%	0%	0%	no

Precipitate Surface									
	Li	C	N	O	Al	Cu	Ag	Sn	Si**
2BD	23%	0%	0%	27%	45%	5%	0%	0%	no
40G	31%	6%	0%	30%	21%	10%	2%	0%	no
2BB	11%	0%	0%	15%	61%	13%	0%	0%	no

Freshly Exposed Hot Crack Surface (Recrystallized HAZ)									
	Li	C	N	O	Al	Cu	Ag	Sn	Si**
40E (Grain E)	24%	4%	0%	29%	27%	12%	1%	2%	yes
40I (Grain E, 30 sec. Sputter)	10%	0%	23%	9%	43%	12%	0%	0%	no
40D (Grain D)	21%	8%	0%	29%	27%	13%	1%	2%	yes
40H (Grain D, 30 sec. Sputter)	15%	5%	14%	5%	49%	7%	4%	0%	no
40F (Grain F)	27%	5%	0%	36%	24%	6%	1%	1%	yes
40J (Grain F, 30 sec. Sputter)	0%	0%	21%	28%	39%	12%	0%	0%	no

Hot Crack Surfaces Exposed to Air When Hot Cracked (Dendritic Fusion Zone)									
	Li	C	N	O	Al	Cu	Ag	Sn	Si**
3CE Dendrite	36%	3%	0%	36%	21%	2%	1%	0%	no
3CF Dendrite 20 sec Sputter	12%	6%	6%	28%	42%	5%	0%	0%	no
3CG Dendrite 100 sec Sputter	6%	8%	11%	23%	48%	4%	0%	0%	no
3CB	34%	2%	0%	37%	27%	0%	0%	0%	no
3A2	30%	0%	0%	39%	28%	4%	0%	0%	yes
3A1	36%	0%	0%	45%	15%	4%	0%	0%	yes
3CC	32%	2%	0%	37%	28%	0%	0%	0%	no

Freshly Fractured Dendrite Interface (Not a Hot Crack)									
	Li	C	N	O	Al	Cu	Ag	Sn	Si**
2BE	18%	0%	0%	22%	42%	17%	0%	0%	no

* $C_i = (I_i/S_i) / \sum (I_j/S_j)$

C_i = Concentration of element i

I_i = peak to peak intensity ($dN(E)/dE$)

S_i = Auger sensitivity factor for element i

Lines used KLL {Li,C,N,O, Al}; LMM{Cu}; MNN {Sn,Ag}

** S_i = MNN line was large but no KLL line was seen. Thus, it was not calculated.

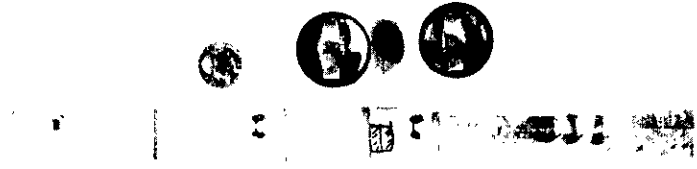


FIGURE 1

Autogenous welded plate supplied by NASA. Weld # 932195N4. The weld was sectioned as shown when we recieved it. The two mounted cross sections from the welded plate shown next to the quarter were also supplied by NASA.

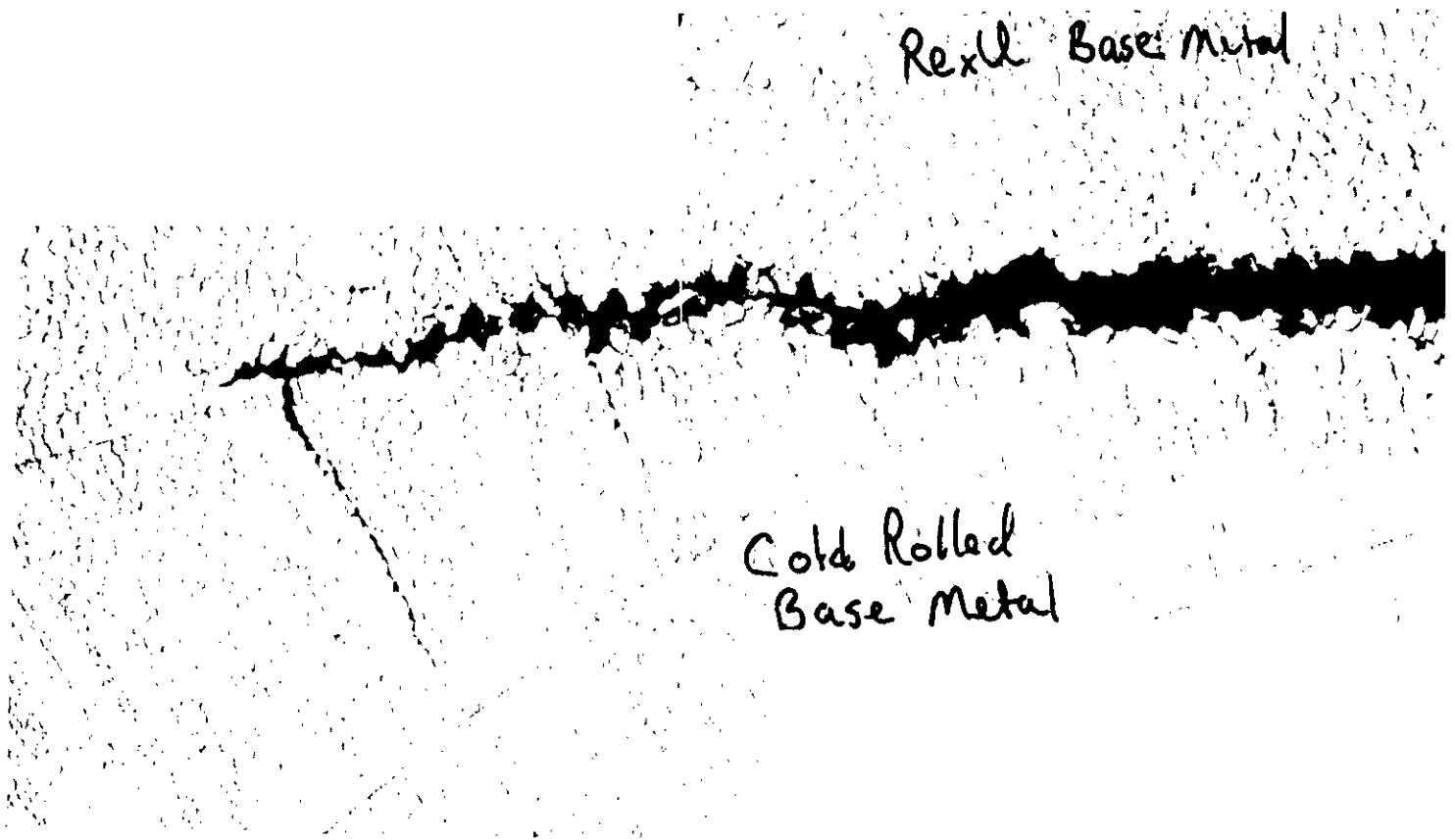
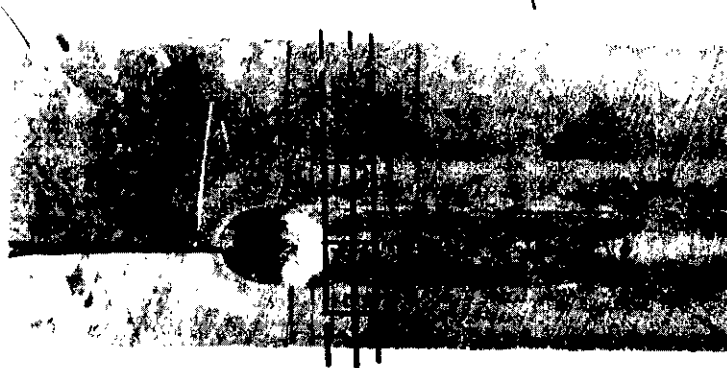


FIGURE 2

A crack in the welded plate that extended from the fusion zone, through the HAZ and into the base metal. Note that the crack extends beyond the recrystallized HAZ into the base metal.

932195N4
Autogenous
NASA 2195 alloy



Auger specimens 1

FIGURE 3

A. The end of the welded plate contained hot cracks. This area was sectioned to produce specimen for the SAM and SEM analysis of fracture surfaces. These are shown below in their cut and etched condition. Letters a,b,c, and d indicate the through-thickness position. (a-weld top, d-weld bottom)

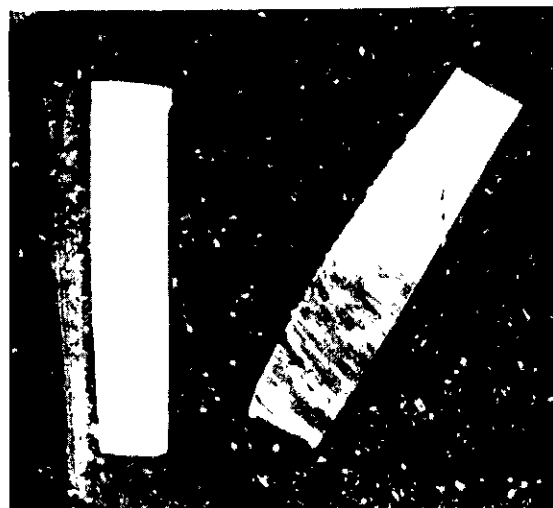


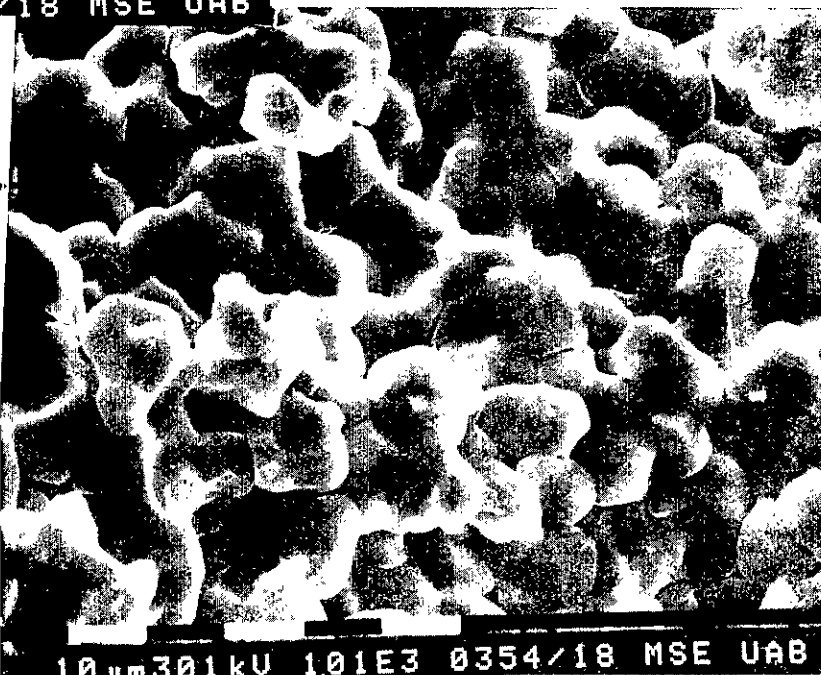
FIGURE 4

B. Interdendritic fracture clearly shows fusion zone dendrites with classic hot crack surface covered by liquid film. SEM x-ray chemical analysis showed only typical Al - Cu matrix chemistry.



A. Fracture surface of specimen 4a. Note that the fracture has a transition from coarse dendritic fracture in the fusion zone to finer intergranular fracture in the recrystallized HAZ. This is seen more clearly in Figures 4.B and 4.C.

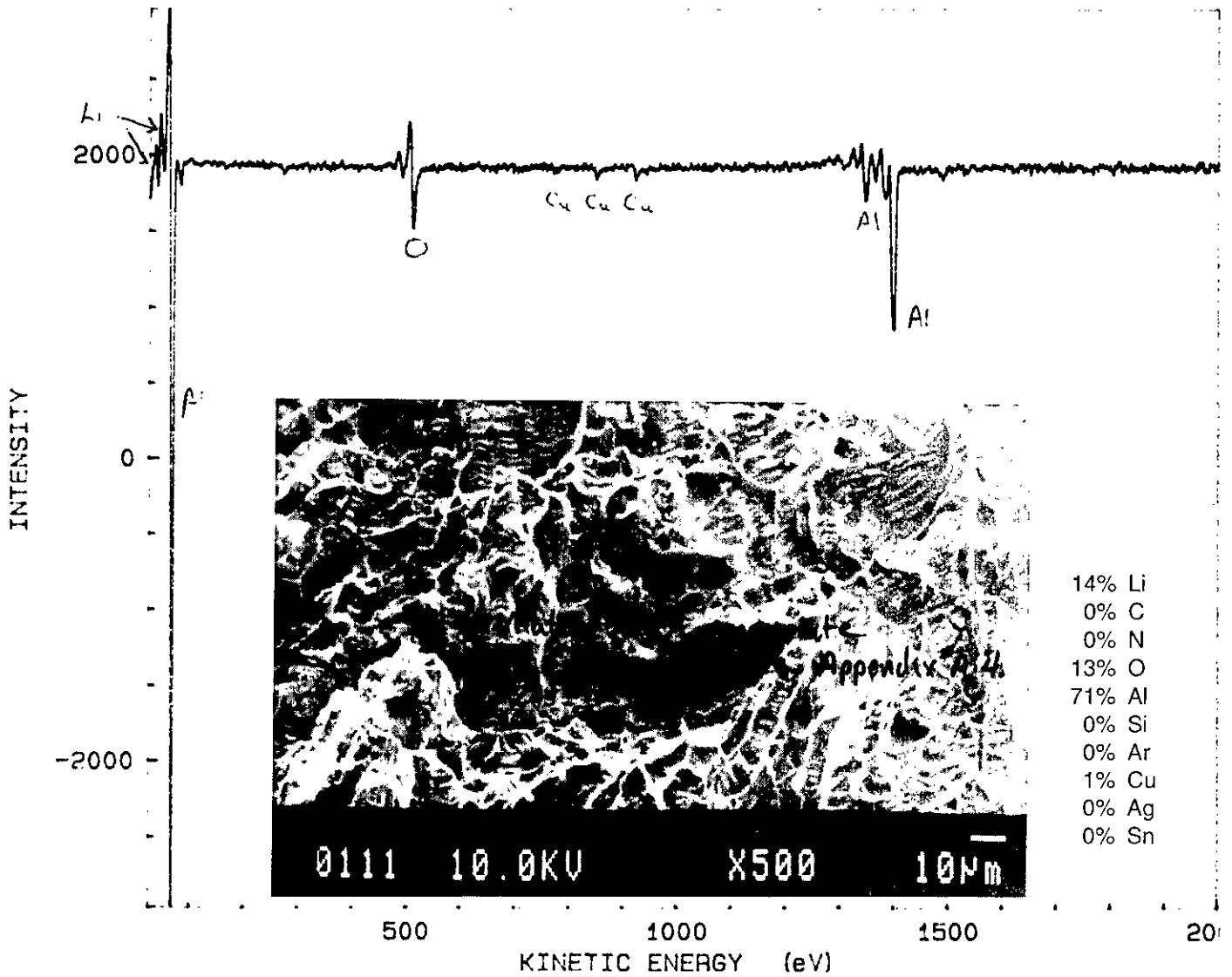
C. Intergranular fracture clearly shows recrystallized HAZ grains with classic hot crack surface covered by liquid film. SEM x-ray chemical analysis showed only typical Al - Cu matrix chemistry



Appendix A.

Matrix, ductile rupture fracture in high vacuum.

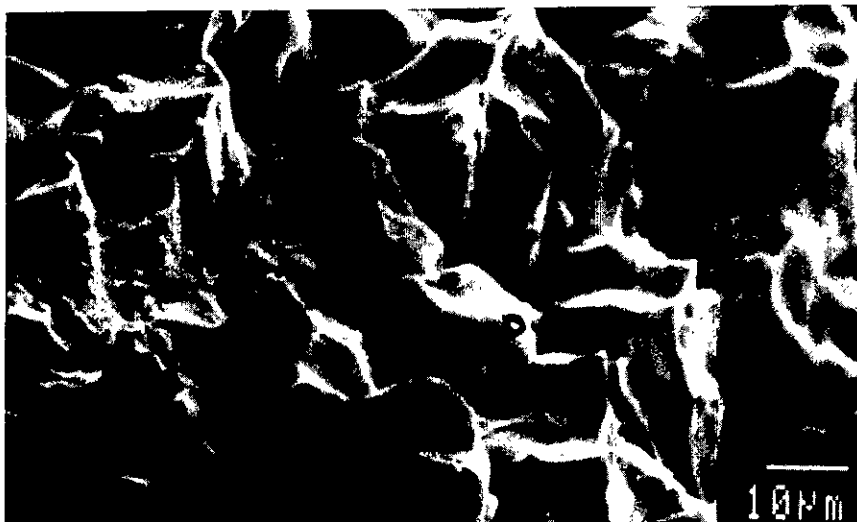
File : NAS4N2BC.SSP



The matrix signature is seen as high Al and low Cu and Li. The O peak probably indicates the gettering power of a fresh Al surface even in a high vacuum.

Appendix B.1

Intergranular hot crack surfaces from the recrystallized HAZ. Surfaces were exposed in high vacuum and had not been open to the air. SAM spectra are attached in B.2.

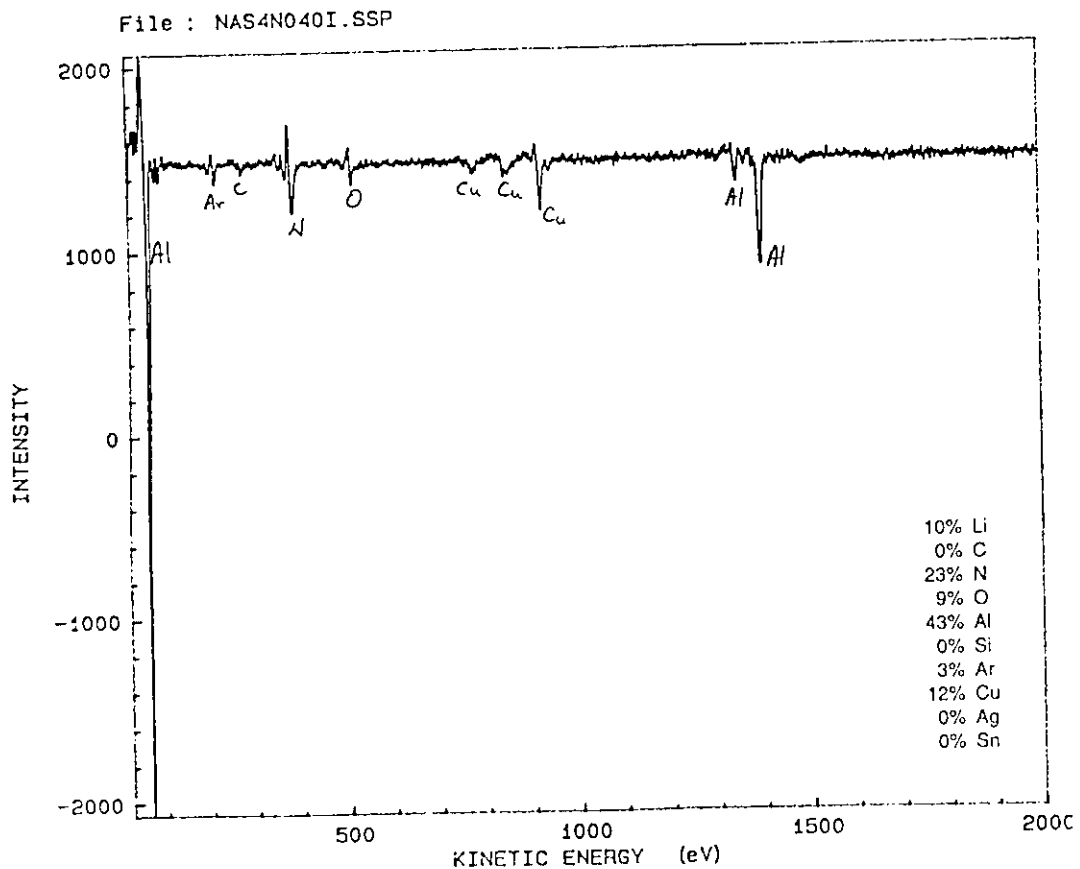
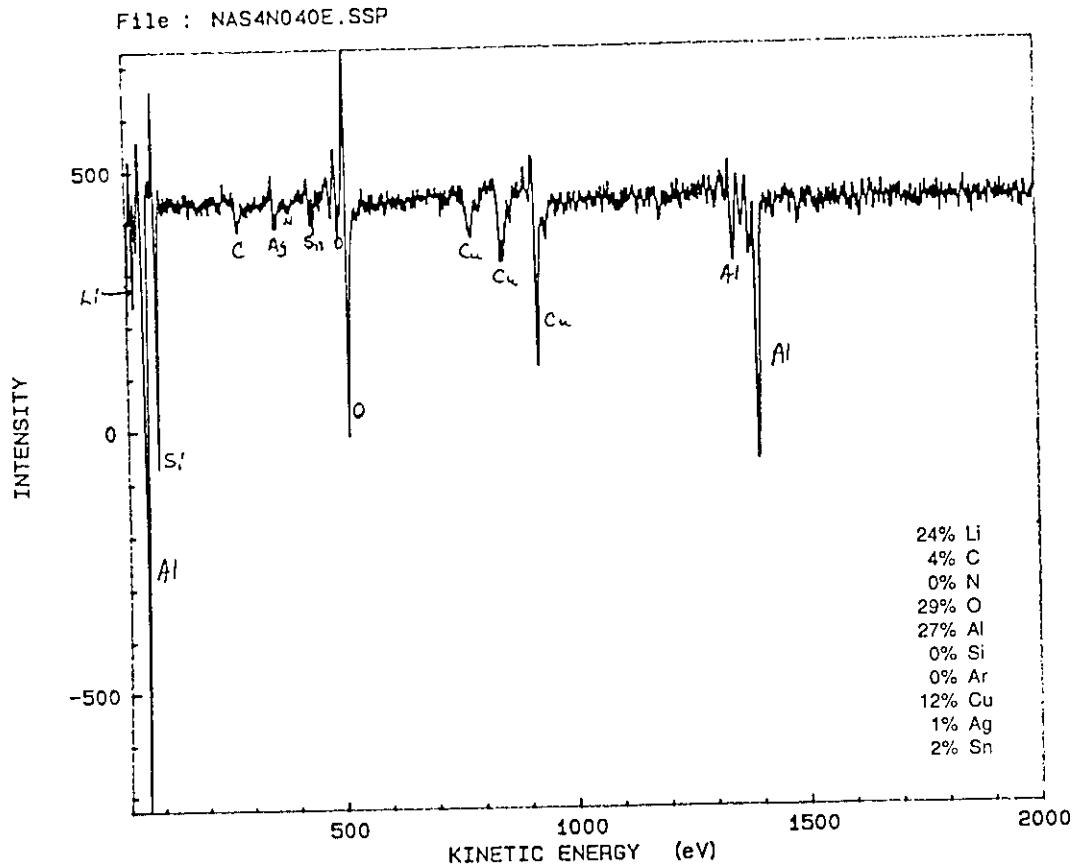


The hot cracks are mixed with ductile rupture fracture as seen in the photograph. Several hot crack surfaces are exposed, those marked D, E, and F were analyzed. Attached are the chemical analysis of the freshly exposed hot crack and the hot crack after sputtering away the top few atom layers of facet E. Other facets gave similar results.

The surface signature of the fresh surface was high in Cu, Li, Si, Sn and Ag. After sputtering the Li, Si, Sn and Ag were removed indicating they existed in the surface layers. Cu persisted indicating it was present in a thicker grain boundary layer. Nitrogen and Ar appeared after sputtering. Argon was implanted in the surface by sputtering. The source of the nitrogen is unknown at this time.

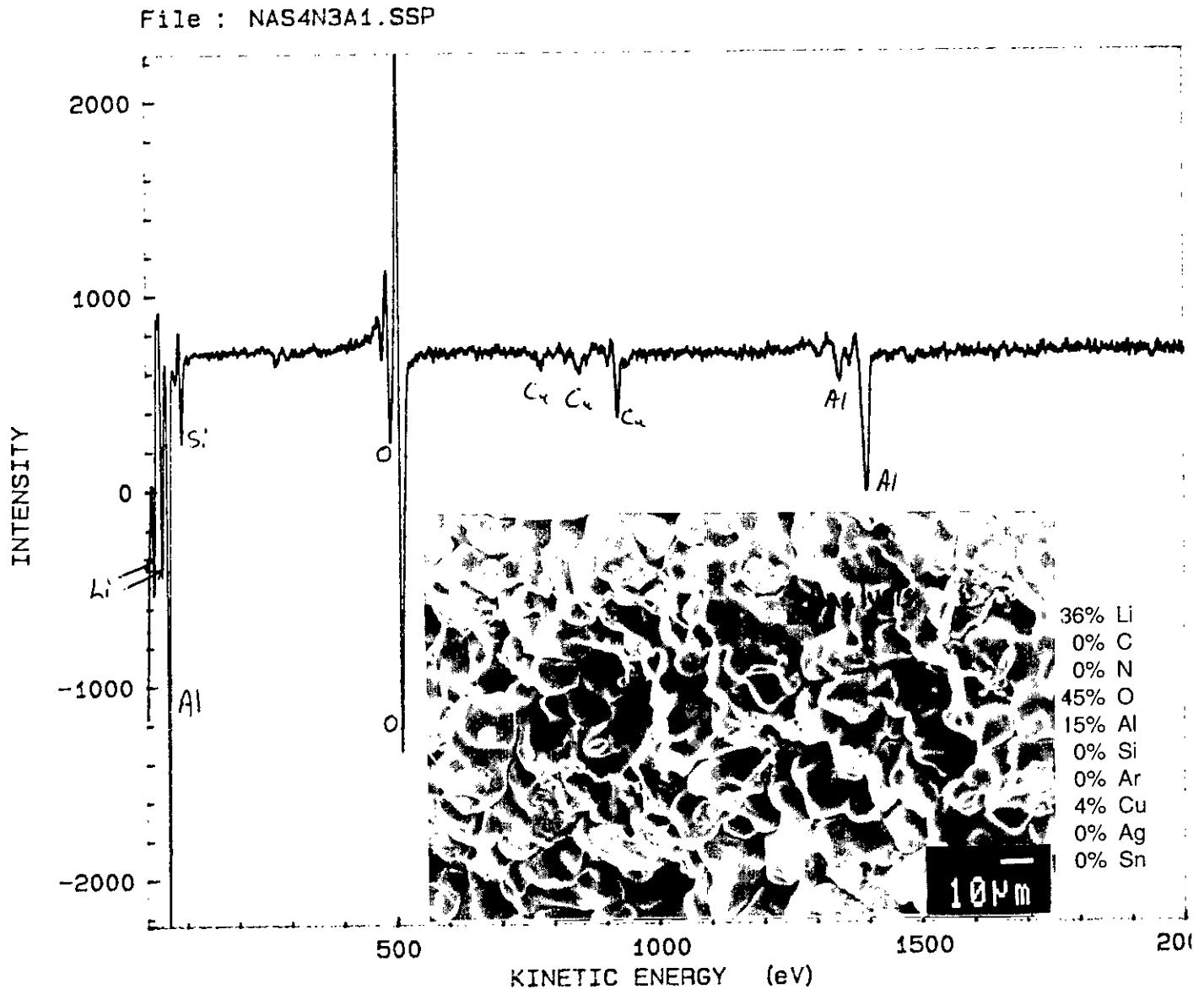
Appendix B.2

SAM spectra of intergranular hot crack surfaces from the recrystallized HAZ facet E.



Appendix C.

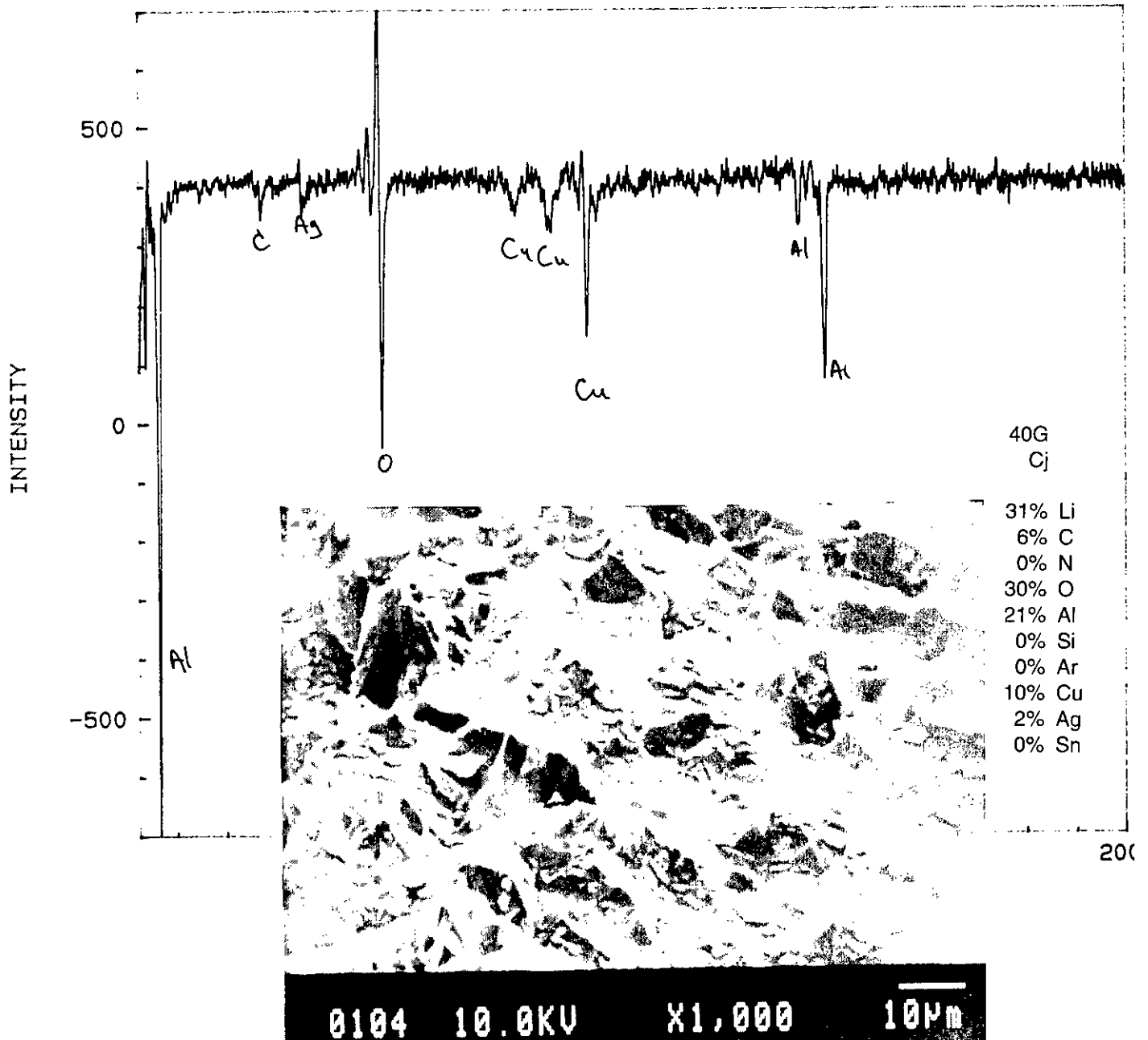
Interdendritic hot cracks exposed in high vacuum. Exposed surfaces had been previously open to air due to the crack being connected to a free surface. Sputtered surfaces are typical of intergranular hot cracks with the exception of a low Cu concentration and the elements Sn and Ag.



The chemistry of the fusion zone hot crack is different from those of the HAZ in that they lack the strong peaks from Si, Sn, Ag and Cu. These are primarily Li rich surfaces which when sputtered quickly loose their Li peak. Once again N is found after sputtering.

Appendix D.

Precipitate exposed by ductile rupture in high vacuum. Typical of several precipitates observed.



The chemical signature of several precipitates observed in both the HAZ and Fusion zone indicate that they are rich in Cu and Li.

Analysis of Weld Hot Cracks in Al-Li Alloy 2195
Ray Thompson

- Q: Joe Pickens (Martin Marietta) Why didn't you measure magnesium via Auger, because magnesium is a mobile element and is associated with segregation in aluminum alloys. Any reason why you did not look for magnesium?
- A: Auger spectroscopy is readily sensitive to magnesium when it is present on the surface being analyzed. We certainly looked for magnesium but its auger signal was not present above the background noise of the instrument. Thus, it can be assumed that its concentration was less than 1 atomic %. It is possible that magnesium was precipitated and not present in the liquid hot-crack film.
- Q: J.P. - My suggestion is go back over the data and look for magnesium, magnesium does lower the solidus temperature and has been associated with a lot of crack formation and aluminum zinc mag welding alloy and it might be worth looking at.
- A: We found that when we looked at these are the Auger spectra there just wasn't magnesium present in the hot crack areas, maybe magnesium was not present in just the ones we looked at.
- Q: John Lippold (Edison Weld Institute) In terms of your fusion zone hot cracking mechanism you propose a mechanism associated with lithium partitioning, but when you sputter a small amount off the surface the lithium disappears and that does not fit very well with a shale type partitioning that would occur during weld solidification. That is to say that lithium should be there and be a much thicker boundary layer particularly if it is tied up as a eutectic. How can you explain the lithium at this point?
- A: Partitioning of solute in the fusion zone to a eutectic would indeed cause a more uniform distribution of Li than found by sputtering in the Auger analysis. I would suggest that Li not only partitioned to the liquid during solidification, but that it continued to be segregated to the liquid film surface both during solidification of any eutectic and after fracture and crack formation.
- Q: J.L. - Typically when you sputter you are removing on the order of nanometers of materials and if you use a standard shale partitioning solidification approach you are going to end up with much thicker layers of lithium rich layers in those regions.
- Q: Roy Crooks (Naval Post Graduate School) I have two quick questions actually, first you refer to this fine grain region near the fusion zone as a heat affected recrystallized zone, how did you conclude to that is a recrystallized region? The other question I had was what was the filler metal you were using?

- A: There is evidence from the Auger analysis that the fine grain zone is recrystallized from the base metal and not a solidified fusion zone. The Auger spectra from the fine grain area had unique copper, tin and silver concentrations not found in the fusion zone. The most likely source of these concentrations is liquated base-metal precipitates, not partitioning from solidification.
- Q: Rich Martikuntz (Applied Research Lab) - I would like to make a comment to that point that gentleman made, a lot of importance is placed on the fine grain region that is assumed to be recrystallized adjacent to the weld and many of the fractures have been traced to that region but I do not believe that it has been definitively described as a fine grain recrystallized zone which would be part of the heat affected zone or very fine solidification structure part of the fusion zone so I think that is still up in the air as far as I am concerned at least from what I have seen.
- Q: Mack Roberts (Martin Marietta) My question is it really important how that zone occurred we know it is grain boundary liquation is causing the problem so the solution is to get rid of the grain boundary liquation regardless of whether that is a recrystallized or part of the fusion zone or part of the heat affected zone or whatever it is.
- A: Rich Martikuntz - Well, the way in which you would get rid of that would be different depending on the mechanism in which it is formed one being solidification partitioning and the other one being by fusion and by liquation. It will certainly effect how you approach it.
- Q: M.R. - Yes, it could but I believe in general the solution is to reduce the heat input and or the cooling rate to get rid of it in either case.
- A: Rich Martikuntz - that seems to be moving in the right direction.

WELD CRACKING SUSCEPTIBILITY OF ALUMINUM-LITHIUM ALLOYS

J.C. Lippold and W. Lin
Edison Welding Institute
Columbus, OH 43212

W.A. Baeslack III and D. Xia
The Ohio State University
Columbus, OH 43210

A. Szabo
Martin Marietta Manned Space Systems
New Orleans, LA

Abstract

The weldability of a number of commercial aluminum-lithium alloys was evaluated relative to susceptibility to both weld solidification cracking and HAZ liquation cracking. The weld solidification cracking susceptibility of alloys 2090, 8090, 2094 and 2195 were evaluated using the Varestraint test. The behavior of alloy 2219 was also investigated to provide a baseline comparison. Using a new assessment methodology based on the brittle temperature range during solidification, alloy 2219 was found to be the most resistant to solidification cracking while alloys 2094 and 2195 were most susceptible.

The HAZ liquation cracking susceptibility of alloy 2195 was determined using the Gleeble hot ductility test. A strong orientation effect with respect to loss of liquation-induced high temperature ductility was observed. Samples transverse to the rolling direction were found to lose on-heating ductility at a much lower temperature than longitudinally oriented samples.

Alloys 2094 and 2195 exhibited a peculiar, equiaxed grain structure along the fusion boundary that was susceptible to cracking. Cracks propagating in the fusion zone would deflect and follow this microstructure preferentially, often resulting in relatively long cracks along the fusion boundary. This equiaxed grain region represents a classic unmixed zone that exists in a narrow region along the fusion boundary.

I. Introduction

The widespread use of aluminum-lithium alloys in aerospace applications will require development of both process technology for joining these materials and a thorough understanding of their welding metallurgy. Considerable research effort has been devoted to the optimization of base metal microstructures and properties of commercial and near-commercial Al-Li alloys. In contrast, little research effort has been directed toward optimizing these materials in terms of weldability.

Aluminum alloys exhibit a propensity for weld metal cracking relative to other alloy systems (such as iron- or titanium-base systems) due to their large solidification temperature range, high coefficient of thermal expansion and tendency to form low melting constituents. These characteristics are also inherent in Al-Li-X alloys and thus suggest that these alloys may be susceptible to cracking during solidification.

Relatively, little work has been published regarding the weld solidification and HAZ liquation cracking susceptibility of Al-Li-X alloys. Cross *et al.* [1] used the Varestraint test to evaluate the solidification cracking susceptibility in autogenous gas tungsten arc (GTA) welds in Al-Li binary alloys containing up to 4.4 weight percent lithium. Their results indicated that a maximum in cracking susceptibility occurred in the composition range from 2 to 3 weight percent lithium.

The weld hot cracking resistance of the soviet alloy 01420 has not been similarly quantified, although it has been reported that this alloy has

"good weldability" [2]. The basis for this assessment involved the evaluation of welds with various filler metal additions and welding processes, but did not address the inherent weldability of the base material.

Martukanitz *et al.* [3] studied the weld cracking sensitivity of alloy 2090-T8E41 in conjunction with various filler materials using the Alcoa "inverted-T" test. Their results suggested that alloy 2090 can be successfully welded using filler alloys 4043, 4047 and 2319, but showed susceptibility to cracking in conjunction with alloy 5356. The inverted-T test is primarily a filler metal test, allowing little dilution by the 2090 base material, and thus did not provide a good measure of the inherent Al-Li alloy weldability.

Weld cracking susceptibility in alloy 8090 was evaluated by Edwards and Stoneham [4] using the Houldcroft test. Their results indicate that the cracking susceptibility of alloy 8090 is comparable to 2014-T6 and superior to 7017-T6 and 7079-T6 when welded autogenously. Gittos [5] reported significant cracking in alloy 8090 during Houldcroft testing. He also observed solidification cracking during gas metal-arc (GMA) welding with 4043 and 2319 filler materials.

More recently, Kramer *et al.* [6] have used the Varestraint test to compare the weld solidification cracking susceptibility of three variants of Weldalite 049 with alloys 2090, 2014 and 2219. Their results show the Al-Li alloys to be less susceptible than 2014 but more susceptible than 2219, with alloy 2090 slightly more susceptible to cracking than the most crack susceptible Weldalite 049 alloy.

Also using the Varestraint test, Lippold [7,8] quantified the susceptibility to weld solidification cracking of alloys 2090 and 8090, and compared this behavior to that of alloys 2219, 5083 and 6061. Both of the Al-Li alloys were found to be more susceptible to cracking than the Li-free alloys. Alloys 2090 and 8090 were found to be more resistant to HAZ liquation cracking.

The purpose of this paper is to evaluate the weldability of Al-Li alloys in the context of recent advances in the understanding and quantification of cracking susceptibility. These advanced techniques provide better insight into the inherent weldability of these materials and the factors that influence solidification and HAZ liquation cracking.

II. Experimental Procedure

The weld solidification cracking susceptibility of alloys 2090, 8090, 2094, 2219 and 2014 was evaluated using the longitudinal Varestraint test [7,9]. The nominal composition of the alloys tested is listed in Table 1. A schematic of the longitudinal Varestraint test is shown in Figure 1. Testing was conducted over a range of augmented strain from 0.25 to 2.0 percent. Welds were produced using the autogenous gas tungsten arc welding (GTAW) process. Welding current, voltage and travel speed were varied over a narrow range in order to produce a weld bead 10 mm wide on the sample surface.

Table 1. Nominal Alloy Composition (wt %)

Alloy	Cu	Li	Si	Fe	Mn	Mg	Zn	Ti	Zr	Ag
2014	4.5	--	0.8	0.7	0.8	0.5	0.25	0.15	--	--
2219	6.3	--	0.2	0.3	0.3	0.02	0.10	0.06	0.15	--
2090	2.7	2.2	0.1	0.12	0.05	0.25	0.10	0.15	0.12	--
2094	4.7	1.3	0.03	0.05	0.05	0.4	0.01	0.02	0.14	0.40
2195	4.0	1.0	0.03	0.05	0.05	0.4	0.01	0.02	0.14	0.40
8090	1.3	2.5	0.2	0.3	0.1	1.0	0.25	0.10	0.12	--

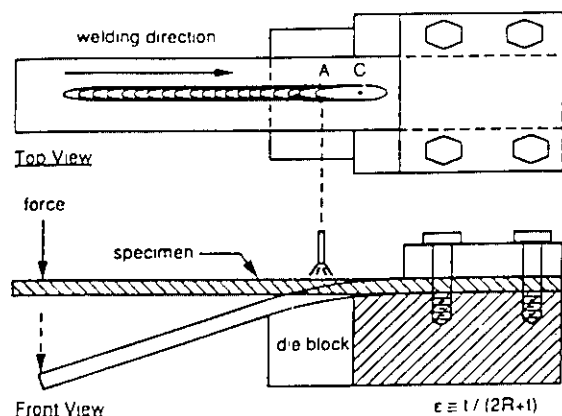


Figure 1. Schematic illustration of the longitudinal V restraint test.

The "saturated" strain was determined for each alloy, where saturated strain is defined as the strain at which the maximum crack distance (MCD) on the surface of the sample is maximized. Testing at strains above saturated strain does not result in any further increase in MCD. The method for evaluating MCD is shown in Figure 2. Weld solidification cooling rates were determined by plunging a thermocouple into the molten pool during the test. By combining the MCD, weld travel speed, and solidification cooling rate, the brittle temperature range (BTR) which defines the temperature range in which cracking occurs was determined.

HAZ liquation cracking susceptibility of alloys 2319, 2090 and 2195 was determined using the hot ductility test. A Gleeble™ thermal simulator was used to conduct the hot ductility tests. Samples were tested on heating at a rate of 55 °C/sec to determine the nil ductility temperature (NDT) and nil strength temperature (NST). Samples were also tested on cooling from the NST to determine the ductility recovery temperature (DRT).

Samples for metallographic analysis were diamond polished through 1 micron and then final polished using 0.05 micron alumina on a vibratory polishing machine. All samples were etched with

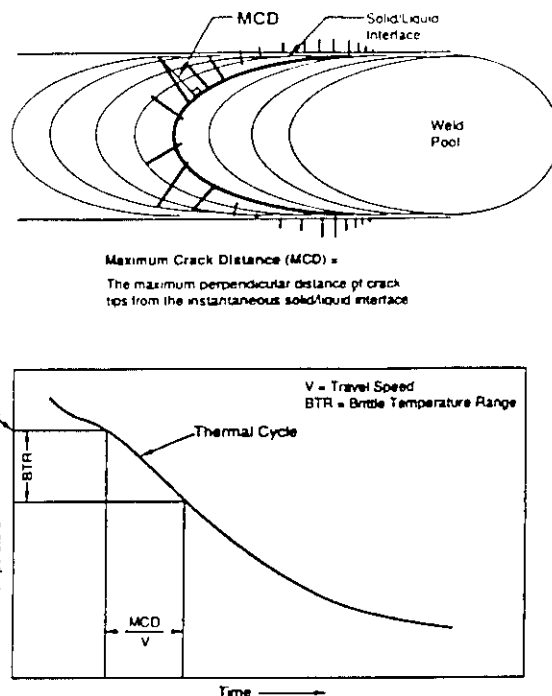


Figure 2. Methodology for determining the brittle temperature range (BTR).

Keller's reagent (2 mL HF, 3 mL HCL, 5 mL HNO₃ and 175 mL H₂O) prior to optical metallographic analysis.

III. Results

Weld Solidification Cracking

Representative weld microstructures from V restraint samples of alloys 2219 and 2195 are shown in Figure 3. The 2219 fusion zone contained considerably more eutectic constituent than 2195. Generally, a relatively thick layer of eutectic was observed along solidification grain boundaries in 2219, as noted by the arrows in Figure 3A. By contrast, the eutectic constituent along solidification grain boundaries in 2195 was extremely thin but continuous.

Weld solidification cracking was restricted to weld solidification grain boundaries in the fusion zone in all the alloys tested. Significant backfilling, or "healing" of cracks was observed in 2219 test samples. Little or no backfilling was associated with cracks in the Li-bearing alloys.

In alloy 2219, fusion zone cracks were observed to propagate into the partially melted zone

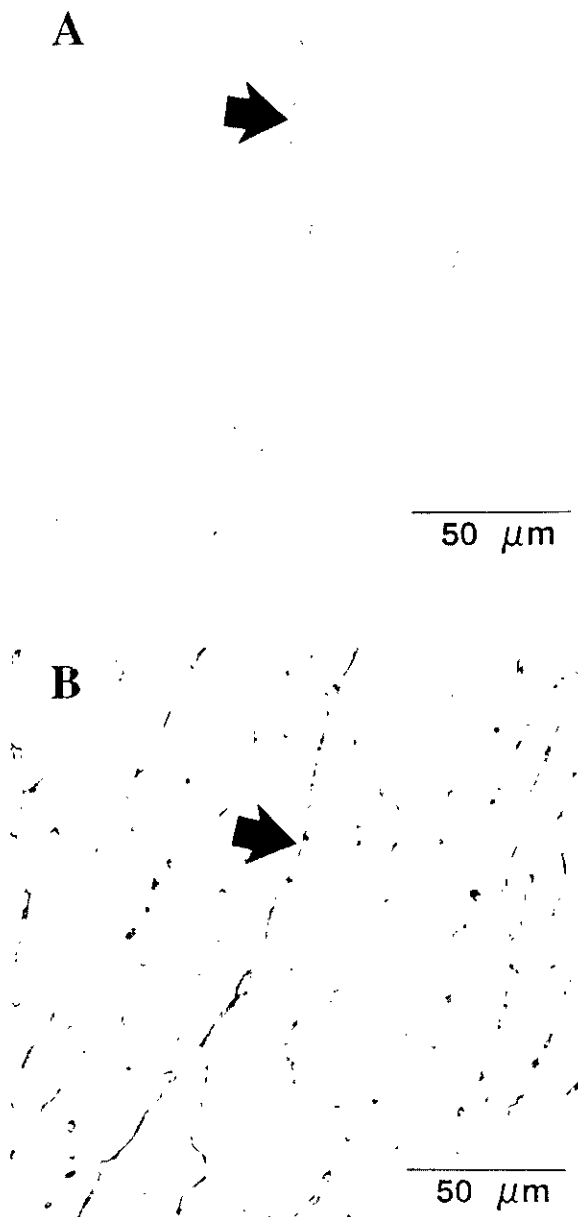


Figure 3. Representative fusion zone microstructure, 400X. A) Alloy 2219, B) Alloy 2195.

adjacent to the fusion boundary along liquated grain boundaries. By contrast, alloys 2094 and 2195 exhibited cracking along a narrow equiaxed grain region at the fusion boundary. These cracks often deviated significantly in order to follow this equiaxed zone, as shown in Figure 4. This equiaxed zone constitutes an unmixed zone (UMZ) along the fusion boundary. By definition, the UMZ represents a stagnant molten boundary layer that does not mix with the rest of the fusion zone. Its nature and origin is discussed in more detail in another paper in this proceedings [10].

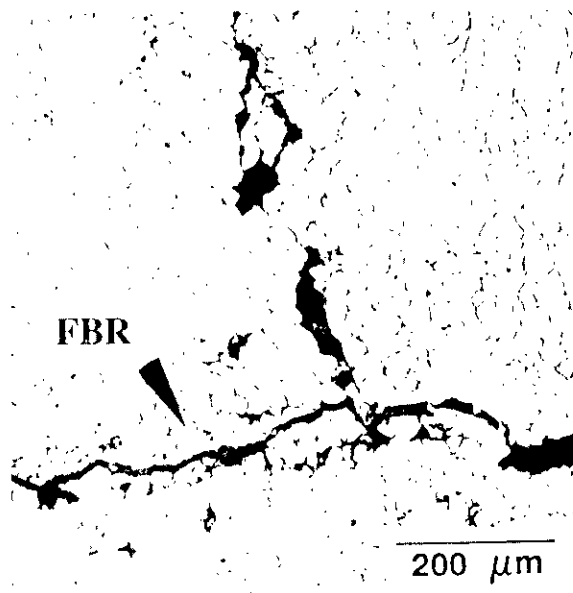


Figure 4. Cracking along the equiaxed zone at the fusion boundary of an alloy 2195 Vareststraint sample, 100X.

The maximum crack distance (MCD) at saturated strain for the alloys tested using the Vareststraint test is plotted in Figure 5A. The BTR, determined based on the MCD, weld travel speed, and cooling rate, is presented in Figure 5B. Note that the weld solidification cracking susceptibility of the Li-bearing alloys is greater than that of alloys 2219 and 2014. The cracking susceptibility of alloys 2195 and 2094 is significantly increased relative to the other alloys due to the cracking along the equiaxed zone. Crack propagation along the fusion boundary was not observed in Vareststraint samples from alloys 2219, 2014, 2090, or 8090.

Hot Ductility Behavior

The hot ductility test provides a measure of base metal HAZ or weld metal liquation cracking susceptibility. By performing on-heating tests to identify the NDT and NST, and on-cooling tests from the NST to determine the ductility recovery temperature (DRT), a liquation cracking "signature" can be developed. On-heating and on-cooling hot ductility curves for alloy 2195 in the longitudinal and transverse orientations relative to the plate rolling direction are shown in Figures 6 and 7, respectively. Note that the on-heating hot ductility in the transverse orientation drops to zero almost 60 °C below that of the longitudinal orientation. The on-cooling behavior is essentially unaffected by orientation effects.

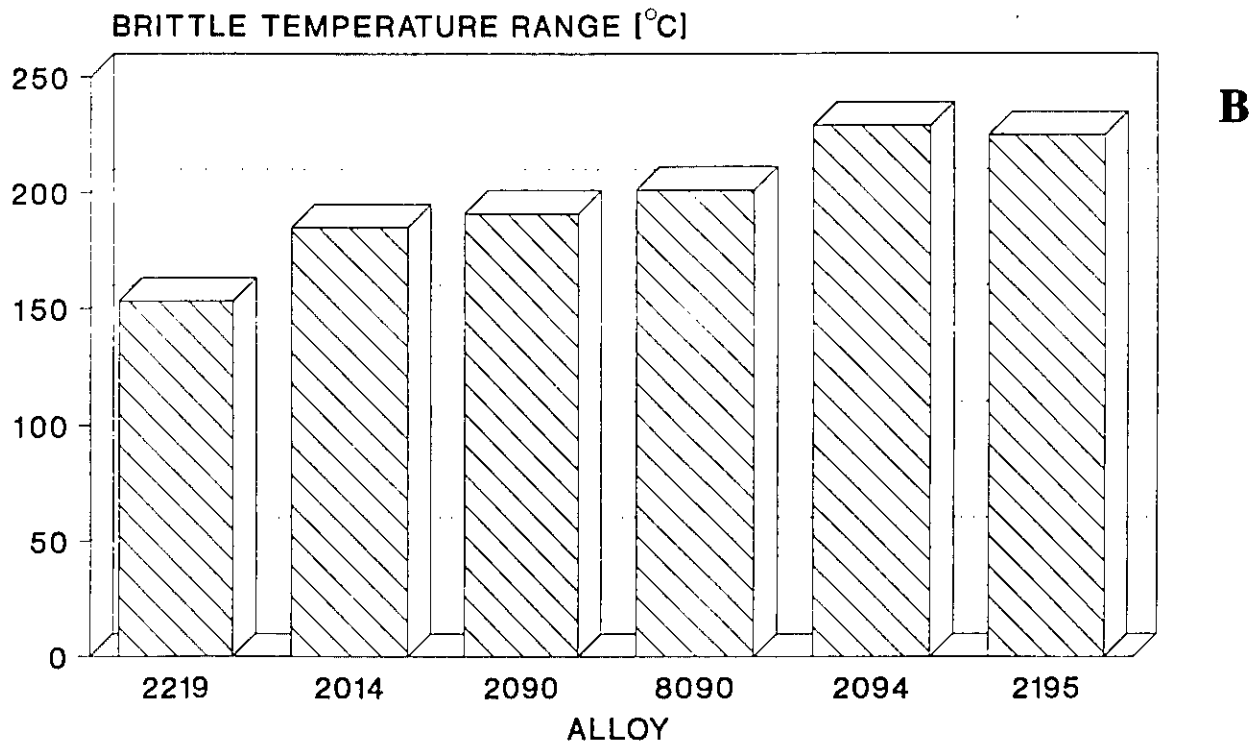
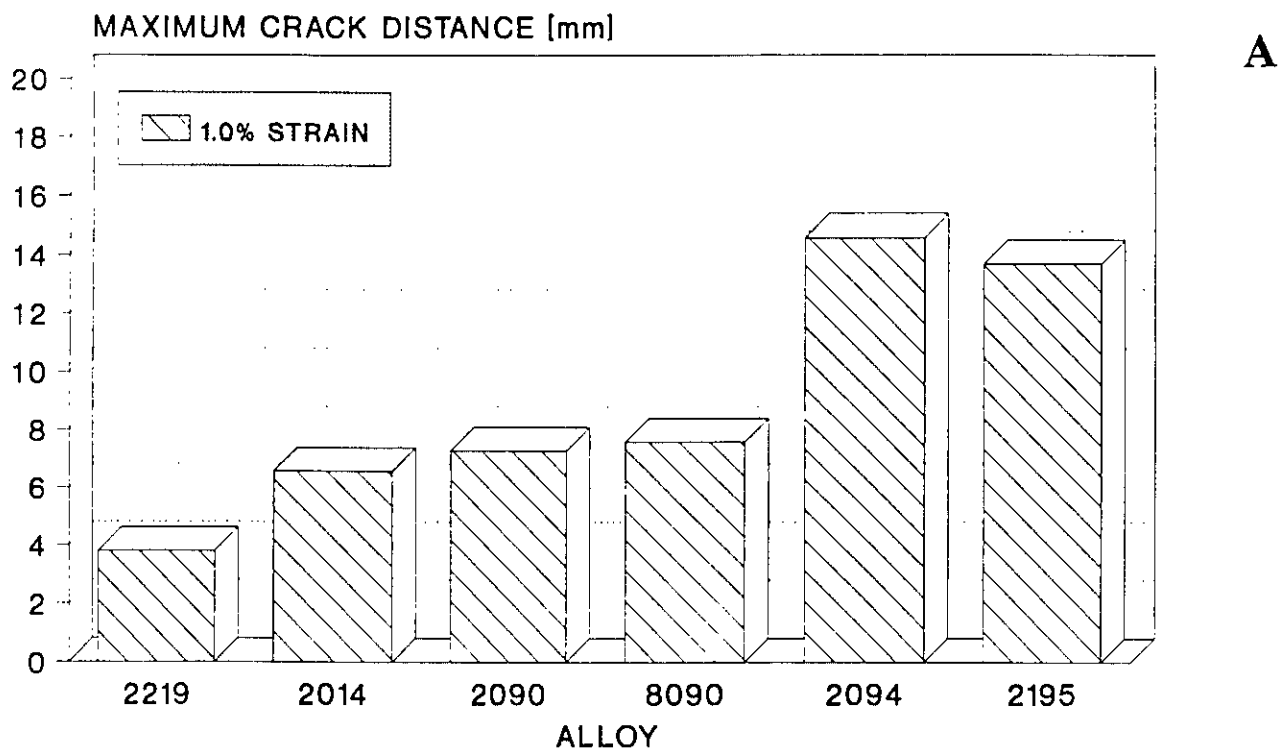


Figure 5. Weld solidification cracking susceptibility in terms of A) maximum crack distance (MCD) and B) brittle temperature range (BTR).

Hot ductility data for alloy 2195 is presented in Table 2 in terms of NDT, NST, DRT and $(NST - DRT_{NST})$. The latter quantity provides a good measure of liquation cracking susceptibility since it defines the range over which liquid films solidify as the microstructure cools. As $(NST - DRT_{NST})$ increases, cracking susceptibility increases. For alloy 2195, this quantity ranges from 135 to 145 °C. For reference, data obtained in a similar manner for alloy 6061 is included in Table 2. Hot ductility data reported in the literature for other alloys is not strictly comparable to these values, since many investigators do not use the NST for a peak temperature during on-cooling tests. As a result, the data may not reflect the true HAZ liquation cracking susceptibility of the alloy.

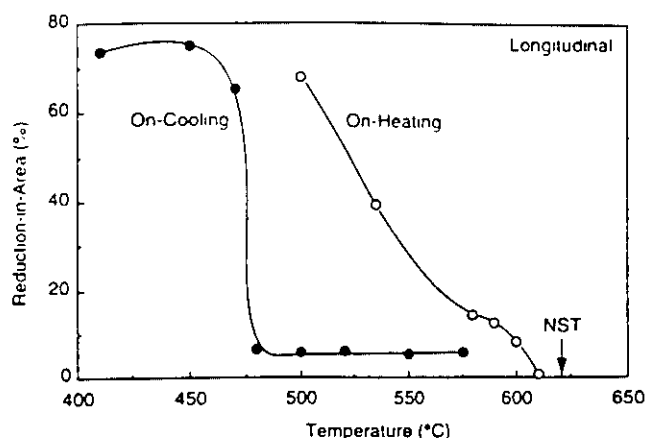


Figure 6. Hot ductility behavior of alloy 2195 in the longitudinal orientation relative to the rolling direction.

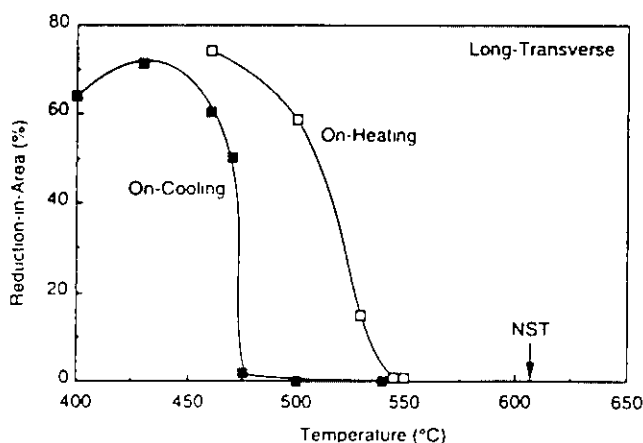


Figure 7. Hot ductility behavior of alloy 2195 in the transverse orientation relative to the rolling direction.

IV. Discussion

Weld solidification cracking in aluminum alloys can be directly related to the magnitude of the BTR. As the BTR increases, the opportunity for stress to build in the system and exceed some threshold for cracking also increases. The BTR is bounded by the non-equilibrium solidification temperature range. For most aluminum alloys, this range is from the alloy liquidus temperature (T_L) to the eutectic temperature (T_E).

Table 2. Hot Ductility Data (°C)			
Alloy/Orientation	NDT	NST	$[NST - DRT_{NST}]$
2195/Transverse	550	610	135
2195/Longitudinal	610	620	145
6061/Transverse	590	632	137

Table 3. Aluminum Binary Alloy Solidification Data			
	Al-Li	Al-Cu	Al-Mg
Partition coefficient k	0.40	0.17	0.42
$(T_L - T_E)$, °C	37	105	133

Alloying elements such as copper, lithium and magnesium partition to the liquid phase during non-equilibrium solidification. In the applicable Al-binary systems, this partitioning drives the composition of the liquid toward the eutectic composition and the final solid to form is of eutectic composition [11,12]. As a result the weld metal solidification range is defined by $T_L - T_E$ and the BTR will be some fraction of this quantity. Values for k , the partition coefficient, and $T_L - T_E$ are provided in Table 3 for the Al-Li, Al-Cu and Al-Mg systems.

Note that the BTR determined for the commercial alloys (Figure 5B), is generally larger than the maximum solidification range predicted by the binary phase diagrams. This suggests that more complex ternary and quaternary systems have an effective solidification range that is much larger than one would predict using binary approximations. This reinforces the utility of using the BTR approach with the Varestraint test for quantifying weld solidification cracking susceptibility.

Although the susceptibility of alloys 2094 and 2195 to solidification cracking appears significantly greater than the other alloys evaluated (Figure 5), the MCD and BTR values may be somewhat exaggerated due the presence of an equiaxed grain structure at the fusion boundary.

Crack backfilling significantly reduces the degree of cracking in 2219. Higher copper content in this alloy, relative to the Li-bearing alloys, promotes the formation of more eutectic liquid during the final stages of non-equilibrium weld solidification. This eutectic liquid, in sufficient quantity, has been shown to be effective in the healing of cracks that form along solidification grain boundaries. The Li-bearing alloys form considerably less eutectic along the solidification grain boundaries, as typified by the microstructure of 2195 in Figure 3B. As a result, the thin liquid film tends to promote cracking but is not present in sufficient quantity to effect any healing.

The hot ductility behavior of 2195 provides some insight into the potential HAZ liquation cracking susceptibility of this alloy. It is interesting to note from Figure 5 that although orientation has a significant effect on the on-heating hot ductility behavior, there is no effect on cooling. Both the longitudinal and transverse orientation has a DRT of approximately 475 °C. This suggests that developing a continuous liquid film network on heating is orientation dependent, but once this network forms the recovery of on-cooling ductility is dependent on the solidification temperature of the liquid grain boundary film.

It is important to note that an equiaxed grain structure, such as that observed along the fusion boundary in the alloy 2195 Varestraint samples, was not observed in the hot ductility samples. Metallographic examination of samples heated to

the NST, a temperature approximating that at the fusion boundary, did not reveal an equiaxed structure reminiscent of that in welded samples.

In closing, it should be pointed out that the formation of an equiaxed grain structure along the fusion boundary in alloys 2094 and 2195 significantly increase the apparent weld solidification cracking susceptibility of these alloys. It is apparent based on careful metallographic examination of welded samples and an inability to simulate this microstructure in the Gleeble, that the equiaxed zone represents a region that has been completely melted and resolidified. It is proposed that this region represents a type of unmixed zone. It is essential that this zone be better understood in order to control and mitigate its effect on weld cracking in Li-bearing aluminum alloys.

V. Conclusions

1. The weld solidification cracking susceptibility of Al-Li alloys was higher than that of other commercial 2000-series alloys, such as 2219 and 2014.
2. Weld metal cracking was associated with eutectic films along solidification grain boundaries. Little backfilling, or crack "healing", was observed in the Al-Li alloys.
3. Cracking in alloys 2094 and 2195 was also observed along an equiaxed grain structure at the fusion boundary. This type of cracking significantly increased the apparent susceptibility of these alloys.
4. Orientation relative to the rolling direction of alloy 2195 plate was found to influence the nil-ductility temperature on heating with transverse samples exhibiting a 60 °C decrease relative to longitudinal samples.
5. The recovery of ductility on cooling from the nil-strength temperature was not influenced by orientation, but was related to the solidification temperature of grain boundary liquid films.

References

1. Cross, C.E., Olson, D.L., Edwards, G.R. and Capes, J.F., **Aluminum-Lithium II**, eds. T.H. Sanders and E.A. Starke, TMS-AIME, Warrendale, PA, pp. 675-682, 1983.
2. Mironenko, V.R., Estifeev, V.S. and Korskunkova, S.A., **Welding Prod.**, **24**, pp. 44-50, 1974.
3. Martukanitz, R.P., Natalie, C.A. and Knoefel, J.O., Alcoa Technical Report "The Weldability of 2090 - An Al-Li-Cu alloy", 1985.
4. Edwards, M.R. and Stoneham, V.E., **Aluminum-Lithium IV**, eds. T.H. Sanders and E.A. Starke, TMS-AIME, Warrendale, PA, p. 285-293, 1987.
5. Gittos, M.F., Welding Institute, Abington, England, 1989, private communication.
6. Kramer, L.S., Heubaum, F.H. and Pickens, J.R., **Aluminum-Lithium V**, eds. T.H. Sanders and E.A. Starke, Materials and Component Engineering Publications Ltd., Birmingham, 1989.
7. Lippold, J.C. **Aluminum-Lithium V**, eds. T.H. Sanders and E.A. Starke, Materials and Component Engineering Publications Ltd., Birmingham, pp. 1365-1375, 1989.
8. Lippold, J.C. **Advances in Joining Newer Structural Materials**, Proc. IIW Conference, Montreal, 1990.
9. Savage, W.F. and Lundin, C. **Welding Journal** **44**(10), pp. 433s-442s, 1965.
10. Hou, K.H., Baeslack, W.A., Lippold, J.C. and Szabo, A. **Proc. of 1994 Conf. on Advanced Earth-to-Orbit Propulsion Technology**.
11. Lippold, J.C., Savage, W.F. and Nippes, E.F. **Welding Journal** **56**(6), pp. 171s-178s, 1977.
12. Borland, J.C. **British Welding Journal** **7**(8), 1960.

Acknowledgements

The authors wish to recognize the financial support of Martin Marietta Space systems, the Army Research Office, and Edison Welding Institute (EWI). Special thanks are extended to Mr. John Rovder, III, of EWI for preparing the metallographic samples.

Weld Cracking Susceptibility of Aluminum-Lithium Alloys
John C. Lippold

- Q: Mack Roberts - John is it possible to have that equiaxed zone without the liquation of the grain boundaries?
- A: Basically what is happening is that you have got a stagnant layer and there appears to be some type of heterogeneous nucleation phenomena that is going on and so basically you are nucleating and solidifying similar to what happens in a weld metal and at the very end of solidification you are ending up with a liquid film and eventually forming some eutectic. I mean if you look at these equiaxed zones what you find is the eutectic constituent that completely circles them and so liquation is inherent I mean we have done some looking at the composition of these eutectic and they appear to be similar to what you see in the weld metal and as a result of that the melting temperature the remelting temperature or the solidification temperature in that region is going to be fairly low and that is one of the reasons why and it is lower than what you get in the adjacent parent material and as a result of that it sort of drives the cracking that you see.
- Q: M.R. - The reason I ask the question is I thought that in some of the DOE welds we say equiaxed grains with very minimal amounts of grain boundary liquation.
- A: You have to be careful in looking at welds in terms of defining what you call an equiaxed zone. Because you can take a section through a weld, a transverse section and you can look out here in the weld metal and see something that looks equiaxed until you section it and look in a different dimension. And what you find is that it is a long cell or dendrite that is growing right out at you whereas in the equiaxed zone you can look at any dimension and they look exactly the same they are truly equiaxed and so you need to be careful in terms of what you are defining as equiaxed.
- Q: M.R. - Well, I guess the whole reason for my question is that I think that equiaxed is a bad term for that because equiaxed grains in themselves are desirable but if they have grain boundary liquid or eutectic then they are undesirable so it is really the grain boundary position rather than the shape of the grain is the problem so people get confused when you say equiaxed they think anytime they see an equiaxed region is bad when actually it is good unless you have the liquation in grain boundary.
- A: As I said we do not have all of the answers and we really do not understand why this microstructure behaves the way it does I mean why a crack coming out of the fusion zone is willing to turn 90 degrees and go along this equiaxed zone rather than plowing through that and going through the PMC, that part is still a mystery.
- Q: MR - Don't you agree that region could be better named so it was not misleading or implied?

A: Yes, we will call it an unmixed zone.

Q: MR - Just call it a grain boundary liquation zone?

A: But you have grain boundary liquation in the partially melted zone right next to it. If you look at the partially melted zone right next to the equiax zone you would have liquation in there too. It is just that the orientation is different. You have these elongated or pancake grains but they are all liquid films along those grain boundaries.

Q: M.R. - Well that is bad too, any place you have it is bad. It does not make any difference whether it is grain shaped.

A: Well, but you have got the geometry of the system going for you. I showed the difference between longitudinal and longitudinal transverse hot ductility behavior and basically you are pulling in the longitudinal direction when you are straining these welds and so point in fact the orientation is advantageous to you whereas in the equiaxed region you know the grains are the same shape in all dimensions and that may be part of the problem, but I am not pretending to know all of the answers at this point in time.

Q: M.R. - I just think that is bad terminology.

A: O.K., we will call it an unmixed zone.

Q: Joe Pickens (Martin Marietta) - I was little surprised to see your hot cracking data with the ranking of the alloys and showing the 2195 and 2094 so much inferior to 2014 and on par with 6061 which is kind of at odds with some of the real world experience our welders in our divisions have reported. I know our machine shop for example who are not skilled welders everytime you give them 6061 you get back a cracked structure and they have never hot cracked a 2195 and I remember a statement by Larry Lackle who is the ALS program manager of so many hundreds of welds of 2195 he never saw any hot cracks. I was just wondering when you do your vareststraint testing you have this mandrel if you could put different mandrels in to get different amounts of strain you think you could perhaps change the ranking of these results by using different mandrels and maybe the mandrels used is not the one that makes the welding experience?

A: Well you have a real difficulty in all weldability testing is relating the actual strain conditions in your weldability test to what happens in service. And we are not trying to do that what we are trying to do is come up with a metallurgically significant parameter in order to rank these things. In different conditions you are going to have different levels of restraint, so you can have a very cracked susceptible microstructure but you fixture it such or you weld it in such a manor that the restraint is below some critical level and it is not going to crack. In making manual welds you know there is

instantaneous feedback there and so a manual welder can adjust things that will influence restraint from one material to another. So again the difficulty here you have a microstructure factoring and you have a restraint factor and we are working on trying to quantify this but coupling these two is an extremely difficult problem. I wanted to show you one thing though that eluded to the fact that this equiaxed zone sort of screws things up in terms of interpreting the data. This is a different data set that includes 2319 to 2195 weld and 4043 to 2195 these are basically VPPA welds. Where you are getting various levels of dilution of 2195 by the 4043. This is a weld for instance made at 25 inches per minute or wire feed speed at 25 inches per minute and this is a wire feed speed of 100 inches per minute. So this one has more 4043 in it and what we have done here is subtracted off the cracking that occurs along the fusion boundary and now we are only looking at cracking that occurs in the weld metal. And what you see is that the cracking susceptibility drops significantly if we forget about what is happening at the fusion boundary region and it follows the trend that you expect, that is that as you get more 4043 into the system the cracking susceptibility decreases in the same with 2319.

Q: Have you done much with 2014 and 2219?

A: Well 2014 and 2219 do not have any fusion boundary cracking and so the data I showed previously would compare very nicely with this. But we have another problem here in that because the fusion boundary region of the unmixed zone wants to crack so readily that it immediately reduces the restraint in the rest of the weld and maybe driving these values down somewhat artificially low. So the approach we are now going to be taking is we are going to be doing a transverse restraint test which loads the weld in the other dimensions so you make a weld in this direction and load it in this manner and in that way we can keep the crack out of the unmixed zone and we can keep it in the weld metal, and that is going to give us some better BTR data. We are in process of doing some of those now.

Comment: And again to back up what Joe is saying 2195 we can weld without any filler material and all homogenous welds and there is no center line cracking at all which is generally what you see in hot crack sensitive alloys such as 6061.

Q: On this orientation dependent hot crack data from the glebol, don't you think that is why the cracks along unzipped between the fusion zone and the base metal, is that do you have that orientation change as you come out into the plate and your stresses are such that it does not it wants to unzip it without penetrating into the base metal?

A: In the transverse restraint samples it does, that is right because if they way most of our transverse restraint samples are oriented in a longitudinal orientation so that crack coming out sees that transverse orientation and perhaps it helps that crack to turn down that boundary. If you look at some of these VPPA welds were they have gotten some cracking due to the E-stops where you get a solidification crack that comes out and

hits that boundary. Often the orientation of the melted zone is oriented in this direction and so it is hard to understand why that crack instead of plowing right through the equiaxed zone to get out of the partially melted zone does not but essentially turns 90 degrees, so orientation does not explain all of it.

Q: The other thing with this equiaxed or unmixed zone, you can hand me a hot crack I do not care you do not have to tell me what zone it is from but I can tell you it comes from the dendritic fusion zone or from this equiaxed zone just by the chemistry of the liquid film on it that I see in the Auger. It is very consistent it is always consistent differences between the level of copper in the two zones that shows up on the hot crack surface and also some of the other elements that we tend to associate more with equilibrium grain boundary diffusion like silver and in this case there was tin we also found. So if it is solidification it has to be a different solidification mechanism that explains that difference in partitioning of the elements to the surface.

A: You are partitioning the same elements, I mean you are partitioning certainly copper. Lithium is obviously fairly hard to detect but we are in the process of looking at some of those issues.

Q: Well I do not have any trouble with detecting lithium, but the copper levels are considerably different in the two zones.

A: The copper levels?

Q: Yes.

A: Well, again we are dealing with a shingle type partitioning and depending on the solidification conditions the temperature gradient the solidification rate etc. you can potentially get different levels of copper although you should be getting essentially to the same eutectic composition all things being equal so I would be surprised if the eutectic in the weld metal and the autogenous weld versus the unmixed zone is significantly different.

Q: If the unmixed zone was just a largely melted the high part of the mushy zone couldn't your stirring also strip off those grains that have long, or as you say zero strength? Couldn't those grains also be stripped off? The data from NIST on recrystallizing these things says that recrystallization temperature is about the same as the solvus temperature so you should not see any recrystallization until you get into the mushy zone.

A: Well, and that is why we did the glebo test, basically we took the sample up as high as we could in the glebo and then it melted and it won't form an equiaxed zone. Now if you take it that next step, if you take it to 645 degrees C the sample literally melts or blows up in the glebo and when you look at that melt zone it is equiaxed. So,

based on what we have seen using some fairly simple experiments I find it very hard to believe that it is a PMZ or a heat affected zone type phenomena and the fact at when you start looking at alot of different weld cross sections you can see it here and not over here so there is something going on with the fluid dynamics is getting rid of it. From partially melted zone heat affected zone standpoint you have essentially got the same temperature gradient on each side of this weld, why is it here and why is it not over here in the same temperature field? From the standpoint of recrystallization I have a hard time explaining how that can happen.

A: Yes, John it is a very interesting concept and everything appears to make sense I might add the addition of lithium to molten aluminum has a known significant effect on changing the surface tension of that liquid metal which could be responsible for that complex fluid dynamics that you are saying.

Q: Joe Pickens (Martin Marietta) We spoke half a dozen or 8 years ago about hot cracking and we looked at this reference together it was Martin or Meister or something where he summarized all the old hot cracking work in the 60's, do you know the reference I mean?

A: Yes.

Q: J.P. - And if I am not mistaken the maximum hot cracking susceptibility in the aluminum copper binaries was somewhere around 3 or 4 in that study weight percent.

A: Yes, somewhere in that regime.

Q: J.P. - Becase I noticed when you showed your plot earlier you had the maximum at 0.4 and it was called normalized composition what does that mean?

A: It is normalized to the maximum solid solubility which is 9.9 copper.

Q: J.P. - So that is 4 over 9.9, Ok that is consistent.

MICROSTRUCTURAL CHARACTERIZATION OF 0.5-INCH WELDED ALUMINUM-LITHIUM ALLOY

J.H. Sanders and B. Panda
IIT Research Institute/Metallurgical Facilities
George C. Marshall Space Flight Center
Marshall Space Flight Center, AL 35812

ABSTRACT

An investigation was performed to relate microstructure to mechanical properties for 0.5-inch welds tensile tested in air, liquid nitrogen (LN₂), and liquid hydrogen (LH₂). The study used three-pass welds in the flat position, made from two alloys in three combinations (2195/2195, 2195/2219, and 2219/2219) using variable polarity plasma arc welding (VPPA) with 2319 filler wire.

This paper discusses intergranular failure in 2195/2195 specimens, characterized by cracking that initiated at the root corner and ran toward the crown along the fusion line, sometimes extending into the weld pool. No direct correlation could be established between the fracture path and mechanical properties. When Cu content was profiled in a 2195/2195 specimen, nonuniform Cu segregation was seen across the weld pool. Such patterns indicate that grain boundary phases varied across the weld, yielding regions susceptible to crack propagation. Many specimens also contained porosity (with diameters on the order of several hundred micrometers) near the fusion line, and large amounts of porosity correlated with low values for ultimate tensile strength (UTS).

I. INTRODUCTION

At present, the Space Shuttle's external fuel tank is primarily constructed from Al-Cu alloy 2219. The next generation tank is the Super Light Weight Tank (SLWT), which will be primarily constructed from Al-Li 2195. Thanks to the increased modulus and strength (as well as reduced density) of 2195, the SLWT should be approximately 8000 pounds lighter than the current tank. This weight advantage is critical to the deployment of Space Station components.

The SLWT design calls for sections of 2195 to be joined to each other, as well as to sections of 2219. Mechanical properties and fracture mechanics data are discussed in detail elsewhere.^[1,2]

This paper focuses on the microstructure of welds that were used to join 0.5-inch-thick sections of 2195, using 2319 filler wire. The results will be discussed in light of mechanical property data in the longitudinal direction for all three weld combinations (2195/2195, 2195/2219, and 2219/2219).

II. EXPERIMENTAL PROCEDURE

Test specimens were provided by Martin Marietta Manned Space Systems, using variable polarity plasma arc (VPPA) welding as described by Nunes *et al.*^[3] These welds joined 2195 to 2195 (2195/2195), 2195 to 2219 (2195/2219), and 2219 to 2219 (2219/2219). The first pass was autogenous, while the second and third passes used 2319 filler wire. The plasma gas was 100 percent argon, and the torch shield gas and root side purge gas were 100 percent helium. Table I gives nominal chemistry values for the alloys.

Table I. Chemical Composition of Al Alloys

Material	Alloys		
	2195	2219	2319
Ag	0.40	-	-
Al	R	R	R
Cu	4.0	6.30	6.30
Fe	0.03	-	-
Li	1.00	-	-
Mg	0.40	-	-
Mn	-	0.30	0.30
Si	0.03	-	-
Ti	0.01	0.06	0.15
Zr	0.14	-	0.17

III. TEST RESULTS

Base Metal

The base metal microstructures were recorded for 2195 and 2219 prior to welding. In the fully heat treated condition, 2195 base metal had a microstructure that consisted of elongated grains stacked onto each other. As viewed in the longitudinal-short transverse direction, the grain boundaries ran parallel to the rolling direction. (See Figure 1a.) Higher magnification revealed clean grain boundaries with no visible second phases. The 2219 base metal had a microstructure that contained more equiaxed grains. (See Figure 1b.)

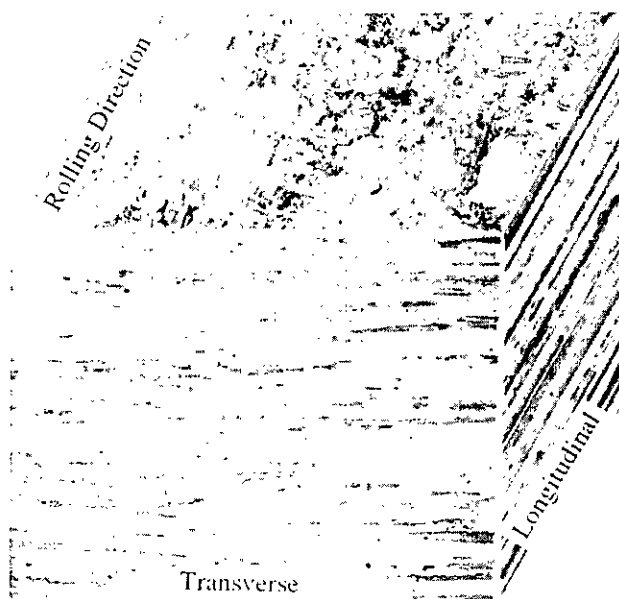
Weld

A typical 2195/2195 butt weld is produced by placing two plates together, with both short-transverse planes in contact with each other. Such a weld usually contains several zones, with a fusion line separating the weld pool from the heat affected zone (HAZ).

The partially melted zone (PMZ) exists in the HAZ on the base metal side of the fusion line. The PMZ retains the directionality of the rolled material and yet has a continuous second phase at the grain boundary. Microprobe analysis indicated that this phase had an Al/Cu ratio of two, which corresponds to θ (Al_2Cu) for the binary Al-Cu system. However, microprobe analysis cannot detect the presence of Li, so this technique cannot be used to rule out the formation of more complex ternary phases. In previous work,^[4] the PMZ did not significantly mix with filler metal. Therefore, the second phase at the grain boundary was probably formed by partial melting of grains in the base metal, with solidification during the post-weld quench.

The equiaxed grain zone (EQZ) exists immediately adjacent to the PMZ on the weld side of the fusion line. The EQZ contains equiaxed grains with dimensions near those of the grain thickness in the PMZ. The EQZ is not always present in 0.5-inch specimens. This region (which may form on initiation sites from resolidification of molten fragments of base metal) usually has continuous second phase along the grain boundaries.

The cellular dendritic zone (CDZ) is a dendritic structure that forms in the weld interior, due to solidification after the torch passes. The CDZ is characterized by large grains, with semicontinuous second phase present in grain boundaries and grains.



(a)



(b)

Fig. 1. Base metal microstructure of (a) 2195 and (b) 2219. (Magnification 50x)

Mechanical Properties

Ultimate tensile strength (UTS) was similar for 2195/2195, 2195/2219 and 2219/2219 at the three temperatures tested. The base metal properties indicated a larger reduction in strength in 2195/2195 than in 2219/2219. As temperature decreased to LH₂ levels, UTS increased for all welds. (See Figure 2.)

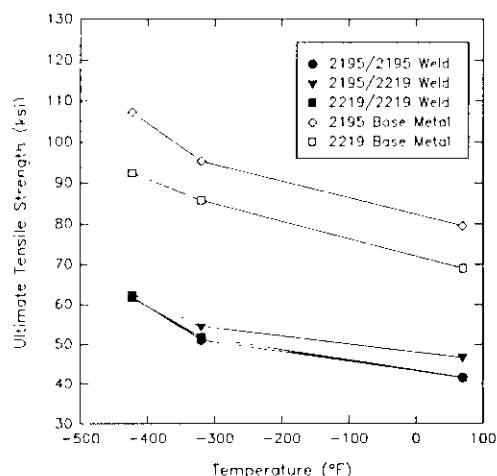


Fig. 2. Ultimate tensile strength for 2195/2195, 2195/2219, and 2219/2219 welds.

Yield strength (YS) was similar for all welds in that YS increased as temperature decreased. Yet each weld type had a different level of YS, with 2195/2195 > 2195/2219 > 2219/2219. (See Figure 3.)

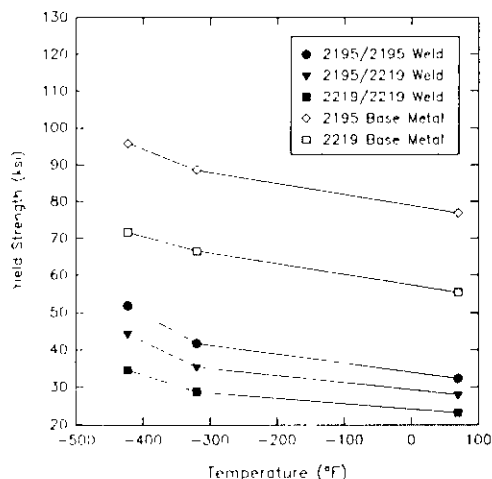


Fig. 3. Yield strength for 2195/2195, 2195/2219, and 2219/2219 welds.

Elongations were made using a 1-inch gauge length. These measurements indicated that 2219/2219 was the most ductile weld at all temperatures. At lower temperatures, 2195/2219 was more ductile than 2195/2195. At ambient temperature, 2195/2219 and 2195/2195 had approximately the same ductility. All weld elongations decreased as temperature decreased. (See Figure 4.)

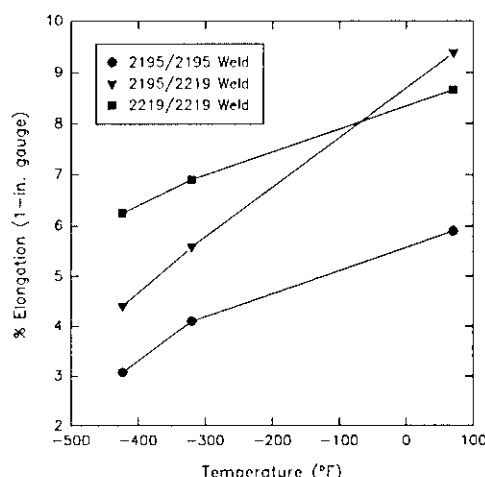


Fig. 4. 1-in. elongations for 2195/2195, 2195/2219, and 2219/2219 welds.

Metallography and Fractography

Similar microstructures were seen in all 2195/2195 specimens at all temperatures. All fractures progressed from a root corner, either propagating directly along the fusion line or going into the CDZ and returning to the fusion line. All fractures were intergranular within the first pass region, failing on one side of the specimen only. Final fracture of most specimens occurred through the second and third passes, normal to the stress direction in a transgranular-ductile fashion.

Figure 5 shows a typical 2195/2195 fracture made at ambient temperature. The fracture apparently initiated in the root corner, since some cracking was observed at the opposite root corner (not shown) and no cracking was seen in the crown regions. The crack propagated into the center of the weld, then went back to the fusion line until it encountered the second pass boundary. Final fracture extended through the second and third passes.

This fracture was examined at a higher magnification. (See Figure 6.) In the root corner, the crack propagated into the weld through the EQZ. The primary crack followed grain boundaries in the CDZ and returned to the fusion line, where no EQZ was evident. Numerous secondary cracks are visible within the weld, due to the separated grain boundaries.



Fig. 5. Optical micrograph showing typical 2195/2195 fracture path made at ambient temperature. (Magnification 5x)

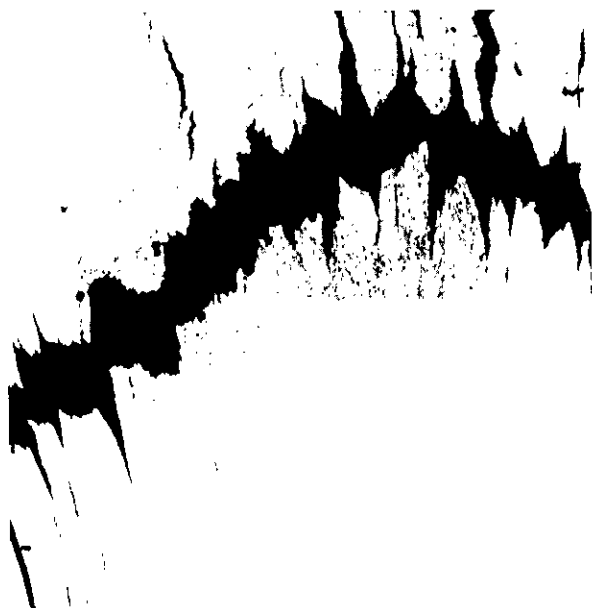


Fig. 6. Optical micrograph of specimen seen in Fig. 5, root corner with intergranular fracture and secondary cracks. (Magnification 50x)

Fractography was performed on the 2195/2195 weld. The root corner revealed a pancake structure of the base metal at the crack initiation site, with extensive porosity throughout the first pass. (See Figure 7.)



Fig 7. Fractograph of specimen seen in Fig. 5, root corner with pores on fracture path. (Magnification 20x)

At higher magnification, the planar structure is seen to contain separated grains that have a smooth surface and grain boundaries with porosity of up to $70\text{ }\mu\text{m}$. (See Figure 8.) A location on the fracture surface near the EQZ is shown in Figure 9. At higher magnification, brittle-intergranular fracture is evident around large spherical pores. Cu-rich second phase is also seen along the grain boundaries of the fine-grained structure. The microstructure near the crown corner (within the diluted filler metal region) is ductile, with only minor amounts of porosity visible.

Other fractographs illustrated the ductility of grains in the HAZ. (See Figure 10.) Figure 10a shows dimpling on the surface of a fractured grain in the root corner of a 2195/2195 specimen tested in LH_2 . Figure 10b shows dimpled structure on a fracture in the CDZ. These fractographs demonstrate that the matrix material is ductile after welding, but the grain boundaries are brittle. In Figure 11, a 2195/2195 specimen fractured in LN_2 shows cracking of the second phase in grain boundaries near the fracture path.



Fig. 8. Fractograph of fracture surface at root corner, showing delamination and porosity. (Magnification 20x)

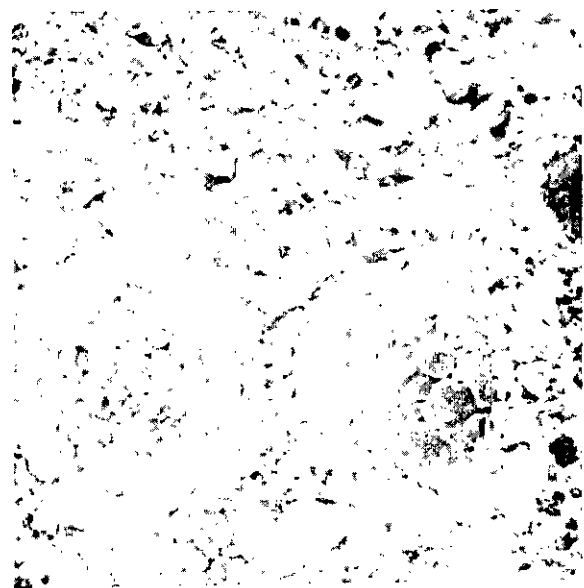
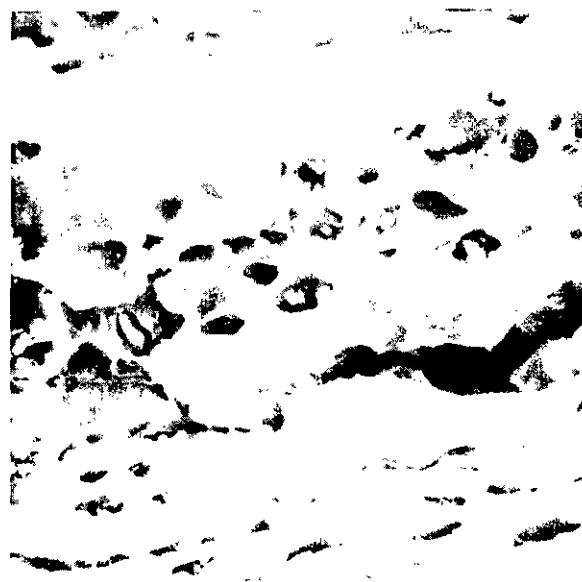
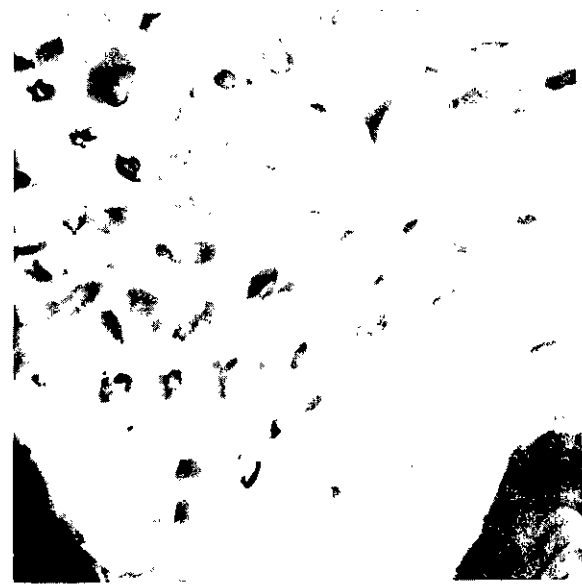


Fig. 9. Fractograph of fine-grained equiaxed region in fracture, showing porosity. (Magnification 200x)



(a)



(b)

Fig. 10. Fractographs showing ductility of the matrix in localized regions on the fracture surface where transgranular fracture occurred, (a) root corner and PMZ and (b) CDZ. (Magnification 1kx)



Fig. 11. Micrograph of cross-section of a fracture surface, showing brittle nature of the Cu-rich second phase. (Magnification 4kx)

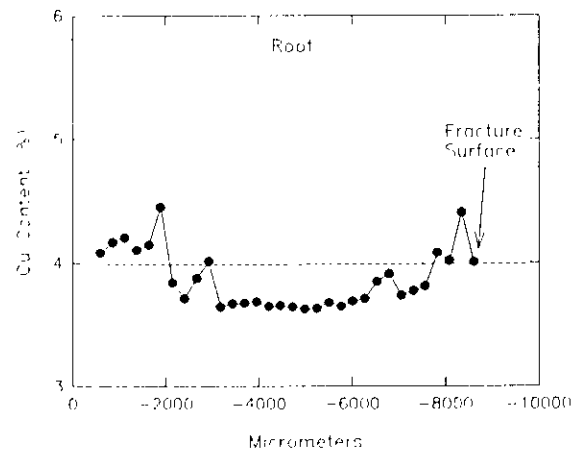
Cu Concentration Profile

To determine segregation within the first pass of a weld, electron microprobe analysis was used to obtain Cu concentration profiles across the weld pool of a 2195/2195 specimen. (See Figure 12.) In the HAZ, Cu content was near the nominal content of the base metal. It increased to about 4.5 percent over a 200- μ m region immediately adjacent to the fusion line on the weld side. In the center of the weld, the Cu content decreased to about 3.6 percent, which is below the nominal amount.

Various regions of the weld were analyzed to determine Cu content within the interior of the grains. All regions within the fusion line had Cu concentrations about 2 weight percent below the base metal, with variation as much as 1 weight percent (1 to 2 weight percent compared to 3.7 weight percent for base metal). These results indicated that additional Cu enrichment at the fusion line resided in the grain boundaries.



(a)



(b)

Fig. 12. Microprobe analysis showing Cu-concentration mapped across root corner of 2195/2195 weld, (a) location (Magnification 4.5x) and (b) results.

Transmission Electron Microscopy

Transmission electron microscopy (TEM) was used to examine the base metal and fusion line regions to determine primary strengthening phases of the matrix. Figure 13a shows morphology in the base metal which corresponds to T_1 (Al_2CuLi). This finding was substantiated by electron diffraction patterns. Figure 13b shows δ' (Al_3Li) precipitates in the matrix near the fusion line. Although some T_1 was present, most of the Cu partitioned to the grain boundary to form continuous Cu-rich second phases. Identification of some of these phases showed that θ (Al_2Cu) was present at grain boundaries. However, additional analysis is required to determine the presence of other phases, including Li-containing phases.

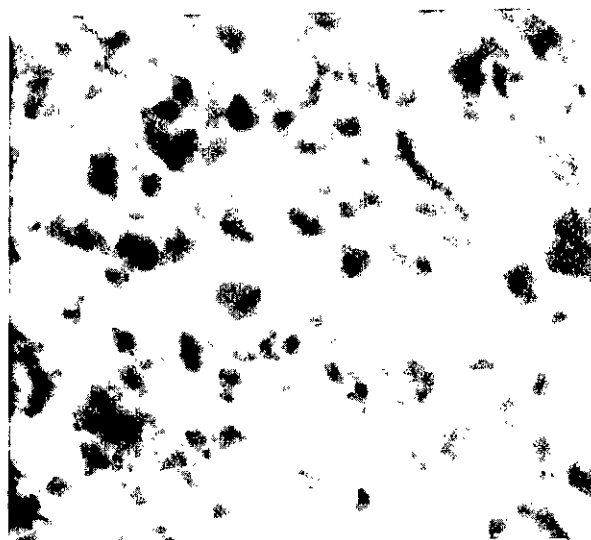
IV. DISCUSSION

Welding 2195 presents technological challenges which exceed those of welding 2219. The 2195 base metal microstructure has an elongated grain structure with anisotropic mechanical properties. Because the strength of 2195 in the longitudinal direction depends in part on this structure, the formation of equiaxed grains within the weld causes a large strength debit relative to the base metal strength. In addition, 2195 contains Li, which is highly reactive with O_2 and H_2O . During welding, the presence of minute amounts of these impurities may degrade properties and cause lack of fusion under conditions that would be adequate for welding 2219. Another significant difference in 2195 chemical composition is the addition of several minor alloying elements (i.e.: Mg, Ag, Zr). These elements segregate during the welding process, which adds complexity to the grain boundary region.

The 2195 grain boundary structure has a critical influence on weld properties, as indicated by analysis of the mechanical property data and comparison of this data with corresponding properties for the wrought alloys. The YS shows that 2195/2195 retains greater matrix strength than both 2195/2219 and 2219/2219. This trend can be related to the difference in matrix precipitates that strengthen the weld. In 2195/2195 welds, the predominant strengtheners are δ' with some T_1 present.



(a)



(b)

Fig. 13. TEM micrographs of 2195 matrix, showing (a) needle-shaped precipitates [T_1] in the base metal outside HAZ and (b) δ' precipitates along the fusion line of a 2195/2195 weld. (Magnification 200kx)

The 2219/2219 specimens are strengthened by a much weaker θ' precipitate (Al_2Cu). The elongations also reflected this difference in matrix strengtheners, as 2219/2219 had over twice the ductility of 2195/2195 at all test temperatures. However, the UTS values did not follow the same trend as YS. The lowest UTS occurred in 2195/2195 at two of the three temperatures tested. This type of behavior indicates that grain boundary integrity was reduced in 2195/2195 welds.

Microstructural evidence complimented the mechanical property data, showing intergranular fracture propagation in 2195/2195. The fracture propagation within the first pass did not necessarily reflect the mechanical properties, but all crack propagation was intergranular. This finding is in agreement with other results obtained for 2090,^[4] which suggest that grain structure within a weld is secondary to chemistry and precipitates as an influence on mechanical properties.

The chemistry has not been clearly established for grain boundary precipitates in 2195/2195 welds using 2319 filler wire. However, some unpublished results on 2195/2195 welds^[5] indicate that grain boundary segregation produces localized regions within the first pass which contain large variations in chemical composition. In these studies, microprobe analysis revealed segregation of alloying constituents across fusion line grain boundaries. Both Ag and Mg were enriched at the grain boundaries, adjacent to Cu-rich phases. Oxygen was commonly found as a segregant, which also segregated to grain boundaries adjacent to the Cu-rich phase.

These findings may have degrading consequences on grain boundary integrity. First, Ag and Mg form low melting eutectics below 500 °C that can melt during application of the cover pass. Incipient melting can lead to microporosity at the grain boundaries, resulting in premature intergranular fracture. Evidence of oxygen at grain boundaries suggests that the welding procedure may need tighter control to reduce infiltration. Oxygen at the grain boundaries will cause Li to segregate and form weak interfaces, due to the strong tendency of Li to oxidize. Preferential segregation and oxidation of Li in Al-Li alloys has been discussed elsewhere.^[6]

These points provide a rationale for weakened grain boundary structure in 2195/2195 welds made with 2319 filler wire, due to segregation within grains. In addition to localized segregation, microprobe analysis verified segregation of Cu from the fusion line to the center of the weld. Within approximately 1000 μm of

the fusion line, the Cu content varied as much as 1 weight percent. The underlying cause has not yet been evaluated, but the segregation indicates that a heterogeneous nature exists in this region of the weld. The likelihood of degrading grain boundaries increases within a zone about 1000 μm from the fusion line to the interior of the weld.

The 2195/2195 microstructure also contained a large amount of porosity on the fracture surfaces. Porosity formation has been shown to result from gas contamination or inadequate surface preparation. The Li-containing alloys are much more susceptible to it than alloys such as 2219.^[7]

In this study, certain specimens contained large amounts of porosity that had a substantial effect on UTS. One specimen tested in LH_2 had about twice the porosity of the other two specimens of its type. The LH_2 specimen had a UTS of only 55.3 ksi, while the others had UTS values of 63.8 and 66.6 ksi. Little variation was seen in YS values for these specimens (51.5, 50.9, and 53.1 ksi, respectively). All 2195/2195 specimens probably contained minor amounts of porosity, which contributed to their low UTS values.

V. CONCLUSIONS

- Due to the segregation of minor alloying elements during rapid solidification, 2195 is inherently more difficult to weld than 2219.
- At all temperatures (ambient, LH_2 , and LN_2) 2195/2195 welds failed intergranularly along one side of the weld, showing no particular association with grain structure.
- Tensile property data for 2195/2195 suggested degraded grain boundary integrity and greatly reduced weld strength relative to the base metal.
- Sources of grain boundary degradation included segregation of minor alloying elements (e.g., Li, Mg, and Ag) adjacent to Cu-rich second phases. These elements can form deleterious phases that reduce grain boundary/matrix cohesion.
- In 2195/2195 welds, the most susceptible regions appeared to occur in a 1000- μm region from the fusion line toward the interior of the weld.
- One factor in 2195 weld degradation is porosity, which reduces UTS but has little effect on YS.

ACKNOWLEDGEMENTS

We gratefully acknowledge contributions from S. Jones of IITRI for specimen preparation and G. Jerman of NASA for microprobe analysis and pertinent discussions. This work was supported by NASA/MSFC Contract NAS8-38258.

REFERENCES

1. Bond, R., Malone, T.W., and Rybicki, D.J., "Mechanical Testing of 0.5-Inch Welded Aluminum-Lithium Alloy," Proceedings of the 1994 Conference on Advanced Earth to Orbit Propulsion Technology, Marshall Space Flight Center, AL, May 17-19, 1994.
2. McGill, P., Watwood, M., and Stafford, C., "Fracture Properties of 0.5-Inch Welded Aluminum-Lithium Alloy," Proceedings of the 1994 Conference on Advanced Earth to Orbit Propulsion Technology, Marshall Space Flight Center, AL, May 17-19, 1994.
3. Nunes, A.C., Jr., Bayless, E.O., Jr., Jones, C.S., III, Munafo, P.M., Biddle, A.P., and Wilson, W.A., "Variable Polarity Plasma Arc Welding on the Space Shuttle External Tank," *Welding Journal*, **63(9)**, 27-35, September 1984.
4. Sunwoo, A.J. and Morris, J.W., Jr., "Influence of Intrinsic and Extrinsic Factors on Mechanical Properties of 2090 Aluminum Alloy Weldments," *Materials Science and Technology*, **7**, 965-971, October 1991.
5. Sanders, J.H. and Jerman, G.A., unpublished results, Materials & Processes Laboratory, Marshall Space Flight Center, AL, 1994.
6. Soni, K.K., Williams, D.B., Newbury, D.E., Gillen, G., Chi, P., and Bright, D.S., "Compositional Changes in Aluminum-Lithium-Base Alloys Caused by Oxidation," *Metallurgical Transactions A*, **24A**, 2279-2288, October 1993.
7. Martinez, L.F., McClure, J.C., and Nunes, A.C., Jr., "Effect of Gas Contamination During Welding of Aluminum-Lithium Alloys," *Welding and Joining Processes*, **51**, 235-243, 1991.

**Microstructural Characterization of 0.5-inch Welded
Aluminum-Lithium Alloy
J. H. Sanders**

Q: I have a quick question, were all of your tensile data basically unshaven welds specimens or did you have shaved and unshaved?

A: No, they were all unshaven.

Q: Because of the flat position welding of such a thickness you had an extremely high reinforcement angle on the root side of your plasma welds, approaching 90 degrees, so I think it would be interesting to shave those welds, retest them in similar combinations and see how the ranking comes out on shaven welds.

A: Yes, there was a lot variability in the drop through these specimens and I believe that may be due in part to control problems in the welding procedure. I know that the weld schedule is being refined and that these welds were from an older weld schedule. These were some of the first 0.5 inch welds that MMMSS produce at MSFC.

Q: I suspect that pulsing that keyhole pass may also help to reduce the extent of drop through.

A: The vertical welds had significantly less drop through; however, the properties were similar.

Q: Diwan - This copper rich phase that you mentioned, are they copper-iron rich hard phase particles that you see on the fusion line?

A: Our suspicion is that the majority of these phases are essentially aluminum copper. I am not convinced that they contain lithium. We have to perform more TEM work or more SIMS work to identify these phases.

Q: Diwan - The last conclusion that you said was that they are copper rich phase, right?

A: I am talking about the second phase in general based on our macroscopic segregation map across the weld. There is definitely more second phase along the grain boundaries within the fusion line regions.

Q: Diwan - I think you should check the composition, it might be copper iron rich.

A: We have not seen any iron, and we have looked.

Q: Have you measured the hardness across the weld?

- A: Not in that specimen in particular, we have measured hardness across alot of other weld specimens.
- Q: I thought we squared this whole thing away about this equiaxed region this morning and early this afternoon but my question is if your data shows high copper near the interface in the fusion zone in the area of the weld where there has been 2219 dilution would that not indicate mixing? You are seeing high copper from the 2219.
- A: Art Nunes (Marshall Space Flight Center) I think it is not commonly known to people even in the welding business, the extent to which the migration of the last fluids to solidify in the weld can be brought about by the strains that occur during the weld. If you will recall, the micro-fissuring range tends to be caused by an expansion of the interlayers toward the weld in the heat affected zone driven by an expansion of pulled apart layers standing outside, as they get hotter, while the inner layers get colder. So there is a tendency, immediately behind the weld puddle, for the outer layer of the weld and in other words the fusion boundary to expand and if there is hot material inside the resevoir inside the weld this will expand into this region. We see some more direct evidences that this causes little filaments of segregate and give rise to straight line x-ray indications, that the so called iganigma. These are apparently caused by the oozing out of a copper rich material in undercuts on the edge of the weld prior to solidification, so you have a clear example of this kind of segregation.

MICROSTRUCTURE EVOLUTION IN THE HEAT-AFFECTED ZONE OF A GAS TUNGSTEN-ARC WELDED Al-2195

K. H. Hou¹, W. A. Baeslack III¹, J. C. Lippold², and A. Szabo³

¹Department of Welding Engineering
The Ohio State University
Columbus, OH 43210

²Edison Welding Institute
Columbus, OH 43212

³Martin Marietta Manned Space Systems
New Orleans, LA 70189

Abstract

In the present study, aluminum alloy 2195 (Al-1.0Li-4.0Cu-0.4Mg-0.4Ag-0.14Zr) in the T3 and T8 tempers was welded autogenously using the gas tungsten-arc (GTA) welding process. Through detailed characterization, relationships between location in the heat-affected zone (HAZ), microstructure, and the corresponding microhardness were established for both the as-welded and postweld heat-treated conditions. HAZ microstructures and hardness were strongly influenced by the base metal (BM) heat treatment, the thermal histories experienced during GTA welding, and postweld heat treatment. The competition between major strengthening precipitates, including T_1 , θ' and Ag-containing α' , determined the resulting microstructure and hardness. It was found that the combination of overaging and dissolution during the on-heating cycle, and re-precipitation of various strengthening precipitates during cooling and postweld heat treatment occurred differently across the HAZ and resulted in substantial hardness variations. Relationships between hardness and microstructure in the HAZ's of the GTA welds in 2195 were established.

I. Introduction

Lithium-containing aluminum alloys have been the focus of considerable research in recent years. The potential use of these low-density, high strength/stiffness materials by the aerospace industry has resulted in vigorous alloy development to meet the demanding requirements for building today's aircraft and aerospace systems. The addition of lithium in aluminum alloys promotes a reduction in density, combined with an increase in stiffness and strength. (refs. 1-2) Alloy 2195 achieves its high strength and stiffness via precipitation strengthening from finely distributed T_1 precipitates. (ref. 3) To achieve full advantage to off-set the high cost of these engineering materials, and to replace highly weldable alloys such as 2219 in the demanding aerospace structural applications, welding procedures must be carefully selected to avoid the formation of various defects and to produce high strength weld joints.

The thermal histories experienced in the HAZ of heat treatable aluminum alloys during welding alter the base metal microstructure, and correspondingly can potentially degrade the mechanical properties. Relatively few studies have been performed to establish the relationship between the HAZ microstructure and the mechanical properties in the heat treatable aluminum alloys. (refs. 4-6) Improvements of FZ properties are achievable by the proper selection of the filler metal and the postweld heat treatment. However, a reduction in the HAZ strength due to the "damaged" microstructure cannot be restored through the modification of the filler metal. Consequently, HAZ regions may become the weakest portions of the welds and ultimately determine the joint efficiency. In the current study, the effect of welding and postweld heat treatment on the microstructure of two differently heat-treated 2195 base metals was evaluated. It was intended to understand the effect of the weld HAZ thermal cycle on the strengthening precipitates in the HAZ and to provide the fundamental knowledge for future alloy design and the optimization of postweld heat treatment.

II. Experimental Procedure

The nominal composition of 2195 was Al-1.0Li-4.0Cu-0.4Mg-0.4Ag-0.14Zr. The base metal was solution heat-treated at 504 °C for 2 hour following by 6% stretching and tempered to naturally-aged T3 and artificially-aged T8 (143 °C for 24 hours) conditions. Autogenous, bead-on-plate GTA welds were produced on 4.8 mm thick plates with the welding direction transverse to the plate rolling direction. The welding parameters are summarized in Table 1. Prior to the welding, the plates were dry machined to remove surface oxide and avoid FZ porosity. To study the postweld aging heat treatment responses in different regions of the weldments, postweld heat treatment was performed at 160 °C for 16 hours. Forced air circulation was used to maintain temperature uniformity during heat treatment. Representative weld cross-sections were cold-mounted in epoxy and prepared for optical metallography and microhardness testing by mechanical polishing with SiC paper, 0.3 micron aluminum oxide and a colloidal silica suspension, and then etched with

Keller's reagent. Microhardness traverses across the GTA welds were measured using a load of 100 g. The hardness traverses were measured 2 mm from the plate surface at a location coincident with the centers of the TEM samples. TEM specimens were prepared from thin slices which were carefully sectioned parallel to the welding direction in increments of 0.64 mm from the weld centerline to the base metal using a low speed diamond saw. TEM samples from the base metal, HAZ and FZ were electrojet-thinned in a solution of 25% nitric acid and 75 % methanol at -40 °C and immersed in a 70% nitric acid solution to remove possible surface contamination. Thin foils were examined in a JEOL 200CX analytical electron microscope equipped with Tracor-Northern TN-2000 energy-dispersive X-ray analysis (EDS) system operating at 200 KeV.

Table 1 Parameters for GTA welding

Shielding Gas:	He at 629 cc/s
Voltage:	16 volts, DCSP
Current:	150 amperes
Travel Speed:	4.23 mm/sec
Electrode Dia.:	2.4 mm
Arc Gap:	1.5 mm

III. Results

III.1. Base Metal Microstructures

The elongated grains in the BM of both T3- and T8-tempered alloy 2195 are shown in Fig. 1A. The TEM bright-field micrograph in Fig. 1B shows the elongated grains and subgrains. The naturally-aged T3 BM contained only sparsely distributed α' and probably δ' and G.P. zones, as shown in Fig. 1C. Consequently, the hardness of the 2195-T3 base metal was only 124 DPH. As shown in Fig. 1D, the artificially-aged 2195-T8 BM contained finely distributed T_1 precipitates that averaged 40 nm in length in the matrix, and fewer θ' and α' precipitates. Correspondingly, this microstructure exhibited a higher hardness of 183 DPH. It should be noted that the α' precipitates observed in 2195-T3 and 2195-T8 alloys were (Ag, Zr)-containing precipitates which exhibited similar L12 superlattice reflections in diffraction patterns as δ' in the alloy 2090. These spherical α' precipitates which were different from occasionally found (Ag, Cl)-containing surface contaminant particles, exhibited certain characteristics of both α' ($Al_3(Zr, Li)$) and β' (Al_3Zr). These particles reprecipitated during weld cooling cycles and provided moderate strengthening to the material that resembled typical δ' in alloy 2090. However, the morphology of discrete particles and dissolution behavior exhibited the characteristics of β' , which was relatively unaffected by the HAZ thermal cycles. It was suggested that these precipitates be designated as Ag-containing α' , which is being investigated. (ref. 7)

III.2. Heat-Affected Zone Study

A. Microhardness Results

Microhardness traverses, for the as-welded and 160°C/16hr-aged conditions, across the GTA welds in the 2195-T3 and 2195-T8 base metals are shown in Figs. 2A and Fig. 2B, respectively. Hardness variations in the weld HAZ's and the related microstructure will be described in detail in the following sections.

B. HAZ Microstructure of 2195-T3 GTA Welds

The microstructural characterization was conducted with TEM on the regions approximately 15, 10, 5, and 2 mm from the fusion line. Partially-melted regions immediately adjacent to the fusion line were also studied. TEM bright-field (BF) and dark-field (DF) images, and selected-area electron diffraction patterns were used for phase identification. This study concentrated on the effect of the evolution of major strengthening precipitates, including T_1 , α' and θ' , on the hardness of the weld HAZ.

(i) As-Welded HAZ in 2195-T3 GTA Welds

HAZ-15mm: As shown in Fig. 3A, spherical α' precipitates were sparsely distributed in the matrix with diameters ranging from 20 nm to 44 nm and an average value of 26 nm, which was smaller than 31 nm in the as-received T3-tempered base metal. Since the only noticeable difference between the BM and the HAZ-15 mm microstructure was the smaller α' precipitates in the latter region, it was suggested that the smaller α' size and possibly the dissolution of G.P. zones induced the observed minor reduction in hardness to 107 DPH.

HAZ-10mm: The high density of T_1 precipitates formed in this region is shown in Fig. 3B. The length of T_1 precipitates ranged from 25 nm to 70 nm and the average was 45 nm. No θ' precipitates were observed. It is believed that the hardness increase in this region to 125 DPH resulted from the occurrence of T_1 precipitation. The fewer yet slightly larger α' precipitates were not expected to have a marked effect on hardness.

HAZ-5mm: The average α' precipitate size was 25 nm in diameter, which was slightly smaller than that of the HAZ-10 mm region. The size of T_1 precipitates increased to from 120 nm to 340 nm, with an average of 215 nm in length. θ' precipitates were observed in the matrix with lengths ranging from 100 nm to 300 nm, with an average of 205 nm. (Fig. 3C) The hardness in this region (101 DPH) was substantially lower than that of the HAZ-10 mm region. The minor change in α' precipitate size should have little effect on the hardness. It is believed that the large size of T_1 and

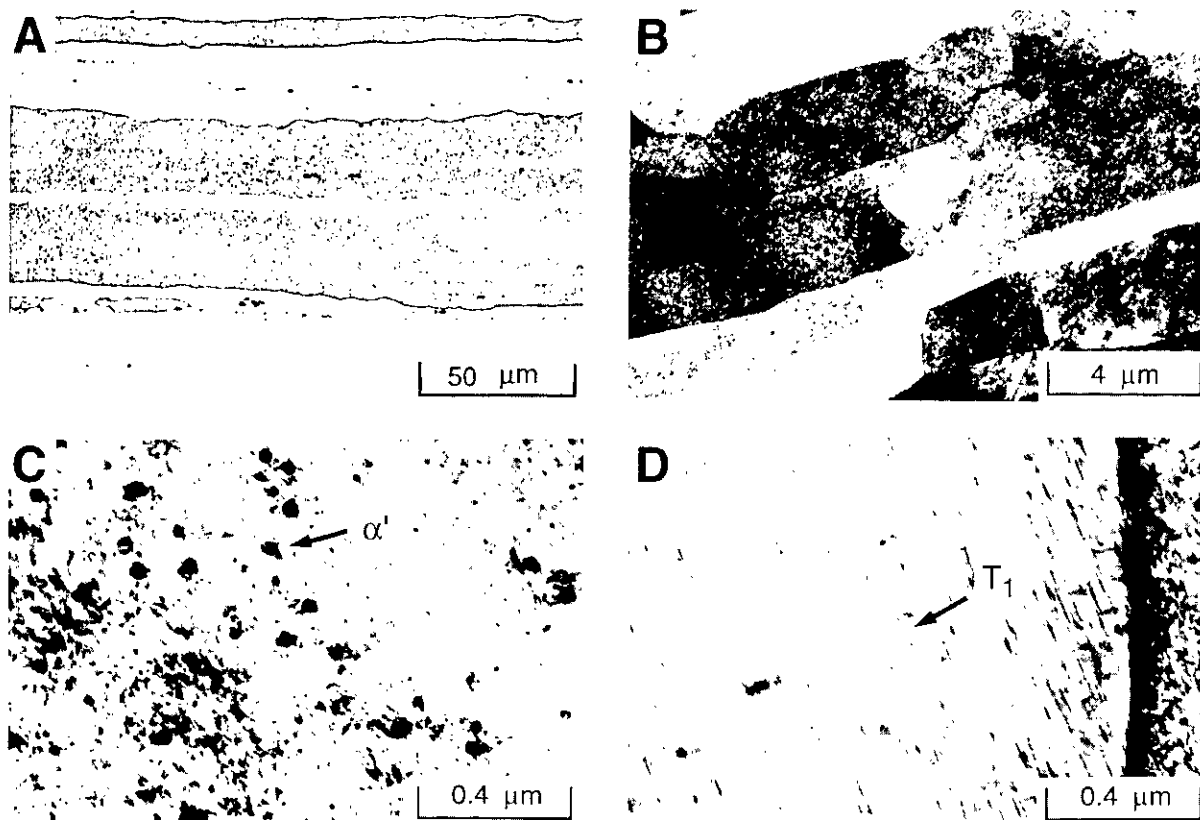


Fig. 1 Base metal microstructure of Al-2195: A) light micrograph; B) TEM BF micrograph; C) TEM BF micrograph of 2195-T3 base metal showing Ag-containing α' precipitates; and D) TEM BF micrograph of 2195-T8 base metal showing T_1 precipitates.

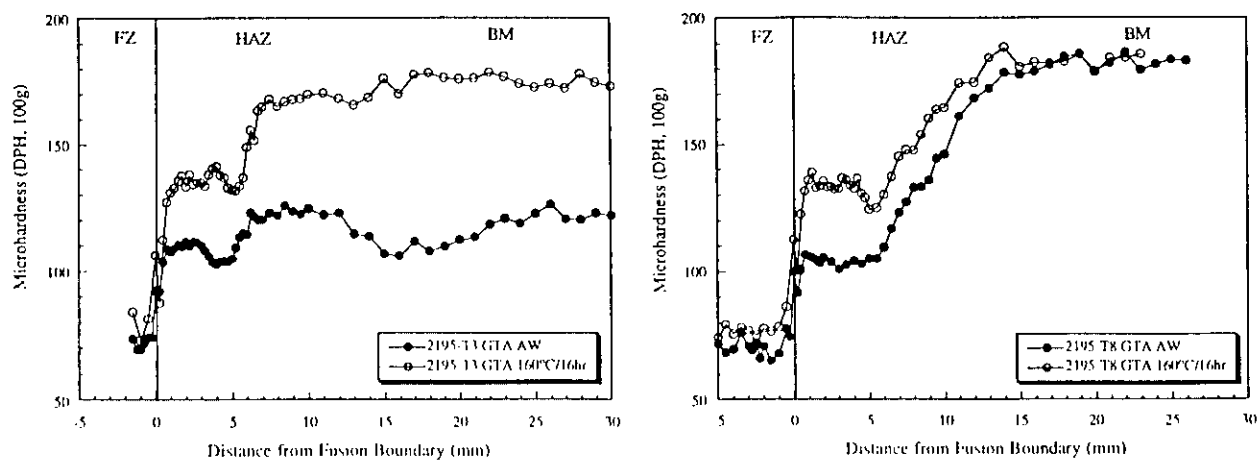


Fig. 2 Microhardness traverses across the as-welded and 160°C/16hr-aged GTA welds in A) 2195-T3; and B) 2195-T8 base metals.

θ' precipitates was responsible for the lower hardness in this region.

HAZ-2mm: Appreciable recrystallization of the base metal microstructure was observed in this region. As shown in Fig. 3D, a high density of α' precipitates was observed in the matrix, with an average diameter of 31 nm. Matrix T_1 precipitates were no longer observed while grain boundary T_1 precipitates up to 240 nm in length were still commonly found. θ' precipitates were not found either in the matrix or at the grain boundaries. Since this region lacked strengthening from T_1 and θ' precipitates, the recovery of hardness to 112 DPH in this region was attributed to the more extensive α' precipitation which produced larger and more importantly, a higher particle density of α' precipitates.

PMZ: Liquid phases formed at the grain boundaries in the partially-melted zone (PMZ) during welding. This region contained a high density of α' precipitates, as shown in Fig. 3E. Occasionally, T_1 precipitates were observed at the high angle grain boundaries. The hardness in this region was 90 DPH, which was lower than the 112 DPH in the HAZ-2 mm region. The lower hardness was attributed to the slightly lower α' precipitate particle density, the lack of T_1 and θ' precipitation, and the lesser degree of solid solution strengthening due to the segregation of matrix solute to grain boundaries.

(ii) 160°C/16hr-Aged HAZ in 2195-T3 GTA Welds

HAZ-15mm: T_1 precipitates were densely distributed in the matrix, as shown in Fig. 4A. The length of T_1 precipitates ranged from 20 nm to 80 nm and averaged 50 nm, which was slightly longer than 45 nm in the aged BM. A small amount of θ' precipitation was also observed. The size of θ' varied widely from 20 nm to 86 nm in length and averaged 45 nm. The non-uniformly distributed α' precipitates were found in the matrix with an average diameter of 35 nm. The hardness increase in this region from 107 DPH to 170 DPH after aging was attributed to T_1 precipitation. Contributions to hardness from the α' and θ' precipitates were considered minimal.

HAZ-10mm: A high density of T_1 precipitates was observed in the matrix ranging from 80 nm to 190 nm in length, as shown in Fig. 4B. The average length of T_1 precipitates was 120 nm, which was considerably larger than 50 nm in the aged HAZ-15 mm region. In the as-welded condition, the formation of T_1 precipitates (45 nm long) resulted in a hardness increase in this region. During the 160°C/16hr aging, these T_1 precipitates coarsened and became slightly overaged. Consequently, the hardness in this region maintained a level slightly lower than that of the aged base metal.

More T_1 precipitates formed in the matrix, which resulted in a hardness increase. A small amount of θ' was found in the matrix with an average length of 45 nm. The amount of θ' precipitation was too small to have any appreciable influence on hardness. The diameters of the spherical α' precipitates ranged from 30 nm to 60 nm with an average of 39 nm. The increase in hardness in this region after aging was considered to be the combined effect of more extensive T_1 and α' precipitation.

HAZ-5mm: The hardness decreased to 130 DPH in this region. As shown in Fig. 4C, a high density of plate-like precipitates, including T_1 and θ' , was observed in the matrix and along the grain boundaries. In the as-welded condition, the average sizes of both T_1 and θ' precipitates were more than 200 nm, which resulted in a hardness reduction. During 160°C/16hr aging, the increase in the particle density of T_1 and θ' precipitates was accompanied with a substantial increase in size. T_1 precipitates with an average length of 500 nm in the matrix and at the grain boundaries were considered severely overaged and not very effective in providing strengthening to the materials. The occasionally observed θ' precipitates in the aged HAZ-10mm matrix became densely distributed in this region and the particle density of θ' was comparable to that of the T_1 precipitates. The average length of θ' precipitates was approximately 200 nm, which was considerably larger than 46 nm in the aged HAZ-10 mm region. The diameter of spherical α' precipitates ranging from 20 nm to 46 nm with an average of 34 nm. The increase in hardness from 105 DPH to 132 DPH after aging was attributed to the more extensive θ' precipitation. Compared to the aged HAZ-10mm region, this region contained severely overaged T_1 precipitates, which resulted in a lower hardness.

HAZ-2mm: As discussed previously, the hardness recovery in the as-welded HAZ-2mm regions resulted from the formation of a high density of fine α' precipitates in the matrix. As shown in Fig. 4D, a high density of plate-like precipitates including θ' and T_1 was observed in this region after aging. In the as-welded condition, the extensive precipitation of α' resulted in an increase in hardness in this region. Consequently, the Li content in the matrix was depleted by the formation of large number of α' precipitates. During postweld aging, the nucleation of T_1 precipitates was hindered by the lack of sufficient Li in the matrix. Consequently, fewer T_1 precipitates formed in the matrix which ranged from 40 nm to 300 nm and averaged at 200 nm. The particle density of the T_1 was much lower than that of the θ' . A large particle size and a low particle density clearly suggested that the T_1 precipitates were overaged and no longer provided effective strengthening to the material. θ' precipitates

were densely distributed in the matrix with an average length of 95 nm. By comparing Fig. 4D with Fig. 4C, it was found that the HAZ-2mm region contained much smaller but more densely distributed θ' precipitates than HAZ-5mm region. Therefore, the higher hardness in this region (138 DPH) compared to that in the aged HAZ-5mm region (132 DPH) resulted from the greater θ' strengthening, which was also attributed to the increase in hardness after the 160°C/16hr aging. A higher α' particle density was found in this region than in the HAZ-5mm region. The average diameter of the α' precipitates was 32 nm, which was comparable to that in the as-welded HAZ-2mm region. Even though this region contained finely distributed θ' precipitates in the matrix, the hardness was considerably lower than that of the aged BM, which was strengthened primarily by T_1 precipitates. Higher BM hardness was attributed to the more potent strengthening from T_1 .

PMZ: The recrystallized α -Al grain structure in this region exhibited solidified liquated phase along α grain boundaries. Within 1 mm from the FL, the hardness decreased abruptly to 108 DPH. As shown in Fig. 4E, relatively fewer but larger T_1 precipitates coexisted with θ' precipitates in the matrix. The average length of T_1 was 110 nm. The low particle

density of T_1 precipitates limited the effectiveness of the strengthening from T_1 . θ' precipitates were more densely distributed in the matrix than T_1 precipitates, with an average length of 50 nm. However, by comparing Fig. 4E with 4D, it was evident that the particle density of θ' precipitates was lower in the aged PMZ than in the aged HAZ-2mm region. In the as-welded condition, this region exhibited a high density of α' precipitates, and low hardness due to the segregation of solute elements to the grain boundaries. During postweld aging, the precipitation of T_1 was limited due to the extensive α' precipitation for the similar reason described in the aged HAZ-2mm region previously. The lower degree of T_1 precipitation also enhanced the nucleation and growth of θ' precipitates. However, the lower solute content in the matrix due to the formation of grain boundary liquated phases resulted in the formation of less and smaller θ' precipitates than in the aged HAZ-2mm region. Consequently, this region exhibited a considerably lower hardness than that in the aged HAZ-2mm region. The average α' diameter in this region was 32 nm, which was identical to that in the aged HAZ-2 mm region. Segregation of precipitates in the regions adjacent to the grain boundary liquated phases was observed and will be discussed more thoroughly in the aged T8-PMZ in a latter section.

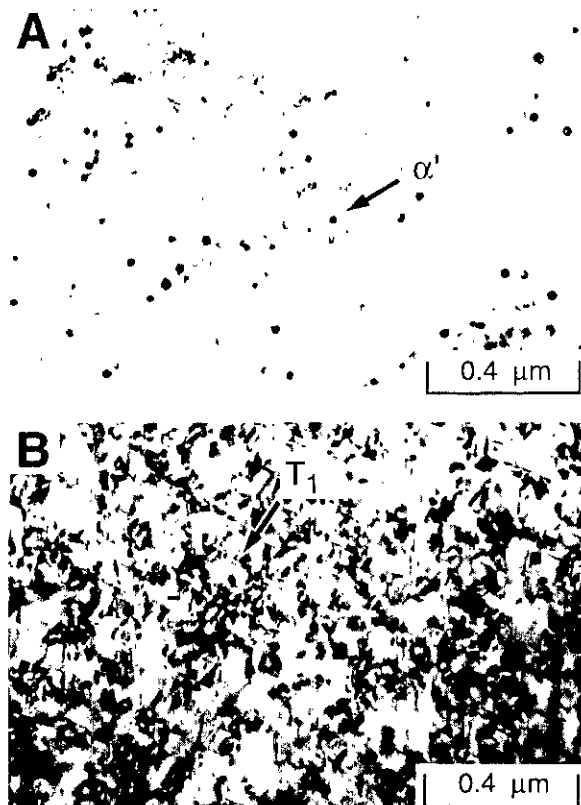


Fig. 3 TEM BF micrographs of the HAZ microstructures in the as-welded GTA welds in 2195-T3: A) HAZ-15mm; and B) HAZ-10mm.

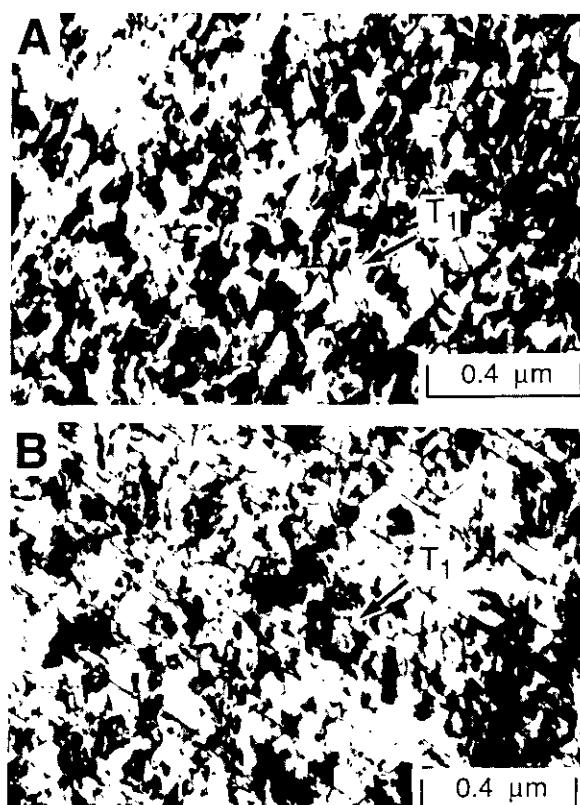


Fig. 4 TEM BF micrographs of the HAZ microstructures in the 160°C/16hr-aged GTA welds in 2195-T3: A) HAZ-15mm; and B) HAZ-10mm.

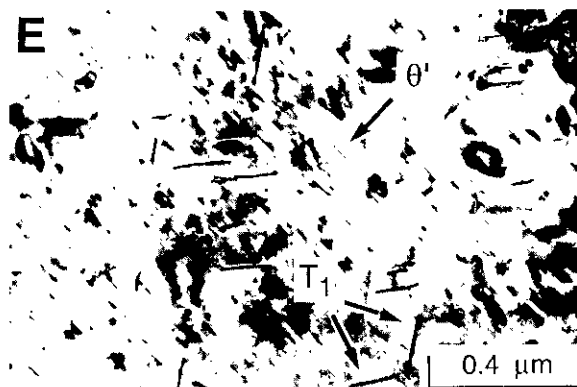
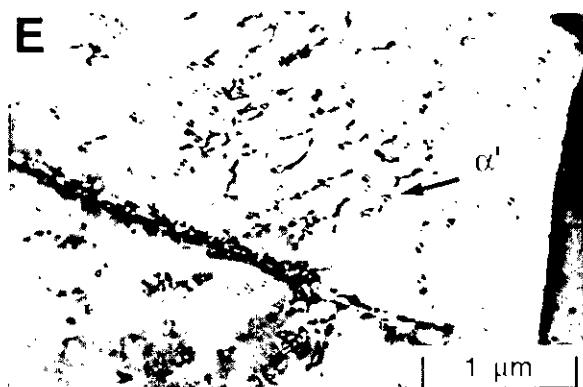
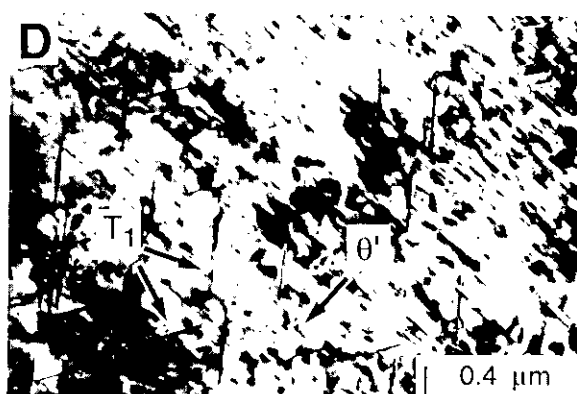
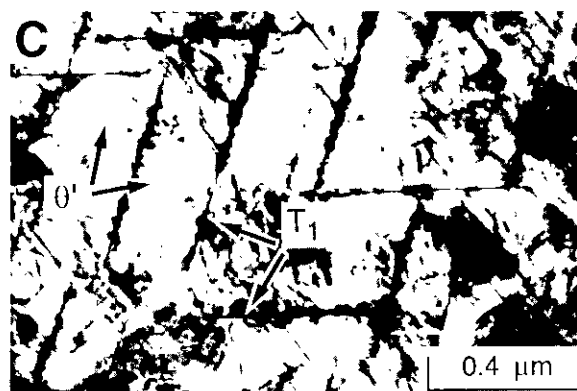
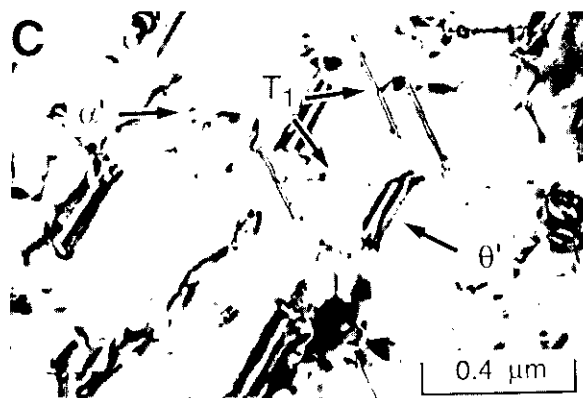


Fig. 3 (cont'd.) TEM BF micrographs of the HAZ microstructures in the as-welded GTA welds in 2195-T3: C) HAZ-5mm; D) HAZ-2mm; and E) PMZ.

Fig. 4 (cont'd.) TEM BF micrographs of the HAZ microstructures in the 160°C/16hr-aged GTA welds in 2195-T3: C) HAZ-5mm; D) HAZ-2mm; and E) PMZ.

C. HAZ Microstructure of 2195-T8 GTA Welds

(i) As-Welded HAZ in 2195-T8 GTA Welds

HAZ-10mm: The hardness of this region was 137 DPH, which was substantially lower than 183 DPH in the base metal. T_1 precipitates increased slightly from 40 nm in the base metal to 45 nm while particle density decreased, as shown in Fig. 5A. The dissolution of base metal θ' precipitates was observed with few particles remaining in the matrix, averaging 15 nm in length. In addition, the size and the particle density of α' were decreased. The reduction in hardness was attributed to the reduction in particle density of T_1 , θ' , and α' precipitates during welding. By comparing Fig. 3B and Fig. 5A, the microstructures of the as-welded HAZ-10mm regions were determined by the base metal heat treatment. In the T3-HAZ-10mm region, the supersaturated base metal provided solute for the nucleation and growth of fine T_1 precipitates during welding thermal cycle. Consequently, the hardness increased. In the T8-HAZ-10mm region, the pre-existing base metal T_1 precipitates coarsened and reduced in particle density and resulted in an reduction in hardness.

HAZ-5mm: As shown in Fig. 5B, the average length of T_1 precipitates increased to 100 nm and the particle density decreased considerably. Few θ' precipitates with an average length of 50 nm were observed in the matrix. Overaging of T_1 precipitates was believed to cause the hardness reduction to 105 DPH. A relatively high α' particle density was found in the matrix with the average diameter of 26 nm. The α' was believed to re-precipitate during cooling from peak temperature to room temperature. Compared to the T3-HAZ-5mm, this region contained less severely overaged T_1 precipitates and fewer θ' precipitates, and a slightly higher hardness.

HAZ-2 mm: The hardness decreased from 105 DPH in the HAZ-5mm region to 101 DPH in the HAZ-3mm region and then increased to 105 DPH in the HAZ-2mm region. Extensive recrystallization was observed in the HAZ-2mm region. Complete dissolution of matrix T_1 and θ' precipitates resulted in a decrease in hardness compared to the BM. As shown in Fig. 5C, a high particle density of α' precipitates was found in the matrix. It was believed that the more prominent reprecipitation of α' , induced by more available solute elements in the matrix, resulted in an increase in the hardness compared with the HAZ-3mm region, where severely overaging of T_1 precipitates was expected. This T8-HAZ-2mm region contained a very similar microstructure to the T3-HAZ-2mm region. The extensive α' precipitation was attributed to the hardness increase in both regions.

PMZ: Solidified eutectic phases were observed along the grain boundaries and inside the α -Al matrix. As shown in Fig. 5D, a high particle density of α' precipitates was observed in the matrix which was similar to that in the HAZ-2mm region described previously. No T_1 or θ' precipitates were observed in the matrix. The hardness of this partially-melted region was only 92 DPH. It was suggested that the segregation of solute elements to the liquated phases resulted in a lower matrix solute content, and consequently reduced the extent of solid solution strengthening. High peak temperatures experienced in the PMZ's in T3- and T8-tempered 2195 base metals resulted in the complete dissolution of BM precipitates and extensive α' precipitation. The microstructures in the as-welded T3-PMZ and T8-PMZ were virtually identical.

(ii) 160°C/16hr-Aged HAZ in 2195-T8 GTA Welds

HAZ-10mm: Postweld heat treatment induced a significant hardness increase from 137 DPH to 164 DPH in this region. A high density of T_1 precipitates was observed with an average length of 60 nm. (Fig. 6A) In addition, more α' precipitates were found in the matrix with an average diameter of 22 nm. Little θ' was found distributed in the matrix. In the as-welded condition, the reduction of hardness in this region was attributed to the decreased particle densities of T_1 , α' and θ' precipitates due to the welding thermal cycle. Postweld aging primarily increased particle density of T_1 precipitates and resulted in the hardness increase.

HAZ-5mm: The hardness in this region was 124 DPH, which was the lowest in the aged HAZ except for the regions immediately adjacent to the fusion line. Extensive coarsening of T_1 precipitates resulted in an average length of 250 nm and a much lower particle density than regions farther from the FL, as shown in Fig. 6B. θ' precipitates coexisted with T_1 precipitates with an average length of 145 nm and exhibited a similar particle density as T_1 . α' precipitates were found relatively densely distributed in the matrix with an average diameter of 23 nm. Compared with the aged HAZ-10mm region, the lower hardness in this region was attributed to the overaging of T_1 precipitates. In the as-welded condition, this region exhibited a lower T_1 particle density and hardness than those in the HAZ-10mm region. A higher α' particle density was observed in the as-welded condition, which ultimately hindered the precipitation of new T_1 precipitates in the matrix during aging. More θ' precipitates formed during aging due to the more available Cu in the supersaturated matrix. The hardness increase in this region after aging was directly related to the higher θ' particle density, which was the result of competition between α' and T_1 precipitates. By comparing the aged T3-HAZ-5mm and

aged T8-HAZ-5mm regions, it was evident that these two regions exhibited similar microstructures. Both regions contained coarse T_1 precipitates and relatively high θ' particle density after aging, and exhibited similar hardness values.

HAZ-2mm: In this region, the hardness was 135 DPH, which was higher than that in the HAZ-5mm region. As shown in Fig. 6C, T_1 precipitates with an average length of 160 nm were found sparsely distributed among the densely distributed θ' precipitates, which were 100 nm in average. A relatively high density of α' precipitates was found in the matrix with the average diameter of 35 nm. The higher hardness in this region was attributed to the θ' and α' precipitates, while the overaged T_1 precipitates were considered insignificant in determining the hardness of this region. In the as-welded condition, the dissolution of both T_1 and θ' precipitates, and the formation of α' precipitates were observed in this region. The available Li in the matrix was consumed by the precipitation and growth of α' , which ultimately inhibited the extensive T_1 precipitation during postweld heat treatment. Consequently, the unused Cu in the solid solution by T_1 was used by the extensive precipitation of θ' during aging. It was noted that the particle density of θ' precipitates was higher in this region than that in the aged HAZ-5mm region, which corresponded to the higher hardness in this region. The microstructures of the aged T3-HAZ-2mm and T8-HAZ-2mm region were very similar. During the welding thermal cycle, high peak temperature dissolved all the precipitates in the matrix and formed a high density of α' precipitates during cooling in both as-welded T3-HAZ-2mm and T8-HAZ-2mm regions. The formation of α' precipitates ultimately enhanced the θ' precipitation and hindered the T_1 precipitation for the aforementioned competition for Li between α' and T_1 precipitates.

PMZ: The hardness in this region was approximately 100 DPH, which was considerably lower than that in the HAZ-2mm region. As shown in Fig. 6D, T_1 and θ' formed adjacent to the liquated phases with the average lengths of 120 nm and 80 nm, respectively. α' precipitates were found located in the vicinity of but not immediately adjacent to the liquated phases. This phenomenon was similar to that observed in the postweld aged FZ. (ref. 8) In the region immediately adjacent to the liquated phases where solute elements highly concentrated. The formation of α' precipitates away from the liquated phases implied that the growth of α' precipitates was determined not only by the total amount of Li in the matrix, but also the Cu/Li ratio. In the region immediately adjacent to the liquated phases, the high Cu content resulted in a higher Cu/Li ratio, which favored the formation of T_1 instead of α' . The lower solute content in the matrix resulted

in a lower particle density of T_1 and θ' precipitates. The non-uniform distribution of precipitates in the matrix resulted in the lowest aged HAZ hardness.

IV. Discussion

The microhardness in the various regions in the as-welded and aged HAZ's of GTA welds in 2195-T3 and 2195-T8 was affected by the distribution and size of the major strengthening precipitates, including T_1 , α' , and θ' . In addition, the base metal heat treatment conditions also influenced the resulting HAZ microstructure and hardness. The microstructures of both the as-welded and postweld heat-treated GTA weld HAZ's in 2195-T3 and 2195-T8 tempered base metals are summarized in Figs. 7A and 7B, respectively.

In the as-welded condition, the occurrence of various metallurgical reactions was influenced by the peak temperature and the base metal microstructure. In both the as-welded 2195-T3 and 2195-T8 HAZ's, different peak temperatures resulted in the dissolution, precipitation, and overaging of the major strengthening precipitates. Therefore, the variations in hardness were observed. Supersaturation of solute elements in the matrix resulted from the dissolution of precipitates during the on-heating welding thermal cycles. Due to the ease of nucleation of α' precipitates, it was noted that the extensive re-precipitation of α' during cooling in the regions 2 mm or closer to the FL not only induced the hardness increase in the as-welded condition, but also consumed the matrix Li and hindered the T_1 precipitation during the postweld heat treatment. Consequently, Cu in the matrix was not consumed, which benefited the precipitation of θ' . The high peak temperatures experienced in the HAZ close to the FL resulted in the complete dissolution of the BM precipitates. It was not unexpected to find out that the hardness traverses of the aged 2195-T3 and 2195-T8 were similar especially in the region closer to the FL.

Postweld aging increased the hardness of the HAZ. In the partially-melted zone where liquated phases formed, the hardness was the lowest in the entire HAZ in both the as-welded and postweld aged condition. The concentration of solute in the liquated phases reduced the effectiveness of solid solution strengthening, which was more significant when limited precipitation strengthening was provided in the as-welded condition. During postweld aging, the formation of precipitates was limited to the regions where a higher solute content was present. Consequently, non-uniform distribution of precipitates occurred similar to that in the aged FZ. The competition between α' and T_1 for Li was observed and was ultimately determined by the Cu/Li ratio. Therefore, α' precipitates were located in the regions not immediately adjacent to the Cu-riched liquated phases.

V. Conclusions

The following conclusions were drawn from the current HAZ study.

1. HAZ hardness and microstructure were influenced both by the thermal cycles and the base metal heat treatment. The HAZ hardness variations in the as-welded and postweld aged conditions were the result of the occurrence of dissolution, precipitation and coarsening of various precipitates in the HAZ.
2. Postweld aged HAZ microstructures were the result of the competition between various precipitates. Extensive precipitation of α' during cooling in the regions close to the FL was enhanced by the supersaturated α -Al matrix due to the dissolution of various precipitates, and resulted in an increase in hardness. During postweld heat treatment, the precipitation of T_1 was hindered because the matrix Li was consumed by α' , which induced the more extensive θ' precipitation.

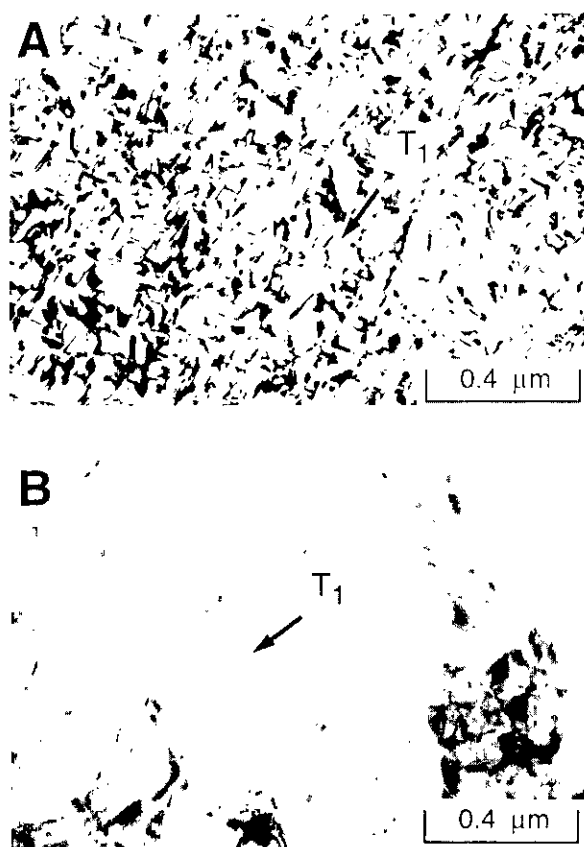


Fig. 5 TEM BF micrographs of the HAZ microstructures in the as-welded GTA welds in 2195-T8: A) HAZ-10mm; and B) HAZ-5mm.

VI. References

1. Balmuth, E. S. and Schmidt, R., Aluminum-Lithium Alloys, ed. by T. H. Sanders and E. A. Starke (TMS-AIME, New York) 1981, pp. 69-88.
2. Tack, W. T. and Loechel, L. W., Proceedings of 5th International Aluminum-Lithium Conference, ed. by T. H. Sanders and E. A. Starke (Williamsburg) 1989, pp. 1457-1467.
3. Pickens, J. R., Heubaum, F. H., Langan, T. J. and Kramer, L. S., Proceedings of 5th International Aluminum-Lithium Conference, ed. by T. H. Sanders and E. A. Starke (Williamsburg) 1989, pp. 1397-1411.
4. Dumolt, S. D., Ph.D. Dissertation, Carnegie-Mellon University, Pittsburgh, PA, 1983.
5. Sunwoo, A. J., Bradley, E. L. III, and Morris, J. W. Jr., Met. Trans., Vol. 21A (1990), pp. 2795-2804.

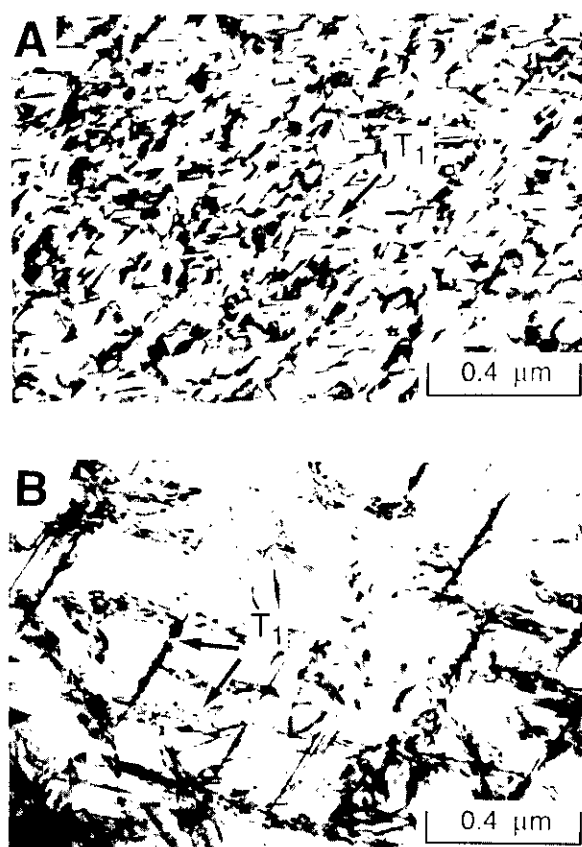


Fig. 6 TEM BF micrographs of the HAZ microstructures in the 160°C/16hr-aged GTA welds in 2195-T8: A) HAZ-10mm; and B) HAZ-5mm.

6. Martukanitz, R. P., Stevens, R. H. and Johnson, L. R., Microstructure Science, Vol. 14, ed. by M. R. Louthan Jr., I. Lemay and G. F. van der Voort (ASM International, 1987) pp. 53-64.

7. Hou, K. H., Baeslack, W. A. III, Szabo, A., and Lippold, J. C., AWS 75th Annual Convention, Philadelphia (1994).

8. Gayle, F. W. and Hou, K. H., private communication regarding Ag-containing α' precipitates. May, 1994.

Acknowledgments

The authors would like to express the appreciation to the Army Research Office for the financial support of this study and to Martin Marietta Corporation for providing the material.

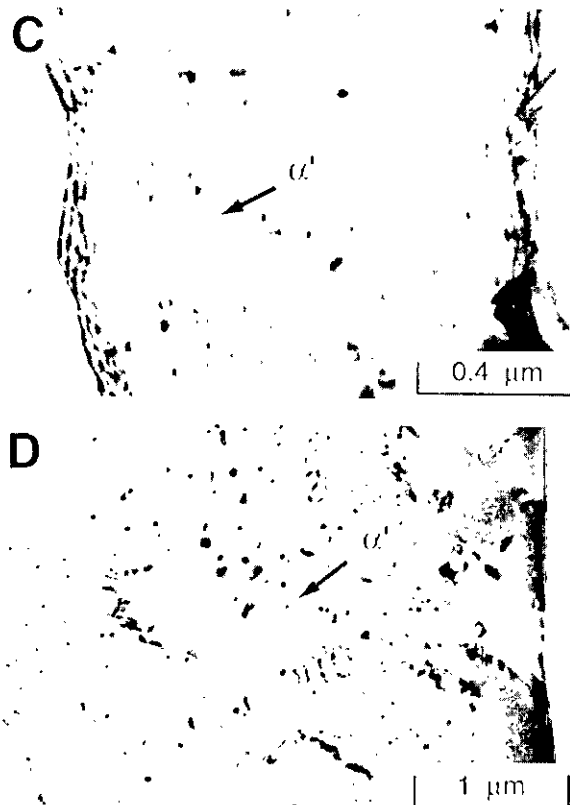


Fig. 5 (cont'd) TEM BF micrographs of the HAZ microstructures in the as-welded GTA welds in 2195-T8: C) HAZ-2mm; and D) PMZ.

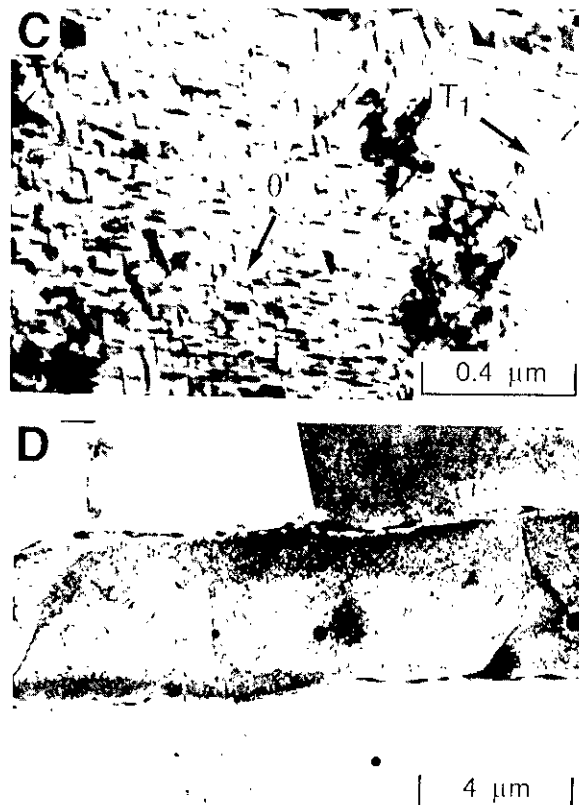
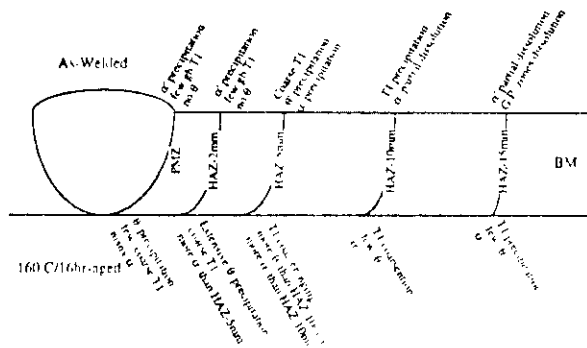


Fig. 6 (cont'd) TEM BF micrographs of the HAZ microstructures in the 160°C/16hr-aged GTA welds in 2195-T8: C) HAZ-2mm; and D) PMZ.

7A: 2195-T3 GTA Weld



7B: 2195-T8 GTA Weld

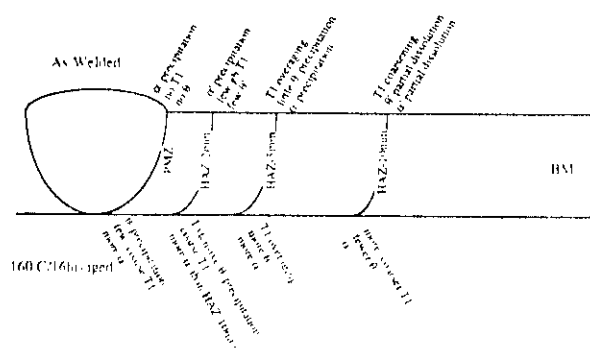


Fig. 7 Microstructures in the as-welded and 160°C/16hr-aged GTA weld HAZ's in A) 2195-T3; and B) 2195-T8. Description of the aged microstructures are relative to the as-welded microstructures.

Microstructure Evolution in the Fusion Welding of Heat-Treatable Al-Cu-Li Alloys
W.A. Baeslack

- Q: Diwan (Southern University) Very much enjoyed your presentation and the characterization of the structures. On this T1 phase, you got this softening dip and so on, quantitatively you have any range sizes that you had on the T1 precipitate.
- A: Yes, I do not have it memorized but it is in the paper though, the paper has measurements lengths of all and I cannot remember....
- Q: Diwan - Was it like twice the size?
- A: Yes. You could probably almost see that from the picture. I had better pictures but I tried to give the all the same magnification and similar pictures. But yes in fact there is quite a difference, in the paper he gives sizes for the Theta prime and plate length and the T1 plate length and also the diameter of the delta prime which is pretty hard to give.
- Q: Diwan - You might have it in the paper maybe.
- A: Yes it is all in the paper
- Q: Diwan - The comment on the same weld, we tested the 2195 VPPA welds and I also noticed the same kind of dips. That is really what prompted this thing. This student was about ready to graduate with the fusion zone work and he did his hardness transverses and he got so excited about this dip that he had to stay around another year.
- Q: ? - You eluded to the fact that in that near heat affected zone you believe that there is a lot of heterogenous nucleation on grain boundaries.
- A: Yes. But I think you have seen the same thing right, in a fusion zone, you get coarse T1 plates and we have seen that in the laser welds to. I have got a whole thesis or draft full of picture that show coarse T1 platelettes emanating growing from the grain boundaries and laser welds and I think in 2090 we still have the same thing not just 2195.
- Q: You may have shown that but I may have missed it, did 2090 did you see that dip in hardness?
- A: Yes.
- Q: Roy Crooks (Naval Postgraduate School) I wanted to make a comment on something that I have observed in 2094. In the heat affected zone of the VPPA welded 2094

and the as welded condition, we found three distinct regions. The closest one which went completely in the solution treatment temperature range and which was pretty much clear of a precipitates. The region that you are talking about when you are getting coarsening of the strengthening precipitates. And then an intermediate region between where the cooling range is slow enough to duplicate conditions you get in quenching a thick plates and that is you are bringing it down through the phase transformation nodes slowly around 350C. You get very coarse T1 precipitates.

A: Right. And that maybe what is happening here in fact that was my point in the beginning and that is why I did not really like to use the word coarsening here or overaging and that is not necessarily the case. It may be that some of these precipitates particularly in that region you are talking about.

Q: R.C. - In the 2094 these T1 plates were several microns.

A: Well some of these are several times longer than the base metal precipitates so...

Q: They difficult to study by TEM we use SEM.

A: That is a good point, when I kept saying overaging I felt that was not entirely clear because you are right some of those coarse ones are probably not overaging from the base metal there in fact forming from the on cooling because from high temperature your hitting the nose of that curve. That is a good point.

Q: Diwan - On this other phases you mentioned S' and so on and T1 of course is there and delta prime do you have any other quantitative measurements done and did you find any TB or any other phases too.

A: We found S', an aluminum zirconium intermetallic and a couple of phases TB, I think you found, and there was a couple of others that he could not identify. He spent a lot of time a couple of weeks trying to look at patterns and just gave up and said they are the unknown phases whatever he called them. I think some other people have found some more types of unknown phases too.

Q: Tim Langan (Martin Marietta Labs) In trying to sort it out, 2 other things you might want to consider would be that the distribution of magnesium and silver which is going to enhance your nucleation of T1 and also the fact that your parent metal, I think probably 6% stretch. So you have lost your stretch in that near heat affected zone region too.

A: Yes that is certainly going to have an effect.

Cracking During Welding of 2195 Aluminum-Lithium Alloy: Experimental Approaches towards Mechanism

Jorge E. Talia¹ and Arthur C. Nunes, Jr.²

¹ Department of Mechanical Engineering
The Wichita State University
Wichita, KS 67208

² Materials and Processes Laboratory
National Aeronautics and Space Administration
Marshall Space Flight Center, AL 35812

Abstract

2195 aluminum-lithium alloy offers significantly more strength per weight than the current 2219 aluminum alloy. The replacement of 2219 alloy by 2195 aluminum alloy provides the basis for the new Space Shuttle Lightweight External Tank design. With its advantages the new alloy also offers certain challenges to technology. The new 2195 alloy has a greater tendency to crack during welding than its 2219 predecessor. Although numerous successful welds have been made in 2195 alloy, occasional cracking has been encountered during repair welding or as a result of sudden loss of arc or broken tack welds. Especially in the case of repair welds, it is important to control cracking. Failure to do so could result in heavy scrap costs. This paper gives a historical account of a study of cracking in 2195 welds with conclusions on the nature of the cracking mechanism.

Introduction:

Lithium, because it stiffens and strengthens while it reduces the density of aluminum alloys, presents itself as an attractive additive to improve the performance of low density aerospace structural alloys. In the mid - 1980's Weldalite 049 (4.5 - 6.3 Cu, 1.3 Li, 0.4 Ag, 0.4 Mg, 0.14 Zr) was developed by Martin Marietta Corporation to replace the 2219 alloy (6.3 Cu, 0.3 Mn, 0.18 Zr, 0.10 V, 0.06 Ti) used to fabricate the Space Shuttle External Tank. 2195 alloy, a modification of Weldalite 049 with reduced copper and lithium (4.0 Cu, 1.0 Li), was ultimately selected as the metal for the new Super Lightweight External Tank.

Because welding is the primary means of fabrication for the External Tank, weldability considerations were heavily weighted in the selection of 2195 aluminum - lithium alloy. As experience with the alloy grew, certain concerns arose, primarily regarding repair cracking, where residual stresses may increase with successive repairs, but also regarding occasional cracking in primary welds.

The most annoying kind of crack observed is the fusion line crack, which results in weld ruptures. This kind of crack appears as an "E-stop" crack, which trails behind a solidified weld pool after a sudden "emergency" or "E-" stop. (In 2219 alloy, cracks produced during an emergency stop confine themselves to the weld pool as "crater cracks.") Fusion line cracks may also form immediately behind the weld pool upon the occasion of a broken tack weld. Fusion line cracks are most commonly the result of repairs. The fracture surface morphology of a repair crack differs from that of an "E-stop" crack; thus, the two kinds of fusion cracks are not identical.

Other somewhat more benign forms of cracking are delamination in the weld heat - affected - zone (HAZ) and interdendritic fissures in the fusion zone. Porosity also is seen, both in the HAZ and the weld fusion zone.

Welding difficulties of aluminum-lithium have generally been attributed to a tendency to intergranular/interdendritic liquation. Dvornak *et al.* [1] report a brittle temperature range (BTR) of 73 °C below the liquidus temperature for Al-2.2 Li - 2.7 Cu with a minimum tolerable strain (ϵ_{min}) of 0.0 to

0.1% in the BTR. "Good welding" alloy 5083 had BTR and e_{\min} 68 °C and 0.3 to 0.5 %; "bad welding" alloy 2024, had 80 °C and 0.1 to 0.3 % respectively. Whether susceptible alloys actually crack on welding depends upon the temperature-strain history encountered during the welding process [2]. R.Thompson [3] reports Auger observations of Li concentrations on 2195 alloy weld fracture surfaces.

Lithium, by virtue of its chemistry, produces certain effects on its alloys with aluminum. It has a tendency to migrate to the surface and reacts with oxygen so as to increase the oxidation rate of the alloy [4]. This feature necessitates more stringent shielding during the welding of aluminum - lithium alloys, i.e., backshielding and reduced torch standoff. If there is moisture present at the surface, lithium can remove the oxygen to release hydrogen [5], which then can dissolve into the alloy. The dissolved hydrogen can form LiH particles, and these particles can nucleate H_2 to form pores. (Since at 550 °C lithium diffuses at a rate about four times faster than aluminum, a Kirkendall-effect vacancy backflow may also generate porosity.) If this surface layer is not removed (to a depth of 0.2 mm), welds made in the metal exhibit porosity [6].

Aluminum welds not containing lithium tend to exhibit "primary" porosity directly upon solidification because the molten metal can absorb much more hydrogen than solid metal can [7]. The Variable Polarity Plasma Arc (VPPA), welding process currently used to fabricate the Space Shuttle External Tank, for the most part eliminates primary porosity due to the flushing action of the plasma jet [8]. Lithium increases liquid solubility of hydrogen and still more solid solubility. Following Anyalebechi et al. [9] we may take the reduced "partition coefficient" to imply that Al-Li alloys have a reduced tendency to primary porosity and an increased tendency for residual hydrogen accumulation in a weld fusion zone.

Porosity in the context of our own observation of Al-Li alloy welds has tended not to be primary porosity but rather secondary porosity emerging out of solid metal as a consequence of exposure to heat. In some cases, both porosity and fissures emerged together out of the solid phase. The question arose whether atmosphere might have a significant effect upon weld cracking. This question stimulated the studies reported herein.

Time-Temperature-Transformation Observations:

A series of microstructures of the fusion zone of an autogenous 1-pass VPPA weld bead in 0.2 inches thick 2195 alloy plates resulting from exposure to differing atmospheres, temperatures, and times were observed. The atmospheres were air, oxygen, nitrogen, and vacuum and the temperatures were 350, 375, 400, 425, and 450 °C. Exposure times consisted of a heat-up time ranging from 6 to 14 minutes followed by a holding time of 0 to 8 minutes.

Nothing beyond minor precipitate coarsening was observed in the vacuum-heated samples (Figure 1), but the air-heated samples (Figure 2) exhibited what appeared to be dendrite boundary reaction associated with secondary porosity.

25 μm

Figure 1. 2195 weld metal fusion zone from weld sample exposed to vacuum at 450 °C for one minute.

By comparison of similar microstructures arrived at under different temperature-time combinations, an activation energy of 14 kilocalories per mole was estimated for the rate controlling reaction.

It is noteworthy that gradients were observed at the surfaces of the dendrites, but that the reaction took place uniformly over the weld cross section. If the reactant came from the atmosphere, the rate of grain boundary diffusion would have had to be fast enough so as not to be rate controlling over distances up to 0.1 inches.

25 μm

Figure 2. 2195 weld metal fusion zone from weld sample exposed to air at 450°C for one minute.

Nitrogen Linked to Weld Cracking:

A laser weld bead penetrating about halfway into a 0.2 inch thick 2195 Al-Li alloy plate was cut into sections which were heated to 450°C over a 6 minute period, held a minute, and gas quenched to cool in place to room temperature. This was done in various atmospheres: vacuum, helium, helium plus 10% nitrogen, 100% nitrogen, oxygen, and air. Cracking occurred in the fusion zone (Figure 3) only for atmospheres containing nitrogen.

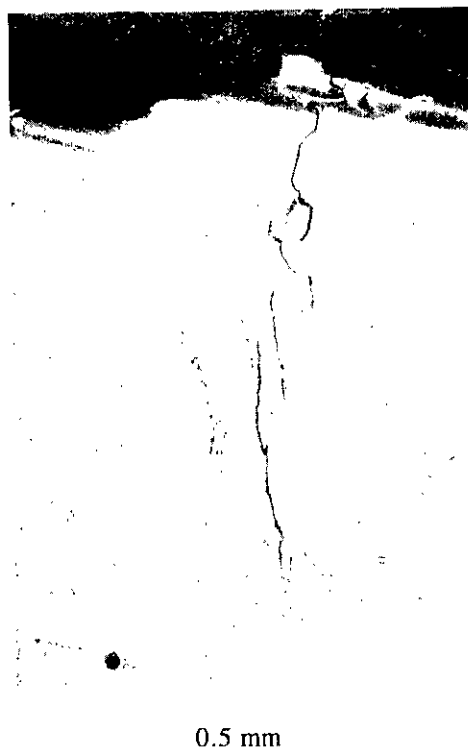


Figure 3. Laser weld bead in 2195 alloy exhibiting cracks after exposure to nitrogen at 450 °C.

Nitrogen Linked to Film Formation and Porosity:

A bottle of helium shield gas, accidentally contaminated with 1.2 % nitrogen, failed spectacularly to produce acceptable welds with 2195 Al-Li alloy although it was observed to produce acceptable quality welds with 2219 aluminum alloy. The weld metal failed to flow together properly behind the plasma keyhole and exhibited a dark surface film. The crinkly bead surface resembled those seen in 2219 welds when the reverse polarity cleaning cycle of the VPPA process is turned off.

Porosity was also exhibited (Figure 4), particularly close to and on either side of the fusion line at the root of the weld. Although this was an example of primary porosity, it is noteworthy that elliptical porosity occurred *in the solid phase* next to the spherical porosity of the liquid phase.

The detrimental effects of surface films on weld quality seem to occur very abruptly. Slight changes in welding conditions can transform a

welding operation to a cutting operation. Two heats of 2195 Al-Li alloy welded under the same conditions yielded the result that one 'would not weld,' i.e., exhibited grossly detrimental surface film effects, while the other welded nicely. The chemistries were almost identical, although the "weldable" alloy exhibited perhaps 5% less lithium. Those unwilling to accept that such a small amount of lithium could make such a difference created the myth of the "mystery metal," yet there is plenty of precedence [10] for large effects from small composition changes, at least where Marangoni effects are involved.



Figure 4. Porosity in 2195 alloy weld beads caused by 1.2% nitrogen contamination of helium shield gas. Note elliptical pores in parent metal.

Thermogravimetric Analysis (TGA):

Weight changes in a dry nitrogen atmosphere at constant temperature and constant-rate rising temperature were measured for 2195 Al-Li samples taken from parent metal and a weld fusion zone. If the weight gain is treated as a thermally activated process, an activation energy of 12 or 13 kilocalories per mole is measured for the process.

At first glance this looks to be about the same as the activation energy for the above microstructural process, but the microstructural figure comes from a comparison of temperature and time and the thermogravimetric, from weight gain rate and time. Where the same microstructure is arrived at by different temperature-time combinations, the product of the diffusivity and the time is a constant. Therefore, the microstructural activation energy should correspond to that of the diffusivity. If the TGA weight gain rate is proportional to the growth of a surface layer through which reactants must diffuse, the simplest model of the process puts the weight gain proportional to the square root of the rate controlling diffusivity. The constant temperature weight gain curves do look plausibly like square root functions of time, although the noses of the curves are obscured in the initial temperature rise domain.

In addition, the reaction produces a brown film on the surface of the specimen. The film attacks the platinum crucible used to hold the specimen when the temperature moves into the neighborhood of the alloy liquidus. These features are characteristic of Li_3N .

Differential Thermal Analysis (DTA):

Differential Thermal Analysis compares the temperature of a given sample of metal with that of a standard. The temperature differences are sensitive to phase changes that produce or absorb heat. Exothermic phase changes produce a temperature rise spike; endothermic phase changes generate a temperature fall spike.

When 2195 weld fusion zone metal was heated from room temperature to a little above 600 °C in nitrogen, oxygen, helium, or air, all samples exhibited a small endothermic transformation at about 530 °C, while those heated in nitrogen or air also exhibited exothermic transformations at about 360 °C (Figure 5). Of the two exothermic spikes at 360 °C, the one for pure nitrogen was significantly larger than that for air. These features may be interpreted as indicating a nitrogen reaction that takes off and then saturates around 360 °C and, perhaps, a partial melting at grain/dendrite boundaries at about 530 °C. When 2195 parent metal was heated over the same temperature range in each of the same four atmospheres, no phase transformation spikes of either type were exhibited (Figure 6). This may be caused by lack of grain boundary penetration to the surface,

and/or by lack of hydrides (introduced during welding ?) and/or by conditioning of phases to reduce or eliminate production of transient grain-boundary-wetting liquid phases.

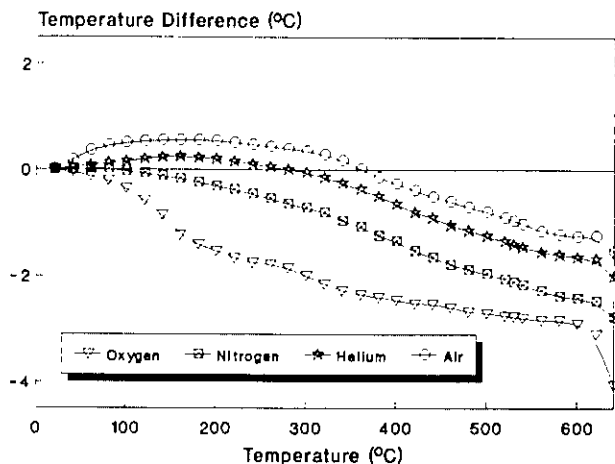


Figure 5. Differential Thermal Analysis curves for 2195 weld metal.

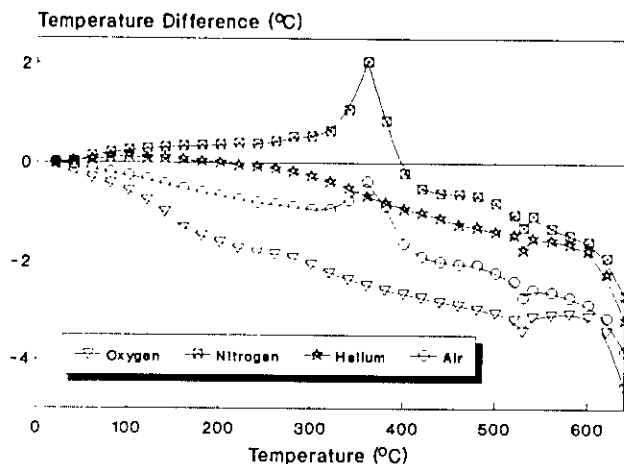


Figure 6. Differential Thermal Analysis curves for 2195 parent metal.

SEM Observations:

The time allowed for this presentation does not permit a detailed presentation of SEM studies of crack/fracture surfaces, pores, and blisters and their environments in 2195 alloy. Some of the visually observed cracks were opened in tension to study the characteristics of the fracture surfaces.

In general, the crack/fracture surfaces exhibit two different aspects: rounded, apparently melted dendritic surfaces (Figure 7) and torn, apparently ductile surfaces (Figure 8). Repair cracks show less melting and more tearing than E-stop cracks (Figure 9).

Pores on crack surfaces (Figure 10) and blisters on plate surfaces (Figure 11) exhibited similar evidence of surface melting. Blisters are form in welds performed without backshielding. Nitrogen induced cracking on laser welds present evidence of melting (Figure 12). Energy Dispersive Spectrometry (EDS) microanalysis of all melted surfaces detects less copper, more nitrogen and oxygen than on the tearing surfaces. (The EDS system is unable to detect lithium.)

In the vicinity of cracks and blisters open to the surface, brown matter presumably expelled from the crack/blister is frequently visible (Figure 13 and 14). EDS analysis detects a high oxygen, nitrogen, and magnesium content in association with the matter.



Figure 7. Evidence of grain boundary melting on a crack fracture surface.



25 μm

Figure 8. Fractography showing a ductile fracture (tearing) on a crack fracture surface.



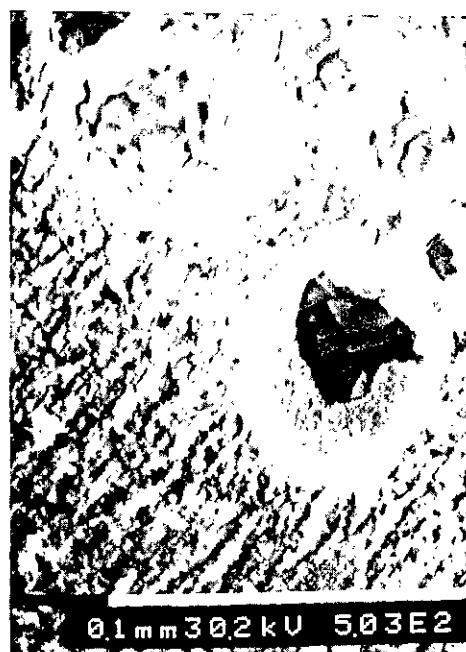
50 μm

Figure 10. Pore on fracture surface showing evidence of surface melting.



25 μm

Figure 9. Internal surface of an E-stop crack showing evidence of melting.



50 μm

Figure 11. Plate external surface formation of "blisters" exhibiting surface melting.



Figure 12. Laser weld showing nitrogen-induced intergranular crack fracture. Note the appearance of the crack surface.



Figure 13. Brown matter morphology observed near a repair crack.

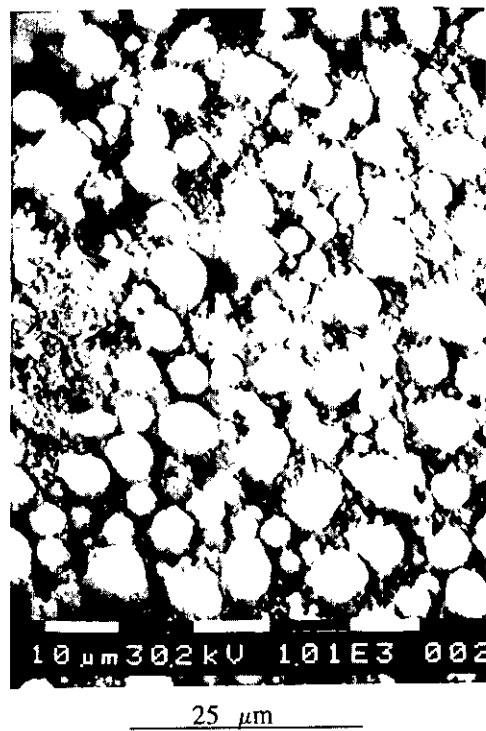


Figure 14. Brown matter with high magnesium content.

Additional evidence of melting and internal gas pressure can be observed in Figure 15. A protuberance or "lip" was formed near a repair crack presenting strong evidence of material displacement. Note that the internal pores and external "blisters," presented in Figures 10 and 11 respectively are produced by gas pressure.

CONCLUSIONS:

2195 weld metal exhibits an endothermic phase transformation at about 530 °C that would be consonant with grain boundary liquation. The wrought parent metal does not exhibit the transformation. Observations of the surface melting on fracture surfaces are also consonant with grain boundary liquation.

Nitrogen reacts with 2195 alloy at temperatures above 360 °C. The reaction results in a surface film having properties of Li_3N when produced in large quantities near alloy melting temperatures. The reaction also produces internal and surface porosity and, in at least one case, has been associated with cracking.



250 μ m

Figure 15.- Overview of a repair crack.

Acknowledgment:

This work was supported by the NASA/ASEE Summer Faculty Fellowship Program, NASA Grants N^o NGT-01-008-021 and N^o NGT-01-002-099.

References:

1.- Dvornak, M.J., Frost, R.H., and Olson, D.L. 1989. The Weldability and Grain Refinement of Al-2.2 Li-2.7 Cu. *Welding Journal* 68 (8), 327-335.

2.- Nunes, A.C., Jr. 1983. Interim Report on the Microfissuring of Inconel 718. NASA Technical Memorandum T-82531. Marshall Space Flight Center.

3.- Thompson, R.G. 1994. Private Communication.

4.- Burke, M. and Papazian, J.M. 1985. Elevated Temperature Oxidation of Al-Li Alloys. Proceedings of the Third International Aluminum-Lithium Conference, University of Oxford 8-11 July. The Institute of Metals: London 1986.

5.- Dickenson, R.C., Lawless, K.R., and Wefers, K. 1988. Internal LiH and Hydrogen Porosity in Solutionized Al-Li Alloys. *Scripta Metallurgica* 22 917-922.

6.- Canaby, J.L., Blazy, F., and Fries, J.F. 1991. Effects of High Temperature Surface Reactions of Aluminum-Lithium Alloy on the Porosity of Welded Areas. *Materials Science and Engineering A* 136, 131-139.

7.- Woods, R.A. 1974. Porosity and Hydrogen Absorption in Aluminum Welds. *Welding Journal* 53 (3), 97- 108..

8.- Nunes, A.C., Jr., Bayless, E.O., Jr., Jones, C.S., III, Munafo, P.M., Biddle, A.P., and Wilson, W.A. 1984. Variable Polarity Plasma Arc Welding on the Space Shuttle External Tank. *Welding Journal* 63 (9), 27-35.

9.- Anyalebechi, P.N., Talbot, D.E., and Granger, D.A. 1989. Hydrogen Solution in Al-Li Alloys. *Light-Weight Alloys for Aerospace Applications*. Ed. by Lee, E.W., Chia, E.H., and Kim, N.J., The Minerals, Metals & Materials Society.

10.- Lambert, J.A. 1991. Cast-to-Cast Variability in Stainless Steel Mechanized GTA Welds. *Welding Journal* 70 (5), 41-52.

**Cracking during Welding of 2195 Aluminum-Lithium Alloy:
Experimental Approaches towards Mechanism
Jorge E. Talia**

No questions.

NEAR-NET FORGING OF ALUMINUM-LITHIUM ALLOY 2195

J.E. Dyer¹, D.B. Sisk², I.K. Hall¹

¹Martin Marietta Space Systems
San Diego, CA 92123

²Martin Marietta Space Systems
Huntsville, AL 35806

Abstract

Aluminum-lithium alloys can reduce the weight of launch vehicle structure 10-15% compared to conventional aluminum alloys. However, the cost of aluminum-lithium is four to five times higher. This higher cost has fueled research into "near-net shape" technologies capable of producing large aluminum-lithium components for launch vehicles structural applications. Near-net shape refers to a class of forming techniques that rely on metal flow to produce thickness changes and integral rings and stiffeners as opposed to the more conventional approach using metal removal (machining). Near-net forming can potentially reduce the recurring cost of launch vehicle structure up to 65% versus conventional methods through more efficient use of raw material, fewer secondary operations and reduced assembly time.

This paper describes the status of an ongoing NASA sponsored program to develop low cost near-net roll forged aluminum-lithium cylindrical structures for launch vehicle propellant tanks and other primary structures. Initially this program has focused on propellant tank applications using the 2195 aluminum-lithium alloy.

The overall program is divided into two phases. The first phase, managed by NASA Langley Research Center, focuses on optimizing the near-net roll forging process for 2195 aluminum-lithium alloy. This effort uses a design of experiments approach to fabricate and test subscale (approximately 1-meter-diameter) near-net forged aluminum-lithium cylinders with integral external axial and internal hoop stiffeners. Detailed forging process parameters, material properties and cost benefit analyses are the primary outputs of this first phase. The second phase of the program, managed by NASA Marshall Space Flight Center, focuses on demonstrating scale-up of the near-net forging process. In this phase, full scale, integrally stiffened, 170-inch-diameter by 18-inch-high 2195 aluminum-lithium near-net forged cylinders will be fabricated and integrated into a structural test tank.

I. Introduction

Background

This project originated as a result of low cost launch vehicle system studies in the late 1980s. These studies addressed a universal concern that excessive launch system costs were limiting the full utilization of space. For a typical expendable launch vehicle, the primary structure, shown in Figure 1, constitutes over 50% of the vehicle dry weight and approximately 20% of the vehicle recurring cost. To achieve significant launch system cost reduction while meeting performance requirements, innovative low cost structures technologies are needed.

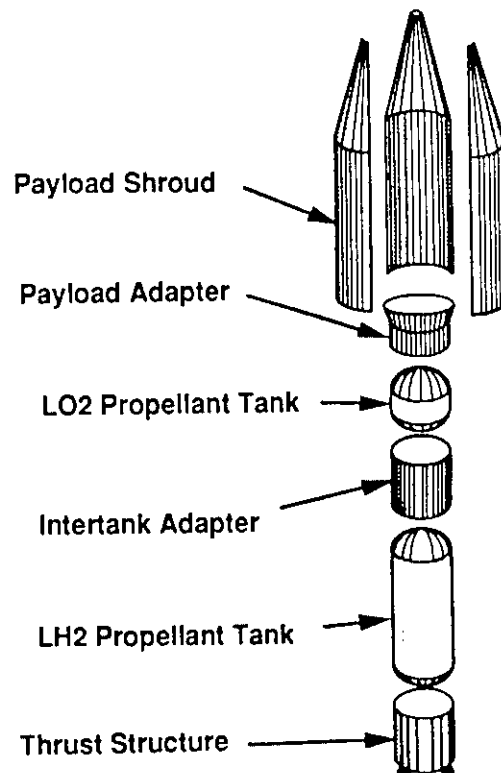


Figure 1. Typical Expendable Launch Vehicle Structures.

Early studies showed that lightweight, high strength aluminum-lithium alloys combined with near-net shape forming technologies provided the needed combination of low cost and good performance. Of the near-net shape technologies, near-net forging is especially attractive in the areas of low material usage, design flexibility and reduced assembly operations.

The problem is that conventional near-net forging technology can not cost-effectively produce

the large integrally stiffened parts, with a plan area in excess of one hundred square feet, needed for launch vehicle primary structure. In 1989, working with the Ladish Company on an internal research and development (IR&D) project, Martin Marietta Space Systems developed a process for producing large near-net forged cylinders (up to 30 feet in diameter) with integral rib stiffeners. Feasibility of the concept was demonstrated in 1991 with the fabrication of a subscale isogrid stiffened aluminum cylinder approximately one meter in diameter, Figure 2.

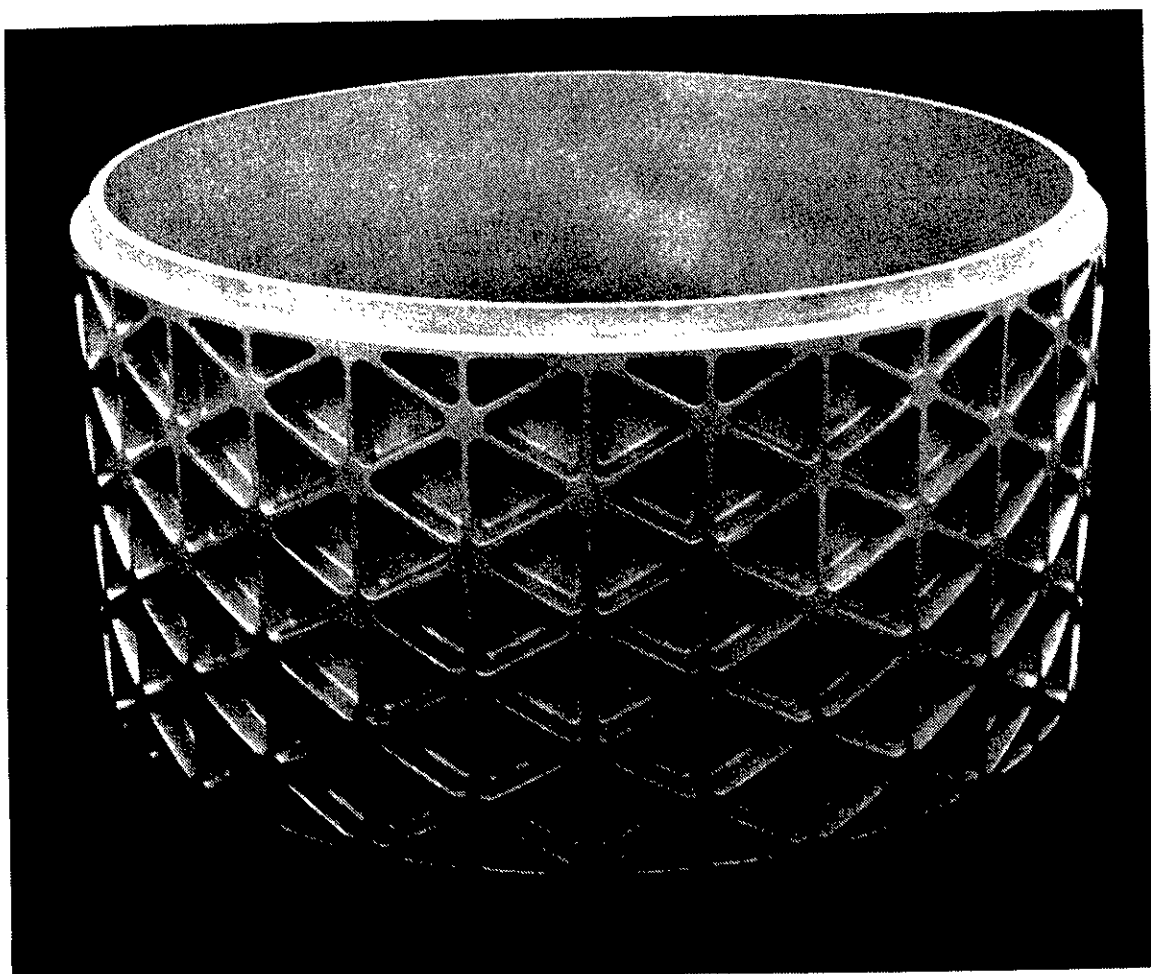


Figure 2. IR&D Near-net forging feasibility demonstration cylinder.

Initial cost-benefit studies identified potential cost savings in excess of 65% for near-net forged aluminum-lithium propellant tank structure when compared to conventional machined plate construction.

Near-Net Forging Process Description

Near-net ring forging offers the potential to produce one piece, integrally stiffened cylinders up to 30 feet in diameter and 10 feet in length using existing commercially available equipment. It is an adaptation of conventional seamless ring rolling with unique tooling and processing operations to forge integral stiffening elements. Figure 3 illustrates the main steps in the process.

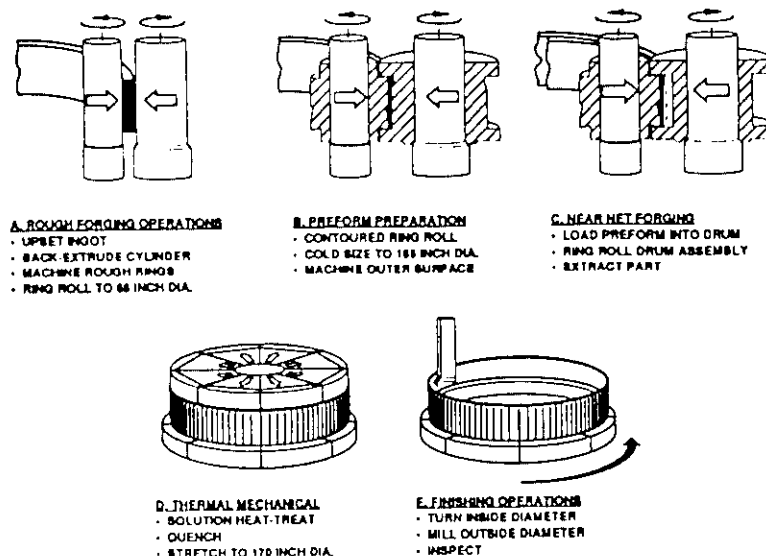


Figure 3. Near-net forging process for producing large integrally stiffened cylinders.

In this process, conventional cast ingot to forged billet conversion, back extrusion and ring rolling are used to create a heavy walled cylindrical aluminum preform. The preform is then rolled in a special set of contoured rolling dies to near final diameter. The contoured dies forge material into areas on the inner surface of the preform where large circumferential features such as internal ring stiffeners will be located in the final part.

The contoured aluminum cylinder preform is then loaded into a steel drum tool that has reliefs machined into its inner surface. These reliefs are a reverse pattern of the external stiffeners to be forged into the outer surface of the aluminum cylinder. The steel tooling, along with the aluminum preform, is heated to forging temperature and then rolled in standard ring rolling equipment. During rolling the aluminum material is forged into the reliefs in the outer drum tool creating a net forged stiffener pattern.

After forging, the aluminum cylinder is removed from the tool, solution heat treated, stretched and artificially aged. A simple machining operation on the inside diameter reduces the as-forged membrane thickness to the final dimension. The goal is to forge all external features to the final dimensions with no additional machining required.

Integrated Aluminum-Lithium Near-Net Forging Development Plan

In 1993, NASA initiated a two phased program with Martin Marietta Space Systems to further develop near-net forging technology, with specific focus on aluminum-lithium alloys. The first phase of the program, managed by NASA Langley

Research Center, is focused on developing aluminum-lithium near-net forging processes, fabricating subscale aluminum-lithium demonstration cylinders and validating near-net forging cost projections. The second phase, managed by NASA Marshall Space Flight Center, demonstrates near-net forging process scale-up by fabricating full scale, 170-inch-diameter, integrally stiffened aluminum-lithium cylinders. At the completion of this effort, the technology should be ready for production implementation.

The aluminum-lithium near-net forging development program is part of a larger integrated NASA effort to demonstrate advanced aluminum-lithium materials and manufacturing technologies for launch vehicle structures. This program, shown in Figure 4, culminates with the fabrication and testing of a full scale 170-inch-diameter launch vehicle propellant tank.

II. Aluminum-Lithium Near-Net Forging Process Development

The 30 month long phase I aluminum-lithium near-net forging process development program, which was initiated in April of 1993, is divided into four major tasks; (1) roll forging parameter development, (2) near-net forging parameter development, (3) near-net forged cylinder demonstration and (4) cost trade studies. In addition to evaluating cost savings associated with near-net forging, this effort develops and demonstrates at the subscale level all the processing parameters needed to produce the full scale demonstration articles in phase II. Since the initial application identified for this technology is cryogenic propellant tanks, forging development focused on aluminum-lithium alloy

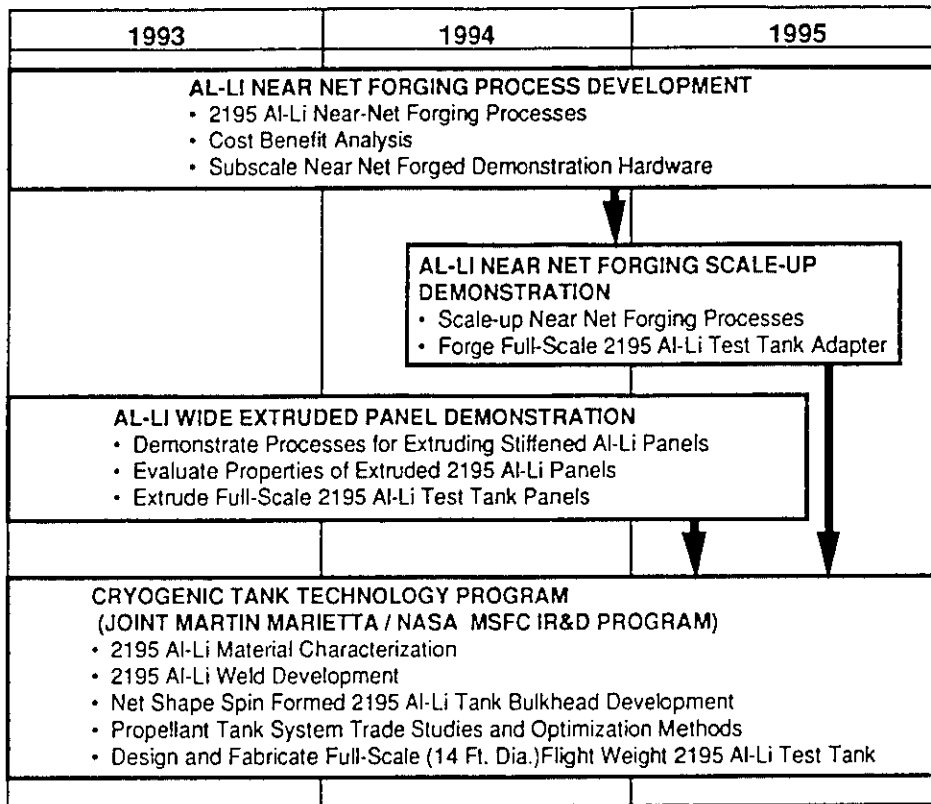


Figure 4. Integrated plan for advanced aluminum-lithium technology demonstration.

2195, which is currently the preferred propellant tank material. At the time of this writing Task 1 is complete and Tasks 2 and 4 are in progress.

Task 1 - Roll Forging Parameter Development

The objective of this task is to develop the basic process parameters for roll forging aluminum-lithium. Included in this task are 2195 aluminum-lithium forgeability evaluation, and 2195 rolled ring forging process development. Roll forging parameters including forging temperature, forging strain rate and total forging strain are optimized using design of experiments (DOE) methods. Metallurgical examination and mechanical testing are used to determine the effects of process parameters on microstructure morphology and mechanical properties of the alloy.

Task 1a - 2195 Forgeability Evaluation

The forgeability evaluation consisted of temperature gradient bar tests, axisymmetric wedge tests and simulated ring rolling experiments, all designed to provide initial rolled ring forging parameter limits.

a. Temperature Gradient Bar Tests. Three bars approximately eight inches long were machined from 2195 cast ingot and three from 2195 forged billet. One end of each bar was heated in a special furnace so that the temperature along the length of the bar varied from 1000 to 520°F. Two bars were held at temperature for one hour, two at eight hours and two at 24 hours. The bars were then examined to identify the incipient melting temperature, structural changes (grain size and recrystallization temperature) as a function of temperature and time, and precipitation reactions (morphology and precipitation temperature range). Results of this evaluation included:

- The incipient melting point could not be determined.
- Heavy precipitation was seen between 520 and 700°F.
- Localized heavy precipitation was seen at 800°F for ingot samples held for one and eight hours.
- 24 hour hold time at 800°F appears to homogenize the ingot samples and eliminate local heavy precipitation.
- Ingot precipitates had a very distinct needle/platelet shape.
- For the billet, uniform precipitation started at 800°F.
- The billet precipitates were spherical to slightly elongated.

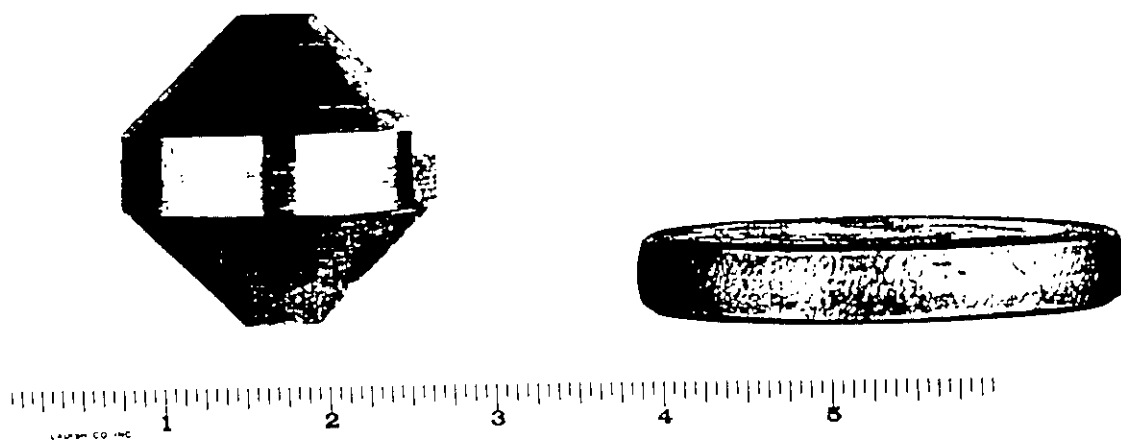


Figure 5. Axisymmetric wedge test specimen-before and after forging.

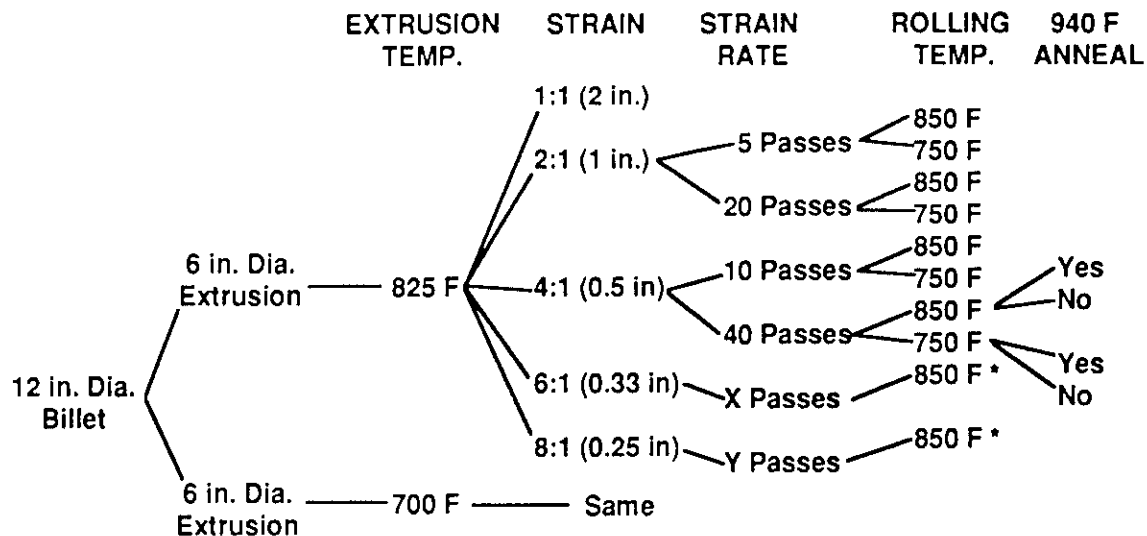
b. Axisymmetric Wedge Tests. Special axisymmetric wedge test specimens, Figure 5, were fabricated from 2195 ingot and forged billet material to evaluate forgeability (surface cracking and flow stresses) and material response (grain size/morphology as a function of forging strain rate, forging temperature and time at temperature). The axisymmetric wedge test specimens were designed to produce a gradient of total strain level from 0.5 at the outer edge to 2.0 at the center of the specimen when forged to the final shape. A total of 10 ingot specimens and six billet specimens were forged over a range of temperatures from 900°F to 400°F. Forging strain rate varied from 2.0 in/in/minute to 0.1 in/in/minute. Specimens were held at temperature for periods from 24 hours to 1 hour prior to forging. Results of the testing included:

- Ingot porosity initiated some minor edge cracking.
- Low temperature working, below 650°F, resulted in poor forgeability (rupturing).
- 2195 flow stress is strain rate sensitive at forging temperatures.
- Time at temperature does not appear to affect forgeability (flow stresses or cracking).
- 2.0 strain level at all strain rates and temperatures produced heavily worked and elongated structure.
- 0.5 strain level at all strain rates and temperatures produced only slightly worked and distorted grain structure.

c. Simulated Ring Rolling Experiments. This effort, designed to simulate rolled ring forging

operations, was conducted at the Reynolds Metals research center in Richmond, Virginia. The objective was to evaluate 2195 aluminum-lithium roll ring forgeability issues and select initial forging parameter values. These controlled experiments used laboratory plate rolling equipment to simulate the roll forging process. Both extruded and upset forged preforms were evaluated.

Two 12-inch-diameter by 12-inch-long forged billets and one 12-inch-diameter by 5-inch-thick forged billet were supplied to Reynolds Metals for these experiments. One of the 12-inch-long billets was extruded at 700°F and the other at 800°F into six inch diameter bar stock (4:1 area reduction). Rectangular blocks 2-inch-thick were machined from the extruded preforms and cross rolled perpendicular to the axial orientation to simulate ring rolling. Rectangular blocks were also machined from the 5-inch-thick forged billet preform and cross rolled to simulate ring rolling. As detailed in Figure 6, a wide range of experiments were conducted to evaluate the effects of extrusion temperature, roll forging temperature, reheat temperature, intermediate annealing, reduction per pass (strain rate), and reduction in area (total strain) on metallurgical structure. Rolling experiments were conducted at two different temperature range; 850-700°F and 750-600°F. Thickness reduction ratios varied from 1:1 to 8:1. To evaluate the effects of intermediate annealing, one specimen from each temperature range received an intermediate anneal at 940°F for two hours approximately half way through the rolling operation.



* Texture Analysis Only
(All Samples Tested in the T-6 Condition)

Figure 6. Simulated ring rolling experiment matrix.

After rolling, all of the specimens were solution heat treated and aged to the -T6 condition. Tensile tests were performed in the axial (L) and transverse (LT) directions and fracture toughness tests were performed in the through-thickness (S-T) direction. Major conclusions from the experimental test results are:

- Differences in tensile strength and fracture toughness were small for the range of experiment parameters evaluated.
- L and LT tensile properties for the extruded preforms were slightly higher than for the forged preform.
- L and LT tensile and S-T fracture properties are generally slightly higher with a high extrusion temperature, high rolling temperature, and high reduction per pass.
- An intermediate anneal during rolling produces only a slight increase in tensile and fracture properties.
- LT tensile yield strength decreases and S-T fracture toughness increases slightly with higher reduction in thickness (total strain).
- LT tensile yield strength decreased and S-T fracture toughness increased slightly with higher reduction in thickness (total strain).

Task 1b - 2195 Rolled Ring Forging Development

Using results from the roll forging parameter development task, six 2195 rolled ring forgings were produced at the Ladish Company in Cudahy, Wisconsin. These rings were used to evaluate the effects of forging temperature and reduction in thickness (total strain) on tensile strength and toughness. The matrix of forging variables is shown in Table 1.

After ingot conversion to billet, a back extrusion process was used to produce a thick walled cylinder 27.8 inches O.D. by 22.1 inches I.D. Individual ring preforms approximately 4.5 inches high were cut from the cylinder and ring rolled to the final ring dimensions. The six completed rings are shown in Figure 7. Metallographic evaluation and tensile and fracture toughness testing is currently being performed on the six rings.

After evaluation of test results for the six rings, optimum values for the forging process parameters will be selected and a process confirmation ring will be roll forged and tested.

Table 1. 2195 aluminum-lithium rolled ring forging variables.

Ring Number (Location in Back-Extruded Preform)	Ring No.	Forging Temp. (F)	Final Ring Dia. (in)
10			
9			
8			
7			
6			
5			
4			
3			
2			
1			
	3	850	55.9
	4	750	55.9
	5	750	31.5
	7	850	31.5
	9	850	55.9
	10	750	31.5

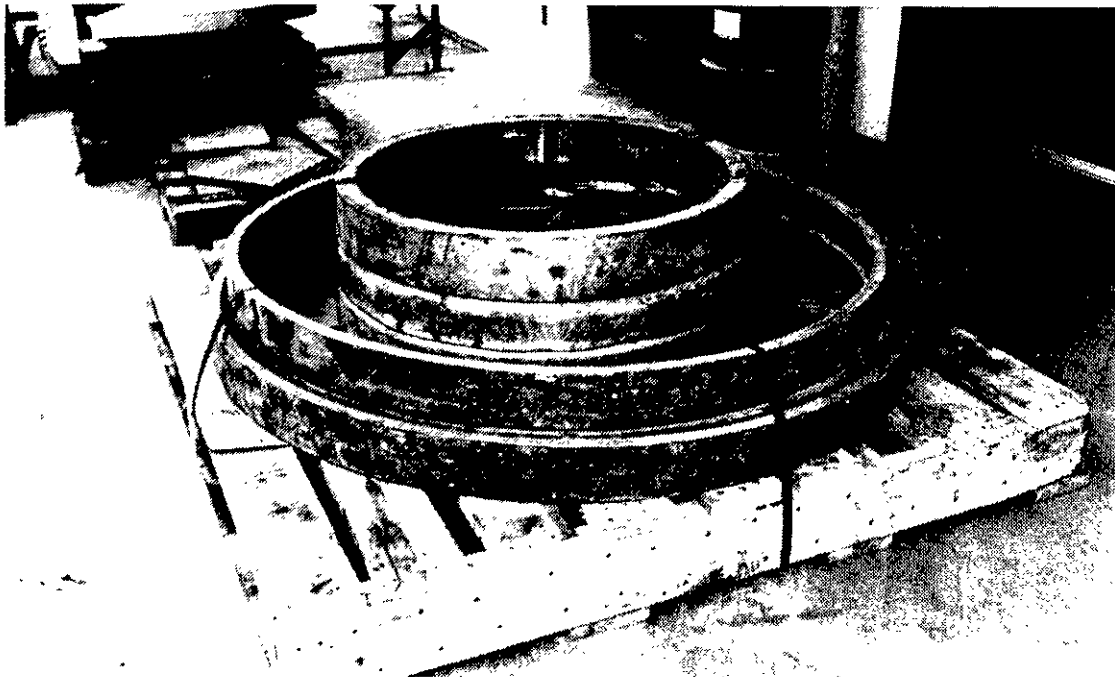


Figure 7. Completed 2195 aluminum lithium rolled ring forgings.

Task 2 - Near-Net Forging Parameter Development

Starting with the results of the 2195 rolled ring forging parameter development task, this effort

will develop designs, tooling and process parameters to roll forge near net cylinders with external axial and internal circumferential stiffeners. Eight subscale (approximately 1-meter-diameter) integrally stiffened cylinders, shown in Figure 8, will be fabricated using

Taguchi design of experiment (DOE) methods to optimize stiffener geometry and roll forging process parameters. The goal is to net forge all external surfaces of the cylinder, including the axial stiffeners. Metallurgical evaluation and tensile and fracture toughness testing will be performed on all eight cylinders.

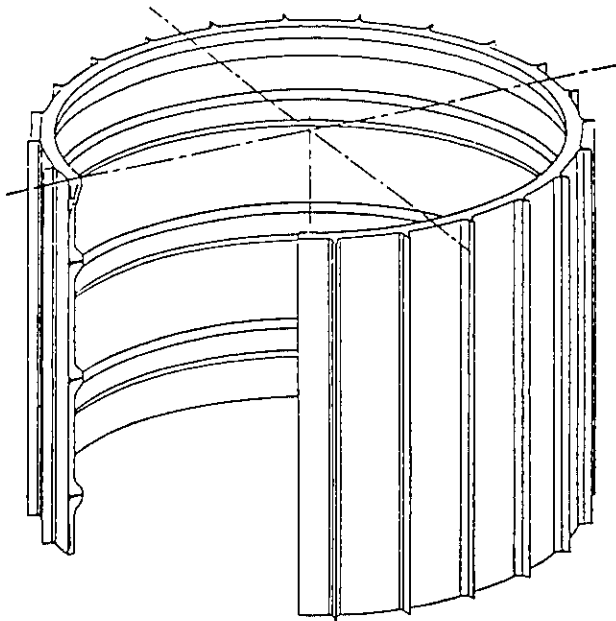


Figure 8. Subscale near-net forged 2195 aluminum-lithium cylinder.

Based on experience with the isogrid stiffened feasibility demonstration cylinder (Figure 2), the most critical issue is forging the external axial stiffeners into the cylinder without defects (laps, cracks and incomplete die cavity fill). A total of four stiffener geometries, four forging preform thicknesses, two forging temperatures and two forging rates will therefore be evaluated. To evaluate the forgings, detailed inspections, metallurgical evaluation, and mechanical properties tests (tensile and fracture toughness) will be performed on critical areas of the near net forged cylinders, with emphasis on the stiffener to cylinder transitions.

Task 3 - Near-Net Forged 2195 Cylinders

Using results from the near-net forging parameter development, this task will demonstrate the application of optimized forging parameters and stiffener geometry to a representative propellant tank structure. Included in this task is the design and fabrication of three subscale (one meter diameter) integrally stiffened cylinders representative of the cylindrical section of a launch vehicle cryogenic

propellant tank. Detailed inspections, metallurgical evaluations and material properties testing will be performed to verify integrity of the near-net forged cylinders.

Task 4 - Manufacturing Plans and Cost Trade Studies

This task, which extends over the full length of the program, develops near net forging manufacturing plans and cost data and conducts cost trade studies to compare alternative methods for producing large integrally stiffened aluminum-lithium cylindrical structures. Actual operations used to produce subscale and full scale near-net forged cylinders will be used to develop manufacturing plans and cost data. A near-net forging cost model will be generated and used to compare costs with other fabrication methods including integrally machined plate, wide near net extrusions and built-up structures.

III. Near-Net Forged Aluminum-Lithium Technology Scale-up Demonstration

The second phase of the near-net forging development program for 2195 aluminum-lithium is scheduled to begin in mid-1994. This phase will focus on the issues associated with scale-up of near-net forging to diameters of practical significance to the launch vehicle industry. Specific phase II objectives include:

- Proofing of the near-net forging tooling concepts and handling procedures.
- Assessment of tolerance control and final part dimensional stability.
- Characterization of room temperature and cryogenic mechanical properties of large near net forged rings.
- System level testing of near-net forged adapters to assess overall structural integrity.

To meet the phase II objectives we will produce four 170-inch-diameter by 18-inch-long near-net forged 2195 aluminum-lithium adapters. These adapters will be stiffened on the outer surface with net forged longitudinal blades and will incorporate an integral circumferential ring on the inner surface. The configuration of these four adapters is illustrated in Figure 9.

Pathfinder Development

The first of the 170-inch-diameter adapters developed during phase II will be a pathfinder article. This article will validate near-net forging tool designs and

process parameters through detailed destructive and non-destructive evaluations.

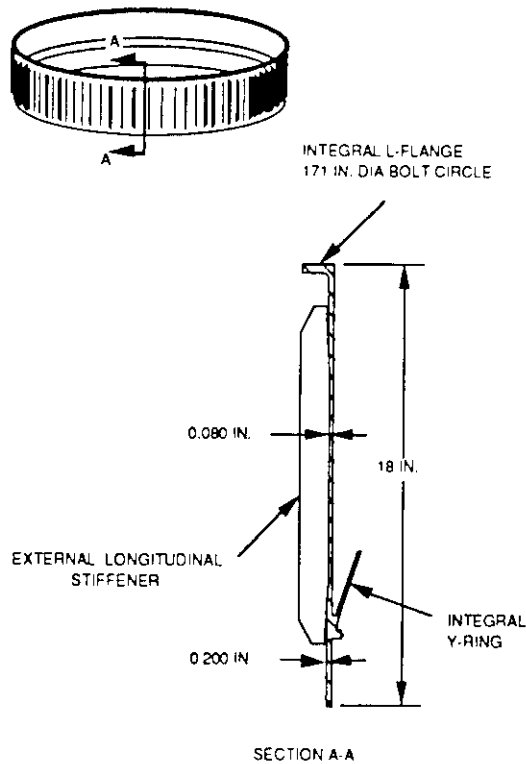


Figure 9. 170-inch-diameter near-net forged adapter configuration.

After near-net forging, solution heat treatment, cold stretch and artificial aging up to the T8 temper the pathfinder will undergo ultrasonic and visual inspection to assess forging quality. A complete dimensional inspection will be performed to evaluate tolerance control on the net features as well as the complete ring. The pathfinder will then be cut into sections so that microstructural evaluations and mechanical property test specimens can be removed. Mechanical properties testing will include tensile and fracture toughness evaluation at both room and cryogenic temperatures.

Flight Quality Adapter Manufacture

The results of the pathfinder article will be used to update the tools and near-net forging process parameters, if required. We will then produce three additional 170-inch-diameter by 18-inch-high near-net forged 2195 adapters. As with the pathfinder, these adapters will be solution heat treated, quenched, stretched and aged to the T8 temper and then inspected for dimensional accuracy and forging quality. In addition, grain structure, tensile properties and KIC fracture toughness will be evaluated using tag end specimens from each of the rings.

Based on the various quality inspections we will select the best two out of the three flight quality adapters and process them for inclusion in the system level test article.

System Level Testing

The final step in our development program will be the testing of near-net forged adapters in a system level test article. Two of the flight quality adapters will be machined on the inside diameter, using simple single point cutter lathe operations, to reduce the forged membrane thicknesses down to flight gauges. These adapters will then be mated to net shape spin formed 2195 aluminum-lithium domes and a cylinder produced from near-net extruded 2195 panels to form an advanced technology launch vehicle propellant tank test article. This tank is illustrated in Figure 10.

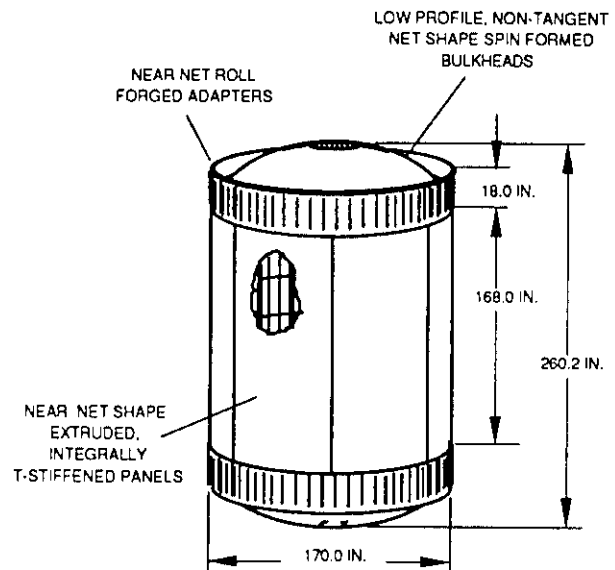


Figure 10. Advanced structural technology demonstration tank.

This advanced technology tank will be tested at NASA Marshall Space Flight Center structurally. The test program will include both internal pressurization and externally applied mechanical loads. Testing will demonstrate both strength and life capability of these technologies in a launch vehicle application. All testing will be performed at room temperature.

Manufacture of the near net forged adapters, assembly into this system level test article, and performance of a rigorous structural test will clear the way for near net forged components to enter full scale development on a future launch vehicle program.

IV. Summary and Conclusions

Aluminum-lithium alloys offer the potential for 10 to 15% weight savings for launch vehicle structures when compared to conventional aluminum alloys. In addition, new near-net forging processes offer a potential recurring cost savings up to 65% for large cylindrical integrally stiffened aluminum lithium structures when compared to conventional machined plate fabrication.

An integrated, multi-year development program has been initiated by NASA to demonstrate technical and cost feasibility of the aluminum-lithium near-net forging technology. During the first phase of this program, Martin Marietta, under NASA contract, has successfully developed rolled ring forging parameters for aluminum-lithium alloy 2195. During the next step in phase I, integrally stiffened 1-meter-diameter aluminum-lithium cylinders will be fabricated and tested to demonstrate feasibility of the near-net forging process. During the final phase of the program, scheduled for completion in 1995, process scale-up and cost feasibility will be demonstrated by near-net forging full scale 170-inch-diameter 2195 aluminum-lithium adapters, integrating these adapters into a representative launch vehicle propellant tank, and performing a structural test program.

Near Net Forging of Aluminum Lithium Alloy 2195
J.E. Dyer

- Q: I was just wondering whether you had any composition variations built into the program?
- A: The answer is no we have not. We have talked about that in terms of just the magnitude of the funding of the program. We are not able to cover all that in the program so we are just taking typical ingots and we are getting some variation from ingot to ingot. We are trying to assess that but we have been relying primarily on the material characterization work that other people have been doing so to give us a feel for the sensitivities. It is a good comment but that is not included currently into the program.
- Q: Kevin Alman (Alcoa) You mentioned in your presentation that you had two orientations that had similar properties. What orientations were those?
- A: Those were the through the thickness and if you think about a cylinder the radial direction and the actual direction. I mention that we had done some preliminary trials if you will a couple of years ago on IR and D on and we found that depending on the forging processing that you go through you can influence the ratio of properties in the 3 directions fairly significantly. We are aiming more to an isotropic as close to isotropic as we can get based on the forging parameters which we are setting. We try to work the material as close as we can in the 3 directions.
- Q: K.A. - One of the questions in the initial preparation for the billet you do for the extrusion process is there any variations in that extrusion process with temperature? And what is the ratio of that extrusion process?
- A: Good question. There is a step before the extrusion process and that is we go through a we call it a forging conversion process where we actually by upsetting the ingot we actually do a forging conversion to basically a wrought material. It is pretty uniform before we ever start the extrusion. And then we go through the back extrusion process which is you know you drop a billet into a pot and punch into it. I will talk a little bit more on that on the next briefing. The ratio's we have been using are not real high. You expect in the area of 2:1. Typically it varies depending on geometries, we have looked at a range of back extrusion ratios but typically around 2:1.
- Q: K.A. - This conversion process you are talking about is sort of like a hand forging?
- A: Yes, exactly and in the next presentation I will talk more about some of those processes.

- Q: Chris Barrett (Marshall) What is the goal date for a flyable superlight ET? The superlight tank what is the goal date for a flyable superlight tank?
- A: Someone else - This technology is not directed at producing a SLWT, IIT is a separate program. I think they are looking at a 1997 date for the SLWT.
- A: I will make one comment as you saw the 14ft. demonstration tank this is planning to go into would be completed in the 95 early 96 timeframe. Potentially for a series of testing programs. That schedule is being worked with for a lot of different reasons right so we can speed up that whole development program.
- Q: You probably mentioned this, but what is the thickness of your thinnest section?
- A: That is a good question because right now we are aiming to get down the order of about 2-3 times of the final thickness. In other words we are looking at the thicknesses in the order of a 1/4 to 3/8 of an inch as forged. But that is one of the parameters we are going to be assessing. We need to find out how thin we can really go and so we have a wide range of preformed thicknesses we are going to start with and try to find out what the problems are as we vary it, that is one of the variables we will be looking at 4 different thicknesses in our matrix. Because that is a very important issue obviously from weight savings but also from forgability so they are kind of conflicting problems and so that is one of our major parameters.
- Q: Eui Lee (Navy) Do you encounter any shape changes during quenching?
- A: It is really not a problem but there is some but we have not, let me answer it this way, in the sections that we have done so far which are really thick sections we have not seen a major change we expect to see more of that when we go to the thinner sections. So the answer is right now we do not see large changes because we have been working primarily with small rings and thick sections but we do anticipate there will be some and that is one of the things we want to evaluate both the subscale and the full scale as what kind of shape changes and you say it is not a real big problem as long as we can get it on the stretching system afterwards. We do not anticipate it will be out....
- Q: E.L. - It could be with the large rings?
- A: Yes, a 14 foot is a large ring and will be fairly thin so it is, actually we are more concerned about stability during the rolling operation than we are during the quenching operation because of the loads of the forces that are put into the ring during the ring rolling operation.
- Q: ? (McDonnell Douglas) We isogrid about 10 years ago and we had problem with shipping and transportation and damage to the rims. Is that a concern to you?

- A: I think if it is recognized as an issue and you package it or you handle it properly, I do not think so. We ship alot stiffened structures around, skin stringer kind of things with external stiffners, extrusions and we do not have problems with that. This is actually no different from some extruded sections. It is certainly you have to address though I agree.
- Q: Mack Roberts (Martin Marietta) You said that you used a modified L8, what is that?
- A: What we are doing if you look at the parameters I showed up there we have two sets of parameters one I call forging parameters and one I call stiffer geometry in the forging parameter because we want to run more than 2 preformed thicknesses there is a technique that you can use up to 4 parameters for 1 variable in the matrix and then you wind up with 3 separate parameters which is temperature, rolling speed, and preformed thickness. It is a technique that has been developed it is part of the basic Taguchi technology that you can use more than 2 values for a variable in the basic Taguchi method and that is what we are talking about. I would like to talk to you about that if you are interested.
- Q: M.R. - I know you were not here yesterday I gave a paper on design of experiments but I would suggest that there might be a better more efficient design you can use for more information.
- A: I would like to talk to you about that, appreciate that.
- Q: Bob DiTolla (Martin Marietta) Just kind of a dose of reality to this whole thing whether your goal is to develop this for a new launch vehicle or integrated within our current inventory I offer the following based on some experience we have had similar types of structures. There have been some great ideas and great cost savers and great weight savers but as you know an adaptor structure when integrated with a launch vehicle becomes very complicated because it has cut outs it is the mounting for avionic boxes or bottles ect., etc. One of the projects that came up a few years ago was a great structure but we were unable to use it for anything because it changed everything else about the launch vehicle. The way everything else was mounted and the cost of requalifying all the other equipment to mounting on that structure was so large that there essentially was no cost saving so I guess the only suggestion I would offer is that when you choose a design or a test maybe to fabricate you look at a real structure that has the same types of cutouts and mounting and so forth may save you some trouble in the long run I do not know.
- A: One of the advantages, one of the things we did do here by the way was the full scale part was really aimed at representing a piece of a real tank in the sense that it had interfaces and so forth that was pretty represented. It was really in areas which were fairly clean structures but in the areas where you do have mounting of the interfaces those have to consider, that is a good comment.

X2096 ALUMINUM-LITHIUM ROLLED RING FORGING DEVELOPMENT

J.E. Dyer¹, I.K. Hall¹, Dr. A. Cho², A.D. Dehbozorgi³

¹Martin Marietta Astronautics Space Systems
San Diego, CA 92123

²Reynolds Metals Company
Richmond, VA 23261

³Shultz Steel Company
South Gate, CA 90280

Abstract

As part of a continuing effort to reduce weight and increase performance on the Atlas/Centaur and Titan/Centaur launch vehicles, an internal research and development project was initiated at Martin Marietta Astronautics Space Systems (Formerly General Dynamics Space Systems) to develop rolled ring forging processes for aluminum-lithium alloys. These roll forged aluminum-lithium rings are to replace conventional aluminum alloy rings on launch vehicle adapter structures.

Based on an evaluation of critical material properties, Reynolds Metal's new aluminum-lithium alloy X2096 was selected for development. The primary objectives of the program were to develop X2096 rolled ring forging process parameters and to demonstrate that X2096 rolled ring forgings meet the requirements for near term implementation on current launch vehicle adapter structures.

A two phased design of experiments approach was used to develop and evaluate X2096 rolled ring forging process parameters. Phase 1, which was supported by Reynolds Metals, included simulated ring rolling experiments in the Reynolds Metals laboratories to identify critical processing parameters. In phase 2, which was supported by Shultz Steel, a Taguchi design of experiments approach was used to roll forge eight full scale X2096 rings representative of launch vehicle applications. Three critical forging parameters; forging temperature, forging strain rate and total forging strain, and their interactions were evaluated. Macrosections, micrographs and tensile test specimens were used to evaluate material properties.

Testing and analysis of the eight X2096 process development rings were very encouraging. Material properties were well above the minimum levels needed to replace the conventional aluminum alloys currently used for the adapter rings. Results were used to select final values for the critical processing parameters,

which were used to fabricate two confirmation rings.

1. Introduction

Recent materials research at Martin Marietta Astronautics Space Systems has focused on implementing lightweight aluminum-lithium alloys on existing Atlas/Centaur and Titan/Centaur launch vehicles. The principle driver behind the use of aluminum-lithium is the significant potential weight savings. Due to lower density, aluminum-lithium alloys offer 5 to 10 percent weight savings when substituted on a gage for gage basis for conventional aluminum alloys. Even greater savings can be realized by designing to take advantage of the superior strength and stiffness properties of aluminum-lithium alloys.

For the Centaur upper stage, used on Atlas and Titan launch vehicles, the payload fairing and various adapter structures, shown in Figure 1, use conventional aluminum built-up skin/stringer/frame construction. These are ideal structures for aluminum-lithium material substitution.

To date, lightweight 2090 aluminum-lithium skins and stringers have been implemented on two production adapters. The heavy interface rings at each end of the adapter structures, shown in Figure 2, are currently machined from 2124 plate or 2219 or 7075 rolled ring forgings. Because of large potential weight savings for aluminum-lithium interface rings, a development program was initiated by Martin Marietta Astronautics Space Systems in 1992 to develop aluminum-lithium rolled ring forgings. The objectives of this program were to select an aluminum-lithium forging alloy, develop aluminum-lithium rolled ring forging process parameters and demonstrate that aluminum-lithium rolled ring forgings meet all the requirements for near term implementation on Centaur adapter structure.

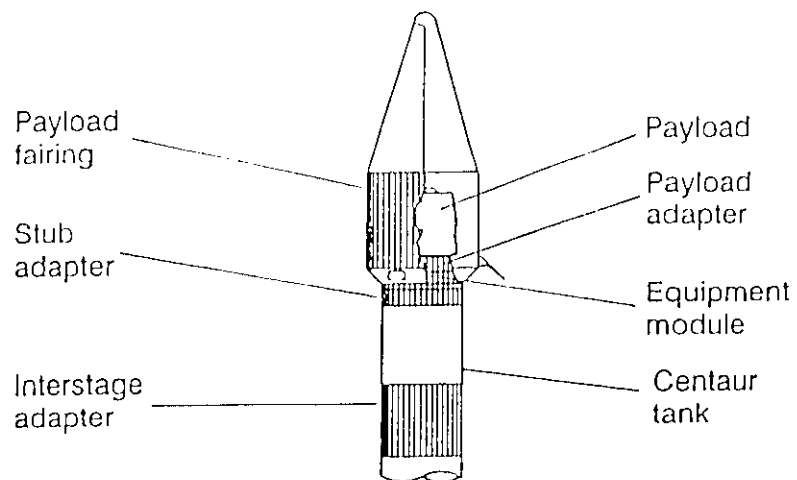


Figure 1. Atlas/Centaur structures - candidates for aluminum-lithium substitution.

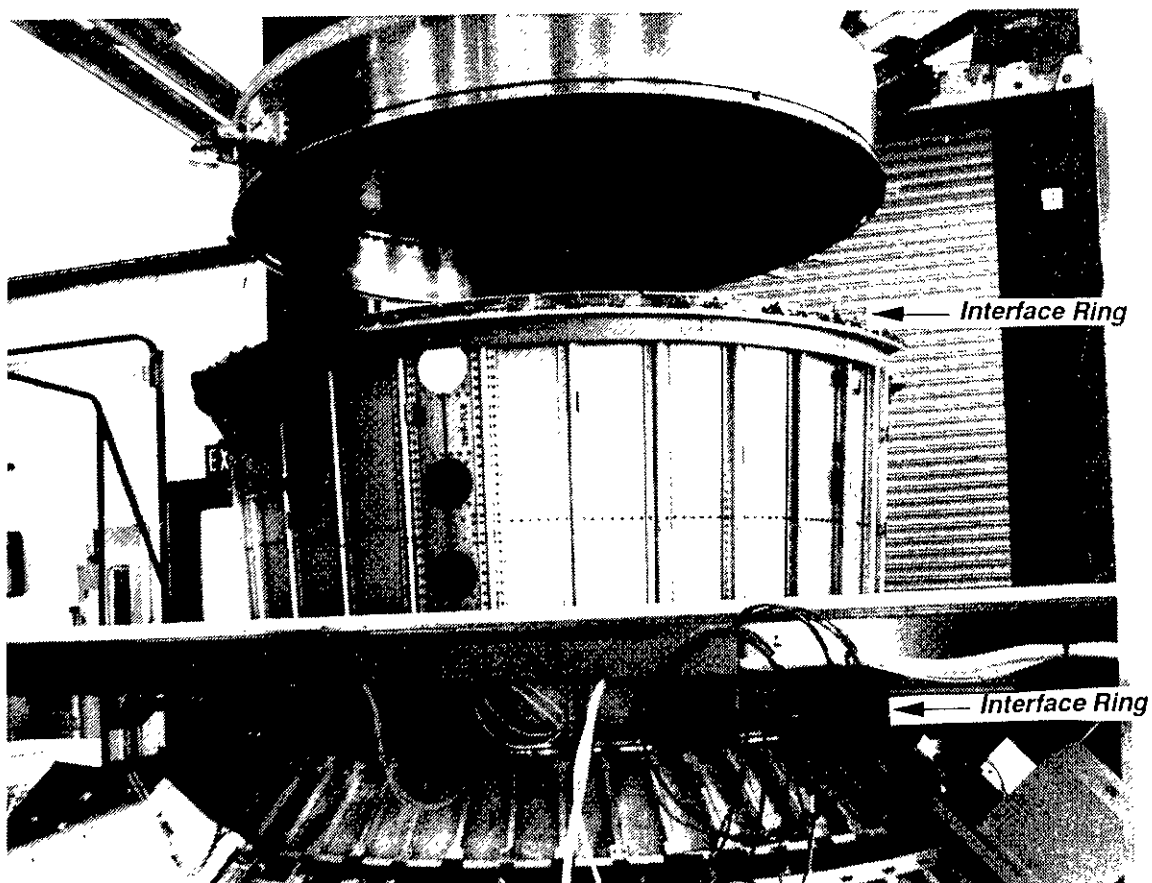


Figure 2. Adapter structures use machined interface rings.

II. Aluminum-Lithium Rolled Ring Forging Development Plan

After evaluating all of the available aluminum-lithium alloys, a new low density, high strength aluminum-lithium alloy, specifically designed to have improved properties in thick sections, was selected for rolled ring forging development. This alloy, designated X2096, was developed by Reynolds Metals for thick plate, extrusions and forging applications. X2096 is a member of the Weldalite family and contains 1.5% Li, 2.5% Cu, 0.4% Mg, 0.4% Ag and 0.13% Zr. Its density is 0.095 lb/in³, which is 7% lower than 2219 aluminum alloy. X2096 has good short transverse strength and toughness which is important for applications such as forged adapter rings which are loaded in the transverse directions.

Two initial X2096 feasibility evaluation rings were forged in 1992. Although results were encouraging, short transverse (radial) properties were lower than expected. For aluminum-lithium alloys, the final grain structure and material properties are heavily dependent on the complete processing history of the material. Selecting the optimum values for all the processes used in fabricating rolled ring forgings is therefore critical to obtaining the desired combination of strength and toughness. Recognizing this sensitivity, a two phased X2096 rolled ring forging process development program was initiated in 1993. This program,

which used a design of experiments approach, focused on selecting values for the critical process parameters at each step of the rolled ring forging process shown in Figure 3.

The integrated design of experiments approach used to evaluate and select values for the critical X2096 rolled ring forging process parameters needed to produce the desired material properties is shown in Figure 4. Details of each major task are discussed in the following sections.

III. Ingot Conversion

A 2150 lb X2096 cast rectangular ingot was supplied by Reynolds Metals for conversion to forged billet stock for initial forging parameter development. The ingot, approximately 10 inches by 41 by 61.5 inches was cut into 4 pieces for conversion into forged material. One piece of ingot was converted into 12 inch diameter bar and shipped to Reynolds Metals for simulated rolled ring forging experiments. The other three pieces were converted into 27 inch diameter billet to be used for back extrusion of rolled ring forging preforms. During the conversion process, the ingot was forged through a series of upsetting, edging and flattening operations to achieve the desired wrought structure. Figure 5 shows typical steps in the ingot conversion process.

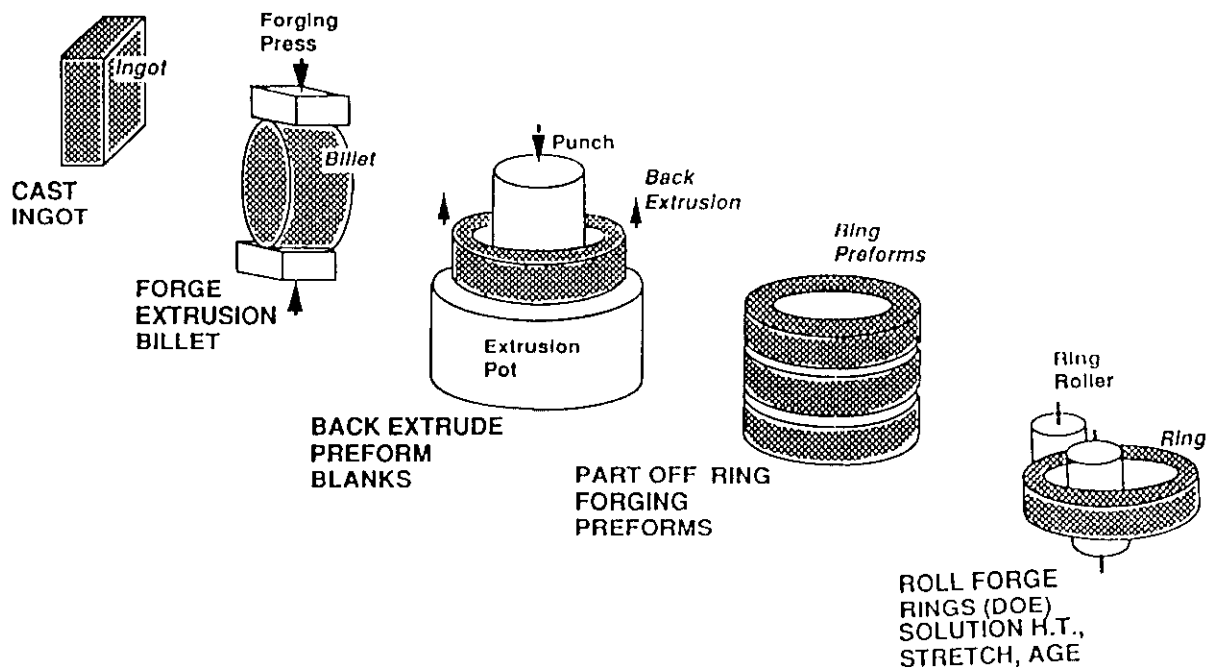


Figure 3. Rolled ring forging process flow.

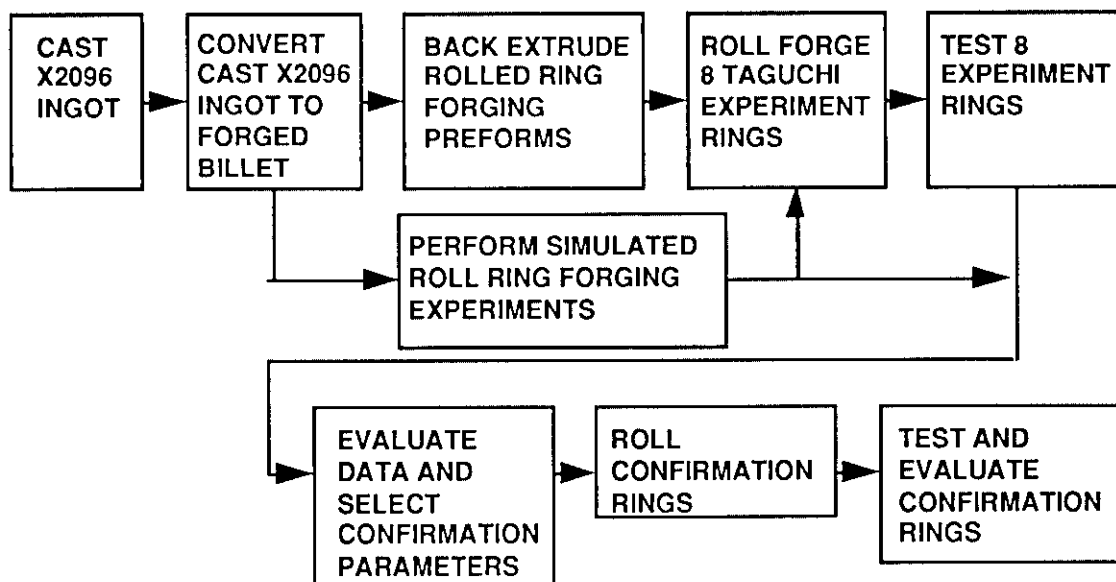


Figure 4. X2096 aluminum-lithium rolled ring forging development program.

IV. Simulated Rolled Ring Forging Experiments

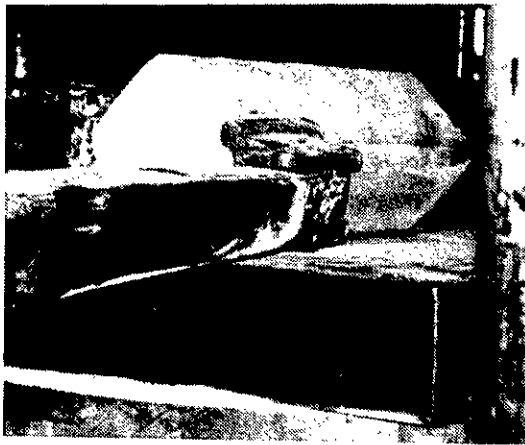
This effort, designed to simulate rolled ring forging operations, was part of a cooperative program with Reynolds Metals at their research center in Richmond, Virginia. The objective was to evaluate X2096 aluminum-lithium roll ring forgeability issues and select initial forging parameter values for the Phase 2 ring rolling experiments to be conducted at Shultz Steel. These controlled experiments at Reynolds Metals used laboratory plate rolling equipment to simulate the roll ring forging process. Both extruded and upset forged preforms were evaluated.

Two 12 inch diameter by 12 inch long and one 12 diameter by five inch thick forged billets were supplied to Reynolds Metals for these experiments. One billet was extruded at 700F

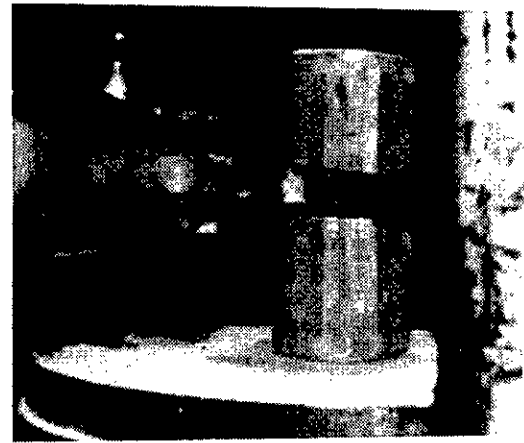
and the other at 820F into 6 inch diameter bar stock (4:1 area reduction). Two inch thick rectangular blocks were machined from the extrusions and rolled perpendicular to the axial orientation to simulate ring rolling. Two inch thick blocks were also machined from the five inch thick forged billet preform and rolled to simulate ring rolling. As detailed in Table 1, a wide range of experiments were conducted to evaluate the effects of extrusion temperature, roll forging temperature, reheat temperature, intermediate annealing, reduction per pass (strain rate), and reduction in area (total strain). Thickness reduction ratios varied from 1:1 to 4:1. Rolling experiments were conducted at two different temperature ranges; 900-750F and 800-650F. To evaluate the effects of intermediate annealing on material properties, two specimens, one from each temperature range, received an intermediate anneal at 990F for two hours.

Table 1. Simulated ring rolling experiment matrix.

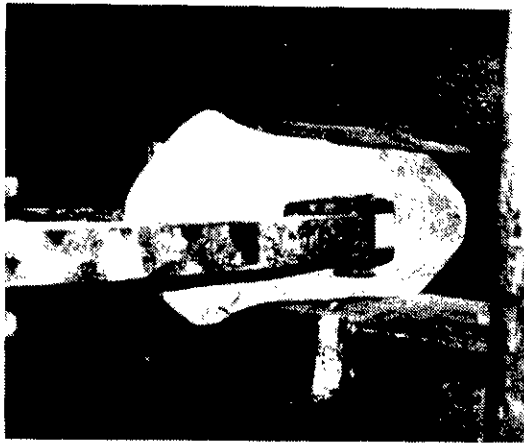
Preform Configuration	Extrusion Temperature	Total Reduction Thickness (total strain)	Thickness reduction per pass (strain rate)	Rolling Temperature	940°F Anneal
Extrusion/ forged billet	820°F/700°F	4:1/2:1	0.14 in./0.04 in.	850-700°F/ 750-600°F	Yes/no



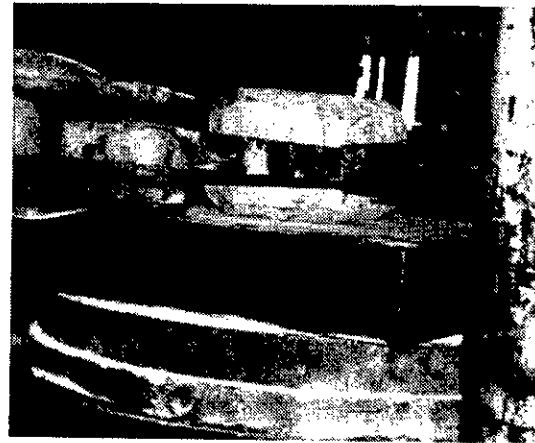
a) Break corners / Edge



b) Upset



c) Draw down



d) Final upset

Figure 5. X2096 ingot conversion process.

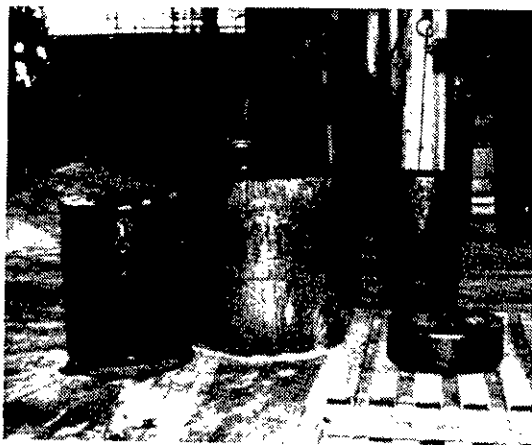
After rolling, all the specimens were solution heat treated and quenched in water than aged to the -T6 condition. Tensile tests were performed in the axial (L) and transverse (L-T) directions and fracture toughness tests were performed in the through-thickness (S-T) direction. Major conclusions derived from the experimental test results include:

- Differences in tensile strength and fracture toughness were small for the range of experiment parameters evaluated.
- L-T tensile strength and S-T fracture toughness for the extruded preforms were higher than for the forged preform.
- L tensile properties were higher for the forged preform.
- L-T tensile strength and S-T fracture toughness for the extruded preforms were higher for low extrusion temperature, high reduction per pass, low rolling temperature and low total reduction.

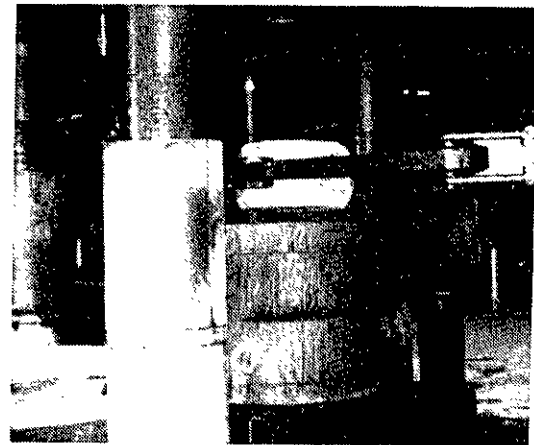
- L tensile strength was higher for high extrusion temperature, low rolling temperature, high reduction per pass and high total reduction.

V. Back Extrusion of Rolled Ring Forging Preforms

After ingot conversion, a back extrusion process was used to produce the cylindrical ring preforms. Back extrusion improves axial grain structure by providing hot working in the axial direction. A 28 inch diameter back extrusion pot and an 18 inch diameter punch (back extrusion ratio of 1.7:1) were used to produce the back extruded preform cylinders. Figure 6 shows the sequence of back extrusion operations. Three 28 inch diameter by 5 inch wall cylindrical preforms were produced. A total of eight rings six inches tall were parted from the three back extruded cylinders to be used for ring rolling experiments.



a) Back extrusion tooling



b) Load upset billet into pot



c) Back extrude



d) 3 back extruded cylindrical preforms

Figure 6. X2096 back extrusion process.

VI. X2096 Rolled Ring Forging Parameter Development

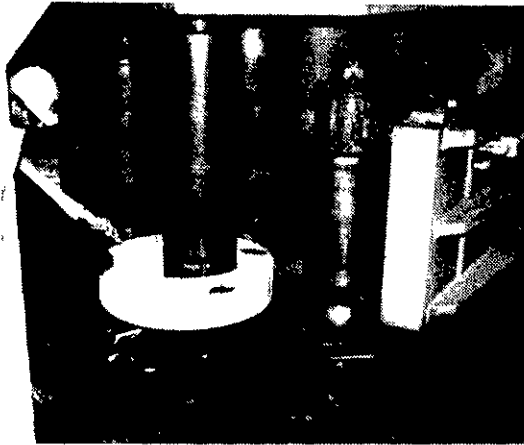
The X2096 rolled ring forging development effort was a cooperative program with Shultz Steel Company of South Gate, California. The objective of this task was to fabricate roll forged X2096 rings and to evaluate critical forging process parameters including rolling temperature, strain rate (thickness reduction per pass) and total strain (total reduction in thickness). This evaluation was accomplished using an L8 Taguchi design of experiments approach to quantify or rank the overall effects of each parameter and to select values for each parameter which collectively result in the highest forging quality and the best mechanical properties.

Taguchi Experiment Parameter Selection

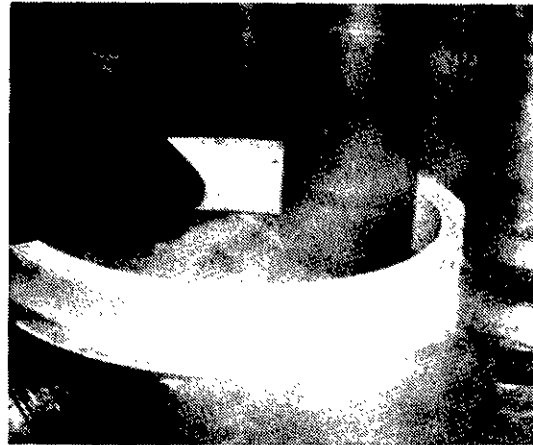
Results of the Phase 1 simulated ring rolling experiments at Reynolds Metals were used to help select the Taguchi L8 experiment with three factors at two levels and four interactions. The Taguchi L8 array is shown in Table 2. The three critical factors selected were; ring forging temperature, ring diameter growth rate (strain rate), and ring final wall thickness (total strain).

Table 2. X2096 rolled ring forging Taguchi design of experiments array.

EXPERIMENT NUMBER	ROLLED RING IDENTIFICATION	A DIAMETER GROWTH RATE (in./sec.)		B ROLLING TEMP RANGE (F)		AXB		C WALL THICKNESS (inches)		AXC		BXC		AXBXC	
		.2	.4	800 650	900 750			2.5	1.5						
		1	2	1	2	1	2	1	2	1	2	1	2	1	2
1	H	1		1		1		1		1		1		1	
2	G	1		1		1		2		2		2		2	
3	F	1		2		2		1		1		2		2	
4	E	1		2		2		2		2		1		1	
5	D	2		1		2		1		2		1		2	
6	C	2		1		2		2		1		2		1	
7	B	2		2		1		1		2		2		1	
8	A	2		2		1		2		1		1		2	



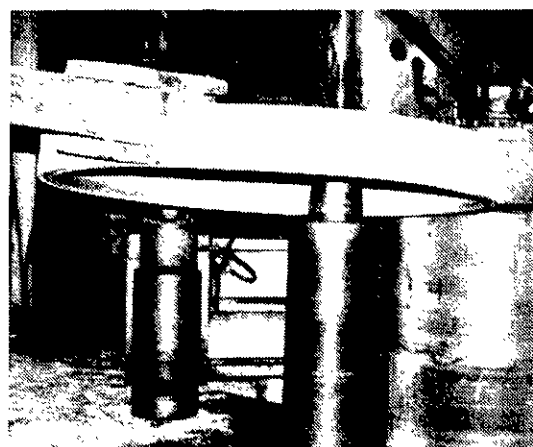
a) Load preform onto ring mill



b) Roll forge



c) Verify dimensions



d) Take to heat treat & stretch

Figure 7. X2096 ring rolling operations.

Ring Rolling Operations

The eight Taguchi experiment rings were rolled from the back extruded preforms as shown in Figure 7. Ring diameter growth rate was programmed into the Shultz Steel computer controlled ring rolling mill and all ring rolling followed the programmed growth rate profiles. The rolling speed remained constant on all rings

at 284 surface feet per minute. All rings were visually inspected and rough machined prior to heat treating and stretching. The 2.5 inch thick rings were solution heat treated at 995F for 2 1/2 hours. The 1.5 inch thick rings were solution heat treated at 995F for 2 hours. All rings were stretched 3-5 percent and then aged to the -T8 condition at 320F for 20 hours.

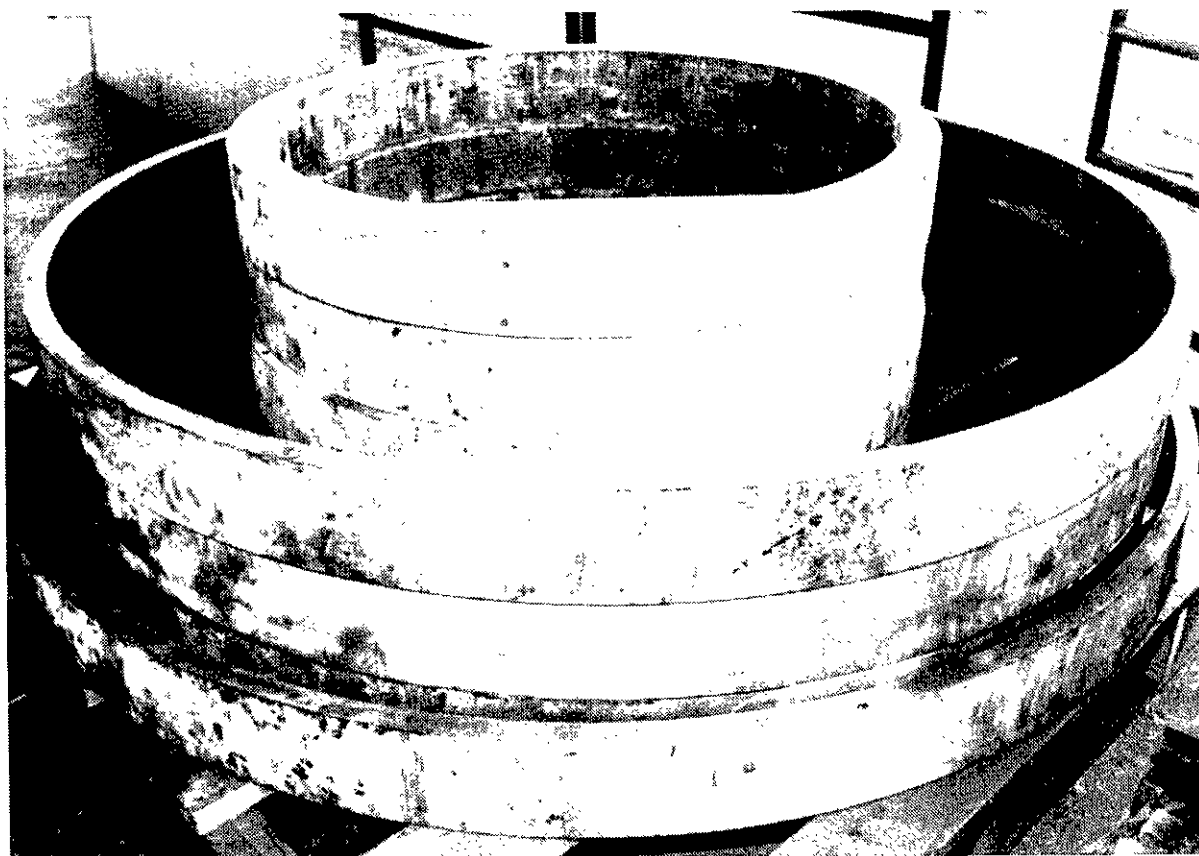


Figure 8. Eight completed X2096 rolled ring forgings. Large and small rings are approximately 73 and 41 inches in diameter respectively.

Table 3. X2096 Rolled Ring Forging Tensile Test Data

Ring	Circumferential			Axial			Radial		
	F _{tu} -ksi	F _{ty} -ksi	e-%	F _{tu} -ksi	F _{ty} -ksi	e-%	F _{tu} -ksi	F _{ty} -ksi	e-%
A	76.1	69.9	9.7	71.9	61.1	12.6	73.9	59.2	4.0
B	78.5	73.0	7.8	72.9	62.2	9.7	69.0	57.0	5.5
C	78.6	74.5	9.3	73.3	65.5	8.6	76.6	64.8	2.0
D	77.2	71.4	7.4	69.2	58.0	12.4	70.7	57.5	3.1
E	79.2	74.5	8.6	74.6	65.8	7.8	73.5	60.8	3.7
F	79.7	76.6	4.6	74.1	64.6	7.3	69.0	59.2	3.1
G	79.3	73.0	8.3	71.6	63.4	10.4	75.2	61.6	4.3
H	79.4	74.3	10.0	69.9	60.2	9.0	67.4	57.6	5.5

Values are averages of three specimens.

Taguchi Experiment Test Results

Figure 8 shows the eight completed test rings. Nine tensile test specimens, consisting of one circumferential, one axial and one radial specimen at three locations, were machined from each ring. For the three radial specimens, one was located at the top, center and bottom of the ring cross-section. The same top, center and bottom locations were used for the circumferential specimens. The axial specimens were located at the outer surface, middle and inner surface of the ring cross-section. Tensile test results for the eight rings are shown in Table 3.

Evaluation of Test Data

In addition to the forging quality (geometry, laps, cracks, grain structure, etc.)

there are nine strength related quality characteristics (F_{tu} , F_{ty} and elongation in three directions). All of these rolled ring forging quality characteristics were evaluated and used to help select forging parameter values for the confirmation rings. The L8 Taguchi experiment response tables for two of the more critical characteristics, radial tensile strength, F_{tu} , and radial elongation, e , are shown in Tables 4 and 5.

As can be seen from the response tables, although none of the effects were large, wall thickness was the dominant parameters for tensile strength and elongation in the radial direction.

Table 4. X2096 rolled ring forging radial f_{tu} response table.

Rolled Ring Forging Identification	Standard Order Trial Number	Response Observed Values - y	A DIAMETER GROWTH RATE (in./in./sec.)		B ROLLING TEMP RANGE (F)		AXB		C WALL THICKNESS (Inches)		AXC		BXC		AXBXC	
			.2	.4	800 650	900 750			2.5	1.5						
			1	2	1	2	1	2	1	2	1	2	1	2	1	2
H	1	67.64	67.64		67.64		67.64		67.64		67.64		67.64		67.64	
G	2	75.22	75.22		75.22		75.22		75.22		75.22		75.22		75.22	
F	3	68.96	68.96		68.96		68.96		68.96		68.96		68.96		68.96	
E	4	73.50	73.50		73.50		73.50		73.50		73.50		73.50		73.50	
D	5	70.68		70.68	70.68		70.68		70.68		70.68		70.68		70.68	
C	6	76.60		76.60	76.60		76.60		76.60		76.60		76.60		76.60	
B	7	69.04		69.04	69.04	69.04		69.04			69.04		69.04		69.04	
A	8	73.88		73.88	73.88	73.88		73.88	73.88		73.88		73.88		73.88	
TOTAL		575.52	285.32	290.20	290.14	285.38	285.78	289.74	276.32	299.20	287.08	288.44	285.70	289.82	285.78	288.74
NUMBER OF VALUES		8	4	4	4	4	4	4	4	4	4	4	4	4	4	4
AVERAGE		71.94	71.33	72.55	72.54	71.35	71.45	72.44	69.08	74.08	71.77	72.11	71.43	72.46	71.70	72.19
EFFECT			+1.22	-1.19			+0.99		+5.72		+0.34		+1.03		+0.49	

Average of three values taken from each ring from locations 120° apart

Table 5. X2096 rolled ring forging radial elongation response table.

Rolled Ring Forging Identification	Standard Order Trial Number	Response Observed Values - y	A DIAMETER GROWTH RATE (in./in./sec.)		B ROLLING TEMP RANGE (F)		AXB		C WALL THICKNESS (inches)		AXC		BXC		AXBXC	
			.2	.4	800	900			2.5	1.5						
			1	2	1	2	1	2	1	2	1	2	1	2	1	2
H	1	5.53	5.53		5.53		5.53		5.53		5.53		5.53		5.53	
G	2	4.33	4.33		4.33		4.33		4.33		4.33		4.33		4.33	
F	3	3.1	3.1			3.1		3.1	3.1		3.1			3.1		3.1
E	4	3.67	3.67			3.67		3.67		3.67		3.67	3.67		3.67	
D	5	3.1		3.1	3.1			3.1	3.1			3.1	3.1			3.1
C	6	2.0		2.0	2.0			2.0		2.0	2.0			2.0	2.0	
B	7	5.5		5.5		5.5	5.5		5.5			5.5		5.5	5.5	
A	8	4.0		4.0		4.0	4.0			4.0	4.0		4.0			4.0
TOTAL		31.23	16.63	14.60	14.95	16.27	19.36	11.87	17.23	14.00	14.63	16.60	16.30	14.93	16.70	14.53
NUMBER OF VALUES		8	4	4	4	4	4	4	4	4	4	4	4	4	4	4
AVERAGE		3.90	4.16	3.65	3.74	4.07	4.84	2.97	4.31	3.5	3.66	4.15	4.08	3.73	4.18	3.63
EFFECT			-0.51		+0.33		-1.87		-0.81		+0.49		-0.35		-0.55	

Average of three values taken from each ring from locations 120° apart

VII. X2096 Rolled Ring Forging Process Confirmation Rings

Using the same ingot conversion, back extrusion and ring rolling processes used for the initial eight test rings, two rings approximately 46.5 inches in diameter were fabricated using the following nominal rolled ring forging parameters:

Forging temperature - 825-650F
Radial growth rate - 0.2 in/sec
Ring wall thickness - 3.0 in

One of the two rings included a secondary saddling operation after back extrusion and prior to ring rolling. In the saddling operation, the back extrusion was heated to forging temperature (900F) and incrementally forged from the back extrusion diameter of 28 in to a diameter of 32.2 inches. The 32.2 inch diameter saddled preform was then ring rolled to the final diameter of 46.5 inches. This saddled ring was used to evaluate potential improvements in radial (through thickness) strength and toughness due to additional radial hot working during the saddling operation.

The two confirmation rings were solution heat treated, stretched and artificially aged to the -T8 condition. Test evaluation is currently in work.

VIII. Concluding Remarks.

Based on this initial evaluation, X2096 rolled ring forgings offer a low cost, low risk approach for reducing weight of existing aluminum interface rings on Centaur and other high performance launch vehicle systems. X2096 rolled ring forgings were successfully fabricated using a range of forging parameters. Preliminary X2096 rolled ring forging tensile strength and elongation are equal to or greater than 2124 plate and 2219 and 7075 forgings currently used for adapter end rings.

Prior to production implementation, additional testing and evaluation of X2096 rolled ring forgings is needed to develop design allowables for the full range of production ring geometries (diameters and thicknesses).

X2096 Aluminum-Lithium Rolled Ring Forging Development
J.E. Dyer

Q: Mack Roberts (Martin Marietta) Why did you select the 2096 alloy?

A: Good question. These are non tank applications this is an area where we are tying into adaptive structures. One of the primary drivers for weight savings which we are after here is density. In most cases the specific strength, specific stiffness for these applications is very important and what we found was that for these applications the weight savings for this particular alloy even though strength is down a bit from the 2195 the density is also significantly down. It was a better choice in terms of weight saving compared to 2195.

Q: There is no welding involved?

A: No welding at all. All mechanically attached so that it is really looking at it purely from here is the geometry, here is the loads, which one is structurally more efficient? We could have made it out of several alloys. The thing we were looking for is something that could be done in thick sections both which 2195 and 2096 can do that. And it just turned out that this alloy did have a fairly significant weight advantage for this application over 2195.

Q: Do you see any unsolved problems for this alloy for this application?

A: Not at this point. I might mention I left one chart out which I see I left out in terms of where we are at. We anticipate this IR and D program to be completed next month. Finish the evaluation of the confirmation rings. We have a contract to implement these rings on adapter structures on Centaur, it is a NASA contract, for some modification program, it IELV. We are in the process of putting together a allowables program to roll fabricate a large series of rings and do a very detail allowables program for this material for that application. As of right now we see no showstoppers but you know how it is.

Q: But everything looks ok?

A: We have some things we are trying to understand in the confirmation rings we saw some interesting, how should I put it, some variations on a couple of areas in the confirmation rings that we are trying to understand and we think it is a aging issue rather than a material issue at this point in time, but that is part of the evaluation we are trying to rap up by the end of the month.

Q: I notice on your experiment with very small process limits, did you try to confirm those ranges?

A: We talked about that, what we tried to do was use our knowledge from all of our previous experience including the work that had been done at Reynolds to set parameter limits that were either in the range of what the forger could produce or that we already knew were established limits. If we already knew we had gone beyond this limit we could create a bad problem. We did not arbitrarily go force it out so what we tried to do is within the limits that we felt were the outer bounds of reasonable numbers we tested. There is no logic that says we should go any wider than that because we already had preexisting material that said that was dumb. So that would just be a waste of a run.

Q: Have you done any trade studies on the weight savings?

A: On this particular case we do have some trade studies looking at the weight settings. I do not remember the pounds of it typically we are looking at maybe 8 percent weight savings.

Q: What is used currently?

A: We make rings out of three different materials currently in one case we machine it out of 2124 plate and then we make some rings out of 7075 ring forgings and 2219 ring forgings so this material what we are trying to do is replace all 3 of those materials with this aluminum lithium alloy.

Q: Can 2195 replace them strength wise?

A: Modulus and obviously specific strength you do because the density is quite a bit lower, that is one of the things we are doing with the allowables program. If you see the range of parameters we saw here one of the obvious things we need to do before we complete our design and production is to do a much more intensive evaluation of properties. We are gathering a statistical base of properties for these rings and once we have done we will have to set our spec allowables. But we are anticipating on after everything we have seen right now that as a minimum we will be as good as the 2124 plate properties, which are the highest of the 3 we have talked about.

Q: Typically the ring structures are very low stress and high stiffness?

A: And obviously there is a big specific stiffness gain over any of those alloys so even for a gage for gage you could actually cut gages down based on stiffness driven as long as you meet the local strength properties.

FORMING OF ALUMINUM-LITHIUM & HIGH ASPECT RATIO ORTHOGRID PANELS

Benny F. Graham

National Aeronautics and Space Administration/MSFC
Marshall Space Flight Center, AL 35812

Abstract

Recent advances in Aluminum - Lithium alloys have made them more attractive for potential use in cryogenic tank applications such as the Space Shuttle External Tank, as a weight saving enhancement. With strength to weight ratios becoming more critical, complex lightweight rib-stiffened structural forms of this alloy will require advances in forming techniques in order to ensure both structural integrity and cost effective producibility. As a result, advanced forming and manufacturing methods have to be developed in order to use these alloys effectively.

I. Introduction

In the past, waffle (isogrid or orthogrid) construction, has been machined flat and subsequently formed¹. Compound curved parts with shallow ribs are usually chemically milled. Traditional methods of shaping light - weight, stiffened structural components made from aluminum have been "bump" (brake) forming on a hydraulic press brake, and high temperature restraint "age" forming. In general, integral structures deep enough to be structurally competitive with built-up structure has been applied only to simple flat or singly curved shapes - flat elements, cylinders, cones and the slightly curved surfaces such as wings or control surfaces for aircraft.

In the aerospace industry, integral construction usually means machining. Intricate shapes are most economically produced by casting, but their mechanical properties are not competitive with those of wrought material. The mechanical properties of forgings are usually the best obtainable, but the classical forging process alone will not deliver the close tolerances and thin stiffening ribs required for weight effective structures. This is particularly true for very large structural components in the sizes necessary for achievement of economy which also combine enough structural features to be classified as "integral". Near-net-shape forging technology is

promising, but not mature enough to be considered for this application. Forgings require finish machining, so machining limitations are an important consideration in the design of integrally stiffened structures.

II. Forming Process Candidates

Due to the geometric complexity of orthogrid structures, the forming processes considered suitable for orthogrid design barrel panels were *bump*, *roll*, and *age* forming.

Bump forming is the process of bending by deflection when a mechanical or hydraulic ram is used to deflect a part or component supported between two points. (Figure 1)

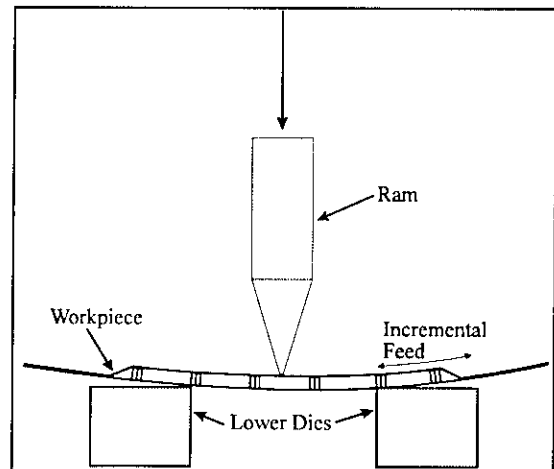


Figure 1. Bump Forming

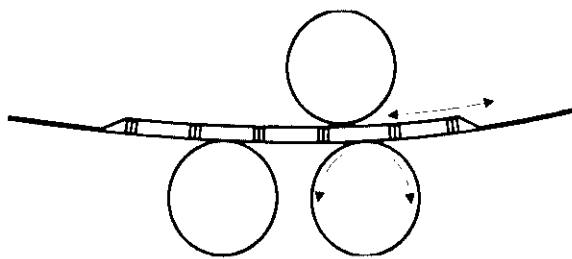


Figure 2. Roll Forming

Roll forming (or three roll bending) is the process of bending a sheet, bar or shaped section between two or three adjustable cylinders. (Figure 2)

Age forming is the process of bending by restraining a component to a predetermined shape, while using high temperature to lower the yield point of the material for attaining permanent deformation.

Since the Space Shuttle External Tank is constructed from "barrel" sections made from segments, Roll forming was thought to be equivalent to bump forming and could possibly result in reduced manufacturing labor costs. Preliminary results from both *roll* and *bump* forming at MSFC are promising, but more development is needed to quantify results and evaluate factors such as curvature and radial surface conformity, stiffening geometry, process economics, and process availability for production quantities. *Age forming* is also a process which will likely be part of the final processing sequence, in order to meet dimensional requirements for manufacturing.

Ongoing efforts are concentrated on age forming development to identify the most effective processing sequence to achieve acceptable panels for cryogenic tankage and other applications.

III. Development Approach

The first forming activity on an orthogrid panel was performed as an effort to evaluate and demonstrate the orthogrid design for structural use on the current STS External Tank as a weight reduction enhancement. Forming development was initiated after a subscale 2195 Aluminum-Lithium test panel experienced rib buckling during bump forming. Since this panel incorporated multiple pocket geometries (and rib heights), buckling was likely

caused when a pliable spacer material on the shorter ribs deformed, resulting in concentrated forming loads on the taller ribs. Also, the design concept and geometry could be evaluated on less expensive and readily available 2219 Aluminum on available equipment.

Forming process development began by machining subscale 48 inch x 48 inch orthogrid panels and forming to ET radius by traditional bump and roll forming techniques. Since rib buckling during forming was a function of geometry rather than material properties², 2219 Aluminum was used because it was relatively inexpensive, readily available, and its physical characteristics were well known.

A technology survey of aerospace manufacturers showed that bump forming was the most familiar process used in the past for forming this type of structure, however roll forming was seen potentially as a simpler forming process which might provide an economic benefit in labor cost savings.

Age forming was also considered as a potential process although this technology was not as simple as bump or roll forming, because it required tooling to be developed. Age forming was anticipated to possibly be needed as a final step for both the bump or roll forming processes in order to meet final dimensional tolerance requirements for longitudinal weld land straightness, circumferential weld land contour, and surface curvature conformity. The primary forming processes investigated are described below.

IV. Roll Forming

Roll forming tests have been conducted at both at Marshall Space Flight Center (MSFC) in Huntsville, AL and at the Michoud Assembly Facility (MAF) in New Orleans, LA where the STS External Tank is manufactured. Three roll forming methods have been used in order to produce a panel formed to a 165.5 inch radius. These methods were: roll forming without a protective cover plate, roll forming with a protective cover plate, and roll forming with a protective cover plate with extensions.

Results varied between methods, and are described as follows.

A. Without a Protective Cover Plate

A 48 inch panel was rolled without a cover plate to a 165.5 inch radius. This produced a uniform contour. One problem that occurred was deformation of the circumferential ribs where they contacted the upper bend roll. Due to the concentrated load applied to the ribs by the upper roller during roll forming, the rib tops were flared, or coined. The longitudinal ribs were unaffected. The flaring had the effect of widening the rib tops by approximately 0.020 inch over an undeformed rib, making the method unacceptable due to the uncertainty of structural integrity and operational concerns. Lead-in and lead-out flats were also produced due to the panel length required to engage the rollers. The flats were approximately 6 inches on each end of the panel for the roll press used at MSFC.

B. With a Protective Cover Plate

A protective cover plate assembly was devised and fabricated for use in roll/bump forming. This consisted of a 0.190 inch thick plate of 6061-T6 aluminum which covered the top (rib side) of the panel during forming. This provided a means of distributing the load during forming, which reduced point loading on the circumferential ribs. Spacers were attached to the cover sheet on the circumferential edges, where the stiffening ribs do not extend to the edges. This filled in the space between the cover sheet and the circumferential weld land surface, enabling the weld lands to be directly formed rather than being formed by loads transferred from the stiffening ribs and skin in the rib area. The use of the cover plate reduced rib flaring to acceptable levels. The maximum recorded flaring was on the order of .002 inch. Lead-in/lead-out flats were still about 6 in. for the 48 inch panels formed. The cover plate was re-usable and was rolled flat between uses.

C. With a Protective Cover Plate and Extensions

In an attempt to eliminate lead-in/lead-out flats, a cover/extension assembly consisting of both a top and bottom cover plate, circumferential weld land spacers, and lead-in and lead-out extensions between the cover plates was fabricated. One 48 inch panel was roll - formed using this method. While flats were eliminated, the cover/extension was extremely cumbersome. Having the panel sandwiched between covers prevented any contour measurements between roll passes and was considered impractical for high production rates on large panels.

V. Bump Forming

Bump forming was investigated because of its wide use in current forming practices. Panel sizes of 48 inch x 48 inch (sub-scale) and 132 inch x 180 inch (full scale) have been bump formed at MSFC and MAF, respectively. Three different bump forming methods have been used to produce a panel formed to a 165.5 inch radius. These were, bump forming on the ribs with no protective cover plate, bump forming on the rib nodes (intersections) with no protective cover plate, and bump forming using a protective cover plate.

A. On Ribs, Without a Protective Cover Plate

The 2219 panel was fed through the press on 1/4 inch increments. A sufficiently uniform radius was produced, however, bumping directly on the transverse ribs produced unacceptable deformation of the ribs. This was the same type of deformation experienced in rolling directly on the ribs, but rather than a uniform deformation, as in rolling, the ribs were deformed at each bump location only. The flaring was, again, on the order of approximately .020 inch. The ribs were flared or coined due to the concentrated load induced on the thin rib tops. As in rolling, the longitudinal ribs were unaffected. This method would be unacceptable for producing flight hardware.

B. On Rib Nodes Without a Protective Cover Plate

This method required bump forming at 5.416 inch intervals (the rib spacing in the formed direction). This method caused no deformation to the ribs, but it produced a radius that was composed of a series of flats, due to the large intervals. Additional forming operations, via aging or some other method, would be required in order to produce uniformly radiused circumferential weld lands of uniform radius and minimize welding mis-match. Since other panel designs have grid sizes as high as 10.832 inch, this method would require tooling for a secondary forming process such as *age* forming to form the pockets of the panels, and was considered uneconomical.

C. Bump Forming With a Cover Plate

A panel was bump formed using a protective cover plate, and was the same as the configuration used for roll forming with a protective cover plate. This enabled bump forming on small increments and prevented any damage to the ribs. A uniform contour was produced which was acceptable for flight hardware requirements. Lead-in/lead-out flats were a function of the die width and appeared to be small enough to minimize weld peaking. This method would be acceptable and practical for hardware production.

VI. Forming Process Comparison

The use of a protective cover plate produced the best results for both roll and bump forming. By using the cover plate, either forming process produced a formed panel with acceptable contour uniformity without damaging the panel stiffening ribs. Roll forming would likely require additional bump forming of the lead-in/lead-out flats, since a roll press large enough to form a 20 ft. long panel would likely have even larger diameter rolls than that used for the tests at MAF. This would produce even larger lead-in and lead-out flats, and would require the use of two machine set-ups in order to produce an acceptable panel. While bump forming is slower and would likely be more labor intensive, it would require the use of only one machine and set-up. This requirement would likely make bump forming a more attractive candidate for a production process.

VII. Age Forming

Age forming offers promise for manufacturing aerospace structural components such as waffle construction.³ One advantage is that contours can be controlled very precisely after the required surface for springback allowances is determined. This is possible due to the forming process taking advantage of reduced mechanical properties at elevated forming temperatures and the creep of grain boundaries to eliminate residual stresses. The only foreseen limitation may be that structures of the required size and deformation depth including springback allowances may require a "staged" or multi-step aging process. If this is the case, the final forming process to produce large barrel panels may include both a mechanical rough forming process, followed by age forming to heat treat, eliminating residual stresses, and removing out-of-tolerance curvatures. Age forming is currently under development and evaluation.

VIII. Curvature

There is one anomaly that has occurred in all bump and roll forming processes tested to date, that has to be addressed. This is the presence of curvature along the longitudinal weld lands after forming. The curvature of

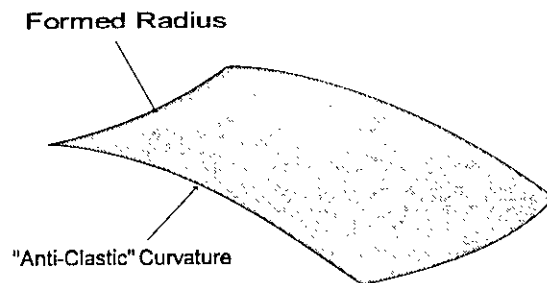


Figure 3. Curvature of Formed Panel

the longitudinal edges is the result of a contour variance along the length of the panel. For instance, a formed 48 inch panel was mapped to determine the effective radius along the length of the panel. The circumferential radius was measured to be 180 inch at one end, varied to 164 inch at mid-length, and was 173 inch at the other end. Thus the panel is slightly "pinched" in the middle, which induces curvature in

the longitudinal edges. This contour deviation is known as "anticlastic" curvature if the inner radius is less than the ends (Figure 3), and "synclastic" curvature when the inner radius is greater than the ends. This longitudinal edge straightness variation has been determined by measuring the arc height at the center of the longitudinal edge, i.e. chord height. Longitudinal edge straightness variation has been measured to be from .070 inch-.260 inch over the 48 inch panel length for panels roll and bump formed using a cover plate. The use of a cover plate with extensions increased curvature to .465 inch on a 48 inch panel, making this method even more undesirable.

The problem of longitudinal edge flatness variation has not been solved to date. Edge flatness deviation was reduced by 50% when three panels were restrained to a true 165.5 inch contour during ageing from T3 to T8. However, a fourth panel experienced only a 25% reduction, suggesting that the small amount of age-forming experienced could vary a great deal. Since it is undesirable to perform any forming operations on a panel after it is in the T8 condition, it is currently thought best not to rely solely on age-forming corrections to edge flatness deviation due to the possible variability of the process. Two alternative methods to reduce/eliminate edge flatness deviation will be investigated in the near term.

A. Elimination of anticlastic curvature by age forming

The first method which could eliminate the edge flatness deviation is an alternate forming method, age forming. Age forming involves taking a flat, unformed, panel and pulling it to contour and restraining it during the ageing process from T3 to T8. This process is currently used in many aerospace forming operations and has a reputation for being repeatable. Longitudinal edge flatness deviation may be eliminated when using this process. Since the panel will spring out when it is released after ageing, springback characteristics will have to be developed in order to determine the proper radius to over form to during ageing so that the panel will spring out to the proper radius. Also, since the ribbed areas possess different springback characteristics than the thicker weld land areas, age form tooling will probably require a compound radiused surface for each panel design configuration.

A potential problem could be panel rib buckling at the tighter radius required during ageing. The current rib height-to-width ratio, or aspect ratio, was determined to be reliably stable at roll or bump forming to a 165.5 inch radius at room temperature, but may not be at a significantly tighter radius and at ageing temperatures..

B. Elimination of anticlastic curvature by compound forming

Another potential method for eliminating edge flatness deviation is the use of shims during bump forming. In this process a panel would be bump formed using a cover sheet as before, but shims would be used to vary the deflection induced along the length of the panel. The effect would be to "over" form the circumferential ends and "under" form the center as the panel is fed through the press, effecting a smaller forming radius on each end varying to a larger forming radius in the center, hopefully yielding a uniform panel with straight longitudinal edges after springback. Again, mechanical springback characteristics of the panel would be required in order to determine the proper amount of overforming. Once this is determined, a tapered punch and die could be machined and used for this purpose.

IX. Conclusions

Forming results to date indicate that Aluminum - Lithium orthogrid stiffened structural panels can be successfully formed. Although the problems of anticlastic curvature and edge flatness have not been eliminated, there are several options available and either one or a combination of these methods should prove to be a solution to these problems.

The most practical method for eliminating both edge flatness and anticlastic curvature would seem to be bump forming the edges and the panel interior with specially contoured brake forming dies. In the case that this solution is unsuccessful, age forming is a probable solution to these problems, and could be successful in forming to final contour in a single operation. Age forming development is currently in progress, but is yet to be qualified as the primary forming process for the Super Lightweight Tank barrel panels.

X. Acknowledgements

The author wishes to acknowledge the support of Gene Golden of Martin Marietta Manned Space Systems for his assistance in preparing this paper.

XI. References

1. McDonnell-Douglas Astronautics Co., "Isogrid Design Handbook", NASA CR 124075, 1973
2. H Taketani, C. F. Pittinato, M. J. Rafanelli, R. Y. Chao., McDonnell-Douglas Astronautics Co., "Brake Forming of Integrally Stiffened Aluminum Isogrid Panels", unpublished work, circa 1987.
3. H. Brewer, "Age Forming Integrally Stiffened, Aluminum Aerospace Structures in an Autoclave", AIAA 89-2087, Textron Aerostructures / Nashville, TENN,

Discussion Session

Q: Unknown(Martin Marietta) What did you use the top material for?

A: For protecting the tops of the ribs. The first one was 0.190 inch thick 6061 Aluminum.

Q: What heat treatment?

A: T6, I believe.

Q: Bob DiTolla - In your process, did you have any type of analytical simulation and if you did, can you briefly describe it, and if not, would you like one?

A: No, we do not have one. Depending on the cost we would like one.

Q: On your brake forming, do you break form it in the T3 or T8 temper?

A: T3.

Q: Will the edges be acceptable for welding? (regarding the edge flatness deviation)

A: No. We feel like it can be implemented. We

can use compound dies if we have to on either bump or roll forming to overform the edges. We think that it will take out the curvature in the weld land area. Also, we think we can remove it by age forming as a secondary process, but that is going to require compound surfaces on your age forming tooling dies. But you can get there. The only problem (with age forming) is that there are so many different configurations of panels (on SLWT) now that you may have to develop several different sets of dies (with compound curvature) to get springback contour on each of the different configurations.

Q: Do you think, that would lead to production problems, with all the dies?

A: That is why we think bump forming is best, and then use shims or overform the edges. We think that if we can do that, and may be bump form the lead in/lead out flats, so that we will not have that much of a problem when we do age them. Textron is planning to put 6 panels in a furnace at a time, if they (Textron) age form them as the primary forming process.

Forming of Aluminum-Lithium & High Aspect Ratio Orthogrid Panels
B. Graham

- Q: Unknown (Martin Marietta) What did you use the top material for?
- A: No it is just protecting the tops of the ribs, the first one we used I think a 0.190 inch thick 6061 aluminum.
- Q: What heat treat?
- A: T6, I believe.
- Q: Bob DiTolla - In your processes did you have any type of analytical stimulation and if you do can you briefly describe it and if you do not would you like one?
- A: Depending on the cost we would like one. No we do not have one.
- Q: On your break forming, do you break form it at T3 or T8?
- A: T3
- Q: Will the edges be acceptable for welding?
- A: No we feel like it can be implemented we can use compound dies if we have to on either bulk or rolled to overform towards the edges we think that will take out the curvature in the weld land area. Also we think we can remove it age forming as a secondary process, that is going to require compounded surfaces on your age forming tooling dies. But you can get there. The only problem is there is so many different configurations of panels now that you may have to develop several different sets of dies to get spring back contour on each of the different configurations.
- Q: Do you think that would lead to production problems with all the dies?
- A: That is why we think that bulk forming is best and going to the shims or overforming on the edges. We think that if we can do that and maybe even do some bulk forming on the lead in lead out flats that we will not have that much problem we do when we age them. Textrons are planning to put 6 pounds at a time if they aged them as the primary process.

NET SHAPE SPINFORMED ALUMINUM-LITHIUM BULKHEADS FOR CRYOGENIC LAUNCH VEHICLE PROPELLANT TANKS

D. B. Sisk¹, E. Sperlich²,
¹Advanced Systems and Technology
Martin Marietta Astronautics
Huntsville, AL 35806
²Zeppelin Technologie
Friedrichshafen, Germany

Abstract

Martin Marietta Astronautics (MMA) has performed studies over the last several years to identify the materials, manufacturing processes and designs for a future cost-optimized expendable launch vehicle. These studies recommend the use of aluminum-lithium for structural components including the propellant tanks and adapters. Among the various aluminum-lithium alloys a weldable Al-Cu-Li-Mg-Ag variant known as 2195 is the leading candidate for use in cryogenic propellant tanks. The 2195 alloy offers a 30% increase in strength, 5% increase in elastic modulus and a 5% reduction in density compared with the conventional 2219 alloy it replaces. However, due to the cost of lithium and the need for special casting and processing techniques 2195 is roughly five times more expensive than 2219. This increase in raw material cost has fueled the development of "net shape" manufacturing technologies for launch vehicle structural components. Net shape technologies refer to a class of manufacturing methods that use precisely controlled metal flow to form integral features or thickness changes in a part as opposed to the more conventional approach that relies on metal removal. This paper summarizes development of net shape spin formed launch vehicle propellant tank bulkheads using the 2195 aluminum-lithium alloy performed by the team of Martin Marietta Astronautics (MMA) and Zeppelin Technologie.

The MMA/Zeppelin net shape spin forming development program began in 1992. This program is divided into two phases. Phase One, which has been completed, involved welding development, spin forming process optimization, heat treatment optimization and mechanical properties testing. All of the Phase One activities were performed on subscale, 1000-mm-diameter, domes with membrane

thicknesses ranging from 1.27 mm to 3.12 mm. The objective of Phase One was to develop and optimize all critical aspects of net shape spin forming for 2195 aluminum-lithium on a subscale level.

In Phase Two, which is partially completed, the optimized processing parameters are being used to produce four 4.3 meter diameter net shape spin formed domes. Two of these domes will be incorporated into an advanced technology liquid hydrogen tank under development at Martin Marietta. The objective of Phase Two is to demonstrate scalability of 2195 aluminum-lithium net shape spin forming to sizes of practical significance to the launch vehicle industry.

Based upon the Phase One results there are no significant technical concerns with net shape spin forming of 2195 aluminum-lithium. Outstanding tolerance control of ± 0.15 mm on the membrane thicknesses was consistently achieved in the finished dome. Mechanical properties tests were performed on several of the 1000-mm-diameter domes that had been heat treated, quenched, stretched and artificially aged to the T8 temper. The minimum observed ultimate strength was 527 MPa (Rm) in the parent material and 513 MPa (Rm) in the welds. Fracture toughness tests were attempted using small edge notch specimens taken from the 1000-mm-diameter domes. However, the severe double curvature of the specimens introduced unacceptable variations in the fracture toughness values. One of the most significant achievements of the program was the development of welding techniques capable of producing a weld that would survive the severe deformation of spin forming. Welding of the starting blank from two pieces is necessary for domes with a diameter greater than 3.7 meters due to plate width limitations from the aluminum mills.

I. Introduction

Application

The existing fleet of launch vehicles were designed for maximum performance. In contrast, a future vehicle will be designed to minimize system cost. Martin Marietta has performed studies over the last several years to identify designs, materials, and processes that significantly reduce the cost of launch vehicle propellant tanks and non-pressurized adapter structures. Our goal is a 50% reduction below current industry standards. We believe that the net shape spin forming process will help us to achieve or exceed this goal.

Net shape spin forming is primarily of interest to the aerospace industry for production of propellant tank end domes. Figure 1 shows the Martin Marietta Titan/Centaur launch vehicle highlighting its eleven propellant tank domes.

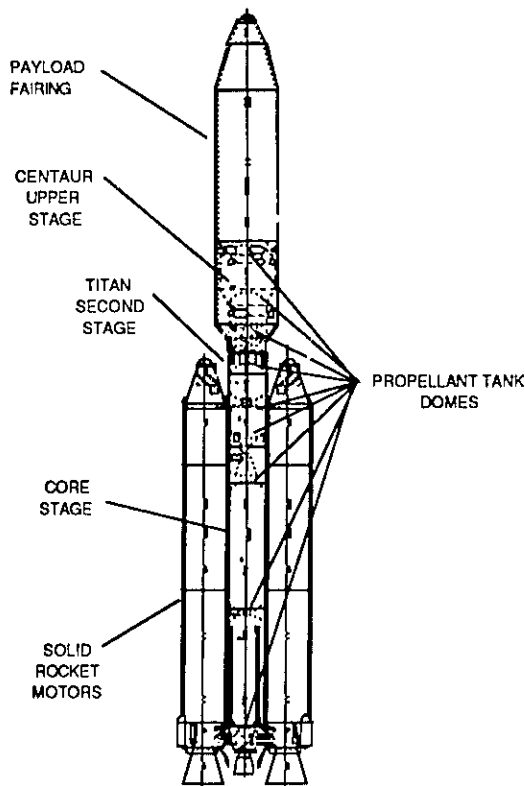


Figure 1. Net shape spin forming will be used to produce propellant tank domes for future versions of our proven Atlas, Centaur and Titan vehicles.

Process Description

Net shape spin forming is a process capable of producing large single piece parts with an axisymmetric inner contour but a non-axisymmetric thickness distribution without the need for post forming mechanical or chemical milling. This manufacturing technique is applicable to a variety of materials including high performance aluminum and aluminum-lithium alloys.

The net shape spin forming process begins with a round, flat blank of plate material, slightly larger in diameter than the finished dome. A dome up to 3.7 meters in diameter can be net shape spin formed using a single, continuous piece of material. As previously stated, over this diameter, plate width limitations from the aluminum mills necessitate welding of multiple plates for the starting blank.

Prior to forming, the starting blank is conventionally machined to close tolerance pre-spinning thicknesses. During this operation axisymmetric and non-axisymmetric thickness buildups are machined into the blank to accommodate weld lands and penetrations in the final product. After inspection, the outer edge of the machined blank is then clamped to the head stock of a conventional spinning lathe. An illustration of the spin forming set-up is presented in Figure 2.

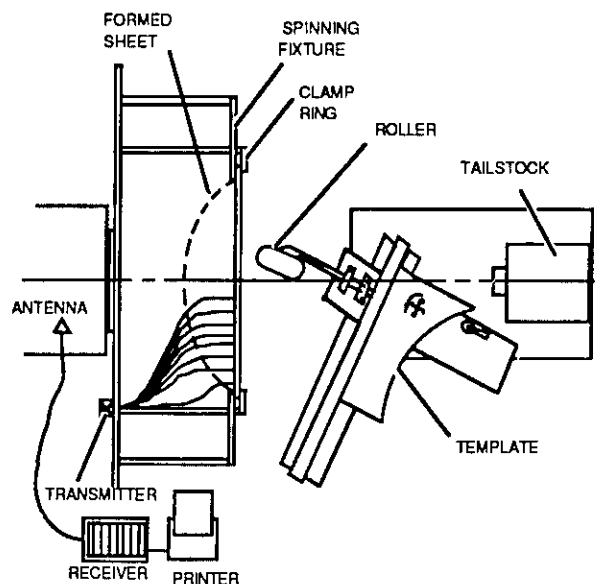


Figure 2. Spin forming equipment.

Forming of the dome is accomplished by a single roller pressing against the inside surface of the rotating blank while simultaneously moving back and forth along the dome meridian.

Initial forming of the dome is accomplished at elevated temperatures in multiple steps. The path of the roller for each step is precisely controlled using a tracer template. Infrared heaters are used to heat the blank prior to spinning and maintain temperature during the spinning operations. A photo of the initial spin forming operations showing the infrared heaters is presented in Figure 3.

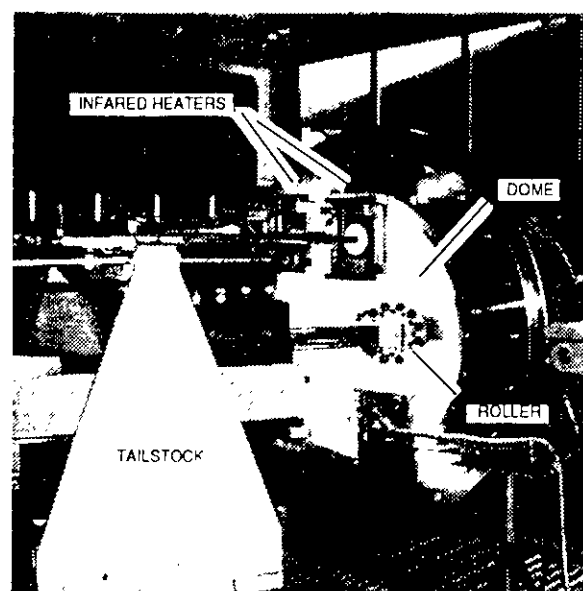


Figure 3. Net shape spin forming operations.

After the initial spin, the dome is solution heat treated and spray quenched. It is then loaded back onto the spinning lathe and formed at room temperature to the final contour. This second spinning operation sets the final contour and induces the necessary permanent stretch into the material to achieve the T8 temper upon subsequent artificial aging. The finished dome is trimmed, protected with a suitable corrosion inhibitor and then readied for next assembly.

Benefits

Conventionally produced propellant tank bulkheads are made from a welded assembly of stretch formed gores or with a non-net, thick plate spin

forming technique. Net shape spin forming is superior to either of these methods. Our cost studies indicate that the net shape spin forming process will reduce the cost to manufacture a comparable bulkhead by 30-45%. Cost savings of this magnitude are possible through the elimination of labor and inspection intensive welding operations, elimination of complex machining tools, and a significant reduction in raw material requirements. Net shape spin forming also eliminates the need for environmentally hazardous, chemical milling. A breakdown of these cost factors is presented in Figure 4.

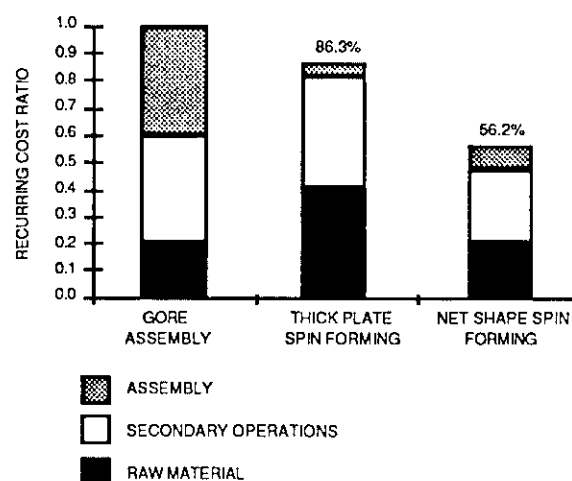


Figure 4. Bar chart for cost savings.

Program Need

In late 1991 and early 1992 Zeppelin Technologie of Germany and Martin Marietta performed a cooperative independent research and development (IRAD) program to demonstrate the feasibility for net shape spin forming 2195 aluminum-lithium. Under this cooperative IRAD two 600-mm-diameter domes were produced from 2.9-mm thick 2195 aluminum-lithium. The first dome was spin formed from a single sheet of material while the second was made from a welded assembly of two sheets. A photo of the welded 600-mm-diameter dome is shown in Figure 5.

The 600-mm-diameter dome development demonstrated feasibility to weld, spin form and heat treat 2195 aluminum-lithium using modified

techniques developed for other aluminum alloys. Mechanical properties testing indicated that the T8 temper was achievable in the parent material and perhaps most significantly that welds in the final dome had both high minimum strength (436 MPa) and reasonable elongation (>3%).

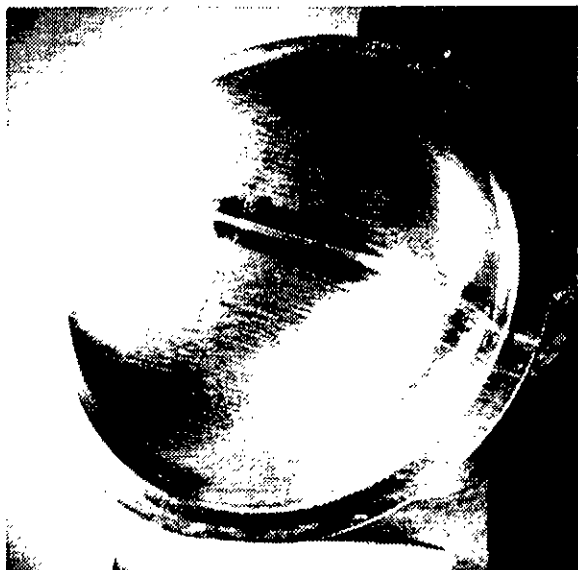


Figure 5. 600-mm-diameter feasibility demonstration article.

After demonstrating feasibility, a detailed investigation was needed to optimize the net shape spin forming process for 2195 aluminum-lithium and to address the critical issues of scaling to the large diameters predicted for future launch vehicles.

II. Phase One Program Overview

As previously stated, our net shape spin forming development program is divided into two phases. The top level objective of Phase One was to refine the entire net shape spin forming process for welded 2195 aluminum-lithium. The following paragraphs summarize the tasks performed during Phase One.

Spin Forming Development

Spin forming process parameters (roller diameter, lathe angular velocity, temperature, number and shape of the guide templates, etc.) were developed by forming six domes from constant thickness starting

blanks, three domes from variable thickness blanks and fourteen domes from welded starting blanks. To minimize raw material cost all Phase One spin forming development was accomplished on 1000-mm-diameter subscale domes.

Aging Optimization

A study was performed to identify the optimum aging practice to be applied to net shape spin formed domes. Samples were removed from one of the constant thickness domes which had been solution heat treated, quenched and cold stretched. Curves of hardness vs. aging time were developed for specimens aged at 143°C, 150°C and 155°C. From these curves, six time/temperature combinations corresponding to a peak aged and slightly under aged condition were selected for further study. Room temperature tensile and fracture toughness tests were performed on spin formed samples aged at each of the six aging time/temperature relationships. From these data, an aging practice with the best combination of strength and toughness was selected.

Welding Development

Welding process parameters were developed for the T0, T3 and T8 tempers of 2195 aluminum-lithium. Welding of the T0 temper is of interest in producing the starting blank. Welding of T3 and T8 were evaluated for next assembly of the door ring and y-ring to the net shape spin formed dome. The option exists to weld the y-ring and door rings prior to aging (T3) and after aging (T8). Both the Variable Polarity Gas Tungsten Arc (VPGTA) and Gas Tungsten Arc (GTA) processes were evaluated. All welds used 2319 as the filler alloy.

Mechanical Properties Testing

After spin forming and artificial aging process parameters had been established, mechanical properties tests were performed on spin formed dome samples to develop preliminary design values. Small "dog bone" tensile and edge notch fracture toughness specimens were cut from three meridians, corresponding to the longitudinal, lateral and 45° orientation in the original plate and two orientations, circumferential and meridional. Tests were performed at both room and LHe temperatures.

III. Phase One Results

Twenty domes were spin formed throughout Phase One to develop and optimize all aspects of the net shape spin forming process. Three additional domes were processed at the end of Phase One using the optimized parameters. A photo of one of these process confirmation domes is shown in Figure 6.



Figure 6. Sample process confirmation dome.

The following paragraphs summarize the typical characteristics of a net shape spin formed 2195 aluminum-lithium dome produced using the optimized Phase One parameters. The dimensional data came from the dome shown in Figure 6. Mechanical properties came from one of the other two confirmation domes which was destructively tested.

Forming degree

Forming degree is a measure of the amount of stretch induced during net shape spin forming. It is calculated using the equation:

$$\text{Forming Degree} = (\text{starting thk}/\text{final thk} - 1) \times 100$$

Forming degree is an important factor because it is used as a guide in selecting pre-spin forming thicknesses. The forming degree for the dome shown in Figure 6, taken along a meridian aligned 90° from the meridional weld land is shown in Figure 7. A forming degree as high as 81.3% was observed for

this dome. Elevated temperatures and a series of small forming steps allow for forming of this magnitude.

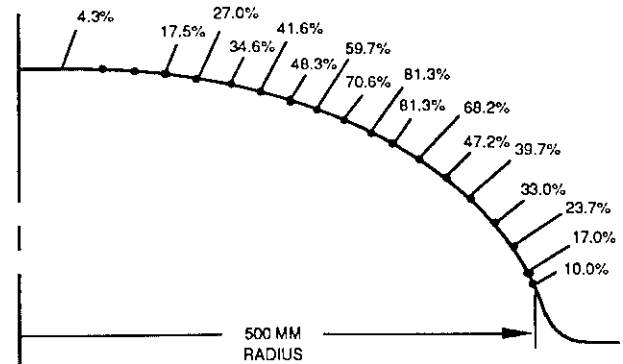


Figure 7. Forming degree.

Percent stretch

After solution heat treatment and quench the dome is stretched to the final contour by spin forming at room temperature. This stretching operation sets the contour and induces permanent strain, improving the final mechanical properties. The goal is to achieve 3-8% percent permanent strain during stretching. The percent stretch along the meridian 90° from the meridional weld seam is shown in Figure 8.

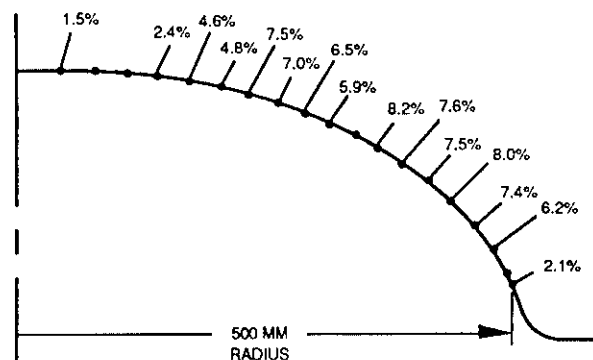


Figure 8. Percent stretch.

As can be seen in the figure we did not quite achieve the goal of 3% stretch in the apex and at the last point near the dome equator. Stretching at the equator can be corrected with minor template changes on the 4.3 meter domes. Stretching degree in the apex will be corrected by slightly raising the 4.3 meter diameter dome profile.

Contour Tolerances

Measurements of the dome after stretch were taken in the longitudinal and lateral directions to evaluate the accuracy of the contour versus the theoretical shape. The variance between the nominal and the as-produced shape measured along the meridian 90° to the weld seam is presented in Figure 9. Negative values indicate that the dome was not formed as deeply as required.

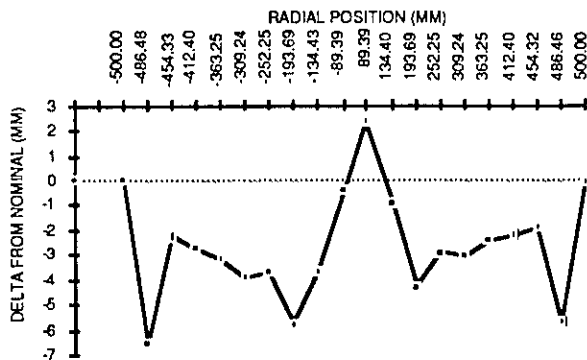


Figure 9. Contour tolerances.

As Figure 9 illustrates the greatest deviation from contour is seen in the equator and apex areas. The deviation near the equator is over a very short distance and is subject to a large uncertainty because we took vertical measurements on a steeply inclined surface. The deviation in the apex is another indicator of how difficult it is to balance the need for stretch after SHT&Q with contour requirements. At the apex the contour is higher than nominal, yet the degree of stretch was below the target 3% value (Figure 8).

Although the variance in the apex appears large at first glance it is not clear that values on this order of magnitude are a significant problem. We recommend, slightly raising the dome contour for the first 4.3-meter-diameter dome, taking detailed contour measurements similar to those shown in Figure 9 and then reevaluating whether to design for these contour tolerances or attempt further improvements through template and dome contour adjustments.

Thickness Tolerances

The membrane thickness tolerances, also measured along the meridian 90° from the weld seam,

are presented in Figure 10. These tolerances are consistent with our expectations.

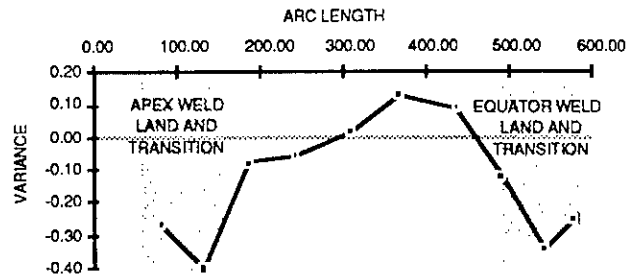


Figure 10. Thickness tolerances.

Strength

Figure 11 summarizes the room temperature ultimate strength of the welded 1000-mm-diameter domes as measured in three meridians and two orientations. Small dog bone specimens were used for the testing. The values shown represent typical values based on multiple specimens.

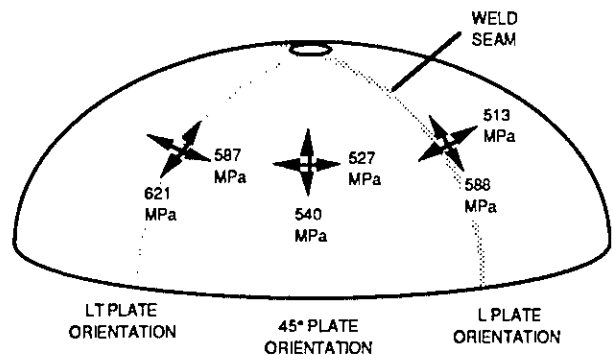


Figure 11. Mapping of room temperature strength.

There are several points that can be observed by studying the tensile strength data summarized in the figure.

The first point is that strength values in net shape spin formed 2195 material are as good as or better than those observed in 2195 RT70 plate. As with plate, the minimum values are associated with the 45° orientation.

The second observation is associated with stretch sensitivity. The net shape spin forming process induces approximately uniform biaxial strain during final stretching. As shown in Figure 11 the ultimate strength in what was the lateral (LT) direction in the original plate achieved 621 MPa. The

ultimate strength along the original longitudinal (L) direction of the plate achieved 588 MPa. These results lead us to conclude that a more significant increase in strength should be expected in the LT orientation when compared to the longitudinal given the same amount of permanent stretch after solution heat treatment.

The third observation regarding the tensile test data is associated with weld efficiency. For simplicity and due to uncertainty with the property variation, we will size a net shape spin formed dome based on minimum properties, in this case those in the 45° orientation. If we compare the 45° circumferential strength with that of the weld we see that we have a weld efficiency factor of nearly 97%. This is due to the fact that the weld undergoes a solution heat treatment, quench, stretch and artificial aging process. Even though we will likely use larger factors of safety on the welds to account for scatter and the influence of defects, this efficiency factor is quite attractive.

Fracture Toughness

Fracture toughness in the 1000-mm-diameter subscale domes was measured by using edge crack tension (ECT) specimens. These small rectangular specimens were selected because the effect of dome contour would be minimized.

Despite small specimen size, there was still a considerable amount of scatter associated with the curvature of the specimen. As a result, the ECT test data was of limited value. Further investigation of fracture properties for net shape spin formed 2195 are planned as a part of Phase Two. It is anticipated that the less severe curvature of the 4.3-meter domes will reduce the scatter in the fracture tests.

IV. Phase Two Program Overview

The objective of Phase Two is to demonstrate our ability to net shape spin form flight size and quality 2195 aluminum-lithium domes using the optimized processing parameters developed in Phase One. During this second phase, which is in progress, we are producing four 4.3-meter-diameter domes. The first dome is a "pathfinder" to prove out the complete net shape spin forming process at this

scale. After forming, the pathfinder will be thoroughly inspected for shape and thickness control and then destructively tested to evaluate final mechanical properties and residual stresses. The three remaining 4.3-meter domes will be flight quality articles. Two of the three will be included in a 4.3-meter-diameter prototype liquid hydrogen tank under joint development by Martin Marietta and NASA Marshall Space Flight Center.

V. Conclusions and Recommendations

1. Producing net shape spin formed domes for launch vehicle propellant tanks from 2195 aluminum-lithium continues to appear feasible based on accomplishments to date.
2. Mechanical properties of net shape spin formed 2195 domes should be as good as or better than those observed for plate material.
3. Tolerance and shape control will be comparable to current industry standards without the need for post form machining or chemical milling.
4. Weld quality during spin forming is the greatest area of technical risk due to severe forming of the weld. Defects present in the initial weld grow during the spinning process. Therefore welds with extremely high quality are required in the starting blank.
5. Although there are areas of risk still present, we believe we have learned all that is necessary at a subscale level and recommend proceeding with Phase Two.

Acknowledgments

This activity was funded under the Martin Marietta Astronautics Independent Research and Development (IRAD).

Net Shape Spinformed Aluminum Lithium Bulkheads for Cryogenic
Launch Vehicle Propellant Tanks
D. Sisk

- Q: Joe Pickens (Martin Marietta) - With your 45 degree properties as your weakest link, I guess you are welding together 2 wide pieces, If you have room on the mill you might want to try 45 degree cross rolling?
- A: It is an interesting idea and yes we would entertain it. Beyond that level of discussion we have not really thought about it that much.
- Q: J.P. - Based on the small scale.
- A: It is an interesting idea for bringing up those minimum strength properties. Of course a dome is strength driven whereas the previous discussion we were talking about rings which are all EI driven. So we are interested in bringing up the minimums as high as we can and the 45 appeared to be the area to concentrate. Good comment.
- Q: ? (Marshall) The contour you used, did it allow adequate stretch?
- A: The contour we used in all the subscale forming work was based on the full scale designs. We found that we could not get adequate stretch in the apex of the dome so in the final design we recountoured slightly. We updated our system level optimizations to determine what impact this contour change had on performance. It was very small.
- Q: ? - I was just curious as to whether a new contour would require some additional propellant slosh tests?
- A: Can't really answer that. We considered slosh and pull-through when we defined the contour. However, we do not really worry too much about slosh on the front dome because the propellant levels are so high and in a hydrogen tank because of the low fluid density there is very little concern about slosh. However, we are concerned about pull-through height. The lower dome contour was defined to balance the structural considerations of weight performance against the propulsion considerations like pull-through and residuals.
- Q: Have you seen any pore formation caused by your processing?
- A: We have done alot of microstructural work on the as-spun products and there really isn't any pore formation or cavitation as you might see with super plastic forming. This is not a stretching operation. Forming is actually accomplished by bending very locally around the roller. It is actually bending low cycle fatigue type of operation versus a gross stretching operation like you do in a stretch forming. And of course

you do have a compressive stress on the inside surface that is preventing pore formation and growth. You would be most concerned with the outside surface where it is free formed. But no we have not seen any cavitation in the material or additional pore formation.

**Attendance List for "The Aluminum-Lithium Alloys
for Aerospace Applications Workshop" May 17-19, 1994**

Raf Ahmed
NASA/MSFC
EH24
MSFC, AL 35812

Chris Barrett
NASA/MSFC
ED15
MSFC, AL 35812

Biliyar N. Bhat
NASA/MSFC
EH23
MSFC, AL 35812

Fred Bickley
NASA/MSFC
EE83
MSFC, AL 35812

Larry Foreman
NASA/MSFC
EH24
MSFC, AL 35812

Cynthia Frost
NASA/MSFC
PP02
MSFC, AL 35812

Nedra Hundley
NASA/MSFC
EE31
MSFC, AL 35812

Michael Karigan
NASA/MSFC
ED54
MSFC, AL 35812

Tina Malone
NASA/MSFC
EH24
MSFC, AL 35812

Preston McGill
NASA/MSFC
EH23
MSFC, AL 35812

Arthur C. Nunes, Jr.
NASA/MSFC
EH23
MSFC, AL 35812

R.J. Schwinghamer
NASA/MSFC
EEA01
MSFC, AL 35812

Janet Sisk
NASA/MSFC
ED24
MSFC, AL 35812

Davis Snoddy
NASA/MSFC
ED72
MSFC, AL 35812

Richard A. Smith
NASA/MSFC
ED51
MSFC, AL 35812

David Stone
NASA/Headquarters

Tim Vaughn
NASA/MSFC
EH43
MSFC, AL 35812

Marc Verhage
NASA/MSFC
ED72
MSFC, AL 35812

Douglas Wells
NASA/MSFC
EH23
MSFC, AL 35812

Ricky Wilbanks
NASA/MSFC
ED72
MSFC, AL 35812

Thomas Bales
NASA/LeRC
21000 Brookpark Rd.
Cleveland, OH 44135

Robert Bond
IIT Research Institute
Building 4618
MSFC, AL 35812

Po Chen
IIT Research Institute
Building 4618
MSFC, AL 35812

Susan Hessler
IIT Research Institute
Building 4618
MSFC, AL 35812

Bob Jacobs
IIT Research Institute
Building 4618
MSFC, AL 35812

Steve Jones
IIT Research Institute
Building 4618
MSFC, AL 35812

Binyak Panda
IIT Research Institute
Building 4618
MSFC, AL 35812

Jeff Sanders
IIT Research Institute
Building 4618
MSFC, AL 35812

James Thayer
IIT Research Institute
Building 4618
MSFC, AL 35812

Ed Vesely, Jr.
IIT Research Institute
Building 4618
MSFC, AL 35812

Mike Watwood
IIT Research Institute
Building 4618
MSFC, AL 35812

Kevin P. Armanie
ALCOA Technical Center
100 Technical Drive
Alcoa Center, PA 15069-0001

Pedro C. Bastias, Ph.D.
Vanderbilt University
P.O. Box 1592 - Station B
Nashville, TN 37205

Brett Boutwell
University of Alabama at Birmingham
Department of Material Science and Engineering
1150 Tenth Ave. South
BEC 360
Birmingham, AL 35294-4461

Alex Cho
Reynolds Metals Co.
P.O. Box 27003
Richmond, VA 23261

Roy Crooks
Naval Postgraduate School
ME/Cr
6699 Dryer Rd/Rm M5
Monterey, CA 93940

Robert DiTolla
General Dynamics - Space Systems
24-5190
P.O. Box 85990
San Diego, CA 92138

Ravinder M. Diwan
Southern University
Mechanical Engineering Dept.
Baton Rouge, LA 70813

Jack E. Dyer
General Dynamics - Space Systems
23-5360
P.O. Box 85990
San Diego, CA 92186-5990

Robert H. Grishom
American Aluminum/ALCOA Technical Center
100 Technical Drive
Alcoa Center, PA 15069-0001

I. Keith Hall
General Dynamics - Space Systems
23-5360
P.O. Box 85990
San Diego, CA 92186-5990

Joe Helmstetter
Technical Analysis Inc.
977 Explorer Blvd.
Huntsville, AL 35805

Alan K. Hopkins
University of Dayton Research Institute
0172
300 College Park Avenue
Dayton, OH 45469-0172

Kumar Jata
WL/MLS
2179 Twelfth Street
Suite 1
WPAFB, OH 4543*-771*

Mark Krutyholowa
Ashurst Corporation
Suite 840
1380 Lawrence St.
Denver, CO 80204

Timothy J. Langan
Martin Marietta Laboratories - Baltimore
1450 South Rolling Road
Baltimore, MD 21227

Eui W. Lee
Naval Air Warfare Center
Code 6063
Marmineter, PA 18974

Richard P. Martukanitz
The Pennsylvania State University
Applied Research Laboratory
P.O. Box 30
State College, PA 16904

John L. Mihelich
Commonwealth Aluminum Technologies
1200 Meidinger Tower
Louisville, KY 40202

Ray Miryekta
McDonnell Douglas Aerospace
A3-243-45-2
5301 Bolsa Ave.
Huntington Beach, CA 92647-2099

John Newman
ALCOA Technical Center
100 Technical Drive
Alcoa Center, PA 15069-0001

Dr. Joseph R. Pickens
Martin Marietta Laboratories - Baltimore
1450 South Rolling Road
Baltimore, MD 21227

Roberto Rioja
ALCOA Technical Center
100 Technical Drive
Alcoa Center, PA 15069-0001

Mack O. Roberts
Martin Marietta Astronautics
T330
P.O. Box 179
Denver, CO 80201

Mary J. Shiflet
University of Virginia - Thornton Hall
Materials Science & Engineering Dept.
School of Engineering & Applied Science
Charlottesville, CA 22903-2442

Jogender Singh
The Pennsylvania State University
Applied Research Laboratory
P.O. Box 30
State College, PA 16804

Dave B. Sisk
Martin Marietta
Suite 200
620 Discovery Dr.
Huntsville, AL 35806

Kamal K. Soni
University of Chicago
Enrico Fermi Institute
5640 South Ellis Avenue
Chicago, IL 60637

Edgar A. Starke, Jr.
University of Virginia - Thornton Hall
Materials Science & Engineering Dept.
School of Engineering & Applied Science
Charlottesville, CA 22903-2442

Scott Szogas
The Aerospace Corporation
M4/922
P.O. Box 92957
Los Angeles, CA 90009-2957

Attila Szabo
Martin Marietta Manned Space Systems
D-4642
P.O. Box 29304
New Orleans, LA 70189

Wm. Troy Tack
Ashurst Corporation
Denver Corp. Ctr., Tower III
7900 E. Union Ave., Suite 1100
Denver, CO 80237

Hideo (Tak) Taketani
McDonnell Douglas Aerospace West
A3-211 /T-50
5301 Bolsa Avenue
Huntington Beach, CA 92647

George E. Talia
The Wichita State University
Department of Mechanical Engineering
1845 Fairmont
Box 35
Wichita, KS 67260-0035

Ray Thompson
University of Alabama at Birmingham
Department of Material Science and Engineering
1150 Tenth Ave. South
BEC 360
Birmingham, AL 35294-4461

A.K. Vasudevan
Office of Naval Research
Code 332
800 N. Quincy St.
Arlington, VA 22217

F. Douglas Wall
University of Virginia
Department of Materials Science
Charlottesville, VA 22903-2442

Chung-Chu Wan
Aerospace Corporation
M2/242
P.O. Box 92957
Los Angeles, CA 90009

John R. Wooten
Rockwell International - Rocketdyne Division
IB15
P.O. Box 7922
6633 Canoga Park
Canoga Park, CA 91309-7922

Dr. Deborah Yaney
Lockheed Missiles and Space Co.
O/93-60 B/204 P/2
3251 Hanover St.
Palo Alto, CA 94304

AUTHOR INDEX

AUTHOR.....	PAGE
W. A. Baeslack, III.....	264,288
P. C. Bastias.....	205
C. G. Bennett.....	84
G. Bjorkman.....	229
C. P. Blankenship, Jr.	6
R. Bond.....	183
J. M. Chabala.....	95
A. Cho.....	17,322
R. Crooks.....	174
A. D. Dehbozorgi.....	322
R. Di Tolla.....	156
M. Diehm.....	205
R. M. Diwan.....	144
J. E. Dyer.....	309,322
P. S. Fielding.....	17
F. W. Gayle.....	57
B. F. Graham.....	334
R. E. Greene.....	17
G. T. Hahn.....	205
I. K. Hall.....	114,309,322
A. K. Hopkins.....	43
K. H. Hou.....	288
P. R. Howell.....	237
V. K. Jain.....	43
K. V. Jata.....	43
K.-Y. Kim.....	205
M. Kral.....	205
T. J. Langan.....	133
K. Lawless.....	216
R. Levi-Setti.....	95
W. Lin.....	264
J. C. Lippold.....	264,288
L. W. Locchell.....	216
K. G. Lysher.....	237
J. Maisano.....	57
T. Malone.....	144,183
B. Malone.....	194
R. P. Martukanitz.....	237
P. E. McCubbin.....	133
P. McGill.....	194
J. L. Mihelich.....	84
M. R. Mitchell.....	174

J. T. Morgan	43
I. Musulin.....	84
D. E. Newbury	95
A. C. Nunes, Jr.....	300
B. Panda.....	277
J. R. Pickens.....	57,133
M. A. Przystupa	26
M. O. Roberts	216
J. H. Sanders.....	277
E. F. Scholz.....	216
R. J. Schwinghammer	1
J. S. Sedlak.....	174
S. R. Shah	205
G. J. Shiflet	105
D. B. Sisk.....	114,309,341
M. H. Skillingberg.....	17
K. K. Soni.....	95
E. Sperlich.....	341
E. A. Starke, Jr.....	3,6
G. E. Stoner	122
E. D. Sweet.....	84
A. Szabo	174,264,288
W. T. Tack.....	57
H. Taketani	167
J. E. Talia.....	300
R. G. Thompson.....	246
P. D. Torres	144
A. K. Vasudevan	26
F. D. Wall.....	122
Z. M. Wang.....	105
M. Watwood.....	194
D. B. Williams.....	95
J. E. Wittig.....	205
D. Xia	264
D. L. Yaney.....	73

REPORT DOCUMENTATION PAGE			Form Approved OMB No. 0704-0188	
Public reporting burden for this collection of information is estimated to average 1 hour per response, including the time for reviewing instructions, searching existing data sources, gathering and maintaining the data needed, and completing and reviewing the collection of information. Send comments regarding this burden estimate or any other aspect of this collection of information, including suggestions for reducing this burden, to Washington Headquarters Services, Directorate for Information Operations and Reports, 1215 Jefferson Davis Highway, Suite 1204, Arlington, VA 22202-4302 and to the Office of Management and Budget, Paperwork Reduction Project (0704-0188), Washington, DC 20503				
1. AGENCY USE ONLY (Leave blank)	2. REPORT DATE December 1994	3. REPORT TYPE AND DATES COVERED Conference Publication		
4. TITLE AND SUBTITLE Aluminum-Lithium Alloys for Aerospace Applications Workshop			5. FUNDING NUMBERS	
6. AUTHOR(S) B.N. Bhat, T.T. Bales*, E.J. Vesely, Jr.**, Editors				
7. PERFORMING ORGANIZATION NAME(S) AND ADDRESS(ES) George C. Marshall Space Flight Center Marshall Space Flight Center, Alabama			8. PERFORMING ORGANIZATION REPORT NUMBER M-769	
9. SPONSORING/MONITORING AGENCY NAME(S) AND ADDRESS(ES) National Aeronautics and Space Administration Washington, DC 20546			10. SPONSORING/MONITORING AGENCY REPORT NUMBER NASA CP-3287	
11. SUPPLEMENTARY NOTES Proceedings of a workshop held at Marshall Space Flight Center during the conference on Earth-to-Orbit Propulsion Technology, May 17-19, 1994. *Langley Research Center, Hampton, VA. **IIT Research Institute, Huntsville, AL				
12a. DISTRIBUTION/AVAILABILITY STATEMENT Unclassified-Limited Distribution Subject Category 26			12b. DISTRIBUTION CODE	
13. ABSTRACT (Maximum 200 words) Aluminum-Lithium (Al-Li) alloys are the new generation of lightweight, high modulus alloys some of which also have high strength and high fracture toughness. These alloys offer high strength-to-weight ratios which make them attractive for aerospace applications. The purpose of the workshop was to disseminate to the propulsion community results emerging from government laboratories, industry and universities, actively engaged in research, development and testing of Al-Li alloys. In all, 32 papers were presented and discussed, covering a wide range of topics: Al-Li alloy development, processing, physical metallurgy, analytical techniques, mechanical properties, corrosion and stress corrosion cracking, texture and anisotropy, fracture toughness, welding and joining, and forming. Most of the workshop focused on the latest generation of Al-Li alloys, i.e., the high strength, Weldalite family of alloys, such as 2195 alloy that has been selected for fabricating the super lightweight external tank of the Space Shuttle. Presentations illustrated that 2195 alloy has good corrosion resistance, excellent fatigue properties, can be near net shape formed and, with proper precautions, can be adequately welded. However, further research is needed to optimize processing to ensure required combination of strength and toughness in the final product.				
14. SUBJECT TERMS Aluminum-Lithium (Al-Li) alloys, Super Lightweight Tank, Welding, Forming, Space Shuttle			15. NUMBER OF PAGES 363	
			16. PRICE CODE A16	
17. SECURITY CLASSIFICATION OF REPORT Unclassified	18. SECURITY CLASSIFICATION OF THIS PAGE Unclassified	19. SECURITY CLASSIFICATION OF ABSTRACT Unclassified	20. LIMITATION OF ABSTRACT	